The Dissertation Committee for Hamoud Ali Al-Anazi
certifies that this is the approved version of the following dissertation:

Experimental Measurements of Condensate Blocking and Treatments in Low and High Permeability Cores

Committee:

Mukul M. Sharma, Supervisor

Gary A. Pope, Co-Supervisor

Russell T. Johns

Steven L. Bryant

Isaac C. Sanchez

Experimental Measurements of Condensate Blocking and Treatments in Low and High Permeability Cores

by

Hamoud Ali Al-Anazi, BS, MSE

Dissertation

Presented to the Faculty of the Graduate School of
The University of Texas at Austin
in Partial Fulfillment
of the Requirements
for the Degree of

Doctor of Philosophy

The University of Texas at Austin
December 2003

Dedication

To my parents and family

Acknowledgements

I would like to thank my supervising professors: Dr. Mukul M. Sharma and Dr. Gary A. Pope for their continuous teaching, invaluable guidance, encouragement, and support. Their advice helped me to understand problems and provided insight to possible solutions. I really enjoyed working with them and will never forget the excellent work we accomplished.

I am grateful to Dr. Russell T. Johns, Dr. Steven L. Bryant, and Dr. Isaac C. Sanchez for serving on my dissertation committee. I would like to thank Dr. Bruce A. Rouse for his help and advise on the setup of the experiments. I appreciate the effort of Dr. Bob Metcalfe for his assistance in the design of the coreflood experiments and the plan to achieve the research tasks. Thanks to Esther Barrientes for help in administrative matters and purchasing, and Joanna Castillo for her assistance in computer programs and formatting the papers I published.

I would like to acknowledge Glen Baum for his efforts in helping me to set-up and calibrate the apparatus used in my research. I also thank Bob Savicki for his assistance in providing reservoir cores and safety guidance. I would like to acknowledge my company Saudi Arabian Oil Company (Saudi Aramco) for its scholarship, support, and confidence in my capabilities. I would like also to express my sincere appreciation to the management of Research and Development

Center of Saudi Aramco for their encouragement and follow-up during my assignment. Thanks to the sponsors of this gas-condensate research project: ChevronTexaco, Saudi Aramco, Conoco, and JNOC for their financial support.

Special thanks go to other members of the gas-condensate group. Rakesh R. Rai and Padmakar Ayyalasomayajula kindly did the calculations needed using UTCOMP. Jaehyuk Lee has been a great office-mate for the first two years and helped me in preparing standard solutions needed to calibrate the GC. Jacob G. Walker was so patient with me when I started to take over his work. He explained to me all the details I need to consider and accomplish in this dissertation. He also contributed in writing the paper we published on the successful field treatment. I also thank David Hackney, ChevronTexaco Crop., for providing us with the field data and the details of the methanol treatment conducted on a gas well in the Hatter's Pond Field in Alabama.

I am really proud to be a graduate student in the Petroleum and Geosystems Engineering Center at the University of Texas at Austin where U.S. News ranked it first among graduate schools. I would like to thank all the professors who taught me in all my classes and helped me in gaining a very strong technical base of knowledge.

I deeply thank my beloved wife and kids, Faisal, Mohamed, and Ghadah, for their patient and encouragement during my graduate studies.

Hamoud Ali Al-Anazi
December 2003

Experimental Measurements of Condensate Blocking and Treatments in Low and High Permeability Cores

Publication No._____________

Hamoud Ali Al-Anazi, PhD
The University of Texas at Austin, 2003

Supervisors: Mukul M. Sharma and Gary A. Pope

Experiments were performed to investigate the effect of condensate and water blocking on gas productivity in both low and high permeability cores. Liquid dropout data for a four-component synthetic gas mixture was measured experimentally. The Peng-Robinson equation-of-state was used to calculate the liquid drop and matched the data closely after a small adjustment in the gas composition.

Coreflood experiments were conducted to measure relative permeability using Berea sandstone and Texas Cream limestone cores and the four-component synthetic gas mixture to quantify the loss in relative permeability caused by condensate blocking. The condensate saturation was established dynamically by precise control of core inlet and outlet pressures. It is well known that retrograde condensate blockage can cause significant productivity loss in low permeability gas reservoirs. This research shows that such productivity losses can also occur in high permeability gas reservoirs. Gas relative permeability reductions of up to 97% were measured in 3 md and 350 md cores during steady state flow of gas and condensate (see **Table 5.1**). Higher initial water saturations resulted in higher reductions in gas relative permeability. Gas and condensate relative permeability values are almost equal at steady state flow of gas and condensate. Values as low as 0.04 were measured at the highest initial water saturation.

Methanol treatments in the same cores increased both gas and condensate relative permeability in both low and high permeability rocks. These coreflood experiments also were used to quantify the methanol treatment volumes required to restore the gas relative permeability. Methanol displaces condensate and maintains improved gas relative permeability for a significant period of time after the treatment even with production below the dew point pressure. Methanol miscibility displaces water, which is also beneficial since water contributes to the total liquid blockage of the gas.

These same coreflood experiments showed that dynamic condensate accumulation is influenced by flow rate. More pore volumes were required to

reach a steady state at high flow rates than a low flow rates. Co-injection equilibrium gas and condensate phases into the core achieved a steady state with fewer pore volumes than the high flow rate dynamic accumulation corefloods. These data show that local equilibrium was not reached at the high flow rates. At the highest flow rates, the residence time in the core was only about 9 minutes, which evidently is not sufficient time for complete mass transfer to occur. However, it is important to note that the steady state values of gas and condensate relative permeability are the same for both methods. These values will be reached very quickly around gas wells with high flow rate due to the large number of pore volumes flowing near the well.

In light of these new data, the common perception that condensate blocking around wells in high-permeability gas reservoirs is not significant should be re-examined. Reservoir engineers should be especially careful to evaluate the damage done in such high-permeability reservoirs if the well's pressure drawdown is high enough to result in pressures below the dew point over a long enough period of time to allow condensate accumulation near the well.

Table of Contents

List of Tables .... **xiv**

List of Figures .... **xxviii**

Chapter 1: Introduction **1**

1.1 Condensate and Water Blockage 1
1.2 Condensate Removal Treatments 3
1.3 Gas-Condensate Reservoir Studies 8
1.4 Objectives 14

Chapter 2: Phase Behavior Studies **16**

2.1 Gas Mixture Preparation 16
2.2 Apparatus 19
    2.2.1 Pumps 19
    2.2.2 Through-Window PVT Cell 19
    2.2.3 Accumulators 20
2.3 Experimental Studies 21
    2.3.1 Liquid Dropout Measurements 21
    2.3.2 Alcohol-Hydrocarbon Solubility 22
2.4 Results and Discussion 23
    2.4.1 Liquid Dropout Measurements 23
    2.4.2 Methanol-Hydrocarbon Solubility 25

Chapter 3: Solubility of Salts in Alcohol-Water Mixtures **34**

3.1 Introduction 34
3.2 Chemicals 34
    3.2.1 Salts 34

3.2.2 Alcohols 35
3.3 Experimental Procedure 35
3.4 Results and Discussion 36
3.4.1 Solubility of Salts in Methanol-Water Mixtures 36
3.4.2 Solubility of Salts in Ethanol-Water Mixtures 38

Chapter 4: Coreflood Apparatus and Experimental Procedure 46
4.1 Introduction 46
4.2 Theory 52
4.3 Apparatus 57
4.3.1 Through-Window PVT Cell 57
4.3.2 Back-Pressure Regulator 58
4.3.3 Accumulators 59
4.3.4 PVT Visual Cell 59
4.3.5 Capillary Tube Viscometer 59
4.3.6 Pressure Transducers 60
4.3.7 Digital Data Recorder 61
4.3.8 Gas Chromatograph 61
4.4 Coreflood Experimental Procedure 63
4.4.1 Core Preparation 63
4.4.2 Water Saturation Procedure 64
4.4.3 Coreflood Procedure 65
4.4.4 GC Calibration 66

Chapter 5: Gas-Condensate Coreflood Results and Discussion 74
5.1 Summary 74
5.2 Condensate Blocking 75
5.2.1 Effect of Core Permeability 77
5.2.1.1 Low Permeability Cores 77
5.2.1.2 High Permeability Cores 79

5.2.2 Effect of Water Saturation 81
5.2.3 Effect of Capillary Number 82
5.3 Effect of Methanol Treatment 83
5.3.1 Methanol Treatments in Low Permeability Cores 84
5.3.2 Methanol Treatments in High Permeability Cores 87
5.4 Summary of the Results 89

Chapter 6: Non-Equilibrium Behavior 112
6.1 Introduction 112
6.2 Effect of Flow Rate on Condensate Accumulation 117
6.3 Co-Injection of Equilibrium Phases 119
6.4 GC Measurements 122
6.5 Compositional Analysis During Two-Phase Flow 124
6.5.1 Dynamic Flashing of Two Phases 124
6.5.2 Co-Injection of Two Phases 128
6.6 Coreflood Simulation 129
6.7 Summary of the Results 132

Chapter 7: Methanol Treatment in the Hatter’s Pond Field 147
7.1 Field History 148
7.2 Well History 150
7.3 Methanol Treatment 151
7.4 Summary of Field Treatment 153

Chapter 8: Revaporization of Condensate by Methane 158
8.1 Introduction 159
8.2 Results and Discussion 163
8.2.1 Condensate Revaporization by Methane 163
8.2.2 Effect of Flow Rate 166
8.2.3 Effect of Pressure 168
8.3 Summary of Results 169

Chapter 9: Conclusions 177

Appendix A 181

A.1 Gas Mixture Preparation 181

A.2 Flow Rates Equations 183

A.3 Properties of Methanol-Water Mixture 185

Appendix B: Gas-Condensate Coreflood Experiments 189

Appendix C: Characterizing Flow Properties of Cores 444

References 464

Vita 474

List of Tables

Table 2.1: Experimental composition of the gas mixture. 27

Table 2.2: Critical properties of hydrocarbons used in PREOS calculations........ 27

Table 2.3: Adjusted composition of the gas mixture. 28

Table 2.4: Measured and calculated dewpoint pressure and maximum liquid dropout of the gas mixture at 145°F.. 28

Table 3.1: Solubility of NaCl in methanol-water mixtures at 78°F. 39

Table 3.2: Solubility of $CaCl_2$ in methanol-water mixtures at 78°F. 40

Table 3.3: Solubility of KCl in methanol-water mixtures at 78°F. 41

Table 3.4: Measured and reported values of salt solubility in water.................... 41

Table 3.5: Solubility of NaCl in ethanol-water mixtures at 78°F. 42

Table 3.6: Solubility of $CaCl_2$ in ethanol-water mixtures at 78°F. 42

Table 4.1: Flow rates of gas and condensate (oil) phases through the core during dynamic flashing of two-phase through the core at 1,200 psig and 145°F. 68

Table 4.2: The capillary viscometer factor determined by flowing methane at 3,000 psig and 145°F at various rates. 68

Table 4.3: Gas viscosity measured with the capillary viscometer. 69

Table 4.4: Properties of low and high permeability cores..................................... 69

Table 5.1: Summary of gas and condensate relative permeability data measured at steady state at 1,200 psig and 145°F. 91

Table 5.2: Experimental core properties of low and high permeability rocks. 92

Table 5.3: Initial gas permeability measured for Texas Cream limestone cores at different initial water saturations.. 92

Table 5.4: Initial gas permeability of Texas Cream limestone core measured using methane at 3,000 psig. 93

Table 5.5: Core permeability measured with the gas mixture (single-phase) at 3,000 psig and 48 cc/hr. 93

Table 5.6: Gas and oil relative permeabilities measured during dynamic condensate accumulation at 1,200 psig and 18 cc/hr. 94

Table 5.7: Relative permeability values in Texas Cream limestone cores during two-phase flow at 1200 psig. 94

Table 5.8: Relative permeability values in Berea cores during two-phase flow at 1,200 psig. 94

Table 5.9: Results of methanol treatments performed after condensate accumulation for Experiment-8.. 95

Table 5.10: Gas relative permeability during the enhanced flow period in Texas Cream limestone cores.. 95

Table 5.11: Oil relative permeability during the enhanced flow period in Texas Cream limestone cores. 96

Table 5.12: Effect of methanol treatment on gas end-point relative permeability in Texas Cream limestone cores. 96

Table 5.13: Gas relative permeability during the enhanced flow period in Berea cores. 97

Table 5.14: Oil relative permeability during the enhanced flow period in Berea cores. 97

Table 5.15: Effect of methanol treatment on gas end-point relative permeability in Berea cores.. 98

Table 6.1: Condensate saturation (S_o) calculated during two-phase flow steady state at various flow rates. 133

Table 6.2: Gas and oil relative permeabilities during co-injection of equilibrium gas (q_{gas}=132 cc/hr) and condensate (q_{oil}=10 cc/hr) phases at 1,200 psig. 133

Table 6.3: Gas and oil relative permeabilities during co-injection of equilibrium gas (q_{gas}=32 cc/hr) and condensate (q_{oil}=2.5 cc/hr) phases at 1,200 psig at steady state. 134

Table 6.4: Flash calculation using the PREOS at 145°F. 134

Table 6.5: Measured and calculated concentration of each component in the equilibrium gas at 145°F and 1,200 psig. 135

Table 6.6: Gas and oil relative permeabilities during dynamic condensate accumulation through the core at 1,200 psig and steady state. 135

Table 6.7: Dynamic condensate fractional flow measured during two-phase in the absence of porous medium at 1,200 psig and various pump rates. 136

Table 6.8: Gas and oil relative permeabilities during co-injection of equilibrium gas (q_{gas}=32 cc/hr) and condensate (q_{oil}=2.5 cc/hr) phases through the core at 1,200 psig and steady state. 136

Table 7.1: Chemical analysis of water sample for Hatter's Pond field. 154

Table 7.2: Test results of Well #3-6 before and after methanol treatment. 154

Table 8.1: Return permeability ratio during revaporization of condensate by methane at 1,200 psig and 99 cc/hr. 170

Table 8.2: Return permeability ratio during revaporization of condensate by methane at 1,200 psig at 132 cc/hr. 170

Table B.1: Initial core permeability measured with methane at 1,200 psig and a flow rate of 44.8 cc/hr. 193

Table B.2: Core permeability measured during gas mixture (single-phase) flow at 1,200 psig and a flow rate of 44.8 cc/hr. 193

Table B.3: Gas and oil relative permeabilities measured during dynamic condensate accumulation before methanol treatment at 1,200 psig and 44.8 cc/hr. 193

Table B.4: Gas end-point relative permeability measured during equilibrium gas flow at 1,200 psig and 44.8 cc/hr. 193

Table B.5: Relative permeabilities measured during dynamic condensate accumulation after methanol treatment at 1,200 psig and 44.8 cc/hr. 194

Table B.6: Gas end-point relative permeability measured during equilibrium gas flow after methanol treatment at 1,200 psig and 44.8 cc/hr. 194

Table B.7: Summary of experimental results for coreflood Experiment-4. 194

Table B.8: Initial core permeability measured with 0.5 wt% $CaCl_2$ solution at atmospheric pressure and a flow rate of 44.8 cc/hr. 205

Table B.9: Gas relative permeability measured during brine displacement with methane at 2,000 psig (S_{wr}=56.24%). 205

Table B.10: Gas relative permeability measured during methane flow at 3,000 psig and 44.8 cc/hr (S_{wr}=44.85%). 205

Table B.11: Gas relative permeability measured during gas mixture (single-phase) flow at 3,000 psig and 44.8 cc/hr. 206

Table B.12: Gas and oil relative permeabilities measured during dynamic condensate accumulation at 1,200 psig and 44.8 cc/hr. 206

Table B.13: Gas end-point relative permeability measured during equilibrium gas flow before methanol treatment at 1,200 psig and 44.8 cc/hr. 206

Table B.14: Gas and oil relative permeabilities measured during condensate accumulation after methanol treatment at 1,200 psig and 44.8 cc/hr. 207

Table B.15: Gas end-point relative permeability measured during equilibrium gas flooding after methanol treatment at 1,200 psig and 44.8 cc/hr. 207

Table B.16: Summary of experimental results for coreflood Experiment-5. 207

Table B.17: Initial core permeability measured using single-phase gases..........222

Table B.18: Core permeability measured with gas mixture (single-phase) at 3,000 psig and 44.8 cc/hr. 222

Table B.19: Oil and gas relative permeabilities measured during condensate accumulation stage before methanol at 1,200 psig and 44.8 cc/hr...222

Table B.20: Gas end-point relative permeability measured during equilibrium gas flow before methanol treatment at 1,200 psig and 44.8 cc/hr....223

Table B.21: Two-phase relative permeability measured during condensate accumulation after the first methanol treatment at 1200 psig..........223

Table B.22: Gas end-point relative permeability measured during equilibrium gas flow after the first methanol treatment at 1200 psig and 44.8 cc/hr..223

Table B.23: Gas and oil relative permeabilities measured during condensate accumulation after the second methanol treatment at 1200 psig. 224

Table B.24: Gas end-point relative permeability measured during equilibrium gas flow after the second methanol treatment at 1,200 psig and 44.8 cc/hr...224

Table B.25: Gas and oil relative permeabilities measured during condensate accumulation after the second methanol treatment at 1,200 psig 224

Table B.26: Gas end-point relative permeability measured during equilibrium gas flow after the third methanol treatment at 1,200 psig and 44.8 cc/hr..225

Table B.27: Gas and oil relative permeability measured during the enhanced flow period of the two-phase flow at 1,200 psig.............................225

Table B.28: Summary of the results for coreflood Experiment-7.......................225

Table B.29: Initial core permeability measured using methane at 3,000 psig and a flow rate of 44.8 cc/hr...244

Table B.30: Gas relative permeability measured during methane flow at S_{wi} =20%. 244

Table B.31: Gas relative permeability measured during gas mixture (single-phase) flow at 3,000 psig and 44.8 cc/hr..244

Table B.32: Gas and oil relative permeabilities measured during condensate accumulation before methanol at 1200 psig and 44.8 cc/hr.............244

Table B.33: Gas end-point relative permeability measured during equilibrium gas flow before methanol at 1,200 psig and 44.8 cc/hr...................245

Table B.34: Gas and oil relative permeability measured during two-phase flow after the first methanol treatment at 1,200 psig and 44.8 cc/hr........245

Table B.35: Gas end-point relative permeability measured during equilibrium gas flow after the first methanol treatment at 1,200 psig and 44.8 cc/hr...245

Table B.36: Gas and oil relative permeabilities measured during condensate accumulation after the second methanol treatment at 1200 psig and 44.8 cc/hr...245

Table B.37: Gas end-point relative permeability measured during equilibrium gas flow after the second methanol treatment at 1,200 psig and 44.8 cc/hr...246

Table B.38: Gas and oil relative permeabilities measured during two-phase flow (4th flow stage) at 1,200 psig and 44.8 cc/hr............................246

Table B.39: Gas end-point relative permeability measured during equilibrium gas flow (4th stage) at 1,200 psig and 44.8 cc/hr.............................246

Table B.40: Gas and oil relative permeabilities measured during two-phase flow (5th stage) at 1,200 psig and 44.8 cc/hr. 246

Table B.41: Gas end-point relative permeability measured during equilibrium gas flow (5th stage) at 1,200 psig and 44.8 cc/hr.............................247

Table B.42: Summary of experimental results for coreflood Experiment-8.......247

Table B.43: Gas and oil relative permeabilities measured during the enhanced flow period. 247

Table B.44: Initial core permeability measured using methane at 3,000 psig. ...263

Table B.45: Core relative permeability to methane at an initial water saturation of 20% and 3,000 psig......263

Table B.46: Gas relative permeability measured during gas mixture (single-phase) flow at 3,000 psig. 263

Table B.47: Gas and oil relative permeabilities measured during condensate accumulation before methanol treatment at 1,200 psig and 60 cc/hr......264

Table B.48: Gas end-point relative permeability measured during equilibrium gas flow before methanol treatment at 1,200 psig and 60 cc/hr......264

Table B.49: Gas and oil relative permeabilities measured during condensate accumulation after the first methanol treatment at 1,200 psig and 60 cc/hr......264

Table B.50: Gas end-point relative permeability measured during equilibrium gas flow after the first methanol treatment at 1,200 psig and 60 cc/hr......265

Table B.51: Summary of experimental results for coreflood Experiment-10......265

Table B.52: Gas and oil relative permeabilities measured during the enhanced flow period. 265

Table B.53: Initial core permeability measured using methane at a flow rate of 600 cc/hr and 3,000 psig. 283

Table B.54: Core permeability measured during gas mixture (single-phase) flow at a flow rate of 600 cc/hr and 3,000 psig......283

Table B.55: Gas and oil relative permeabilities measured during condensate accumulation before methanol treatment at 600 cc/hr and 1,200 psig. 283

Table B.56: Gas end-point relative permeability measured during equilibrium gas flow before methanol treatment at 600 cc/hr and 1,200 psig......283

Table B.57: Gas and oil relative permeabilities measured during condensate accumulation after the first methanol treatment at 600 cc/hr and 1,200 psig. 284

Table B.58: Gas end-point relative permeability measured during equilibrium gas flow after the first methanol treatment at 600 cc/hr and 1,200 psig. 284

Table B.59: Gas and oil relative permeabilities measured during condensate accumulation after the second methanol treatment at 600 cc/hr and 1,200 psig. 284

Table B.60: Gas end-point relative permeability measured during equilibrium gas flow after the second methanol treatment at 600 cc/hr and 1,200 psig. 285

Table B.61: Gas and oil relative permeabilities measured during condensate accumulation after the third methanol treatment in the reverse direction (upward flow) at 600 cc/hr and 1,200 psig. 285

Table B.62: Gas end-point relative permeability measured during equilibrium gas flow after the third methanol treatment in the reverse direction (upward flow) at 600 cc/hr and 1,200 psig. 285

Table B.63: Gas and oil relative permeabilities measured during condensate accumulation after the fourth methanol treatment in the horizontal direction at 600 cc/hr and 1,200 psig. 286

Table B.64: Gas end-point relative permeability measured during equilibrium gas flow after the fourth methanol treatment in the horizontal direction at 600 cc/hr and 1,200 psig. 286

Table B.65: Gas and oil relative permeabilities measured during condensate accumulation after the fifth methanol treatment in the downward direction at lower rates and 1,200 psig.......... 286

Table B.66: Gas end-point relative permeability measured during equilibrium gas flow after the fifth methanol treatment in the downward direction at lower flow rates and 1,200 psig. 287

Table B.67: Summary of experimental results for coreflood Experiment-12. 287

Table B.68: Gas and oil relative permeabilities measured during the enhanced flow period. 287

Table B.69: Initial core permeability measured using methane at 1,200 psig. 309

Table B.70: Core permeability measured using brine at 1,200 psig. 309

Table B.71: Gas relative permeability measured during brine displacement with methane at 1,200 psig and various flow rates. 309

Table B.72: Core relative permeability at $S_{wr} = 38\%$ measured during methane flow at 3,000 psig. 310

Table B.73: Gas relative permeability measured during gas mixture (single-phase) flow at 600 cc/hr and 3,000 psig. 310

Table B.74: Gas and oil relative permeabilities measured during condensate accumulation stage before methanol treatment at 600 cc/hr and 1200 psig. 310

Table B.75: Gas end-point relative permeability measured during equilibrium gas flow before methanol at 600 cc/hr and 1,200 psig. 311

Table B.76: Gas and oil relative permeabilities measured during condensate accumulation after the first methanol treatment at 600 cc/hr and 1,200 psig. 311

Table B.77: Gas end-point relative permeability measured during equilibrium gas flow after the first methanol treatment at 600 cc/hr and 1,200 psig. 311

Table B.78: Gas and oil relative permeabilities measured during condensate accumulation after the second methanol treatment at 600 cc/hr and 1,200 psig. 312

Table B.79: Gas end-point relative permeability measured during equilibrium gas flow after the second methanol treatment at 600 cc/hr and 1,200 psig. 312

Table B.80: Gas and oil relative permeabilities measured during condensate accumulation after the third methanol treatment at 138 cc/hr and 1,200 psig. 312

Table B.81: Effect of methanol treatment on two-phase relative permeabilities during condensate accumulation at 1,200 psig. 313

Table B.82: Gas and oil relative permeabilities measured during the enhanced flow period. 313

Table B.83: Initial core permeability measured during methane flow at 1,200 psig and various flow rates. 333

Table B.84: Core permeability to brine (3wt% NaCl) at atmospheric pressure. 333

Table B.85: Gas relative permeability measured during brine displacement with methane at 1,200 psig. 333

Table B.86: Gas and oil relative permeabilities measured during condensate accumulation stage before methanol treatment at 60 cc/hr and 1200 psig. 334

Table B.87: Gas end-point relative permeability measured during equilibrium gas flow before methanol treatment at 99 cc/hr and 1,200 psig. 334

Table B.88: Gas and oil relative permeabilities measured during condensate accumulation after the first methanol treatment at 60 cc/hr and 1,200 psig. 334

Table B.89: Gas end-point relative permeability measured during equilibrium gas flow after the first methanol treatment at 99 cc/hr and 1,200 psig. 335

Table B.90: Gas and oil relative permeabilities measured during condensate accumulation after the second methanol treatment at 1,200 psig. 335

Table B.91: Gas end-point relative permeability measured during equilibrium gas flow after the second methanol treatment at 99 cc/hr and 1,200 psig. 335

Table B.92: Gas and oil relative permeabilities measured during the enhanced flow period. 336

Table B.93: Gas and oil relative permeabilities measured at steady state during condensate accumulation at 60 cc/hr and 1,200 psig. 336

Table B.94: Initial core permeability measured during methane flow at 3,000 psig. 348

Table B.95: Core permeability measured during flow of gas mixture (single-phase) at 3,000 psig. 348

Table B.96: Gas and oil relative permeabilities measured during condensate accumulation stage at 1,200 psig and various flow rates. 348

Table B.97: Initial core permeability measured using methane at 3,000 psig. ... 360

Table B.98: Core permeability measured with gas mixture (single-phase) at a flow rate of 48 cc/hr and 3,000 psig.. 360

Table B.99: Gas and oil relative permeabilities measured during condensate accumulation stage at 1,200 psig and 18 cc/hr................................ 361

Table B.100: Gas end-point relative permeability measured during equilibrium gas flow before methanol at 1,200 psig and 99cc/hr....................... 361

Table B.101: Gas and oil relative permeabilities measured during condensate accumulation after the first methanol treatment at 1,200 psig and 18 cc/hr.. 362

Table B.102: Measured gas and oil rates during two-phase flow at steady state at 1,200 psig and different pump rates. 362

Table B.103: Gas end-point relative permeability measured during equilibrium gas flow after the first methanol treatment at 1,200 psig and 99 cc/hr.. 363

Table B.104: Gas and oil relative permeabilities measured during the enhanced flow period of the two-phase after the second methanol treatment at 1,200 psig and 18 cc/hr. 363

Table B.105: Gas and oil relative permeabilities measured during condensate accumulation at steady state after the second methanol treatment at 1,200 psig and 18 cc/hr. 364

Table B.106: Gas end-point relative permeability measured during equilibrium gas flow after the second methanol treatment at 1,200 psig and 99 cc/hr.. 364

Table B.107: Gas and oil relative permeabilities measured during condensate accumulation at steady state at 1,200 psig. 365

Table B.108: Initial core permeability measured using methane at 3,000 psig. . 379

Table B.109: Core permeability measured with gas mixture (single-phase) at 3,000 psig. 379

Table B.110: Gas and oil relative permeabilities measured during condensate accumulation stage at 6 cc/hr and 1,200 psig. 380

Table B.111: Measured gas and oil rates during two-phase flow at steady state at 1,200 psig and different pump rates (@ 3,000 psig). 380

Table B.112: Gas and oil relative permeabilities measured during condensate accumulation at 1,200 psig and various pump rates. 381

Table B.113: Gas end-point relative permeability measured during equilibrium gas flow at 1,200 psig and 99 cc/hr. 381

Table B.114: Initial core permeability measured using methane at 3,000 psig. 392

Table B.115: Core permeability measured during gas mixture (single-phase) flow at 3,000 psig. 392

Table B.116: Gas and oil relative permeabilities measured during condensate accumulation stage at 1,200 psig and 2 cc/hr. 393

Table B.117: Gas permeability measured during revaporization of condensate by methane flow at 1,200 psig and different flow rates. 393

Table B.118: Initial core permeability measured using methane at 1,200 psig. 409

Table B.119: Gas and oil relative permeabilities measured during co-injection of equilibrium gas (q=132 cc/hr) and condensate (q=10 cc/hr) phases at 1,200 psig. 409

Table B.120: Gas and oil relative permeabilities measured during co-injection of equilibrium gas (q=32 cc/hr) and condensate (q=2.5 cc/hr) phases at 1,200 psig and steady state. 409

Table B.121: Gas end-point relative permeability measured during equilibrium gas flow at 99 cc/hr and 1,200 psig. 410

Table B.122: Gas and oil relative permeabilities measured during co-injection of equilibrium gas (q=64 cc/hr) and condensate (q=5 cc/hr) phases after the first methanol treatment at 1,200 psig. 410

Table B.123: Gas end-point relative permeability measured during equilibrium gas flow after the first methanol treatment at 99 cc/hr and 1,200 psig. 410

Table B.124: Gas and oil relative permeabilities measured during co-injection of equilibrium gas (q=64 cc/hr) and condensate (q=5 cc/hr) phases after the second methanol treatment at 1,200 psig. 411

Table B.125: Gas end-point relative permeability measured during equilibrium gas flow after the second methanol treatment at 99 cc/hr and 1,200 psig. 411

Table B.126: Gas and oil relative permeabilities measured during dynamic condensate accumulation (flashing method) after the third methanol treatment at 1,200 psig and a pump rate of 20 cc/hr (@3,000 psig). 411

Table B.127: Gas end-point relative permeability measured during equilibrium gas flow after the third methanol treatment at 99 cc/hr and 1,200 psig. 412

Table B.128: Gas and oil relative permeabilities measured during dynamic condensate accumulation (flashing method) after the fourth methanol treatment at 1,200 psig and a pump rate of 2 cc/hr (@3,000 psig). 412

Table B.129: Initial core permeability measured during revaporization of condensate with methane flow at 1,200 psig. 434

Table B.130: Core permeability measured during methane flow at 3,000 psig. .. 434

Table B.131: Core permeability measured during gas mixture (single-phase) flow at 3,000 psig. 434

Table B.132: Gas and oil relative permeabilities measured during dynamic condensate accumulation at 42 cc/hr and 1,200 psig. 435

Table B.133: Core permeability measured during revaporization of methanol by methane flood at 1,200 psig. 435

Table B.134: Core permeability measured during methane flow at 2,500 psig. .. 435

Table B.135: Flash calculation using the PREOS at 145°F. 436

Table B.136: Gas and oil relative permeabilities measured during dynamic condensate accumulation through the core at 42 cc/hr and 2,500 psig. 436

Table C.1: UV readings for standard solutions of KI used for calibration. 456

Table C.2: Summary of the results for tracer tests. 456

List of Figures

Figure 1.1: Productivity index for the Arun gas-condensate reservoir (Afidick et al., 1994)........15

Figure 2.1: Measured liquid dropout (V/V_t) curve of the gas mixture at 145°F...29

Figure 2.2: Measured liquid dropout (V/V_{dew}) curve of the gas mixture at 145°F........29

Figure 2.3: Liquid dropout (V/V_t) curves of the gas mixture at 145°F........30

Figure 2.4: Phase envelope of the gas mixture generated by the PREOS........30

Figure 2.5: Phase envelope (vapor/liquid =1.0) calculated for experimental and adjusted composition of the gas mixture........31

Figure 2.6: Methanol-n-heptane binary mixture at 25°C........31

Figure 2.7: Methanol-n-heptane binary mixture at different temperatures........32

Figure 2.8: Methanol-n-decane binary mixture at 25°C........32

Figure 2.9: Methanol-n-decane binary mixture at different temperatures........33

Figure 3.1: Solubility of NaCl in methanol-water mixtures at 78°F........43

Figure 3.2: Solubility of $CaCl_2$ in methanol-water mixtures at 78°F........43

Figure 3.3: Solubility of KCl in methanol-water mixtures at 78°F........44

Figure 3.4: Solubility of salts in methanol-water mixtures at 78°F........44

Figure 3.5: Solubility of NaCl in ethanol-water mixtures at 78°F........45

Figure 3.6: Solubility of $CaCl_2$ in ethanol-water mixtures at 78°F. 45

Figure 4.1: A photograph of gas-condensate laboratory (CPE 5.166). 70

Figure 4.2: A photograph of HPHT coreflood apparatus. 70

Figure 4.3: Schematic diagram of the coreflood apparatus. 71

Figure 4.4: Schematic diagram of the back-pressure regulator (courtesy of TEMCO, Inc.). 71

Figure 4.5: Schematic diagram of the gas chromatograph. 72

Figure 4.6: Calibration curve for n-butane. 72

Figure 4.7: Calibration curve for n-heptane. 73

Figure 4.8: Calibration curve for n-decane. 73

Figure 5.1: Measured initial gas permeability of Texas Cream limestone cores at 100% S_g. 99

Figure 5.2: Gas relative permeability data at different initial water saturations. .. 99

Figure 5.3: Pressure drop for different sections across the core during methane flow at 3,000 psig and at various flow rates. 100

Figure 5.4: Pressure drop for different sections of the core during gas mixture flow at 3,000 psig and 48 cc/hr. 100

Figure 5.5: Pressure drop across different sections of a Texas Cream limestone core during dynamic condensate accumulation at 1,200 psig and a flow rate of 18 cc/hr. 101

Figure 5.6: Pressure drop across the cores during condensate accumulation at 1,200 psig and different flow rates and water saturations. 101

Figure 5.7: Pressure drop across Berea cores during dynamic condensate accumulation at 1,200 psig and 600 cc/hr. 102

Figure 5.8: Effect of condensate blocking on productivity index of Texas Cream limestone and Berea sandstone cores at different water saturations. 102

Figure 5.9: Normalized productivity index ratio during condensate accumulation at different water saturations. 103

Figure 5.10: Effect of initial water saturation on gas and condensate relative permeabilities during two-phase flow at 1,200 psig. 103

Figure 5.11: Gas and condensate relative permeabilities as a function of capillary number for Texas Cream limestone cores........................ 104

Figure 5.12: Gas and condensate relative permeabilities as a function of capillary number for Berea cores. 104

Figure 5.13: Steady state flow periods before and after methanol treatment during two-phase flow through the core. 105

Figure 5.14: Effect of methanol treatment on condensate accumulation in Texas Cream limestone core at S_{wi}=20%....................................... 105

Figure 5.15: Effect of methanol treatment on PI during condensate accumulation in Texas Cream limestone core at S_{wi}=20%. 106

Figure 5.16: Effect of methanol treatment volume on gas relative permeability ratio during the enhanced flow period in Texas Cream limestone cores. 106

Figure 5.17: Effect of methanol treatment volume on oil relative permeability ratio during the enhanced flow period in Texas Cream limestone cores. 107

Figure 5.18: Effect of methanol treatment volume on duration of the enhanced flow period in Texas Cream limestone cores................................. 107

Figure 5.19: Effect of methanol treatment volume on gas relative permeability end-point ratio in Texas Cream limestone cores............................. 108

Figure 5.20: Effect of methanol treatment volume on condensate accumulation in Berea core at S_{wi}=38%. 108

Figure 5.21: Effect of methanol treatment on PI during condensate accumulation in Berea core at S_{wi}=38%. 109

Figure 5.22: Effect of methanol treatment on PI during condensate accumulation in Berea core at S_{wi}=0%. 109

Figure 5.23: Effect of methanol treatment volume on gas relative permeability ratio during the enhanced flow period in Berea cores..................... 110

Figure 5.24: Effect of methanol treatment volume on oil relative permeability ratio during the enhanced flow period in Berea cores..................... 110

Figure 5.25: Effect of methanol treatment volume on duration of the enhanced flow period in Berea cores. 111

Figure 6.1: Pressure drop at different sections across the core during dynamic condensate accumulation at 42 cc/hr and 1,200 psig. 137

Figure 6.2: Pressure drop at different sections across the core during dynamic condensate accumulation at 6 cc/hr and 1,200 psig. 137

Figure 6.3: Pressure drop at different sections across the core during dynamic condensate accumulation at 2 cc/hr and 1,200 psig. 138

Figure 6.4: Pore volumes required to reach steady-state during dynamic condensate accumulation as a function of flow rate at 1,200 psig... 138

Figure 6.5: Residence time as a function of flow rate....................................... 139

Figure 6.6: Pressure drop at different sections across the core during co-injection of equilibrium gas and condensate phases at 1,200 psig... 139

Figure 6.7: Pressure drop at different sections across the core during co-injection of equilibrium gas and condensate phases at 1,200 psig and steady state. 140

Figure 6.8: Compositional analysis of the equilibrium gas at 1,200 psig. 140

Figure 6.9: Normalized concentrations of the flowing equilibrium gas composition at 145°F and 1,200 psig... 141

Figure 6.10: Normalized concentration of the equilibrium gas at 145°F and 1,200 psig. 141

Figure 6.11: Pressure drop at different sections across the core during dynamic condensate accumulation at steady state and 1,200 psig................. 142

Figure 6.12: Normalized concentration of the gas during dynamic condensate accumulation through the core at 1,200 psig and steady state. 142

Figure 6.13: Normalized concentrations of the gas in equilibrium with the condensate in the PVT cell at 1,200 psig. 143

Figure 6.14: Normalized concentrations of the gas phase composition during two-phase flow in the absence of the core at 1,200 psig. 143

Figure 6.15: Cumulative condensate volume collected in the PVT during two-phase flow at 1,200 psig and various flow rates. 144

Figure 6.16: Pressure drop at different sections across the core during co-injection of gas and condensate phases at steady state and 1,200 psig. 144

Figure 6.17: Normalized concentrations of gas composition during co-injection of equilibrium phases through the core at steady state and 1,200 psig. 145

Figure 6.18: Normalized concentrations of the gas-phase during co-injection of equilibrium phases in the absence of the core at 1,200 psig. 145

Figure 6.19: Simulated and measured pressure drop across the core during dynamic condensate accumulation at 2 cc/hr (Experiment-17, 1,200 psig and 145°F). 146

Figure 6.20: Simulated and measured pressure drop across the core during co-injection of equilibrium gas and condensate phases at 1,200 psig (Experiment-18, q_g=132 cc/hr, q_o=10 cc/hr). 146

Figure 7.1: Hatter's Pond type log. 155

Figure 7.2: Wellbore sketch for Hatter's Pond Unit 3-6 #1, Hatter's Pond Field, Mobile Co., Alabama. 156

Figure 7.3: Gas and condensate production rates for Hatter's Pond Unit 3-6 #1 before and after methanol treatment. 157

Figure 8.1: Pressure drop at different sections across the core during revaporization of condensate by methane at 1,200 psig. 171

Figure 8.2: Pressure drop at different sections across the core during revaporization of condensate by methane at 1,200 psig. 171

Figure 8.3: Return permeability ratio at different sections across the core during revaporization of condensate by methane at 1,200 psig. 172

Figure 8.4: Composition of the core effluent during revaporization of condensate by methane at 1,200 psig and various flow rates. 172

Figure 8.5: Pressure drop at different sections across the core during revaporization of condensate by methane at 1,200 psig. 173

Figure 8.6: Return permeability ratio at different sections across the core during revaporization of condensate by methane at 1,200 psig. 173

Figure 8.7: Composition of the core effluent during revaporization of condensate by methane at 1,200 psig. 174

Figure 8.8: Concentration of n-butane in the core effluent during revaporization of condensate by methane at 1,200 psig and various flow rates. 174

Figure 8.9: Concentration of n-heptane in the core effluent during revaporization of condensate by methane at 1,200 psig and various flow rates. 175

Figure 8.10: Concentration of n-decane in the core effluent during revaporization of condensate by methane at 1,200 psig and various flow rates. 175

Figure 8.11: Pressure drop across the core during revaporization of condensate by methane at 3,000 psig. 176

Figure 8.12: Return permeability ratio as a function of methane volume injected in Texas Cream limestone cores. 176

Figure A.1: A schematic diagram of upstream back-pressure regulator (BPR-1) during two-phase flow. 187

Figure A.2: Viscosity of methanol-water mixtures at different temperatures (Mikhail and Kimel, 1961). 187

Figure A.3: Viscosity of methanol as a function of temperature. 188

Figure B.1: Pressure drop across the core during methane flow at 3,000 psig and 44.8 cc/hr. 195

Figure B.2: Pressure drop across the core during gas mixture (single-phase) flow at 3,000 psig and 44.8 cc/hr. 195

Figure B.3: Pressure drop across the core during dynamic condensate accumulation at 1,200 psig and 44.8 cc/hr. 196

Figure B.4: Pressure drop across the core during equilibrium gas flow at 1,200 psig and 44.8 cc/hr. 196

Figure B.5: Pressure drop across the core during methanol treatment at 1,200 psig. 197

Figure B.6: Pressure drop across the core during condensate accumulation after the methanol treatment at 12,00 psig and 44.8 cc/hr....................... 197

Figure B.7: Pressure drop across the core during equilibrium gas flow after the first methanol treatment at 1200 psig and 44.8 cc/hr. 198

Figure B.8: Pressure drop across the core during dynamic condensate accumulation before and after methanol treatment at 1,200 psig and 44.8 cc/hr. 198

Figure B.9: Pressure drop across the core during equilibrium gas flow before and after methanol treatment at 1,200 psig and 44.8 cc/hr. 199

Figure B.10: Pressure drop across the core during brine (0.5 wt% $CaCl_2$) injection at atmospheric pressure and 44.8 cc/hr. 208

Figure B.11: Pressure drop across the core during methane flow to displace water from the core at 2,000 psig and various flow rates. 208

Figure B.12: Pressure drop across the core during methane flow at 3,000 psig and a flow rate of 44.8 cc/hr... 209

Figure B.13: Pressure drop across the core during gas mixture (single-phase) flow at 3,000 psig and 44.8 cc/hr. 209

Figure B.14: Pressure drop across the core during dynamic condensate accumulation at 1,200 psig and 44.8 cc/hr. 210

Figure B.15: Pressure drop across the core during equilibrium gas flow before methanol treatment at 1,200 psig and 44.8 cc/hr. 210

Figure B.16: Pressure drop across the core during methanol treatment at 1,200 psig and 44.8 cc/hr. 211

Figure B.17: Pressure drop across the core during condensate accumulation after methanol treatment at 1,200 psig and 44.8 cc/hr. 211

Figure B.18: Pressure drop across the core during equilibrium gas flow after methanol treatment at 1,200 psig and 44.8 cc/hr. 212

Figure B.19: Pressure drop across the core during condensate accumulation before and after methanol treatment at 1,200 psig and 44.8 cc/hr. .. 212

Figure B.20: Pressure drop across the core during equilibrium gas flow before and after methanol treatment at 1,200 psig and 44.8 cc/hr. 213

Figure B.21: Gas (methane) relative permeability data at different residual water saturations. 213

Figure B.22: Pressure drop across the core during nitrogen flow at 2,000 psig and 44.8 cc/hr. 226

Figure B.23: Pressure drop across the core during methane flow at 2,000 psig and 44.8 cc/hr. 226

Figure B.24: Pressure drop across the core during methane flow at 3,000 psig and 44.8 cc/hr. 227

Figure B.25: Pressure drop across the core during gas mixture (single-phase) flow at 3,000 psig and 44.8 cc/hr. 227

Figure B.26: Pressure drop across the core during condensate accumulation before methanol treatment at 1,200 psig and 44.8 cc/hr. 228

Figure B.27: Pressure drop across the core during equilibrium gas flow before methanol treatment at 1,200 psig and 44.8 cc/hr. 228

Figure B.28: Pressure drop across the core during the first stage of methanol treatment at 1,200 psig and 44.8 cc/hr. 229

Figure B.29: Pressure drop across the core during condensate accumulation after the first methanol treatment at 1,200 psig and 44.8 cc/hr. 229

Figure B.30: Pressure drop across the core during equilibrium gas flow after the first methanol treatment at 1,200 psig and 44.8 cc/hr. 230

Figure B.31: Pressure drop across the core during the second methanol treatment at 1,200 psig and 44.8 cc/hr. 230

Figure B.32: Pressure drop across the core during condensate accumulation after the second methanol treatment at 1,200 psig. 231

Figure B.33: Pressure drop across the core during equilibrium gas flow after the second methanol treatment at 1,200 psig and 44.8 cc/hr. 231

Figure B.34: Pressure drop across the core during the third methanol treatment at 1,200 psig and 44.8 cc/hr. 232

Figure B.35: Pressure drop across the core during condensate accumulation after the third methanol treatment at 1,200 psig. 232

Figure B.36: Pressure drop across the core during equilibrium gas flow after the third methanol treatment at 1,200 psig and 44.8 cc/hr. 233

Figure B.37: Pressure drop across the core during dynamic condensate accumulation before and after methanol treatments at 1,200 psig and 44.8 cc/hr. 233

Figure B.38: Pressure drop across the core during equilibrium gas flow before and after methanol treatments at 1,200 psig and 44.8 cc/hr. 234

Figure B.39: Pressure drop across the core during methane flow before introducing water saturation at 3,000 psig and 44.8 cc/hr. 248

Figure B.40: Pressure drop across the core during methane flow at an initial water saturation of 20% at 3,000 psig and 44.8 cc/hr. 248

Figure B.41: Pressure drop across the core during gas mixture (single-phase) flow at 1,200 psig and 44.8 cc/hr. 249

Figure B.42: Pressure drop across the core during condensate accumulation before methanol treatment at 1,200 psig and 44.8 cc/hr. 249

Figure B.43: Pressure drop across the core during equilibrium gas flow before methanol treatment at 1,200 psig and 44.8 cc/hr. 250

Figure B.44: Pressure drop across the core during the first methanol treatment at 1,200 psig and 44.8 cc/hr. 250

Figure B.45: Pressure drop across the core during condensate accumulation after the first methanol treatment at 1,200 psig and 44.8 cc/hr. 251

Figure B.46: Pressure drop across the core during equilibrium gas flow after the first methanol treatment at 1,200 psig and 44.8 cc/hr. 251

Figure B.47: Pressure drop across the core during the second methanol treatment at 1,200 psig and 44.8 cc/hr. 252

Figure B.48: Pressure drop across the core during condensate accumulation after the second methanol treatment at 1,200 psig and 44.8 cc/hr. .. 252

Figure B.49: Pressure drop across the core during equilibrium gas flow after the second methanol treatment at 1,200 psig and 44.8 cc/hr. 253

Figure B.50: Pressure drop across the core during condensate accumulation (4th flow) at 1,200 psig and 44.8 c/hr. 253

Figure B.51: Pressure drop across the core during equilibrium gas flow (4th flow) at 1,200 psig and 44.8 cc/hr. 254

Figure B.52: Pressure drop across the core during condensate accumulation (5th flow) at 1,200 psig and 44.8 cc/hr. 254

Figure B.53: Pressure drop across the core during equilibrium gas flow (5th flow) at 1,200 psig and 44.8 cc/hr. 255

Figure B.54: Pressure drop across the core during condensate accumulation before and after methanol treatments at 1,200 psig and 44.8 cc/hr. .. 255

Figure B.55: Pressure drop across the core during equilibrium gas flow before and after methanol treatments at 1,200 psig and 44.8 cc/hr. 256

Figure B.56: Pressure drop across the core during methane flow before introducing water saturation at 3,000 psig. 266

Figure B.57: Pressure drop across the core during methane flow at an initial water saturation of 20% and 3,000 psig. 266

Figure B.58: Pressure drop across the core during gas mixture (single-phase) flow at 3,000 psig. 267

Figure B.59: Pressure drop across the core during dynamic condensate accumulation before methanol treatment at 1,200 psig and 60 cc/hr. 267

Figure B.60: Pressure drop across the core during equilibrium gas flow before methanol treatment at 1,200 psig and 60 cc/hr. 268

Figure B.61: Pressure drop across the core during the first methanol treatment at 1,200 psig and 60 cc/hr. 268

Figure B.62: Pressure drop across the core during condensate accumulation after the first methanol treatment at 1,200 psig and 60 cc/hr. 269

Figure B.63: Pressure drop across the core during equilibrium gas flow after the first methanol treatment at 1,200 psig and 60 cc/hr. 269

Figure B.64: Pressure drop across the core during condensate accumulation before and after methanol treatment at 1,200 psig and 60 cc/hr. 270

Figure B.65: Pressure drop across the core during equilibrium gas flow before and after methanol treatment at 1,200 psig and 60 cc/hr. 270

Figure B.66: Pressure drop across the core during methane flow at 600 cc/hr and 3,000 psig. 288

Figure B.67: Pressure drop across the core during gas mixture (single-phase) flow at 600 cc/hr and 3,000 psig. 288

Figure B.68: Pressure drop across the core during condensate accumulation before methanol treatment in downward flow at 600 cc/hr and 1,200 psig. 289

Figure B.69: Pressure drop across the core during equilibrium gas flow before methanol treatment at 600 cc/hr and 1,200 psig. 289

Figure B.70: Pressure drop across the core during the first methanol treatment at 300 cc/hr and 1,200 psig. 290

Figure B.71: Pressure drop across the core during condensate accumulation after the first methanol treatment at 600 cc/hr and 1,200 psig. 290

Figure B.72: Pressure drop across the core during equilibrium gas flow after the first methanol treatment at 600 cc/hr and 1,200 psig. 291

Figure B.73: Pressure drop across the core during the second methanol treatment at 300 cc/hr and 1,200 psig. 291

Figure B.74: Pressure drop across the core during condensate accumulation after the second methanol treatment at 600 cc/hr and 1,200 psig. ...292

Figure B.75: Pressure drop across the core during equilibrium gas flow after the second methanol treatment at 600 cc/hr and 1,200 psig. 292

Figure B.76: Pressure drop across the core during the third methanol treatment at 300 cc/hr and 1,200 psig. 293

Figure B.77: Pressure drop across the core during condensate accumulation in the reverse direction (upward flow) after the third methanol treatment at 600 cc/hr and 1,200 psig. 293

Figure B.78: Pressure drop across the core during equilibrium gas flow in the reverse direction (upward flow) after the third methanol treatment at 600 cc/hr and 1,200 psig. 294

Figure B.79: Pressure drop across the core during the fourth methanol treatment in horizontal direction at 300 cc/hr and 1,200 psig..........294

Figure B.80: Pressure drop across the core during condensate accumulation in the horizontal direction after the fourth methanol treatment at 600 cc/hr and 1,200 psig. 295

Figure B.81: Pressure drop across the core during equilibrium gas flow in the horizontal direction after the fourth methanol treatment at 600 cc/hr and 1,200 psig. 295

Figure B.82: Pressure drop across the core during the fifth methanol treatment in the downward direction at 300 cc/hr and 1,200 psig. 296

Figure B.83: Pressure drop across the core during condensate accumulation after the fifth methanol treatment at various rates and 1,200 psig...296

Figure B.84: Pressure drop across the core during equilibrium gas flow after the fifth methanol treatment at various rates and 1,200 psig. 297

Figure B.85: Pressure drop across the core during condensate accumulation before and after methanol treatments at 600 cc/hr and 1,200 psig... 297

Figure B.86: Effect of methanol on post-treatment condensate accumulation delay followed the enhanced flow period in Berea core. 298

Figure B.87: Pressure drop across the core during methane flow before introducing water saturation at 1,200 psig. 314

Figure B.88: Pressure drop across the core during methanol flow to clean the core at 300 cc/hr and 1,200 psig.. 314

Figure B.89: Pressure drop across the core during brine (3wt% NaCl+0.5wt% $CaCl_2$) flooding at 1,200 psig... 315

Figure B.90: Pressure drop across the core during brine displacement by methane at 1,200 psig and various flow rates. 315

Figure B.91: Pressure drop across the core during methane flow at 3,000 psig. 316

Figure B.92: Pressure drop across the core during gas mixture (single-phase) flow at 600 cc/hr and 3,000 psig. 316

Figure B.93: Pressure drop across the core (Berea) during dynamic condensate accumulation before methanol treatment at 600 cc/hr and 1,200 psig. 317

Figure B.94: Pressure drop across the core during equilibrium gas flow before methanol treatment at 600 cc/hr and 1,200 psig. 317

Figure B.95: Pressure drop across the core during the first methanol treatment at 300 cc/hr and 1,200 psig. 318

Figure B.96: Pressure drop across the core (Berea) during condensate accumulation after the first methanol treatment at 600 cc/hr and 1,200 psig. 318

Figure B.97: Pressure drop across the core during equilibrium gas flow after the first methanol treatment at 600 cc/hr and 1,200 psig. 319

Figure B.98: Pressure drop across the core during the second methanol treatment at 300 cc/hr and 1,200 psig. 319

Figure B.99: Pressure drop across the core during condensate accumulation after the second methanol treatment at 600 cc/hr and 1,200 psig. ... 320

Figure B.100: Pressure drop across the core during equilibrium gas flow after the second methanol treatment at 600 cc/hr and 1,200 psig. 320

Figure B.101: Pressure drop across the core during the third methanol treatment at 300 cc/hr and 1,200 psig. 321

Figure B.102: Pressure drop across the core during condensate accumulation after the third methanol treatment at 138 cc/hr and 1,200 psig........ 321

Figure B.103: Pressure drop across Berea core during condensate accumulation before and after methanol treatments at 600 cc/hr and 12,00 cc/hr. 322

Figure B.104: Pressure drop across the core during equilibrium gas flow before and after methanol treatments at 600 cc/hr and 1,200 psig............. 322

Figure B.105: Effect of methanol treatment volume on condensate bank delay in Berea cores.. 323

Figure B.106: Effect of methanol treatment on the productivity index (PI) profile in Berea cores. 323

Figure B.107: Gas-water relative permeability data for Berea sandstone core... 324

Figure B.108: Pressure drop across the core during methane flow at 1,200 psig.337

Figure B.109: Pressure drop across the core during flow of brine (3wt% NaCl) at atmospheric pressure and 145°F. 337

Figure B.110: Pressure drop across the core during displacement of brine by methane flow at 12,00 psig and various flow rates......................... 338

Figure B.111: Cumulative water volume collected in the core effluent during the displacement of brine by methane at 99 cc/hr and 1,200 psig. .. 338

Figure B.112: Gas-water relative permeability data for Texas Cream limestone core.. 339

Figure B.113: Pressure drop across the core during condensate accumulation before methanol treatment at 60 cc/hr and 1,200 psig. 339

Figure B.114: Pressure drop across the core during equilibrium gas flow before methanol treatment at 99 cc/hr and 1,200 psig. 340

Figure B.115: Pressure drop across the core during the first methanol treatment at 99 cc/hr and 1,200 psig. 340

Figure B.116: Pressure drop across the core during condensate accumulation after the first methanol treatment at 60 cc/hr and 1,200 psig. 341

Figure B.117: Pressure drop across the core during equilibrium gas flow after the first methanol treatment at 99 cc/hr and 1,200 psig. 341

Figure B.118: Pressure drop across the core during the second methanol treatment at 99 cc/hr and 1,200 psig. 342

Figure B.119: Pressure drop across the core during condensate accumulation after the second methanol treatment at 1,200 psig. 342

Figure B.120: Pressure drop across the core during equilibrium gas flow after the second methanol treatment at 99 cc/hr and 1,200 psig. 343

Figure B.121: Pressure drop across the core during condensate accumulation before and after methanol treatments at 60 cc/hr and 1,200 psig..... 343

Figure B.122: Pressure drop across the core during equilibrium gas flow before and after methanol treatments at 99 cc/hr and 1,200 psig. 344

Figure B.123: Pressure drop across the core during methane flow at various flow rates and 3,000 psig. 349

Figure B.124: Pressure drop across the core during gas mixture (single-phase) flow at 3,000 psig and different flow rates. 349

Figure B.125: Pressure drop across the core during dynamic condensate accumulation at 1,200 psig and different flow rates. 350

Figure B.126: Pressure drop at different sections across the core during methane flow at 3,000 psig and various rates. 366

Figure B.127: Pressure drop at different sections across the core during gas mixture (single-phase) flow at 48 cc/hr and 3,000 psig. 366

Figure B.128: Pressure drop at different sections across the core during condensate accumulation at 18 cc/hr and 1,200 psig. 367

Figure B.129: Cumulative hydrocarbon liquid volume during two-phase flow at steady state at 18 cc/hr and 1,200 psig. 367

Figure B.130: Cumulative volume of water displaced by gas-phase during two-phase flow at steady state at 18 cc/hr and 1,200 psig. 368

Figure B.131: Pressure drop at different sections across the core during equilibrium gas flow at 99 cc/hr and 1,200 psig. 368

Figure B.132: Pressure drop across the core during the first methanol treatment at 99 cc/hr and 1,200 psig. 369

Figure B.133: Pressure at different sections across the core during condensate accumulation after the first methanol treatment at 1,200 psig. 369

Figure B.134: Cumulative hydrocarbon liquid volume during two-phase flow at steady state at 1,200 psig and various pump rates. 370

Figure B.135: Cumulative volume of water displaced by gas-phase during two-phase flow at steady state at 1,200 psig and various pump rates. 370

Figure B.136: Pressure drop at different sections across the core during equilibrium gas flow after the first methanol treatment at 99 cc/hr and 1,200 psig. 371

Figure B.137: Pressure drop across the core during the second methanol treatment at 20 cc/hr and 1,200 psig. 371

Figure B.138: Pressure drop at different sections across the core during condensate accumulation after the second methanol treatment at 18 cc/hr and 1,200 psig. 372

Figure B.139: Pressure drop at different sections across the core during equilibrium gas flow after the 2nd methanol treatment at 99 cc/hr and 1,200 psig. 372

Figure B.140: Pressure drop at different sections across the core during methane flow at 1,200 psig and various flow rates. 382

Figure B.141: Pressure drop at different sections across the core during methane flow at 3,000 psig and various flow rates. 382

Figure B.142: Pressure drop at different sections across the core during gas mixture (single-phase) flow at 3,000 psig. 383

Figure B.143: Pressure drop at different sections across the core during condensate accumulation at 1,200 psig and a pump rate of 6 cc/hr. 383

Figure B.144: Cumulative hydrocarbon (HC) liquid volume collected during two-phase flow at steady state at 1,200 psig and various pump rates. 384

Figure B.145: Cumulative volume of water displaced by gas during two-phase flow at steady state at 1,200 psig and various pump rates. 384

Figure B.146: Pressure drop across the core during two-phase flow at steady state at 1,200 psig and different pump rates. 385

Figure B.147: Pressure drop at different sections across the core during equilibrium gas flow at 1,200 psig and 99 cc/hr. 385

Figure B.148: Effect of flow rate (@3,000 psig) on condensate accumulation. 386

Figure B.149: Gas and oil relative permeabilities as a function of capillary number. 386

Figure B.150: Pressure drop at different sections across the core during methane flow at 1,200 psig and various flow rates. 394

Figure B.151: Pressure drop at different sections across the core during methane flow at 3,000 psig and various flow rates. 394

Figure B.152: Pressure drop at different sections across the core during gas mixture (single-phase) flow at 3,000 psig. 395

Figure B.153: Pressure drop at different sections across the core during dynamic condensate accumulation at 1,200 psig and 2 cc/hr. 395

Figure B.154: Pressure drop at different sections across the core during revaporization of condensate by methane flow at 1,200 psig. 396

Figure B.155: Components concentrations in the effluent of the core during revaporization of condensate by methane flooding at 1,200 psig. ... 396

Figure B.156: Pressure drop at different sections across the core during methane flow at 1,200 psig and various rates. ... 413

Figure B.157: Pressure drop at different sections across the core during co-injection of equilibrium gas and condensate phases at 1,200 psig... 413

Figure B.158: Pressure drop at different sections across the core during co-injection of equilibrium gas and condensate phases at 1,200 psig at steady state. ... 414

Figure B.159: Pressure drop at different sections across the core during equilibrium gas flow at 99 cc/hr and 1,200 psig. ... 414

Figure B.160: Pressure drop across the core during the first methanol treatment at a flow rate of 20 cc/hr and 1,200 psig. ... 415

Figure B.161: Methanol-rich phase measured during the first methanol treatment. ... 415

Figure B.162: Pressure drop at different sections across the core during co-injection of equilibrium gas and condensate phases after the first methanol treatment at 1,200 psig. ... 416

Figure B.163: Pressure drop at different sections across the core during equilibrium gas flow after the first methanol treatment at 99 cc/hr. 416

Figure B.164: Pressure drop across the core during the second methanol treatment at a flow rate of 20 cc/hr and 1,200 psig. ... 417

Figure B.165: Methanol-rich phase measured during the second methanol treatment. ... 417

Figure B.166: Pressure drop at different sections across the core during co-injection of equilibrium gas and condensate phases after the second methanol treatment at 1,200 psig. ... 418

Figure B.167: Pressure drop at different sections across the core during equilibrium gas flow after the first methanol treatment at 99 cc/hr. 418

Figure B.168: Components concentrations during equilibrium gas flow after the second methanol treatment. 419

Figure B.169: Pressure drop across the core during the third methanol treatment at a flow rate of 20 cc/hr and 1,200 psig. 419

Figure B.170: Pressure drop at different sections across the core during dynamic condensate accumulation after the third methanol treatment at a pump rate of 20 cc/hr and 1,200 psig. 420

Figure B.171: Pressure drop at different sections across the core during equilibrium gas flow after the third methanol treatment at 99 cc/hr and 1,200 psig. 420

Figure B.172: Components concentrations during equilibrium gas flow after the third methanol treatment. 421

Figure B.173: Pressure drop across the core during the fourth methanol treatment at a flow rate of 20 cc/hr and 1,200 psig. 421

Figure B.174: Pressure drop at different sections across the core during dynamic condensate accumulation after the fourth methanol treatment at a flow rate of 2 cc/hr and 1,200 psig. 422

Figure B.175: Pressure drop at different sections across the core during revaporization of condensate with methane at 1,200 psig. 437

Figure B.176: Composition of the core effluent during revaporization of condensate with methane at 1,200 psig. 437

Figure B.177: Pressure drop at different sections across the core during methane flow at 3,000 psig and various flow rates. 438

Figure B.178: Pressure drop at different sections across the core during gas mixture (single-phase) flow at 3,000 psig. 438

Figure B.179: Pressure drop at different sections across the core during dynamic condensate accumulation at 42 cc/hr and 1,200 psig. 439

Figure B.180: Composition of the core effluent during dynamic condensate accumulation at 1,200 psig and 42 cc/hr. 439

Figure B.181: Normalized concentration of the core effluent during dynamic condensate accumulation at 1,200 psig and 42 cc/hr. 440

Figure B.182: Normalized concentrations of the gas phase that was in equilibrium with condensate phase inside the PVT cell at 1,200 psig. 440

Figure B.183: Pressure drop across the core during methanol flow at 1,200 psig and 36 cc/hr. 441

Figure B.184: Pressure drop at different sections across the core during revaporization of methanol with methane at 1,200 psig. 441

Figure B.185: Pressure drop at different sections across the core during methane flow at 2,500 psig. 442

Figure B.186: Pressure drop at different sections across the core during dynamic condensate accumulation at 42 cc/hr and 2,500 psig. 442

Figure B.187: Cumulative hydrocarbon liquid volume collected during two-phase flow through the core at 2,500 and 42 cc/hr. 443

Figure B.188: Normalized concentrations of the gas phase composition during dynamic condensate accumulation through the core at 42 cc/hr and 2,500 psig. 443

Figure C.1: Calibration curve for measuring concentration of KI in solutions... 457

Figure C.2: Normalized tracer concentration profile for Texas Cream limestone core. 457

Figure C.3: Breakthrough curve for tracer test in Texas Cream limestone core. 458

Figure C.4: Growth of mixing zone length with time in Texas Cream limestone core. 458

Figure C.5: Experimental and analytical concentration profiles for the tracer test in Texas Cream limestone core. 459

Figure C.6: Fractional flow curves for the first drainage process for Texas Cream limestone core... 459

Figure C.7: Fractional flow curves for the forced imbibition process for Texas Cream limestone core. 460

Figure C.8: Fractional flow curves for the second drainage process for Texas Cream limestone core. 460

Figure C.9: Water and oil end-point relative permeability data for Texas Cream limestone core. 461

Figure C.10: Normalized tracer concentration profile for Antolini core. 461

Figure C.11: Breakthrough curve for tracer test in Antolini core. 462

Figure C.12: Growth of mixing zone length with time Antolini core. 462

Figure C.13: Experimental and analytical concentration profiles for the tracer test in Antolini core. 463

Chapter 1: Introduction

1.1 CONDENSATE AND WATER BLOCKAGE

Gas production from reservoirs having a bottom hole flowing pressure below the dewpoint pressure results in an accumulation of a liquid hydrocarbon phase near the wellbore. This condensate accumulation reduces the gas relative permeability, and thus the well's productivity. This is known as condensate blocking. Condensate saturations near the well can reach as high as 50-60% under pseudo steady-state flow of gas and condensate (Mott et al., 2000). Even when the gas is very lean (such as in the Arun field), condensate blocking can cause a drastic decline in well productivity (Afidick et al., 1994; Narayanaswamy et al., 1999; Whitson et al., 1999; Pope et al., 2000).

The Arun field is one of the world's largest retrograde gas reservoirs and is located in the northern coast of Aceh Province in North Sumatra, Indonesia (Afidick et al., 1994). The produced gas is considered very lean, with a maximum liquid dropout of about 1.1%. Experimental PVT analysis of reservoir fluids showed that the dewpoint pressure is 4,400 psi. The productivity of wells declined by a factor of 2 as the average reservoir pressure dropped below the dewpoint pressure as shown in **Figure 1.1**. Well tests were conducted and showed strong evidence of condensate accumulation that restricts gas production. As the condensate accumulates around the wellbore region, the condensate does not flow until it reaches the critical condensate saturation. Experiments conducted on core samples showed that the critical condensate saturation was 51%, which corresponds to a gas relative permeability of 0.18. This high critical condensate saturation resulted in a severe decline in gas productivity (Afidick et al., 1994).

Barnum et al. (1995) reported that critical condensate saturations ranged from 10% to 30% based on history matched simulations. They studied a gas condensate well that produced at an initial rate over 1 MSCF/D. The well died after the flowing bottom hole pressure reached the dewpoint pressure. Liquid condensate resulted in severe loss of well deliverability and gas recovery when the reservoir pressure declined below the dewpoint pressure.

The Cal Canal Field in California produces a rich gas condensate from an average depth of 11,500 feet (Engineer, 1985). The reservoir is classified as a tight abnormally pressured gas condensate reservoir. The average reservoir porosity is 12% and the permeability ranged from 0.01 to 0.1 md. The reservoir had an estimated connate water saturation of 59%. PVT analysis showed that the dewpoint pressure at the reservoir temperature of 271°F is 5,835 psig, which is lower than the initial reservoir pressure by 1,508 psig. The recovery from this field was estimated to be 10% of the original gas-in-place. This poor recovery is due to a combination of condensate accumulation and water saturation around the wellbore. Liquid condensate banking and presence of water in the near wellbore region decrease the relative permeability to gas and tend to reduce the total recovery.

High water saturation in the formation after a stimulation or workover treatment reduces the gas relative permeability. The adverse effect of condensate banking increases in the presence of high water saturation. A water block may occur when capillary forces exceed formation gas pressure. During the flow of gas, some water was produced in a very slow process. For example, some wells required a period of 3 months to a year to restore the initial gas productivity following liquid injection into the formation. Water blocking difficulty increases in a low permeability formation where the capillary forces are high or in reservoirs that have low pressure (McLeod et al., 1966; Kamath and Laroche, 2000; Antoci et al., 2001).

1.2 CONDENSATE REMOVAL TREATMENTS

Several methods have been proposed to restore gas production rates after a decline owing to condensate and/or water blocking (Kamath and Laroche, 2000; Du et al., 2000; Al-Anazi et al., 2002). The main objective of such treatments is to decrease the hydrocarbon liquid or water saturations near the well to increase gas productivity (Barnum et al., 1995). Gas cycling has been used to maintain reservoir pressure above the dewpoint pressure. There are two schemes of gas cycling: full pressure or partial pressure maintenances (Abel et al., 1970). In the full pressure maintenance, gas is being cycled continuously at the same time of withdrawal of gas condensate from reservoirs. However, gas is being cycled into the reservoir after previous depletion in the partial pressure maintenance. Both methods of gas cycling require gas cycling plants that increase the initial capital costs. Engineer (1985) discussed other methods, such as optimization of tubing size, installation of rod pump, and installation of gas lift systems to improve the hydrocarbon recovery in the Cal Canal Field.

Injection of dry gas into a retrograde gas-condensate reservoir vaporizes condensate and increases its dewpoint pressure. Contact of injected dry gas with gas condensate leads to enrichment of the dry gas due to the mass transfer (Luo et al., 2001). They found experimentally that the injected dry gas vaporized efficiently both intermediate and some heavy hydrocarbons. The cumulative condensate recovery in the long-core tests was found to be higher than that in the PVT cell at the same gas injection volume. This means that flow in the porous medium might improve the revaporization process. Li et al. (2001) found that the full pressure maintenance yielded a higher condensate recovery than the partial pressure maintenance. Injection of propane was experimentally found to decrease the dewpoint and vaporize condensate more efficiently than carbon dioxide (Jamaluddin and Thomas, 2001).

Nitrogen has been applied in gas injection due to its economic feasibility (Eckles et al., 1981; Huang et al., 1986). Sänger and Hagoort (1998) used a slim tube to investigate the efficiency of nitrogen to evaporate condensate compared to methane. They found that methane re-evaporated the condensate and resulted in complete recovery of all condensate. The recovery due to nitrogen injection reached up to 94%, but it decreased when the pressure was lowered below the dewpoint pressure. The recovery of condensate was found to be more sensitive to dispersion during nitrogen injection than that during methane flooding. They recommended using nitrogen for gas injection based on availability and cost.

Methane can evaporate more condensate than nitrogen. Siregar et al. (1992) reported that the evaporation capacity of methane is more than 20 times higher than that of nitrogen. The only disadvantage of using nitrogen injection is raising the dewpoint pressure and the liquid dropout of the base reservoir fluid/injected gas mixture (Moses and Wilson, 1981; Sänger and Hagoort, 1998; Siregar and Hagoort, 1992; Piers et al., 1995). Water flooding may be selected as an option for reservoir pressure maintenance, especially if there is an underlying aquifer that is providing a strong water drive. For rich gas-condensate reservoirs, water flooding above the dewpoint pressure would be the preferred option for maximizing condensate recovery (Henderson et al., 1991).

Hydraulic fracturing has been used to enhance gas productivity, but is not always feasible or cost-effective (Engineer, 1985; Rajeev, 2000; Antoci et al., 2001). The success of a hydraulic fracture treatment depends on the placement of sufficient quantity of proppant without changing the integrity of the formation and the clean up rate of fracture fluids after the treatment. Inducing hydraulic fractures into the formation can increase the bottom hole pressure. Hydraulic fracturing successfully restored the gas productivity of a well that died after the flowing bottom hole pressure dropped below the dewpoint (Barnum et al., 1995).

Alcohols have been used to enhance gas and oil recovery. Gatlin (1959) investigated the use of various alcohols to recover oil. He found experimentally that a slug of isopropyl alcohol (IPA) completely displaces both oil and water. Total oil recovery was achieved with a smaller slug of either IPA or a mixture of methanol and IPA.

Stimulation fluids containing alcohol have been shown to be highly successful in stimulating gas production from problem wells in sandstone formations (McLeod and Coulter, 1966). Use of alcoholic hydrochloric acid as a pre-flush and after-flush resulted in an increase in gas injection rates by a factor of seven.

Hernández et al. (1994) described the use of methanol as a fracture fluid in gas wells. Methanol has the following desirable properties (Malone, 2001; Antoci et al., 2001), miscibility with water, low surface tension (22.6 dynes/cm), and high vapor pressure. Mixing methanol with the formation water near the face of the fracture produces a reduction of the surface tension of the aqueous phase. This expedites the clean up process of the formation water, where it decreases the saturation of water and increases the permeability of the gas. The methanol can displace water it mixes with even below residual water saturation (Malone, 2001). Core flow experiments showed that flowing methanol after kerosene increased the permeability by a factor of 1.7, while flowing 2% KCl brine reduced the permeability by 60%. Field applications showed that wells fractured with methanol gave higher productivity than the others treated with other fracture fluids (Hernández et al., 1994; Malone, 2001; Antoci et al., 2001).

Methanol was used as a prepad of fracture fluid to stimulate a water-sensitive sandstone formation (Ortiz and McLane, 1986). Several wells treated with the conventional crosslinked 40/60-lbm hydroxypropyl guar (HPG) in KCl-water-based fluids resulted in a very low productivity enhancement. Treated wells showed a rapid decline in production after the conventional treatments due to water blocking. An average recovery of 20% of the treating fluid after proppant placement confirms the effect of water blocking on gas productivity. The use of methanol showed an effective enhancement compared to the conventional water-based completion fluid.

Methanol increases the vaporization rate of water from solution. Interfacial tension reduction reduces the capillary forces holding a liquid in the rock. Production of a gas well stimulated with alcoholic acid increased from 870 MSCF/D to 6200 MSCF/D (McLeod et al., 1966). Adding volatile solvents, such as methanol, to the completion fluids increases the gas deliverability by decreasing the clean up process after the treatment (Kamath and Laroche, 2000).

Recently, a new strategy of using solvents was developed to increase gas relative permeability reduced by condensate blocking (Du et al., 2000; Al-Anazi et al., 2002). Methanol was found to be effective for removing condensate and water and restore gas productivity in low permeability limestone cores. This study is a continuation of that research to explore the effect of condensate blocking in high permeability cores and quantifies the volumes of methanol required.

1.3 GAS-CONDENSATE RESERVOIR STUDIES

As mentioned before, a decrease in well productivity occurs due to condensate blockage near a well when the bottom hole flowing pressure falls below the dewpoint. The condensate phase is trapped by the capillary forces in the rock pores near the well causing its saturation to increase until it reaches a critical value. This residual oil saturation combined with the residual water saturation reduces the gas relative permeability, therefore causing a significant decline in the productivity of the well.

Gas relative permeability is a function of interfacial tension between gas and condensate among other variables. Many experimental studies have shown the effect of interfacial tension on the gas relative permeability. The gas relative permeability increases as the interfacial tension between gas and condensate decreases. However, it was recognized long ago (Brownell and Katz, 1947) that in general, relative permeabilities are functions of the ratio of viscous to interfacial forces on the trapped phase. This ratio was defined as the capillary number. The Bond number was defined to quantify the ratio of the buoyancy forces to the interfacial forces, which also contributed to the total force on the trapped phase (Bardon and Longeron, 1980).

Leemput et al. (1995) investigated the well impairment in Central Oman gas-condensate fields due to near well condensate accumulation. Damage was assessed using measured, capillary number dependent, relative permeability curves. Henderson et al. (1996) found that the key parameter controlling the increase in relative permeability is the Bond and capillary numbers and not the IFT alone.

Fevang and Whitson (1996) developed a pseudo-pressure method for modeling the deliverability of gas condensate wells. Well deliverability was calculated using a modified pseudo-pressure function and required producing GOR data along with PVT properties and gas-oil relative permeabilities. The gas-condensate reservoir was represented by three regions: a near-well region where both oil and gas are mobile, a region where condensate accumulates and only gas flows, and a region containing single-phase original reservoir gas. The method was successfully tested for radial, vertically fractured, and horizontal wells. Whitson and Brule (2000) discussed a modified black oil PVT formulation of this problem. Both the presence of liquid content in gas and gas content in liquid were taken into account. Their formulation requires accurate producing GOR data.

Blom and Hagoort (1998) presented a numerical method to calculate the well impairment based on steady-state radial flow. The method incorporated near-critical relative permeability and saturation-dependent inertial resistance. Their results showed that the improved mobility of the gas phase caused by a higher capillary number enhances the importance of the inertial resistance. The effect of non-Darcy flow was shown to be much more pronounced in gas-condensate reservoirs than in dry gas reservoirs.

Narayanswamy (1998) and Narayanswamy et al. (1999) studied the effects of non-Darcy flow and changes in relative permeability due to capillary number on well productivity index (PI). These results show that when considering only non-Darcy flow, the condensate bank can cause an order of magnitude reduction in PI, but a more accurate prediction of PI is possible when both non-Darcy flow and capillary number effects are considered.

Pope et al. (2000) developed a new model to relate phase relative permeabilities to trapping number, which is a generalization of the capillary and Bond numbers to account for both effects on phase trapping. Kumar (2000) studied the effect of hydraulic fractures to improve the productivity of gas-condensate wells by conducting numerical simulations. His results showed a significant increase in productivity after fracturing. The effects of various factors such as fracture length, fracture conductivity, formation permeability, gas relative permeability, production mode, gas composition, and permeability heterogeneity were studied.

Marker (2000) simulated the use of solvents in gas condensate reservoirs to improve the productivity. These simulations showed a significant increase in the well productivity after methanol injection in a gas condensate reservoir that has been produced under the dewpoint pressure. Due to higher liquid dropout, injection of 2-propanol and 2-butanol yielded a lower increase in the productivity than the increase with the use of methanol.

Wheaton and Zhang (2000) developed a new analytical model in order to understand the accumulation of heavier components near the well. The rate of change in heavy component composition was shown to be higher for rich gas and the effect of condensate blocking more acute for low-permeability, high-yield reservoirs. Also, once condensate accumulation has occurred, it is not possible to remove the bank by shutting in the well and letting the pressure increase above the initial dewpoint pressure.

Ahmed et al. (2002) presented a study of the impact of pressure depletion on production for Ghawar gas-condensate reservoirs in Saudi Arabia. Effects of condensate dropout on the well productivity with and without hydraulic fractures were shown. Effects of non-Darcy flow were also investigated. Results showed that condensate saturation is lower in fractured case than that without fractures and hence the decline in well productivity is less. It was also shown that hydraulic fractures minimize the non-Darcy effects for gas wells.

Briones et al. (2002) studied the phenomenon of condensate stripping near the well for Santa Barbara Field in Venezuela using well test analysis. A decrease in gas relative permeability from 90 % to 15 % was reported. Success of a hydraulic fracture in bypassing condensate bank was shown to depend on a good design. Despite a big improvement in pressure differential, the condensate bank was not bypassed completely.

Mott (2002) further developed the pseudo-pressure approach by including the region where only gas flows and condensate builds up. The expansion of the condensate bank was also taken into account and was calculated on the basis of a material balance. The method was tested by comparison with the results of fine grid simulations.

Ayyalasomayajula et al. (2002) studied the phase behavior of a four-component gas-condensate mixture with water and methanol using Peng-Robinson and SAFT equations-of-state. Their study showed that the SAFT equation-of-state could model the water-methanol-hydrocarbon mixtures with better accuracy than the PREOS. Ayyalasomayajula (2003) implemented the SAFT equation-of-state in the University of Texas compositional simulator (UTCOMP) and used it for predicting bulk and interfacial thermodynamic properties of polar mixtures.

Sharma (2003) performed a simulation on the Hatter's Pond gas-condensate reservoir to understand the effect of near-well condensate build up and the related decrease in gas relative permeability including the trapping number (interfacial tension) effect. He found that the effect of condensate blocking on the well productivity was very large and the total liquid saturation (condensate and water) was very large, so the gas relative permeability was very small. The trapping number has a significant effect on well productivity. Production rates with trapping number were found to be 20 to 30% higher than those without the trapping number. Sharma developed a new hybrid well model for better resolution close to wells. The new hybrid model captures the near-well behavior accurately and is much faster compared to a fine-grid compositional simulation.

1.4 OBJECTIVES

The objectives of this research were to investigate:

- The effect of condensate blocking on gas relative permeability in low and high permeability cores.
- The effect of initial water saturation on the reduction in gas relative permeability.
- The effect of flow rate on gas relative permeability.
- The effect of methanol treatment size on gas productivity improvement.
- The effect of multiple methanol treatments.
- The revaporization of condensate with methane flooding.
- The impact of non-equilibrium effects on condensate accumulation.

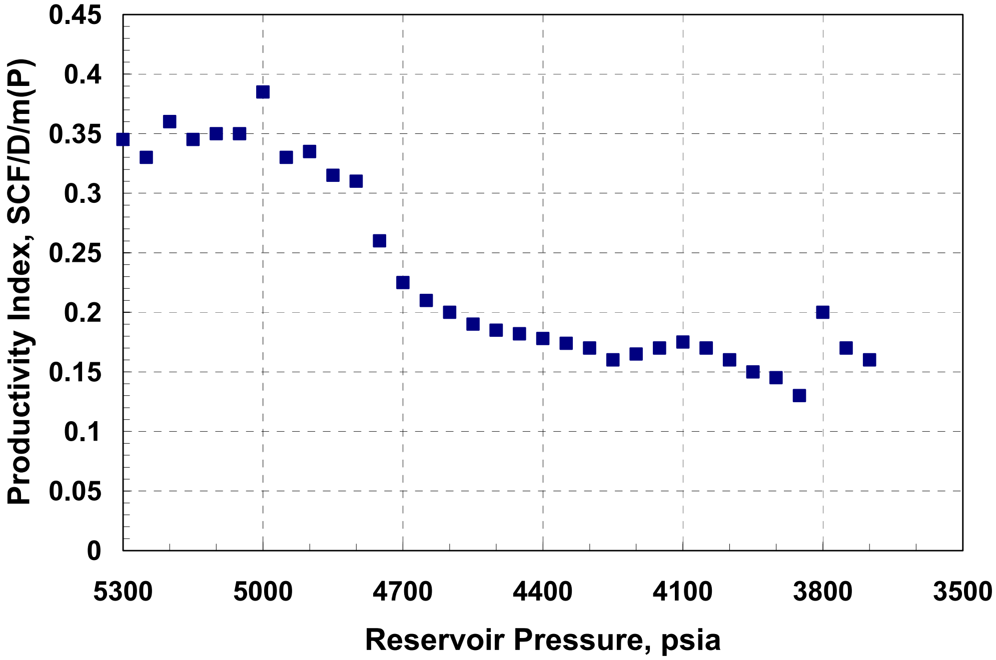

Figure 1.1: Productivity index for the Arun gas-condensate reservoir (Afidick et al., 1994).

Chapter 2: Phase Behavior Studies

This chapter describes pressure-volume-temperature (PVT) experiments conducted to study the phase behavior of several multi-component mixtures. The objectives of this study were to understand the phase behavior of the selected mixtures and to select the proper temperature and pressure conditions for the coreflood experiments. Two types of phase behavior experiments were used in this study: liquid dropout measurements and miscibility of methanol with hydrocarbons.

2.1 GAS MIXTURE PREPARATION

The synthetic gas-condensate mixture used in this study consisted of four components: methane (C_1), n-butane (n-C_4), n-heptane (n-C_7), and n-decane (n-C_{10}). The experimental composition of the gas mixture is given in **Table 2.1**. The gas mixture was prepared in the laboratory using the following procedure. A high-pressure accumulator with a rodded piston was cleaned and vacuumed. The volume of the accumulator was measured with distilled water. Water was injected into the vacuumed accumulator until it was full and the piston reached the other end. The water was displaced with compressed air and collected in a two-liter flask. The weight of the collected water was measured using a digital balance. From the measured weight and density (0.997 gm/mL) of water, the volume of the accumulator was found to be 1,431 mL.

In the preparation of the gas mixture, heavy components (n-C_{10} and n-C_7) were mixed together and added first into the accumulator as liquids. n-C_4 and C_1 were then metered in. Methane is supplied in a high-pressure cylinder. The molar volume of methane was calculated using the Peng-Robinson equation-of-state (PREOS) at a selected pressure and room temperature (25°C). From that the total moles of gas mixture can be found. Then, number of moles of each component can be calculated using the desired mole fractions. The amount of each n-C_{10} and n-C_7 in weight was determined from its number of moles using the molecular weight. The weighed amounts of both n-C_{10} and n-C_7 are mixed together and poured in a burette that has a screwed tube connected to its nozzle. The burette's tip and tube were flushed with hydrocarbon to assure they are free from air. The dispensed amount of liquid was returned back into the mixture in the burette. The line was connected to the vacuumed accumulator. The n-C_{10} and n-C_7 mixture transferred into the accumulator with the care that the system is an air-free.

Normal butane (n-C_4) was supplied in a compressed liquid form at 25 psig with a purity of >99.63%. The n-C_4 was transferred in a 1,000 mL RUSKA pump that has a pressure relief value set to 1,000 psig. The n-C_4 was compressed into the RUSKA pump at 1,000 psig. Once the pressure reaches the set pressure, n-C_4 starts to flow from the pump. The molar volume of n-C_4 was determined using the PREOS at 1,000 psig and 25°C. Then, the volume of n-C_4 that corresponds to the required moles can be calculated using the molar volume and its number of moles. The pump line was flushed with n-C_4 and then connected to the accumulator that has n-C_7 and n-C_{10} mixture. The compressed n-C_4 was continuously injected by volume. The accumulator was disconnected from the n-C_4 pump and rocked well to mix the components. A RUSKA hand pump was filled with methane at the selected pressure. The pump lines were flushed with methane and connected to the mixture accumulator. The required volume of methane at this selected pressure was injected into the accumulator.

Finally, the accumulator was rigorously mixed and placed inside the oven at 145°F. Then, it was pressurized to 3,000 psig by injecting water from the bottom-side of the piston using the RUSKA pump. The accumulator was removed from the oven and rocked to ensure mixing and then returned back into the oven. The accumulator pressure was monitored over time. More water was pumped to raise the pressure to 3,000 psig. The gas mixture was kept inside the oven at 145°F and 3,000 psig at least 24 hours to assure it reached an equilibrium state before it was used in the experiment. A more detailed example illustrating the gas preparation procedure is given in **Appendix A**. The same procedure was followed to prepare other gas mixtures.

2.2 APPARATUS

2.2.1 Pumps

A RUSKA pump (Model 1458) was used to inject fluids at a constant rate. This pump was rated to a maximum pressure of 10,000 psi and has two cylinders with a capacity of 500 mL each. The pump can deliver variable rates from 1 to 224 mL/hr using one cylinder. Running both cylinders at the same time can double the pump rate. An ISCO syringe pump (Model LC-5000) was also used in these studies. The ISCO pump can deliver fluids either at a constant flow rate or constant flowing pressure. The LC-5000 pump has a capacity of 500 mL. Flow rates range from 0.06 to 400 mL/hr at a pressure rating of 3,700 psi. Any flow rate may be selected by setting a range switch calibrated in mL/hr and a 0-100% knob to determine the desired percentage of the range setting.

2.2.2 Through-Window PVT Cell

A through-window PVT Cell (Model 2329) purchased from RUSKA was used in our PVT tests. The cell has two windows mounted opposite each other to allow see-through visibility. The windows are made of optical quality glass and chemically treated for hardness. They are approximately 1 inch thick and bolted to the cell body to minimize stress around the edges, which could crack the glass. The PVT cell was rated for a temperature range of ambient to 300°F and a working pressure of 10,000 psi at 300°F. The manufacturer tested the cell for a pressure of 15,000 psi at 300°F. The volume of the cell was measured using distilled water and found to be 96.49 mL. The inside diameter of the cell is 3.5682 cm. Therefore, one millimeter of height viewed through the windows corresponds to 1 mL of volume in the cell. A light was placed behind one window to allow easy detection of the gas-liquid interface level.

2.2.3 Accumulators

Accumulators purchased from TEMCO, Inc. were used in this study. Two types of accumulators were used: rodded and floating piston accumulators. All the accumulators are rated for a temperature up to 350°F and a working pressure of 5,000 psi. The manufacturer tested them for 7,500 psi. The diameter of the piston is 2.5 inches. The volume of the accumulators is approximately 1,500 mL. A Teflon® piston is used in these accumulators to allow easier movement of the piston inside the honed cylinder.

2.3 EXPERIMENTAL STUDIES

2.3.1 Liquid Dropout Measurements

Liquid dropout of the selected gas mixture was measured using the through-window PVT Cell (RUSKA Model 2329). The volume of the cell is 96.49 mL and its inside diameter is 3.5682 cm. The PVT cell was pressurized to 3,000 psig with distilled water. The gas mixture was transferred into the PVT cell by drawing the water from the bottom while injecting the gas mixture from the top at a constant pressure of 3,000 psig using the ISCO syringe-pump. The volume of gas injected was one-third of the total volume of the cell at a pressure of 3,000 psig. The liquid dropout measurements for the gas mixture were performed at 145°F using a constant composition expansion (CCE) method. The pressure of the cell was slowly decreased in steps by drawing water from the bottom with the RUSKA pump while the top valve was closed. The volume of the liquid formed was measured with a cathetometer. The accuracy of the cathetometer is ±0.01 cm.

Once pressure of the cell reached the dewpoint pressure, the color of the gas-phase changed from clear to dark brown. The first droplets of liquid formed when the color changes to foggy white. After the dewpoint pressure was determined, the pressure was gradually decreased by 10-30 psig. The cell was rocked to reach equilibrium. When the pressure of the cell did not change with time, the hydrocarbon liquid volume was measured. Measurements were carried on until the gas phase filled the PVT cell. The liquid dropout (LDO) of the gas mixture was calculated using the following equation:

$$\mathrm{LDO} = \frac{V}{V_t} \times 100 \tag{2.1}$$

where V is the volume of liquid (condensate) collected at a given pressure, and V_t is the total volume of the gas mixture (gas and condensate) at this pressure. The LDO can also be calculated referenced to the volume of the gas mixture at the dewpoint pressure (V_{dew}) as follows:

$$(\mathrm{LDO})_d = \frac{V}{V_{dew}} \times 100 \tag{2.2}$$

2.3.2 Alcohol-Hydrocarbon Solubility

The phase behavior of the gas mixture was investigated in the presence of methanol. A predetermined amount of methanol was placed inside a glass vial with a capacity of 20 mL. Then, a small amount of liquid hydrocarbon was added to the vial. The mixture was vigorously shaken. An additional hydrocarbon amount was added until it formed two phases. The volume of each phase was measured. Each mixture was placed in a water bath at room temperature. Next, the temperature of the bath was increased by 10°C until it stabilized (based on a reading of the thermometer). The volume of each phase was quickly measured at the stabilized temperature and the vial was returned back into the water bath. The solubility of both normal heptane and decane in methanol was measured at 1 atm and various temperatures ranging from 25 to 97°C.

2.4 RESULTS AND DISCUSSION

2.4.1 Liquid Dropout Measurements

Figure 2.1 shows the liquid dropout (V/V_t) curve for the gas mixture measured at 145°F using the CCE method. The measured dewpoint pressure for this gas mixture was found to be 2,792 psig. Since there are several ways to represent the liquid dropout of such a gas mixture, the measured liquid dropout can be illustrated with reference to the volume at the dewpoint pressure (V_{dew}). **Figure 2.2** depicts the liquid dropout (V/V_{dew}) data for the gas mixture.

The Peng-Robinson equation-of-state (PREOS) with zero binary interaction coefficients and using the critical properties given in **Table 2.2** was used to calculate the liquid dropout for the gas mixture. The volume shift parameter was set to zero in the PREOS. The use of a volume shift parameter affects the PREOS values of liquid dropout since the liquid density is corrected to agree with experimental densities, so it should be used in future calculations to make them more accurate. The PREOS predicted a higher liquid dropout compared with the measured data. The most likely source of this variation is inaccuracy in the gas composition. Therefore, the composition of the gas mixture was adjusted so that the PREOS curve would match the data. **Table 2.3** gives the adjusted composition of the gas mixture. Only small adjustments were needed.

Figure 2.3 compares the measured and the calculated liquid dropout at 145°F. **Table 2.4** compares the measured and calculated dewpoint pressure and maximum liquid dropout at 145°F. The difference between the measured and calculated values is very small. Another possible source of error is due to use of the PREOS to calculate the density of each component. Error in calculating the density affects the number of moles used to prepare the gas mixture. In addition, fluctuations in the temperature of the laboratory could cause the actual and calculated densities to be different (Walker, 2000).

The adjusted composition of the gas mixture was used in all further calculations. **Figure 2.4** shows the phase envelope computed from the PREOS using the adjusted composition. The critical point of the gas mixture is at 96.37°F and 2,756.14 psia. The phase envelope shows that the selected coreflood conditions (1,200 psig and 145°F) are in the retrograde region. Based on the calculations, the expected liquid dropout at 1,200 psig and 145°F is 7.14%.

Figure 2.5 compares the phase envelope of the experimental and adjusted composition of the gas mixture. Increasing the concentration of heavy components shows a small shift in the phase envelope.

2.4.2 Methanol-Hydrocarbon Solubility

Solubility of methanol with both n-heptane and n-decane was studied at various temperatures ranging from room temperature (25°C) to 97°C. Methanol was found to be miscible with both hydrocarbons at 25°C up to 8.58 mole% of n-C_7 and 3.21 mole% n-C_{10}. Above these concentrations, the mixture forms two phases: a hydrocarbon phase and a methanol-rich phase. **Figure 2.6** shows a methanol-n-heptane binary mixture at 25°C. As the concentration of n-C_7 increases, the methanol-rich phase decreases. Miscible displacement occurs when the concentration of n-C_7 is less or equal to 8.58 mole%. Since the concentration of n-C_7 in the gas mixture is less than this value, miscible displacement is expected to be dominant during core treatments with methanol.

Figure 2.7 depicts a methanol-n-C_7 binary mixture at different temperatures. The methanol-rich phase decreased as the temperature was increased. Since these tests were performed at atmospheric pressure, the miscibility is expected to increase at higher pressure. As the temperature reached the boiling point of methanol (T_b = 64.5°C), methanol evaporated leaving a very small volume of the methanol-rich phase. Above this temperature, most of the methanol exists at small concentrations in the n-C_7 phase until the boiling temperature of n-C_7 (T_b = 98.43°C) is reached. At the highest temperature (97°C) examined, a single vapor phase was obtained because both methanol and n-C_7 reached their boiling point temperatures.

Figure 2.8 shows a methanol-n-decane binary mixture at 25°C. The methanol-rich phase decreased as the concentration of n-C_{10} was increased. It shows the same trend as that observed with n-C_7, except the volume of the methanol-rich phase is less. This is because the miscibility of methanol with n-C_{10} (3.21 mole%) is less than that with n-C_7 (8.58 mole%). The effect of temperature on a methanol-n-decane binary mixture is illustrated in **Figure 2.9**. The effect of temperature on the miscibility of n-C_{10} with methanol is less compared to that of n-C_7 due to the high boiling point temperature (T_b = 174°C) of n-C_{10}. Walker (2000) investigated the solubility of the gas mixture in methanol and water at 1,200 psig and 145°F.

Table 2.1: Experimental composition of the gas mixture.

Component	Mole Fraction
Methane	0.785
n-Butane	0.150
n-Heptane	0.050
n-Decane	0.015

Table 2.2: Critical properties of hydrocarbons used in PREOS calculations.

Component	MW	T_c, °K	P_c, atm	ω	Z_c
Methane	16.040	190.60	45.40	0.0080	0.7614
n-Butane	58.120	425.20	37.50	0.1930	0.1665
n-Heptane	100.250	540.30	27.40	0.3510	0.0555
n-Decane	142.290	617.60	20.80	0.4900	0.0166

Table 2.3: Adjusted composition of the gas mixture.

Component	Mole Fraction
Methane	0.800
n-Butane	0.150
n-Heptane	0.038
n-Decane	0.012

Table 2.4: Measured and calculated dewpoint pressure and maximum liquid dropout of the gas mixture at 145°F.

	Measured	Calculated
Dewpoint Pressure, psig	2,792	2,795
Maximum Liquid Dropout, vol.%	18.18	18.23

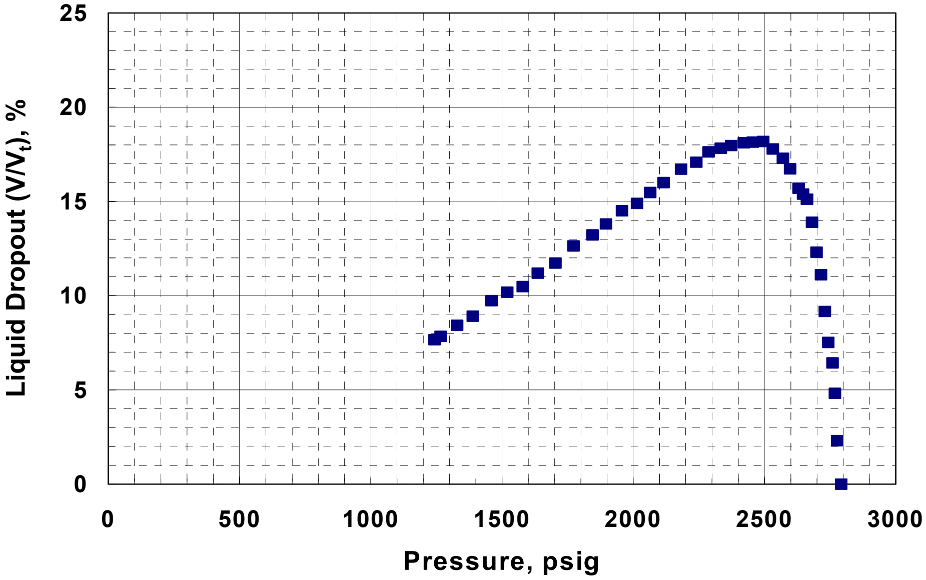

Figure 2.1: Measured liquid dropout (V/V$_t$) curve of the gas mixture at 145°F.

Figure 2.2: Measured liquid dropout (V/V$_{dew}$) curve of the gas mixture at 145°F.

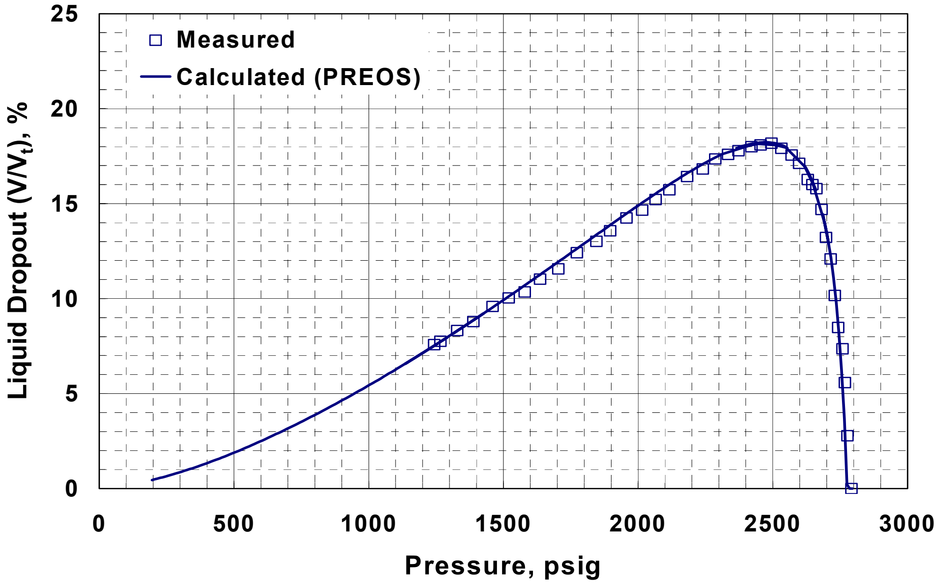

Figure 2.3: Liquid dropout (V/V_t) curves of the gas mixture at 145°F.

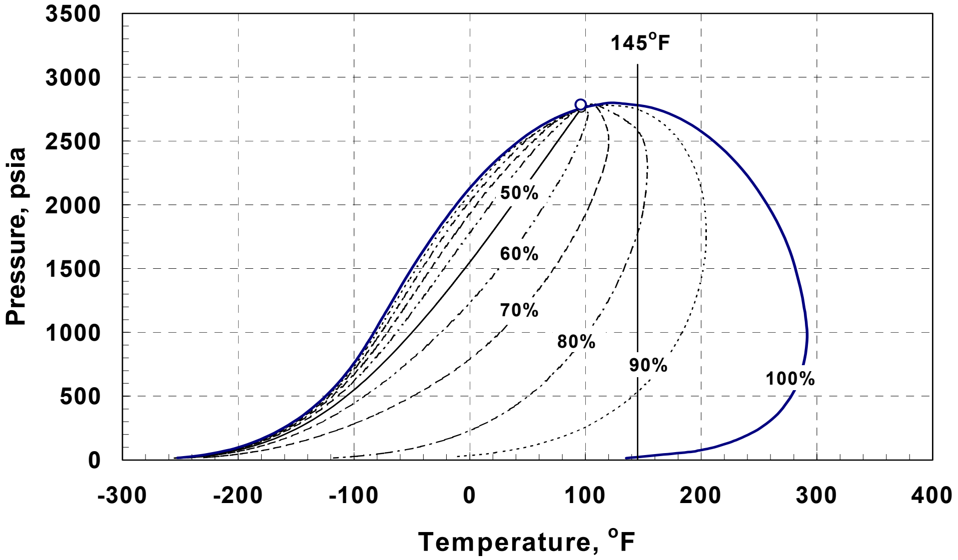

Figure 2.4: Phase envelope of the gas mixture generated by the PREOS.

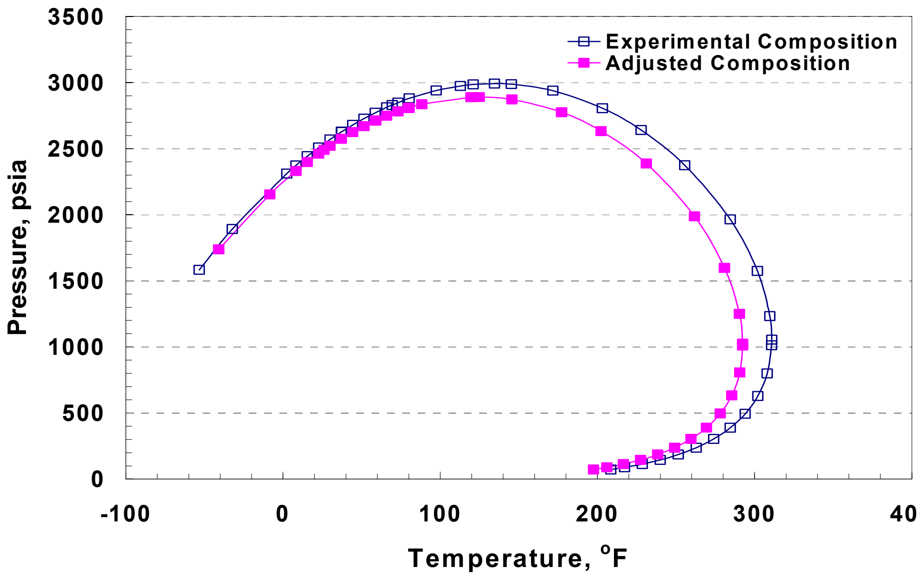

Figure 2.5: Phase envelope (vapor/liquid =1.0) calculated for experimental and adjusted composition of the gas mixture.

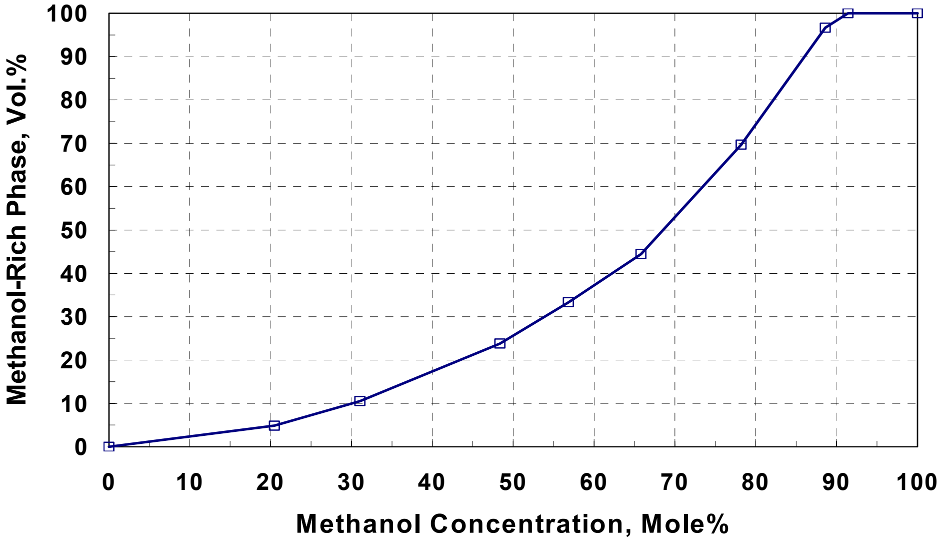

Figure 2.6: Methanol-n-heptane binary mixture at 25°C.

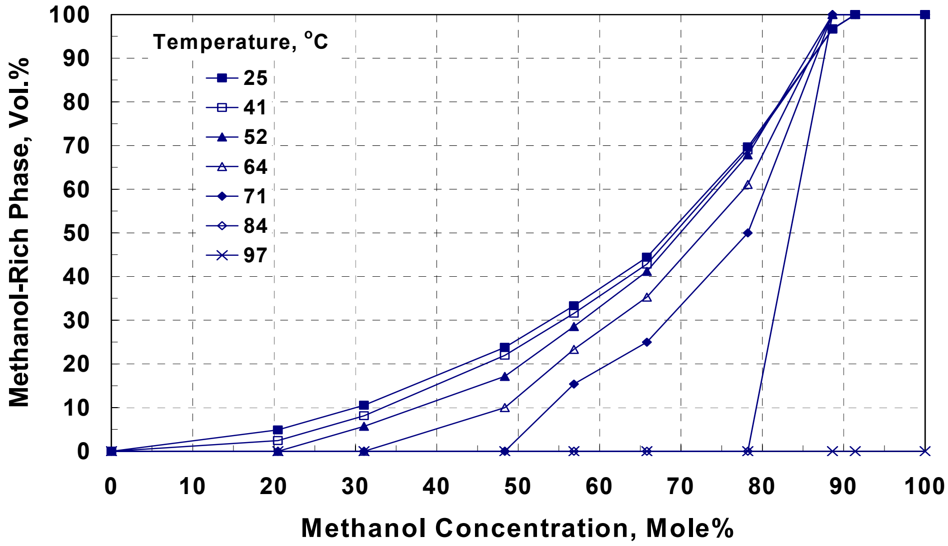

Figure 2.7: Methanol-n-heptane binary mixture at different temperatures.

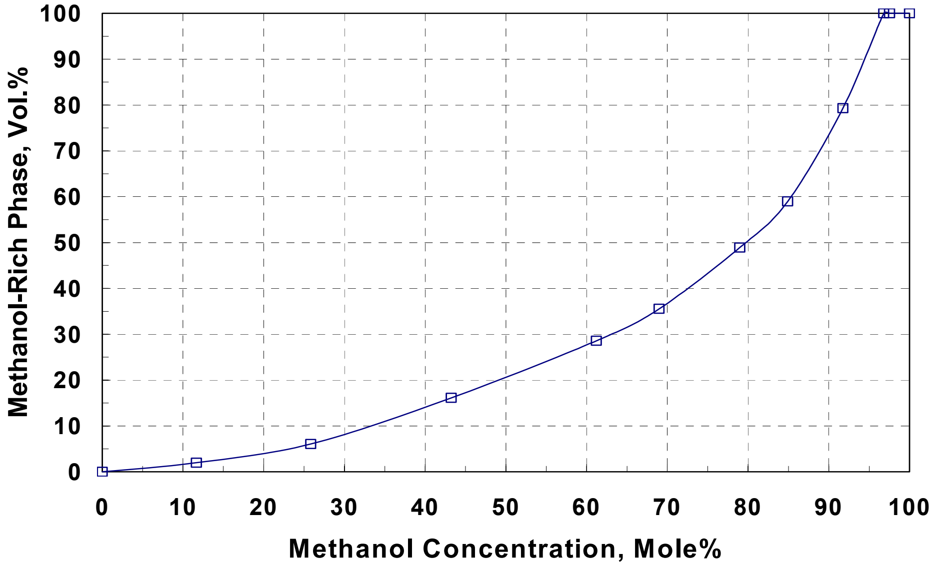

Figure 2.8: Methanol-n-decane binary mixture at 25°C.

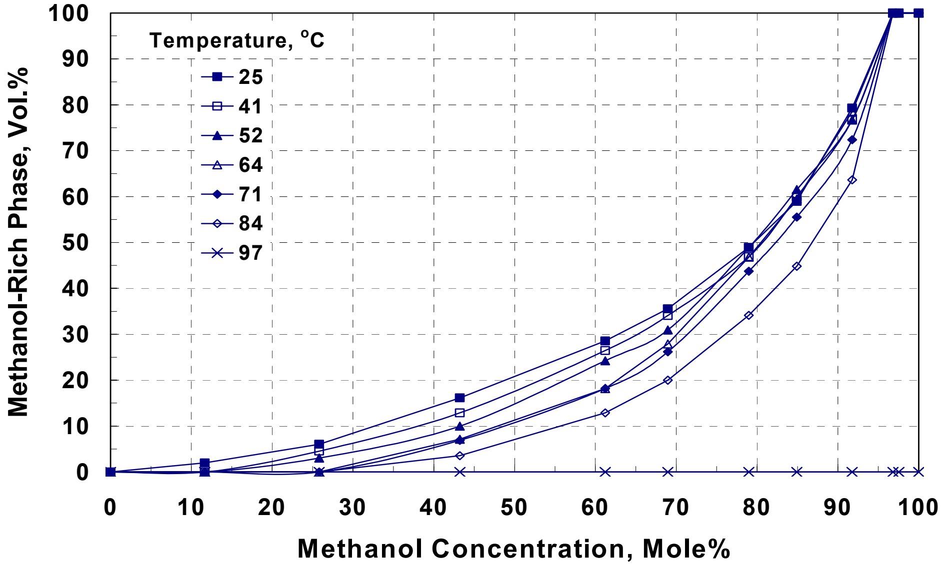

Figure 2.9: Methanol-n-decane binary mixture at different temperatures.

Chapter 3: Solubility of Salts in Alcohol-Water Mixtures

3.1 INTRODUCTION

The objective of this chapter is to investigate the solubility of salts in alcohol-water mixtures. It has been found that mixing alcohol with a high salinity solution can result in salt precipitation (Kamath and Laroche, 2000; Walker, 2000). For example, mixing alcohol with highly concentrated sodium chloride brines can cause sodium chloride to precipitate (McLeod and Coulter, 1966). Therefore, the compatibility of methanol with different brines needs to be explored before using it as a solvent to remove condensate and water blocks.

3.2 CHEMICALS

3.2.1 Salts

Sodium chloride (NaCl) was supplied from EM Science in a 2.5 kg plastic container. It is a 99% pure analytical grade salt. Calcium chloride ($CaCl_2$) anhydrous was purchased from Fisher Scientific in the form of pellets of 4-20 mesh in a 500gm container. Potassium chloride (KCl) was from J. T. Baker Inc. with a purity of 99.3%. The insoluble matter was reported to be less than 0.002%.

3.2.2 Alcohols

Methanol (CH_3OH) was purchased from Mallinckrodt AR in a 1.06 gal glass bottle. It meets ACS specifications. Ethyl alcohol was obtained from AAPER Alcohol and Chemical Co. in a 1.0 gal plastic container. Purity was not reported on the container.

3.3 EXPERIMENTAL PROCEDURE

A digital balance (Model Mettler PL200) with an accuracy of ±0.001gm was used in this experimental study. The experiments were conducted at ambient conditions (1 atm, 78°F). A pre-weighed amount of distilled water was placed in a glass tube. The weight of the distilled water was recorded. A certain amount of alcohol was weighed and mixed with distilled water inside the glass tube. A very small amount of salt was weighed and added to the alcohol-water mixture and mixed well. Sodium/calcium chloride was added to the mixture in steps and mixed vigorously until it formed a precipitate. Then, distilled water was carefully added until the precipitate started to dissolve. The total weight of water was recorded. The salt concentration is reported in parts per million (ppm).

The same procedure was performed on other mixtures with various alcohol-water ratios. Solubility of salts was also measured in both distilled water and alcohols.

3.4 RESULTS AND DISCUSSION

3.4.1 Solubility of Salts in Methanol-Water Mixtures

Table 3.1 gives the solubility of NaCl in methanol-water mixtures at 78°F. The maximum soluble concentration of NaCl in water was found to be 24.5 wt%. This value is close to that measured (25.8 wt%) by Walker (2000). Mixing the methanol with brines containing more than > 24.5 wt% of NaCl will result in precipitation. It is very important to know the chemical analysis of the brine present in the reservoir before the treatment with methanol to avoid such precipitation that may have an impact on well productivity. **Figure 3.1** shows the solubility curve of NaCl in methanol-water mixtures at 78°F. Precipitation occurs above the curve. As the amount of methanol in the mixture is increased, the solubility of NaCl decreases. The solubility of NaCl in pure methanol was found to be 0.1 wt%. This solubility was measured at ambient temperature; we expect it to be higher at elevated temperatures since the dissolution of NaCl in water is an endothermic process.

The solubility of $CaCl_2$ in methanol-water mixtures at 78°F is given in **Table 3.2**. The solubility of $CaCl_2$ is higher than that of NaCl in a methanol-water mixture at the measured temperature. Precipitates form in water when $CaCl_2$ concentration gets higher than 41.6 wt%. **Figure 3.2** shows the solubility curve of $CaCl_2$ in methanol-water mixtures at 78°F. This figure shows that the solubility of $CaCl_2$ decreases as the methanol fraction increases in the mixture. In pure methanol, $CaCl_2$ has a higher solubility (6.41 wt%) than NaCl. The solubility of $CaCl_2$ increases with temperature (Perry, 1984).

Since KCl brine is widely used during completion operations, its solubility was measured in alcohol-water mixtures. **Table 3.3** gives the solubility of KCl in methanol-water mixtures at 78°F. The solubility curve is shown in **Figure 3.3**. The solubility behavior of KCl is similar to that of NaCl in methanol-water mixtures. The solubility of salts in methanol-water mixtures is summarized in **Figure 3.4**.

The measured solubility of salts in water was compared with that reported in the literature. **Table 3.4** gives comparison between the measured and reported (Perry, 1984) values of salts solubility in water. There is good agreement between the measured and reported values.

3.4.2 Solubility of Salts in Ethanol-Water Mixtures

The solubility of NaCl in ethanol-water mixtures is given in **Table 3.5**. It can be seen that the solubility of NaCl in ethanol is less than that in methanol. The solubility curve for NaCl in ethanol-water mixtures at 78°F is shown in **Figure 3.5**. The solubility of NaCl decreases as the ethanol content increases. The maximum concentration of NaCl that dissolves in pure ethanol is 328 ppm.

Table 3.6 gives the solubility of $CaCl_2$ in an ethanol-water mixture and the solubility curve for $CaCl_2$ in an ethanol-water mixture at 78°F is shown in **Figure 3.6**. The solubility of $CaCl_2$ seems similar in both ethanol and methanol-water mixtures up to 50 wt% alcohol. Then, the solubility becomes less in ethanol than in methanol. For instance, the solubility of $CaCl_2$ in pure ethanol is less than that in methanol by a factor of 20.

Table 3.1: Solubility of NaCl in methanol-water mixtures at 78°F.

Methanol, g	Water, g	NaCl, g	Methanol, wt%	NaCl, ppm
0.0	11.826	3.853	0.0	245,742.71
1.262	10.125	2.907	8.83	203,372.04
2.010	9.114	2.302	14.97	171,458.36
3.081	8.142	1.914	23.45	145,695.36
4.226	7.376	1.613	31.98	122,058.27
5.018	5.200	0.813	45.49	73,701.39
6.037	4.134	0.377	57.23	35,741.37
7.051	3.170	0.184	67.77	17,683.81
8.082	2.572	0.120	75.01	11,137.92
9.197	1.532	0.068	85.18	6,298.05
10.025	0.973	0.014	91.04	1,271.34
10.117	0.860	0.011	92.07	1,001.09
10.068	0.0	0.010	99.90	992.26

Table 3.2: Solubility of $CaCl_2$ in methanol-water mixtures at 78°F.

Methanol, g	Water, g	$CaCl_2$, g	Methanol, wt%	$CaCl_2$, ppm
0.0	11.543	8.234	0.0	416,342.22
0.410	10.915	7.769	2.15	406,881.74
1.004	10.629	7.403	5.27	388,894.73
1.972	10.357	7.130	10.13	366,411.43
3.029	9.150	6.286	16.40	340,427.84
4.472	9.330	6.245	22.31	311,517.93
5.246	8.322	5.418	27.63	285,368.17
6.193	6.083	3.816	38.48	237,136.47
6.821	4.798	2.959	46.79	202,977.09
7.410	3.687	2.220	55.64	166,704.21
8.554	3.087	1.901	63.17	140,378.08
9.788	2.406	1.484	71.56	108,495.39
10.483	1.895	1.171	77.37	86,427.04
10.555	1.221	0.979	82.75	76,754.21
11.230	0.637	0.876	88.13	68,743.62
10.038	0.218	0.716	91.49	65,257.02
10.010	0.0	0.686	100.00	64,136.13

Table 3.3: Solubility of KCl in methanol-water mixtures at 78°F.

Methanol, g	Water, g	KCl, g	Methanol, wt%	KCl, ppm
0.0	13.149	4.211	0.0	242,569.12
1.082	10.447	3.166	7.36	215,447.43
1.082	8.910	2.498	8.66	200,000.00
2.394	13.278	3.424	12.54	179,304.57
2.394	9.043	2.077	17.71	153,692.47
3.577	7.644	1.296	28.58	103,539.19
5.012	6.600	0.670	40.81	54,551.38
7.440	5.703	0.226	55.65	16,904.78
8.866	4.872	0.054	64.28	3,915.31
10.022	2.307	0.010	81.22	810.44
10.022	0.0	0.0	100.00	0.0

Table 3.4: Measured and reported values of salt solubility in water.

	Solubility, ppm	
Salt	Measured at 78°F	Reported[a] at 68°F
KCl	242,569.12	253,731.34
NaCl	245,742.71	264,705.88
$CaCl_2$	416,342.22	426,934.10

[a]Perry (1984).

Table 3.5: Solubility of NaCl in ethanol-water mixtures at 78°F.

Ethanol, g	Water, g	NaCl, g	Ethanol, wt%	NaCl, ppm
0.0	11.826	3.853	0.0	245,742.71
0.522	12.608	4.054	3.04	235,917.13
1.389	11.865	2.912	8.59	180,131.14
4.175	8.482	0.516	31.69	39,171.03
7.030	8.650	0.215	44.23	13,526.27
7.030	6.343	0.088	52.22	6,537.40
8.057	6.519	0.057	55.06	3,895.31
9.144	4.45	0.020	67.17	1,469.08
9.144	0.0	0.003	99.97	327.98

Table 3.6: Solubility of $CaCl_2$ in ethanol-water mixtures at 78°F.

Ethanol, g	Water, g	$CaCl_2$, g	Ethanol, wt%	$CaCl_2$, ppm
0.0	11.543	8.234	0.0	416,342.22
0.928	9.873	6.855	5.26	388,253.29
1.948	9.975	6.363	10.65	347,971.13
3.105	7.681	4.797	19.93	307,835.46
4.242	6.806	4.046	28.10	268,053.53
6.110	6.515	3.921	36.93	236,975.70
6.110	4.246	2.458	47.68	191,821.45
10.054	3.578	1.377	66.99	91,744.95
10.054	3.137	0.863	71.54	61,406.01
10.054	2.199	0.491	78.89	38,527.93
10.054	1.516	0.310	84.63	26,094.28
10.054	0.525	0.121	93.96	11,308.41
10.054	0.205	0.044	97.58	4,270.60
10.054	0.0	0.034	100.00	3,370.34

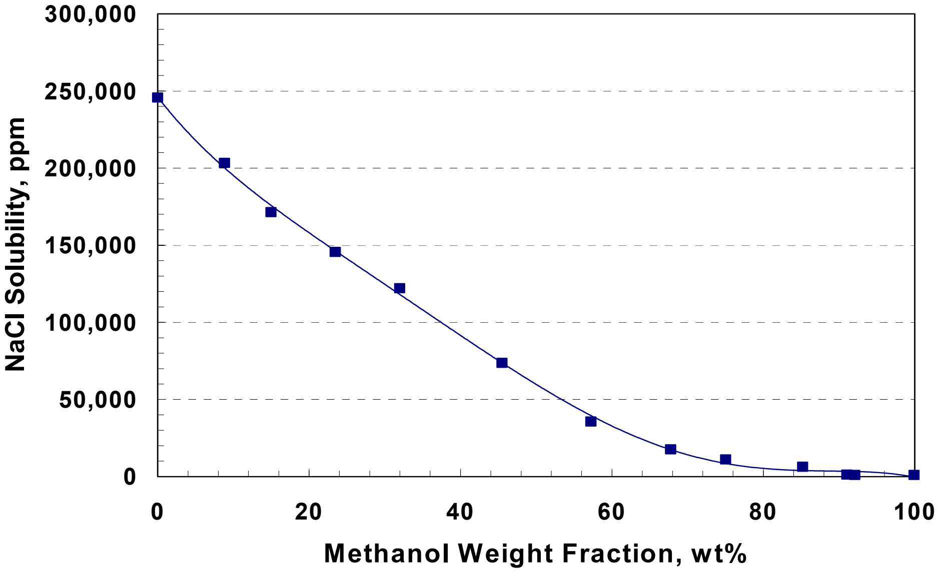

Figure 3.1: Solubility of NaCl in methanol-water mixtures at 78°F.

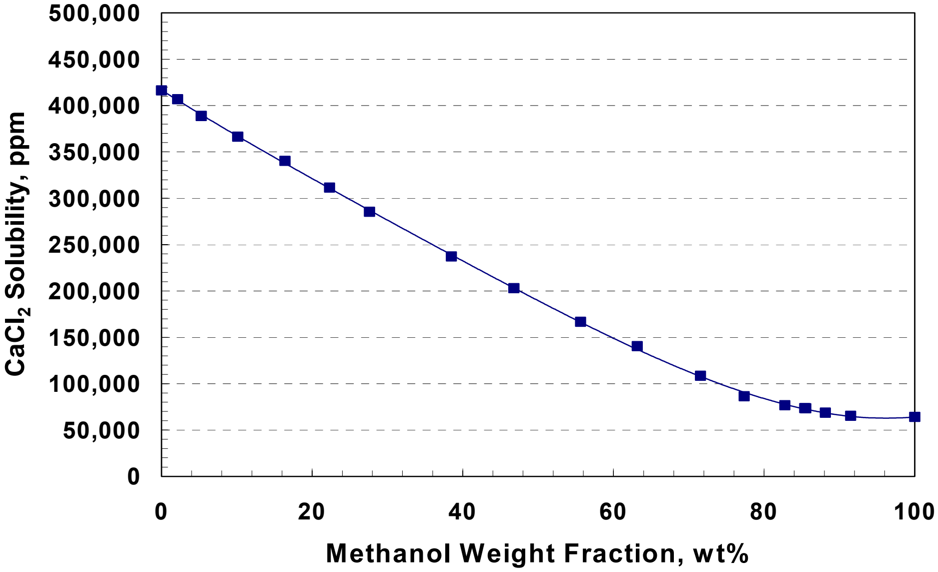

Figure 3.2: Solubility of $CaCl_2$ in methanol-water mixtures at 78°F.

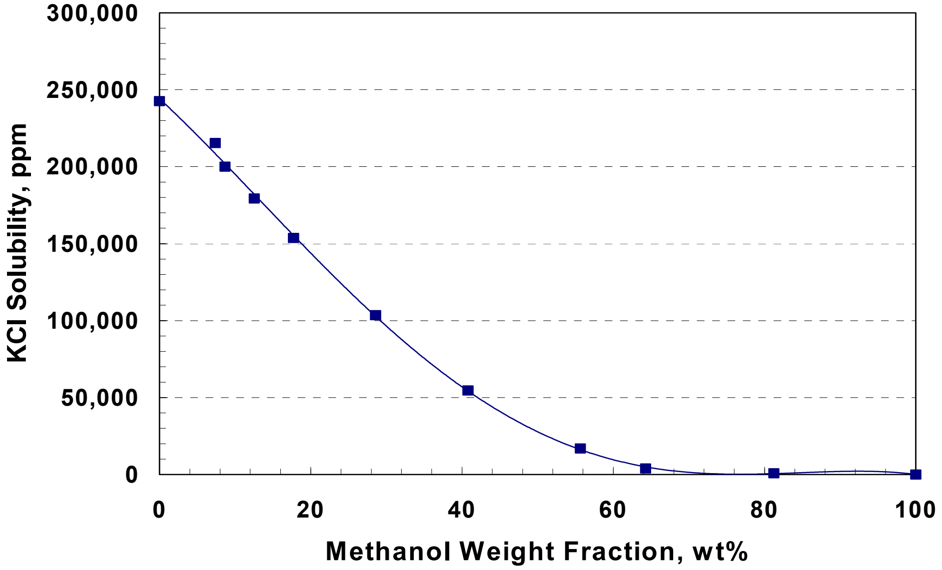

Figure 3.3: Solubility of KCl in methanol-water mixtures at 78°F.

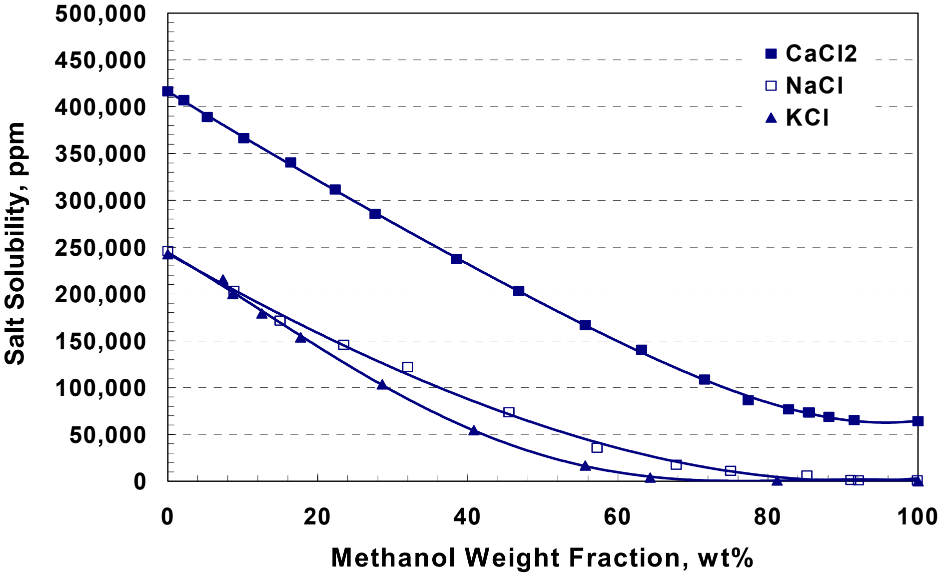

Figure 3.4: Solubility of salts in methanol-water mixtures at 78°F.

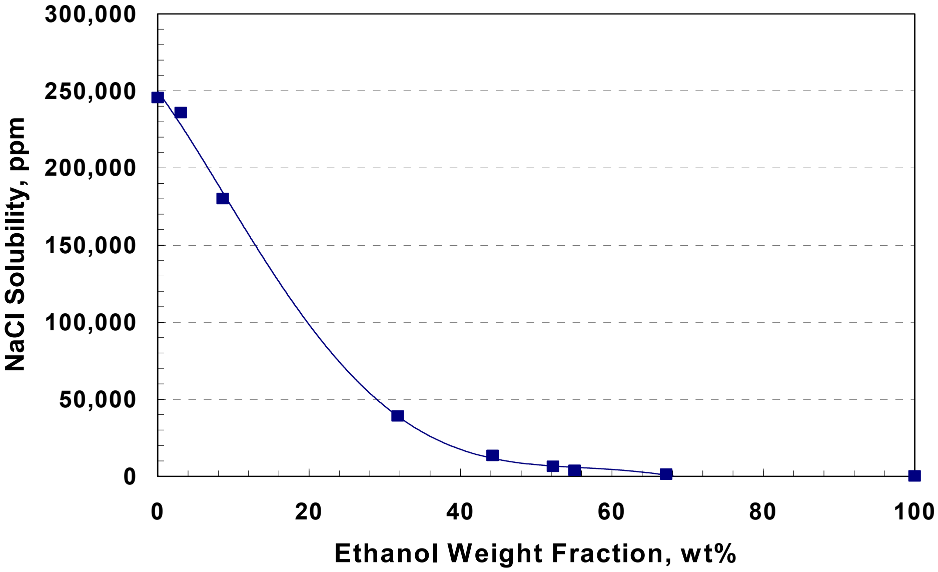

Figure 3.5: Solubility of NaCl in ethanol-water mixtures at 78°F.

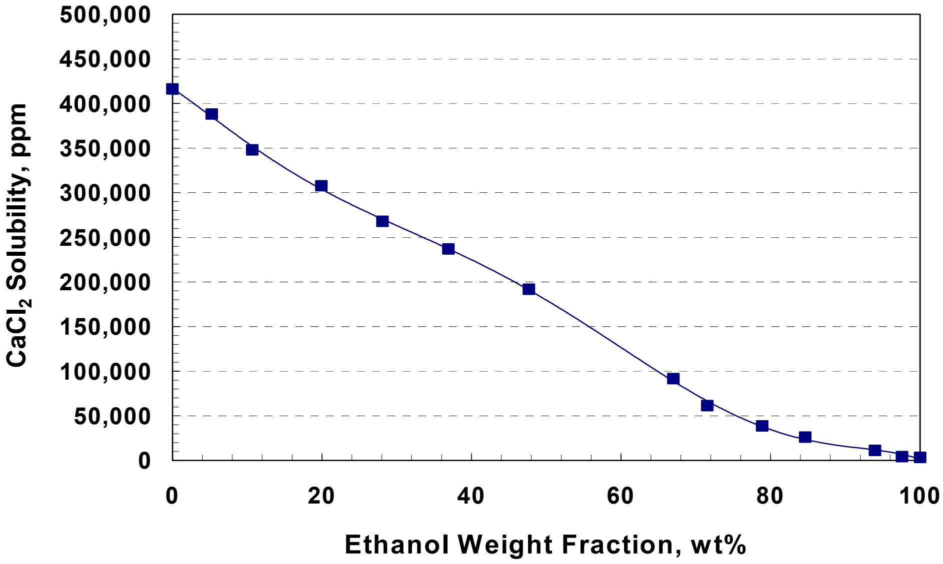

Figure 3.6: Solubility of $CaCl_2$ in ethanol-water mixtures at 78°F.

Chapter 4: Coreflood Apparatus and Experimental Procedure

This chapter describes gas-condensate coreflood experiments conducted to study condensate blocking and treatments in both low and high permeability cores. This chapter starts with an introduction section that summarizes past experimental work performed on two-phase flow through porous media. Then, a theoretical section describes the equations used in the calculations needed to analyze the results. The apparatus section gives a detailed description of the apparatus and equipment used in the coreflood experiments. Finally, an experimental procedure section provides an inclusive summary of each stage used in the coreflood experiments. More details of each experiment can be found in **Appendix B**. The last section describes calibration of the gas chromatograph (GC) to obtain compositional data on the effluent gas.

4.1 INTRODUCTION

The effect of condensate blocking on gas productivity has been studied experimentally and theoretically using relative permeability during two-phase flow. Several researchers investigated several factors affecting gas relative permeability. These include: saturation, wettability, capillary forces, interfacial tension, and trapping number. Odeh (1959) suggested that the viscosity ratio of two phases could affect relative permeabilities.

Thomas and Ward (1972) studied the effect of overburden pressure and water saturation on gas permeability of tight sandstone cores (k < 2 md). They found that the gas permeability decreased with increase in the overburden pressure. For instance, the permeability decreased by 75% at an overburden pressure of 3,000 psi. The reduction of gas permeability reached 90% of the original permeability at 6,000 psi. It was found that cores with micro-fractures lost permeability by 90% at 3,000 psi. However, the gas relative permeability is not significantly affected by increasing overburden pressure. Increasing water saturation of the core reduced the gas relative permeability. This finding is in agreement with the results of Wilson (1956).

The critical condensate saturation is the minimum saturation required for condensate phase to flow in a porous medium when the pressure is reduced below the dewpoint. Saeidi and Handy (1974) studied the flow and phase behavior for a binary mixture of methane-propane in a sandstone core (k = 86 md). They found that condensate saturation as high as 30% was needed for the condensate phase to flow even in the presence of irreducible water. Their results showed that the critical condensate saturations were lower in the presence of water than for condensate alone.

Walls et al. (1982) measured permeability to gas at various brine saturations for several tight sandstone cores from the Spirit River formation of Alberta, Canada. Their results showed that the gas permeability depends very strongly on the residual water saturation. At a water saturation of 40%, the gas permeability was an order of magnitude lower relative to the dry core. They also studied the effect of confining pressure on gas permeability. Experiments showed that confining pressure caused a significant permeability reduction. The sensitivity of the gas permeability to changes in confining pressure increased as the brine saturation was increased.

Gravier et al. (1986) studied rock samples (0.4-50 md) from a carbonate gas field to determine gas and condensate relative permeabilities using a ternary pseudo-reservoir fluid of methane/pentane/nonane. They measured the critical condensate saturation and the extent of the reduction of permeability to gas in the presence of immobile condensate saturation. Their results showed that the gas relative permeability decreased from an average value of 0.68 to about 0.10 when the condensate saturation increased from 0 to 30%. The gas relative permeability decreased when the initial water saturation increased. The measured critical condensate saturation was found to be high, ranging from 24.5 to 50.5%.

Asar and Handy (1988) investigated the effect of interfacial tension on gas/oil relative permeability. They conducted coreflood experiments on Berea cores with an absolute permeability of 193 md, measured using nitrogen as the flowing fluid, and no water. The gas-condensate mixture consisted of methane and propane at 70°F. They found that relative permeability is a strong function of interfacial tension and saturation. Relative permeability curves tend to be straight lines as the interfacial tension becomes very low.

Danesh et al. (1988) measured critical condensate saturation in low (23 md) and high (902 md) permeability sandstone cores both horizontally and vertically using depletion tests on a six-component synthetic gas mixture. They found that the critical condensate saturation values varied in highly permeable cores depending on the orientation of the core: 9% when vertical and 33% when horizontal positions. On the other hand, the critical condensate saturation was about the same value in low permeability cores regardless of their flow positions: 12% when vertical and 14% when horizontal.

Danish et al. (1991) experimentally investigated the effect of residual water saturation on the critical condensate saturation using highly permeable (335 and 902 md) sandstone cores. They found that gravity could mobilize condensate in the absence of residual water saturation in high permeability cores, but the recovery of condensate was very low. They concluded that the residual water saturation reduced the critical condensate saturation and restricted condensate drainage. Capillary and gravity forces largely controlled the critical condensate saturation, which is decreased by increasing the initial water saturation.

Morel et al. (1992) performed depletion tests on low permeability (8.1 md) cores to study the effect of gravitational forces on the mobility of condensate. They found that the condensate could be mobilized under the effect of gravity at the dewpoint pressure.

Bourbiaux and Limborg (1994) developed an experimental methodology to measure the critical condensate saturation and relative permeabilities of gas-condensate fluids. They performed experiments on low permeability (4.1 md) sandstone cores using methane-propane binary mixture at various interfacial tensions and in the presence of interstitial water saturation. The steady state condensate saturations were found to be very high, 53% and 41% for condensate liquid dropouts of 9 and 7%, respectively. This high condensate saturation caused a severe reduction in both gas (k_{rg}) and condensate (k_{ro}) relative permeabilities. At liquid dropout values of 9% and 7%, k_{rg} values were 0.10 and 0.25 and k_{ro} values were 0.028 and 0.033, respectively.

Boom et al. (1996) found that a significant increase in gas-condensate mobility is controlled by the capillary number and not by the interfacial tension alone.

Non-steady state experiments showed that relative permeability changed from curved to straight lines with increasing velocity and decreasing interfacial tension (Blom et al., 1997).

Whitson et al. (1999) developed steady-state experiments to measure gas relative permeability using sandstone cores (10 and 140 md). Due to condensate blocking, the gas relative permeability was only 0.07. They proposed a relationship between the gas relative permeability and capillary number.

Chen et al. (1999) described an example where the condensate relative permeability decreases with increasing liquid saturation. They found that the critical condensate saturation and relative permeability were sensitive to flow rate and interfacial tension. The in-situ condensate accumulation reduced gas relative permeability by 10-fold. Increasing the gas injection rate increased the gas relative permeability. The effect of rate on the relative permeability becomes more predominant as the condensate saturation increased. Increasing the condensate saturation is also increased the differential pressure and the interfacial tension. Gas and condensate relative permeabilities increased as the injection rate increased. The interfacial tension increased as the condensate saturation increased, therefore the gas relative permeability decreased. At lower interfacial tension, the relative permeability curves become straighter. This is in agreement with the results found by Asar and Handy (1988). They also found that the flow rate of condensate increased as the IFT decreased. Condensate was immobile to gas for the high permeability and was mobile for the lower permeability.

Water injection recovery is more efficient when the condensate saturation prior to water injection exceeded the critical condensate saturation. Bourbiaux and Limborg (1994) concluded that the higher the condensate saturation above the minimum value of the critical condensate saturation, the greater the potential condensate recovery by water injection.

Mott et al. (2000) performed relative permeability experiments on a low permeability sandstone (k = 12 md) using a 5-component gas-condensate mixture. They found that gas relative permeability increased at high velocity at a fixed IFT and decreased with velocity at a constant capillary number. They claimed that the decrease in gas relative permeability with velocity at fixed capillary number suggested that the gas permeability may be subject to inertial (non-Darcy) flow effects.

4.2 THEORY

Permeability (k) was calculated using the following form of Darcy's law for single-phase flow:

$$k = \frac{q \mu L}{A \Delta P} \tag{4.1}$$

where q is the injection flow rate , μ is the injected fluid viscosity, L is the length of the core, A is the cross-sectional area of the core, and ΔP is the pressure drop across the core. The relative permeability (k_{rj}) of each phase j is defined as:

$$k_{rj} = \frac{k_j}{k} \tag{4.2}$$

where k_j is the permeability of fluid j and k is the initial gas permeability at 100% gas saturation. The two-phase relative permeability of each phase j at steady-state can be calculated using Darcy's law:

$$k_{rj} = \frac{q_j \mu_j L}{k A \Delta P_j} \tag{4.3}$$

where j refers for either gas or oil (condensate) phase. The gas viscosity used to calculate all gas relative permeability values at 1,200 psig was 0.01594 cp (from **Table 4.3**). The oil viscosity used to calculate all oil relative permeability values at 1,200 psig was 0.23711 cp. If the capillary pressure is negligible, then the pressure drop of each phase is equal to the total pressure drop across the core during the two-phase flow ($\Delta P_g = \Delta P_o = \Delta P$). A single gas phase enters the back-pressure regulator at 3,000 psig and flashes downstream into gas and condensate (oil) phases at 1,200 psig. Flow rate of each oil and gas phase can be calculated using a mass balance across the back-pressure regulator. This mass balance, derived in **Appendix A**, yields the following flow rate equations for oil and gas phases:

$$q_o = \frac{f_o \, q \, \rho}{f_o \, \rho_o + f_g \, \rho_g} \qquad (4.4)$$

$$q_g = \frac{f_g \, q \, \rho}{f_o \, \rho_o + f_g \, \rho_g} \qquad (4.5)$$

where

q = total flow rate of gas mixture at 3,000 psig

q_g = flow rate of gas-phase at 1,200 psig

q_o = flow rate of oil-phase at 1,200 psig

ρ = molar density of gas mixture at 3,000 psig

ρ_g = molar density of gas-phase at 1,200 psig

ρ_o = molar density of oil-phase at 1,200 psig

f_g = fractional flow of gas-phase at 1,200 psig

f_o = fractional flow of oil-phase at 1,200 psig

Density of each phase and the liquid dropout were calculated using the PREOS at the experimental conditions. The values obtained are: $\rho = 0.6719$ lbmole/ft^3, $\rho_g = 0.2263$ lbmole/ft^3, $\rho_o = 0.5659$ lbmole/ft^3, and $f_o = 7.14\%$. The actual flow rate of each phase through the core was calculated using Equations (4.4) and (4.5) as given in **Table 4.1**.

The capillary number (N_c) is a dimensionless number that measures the ratio of viscous to capillary forces:

$$N_c = \frac{k\,\Delta P}{\sigma L} \tag{4.6}$$

where

k = core permeability, cm^2

ΔP = pressure drop across the core, $dynes/cm^2$

σ = interfacial tension between the two phases, dynes/cm

L = length of the core, cm

By using experimental units: k in md, ΔP in psia, σ in dynes/cm, and L in inches, the capillary number can be written including the conversion factor as:

$$N_c = 2.6784 \times 10^{-7} \left(\frac{k\,\Delta P}{\sigma L} \right) \tag{4.7}$$

For large capillary numbers, viscous forces dominate and relative permeabilities tend to approach a straight line, while at very low capillary number capillary forces dominate and immiscible relative permeability behavior exists (Whitson et al., 1999). The values of capillary numbers that are most important and affect well productivity calculations are in the range between 10^{-6} and 10^{-3} (Mott et al., 2000).

Hagen-Poiseuille's equation gives the relationship between the flow rate and the forces causing the flow (Bird et al., 1960). The Hagen-Poiseuille law for a steady flow through a circular tube is given by:

$$q = \frac{\pi r^4 (P_1 - P_2)}{8 \mu L} \tag{4.8}$$

where

q = volumetric flow rate, cm^3/s
r = radius of tube, cm
L = length of tube, cm
P_1 = inlet pressure, $dynes/cm^2$
P_2 = outlet pressure, $dynes/cm^2$
μ = fluid viscosity, poise

This equation is valid only for single-phase incompressible flow. The viscosity of a single phase can be measured by recording the pressure drop across a capillary tube, with a known diameter and length, at a given flow rate. Correlations developed by Lee et al. (1966) for calculating the viscosity of natural gases at elevated temperatures and pressures were also used to estimate the viscosity of the gas.

4.3 APPARATUS

Figure 4.1 shows a photograph of the gas condensate laboratory. Coreflood apparatus was designed for high-pressure and high-temperature experiments as given in **Figure 4.2**. **Figure 4.3** shows a schematic diagram of the coreflood apparatus. A RUSKA pump was used to inject fluid at a constant rate at variable speeds. Multiple pressure ports were used to measure pressure drop across four sections (2 inches in length each) of the core. Two back-pressure regulators were used to control the flowing pressure upstream (BPR-1) and downstream (BPR-2) of the core. A TEMCO PVT visual cell was installed in-line to observe fluid phases. The flow is downward to eliminate gravity segregation effects. The through-window PVT cell was installed in-line to measure fractional flow of the flowing mixture any time through the experiment. The core holder, back-pressure regulators, fluid accumulators, PVT cells, and flow lines are inside a temperature-controlled, forced-air circulation oven at 145°F. The oven temperature is measured with a metal thermocouple and displayed on a digital indicator with an accuracy of ±1°C.

4.3.1 Through-Window PVT Cell

The through-window PVT Cell (Model 2329) used in our experiments was purchased from RUSKA. It has two windows mounted opposite each other to allow see-through visibility. The windows are made of optical quality glass and chemically treated for hardness. They are approximately 1 inch thick and bolted to the cell body in a manner to minimize stress around the edges which could crack the glass. The PVT cell was rated for a temperature range from ambient to 300°F and a working pressure of 10,000 psi at 300°F. The manufacturer tested the cell for a pressure of 15,000 psi at 300°F. The volume of the cell was measured using distilled water and found to be 96.49 mL. The inside diameter of the cell is 3.5682 cm. Therefore, one millimeter of height viewed through the windows corresponds to 1 mL of volume in the cell. A light was placed behind one window to allow easy detection of the gas-liquid interface level.

4.3.2 Back-Pressure Regulator

Back-pressure regulators (BPR) used in the core flow experiments are from TEMCO, Inc. with a Model BPR-5. This model of back-pressure regulator has two sections separated by a diaphragm as illustrated in **Figure 4.4**. The diaphragm is very thin and made from 360 Steel. The compressed gas is in the dome and the flowing fluid in the body section. To avoid rupturing the diaphragm, the two sections were pressurized simultaneously. Nitrogen was used as the compressed gas. The pressure of the compressed gas in the dome is monitored using a digital Heise gauge. When the desired pressure was reached, the nitrogen source was closed and the pressurized gas was allowed to reach the experimental temperature. Two back-pressure regulators were used to control the flow pressure in the upstream and downstream of the core. The upstream and downstream back-pressure regulators are called BPR-1 and BPR-2, respectively.

4.3.3 Accumulators

Accumulators used in this study were purchased from TEMCO, Inc.. Two types of accumulators are used: rodded and floating piston accumulators. All the accumulators are rated for a temperature up to 350°F and a working pressure of 5,000 psi. The manufacturer tested them for 7,500 psi. The diameter of the piston is 2.5 inches. The volume of the accumulators is approximately 1,500 mL. A Teflon® piston is used in these accumulators to allow easier movement of the piston inside the honed cylinder.

4.3.4 PVT Visual Cell

A PVT visual cell from TEMCO, Inc. was installed in-line to observe fluid phases. This type of visual cell has been tested by the manufacturer to temperatures as high as 600°F and 20,000 psi. The visual cell has opposed windows with an adjustable volume ranged from 0 to 9 mL. With the mechanical volume adjustment, the end piece rotates to change the spacing between the two windows.

4.3.5 Capillary Tube Viscometer

A capillary tube viscometer with a diameter of 0.005 inches was installed in-line parallel to the core holder. A pressure transducer was connected to measure the pressure drop across the viscometer during the flow of fluids. The Hagen-Poiseuille equation can be written in the following form:

$$q = f \frac{\Delta P}{\mu} \tag{4.9}$$

where q is the flow rate, ΔP is the pressure drop across the capillary tube viscometer, μ is the flowing fluid viscosity, and *f* is the viscometer factor that was determined by flowing a reference fluid (e.g. methane at 3,000 psig) through the viscometer and measuring the resulting pressure drop. **Table 4.2** gives the capillary viscometer factor determined by flowing methane at 3,000 psig and 145°F at different flow rates. The average value of these measurements is equal to 0.04424. The viscosity of each gas phase was measured experimentally using the capillary viscometer calibrated with methane at 3,000 psig, as listed in **Table 4.3**. The measured viscosity for each gas was found to agree favorably with the calculated value.

4.3.6 Pressure Transducers

Validyne DP 15 Variable Reluctance Pressure Transducers were used to measure pressure drop across the core in coreflood experiments. Each transducer has a stainless steel diaphragm that is clamped between two blocks of stainless steel. An inductance coil is embedded in each block and covered by a disc to provide a corrosion resistant surface. When a pressure difference is applied through the pressure ports, the diaphragm deflects and changes the magnetic field between the two coils. Validyne transducers are equipped with bleed ports to facilitate cleaning or filling the pressure cavity. The transducers are calibrated with a known source of pressure.

4.3.7 Digital Data Recorder

A digital data recorder DDR10 was used to read data from pressure transducers and transfer it to a personnel computer. The DDR10 integrates the functions of a multi-point recorder, data logger, and digital indicator into a single instrument. The input voltage of the DDR10 ranges from ±1 mV to ±10 V DC. It is also capable to take varies input currents: 4-20 mA, 10-50 mA, or any current value that can be converted to a voltage using up to a special 1 Kohm shunt resistance. The recorded pressure transferred to a PC using a data acquisition program called HISTORY.

4.3.8 Gas Chromatograph

A gas chromatograph (Model 8610C) purchased from SRI Instrument was used to analyze hydrocarbon composition. The column oven is capable of operation from ambient temperature to 400°C, both isothermally and by temperature programming with unlimited ramps and holds. Ramp rates of up to 40°C per minute, and assisted cooling from 250°C to ambient in 5 minutes or less are easily achieved. All gases are precisely regulated under Electronic Pressure Control (EPC). All temperatures, pressures, voltages, and currents are displayed on a bright red digital display. The GC is equipped with a built-in 4-channel serially-interfaced data system which is compatible with SRI PeakSimple data system software which is used for integration, hardware automation, and control. The software makes the GC operation fully automated. The GC equipped with a 10-port system-controlled gas sampling valve and an on-column injector port. This port permits on-column manual injections with traditional chromatography syringes. The on-column injector port has a septum that is a plug of silicon rubber that allows the syringe to penetrate and prevents the carrier gas from escaping.

The GC is equipped with a Thermal Conductivity Detector (TCD) and Flame Ionization Detector (FID). The TCD measures the difference in thermal conductivity in the carrier gas flow and the analyte peaks. Nitrogen was used as the carrier gas at a flowing pressure of 9 psi. The TCD consists of four tungsten-rhenium filaments housed in a stainless steel detector block. Two of the filaments are exposed to the sample-laden carrier gas flow and provide the actual chromatographic signal. The other two filaments are provided with clean carrier gas flow, enabling them to be used as a baseline reference signal. The Flame Ionization Detector (FID) responds to any molecule with a carbon-hydrogen bond. Since the FID is mass sensitive, but not concentration sensitive, changes in carrier gas flow rate have little effect on the detector response. The FID is preferred for general hydrocarbon analysis. Hydrogen and air are used as a combustion mixture for the FID and are controlled using electronic pressure controllers. The flowing pressure of hydrogen and air were set to 29 and 6 psi, respectively.

The GC was installed on-line to analyze either the feed or the effluent of the core. **Figure 4.5** shows a schematic diagram of the gas chromatograph. A back-pressure regulator was installed at the outlet end of the GC to control the flowing pressure in the sampling loop. During the experiment, the gas mixture flowed continuously through the GC valve that was in the bypass position. Samples were analyzed only when the sampling valve was switched on. The sampling loop has a volume of 15 μL.

4.4 COREFLOOD EXPERIMENTAL PROCEDURE

4.4.1 Core Preparation

A core with a diameter of 0.972 inches and a length of 8.01 inches was cut from a source rock block. Two types of cores were used: Texas Cream limestone and Berea sandstone. Experimental core properties are listed in **Table 4.4**. The core was dried in an oven at 95°C for more than 2 weeks. The core was wrapped with an aluminum foil and heat-shrink Teflon® to prevent diffusion of injected fluids through the Viton® rubber sleeve. The wrapped core was placed into a core holder inside the oven at 145°F. After 4 hours, an axial pressure was applied by screwing the end pieces of the core holder. Then, an overburden pressure of 3,400 psig was applied. Holes were drilled thorough the pressure taps using a small drill (~1/8”). These holes will allow gas to flow through the pressure ports to the connected pressure transducers to record the pressure drop across each section of the core. The initial gas permeability (at S_g=100%) was measured using methane at a flowing pressure of 3,000 psig.

4.4.2 Water Saturation Procedure

Water was introduced into the core using a vacuum push-pull technique. The coreholder was taken outside the oven to cool at room temperature. The outlet end of the core holder was connected to a vacuum pump and a full vacuum was applied for 5 hours. The inlet end was closed. A predetermined amount of brine was injected from the inlet of the core holder using a burette while a vacuum was pulled from the outlet end of the core holder. The core holder was placed inside the oven at 145°F and opened to atmospheric pressure. The core holder was allowed to reach an equilibrium temperature. Then, a series of push-pull cycles were applied using a RUSKA hand pump through the outlet of the core holder. Between each push and pull cycle, a break of 15 minutes was taken to allow water vapor to distribute through the core. The water saturation procedure was completed after 32 push-pull cycles.

4.4.3 Coreflood Procedure

Gas permeability was first measured using methane at initial water saturation. Then, the gas mixture was flowed through the core at a pressure (3,000 psig) greater than its dewpoint pressure until steady state was reached. Before the start of the two-phase flow of the coreflood experiment, the inlet and outlet valves of the core holder were closed. The pressure of the downstream back-pressure regulator (BPR-2) controlling the core pressure was slowly decreased to 1,200 psig, while the pressure in the upstream back-pressure regulator (BPR-1) controlling the pressure of the gas feed was kept at 3,000 psig. Flow was started while the bypass valve was open until the pressure in the lines stabilized. Then, the bypass valve was closed and the inlet and outlet valves of the core holder were opened simultaneously. This procedure allowed the condensate to dynamically accumulate in the core in a way that is similar to condensate accumulation near a well producing below the dewpoint pressure of a retrograde gas-condensate reservoir.

Both Du et al. (2000) and Whitson et al. (1999) have measured relative permeabilities using this dynamic condensate accumulation procedure as a function of pressure rather than establishing steady state by constant rate injection of both gas and condensate separately. The resulting relative permeabilities can be considered a function of pressure rather than saturation. The single-phase gas mixture is injected at a constant pump rate (@ 3,000 psig) while flashing two-phase through the core until the pressure drop reaches steady state. The gas and condensate relative permeabilities are then calculated directly from Darcy's law as previously described. Next, the end-point gas relative permeability was measured using the equilibrium gas at 1,200 psig. During the second stage of the experiment, methanol was injected to remove the condensate followed by a repeat of the first stage.

4.4.4 GC Calibration

The GC is equipped with an Alumina PLOT Fused Silica (SUPELCO Inc.) capillary column with a length of 30 m and an internal diameter of 0.53 mm. A temperature profile was set to obtain a good separation between the peaks of the desired hydrocarbon components. The temperature of the GC oven was set initially to 40°C and held for 6 minutes. Then, it increases to 160°C with a ramp of 20°C/minute. The temperature was held for 15 minutes at 160°C. Finally, the oven is cooled down to the initial temperature of 40°C using a ramp of -50°C. The sampling loop pressure was set to 300 psig by adjusting the dome pressure of the back-pressure regulator at the outflow end of the GC.

Standard solutions were prepared to calibrate the GC. The gas is a mixture of four components. Binary mixtures of n-butane, n-heptane, and n-decane were made for GC standards but none were made with methane. Standard solutions of n-butane were prepared by bubbling n-butane through n-heptane in a sealed-glass vial. This was done by recording the initial weight of n-heptane and the final weight of n-butane/n-heptane mixture. The difference in weight gives the mass of n-butane that dissolved in the mixture. This is a tedious effort since the amount of dissolved n-butane could not be controlled and predicted in advance. When too much n-butane was dissolved, the sealed vial was opened to allow some of the n-butane to evaporate until the target concentration reached. Standard solutions for n-heptane and n-decane were prepared by diluting each one with the other as a solvent. Binary mixtures of n-butane and n-decane were prepared in sealed-glass vials at different mass proportions. The same method was used for n-decane standard solutions using n-heptane as a solvent.

Samples of each mixture were charged manually into the GC through the on-column injector port using a chromatograph syringe. The volume of each sample injected was 1 μL. **Figures 4.6** to **4.8** show the calibration curve for each component. The concentration of methane can be determined from the difference between the total mass in the sampling loop, calculated using the ideal gas law, and sum of the other masses.

Table 4.1: Flow rates of gas and condensate (oil) phases through the core during dynamic flashing of two-phase through the core at 1,200 psig and 145°F.

Pump Rate (q) at 3,000 psig, cc/hr	Gas-Phase Flow Rate (q_g) at 1,200 psig, cc/hr	Oil-Phase Flow Rate (q_o) at 1,200 psig, cc/hr	Total Flow Rate at 1,200 psig. cc/hr
2	4.98	0.38	5.36
4	9.96	0.77	10.73
6	14.94	1.15	16.09
18	44.82	3.45	48.27
44.8	111.56	8.58	120.14
60	149.42	11.49	160.49
600	1494.15	114.89	1609.04

Table 4.2: The capillary viscometer factor determined by flowing methane at 3,000 psig and 145°F at various rates.

q, cc/hr	ΔP, psi	*f*
8	3.29	0.04618
12.8	5.32	0.04569
16	7.44	0.04084

Table 4.3: Gas viscosity measured with the capillary viscometer.

		Viscosity, cp	
Gas	Pressure, psig	Measured	Calculated
Methane	3,000	0.01879	0.01899
Gas Mixture	3,000	0.03261	0.03674
Equilibrium gas	1,200	0.01682	0.01594

Table 4.4: Properties of low and high permeability cores.

Rock Type	Texas Cream Limestone	Berea Sandstone
Diameter, in.	0.972	0.972
Length, in.	8.01	8.01
Pore Volume, mL	~20	~20
Porosity, %	20.8	20.5
k, md	1-6	220-380

Figure 4.1: A photograph of gas-condensate laboratory (CPE 5.166).

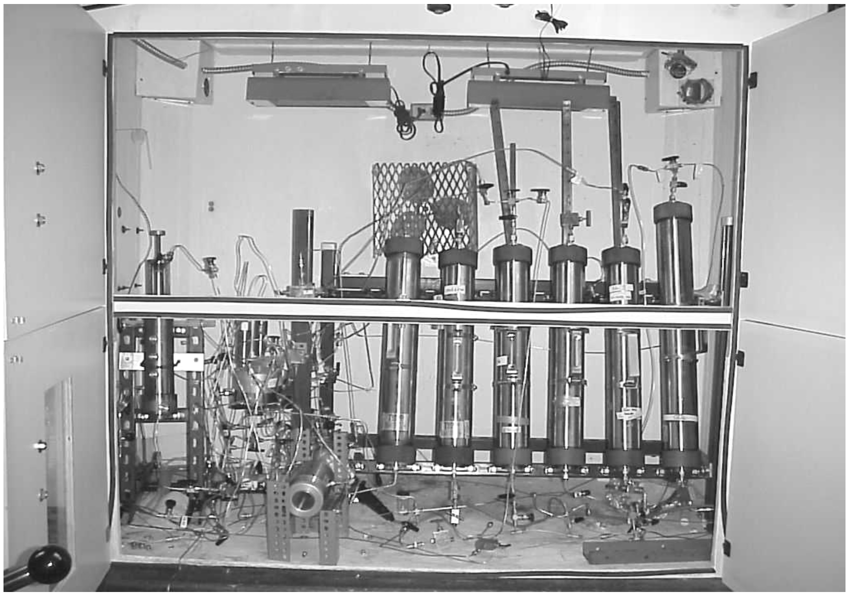

Figure 4.2: A photograph of HPHT coreflood apparatus.

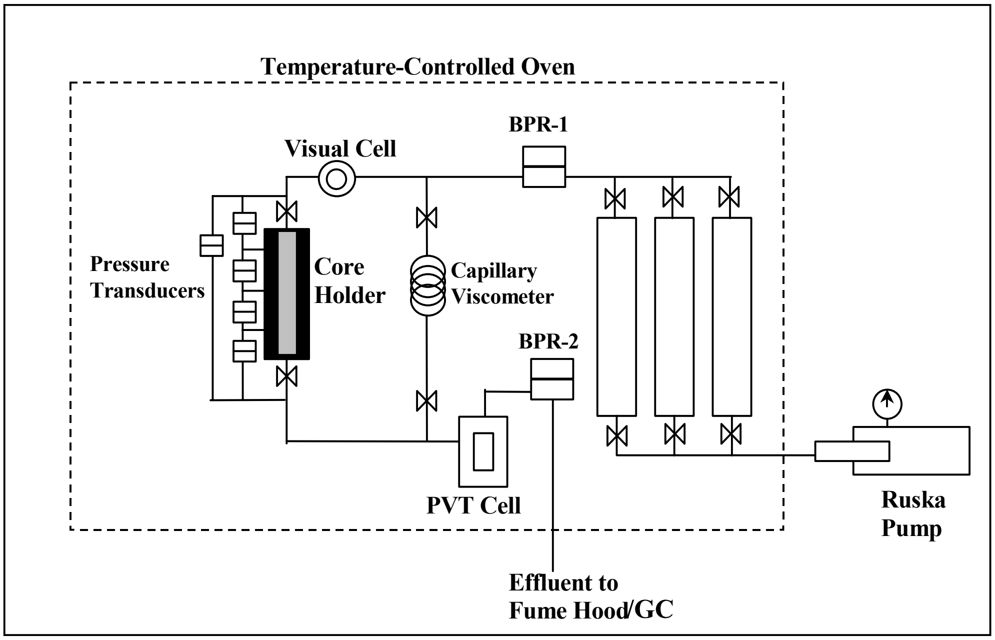

Figure 4.3: Schematic diagram of the coreflood apparatus.

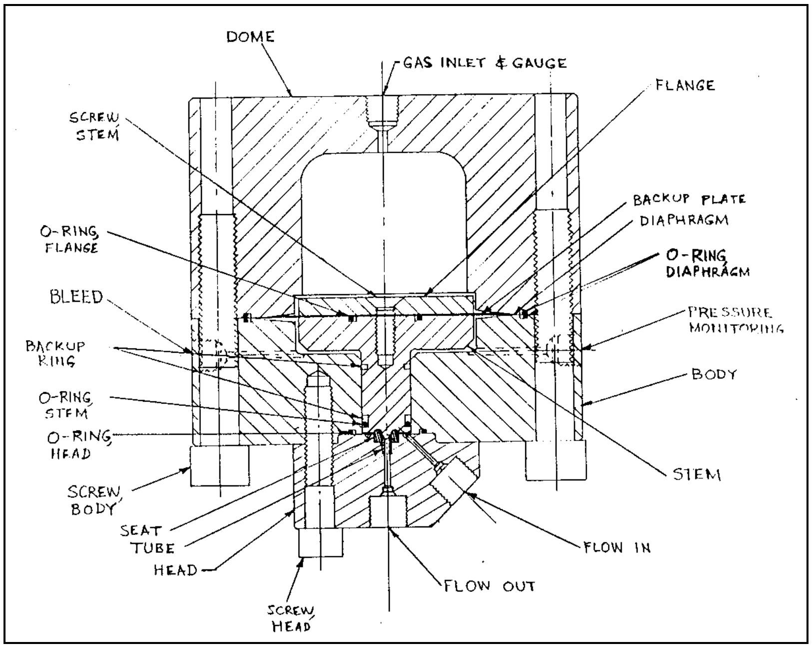

Figure 4.4: Schematic diagram of the back-pressure regulator (courtesy of TEMCO, Inc.).

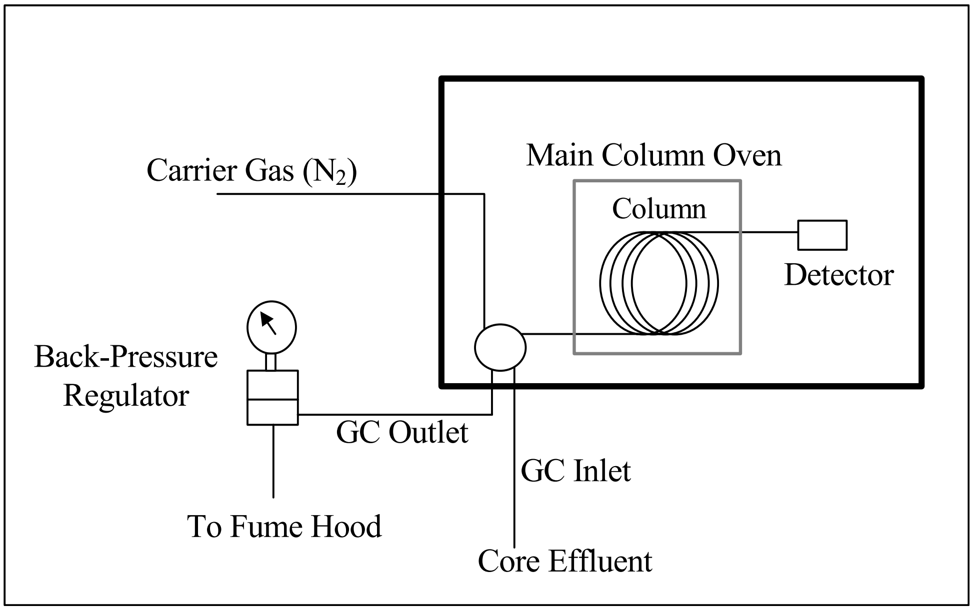

Figure 4.5: Schematic diagram of the gas chromatograph.

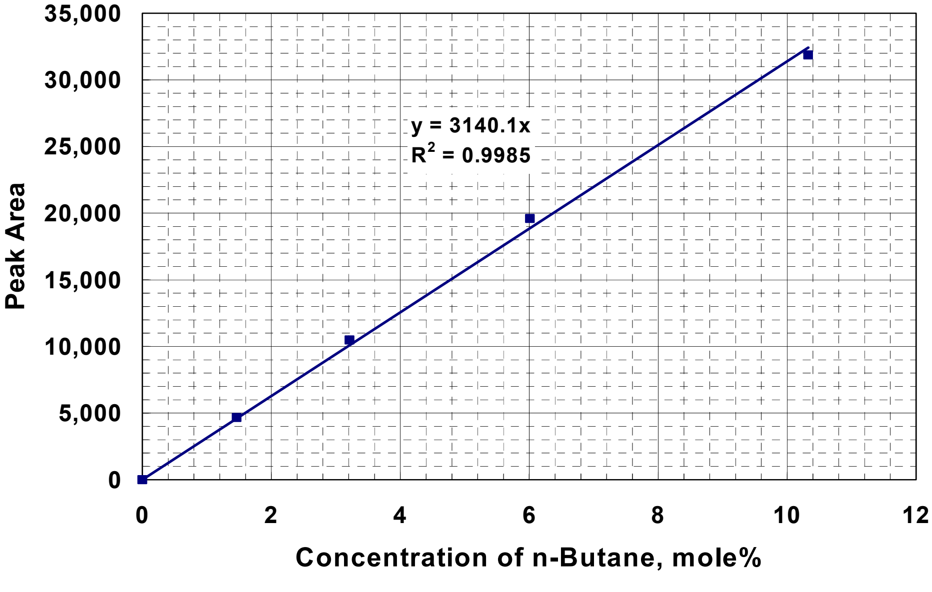

Figure 4.6: Calibration curve for n-butane.

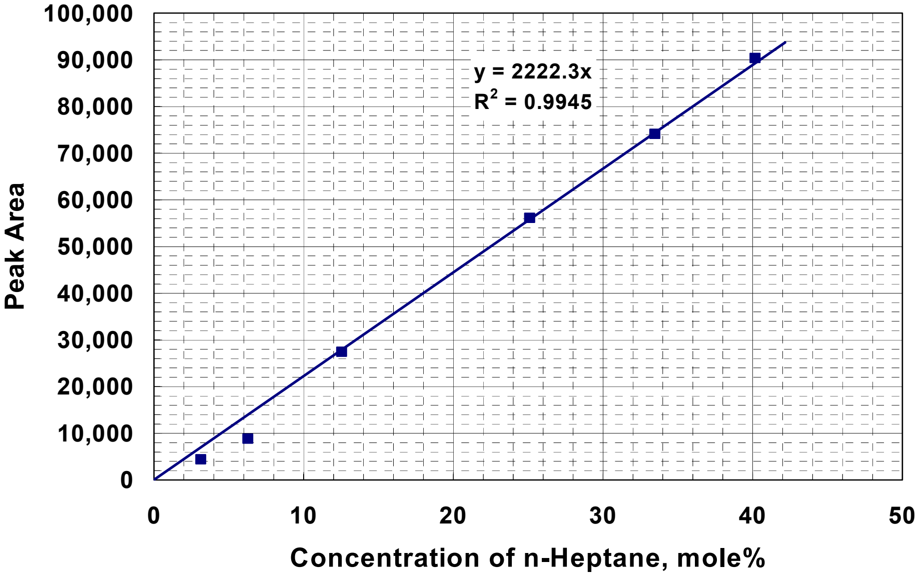

Figure 4.7: Calibration curve for n-heptane.

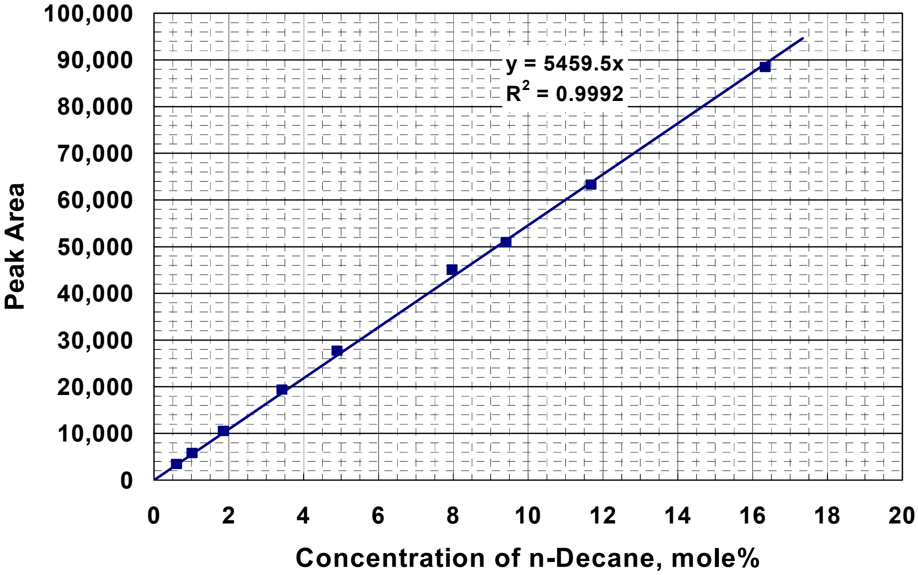

Figure 4.8: Calibration curve for n-decane.

Chapter 5: Gas-Condensate Coreflood Results and Discussion

This chapter describes gas-condensate coreflood results obtained using the experimental procedures given in the previous chapter. A summary of the results will be given in the first section of this chapter. Then, the chapter discusses the effect of condensate blocking on gas relative permeability when the pressure drops below the dewpoint. Several factors that affect on condensate blocking are investigated including: core permeability, water saturation, and capillary number. Then, the effect of methanol treatment on gas relative permeability will be discussed.

5.1 SUMMARY

Coreflood experiments were conducted in Berea sandstone and Texas Cream limestone cores to quantify the loss in relative permeability caused by condensate accumulation. The in-situ condensate saturation was established dynamically by precise control of core inlet and outlet pressures. It is well known that retrograde condensate dropout can cause significant productivity loss in low permeability reservoirs. This study shows that such losses can also occur in high permeability reservoirs. **Table 5.1** gives a summary of gas and condensate relative permeability data measured at steady state at 1,200 psig and 145°F. Gas relative permeability reductions of 88% to 96% were seen in 2-5 md limestone cores and 94% to 97% in 246-378 md sandstone cores.

This study also showed that methanol can be used to remove condensate and water blocking and thus increase gas relative permeability in both low and high permeability cores. Different volumes of methanol were injected following condensate accumulation in the cores to determine how much methanol is needed to remediate the cores and establish how long the treatment lasts.

These results can be used to help reservoir engineers evaluate and treat gas-condensate wells with reduced productivity. Reservoir engineers should be especially careful to evaluate the damage done in such high-permeability reservoirs if the well's pressure drawdown is high enough to result in pressures below the dewpoint pressure.

5.2 CONDENSATE BLOCKING

Coreflood experiments were conducted using both Texas Cream limestone and Berea sandstone cores with water saturations between 0 and 54% established using the vacuum push-pull method except for the highest value of 54%, which was achieved by displacement of water by methane. **Table 5.2** shows core properties of low and high permeability rocks. Texas Cream limestone cores are classified as low permeability rocks, while Berea sandstone cores are high permeability cores. The initial gas permeability (k) was measured with methane in all experiments.

Figure 5.1 shows the measured initial gas permeability of Texas Cream limestone cores at S_g=100%. The gas relative permeability (k_{rg}) in this dissertation is defined as the gas permeability divided by the gas permeability at 100% gas saturation. The measured gas relative permeability data for both cores are shown in **Figure 5.2**. The data for Berea was obtained by displacement of water with methane at various flow rates. As can be seen in this figure, the range of saturations for Berea cores is very narrow compared to the Texas Cream limestone cores due to their high initial permeability.

A Productivity Index (PI) is defined as the ratio of total flow rate to pressure drop. For the sake of comparison, the PI was normalized to the initial productivity index (PI_o), which is the productivity index before condensate accumulation. Gas enters the back-pressure regulator at 3,000 psig and flashes downstream into gas and condensate (oil) phases at 1,200 psig. This experimental procedure simulates what happens around the well when the bottom hole flowing pressure drops below the dewpoint pressure.

5.2.1 Effect of Core Permeability

5.2.1.1 Low Permeability Cores

Several coreflood experiments were performed on Texas Cream limestone cores at 145°F. A list of these experiments is provided in **Table 5.3**. **Figure 5.3** shows the pressure drop for different sections across the core during methane flow at 3,000 psig and at various flow rates for Experiment No. 15. Further details of Experiment No. 15 are given in **Appendix B**. The initial gas permeability at S_g = 100% measured for each section of the core is given in **Table 5.4**. The variation of the measured gas permeability between the sections of the core indicates the heterogeneity of the core. **Figure 5.4** shows the pressure drop for different sections of the core during gas mixture flow at 3,000 psig and a flow rate of 48 cc/hr. The measured gas permeabilities at S_g = 100% are given in **Table 5.5**. The gas permeabilities measured with the gas mixture are almost the same as those measured with methane. This is an important consistency check to ensure that the gas mixture is not dropping out any condensate at 3,000 psig. The flow of gas mixture at 1,200 psig yields two-phase flow since the pressure is below the dewpoint (2,792 psig).

Figure 5.5 shows the pressure drop across different sections of a Texas Cream limestone core during dynamic condensate accumulation at 1,200 psig and a flow rate of 18 cc/hr (Experiment-15). There was no water present in the core.

The pressure drop in the first section gradually increased until it reached a plateau value after 4.0 pore volumes (PV). Then, the pressure drop in the second section started to increase. The condensate accumulates in each section of the core until it reaches a steady state flow. The pressure drop in each section reached a stabilized value after about 4.0 PV. The condensate bank breaks through after 16.0 PV of two-phase flow. **Table 5.6** shows gas and oil relative permeabilities measured during condensate accumulation at 1200 psig and 18 cc/hr. After condensate accumulation the gas and oil relative permeabilities at steady state decreased to 0.165 and 0.215, respectively.

Figure 5.6 shows the pressure drop across Texas Cream limestone cores during two-phase flow at different flow rates and water saturations. **Table 5.7** shows the gas and oil relative permeability values during steady-sate two-phase flow at 1,200 psig. At a steady-state, the gas relative permeability decreased by 88% at zero water saturation and by 96% at the highest water saturation. Initially, the condensate phase started to fill-up the pores while the gas phase is flowing. When the pressure drop reached a steady-state, both gas and condensate reached steady-state fractional flow values. The steady-state relative permeability values for the gas and condensate given in **Table 5.7** show that as the water saturation increased from 0 to 53.96%, k_{rg} decreased from 0.12 to 0.04 and k_{ro} decreased from 0.15 to 0.05.

More pore volumes were needed for the pressure drop to reach a steady state value as the flow rate increased. This was an unexpected result and indicates there was insufficient time for local equilibrium to be achieved in at least the higher flow rate corefloods. The effect of non-equilibrium flow on condensate accumulation was investigated by conducting new corefloods at lower flow rates, as will be discussed later. However, the steady state relative permeabilities reported in this dissertation are still valid.

5.2.1.2 High Permeability Cores

A dynamic condensate accumulation procedure has been used to measure gas and oil relative permeabilities for high permeability sandstone cores (k =220-380 md). It is commonly said that condensate blocking is more of a problem in low permeability formations than in high permeability formations, but little if any experimental coreflood data in the literature support this key conclusion. Experiments 12 and 12a were performed on Berea cores at 0 and 38% water saturation, respectively. The same coreflood procedure used in low permeability cores was followed in these experiments. Further details of Berea experiments are given in **Appendix B**.

Figure 5.7 shows the pressure drop across Berea cores during two-phase flow at 1,200 psig. The pressure buildup data show the same trend as observed for low permeability corefloods. The gas relative permeability decreased to 0.03 and 0.06 for the two Berea corefloods summarized in **Table 5.8**. At 38% water saturation, the gas relative permeability is lower than with 0% water saturation. As with the limestone core this is likely due to the combined effects of condensate and water blocking. Although these Berea cores had a permeability 80-fold higher than the Texas Cream limestone cores, condensate blocking resulted in the same extent of reduction in gas productivity (95%). Although Whitson et al. (1999) reported k_{rg} of 0.07 (at S_w=12%) in a 140 md Berea sandstone with a synthetic gas, we believe this is the first quantification of such an effect in high permeability rocks (k=250-378 md) is reported.

Figure 5.8 illustrates the decline in productivity index during condensate accumulation for both rocks at different water saturations. **Figure 5.9** compares the normalized PI of Texas Cream limestone with Berea sandstone cores during two-phase flow at 1,200 psig. This result shows that condensate blocking reduces gas productivity in both low and high permeability cores to the same extent. These results can be used to help reservoir engineers evaluate and treat gas-condensate wells with reduced productivity. In light of these new data, the common perception that condensate blocking around wells in high-permeability reservoirs is not significant should be re-examined. Reservoir engineers should be especially careful to evaluate the damage done in such high-permeability reservoirs if the well's pressure drawdown is high enough to result in pressures below the dewpoint over a long enough period of time to allow condensate accumulation near the well.

5.2.2 Effect of Water Saturation

The effect of initial water saturation on gas and condensate relative permeabilities was investigated in both low and high permeability cores. Low initial water saturation was established using the push-pull method described in the previous chapter. On the other hand, water displacement by a methane flood was used to get a high initial water saturation. It was found that the presence of a higher initial water saturation resulted in a larger reduction in gas productivity when the flowing pressure dropped below the dewpoint. **Figure 5.10** shows the effect of initial water saturation on gas and condensate relative permeabilities in Texas Cream limestone cores. As the initial water saturation increases, the relative permeability to gas and condensate phases decreases.

The presence of water in the core also decreased the number of pore volumes of two-phase flow needed to reach a steady-state. For example, two-phase flow reached steady-state during condensate accumulation after injection of 68.5 and 58.9 PV at 0 and 20% water saturation, respectively. The presence of water reduces the available pore volume and consequently decreases gas permeability and the available pore space. The same trend was observed in high permeability (Berea) cores as reported in **Table 5.8**. Well productivity will be reduced faster due to condensate blocking in the presence of a high water saturation as illustrated in **Figure 5.8**.

5.2.3 Effect of Capillary Number

Gas and condensate relative permeabilities were measured at different flow rates during dynamic condensate accumulation in low and high permeability cores. The reported relative permeabilities were measured at steady state two-phase flow. The capillary number was calculated for each flow rate using Equation (4.7). **Figure 5.11** shows gas and condensate relative permeabilities as a function of capillary number for Texas Cream limestone cores. The gas relative permeability increases with the flow rate (capillary number).

Since these experiments were performed using the same gas mixture and pressure and temperature conditions, the IFT between gas and condensate phases was constant (4.1 dynes/cm, measured by Walker (2000)). Therefore, the increase in the gas relative permeability with flow rate is due to higher viscous forces at higher flow rates. The measured condensate relative permeability was found to be higher than that of the gas phase due to its high saturation. At higher flow rate, the flowing gas phase stripped some of the condensate and resulting in a decrease in the condensate saturation. Accordingly, the gas relative permeability increases. **Figure 5.12** shows gas and condensate relative permeabilities as a function of capillary number for Berea cores. It shows the same trend where relative permeability of gas and condensate increases with flow rate. The results obtained are in agreement with those reported in the literature (Lefebvre du Prey, 1973; Amaefule and Handy, 1982; Chen et al., 1999; Mott et al., 2000; Pope et al., 2000; Du et al.; 2000).

5.3 EFFECT OF METHANOL TREATMENT

Coreflood data reported by Du et al. (2000) clearly show increases in gas relative permeability after methanol injection following condensate accumulation in Texas Cream limestone cores. However, they did not determine how the increase in gas relative permeability varied with the volume of the methanol treatment. The methanol volume was varied in these new corefloods for this purpose in both Texas Cream limestone and Berea sandstone cores (Al-Anazi et al., 2002). **Figure 5.13** defines three steady-state flow periods observed in these corefloods: (1) pre-treatment accumulation of condensate occurs when the flowing pressure falls below the dewpoint pressure, (2) an enhanced flow period (lower pressure drop) occurs following the methanol injection, and (3) post-treatment accumulation of condensate takes place following the methanol treatment and the pressure drop increases to about its pre-treatment level once the methanol is displaced from the core.

5.3.1 Methanol Treatments in Low Permeability Cores

Figure 5.14 shows pressure drop across the core during dynamic condensate accumulation before and after methanol treatments for Experiment-8 (see **Appendix B** for details). In this experiment, two methanol treatments with a volume of 20 PV each were performed after each condensate accumulation flood (**Table 5.9**). Pressure drop profiles for methanol treatments are given in **Figures B.44** and **B.47**. Before methanol treatment, condensate decreased the relative permeability of gas to 0.06 and of oil to 0.07. After the first methanol treatment (20 PV), there is an enhanced flow period. The pressure drop reaches a minimum value at about 36 PV. The enhanced flow period indicates a delay in the condensate accumulation. This delay in condensate blocking is due to the presence of a methanol-rich phase that is miscible with both water and condensate at the coreflood temperature and pressure and sufficiently high methanol concentrations. As the liquid methanol is stripped out by mass transfer into the flowing gas phase, the condensate starts to accumulate and eventually the pressure drop increases to about the same level as before the treatment. The gas and oil relative permeability values during the post-treatment accumulation reached 0.06 and 0.09, which are close to those during the pre-treatment accumulation period.

The second methanol treatment extended the enhanced flow period by a factor of 2 indicating an insufficient volume of methanol was injected the first time. The effect of methanol treatment on PI during condensate accumulation is shown in **Figure 5.15**. Initially, the PI decreased from 33 to 1 cc/hr/psi due to condensate blocking. During the enhanced flow period after each methanol treatment, the PI increased by a factor on the order of 10. **Table 5.10** summarizes the gas relative permeability during the enhanced flow period in Texas Cream limestone cores. All the results indicate an enhancement in gas productivity after methanol treatment.

Figure 5.16 shows the effect of methanol treatment volume on the gas relative permeability ratio ($k_{rg}/k_{rg\ damage}$) during the enhanced flow period in Texas Cream limestone cores. The gas productivity improvement is much higher in cores with high initial water saturation. For example, k_{rg} increased by a factor of 10 in cores with water saturation in the range of 20 to 54%. **Table 5.11** summarizes the oil (condensate) relative permeability during the enhanced flow period in Texas Cream limestone cores. These results show an enhancement in condensate relative permeability after methanol treatment. **Figure 5.17** shows the effect of methanol treatment volume on the oil relative permeability ratio ($k_{ro}/k_{ro\ damage}$) during the enhanced flow period in Texas Cream limestone cores. The results show the same trend of improvement as that observed in the gas relative permeability ratio (**Figure 5.16**). These results confirm that methanol treatment was effective in removing both condensate and water from the cores. Therefore, reservoirs with high interstitial water saturation are good candidates for methanol treatment even though they may not be encountering any condensate blocking.

Figure 5.18 shows the duration of the enhanced flow period in Texas Cream limestone cores for different methanol treatment volumes. The duration shown on **Figure 5.18** is defined based upon the minimum in the pressure drop. The duration of the enhanced flow period increases with the volume of the methanol treatment. A two-stage methanol treatment (20 PV each) doubled the duration of the enhanced flow period. However, the third stage of methanol increased the enhanced flow period by only 17% relative to the second treatment. More delay was observed at higher water saturation for the same volume of methanol. Sufficient volumes of methanol can apparently displace both the condensate and water from the core and enhance the gas relative permeability.

Table 5.12 gives the gas end-point relative permeabilities before and after methanol treatment. The effect of methanol on the gas end-point relative permeability ratio is illustrated in **Figure 5.19**. This ratio is defined as k^o_{rg} after methanol treatment to k^o_{rg} before methanol treatment ($k^o_{rg\ damage}$). This figure shows that methanol treatments were effective in increasing k^o_{rg} and the increase was larger at higher initial water saturations. The first methanol treatment increased the gas end-point relative permeability by about 25, 35, and 54% at initial water saturations of 0, 20, and 54%, respectively. Larger increase in gas end-point relative permeability at high initial water saturations indicates that the combined effect of condensate and water blocking reduces the gas relative permeability.

5.3.2 Methanol Treatments in High Permeability Cores

Methanol treatments performed in high permeability cores showed the same behavior as that observed in low permeability cores. **Figure 5.20** shows the effect of methanol treatments on condensate accumulation in a Berea core at S_{wi}=38% (Experiment-12a). Condensate blocking decreased the relative permeability to the gas and oil phases to 0.03 and 0.04, respectively. This is the same behavior as that observed with the low permeability cores. Methanol treatments produced an enhanced flow period where the gas productivity reached a maximum as shown by the high values of PI (**Figure 5.21**). The first methanol treatment increased the PI by 10-fold, while the second treatment increased it by a factor of 15. Since this core had a high water saturation (38%), the first methanol treatment was probably effective in removing most of the water from the core since water and methanol are miscible in all proportions. The second methanol treatment may have been needed to remove all of the condensate.

Figure 5.22 shows the effect of methanol on PI during condensate accumulation in a dry Berea core (S_{wi}=0%). The PI after the second treatment showed the same trend as that after the first one, except it declined later. With no water present in the core, methanol filled the same pore volume during each treatment. **Table 5.13** gives the gas relative permeability during the enhanced flow period in Berea cores. The enhancement in gas productivity in a water-saturated core is higher than that in a dry core as illustrated in **Figure 5.23**. The first methanol treatment (20 PV) increased the gas relative permeability during the enhanced flow period at S_{wi} of 38% by a factor of 10.5 and the second treatment increased it to a factor of 15.

Table 5.14 shows the oil relative permeability during the enhanced flow period in Berea cores. Methanol treatments improved the oil relative permeability by more than 10-fold during the enhanced flow period. **Figure 5.24** shows the effect of methanol treatment volume on oil relative permeability ratio ($k_{ro}/k_{ro\ damage}$) during the enhanced flow period in Berea cores. Methanol is more effective at increasing k_{ro} in the presence of high water saturation. **Figure 5.25** shows the effect of methanol on the duration of the enhanced flow period in Berea cores. Larger cumulative volumes of methanol resulted in a longer enhanced flow period.

Table 5.15 gives the gas end-point relative permeability in Berea cores before and after methanol treatment. Before methanol treatment, a high water saturation contributed to a severe reduction in k^o_{rg}. At S_{wi} = 38%, k^o_{rg} is about 42% of that in dry cores. The impact of water saturation together with condensate blocking in high permeability cores resulted in a severe reduction in gas relative permeability. The improvement in the gas end-point relative permeability after methanol treatment is greater than that in low permeability cores, especially in the presence of a high water saturation. After the first methanol treatment, k^o_{rg}

increased by a factor of 2.5 in a Berea core with S_{wi} = 38%, while k^o_{rg} increased by a factor of 1.5 in the Texas Cream limestone core with the highest water saturation (S_{wi}=54%).

5.4 SUMMARY OF THE RESULTS

Gas relative permeability during two-phase steady state corefloods decreased by 88 to 97% due to condensate and water blocking. Gas relative permeability decreased about the same percentage in high permeability cores (Berea) as in low permeability cores (Texas Cream limestone). A more severe reduction in gas relative permeability during two-phase flow of gas and oil occurred at high water saturations than at low water saturations. Gas relative permeability was found to increase with capillary number at a fixed IFT.

After methanol treatment, an enhanced flow period is observed in both low and high permeability cores. Condensate accumulation is delayed for a certain time. During this time, the productivity index can be increased by an order of magnitude in both low and high permeability cores. Duration of the enhanced flow period is controlled by the volume of methanol injected and its rate of mass transfer into the flowing gas phase after the treatment. Methanol treatments remove both water and condensate by a multi-contact miscible displacement if sufficient methanol is injected.

Methanol treatments resulted in a significant but temporary enhancement in productivity for both low and high permeability cores. The removal of water-blocks would be expected to have a long lasting impact on a well's PI. The condensate phase will reform and cause the PI to decrease again if the bottom hole pressure is the same following the treatment. However, in some cases the temporary removal of the condensate and/or water block may allow gas production at significantly lower pressure drawdown resulting in less condensate accumulation, perhaps even allowing the well to be produced at a bottom hole pressure above the dew point for a longer period of time than would otherwise be economic. In other cases due to operations such as lean gas injection in other wells some time in the past, the gas flowing to a given gas-condensate well may be less rich than what caused the original condensate block. Therefore, further investigation is needed to evaluate the expected duration of the enhanced flow period under a variety of field conditions.

Table 5.1: Summary of gas and condensate relative permeability data measured at steady state at 1,200 psig and 145°F.

Experiment #	4	5	7	8	10	13	12	12a	14	15	16	17	18	19
Type	TCL	TCL	TCL	TCL	TCL	TCL	BS	BS	TCL	TCL	TCL	TCL	TCL	TCL
k, md	2.72	1.94	2.32	4.43	5.10	4.50	246	378	4.16	2.83	2.65	3.02	3.74	3.70
S_{wi}, %	0	44.85	0	20	20	53.96	0	38	0	0	0	0	0	0
q, cc/hr	44.8	44.8	44.8	44.8	60	60	600	600	6	18	6	2	52.9	42
N_c	2×10^{-7}	2×10^{-7}	2×10^{-7}	2×10^{-7}	2×10^{-7}	3×10^{-7}	3×10^{-6}	3×10^{-6}	3×10^{-8}	9×10^{-8}	3×10^{-8}	5×10^{-9}	3×10^{-7}	1×10^{-7}
Accumulation Method	Flash	Flash	Flash	Flash	Flash	Flash	Flash	Flash	Flash	Flash	Flash	Flash	co-injection	Flash
MeOH=0PV														
k_{rg}	0.18	0.14	0.12	0.06	0.05	0.04	0.06	0.03	0.08	0.17	0.18	0.13	0.16	0.16
k_{ro}	0.24	0.18	0.15	0.07	0.07	0.05	0.08	0.04	0.10	0.22	0.24	0.17	0.21	0.20
$k°_{rg}$	0.384	0.300	0.517	0.675	0.690	0.519	0.901	0.386	-	0.577	0.510	-	0.598	-
MeOH=20PV														
k_{rg}	0.14	0.06	0.09	0.06	0.06	0.06	0.06	0.04	-	0.19	-	-	0.14	
k_{ro}	0.24	0.08	0.11	0.08	0.08	0.08	0.08	0.05		0.24			0.18	
$k°_{rg}$	0.580	0.313	0.647	0.829	0.933	0.819	0.960	0.967		0.684			0.599	
MeOH=40PV														
k_{rg}	-	-	0.06	0.05	-	0.07	0.07	0.04	-	0.10	-	-	0.18	
k_{ro}			0.08	0.07		0.09	0.09	0.05		0.13			0.24	
$k°_{rg}$			0.704	0.916		0.729	0.984	0.807		0.918			0.607	
MeOH=60PV														
k_{rg}	-	-	0.03	-	-	-	-	-	-	-	-	-	-	
k_{ro}			0.04											
$k°_{rg}$			0.547											

TCL: Texas Cream Limestone
BS: Berea Sandstone
MeOH: Methanol

Table 5.2: Experimental core properties of low and high permeability rocks.

Rock Type	Texas Cream Limestone	Berea Sandstone
Diameter, in.	0.972	0.972
Length, in.	8.01	8.01
Pore Volume, mL	~20	~20
Porosity, %	20.8	20.5
k, md	1-6	220-380

Table 5.3: Initial gas permeability measured for Texas Cream limestone cores at different initial water saturations.

Experiment No.	S_{wi}, %	k, md
4	0	2.72
5	45	1.94
7	0	2.32
8	20	4.43
10	20	5.10
13	54	4.50
14	0	4.16
15	0	2.83
16	0	2.65
17	0	3.02
18	0	3.74
19	0	3.70
20	0	3.50
21	0	3.58

Table 5.4: Initial gas permeability of Texas Cream limestone core measured using methane at 3,000 psig.

	Gas Permeability, md	
	q = 69 cc/hr	q = 99 cc/hr
Section-1	2.57	2.41
Section-2	4.49	4.50
Section-3	3.22	2.95
Section-4	4.01	3.83
Whole Core	3.14	2.94

Table 5.5: Core permeability measured with the gas mixture (single-phase) at 3,000 psig and 48 cc/hr.

	Gas Permeability, md
Section-1	2.40
Section-2	4.09
Section-3	2.79
Section-4	3.67
Whole Core	2.79

Table 5.6: Gas and oil relative permeabilities measured during dynamic condensate accumulation at 1,200 psig and 18 cc/hr.

	ΔP, psia	k_{rg}	k_{ro}
Section-1	5.65	0.118	0.154
Section-2	3.25	0.204	0.266
Section-3	3.35	0.198	0.259
Section-4	3.93	0.169	0.221
Whole Core	16.13	0.165	0.215

Table 5.7: Relative permeability values in Texas Cream limestone cores during two-phase flow at 1200 psig.

	Exp.-7	Exp.-8	Exp.-10	Exp.-13
k, md	2.32	4.43	5.10	4.50
S_{wi}, %	0	20	20	53.96
N_c	2.0×10^{-7}	2.4×10^{-7}	2.5×10^{-7}	2.9×10^{-7}
k_{rg}	0.12	0.06	0.05	0.04
k_{ro}	0.15	0.07	0.07	0.05

Table 5.8: Relative permeability values in Berea cores during two-phase flow at 1,200 psig.

	Exp.-12	Exp.-12a
k, md	246	378
S_{wi}, %	0	38
N_c	2.9×10^{-6}	2.8×10^{-6}
k_{rg}	0.06	0.03
k_{ro}	0.08	0.04

Table 5.9: Results of methanol treatments performed after condensate accumulation for Experiment-8.

	First Treatment	Second Treatment
P, psig	1,200	1,200
Volume, PV	20	20
q, cc/hr	44.8	44.8
ΔP, psia	55.39	62.63
k, md	4.72	4.18

Table 5.10: Gas relative permeability during the enhanced flow period in Texas Cream limestone cores.

	Exp.-4	Exp.-7	Exp.-8	Exp.-10	Exp.-13
k, md	2.72	2.32	4.43	5.10	4.50
S_{wi}, %	0	0	20	20	53.96
N_c	1.6×10^{-7}	2.0×10^{-7}	2.4×10^{-7}	2.5×10^{-7}	2.9×10^{-7}
k_{rg} Before Methanol	0.18	0.12	0.06	0.05	0.04
k_{rg} After the First Methanol	0.24	0.16	0.48	0.58	0.46
k_{rg} After the Second Methanol	-	0.48	0.62	-	-

Table 5.11: Oil relative permeability during the enhanced flow period in Texas Cream limestone cores.

	Exp.-4	Exp.-7	Exp.-8	Exp.-10	Exp.-13
k, md	2.72	2.32	4.43	5.10	4.50
S_{wi}, %	0	0	20	20	53.96
N_c	1.6×10^{-7}	2.0×10^{-7}	2.4×10^{-7}	2.5×10^{-7}	2.9×10^{-7}
k_{ro} Before Methanol	0.24	0.15	0.07	0.07	0.05
k_{ro} After the First Methanol	0.87	0.42	0.63	0.75	0.61
k_{ro} After the Second Methanol	-	0.63	0.80	-	-

Table 5.12: Effect of methanol treatment on gas end-point relative permeability in Texas Cream limestone cores.

	Exp.-4	Exp.-7	Exp.-8	Exp.-10	Exp.-13
k, md	2.72	2.32	4.43	5.10	4.50
S_{wi}, %	0	0	20	20	53.96
N_c	1.6×10^{-7}	2.0×10^{-7}	2.4×10^{-7}	2.5×10^{-7}	2.9×10^{-7}
k^o_{rg} Before Methanol	0.384	0.517	0.675	0.690	0.529
k^o_{rg} After the First Methanol	0.580	0.647	0.829	0.933	0.819
k^o_{rg} After the Second Methanol	-	0.704	0.916	-	-

Table 5.13: Gas relative permeability during the enhanced flow period in Berea cores.

	Exp.-12	Exp.-12a
k, md	246	378
S_{wi}, %	0	38
N_c	2.9×10^{-6}	2.8×10^{-6}
k_{rg} Before Methanol	0.06	0.03
k_{rg} After the First Methanol	0.60	0.33
k_{rg} After the Second Methanol	0.65	0.39
k_{rg} After the Fifth Methanol	0.72	-

Table 5.14: Oil relative permeability during the enhanced flow period in Berea cores.

	Exp.-12	Exp.-12a
k, md	246	378
S_{wi}, %	0	38
N_c	2.9×10^{-6}	2.8×10^{-6}
k_{ro} Before Methanol	0.08	0.04
k_{ro} After the First Methanol	0.78	0.43
k_{ro} After the Second Methanol	0.85	0.51
k_{ro} After the Fifth Methanol	0.94	-

Table 5.15: Effect of methanol treatment on gas end-point relative permeability in Berea cores.

	Exp.-12	Exp.-12a
k, md	246	378
S_{wi}, %	0	38
N_c	2.4×10^{-6}	2.2×10^{-6}
k^o_{rg} Before Methanol	0.901	0.386
k^o_{rg} After the First Methanol	0.960	0.967
k^o_{rg} After the Second Methanol	0.984	0.807
k^o_{rg} After the Fifth Methanol	0.946	-

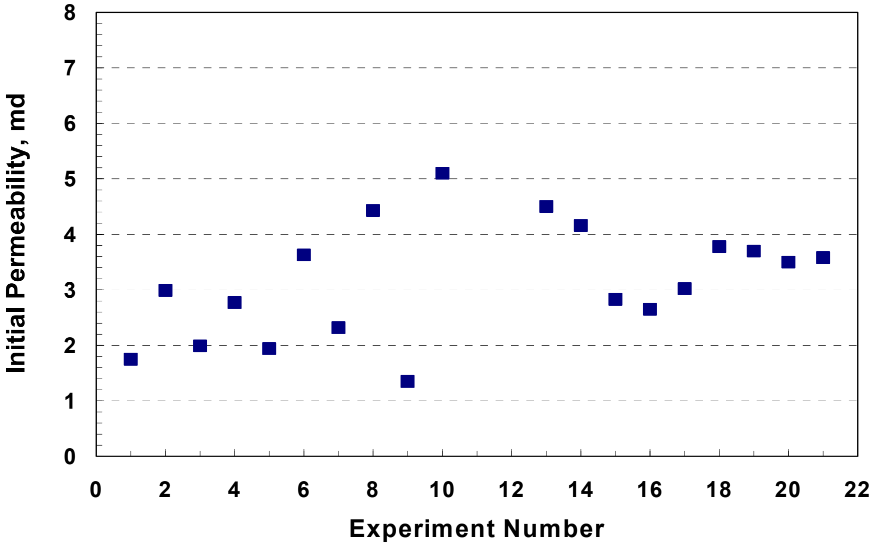

Figure 5.1: Measured initial gas permeability of Texas Cream limestone cores at 100% S_g.

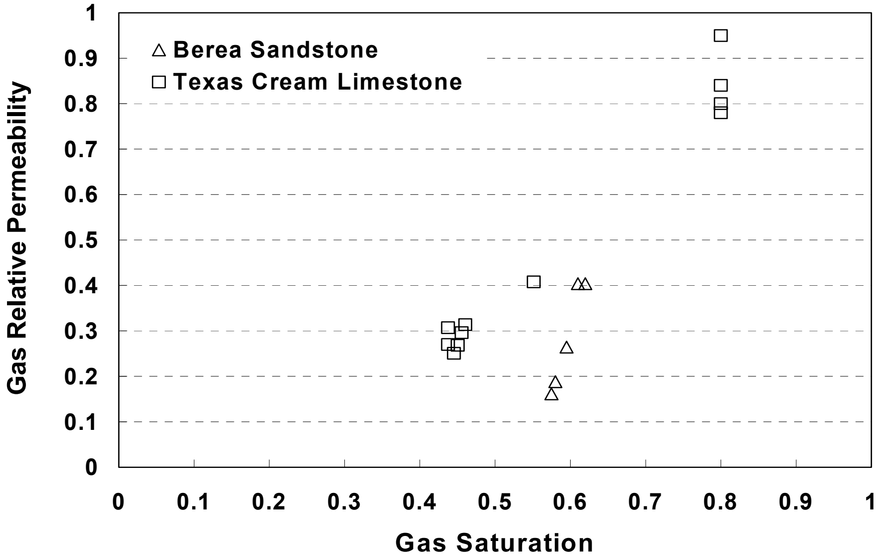

Figure 5.2: Gas relative permeability data at different initial water saturations.

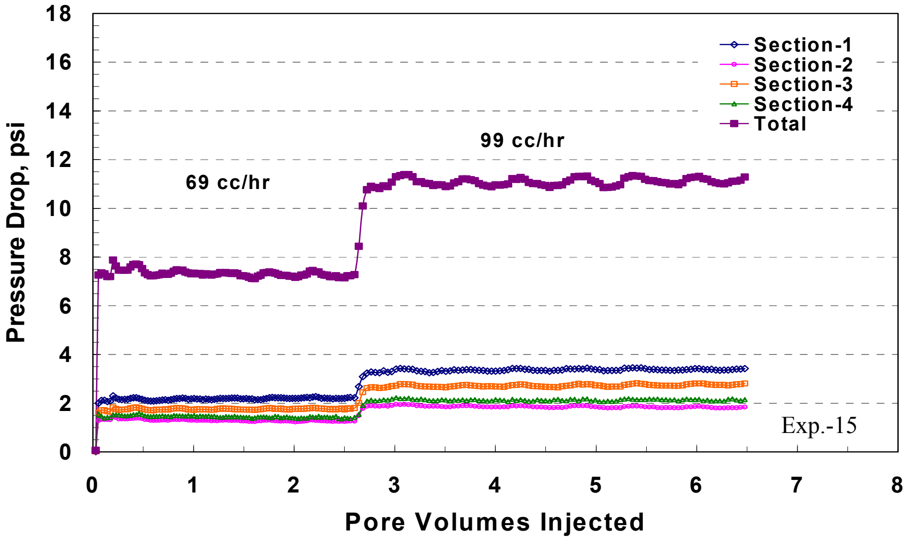

Figure 5.3: Pressure drop for different sections across the core during methane flow at 3,000 psig and at various flow rates.

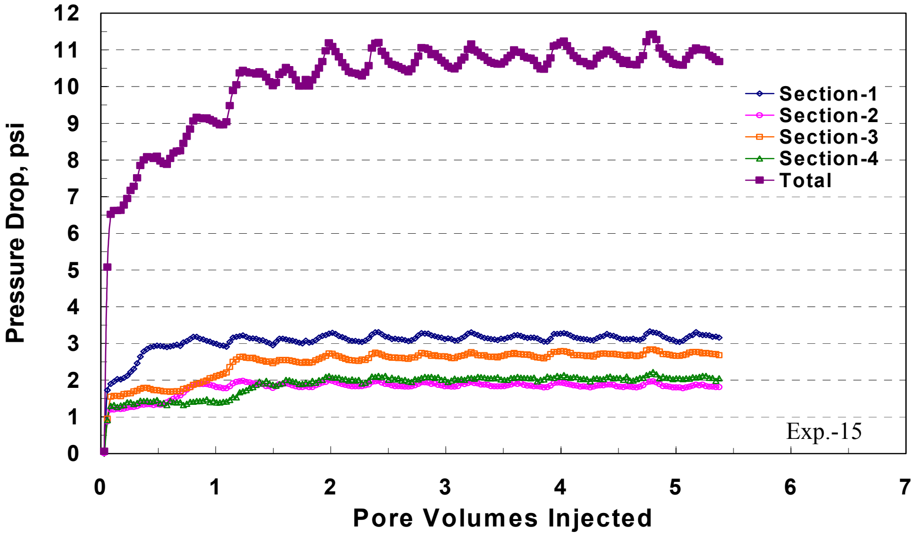

Figure 5.4: Pressure drop for different sections of the core during gas mixture flow at 3,000 psig and 48 cc/hr.

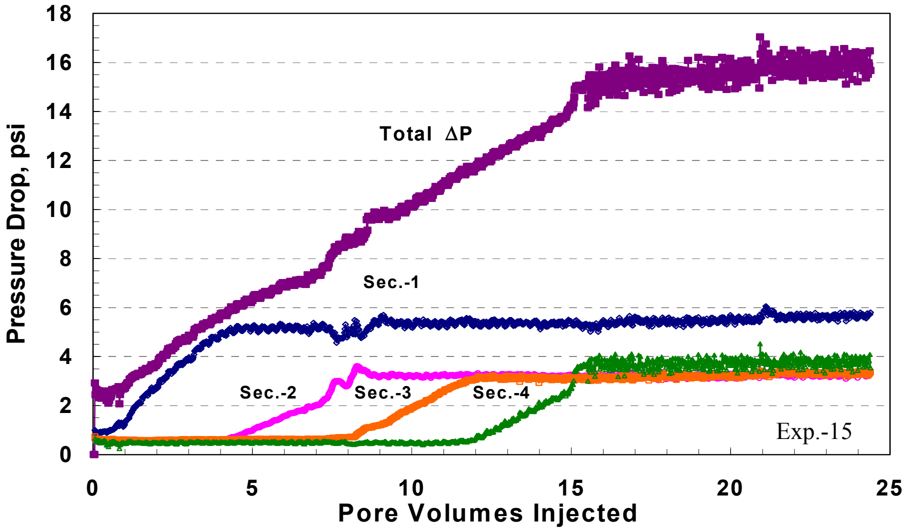

Figure 5.5: Pressure drop across different sections of a Texas Cream limestone core during dynamic condensate accumulation at 1,200 psig and a flow rate of 18 cc/hr.

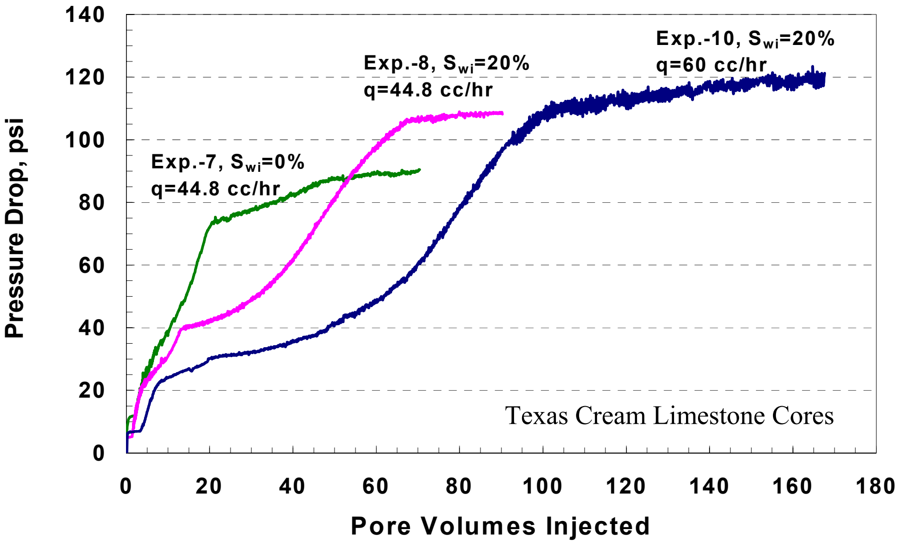

Figure 5.6: Pressure drop across the cores during condensate accumulation at 1,200 psig and different flow rates and water saturations.

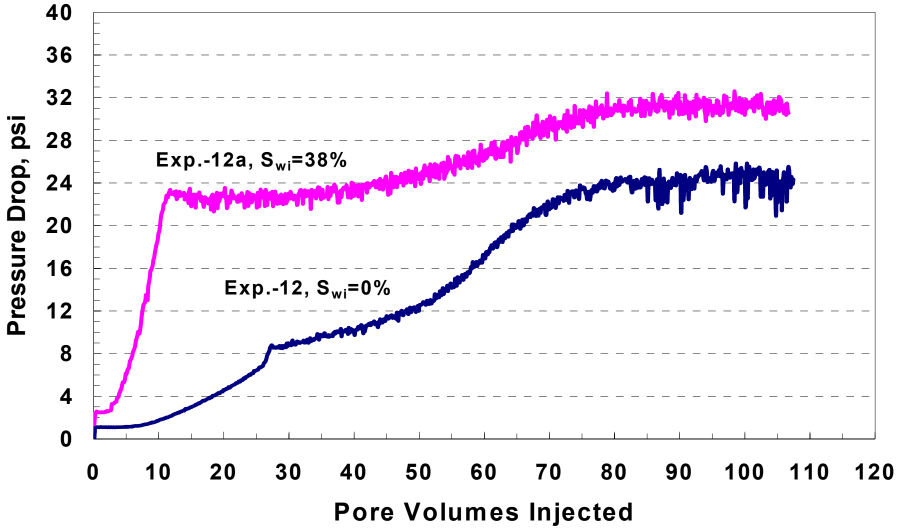

Figure 5.7: Pressure drop across Berea cores during dynamic condensate accumulation at 1,200 psig and 600 cc/hr.

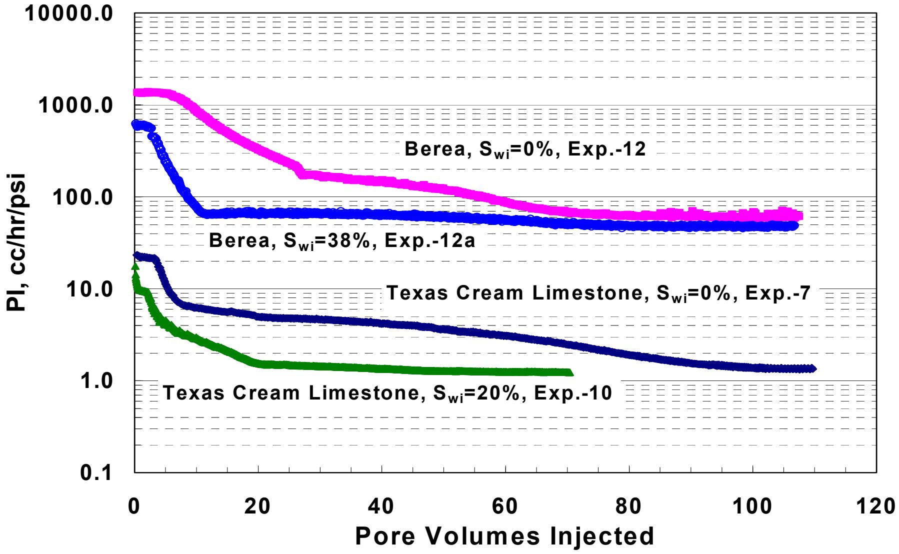

Figure 5.8: Effect of condensate blocking on productivity index of Texas Cream limestone and Berea sandstone cores at different water saturations.

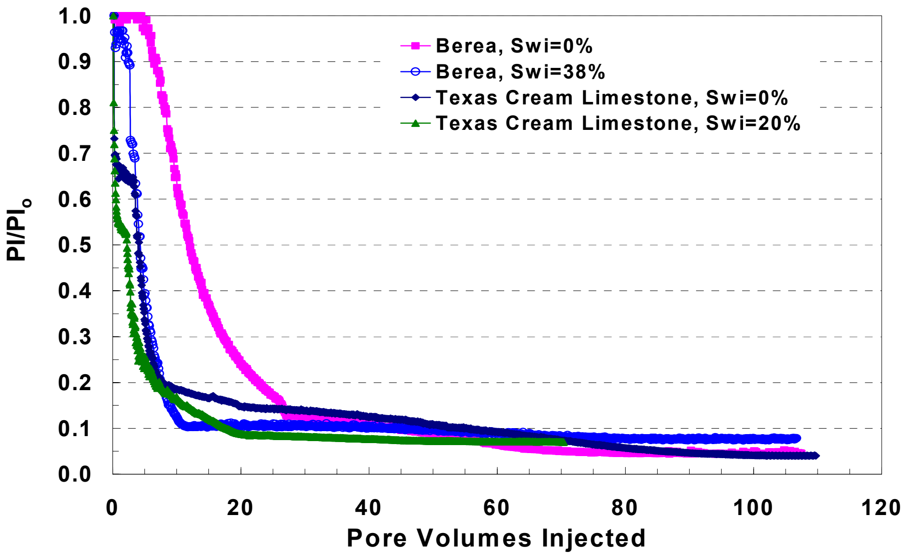

Figure 5.9: Normalized productivity index ratio during condensate accumulation at different water saturations.

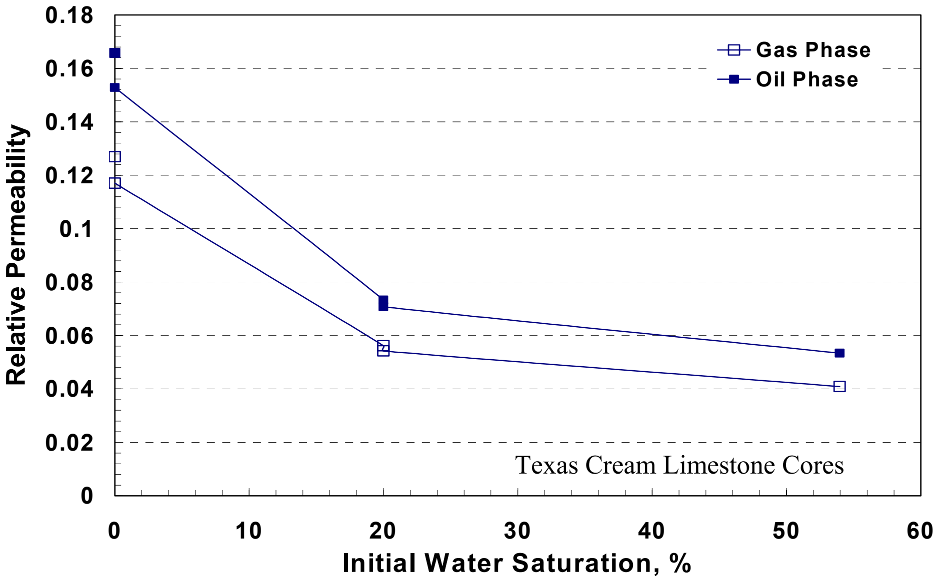

Figure 5.10: Effect of initial water saturation on gas and condensate relative permeabilities during two-phase flow at 1,200 psig.

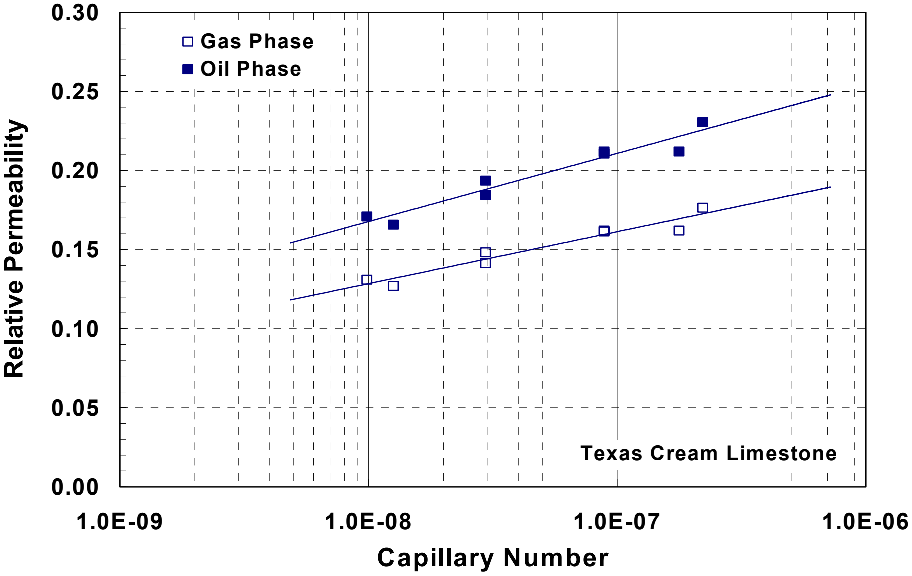

Figure 5.11: Gas and condensate relative permeabilities as a function of capillary number for Texas Cream limestone cores.

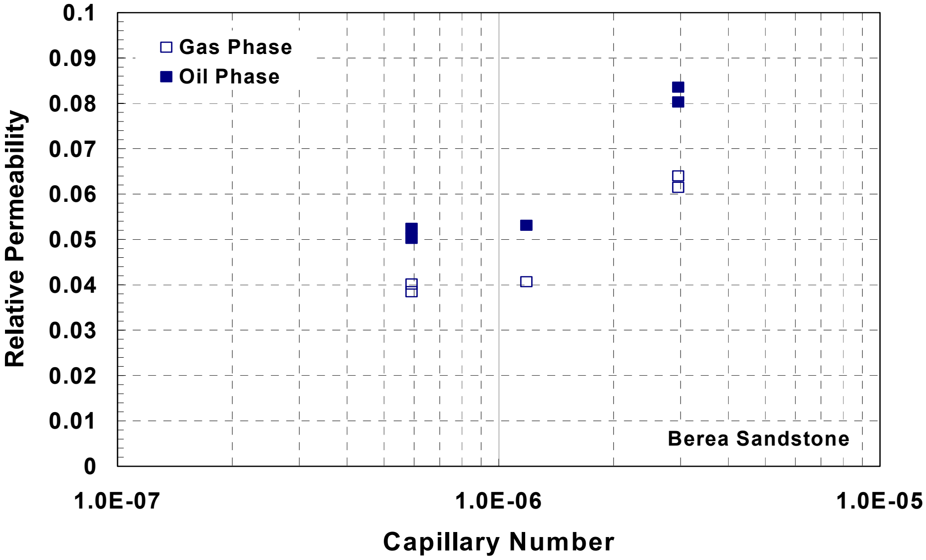

Figure 5.12: Gas and condensate relative permeabilities as a function of capillary number for Berea cores.

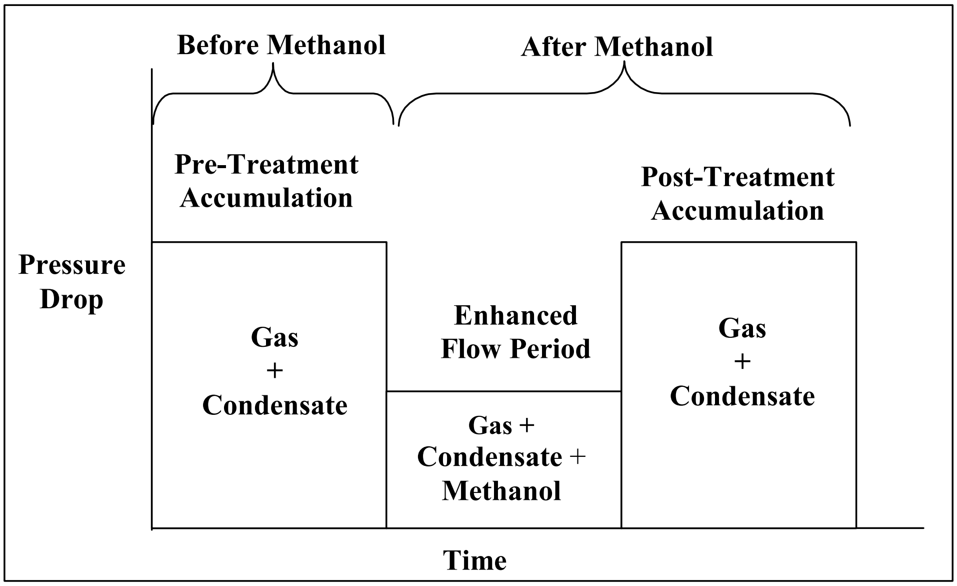

Figure 5.13: Steady state flow periods before and after methanol treatment during two-phase flow through the core.

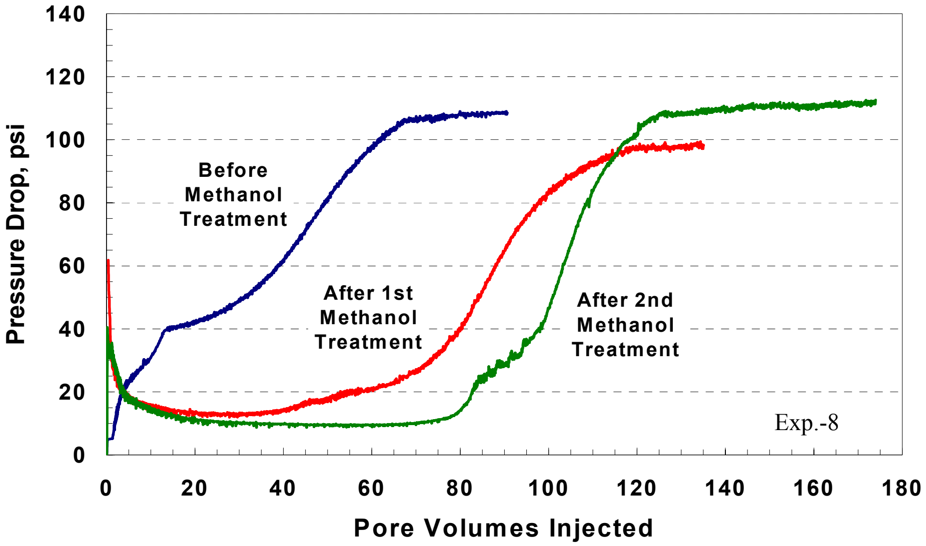

Figure 5.14: Effect of methanol treatment on condensate accumulation in Texas Cream limestone core at S_{wi}=20%.

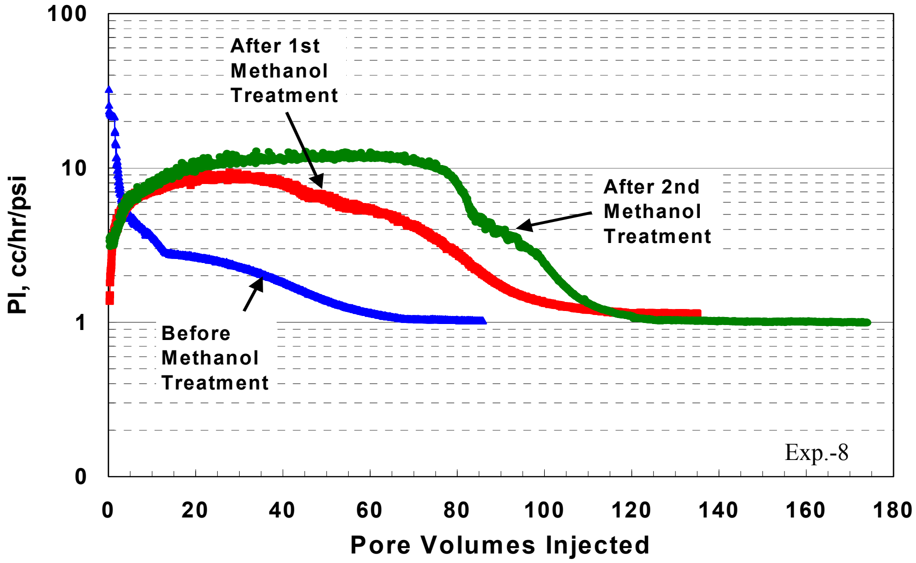

Figure 5.15: Effect of methanol treatment on PI during condensate accumulation in Texas Cream limestone core at S_{wi}=20%.

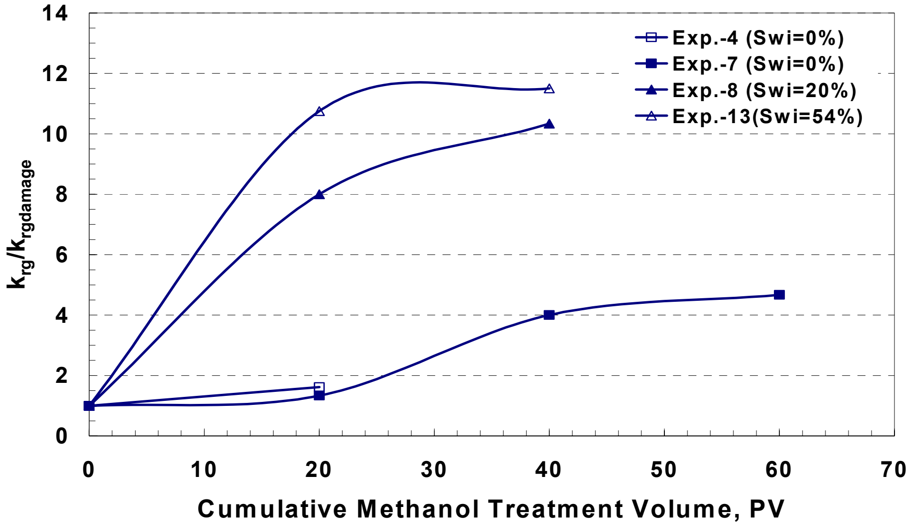

Figure 5.16: Effect of methanol treatment volume on gas relative permeability ratio during the enhanced flow period in Texas Cream limestone cores.

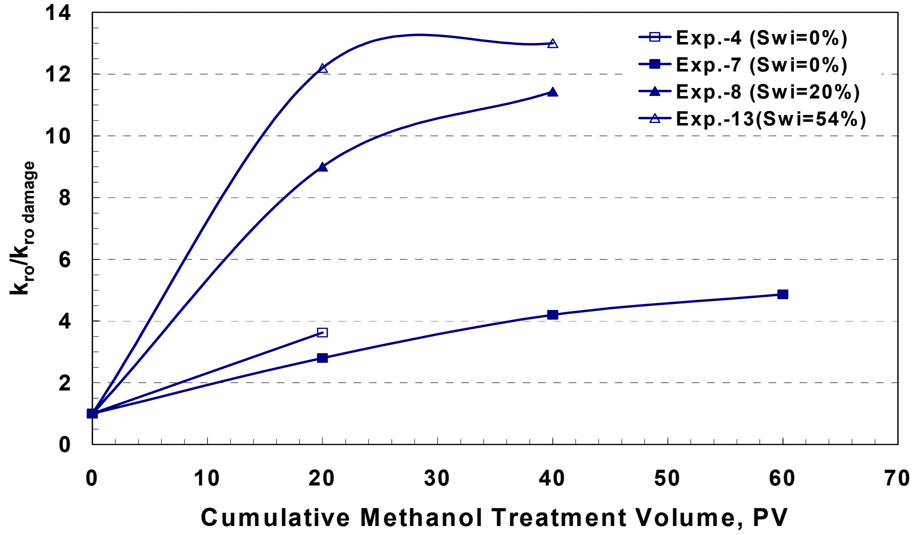

Figure 5.17: Effect of methanol treatment volume on oil relative permeability ratio during the enhanced flow period in Texas Cream limestone cores.

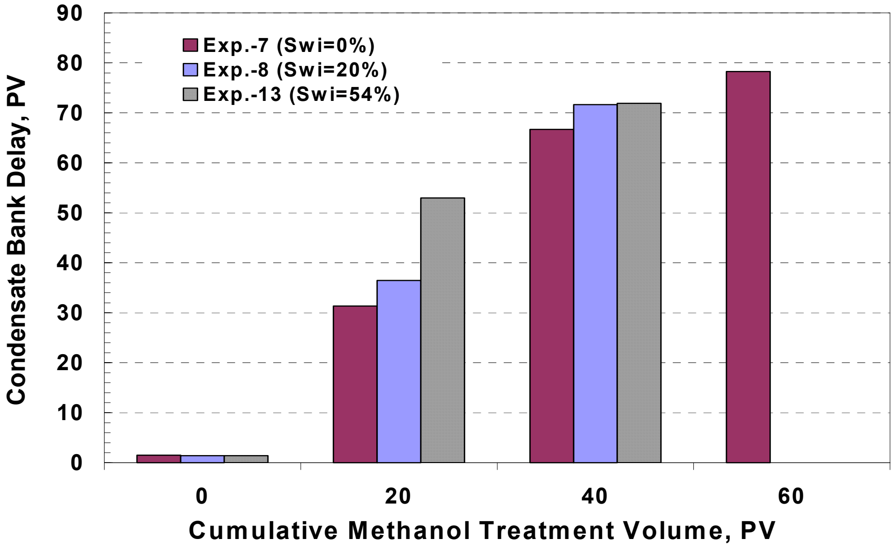

Figure 5.18: Effect of methanol treatment volume on duration of the enhanced flow period in Texas Cream limestone cores.

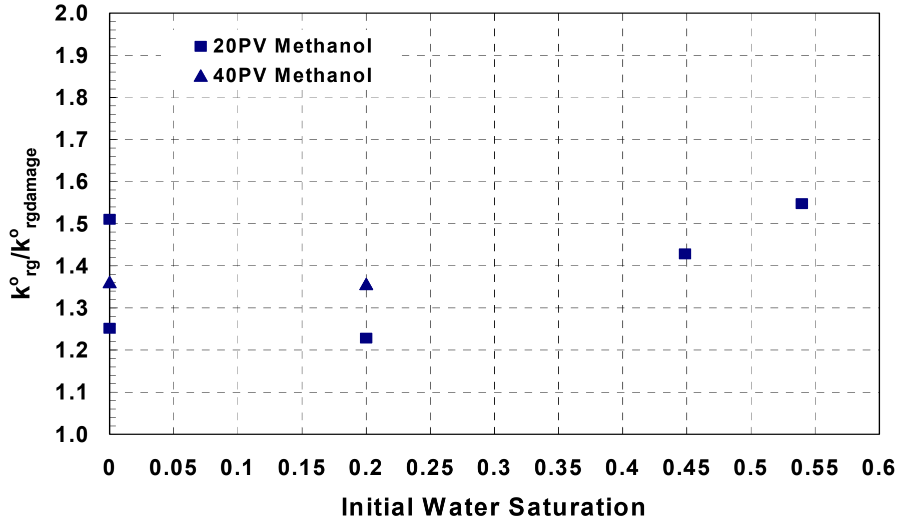

Figure 5.19: Effect of methanol treatment volume on gas relative permeability end-point ratio in Texas Cream limestone cores.

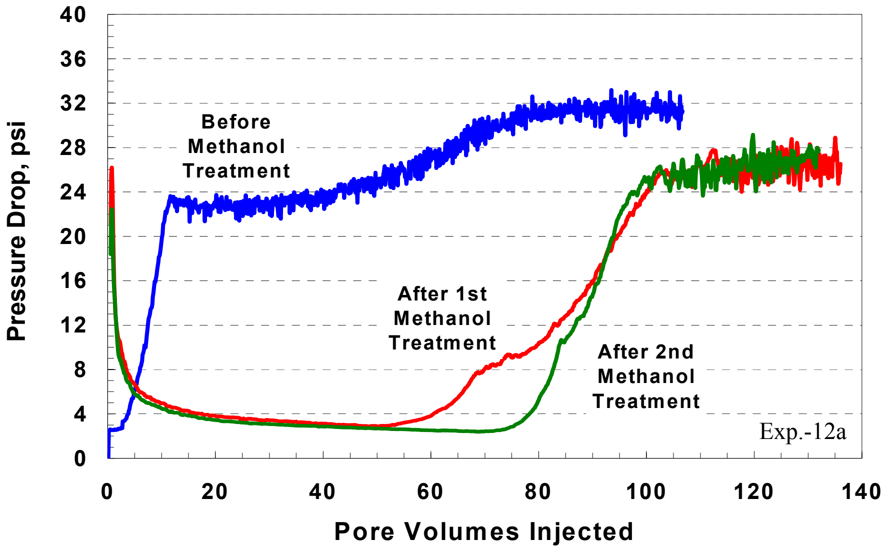

Figure 5.20: Effect of methanol treatment volume on condensate accumulation in Berea core at S_{wi}=38%.

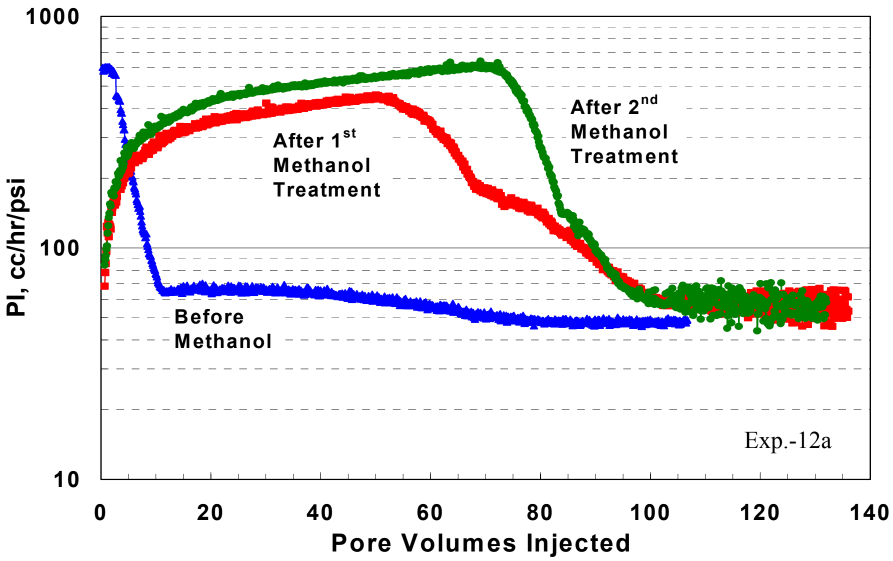

Figure 5.21: Effect of methanol treatment on PI during condensate accumulation in Berea core at S_{wi}=38%.

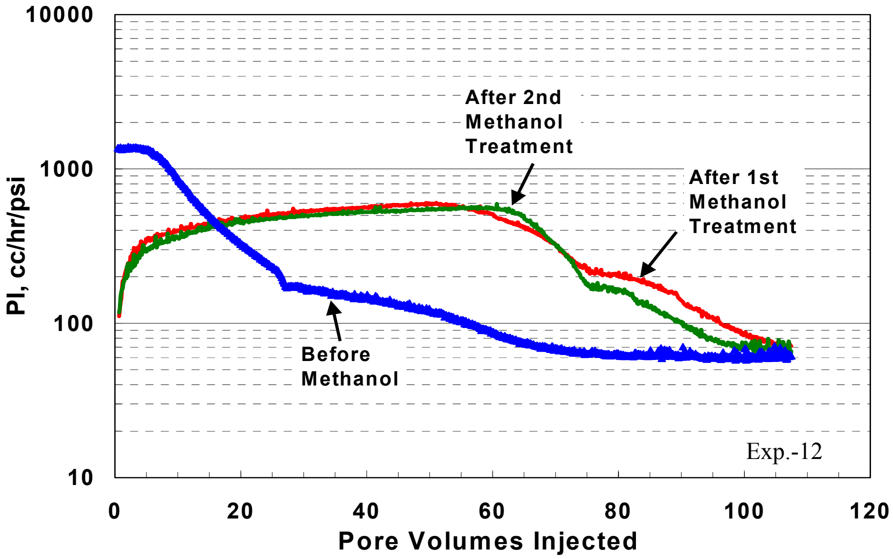

Figure 5.22: Effect of methanol treatment on PI during condensate accumulation in Berea core at S_{wi}=0%.

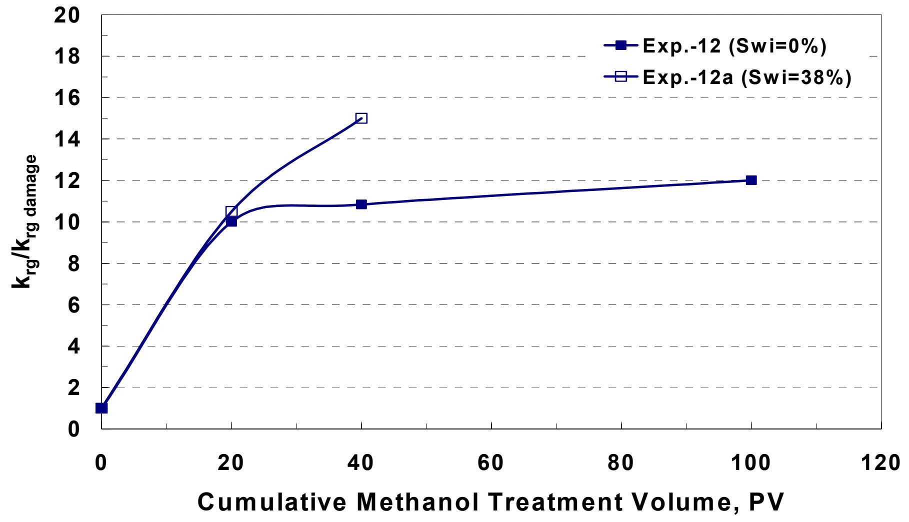

Figure 5.23: Effect of methanol treatment volume on gas relative permeability ratio during the enhanced flow period in Berea cores.

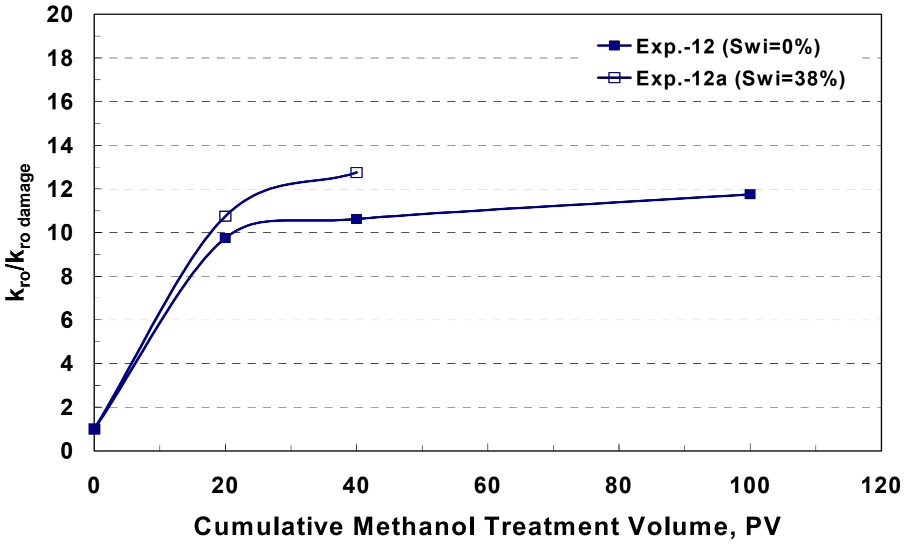

Figure 5.24: Effect of methanol treatment volume on oil relative permeability ratio during the enhanced flow period in Berea cores.

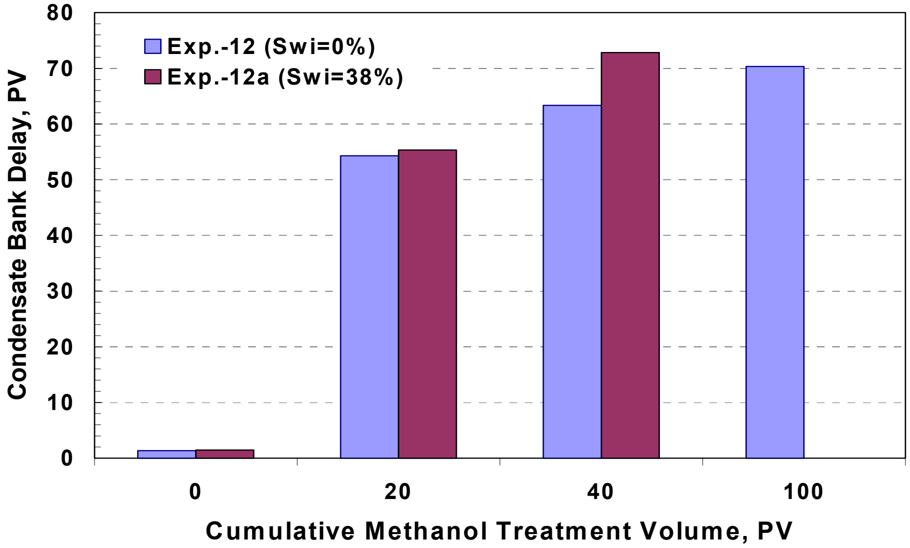

Figure 5.25: Effect of methanol treatment volume on duration of the enhanced flow period in Berea cores.

Chapter 6: Non-Equilibrium Behavior

Coreflood results discussed in Chapter 5 showed that more pore volumes were needed for the pressure drop during dynamic condensate accumulation to reach a steady state value at higher flow rates than at lower flow rates. This chapter describes the experiments performed to investigate the effect of non-equilibrium behavior on two-phase flow. It starts with a literature review of the published papers related to non-equilibrium effects. Then, experimental results will be discussed in detail.

6.1 INTRODUCTION

There have been a limited number of papers that have been published on the non-equilibrium behavior of gas-condensate mixtures. A literature review is provided here on the papers that address this issue.

Gondouin et al. (1967) performed experiments and numerical simulation to predict the well deliverability in gas condensate wells producing at high rates. The distribution of the wetting and non-wetting phases in the pores using retrograde condensation (natural imbibition) was found to be different from the distribution resulting from simultaneous flow of the two phases. At high flow rates, the increased pressure drop in the gas phase near the wellbore causes a higher flow rate of the liquid phase. High pressure gradient provides a better sweep of the liquid phase, thus resulting in lower liquid saturations near the wellbore. Numerical simulations showed that the radius of the liquid saturation accumulated in the Darcy zone increases with cumulative gas production. Simultaneously, some of the condensate brought near the wellbore by Darcy flow is swept away by the increased pressure drop resulting from non-Darcy effects.

Saeidi and Handy (1974) investigated the effects of dynamic fluid flow in consolidated sandstone porous media (k=86 md) on the phase behavior of a binary hydrocarbon mixture (methane/propane system). They found that at low pressure depletion rates, equilibrium was maintained during transient flow of the hydrocarbon mixture through the porous media, while some non-equilibrium behavior was observed at high pressure depletion rates. They also found differences between the fluid composition undergoing depletion while flowing through a porous medium and fluid composition measured in a PVT cell. The differences are due to non-equilibrium behavior related to the high rate of pressure depletion. They also found that the extent of non-equilibrium behavior is dependent on depletion rates. This result agrees with the results obtained by Morel et al. (1997). At a very low depletion rate (0.03 psi/sec), there was no obvious indication of the existence of non-equilibrium behavior. They got good agreement between dynamic and static depletion tests using the same gas mixture.

Henderson et al. (1993) conducted experiments on long Berea cores using a synthetic gas-condensate fluid to study the flow of gas and condensate in the area near the wellbore and the region of the reservoir far way from the producing wells. In the near wellbore region, the flow of gas and condensate is increasingly viscous dominated, as opposed to capillary and gravity dominated away from the wellbore. The higher the flow rate and greater the viscous forces, the greater the recovery of condensate. They found that during the establishment of the condensate saturation required for steady-state flow in Berea sandstone (k = 100 md) the condensate saturation increased to 27.3%, compared to a value of 20.9% in the higher permeability Clashach sandstone (k = 700 md). The increase in condensate saturation required for flow in the Berea core is attributed to the smaller pore size and, therefore, greater capillary retention of condensate in the lower permeability sample. Experimental results showed that the injection of equilibrium gas significantly reduced the condensate saturation in the horizontal cores after steady-state flow had been established. They attributed the recovery of condensate by gas injection from the horizontal core tests to continuity of the condensate phase. The condensate saturation for steady-state flow at a given phase ratio was found to be slightly dependent on the flow velocity, particularly at low capillary numbers.

Yu et al. (1996) observed that the condensate accumulation in the producing region is much greater than the value measured experimentally using the CVD method. The results of several experimental studies indicate that the presence of a porous medium has a significant influence on the equilibrium behavior of hydrocarbon mixtures (Ping et al., 1996; Yu et al., 1996).

Ali et al. (1997) reported experimental studies to evaluate the characteristic effects of immobile and mobile condensate saturations on the mobility of gas in the near-wellbore region. They used Berea sandstones (k=190 md) and a six-component synthetic mixture. The gas relative permeability was found to decrease with the increase in the total liquid saturation and the flow rate of the gas. They found that the reduction in gas relative permeability in the presence of immobile condensate and water is greater than when the same total liquid saturation was established by water only. They reported that as the flow rate of the gas increases, it deviated from Darcy's law and inertial effects play more roles in the flow behavior.

Shapiro et al. (2000) compared the liquid dropout and composition during constant volume depletion (CVD) experiments performed in the absence and in the presence of the porous medium. Their experimental results showed large discrepancies between the liquid dropout data and condensate composition obtained with and without porous media. They claimed that these differences between the mixture behavior in a porous medium and in bulk are due to the presence of non-equilibrium effects. They also said that the porous medium causes a chromatographic effect on the mixture and different components may be produced with different rates. Under reservoir conditions, an equilibrium area (like static PVT test) located far away from the wellbore and a non-equilibrium (dynamic PVT test) zone is close to it.

Wu et al. (2000) performed several simulations to evaluate the effects of non-equilibrium mass transfer on the flow behavior in the region near the wellbore in a gas condensate reservoir. They compared the results with those obtained under the local equilibrium assumption. Their results revealed that non-equilibrium phase behavior led to a reduction in the condensate saturation in the region near the wellbore. The mole fractions for light and heavy components in the oil phase were noticeably different. In high-velocity layers, these differences became more significant.

As can be seen from the literature review, there are several explanations for the non-equilibrium behavior during two-phase flow. To better understand the non-equilibrium behavior, experiments were performed. The aims of these experiments were:

- To study the effect of flow rate on dynamic condensate accumulation.
- To investigate the propagation of condensate bank through the core using co-injection of equilibrium gas and condensate phases simultaneously at a high flow rate.

- To study the non-equilibrium behavior during two-phase flow.
- To analyze the effluent composition during two-phase flow.
- To investigate the effect of flow rate on the composition.

6.2 EFFECT OF FLOW RATE ON CONDENSATE ACCUMULATION

Coreflood experiments described in Chapter 5 showed that two-phase flow required many pore volumes to reach steady state during dynamic condensate accumulation in both low and high permeability cores (**Figures 5.6 and 5.7**). More pore volumes were required to reach steady-state as the flow rate of the two-phase flow was increased. **Figure 6.1** shows the pressure drop for different sections across the core (Texas Cream limestone) during dynamic condensate accumulation at 1,200 psig and a flow rate of 42 cc/hr (Experiment-19, S_w=0%, see **Appendix B** for details). This figure shows how the condensate bank propagates through the core. The pressure drop across Section 1 reached a plateau value after 5.7 PV. Then, the pressure drop across Section 2 started to increase at the arrival of the condensate bank and so on. The condensate bank took around 5.7 PV in each section of the core. The two-phase flow reached a steady state in the core after an injection of 22.6 PV. However, it took only 16 PV to reach a steady-state when the condensate was accumulated at a lower rate of 18 cc/hr (**Figure 5.5**).

The fractional flow of oil (f_o) measured for the gas mixture is 6.82% at 1,200 psig and 145°F. Condensate saturation (S_o) can be calculated, assuming S_w =0%, as follows: $S_o=f_o+f_o\,t_D$, where t_D is pore volumes of two-phase flow required to reach steady state. **Table 6.1** gives condensate saturation calculated for two-phase flow at various flow rates. The calculated condensate saturations for two-phase flows presented in **Figures 5.5** and **6.1** are greater than 100%, which makes no sense. Thus, non-equilibrium behavior influenced two-phase flow and extended the duration of the condensate accumulation at high flow rate.

However, when condensate was dynamically accumulated through the core at lower rates, the pressure drop reached steady state at less pore volumes. **Figure 6.2** shows the pressure drop across different sections of the core during dynamic condensate accumulation at 1,200 psig and a flow rate of 6 cc/hr (Experiment-16, S_w=0%, see **Appendix B** for details). This figure shows the same trend as that observed at higher flow rates, except that the pressure drop reaches a stabilized value after only 9.6 PV. At this point it was suspected that the flow rate might be too high for local equilibrium in the core. To test this hypothesis, another coreflood experiment using the same core, but at very low flow rate, was conducted. **Figure 6.3** shows the pressure drop across the core during dynamic condensate accumulation at 1,200 psig and a flow rate of 2 cc/hr (Experiment-17, S_w=0%, see **Appendix B** for details). The condensate bank takes 1.4 PV to reach steady state in each section. The pressure drop across the core reached steady state after 5.5 PV. Using the measured oil fractional flow (f_o) of

6.82% and t_D =5.5 PV, the condensate saturation (S_o) is equal to 44.3%. The calculated condensate saturation is reasonable. Thus, local equilibrium was achieved in this flow since the flow rate was low. These results indicate that the condensate accumulation depends on the flow rate.

Figure 6.4 is a plot of the pore volumes needed to reach steady-state as a function of flow rate. All flow rates above 5.4 cc/hr appear to show non-equilibrium behavior. **Figure 6.5** shows the residence time as a function of flow rate. The residence time sharply decreases with flow rate. This means that the residence time for two-phase flow to achieve local equilibrium is insufficient to achieve local equilibrium at higher flow rates. However, at a flow rate of 5.4 cc/hr, the residence time of 3.7 hours was adequate to reach steady state, as discussed above for **Figure 6.3**. This implies that on the order of 10, more residence time is required for local equilibrium flow in the core.

6.3 CO-INJECTION OF EQUILIBRIUM PHASES

In the previous coreflood experiments, a single-phase gas mixture was injected at a flowing pressure (3,000 psig) above the dewpoint and flashed into gas and condensate phases at the inlet of the core that was kept at a pressure below the dewpoint (1,200 psig). This method allowed dynamic condensate accumulation through the core. For the purpose of further investigation of the non-equilibrium behavior, equilibrium gas and condensate phases were simultaneously pumped into the core at the same fractional flow and pressure used in the flashing method.

The equilibrium gas and condensate phases were each stored in a separate rodded-piston accumulator. Each accumulator was placed vertically inside the oven and connected to a RUSKA pump. The equilibrium gas phase accumulator was connected to the pump from the bottom, so the gas flow will be from the top-end of the accumulator. On the other hand, the condensate accumulator was connected to the pump from the top-end where the condensate will flow from the bottom end. The flow rate of each pump was selected in order to get a constant fractional flow of around 7%. The injected phases were mixed together before they enter the upstream back-pressure regulator. Before the start of this stage, the inlet and outlet valves of the core were closed. Pressure of the upstream and downstream back-pressure regulators was set to 1,200 psig. Flow was started while the bypass valve was open until the pressure in the lines stabilized. Then, the bypass valve was closed and inlet and outlet valves were opened simultaneously. This stage allowed flow of equilibrium gas and condensate phases simultaneously through the core. The flow was stopped when the pressure drop across the core reached stable values. A Texas Cream limestone core was used in this experiment.

The gas flow rate was 132 cc/hr and the condensate flow rate was 10 cc/hr. These flow rates give a liquid fractional flow of 7.0% that is very close to that one measured (6.82%) using the dynamic accumulation. These flow rates are equivalent to a single-phase flow rate of 52.9 cc/hr at 3,000 psig and flashing at 1,200 psig. **Figure 6.6** shows the pressure drop across different sections of the core during co-injection of equilibrium gas and condensate phases at 1,200 psig. The pressure drop in the first section gradually increased until it reached a plateau value after injection of 2.7 PV. Then, the pressure drop in Section 2 started to increase. The condensate bank propagates through each section until it reaches a steady state. The condensate accumulation in the whole core reached steady state after cumulative injection of 11.5 PV.

Co-injection of condensate and gas phases allowed condensate accumulation to reach a steady state faster compared to the dynamic flashing method at the same flow rate and fractional flow. For instance, two-phase flow using the flashing method reached a steady state after 60 and 152 PV at a flow rate of 44.8 and 60 cc/hr, respectively. Therefore, local equilibrium between gas and condensate phases was not achieved during dynamic flashing, except at very low flow rates.

Gas and oil relative permeabilities during co-injection of the two phases are given in **Table 6.2**. Gas and oil relative permeabilities were 0.161 and 0.207, respectively, at steady state. These results are close to those obtained in the previous experiments since the same core was used in both experiments (No. 17 and 18), even though the condensate accumulation methods were different. Next, the co-injection of two phases was resumed at a lower flow rate. The flow rates of gas and condensate phases were 32 and 2.5 cc/hr, respectively. **Figure 6.7** shows the pressure drop at different sections across the core during co-injection of two phases at 1,200 psig at steady state. The measured gas and oil relative permeabilities are given in **Table 6.3**. Gas and oil relative permeabilities were 0.112 and 0.149, respectively, at steady state. One explanation for these lower values is the lower capillary number at the lower flow rate. The capillary number calculated from $N_c = \frac{k\,\Delta P}{\sigma L}$ is 6.3×10^{-8}.

6.4 GC MEASUREMENTS

The pressure of the upstream and downstream back-pressure regulators was set to 1,200 psig. The equilibrium gas, at 1,200 psig, was flowed through the windowed-through PVT cell while bypassing the core. The flow rate was 48 cc/hr at 1,200 psig. The effluent of the PVT cell was charged into the GC feed line at 300 psig controlled by a third back-pressure regulator. The GC pressure was chosen to be 300 psig because it gives a good separation between the peaks within the limit of the FID detector. The calibration data described in Chapter 4 was used to convert GC peak area to mole fraction for n-C_4, n-C_7, and n-C_{10}

components and C_1 was calculated from the ideal gas law applied on the 15 μL sampling loop.

Table 6.4 shows results from the flash calculation of the gas mixture at 145°F using the PREOS. **Figure 6.8** shows the mole percent of each component of the flowing equilibrium gas at 1,200 psig measured by the GC. The concentration of both C_1 and n-C_4 were almost stable during the flow. However, small variations were observed for n-C_7 and n-C_{10}. In **Table 6.5**, the measured gas concentrations are compared to the values from the flash calculation using the PREOS. The measured concentration of each component was based on an average value of several GC samples. The GC values for n-C_7 and n-C_{10} are lower than the PREOS values. One possibility for this variation is that some of the heavy components were trapped in the PVT cell causing a decrease in their concentrations in the gas samples.

Therefore, all the lines and the PVT cell were flushed with methane until methane was the only component shown in the GC analysis. Then, the flow of the equilibrium gas was resumed through the PVT cell and bypassing the core. To get a comparison, the component concentrations of equilibrium gas were normalized to the values of the flash calculation (**Table 6.4**). **Figure 6.9** depicts the normalized concentration of each component in the flowing equilibrium gas at 145°F and 1,200 psig. There is a very good match between the measured and calculated concentration of C_1 and n-C_4, whereas the GC values for n-C_7 and n-

C_{10} are again lower than the PREOS values. There are likely some problems with the GC measurements for the heavy components that need to be further investigated.

The equilibrium gas was kept in the PVT cell for 2 days at 145°F and 1,200 psig. Samples from the PVT cell were charged into the GC without pumping from the equilibrium gas accumulator (static analysis). This procedure is a constant volume depletion test. The GC was programmed to analyze samples each sample for one hour. **Figure 6.10** shows the normalized concentration of the equilibrium gas components at 145°F and 1,200 psig. The measured concentrations of n-C_4, n-C_7, and n-C_{10} in the first 4 samples were less than the values calculated from the PREOS. The opposite is true for the last 5 samples. One explanation is that some liquid formed in the cell initially and then gradually decreased with time as the pressure in the cell decreased.

6.5 COMPOSITIONAL ANALYSIS DURING TWO-PHASE FLOW

6.5.1 Dynamic Flashing of Two Phases

The pressure of the upstream back-pressure regulator was increased to 3,000 psig, while the downstream back-pressure regulator was kept at 1,200 psig. The core had been saturated with condensate from the previous experiment

(Experiment No. 18). The gas mixture was flowed as a single phase (@ 3,000 psig) and flashed through the core (@ 1,200 psig) into gas and condensate phases. The effluent of the core was passed through the PVT cell to separate the condensate and the gas. The gas was fed into the GC line for compositional analysis. Flow rates of 18 and 6 cc/hr (measured at 3,000 psig) were used in sequence. **Figure 6.11** shows pressure drop data for different sections of the core during dynamic condensate accumulation 1,200 psig. Steady state is reached very quickly since the core had already been flooded with the same mixture at the same pressure. The measured gas and condensate relative permeabilities during two-phase flow are given in **Table 6.6**. The relative permeabilities are almost the same as those previously measured at the same flow rate.

Figure 6.12 shows the normalized concentrations of the effluent gas during dynamic condensate accumulation. The GC data for the gas phase created using the flashing method is not the same as the equilibrium gas. One possible explanation for this difference is that local equilibrium did not exist during the two-phase flow. As a result, the gas phase lost most of the heavy components into the condensate phase that was trapped in the PVT cell.

The gas-condensate volume ratio in the PVT cell was adjusted to about 7% by drawing some of the condensate from the cell while maintained the pressure at 1,200 psig. Then, the PVT cell was shut-in for 2 days to reach local equilibrium. The gas phase was charged directly from the PVT cell into the GC for compositional analysis without any further pumping (static sampling). **Figure 6.13** shows the normalized concentrations of the gas in equilibrium with the condensate in the PVT cell at 1,200 psig. This figure reveals that the gas became more rich with the heavy components than that analyzed with a continuous flow (**Figure 6.12**). As a result, the local equilibrium was achieved between the gas and condensate phases when they kept in contact for some period of time. However, the shut-in period was not sufficient to attain a full equilibrium since the normalized concentration (< 1) of n-C_4, n-C_7 and n-C_{10} components did not reached the values in the equilibrium gas. This test confirms that the local equilibrium is very sensitive to the flow. From a practical point of view, non-equilibrium behavior would be expected to be dominant in gas-condensate reservoir since the production rate is much higher than that performed in the laboratory.

The effect of porous medium on the equilibrium of two-phase flow was investigated. This was accomplished by flowing the two-phase directly through the PVT cell while bypassing the core since the previous analyses were performed in the presence of the core. The gas mixture (at 3,000 psig) was flashed into gas and condensate phases through the PVT cell (at 1,200 psig) at different pump rates. The GC analyzed composition of the gas phase, while the condensate phase accumulated inside the PVT cell. The dynamic condensate fractional flow was determined at each flow rate by measuring the cumulative hydrocarbon liquid volume gathered in the PVT cell as a function of time using the cathetometer.

Figure 6.14 shows the normalized concentrations of the gas during a dynamic two-phase flow through the PVT cell and in the absence of porous medium at 1,200 psig and various flow rates. The normalized concentrations in the absence of the porous medium are close to those measured in the effluent from the core (**Figure 6.12**). The normalized concentrations of n-C_7 and n-C_{10} components increased to a value close of 1.0 when the flow rate was increased to 40 cc/hr. Then, they gradually decreased to the same values measured at the lower flow rates (2, 6,and 18 cc/hr). The reason for the increase in the heavy components concentrations was the flow at 40 cc/hr was started after a shut-in period over the weekend. Thus, the gas-phase was given some time (over the weekend) to equilibrate with the condensate phase in the PVT cell and gained some of the heavy components. When the flow was started, the first sample analyzed was similar to the equilibrium gas. As the flow proceeded, the local equilibrium was disturbed by the flow. The increase in the heavy component concentrations after the shut-in period strongly supports the results obtained in **Figure 6.13**. Therefore, the main factor affecting the local equilibrium is the flow rate.

Figure 6.15 shows the cumulative hydrocarbon volume measured during the two-phase flow as a function of time. The dynamic condensate fractional flow (f_o) measured during two-phase flow in the absence of porous medium at 1,200 psig and various flow rates is given in **Table 6.7**. The measured dynamic condensate fractional flow (8.15%) is close to the value measured (6.82%) from the core as well as the value (7.14%) calculated using the PREOS.

6.5.2 Co-Injection of Two Phases

Next, the equilibrium gas and condensate phases were co-injected through the core at a flow rate of 32 and 2.5 cc/hr, respectively. These flow rates give a condensate fractional flow of 7.2%. The effluent gas was analyzed with the GC. **Figure 6.16** shows the pressure drop for different sections of the core during co-injection at 1,200 psig. The pressure drop did not show any build up because the core was already saturated with condensate. **Table 6.8** lists gas and condensate relative permeabilities measured during the co-injection of two phases through the core at 1,200 psig at steady state. The measured relative permeabilities are higher than those obtained using the flashing method (**Table 6.6**) because the flow rate is higher. Increasing the flow rate increases the relative permeability.

Figure 6.17 shows the normalized concentrations of the gas during co-injection of equilibrium phases through the core at steady state and 1,200 psig. This figure shows the same trend observed using the flashing method through the core (**Figure 6.12**) where the concentration of each component is below the expected values in the equilibrium gas.

The equilibrium gas and condensate phases were then co-injected through the PVT while bypassing the core to investigate the effect of porous medium on the equilibrium. **Figure 6.18** depicts the normalized concentrations of the gas in the absence of the core. The concentrations of n-C_4, n-C_7 and n-C_{10} were larger than those measured in the presence of the core. The concentration of n-C_4 was almost stable and close to its content in the equilibrium gas. The gas phase became richer with the heavy hydrocarbons in the absence of the porous medium. It seems that the porous medium acts as a filter for the heavy components when they are in equilibrium with each other and makes the gas phase leaner. This is in agreement with the results found by Jianfen et al. (1998) and Saeidi and Handy (1974).

6.6 COREFLOOD SIMULATION

Rai (2003) simulated the gas-condensate coreflood experiments performed in this study using the University of Texas Compositional Simulator (UTCOMP). He used a 1-D homogenous model with 12×1×1 grid. The simulated length and the cross-sectional area are equal to the length and the area of the core. The model has a constant rate injector and a constant pressure producer. A Corey-type relative permeability model with the trapping number effects, as suggested by Pope et al. (2000), was used for coreflood simulations. Experimentally measured values of gas end-point relative permeability (k°_{rg}) were used as model inputs. Details of these simulations can be found in Rai (2003).

Figure 6.19 compares simulated and measured pressure drop across the core during dynamic condensate accumulation at 2 cc/hr for Experiment-17. The simulation shows a pressure buildup during condensate accumulation until steady state is reached at about 6.2 PV. Since the simulation was based on the assumption of local equilibrium , steady state was reached within 6.2 PV, which is close to the measured value (5.5 PV) obtained at a low flow rate of 2 cc/hr. This result is consistent with the interpretation that local equilibrium was achieved during two-phase flow at a low flow rate. The simulation gave a condensate saturation of about 58.3% at steady state, which is higher than the estimated experimental value of 44.3% (**Table 6.1**) at 2 cc/hr, but the relative permeability parameters assumed for the simulation input might account for this difference.

Figure 6.20 compares simulated and measured pressure drop across the core during co-injection of equilibrium gas and condensate phases (Experiment-18). Simulation results show a similar trend to that measured in Experiment-18. The simulated co-injection of equilibrium gas and condensate phases reached a steady state at 9.6 PV. This value is close to that measured (11.5 PV) in Experiment-18. However, these pore volumes are higher than that based on equilibrium behavior (6.1 PV for f_o=7% and S_o=50%). One explanation for this small difference is that the initial conditions for flashing and co-injection methods were not the same. In the flashing method, the initial condensate saturation was about 7%, while there was no condensate present in the core at the start of the co-injection method. Therefore, it is expected that two-phase flow needs 7.3 PV to reach a steady state in the co-injection method compared to the flashing method (6.2 PV). On the other hand, simulations of the high flow experiments predict steady state will be reached at much lower pore volumes than the high flow rate coreflood experiments, which is a strong indication that local equilibrium is not a good assumption for high flow rates (low residence times). Residence times were as low as 9 minutes for the highest flow rates.

6.7 SUMMARY OF THE RESULTS

Coreflood experiments showed non-equilibrium behavior during the flow of two-phase through cores. This behavior was found to be sensitive to injection flow rates. Lower flow rates resulted in a faster condensate accumulation in the core than at higher rates. Dynamic condensate accumulation at a low flow rate reached a steady state at about the same cumulative pore volumes required when the equilibrium gas and condensate phases were co-injected through the core at the same fractional flow and pressure when adjusted for the difference in initial conditions. Local equilibrium between the flowing gas and condensate phases can be achieved at a low flow rate. At high flow rates, dynamic condensate accumulation using the flashing method needed 5 to 10 times more pore volumes to reach steady state compared to co-injection or low flow rate.

Table 6.1: Condensate saturation (S_o) calculated during two-phase flow steady state at various flow rates.

q, cc/hr	t_D, PV	S_o, %
2	5.5	44.3
6	9.6	72.3
18	16.0	>100
42	22.8	>100
44.8	59.0	>100
60	108.0	>100

Table 6.2: Gas and oil relative permeabilities during co-injection of equilibrium gas (q_{gas}=132 cc/hr) and condensate (q_{oil}=10 cc/hr) phases at 1,200 psig.

	ΔP, psia	k_{rg}	k_{ro}
Section-1	23.41	0.089	0.115
Section-2	8.70	0.241	0.310
Section-3	9.35	0.224	0.288
Section-4	10.61	0.197	0.254
Whole Core	52.07	0.161	0.207

Table 6.3: Gas and oil relative permeabilities during co-injection of equilibrium gas (q_{gas}=32 cc/hr) and condensate (q_{oil}=2.5 cc/hr) phases at 1,200 psig at steady state.

	ΔP, psia	k_{rg}	k_{ro}
Section-1	6.52	0.078	0.103
Section-2	2.88	0.176	0.234
Section-3	2.67	0.190	0.252
Section-4	3.75	0.135	0.180
Whole Core	18.07	0.112	0.149

Table 6.4: Flash calculation using the PREOS at 145°F.

	Concentration, mole%		
Component	Single-Phase at 3,000 psig	Gas at 1,200 psig	Liquid at 1,200 psig
C_1	78.50	89.582	31.504
n-C_4	15.00	9.579	37.990
n-C_7	5.00	0.795	22.832
n-C_{10}	1.50	0.044	7.674

Table 6.5: Measured and calculated concentration of each component in the equilibrium gas at 145°F and 1,200 psig.

	Concentration, mole%	
Component	Measured	Calculated
C_1	91.949	89.582
n-C_4	8.040	9.579
n-C_7	0.010	0.795
n-C_{10}	0.001	0.044

Table 6.6: Gas and oil relative permeabilities during dynamic condensate accumulation through the core at 1,200 psig and steady state.

	q= 18 cc/hr		q= 6 cc/hr	
	k_{rg}	k_{ro}	k_{rg}	k_{ro}
Section-1	0.085	0.111	0.067	0.087
Section-2	0.205	0.267	0.170	0.222
Section-3	0.211	0.275	0.207	0.271
Section-4	0.175	0.229	0.115	0.151
Whole Core	0.162	0.212	0.141	0.185

Table 6.7: Dynamic condensate fractional flow measured during two-phase in the absence of porous medium at 1,200 psig and various pump rates.

Flow rate, cc/hr	f_o, vol.%
2	8.81
6	8.58
18	6.97
40	7.75
90	8.66

Table 6.8: Gas and oil relative permeabilities during co-injection of equilibrium gas (q_{gas}=32 cc/hr) and condensate (q_{oil}=2.5 cc/hr) phases through the core at 1,200 psig and steady state.

	k_{rg}	k_{ro}
Section-1	0.422	0.560
Section-2	0.565	0.750
Section-3	0.408	0.541
Section-4	0.204	0.271
Whole Core	0.341	0.453

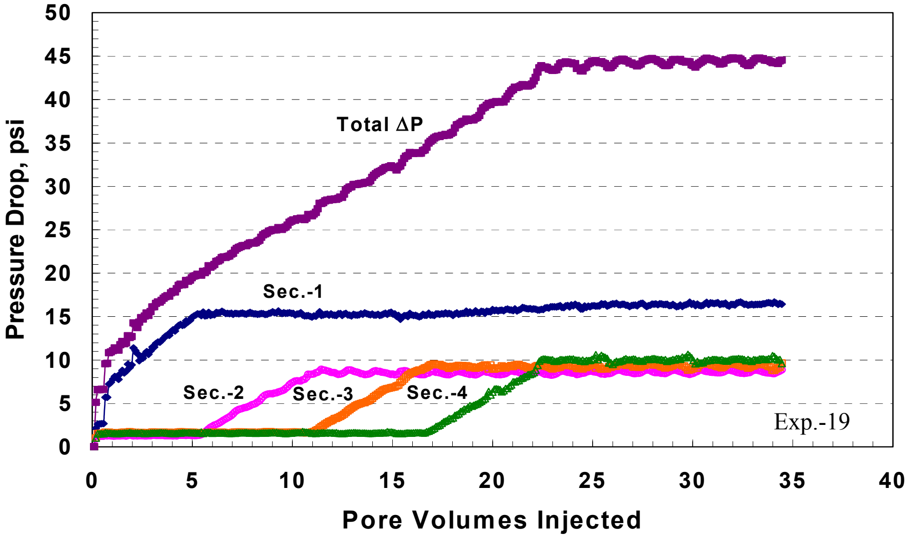

Figure 6.1: Pressure drop at different sections across the core during dynamic condensate accumulation at 42 cc/hr and 1,200 psig.

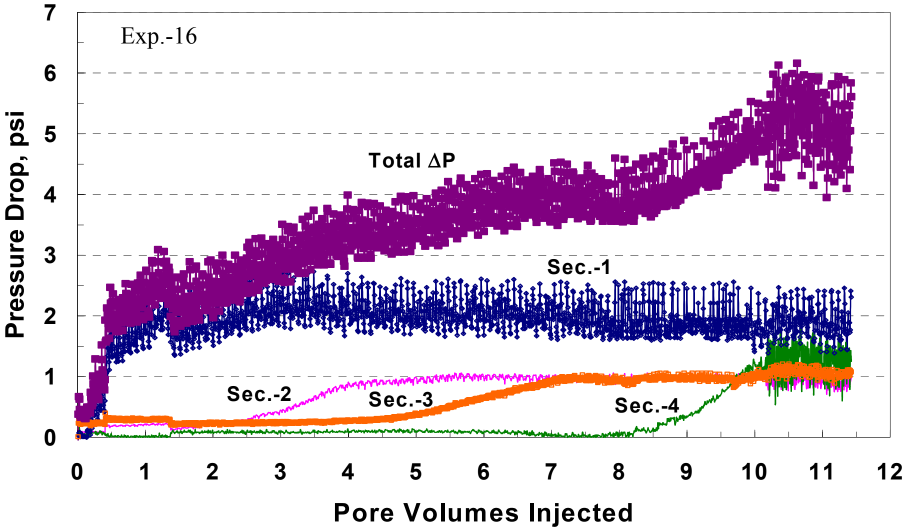

Figure 6.2: Pressure drop at different sections across the core during dynamic condensate accumulation at 6 cc/hr and 1,200 psig.

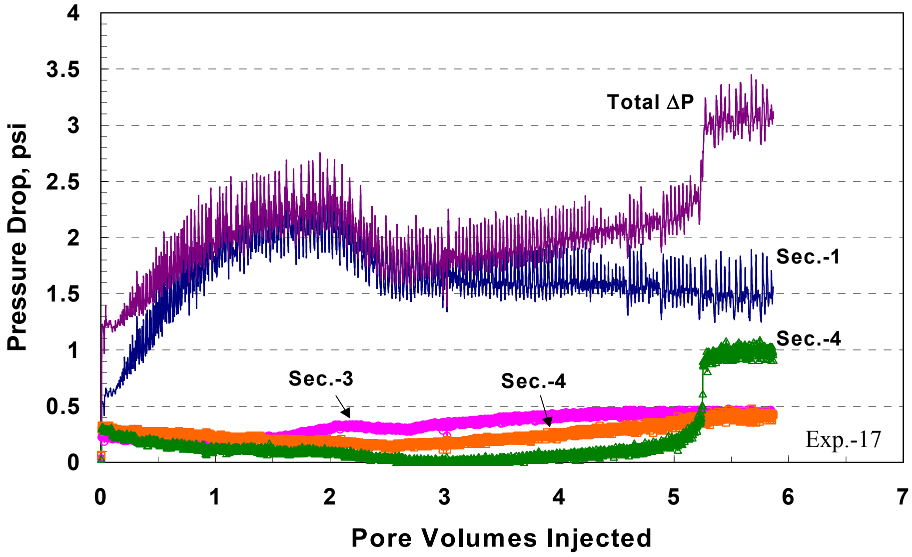

Figure 6.3: Pressure drop at different sections across the core during dynamic condensate accumulation at 2 cc/hr and 1,200 psig.

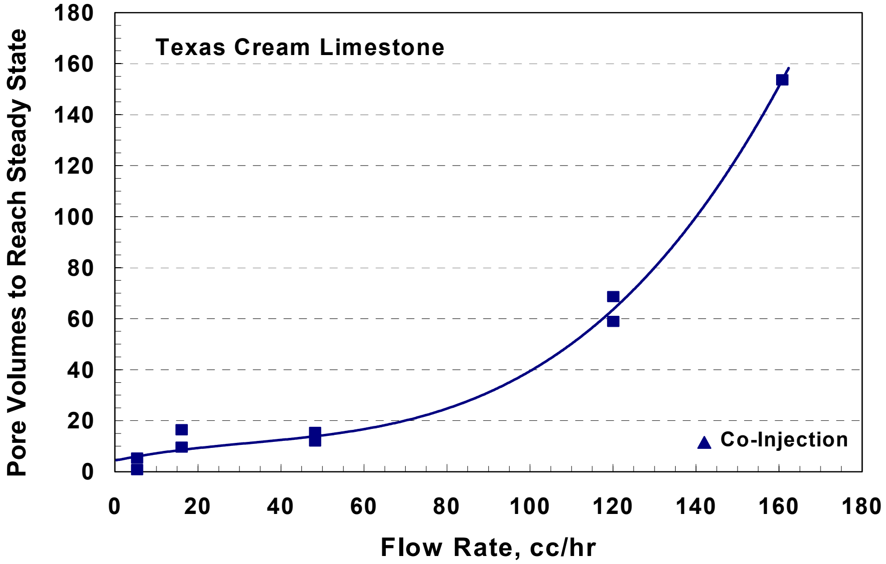

Figure 6.4: Pore volumes required to reach steady-state during dynamic condensate accumulation as a function of flow rate at 1,200 psig.

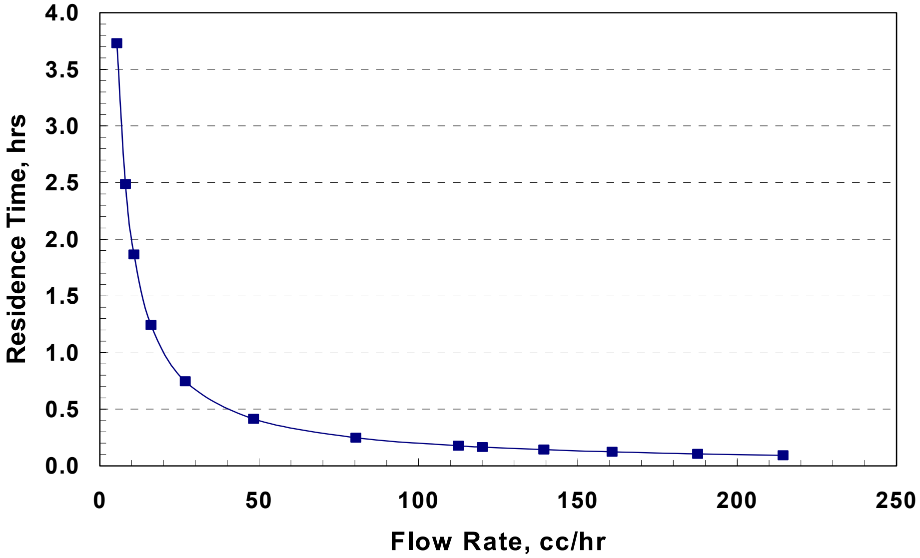

Figure 6.5: Residence time as a function of flow rate.

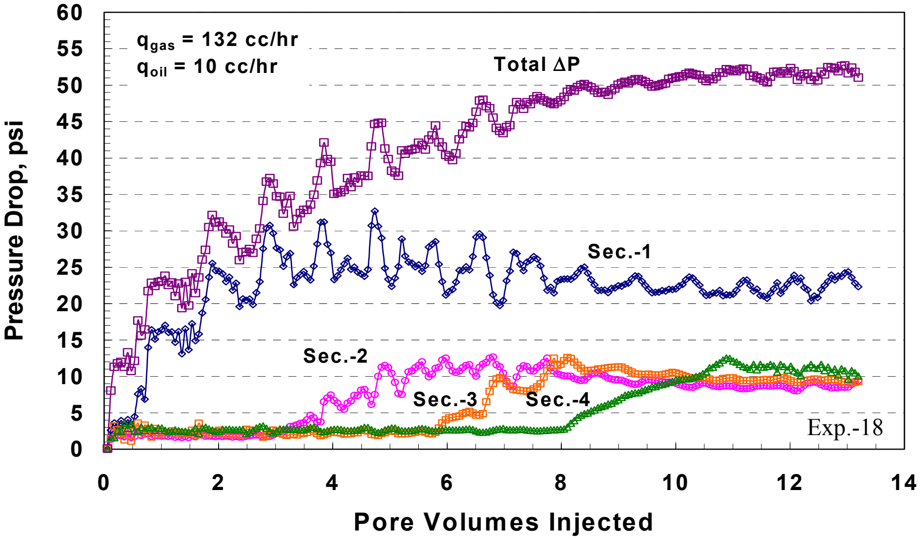

Figure 6.6: Pressure drop at different sections across the core during co-injection of equilibrium gas and condensate phases at 1,200 psig.

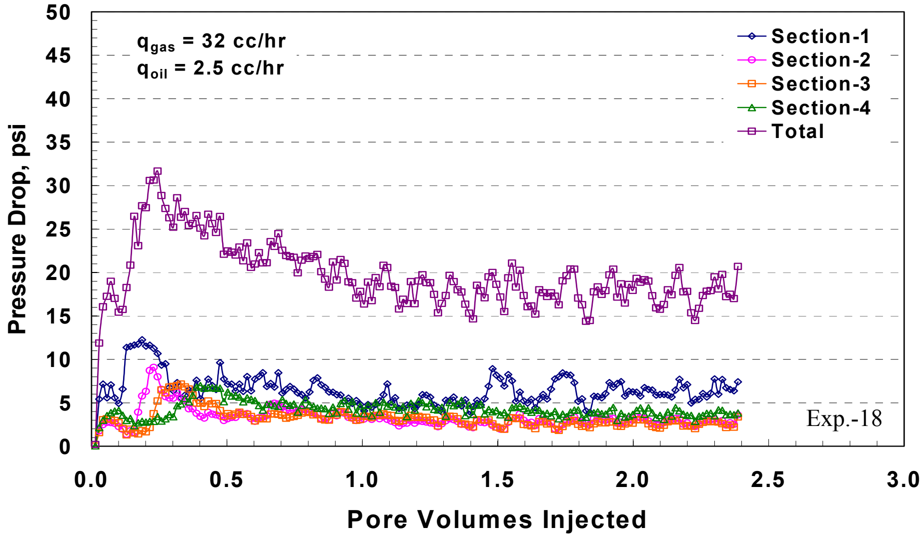

Figure 6.7: Pressure drop at different sections across the core during co-injection of equilibrium gas and condensate phases at 1,200 psig and steady state.

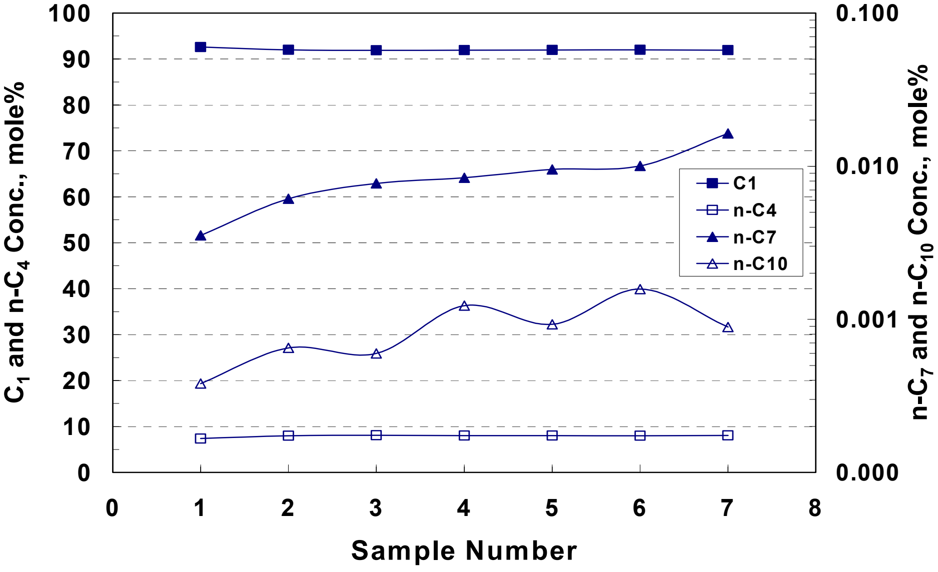

Figure 6.8: Compositional analysis of the equilibrium gas at 1,200 psig.

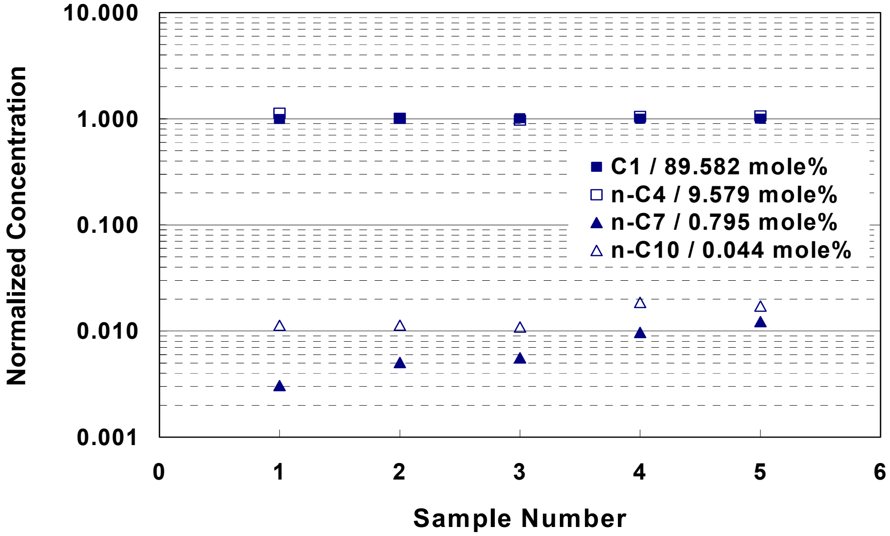

Figure 6.9: Normalized concentrations of the flowing equilibrium gas composition at 145°F and 1,200 psig.

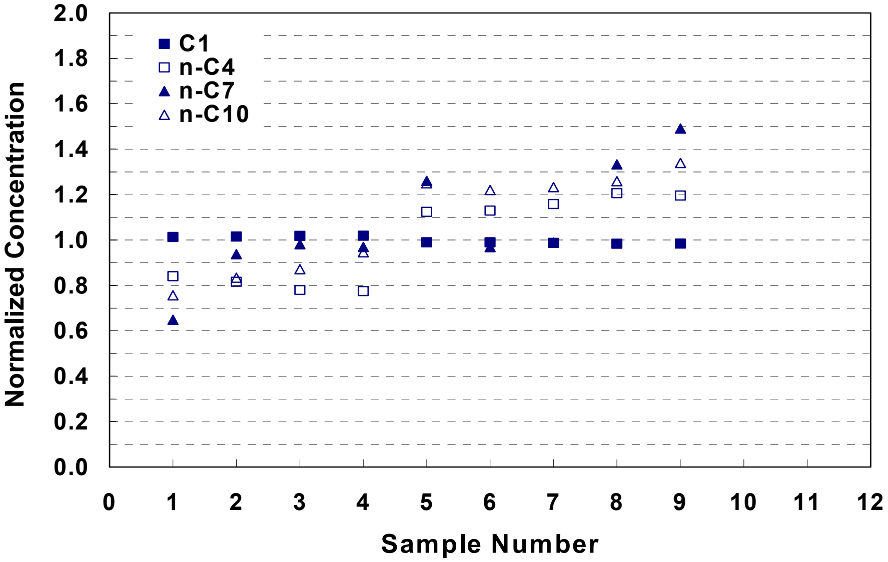

Figure 6.10: Normalized concentration of the equilibrium gas at 145°F and 1,200 psig.

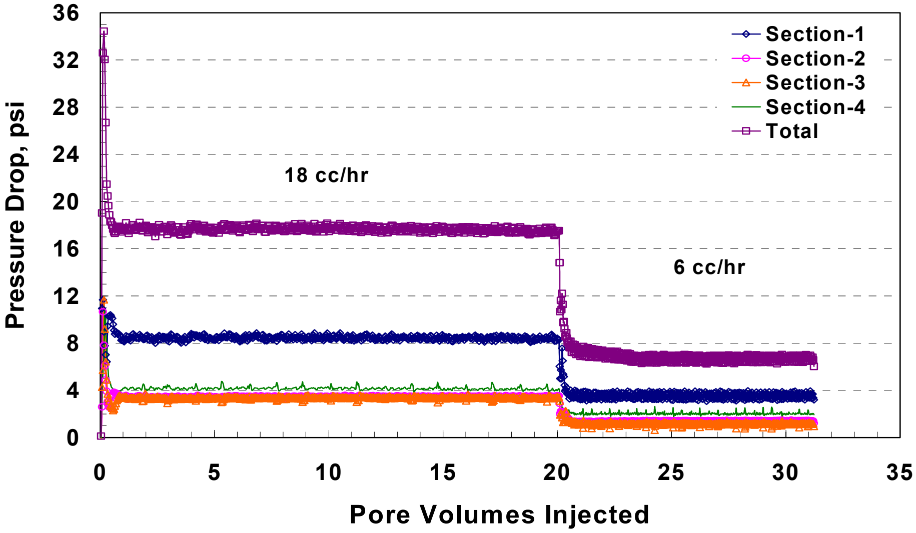

Figure 6.11: Pressure drop at different sections across the core during dynamic condensate accumulation at steady state and 1,200 psig.

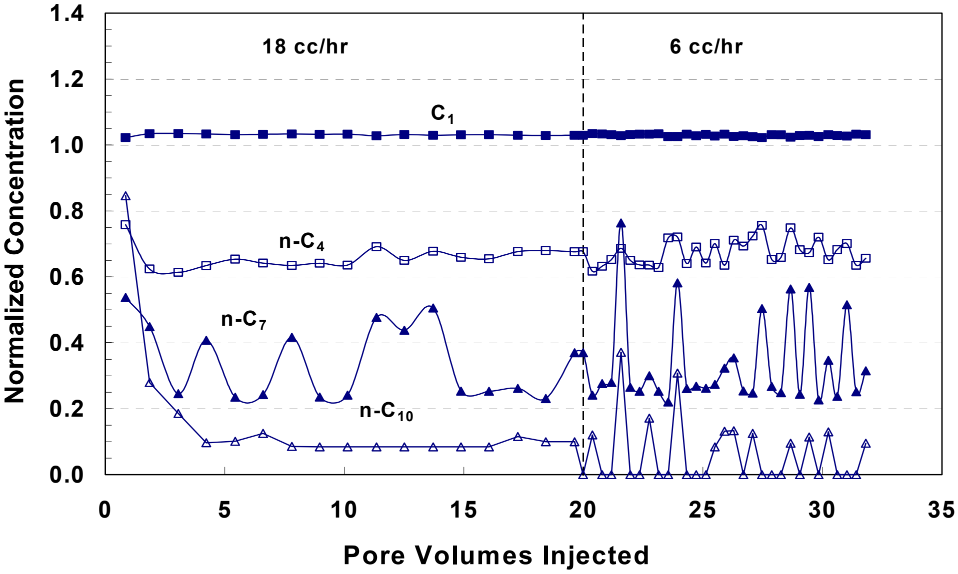

Figure 6.12: Normalized concentration of the gas during dynamic condensate accumulation through the core at 1,200 psig and steady state.

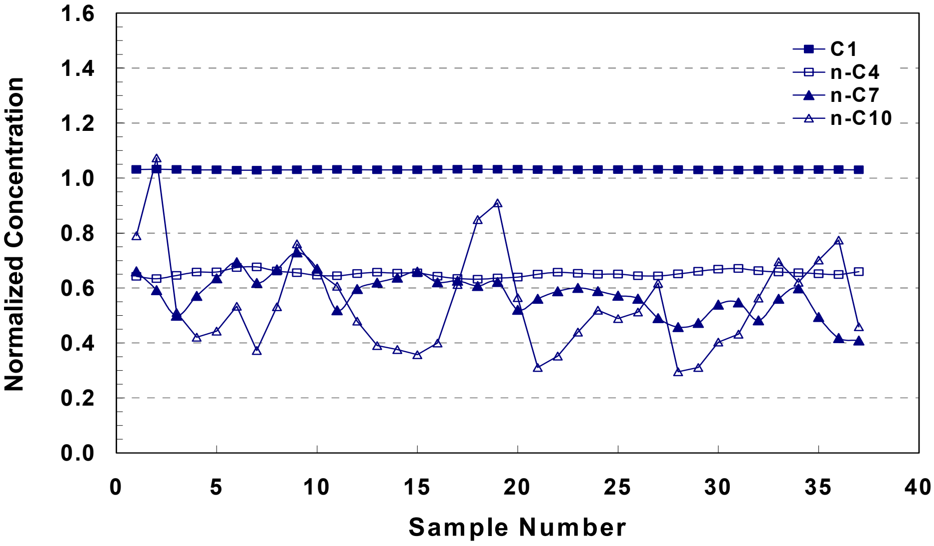

Figure 6.13: Normalized concentrations of the gas in equilibrium with the condensate in the PVT cell at 1,200 psig.

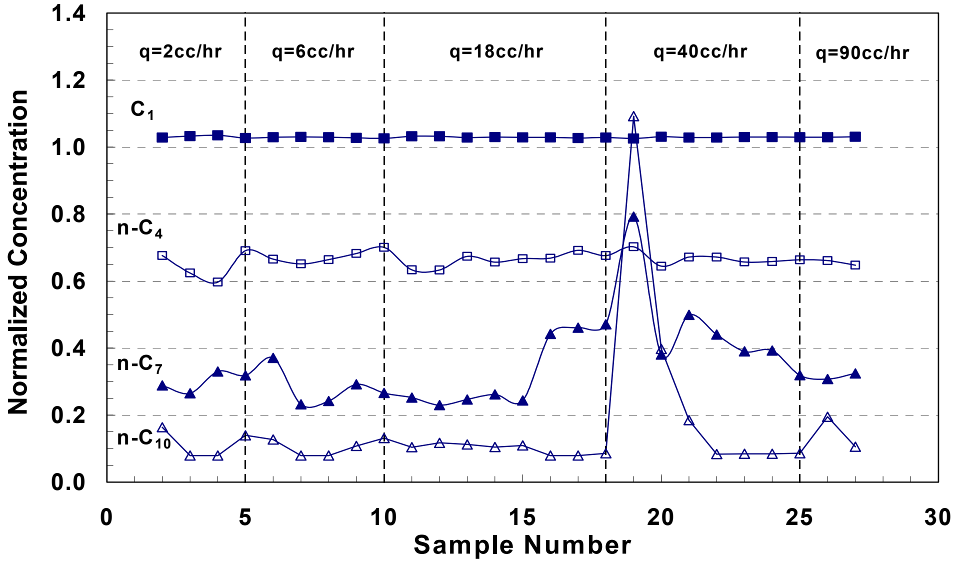

Figure 6.14: Normalized concentrations of the gas phase composition during two-phase flow in the absence of the core at 1,200 psig.

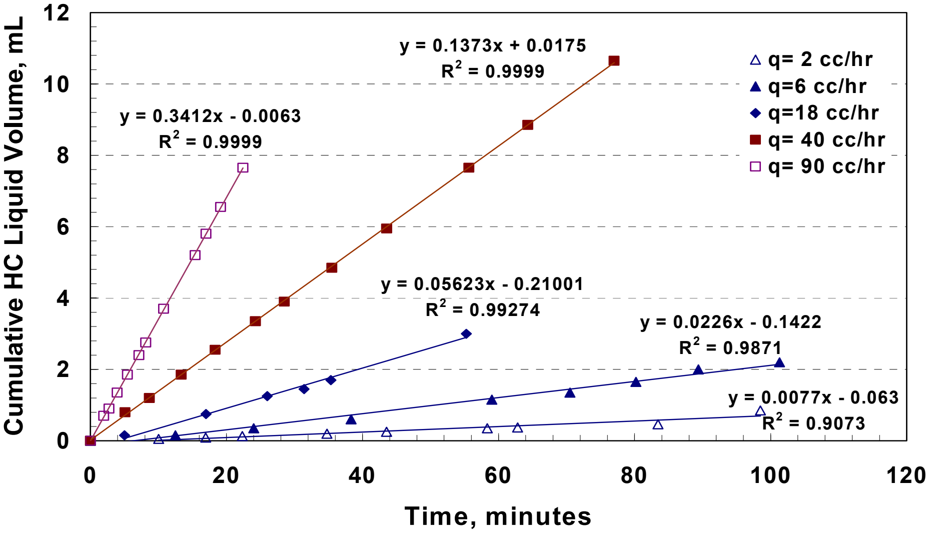

Figure 6.15: Cumulative condensate volume collected in the PVT during two-phase flow at 1,200 psig and various flow rates.

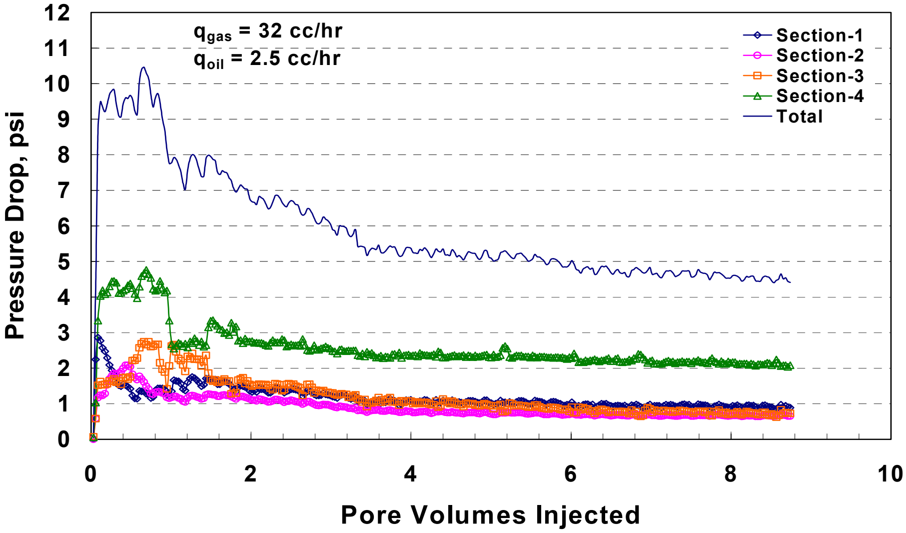

Figure 6.16: Pressure drop at different sections across the core during co-injection of gas and condensate phases at steady state and 1,200 psig.

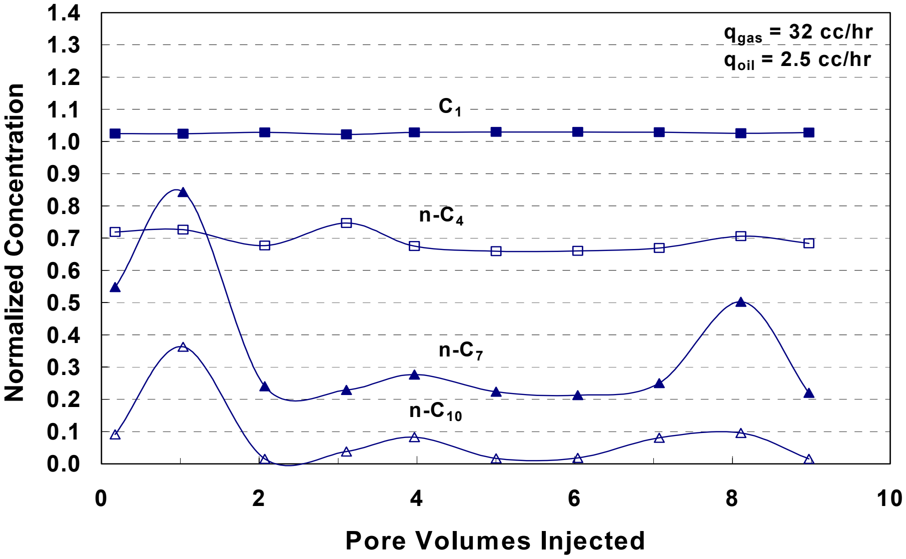

Figure 6.17: Normalized concentrations of gas composition during co-injection of equilibrium phases through the core at steady state and 1,200 psig.

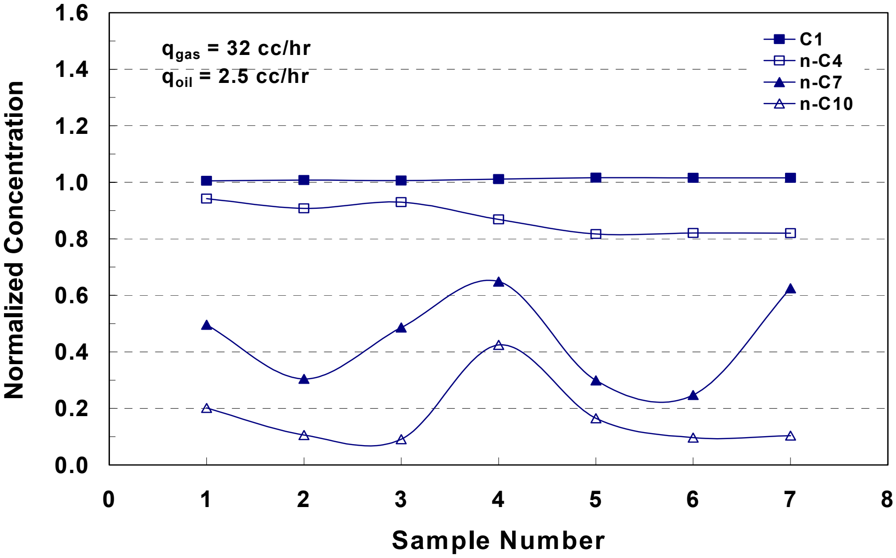

Figure 6.18: Normalized concentrations of the gas-phase during co-injection of equilibrium phases in the absence of the core at 1,200 psig.

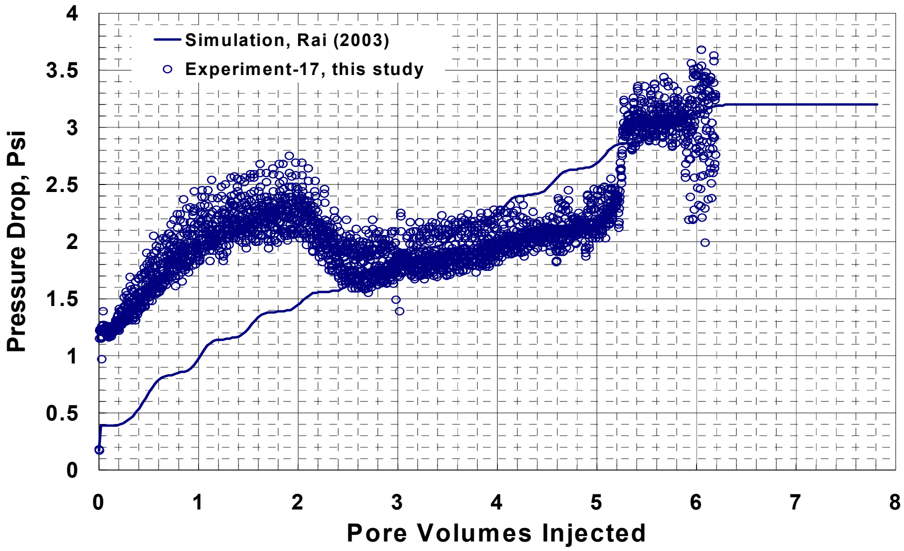

Figure 6.19: Simulated and measured pressure drop across the core during dynamic condensate accumulation at 2 cc/hr (Experiment-17, 1,200 psig and 145°F).

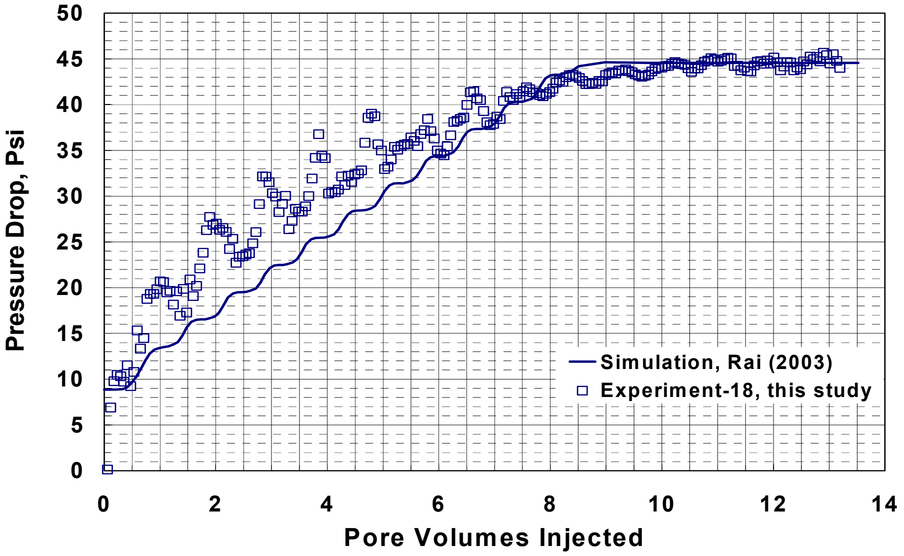

Figure 6.20: Simulated and measured pressure drop across the core during co-injection of equilibrium gas and condensate phases at 1,200 psig (Experiment-18, q_g=132 cc/hr, q_o=10 cc/hr).

Chapter 7: Methanol Treatment in the Hatter's Pond Field

This chapter describes the successful methanol treatment implemented on a gas well in the Hatter's Pond field in Alabama. A field test was conducted to investigate the effectiveness of methanol as a solvent for removing condensate banks that form when pressure in the near wellbore region falls below the dewpoint. Core flood experiments on Texas Cream limestone and Berea sandstone show that condensate accumulation can cause a severe reduction in gas relative permeability, especially in the presence of high water saturation. This can result in well productivity declining by a factor of 3 to 5 as bottom hole pressure declines below the dewpoint.

PVT analysis performed on field samples taken from the Hatter's Pond field in Alabama indicates a retrograde condensate behavior. These high-temperature deep gas wells showed low gas productivity and large skin. A preliminary analysis of the data indicated the possibility of condensate and water blocking due to the loss of water-based drilling fluids. Walker (2000) conducted compatibility tests were conducted to ensure that the injection of filtrate and methanol did not cause any damage to the core. Since the formation brine is very saline, tests were conducted to check for salt precipitation during methanol injection. Based on these laboratory results and a single-well numerical simulation (Marker, 2000), a damaged gas well in the Hatter’s Pond field was found to be a good candidate for a methanol treatment to restore its productivity. Details of the experimental studies have been given by Walker (2000) and Al-Anazi et al. (2003).

7.1 FIELD HISTORY

Hatter's Pond field, located in southwestern Alabama, was discovered in 1974. The field produces from two formations, the Smackover, a shallow marine dolomite and the Norphlet, an aeolian sandstone. The formations have average permeability in the range of 2 to 6 md and porosities in the range of 12 to 15%. The combined pay of the Smackover and Norphlet formations averages 200 to 300 feet at subsea depths ranging from approximately 18,000 ft to 18,300 ft (Stoudt et al, 1992). During the first phase of field development (1974-1985), a total of 40 wells were drilled. 25 of these wells were plugged and abandoned leaving only 15 wells as producers. In the second phase of development (1985-present), 11 wells were drilled (7 new producers, 3 replacements, and 1 gas injector) and 2 sidetracks (1 producer and 1 gas injector). During January 2002, the field was producing 4,700 BPD of condensate (API~50°), 2,200 BPD NGL, and 33 MMSCF/D of gas.

With an average reservoir temperature of 315°F, this is a relatively deep and hot formation with connate water that is very saline. The salinity of the formation brine ranges from 164,000 to 206,000 mg/L TDS. The predominant ions are Na^+, Ca^{2+}, K^+, and Cl^-. The salinity of the formation water at Hatter's Pond field is an important parameter when considering methanol injection to treat condensate and/or water blocking. The water sample obtained from Hatter's Pond was initially thought to be very saline since the formation brine is known to be very saline. The viscosity and density of the sample were measured at 20°C and found to be 0.99 cp and 0.9998 g/mL, respectively (nearly identical to pure water at this temperature). The resistivity was measured to be 12.3 Ω-m, which corresponds to 300 ppm of NaCl equivalent (Walker, 2000). The sample was analyzed for electrolytes (**Table 7.1**) and found to have 43 ppm Na^+ and 32 ppm Ca^{2+}. The water sample from Hatter's Pond was apparently fresh.

The above data cast doubt on the assumption that the brine in the near wellbore region is very saline. Texaco has been circulating fresh water into these gas-condensate wells to deliver anti-corrosion agents and remove scale. Also, loss of water based drilling fluids may have influenced the salinity in the near wellbore region. This might account for the low salinity of the water sample compared to several estimates of the formation salinity that are all very high. Indeed, the brine salinity in the near wellbore region is uncertain and probably not uniform.

7.2 WELL HISTORY

Hatter's Pond Unit Well 3-6 #1 was drilled to 18,550 ft and initially completed in the Norphlet formation in June of 1997. A typical log section of the formations are shown in **Figure 7.1**. The Norphlet formation had 126 ft of pay, with k = 1.25 md and porosity = 11.7%. The Smackover had 23 ft of pay with k = 0.34 md and porosity = 8.0%. A 5-1/2 inch liner was run and cemented. The 5-1/2" liner was then tied back to the surface. A 2-7/8" packerless tubing string was run inside the 5-1/2" casing. Production flows up the annulus, with the 2-7/8" tubing serving as a treating string (**Figure 7.2**). Fresh water to dissolve salt and corrosion inhibitors are injected in the tubing and chased with sweetened, gaslift gas. The lower Norphlet was perforated at 18,290 to 18,345 ft with 6 spf and acidized with HF mud acid. An initial static BHP was 3,230 psi. The lower Norphlet was tested at 2.7 MMSCF/D and 348 BPD of condensate. The upper Norphlet was perforated at 18,259 to 18,267 ft, but had no effect on production. Perforations were added to the Smackover formation at 18,228 to 18,253. Again, no significant changes in rates were observed.

The dewpoint pressure of reservoir gas mixture is about 3,030 psi. The well was produced at a BHP of ~2,000 psi with an initial average reservoir pressure of about 2,700 psig. The productivity of well 3-6 #1 gradually decreased with time until it reached about 0.25 MMSCF/D and 87 BCPD. The productivity decline may be due to skin induced by loss of water-based mud filtrates and completion fluids, as well as condensate blocking due to production below the dewpoint pressure. Tests conducted on this well showed a P* of 3,519 psi, a permeability of 0.039 md, and a total skin of 0.68.

7.3 METHANOL TREATMENT

In December of 2000, Well #3-6 was treated with 1,000 bbl of methanol. Methanol was bullheaded down the tubing at a rate of 5 to 8 bbl/min. Due to the high injection pressures encountered during the treatment, balls were not used as diverters. Production from the well, both before and after the treatment are shown in **Figure 7.3**. As seen in the figure, the gas production increased from an average of 0.25 MMSCF/D to 0.5 MMSCF/D and the condensate production increased from 87 BPD to 157 BPD. Well tests (**Table 7.2**) performed on the well before and after the treatment showed a permeability of 0.04 md while the total skin improved from 0.68 to –1.9. This indicates that the methanol treatment effectively removed the condensate/water bank near the wellbore resulting in improvements to both the gas and condensate production. The production remained above the baseline production rate for about 10 months. The longer term stabilized post-treatment rates were also 50% higher than the average production rates for the two months prior to the treatment (**Figure 7.3**).

There are several possible explanations for the sustained increase in gas and condensate production. Removal of condensate and water from the near wellbore region are clearly the primary mechanisms of stimulation. The primary concern with these treatments was their longevity. The removal of water introduced into the formation by drilling, completion and stimulation fluids is a permanent improvement. However, the removal of the condensate bank is only temporary as it is expected to reform. The results from this test indicate that the reformation of a condensate bank does not occur immediately. We can only speculate about the possible reasons for this. A residual phase of methanol will remain in the pore space and can modify the phase behavior of the flowing gas and oil. The removal of the water from the near wellbore region results in a smaller pressure gradient in the near wellbore region resulting in less condensate dropout. The reservoir gas composition is leaner than the original gas due to gas cycling during part of production history.

Production logs indicate that most of the production is coming from about 10 percent of the producing pay. This suggests that the methanol (used without diverting agents) probably went into a small but productive section of the formation. This almost certainly results in a deeper treatment depth than would be expected with uniform placement.

7.4 SUMMARY OF FIELD TREATMENT

A methanol treatment applied to a gas condensate well in the Hatter's Pond field was found to increase both gas and condensate production by a factor of 2 over the first four months and 50% thereafter. The increased rates were sustained over at least a ten-month period. Removal of water and condensate phases by the methanol resulted in a reduction in skin from 0.68 to –1.9.

Precautions must be taken to ensure that the methanol injected is compatible with both the reservoir brine and the formation fines. Corefloods conducted with reservoir cores from the Norphlet sandstone formation of the Hatter's Pond field indicated little sensitivity to methanol. The cores were found to be sensitive to fresh water. Additional work needs to be done to investigate the optimal treatment size and placement method.

Table 7.1: Chemical analysis of water sample for Hatter's Pond field.

Ions	Concentration, ppm
Ca^{2+}	32
Mg^{2+}	6
Na^{-}	43
Cl^{-}	140

Table 7.2: Test results of Well #3-6 before and after methanol treatment.

	Before Methanol Treatment	After Methanol Treatment
P*, psi	3,519	3,413
k, md	0.039	0.04
Total Skin	0.68	-1.9
Gas Rate, MMSCF/D	0.25	0.50
Condensate Rate, BPD	87	157

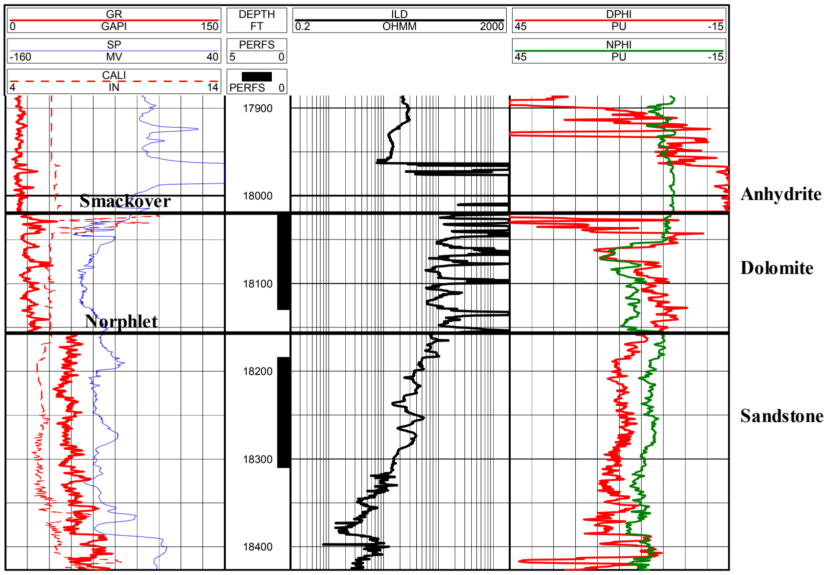

Figure 7.1: Hatter's Pond type log.

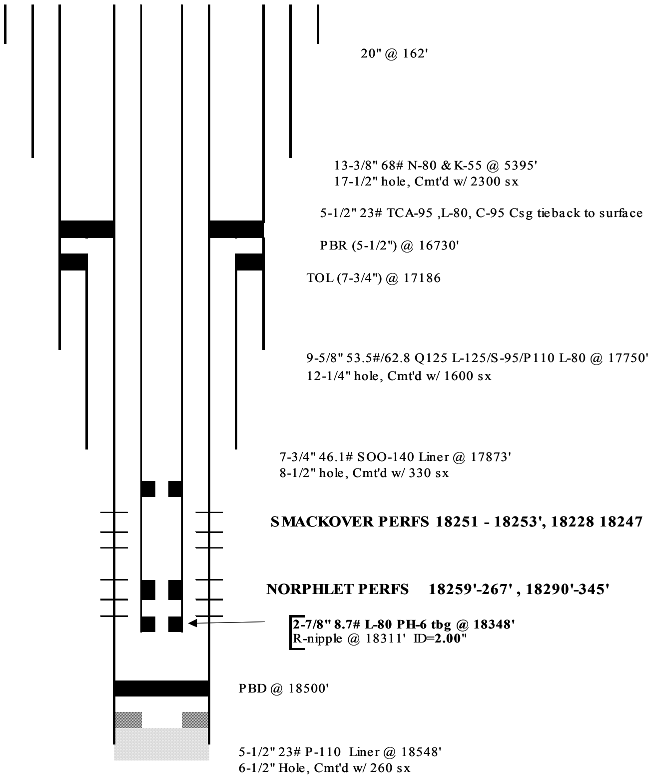

Figure 7.2: Wellbore sketch for Hatter's Pond Unit 3-6 #1, Hatter's Pond Field, Mobile Co., Alabama.

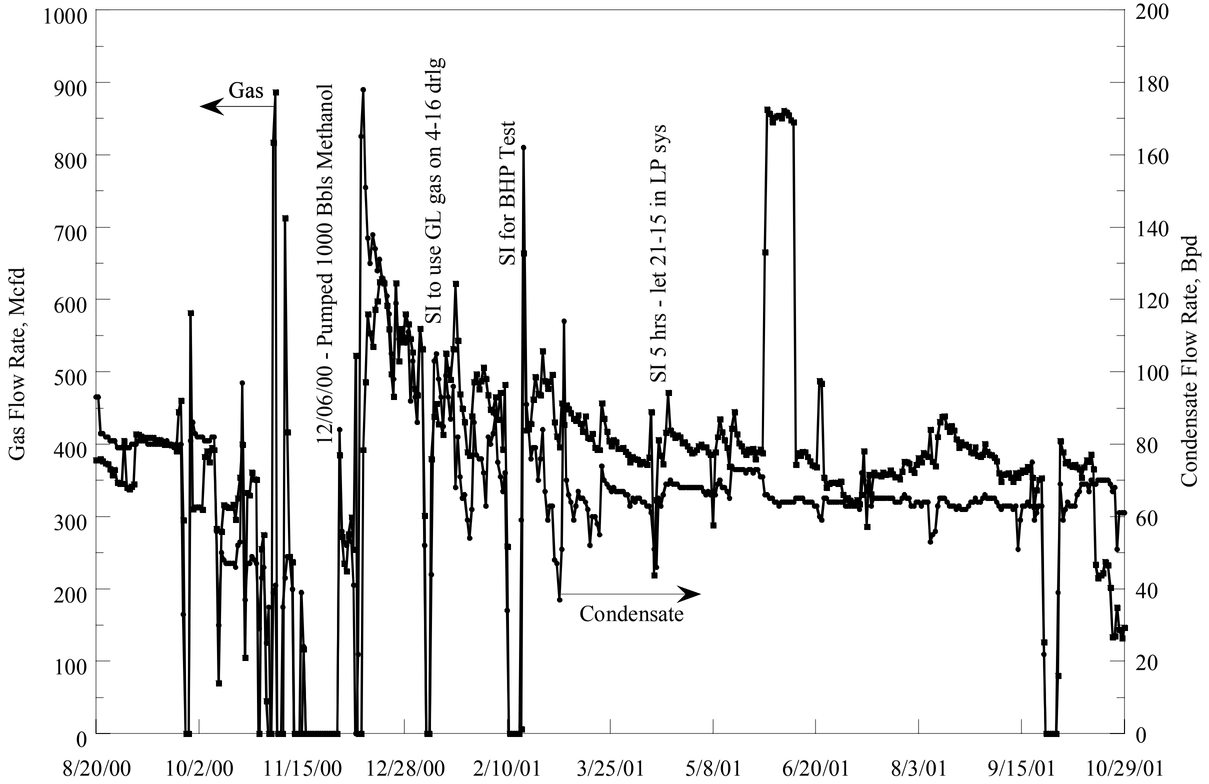

Figure 7.3: Gas and condensate production rates for Hatter's Pond Unit 3-6 #1 before and after methanol treatment.

Chapter 8: Revaporization of Condensate by Methane

In the previous chapters, condensate blocking was found to reduce gas productivity in both low and high permeability cores when the pressure dropped below the dewpoint. Methanol injection enhanced gas relative permeability by removing condensate and/or water blocking. However, the methanol treatment is a temporary cost-effective solution for stimulating gas productivity. Gas cycling has been used as an alternative technique to maintain reservoir pressure above the dewpoint and to displace residual retrograde liquid in gas-condensate reservoirs.

In this chapter, an experimental study of revaporization of liquid condensate from cores by methane injection is presented. A literature review on revaporization of condensate is presented first. Then, experimental results on the revaporization of condensate from the core by methane will be discussed. Several factors that affect the condensate revaporization process were investigated including: compositional analysis, flow rate, and pressure. Finally, the results and findings are summarized.

8.1 INTRODUCTION

Gas cycling has been used to maintain reservoir pressure above the dewpoint pressure. There are two schemes of gas cycling: full pressure or partial pressure maintenance (Abel et al., 1970). In full pressure maintenance, gas is cycled continuously while condensate (or oil) is withdrawn from the reservoir. In partial pressure maintenance, gas is injected into the reservoir but depletion is allowed to occur. Both methods of gas cycling require gas cycling plants that increase the initial capital costs.

Injection of dry gas (N_2, CO_2, or CH_4) into a retrograde gas-condensate reservoir vaporizes condensate and increases its dewpoint pressure. Contact of injected dry gas with gas condensate leads to enrichment of the dry gas due to mass transfer. Luo et al. (2001) found experimentally that the injected dry gas efficiently vaporized both intermediate and some heavy hydrocarbons. Li et al. (2001) found that full pressure maintenance yielded a higher condensate recovery than partial pressure maintenance.

Boersma and Hagoort (1994) compared displacement characteristics of nitrogen and methane injection into volatile-oil reservoirs based on phase behavior analysis, compositional reservoir simulation, and slim-tube experiments. They used a synthetic three-component gas mixture (60 mole% methane, 20 mole% n-butane, and 20 mole% n-tetradecane). Their results showed that methane revaporized the liquid phase more efficiently than nitrogen. A significant liquid saturation was left behind in the nitrogen-invaded zone during nitrogen flooding. The liquid recovery for both methane and nitrogen flooding increases with increasing pressure. They also reported that the recovery of methane floods increased at higher Peclet numbers (decreasing dispersion level).

Nitrogen has been applied in gas injection due to its economic feasibility (Eckles et al., 1981; Huang et al., 1986). Sänger and Hagoort (1998) investigated the efficiency of nitrogen to evaporate gas-condensate compared to methane using a slim tube. They found that methane re-evaporated the condensate and resulted in complete recovery of all condensate. The recovery of nitrogen injection reached 94%, but it decreased when the pressure is lowered below the dewpoint pressure. The recovery of condensate was found to be more sensitive to dispersion during nitrogen injection than that during methane flooding. They recommended using nitrogen for gas injection based on availability and cost.

Ahmed et al. (1998) studied the mechanism of gas injection in reducing gas well productivity loses due to condensate blocking in near-well region. The effectiveness of lean gas, N_2 and CO_2 injection in recovering the well productivity was evaluated. Results indicated the importance of optimum volume and pressure for successful use of injection techniques in gas condensate reservoirs.

Lee and Chaverra (1998) presented a study on the mechanisms controlling the productivity of low-permeability condensate wells in the giant, near-critical Cupiagua field in Colombia. It was found that in-situ condensate revaporization is directly related to increase of the production GOR and loss of productivity.

Methane can evaporate more condensate than nitrogen. Siregar et al. (1992) reported that the evaporation capacity of methane is more than 20 times higher than that of nitrogen. Another disadvantage of using nitrogen injection is raising the dewpoint pressure and the liquid dropout of the base reservoir fluid/injected gas mixture (Moses and Wilson, 1981; Siregar and Hagoort, 1992; Chaback and Williams, 1994; Piers et al., 1995; Sänger and Hagoort, 1998).

Water flooding may be selected as an option for reservoir pressure maintenance especially if there is an underlying aquifer that is providing a strong water drive. For rich gas-condensate reservoirs, water flooding above the dewpoint pressure would be the preferred option for maximizing condensate recovery (Henderson et al., 1991).

Jamaluddin and Thomas (2001) studied the effect of adding light hydrocarbon gases on the phase behavior of condensate using the CCE method. They found that adding CO_2 to the gas-condensate mixture resulted in an increase in the dewpoint pressure and a decrease in the liquid dropout. However, injection of propane was experimentally found to decrease the dewpoint and vaporize condensate more efficiently than CO_2.

Smith and Yarborough (1968) performed flow tests in long sand packs at 100°F and 1,500 psi to study retrograde condensate recovery by revaporization into dry gas. Their results showed that methane revaporized the liquid condensate from a n-pentane-methane binary mixture. Complete recovery of n-pentane was achieved after 2.5 PV. They also used a methane-hydrogen sulfide mixture to revaporize a synthetic light-sour condensate. The heavy component, n-C_7, was removed from the core after 6.0 PV. They concluded that the quantity of dry gas required for complete recovery of retrograde liquid by contact is influenced by the heaviest components of the liquid phase.

In addition, the volume of dry-gas injection necessary to revaporize and produce the retrograde liquid phase is a function of temperature, pressure, composition of the condensate system, and composition of the dry gas injected (Givens, 1969). Since the over-all composition in the retrograde liquid is changing during the revaporization process, there will be a shift in the equilibrium composition. The existence of equilibrium depends on the relative velocity between phases (Raimondi and Torcaso, 1965).

8.2 RESULTS AND DISCUSSION

The experimental apparatus and procedures used have been discussed in detail in Chapter 4. The results are presented below.

8.2.1 Condensate Revaporization by Methane

The effectiveness of a methane flood for revaporizing the residual condensate in the four-component lab mixture was measured in a coreflood. The cores used in these experiments were saturated with condensate by flowing two-phase flow until they reached a steady state. Before injecting methane into the core, equilibrium gas and liquid phases were flooded through the core at 1,200 psig until steady state was achieved. Methane gas was flowed through the core at 1,200 psig to restore its initial gas permeability.

Figure 8.1 shows the pressure drop across different sections of the core during revaporization of condensate by methane at 1,200 psig at various flow rates. **Table 8.1** gives the return permeability ratio during revaporization of condensate by methane at 1,200 psig. The return permeability is the ratio of the measured methane permeability (k_g) during the revaporization process to the initial gas permeability (k @ $S_g = 100\%$). As the amount of the injected methane increased, the return permeability ratio increased. At the end of the methane flood, the restored gas permeability (k=3.82 md) after revaporization of condensate is very close to the initial gas permeability (k=3.87 md) measured before condensate accumulation, which indicates that the methane evaporated all the condensate from the core after injection of about 50 pore volumes.

The same experiment was repeated using the same core. The core was saturated with the condensate as before (Experiment-18) until it reached a steady state where k_{rg} and k_{ro} were reduced to 0.141 and 0.185, respectively, due to condensate accumulation. Methane gas was flowed through the core at 1,200 psig at various flow rates to revaporize the condensate. **Figure 8.2** shows pressure drop across different sections of the core during revaporization of condensate by methane at 1,200 psig. At a flow rate of 99 cc/hr, the pressure drop across the core gradually decreased until it reached a stabilized value after 40 PV. This result also indicates that the removal of condensate by methane flooding is a slow process.

Figure 8.3 illustrates the return permeability ratio for different sections of the core during revaporization of condensate by methane at 99 cc/hr and 1200 psig. At the end of the methane flood, the average restored gas permeability (k = 3.70 md) is very close to the initial gas permeability (k = 3.82 md). This second test confirms that a large volume of methane is needed to revaporize all the condensate from the core.

Figure 8.4 shows the composition of the core effluent during revaporization of condensate by methane flow at 1,200 psig. As methane was flowed through the core, it displaced the condensate phase. The concentrations of n-C_4, n-C_7, and n-C_{10} components increased to maximum values of 8.36, 1.30, and 1.31 mole%, respectively, after injection of 3.2 PV of methane. The increases in these concentrations are correlated with an increase in the pressure drop across the core (**Figure 8.2**). The difference between the maximum pressure drop and the stabilized value, flow initiation pressure, was found to be 17 psia. Such a flow initiation pressure is commonly observed when a high mobility fluid displaces a low mobility fluid (Roy and Sharma, 2001). Heavy component concentrations gradually decreased in the effluent. Methane removed all the n-C_4 from the core after injection of 10 PV. However, the revaporization of n-C_7, and n-C_{10} is a very slow process since they don't partition as readily into the gas phase. As the flow rate was increased to 132 cc/hr, the concentrations of n-C_7, and n-C_{10} increased again in the effluent. This may be because methane flowed through pores that may not have been accessible at the lower rate. Although the core permeability was restored after 70 PV of methane, trace amounts of n-C_{10} were detected in the core effluent. This shows that revaporization of heavy components by methane is very slow process and may require several 10s or 100s of pore volumes to achieve.

8.2.2 Effect of Flow Rate

To check if non-equilibrium effects were playing an important role in condensate revaporization, experiments were conducted at high and low rates. The flowing pressure was kept constant at 1,200 psig, while the flow rate was the only factor changed. **Figure 8.5** shows the pressure drop across different sections of the core during revaporization of condensate by methane at 1,200 psig. Methane was injected at high flow rates of 132 and 195 cc/hr at 1,200 psig. Results show the same trend as that observed in the previous experiments, where the pressure drop across the core decreases gradually as methane vaporized the heavy components from the liquid phase.

Figure 8.6 shows the return permeability ratio at different sections across the core during revaporization of condensate by methane at 132 cc/hr and 1,200 psig. The return permeability ratio increases in all sections at the same time during the methane flood. Thus, the removal of components from the liquid condensate phase takes place in the whole core. Fewer pore volumes of methane were needed to restore the gas permeability at a high flow rate (**Table 8.2**) than that at a low flow rate. For instance, the methane flood restores the gas permeability at 132 cc/hr after 25.41 PV as shown in **Figure 8.6**, while it requires 37.25 PV of methane to restore the permeability at the lower flow rate of 99 cc/hr as given in **Figure 8.3.**

Figure 8.7 shows the composition of the core effluent during revaporization of condensate by methane at 1,200 psig. The concentration of n-C_4 in the effluent increased to a maximum value of 3.58 mole% after injection of 5.2 PV of methane. Then, it gradually decreased to a very small concentration (<0.003 mole%) after 12 PV. The amount of both n-C_7 and n-C_{10} is very small (<0.008 mole%) in the effluent since the mole fraction of these components in the gas phase is very small and difficult to measure accurately. There are likely some problems with the GC measurements for the heavy components that need to be further investigated.

Figure 8.8 compares the concentration of n-C_4 in the effluent of the core during revaporization of condensate by methane at 1,200 psig at different flow rates. There is a sharp decrease in n-C_4 mole% at about 10 PV followed by a low concentration tail up to 30 PV. The greater tailing at the higher flow rates indicates a small departure from equilibrium may have occurred at these high rates. At 132 cc/hr, the residence time is only about 9 minutes. However, this departure is minor in terms of total n-C_4 mass removed.

Figure 8.9 shows the concentration of n-C_7 in the core effluent during revaporization of condensate by methane at 1,200 psig at various flow rates. The revaporization rate of n-C_7 from the core increases with the injection rate of methane. The same results were also observed for the concentration of n-C_{10} in the core effluent, as shown in **Figure 8.10**. These results indicate that the revaporization rate of n-C_4 is higher than that of n-C_7 and n-C_{10}. Therefore, the revaporization of liquid condensate phase depends on the composition of the liquid phase.

8.2.3 Effect of Pressure

The effect of pressure on the revaporization of condensate by methane was also investigated. The core used in this experiment was the same core used in coreflood Experiment number 13 where condensate was accumulated in the core and decreased k_{rg} to 0.066 and k_{ro} to 0.086. The core was flooded with methane at a flowing pressure of 3,000 psig to remove the residual condensate and to restore the initial gas permeability (k = 4.50 md). **Figure 8.11** shows the pressure drop across the core during revaporization of condensate by methane at 3,000 psig and various flow rates. The pressure drop increased initially while the condensate was being displaced from the core. Then, it decreased gradually after methane break through from the core. The pressure for a multiple contact miscible displacement of this mixture (the MMP) is estimated to be about 3,000 psig, so this displacement showed have been much more efficient than that at 1,200 psig. The pressure drop stabilized at only 3 PV. The measured gas permeability was 3.91 md after 7.0 PV (at 99 cc/hr) and 3.92 md (at 132 cc/hr) at the end of methane flood. The miscible displacement is far from ideal since the core is short and the flow rate very high, but clearly it is more efficient than the displacement at 1,200 psig, which requires extraction of heavy components from the condensate.

8.3 SUMMARY OF RESULTS

Methane flooding revaporizes condensate from the core and restores the gas permeability to its initial value. The revaporization of condensate is controlled by the partitioning of the hydrocarbon components into the flowing gas phase when the pressure is below the minimum miscibility pressure (MMP). Increasing methane pressure and flow rate expedites the revaporization of condensate. The revaporization of the heavy components in the condensate phase was slightly affected by non-equilibrium behavior at the high flow rates. The return permeability ratio increases with methane volume injected (**Figure 8.12**) and is relatively insensitive to flow rate, indicating that non-equilibrium effects are of secondary importance. There are likely some problems with the GC measurements for the heavy components that need to be further investigated.

Table 8.1: Return permeability ratio during revaporization of condensate by methane at 1,200 psig and 99 cc/hr.

Methane Volume Injected, PV	Return Permeability Ratio (k_g/k)
20.02	0.88
36.58	0.95
47.31	0.94
55.01	0.99

Table 8.2: Return permeability ratio during revaporization of condensate by methane at 1,200 psig at 132 cc/hr.

Methane Volume Injected, PV	Return Permeability Ratio (k_g/k)
25.52	0.92
44.13	0.98

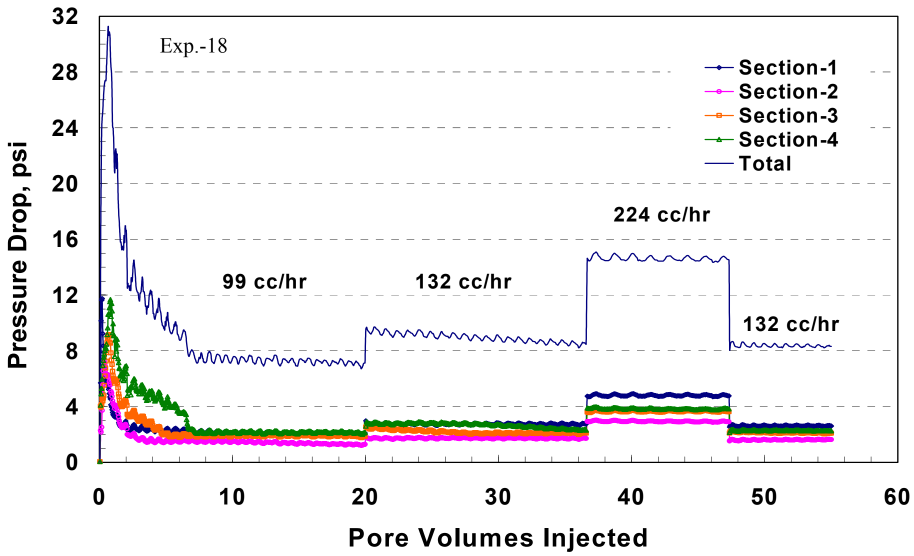

Figure 8.1: Pressure drop at different sections across the core during revaporization of condensate by methane at 1,200 psig.

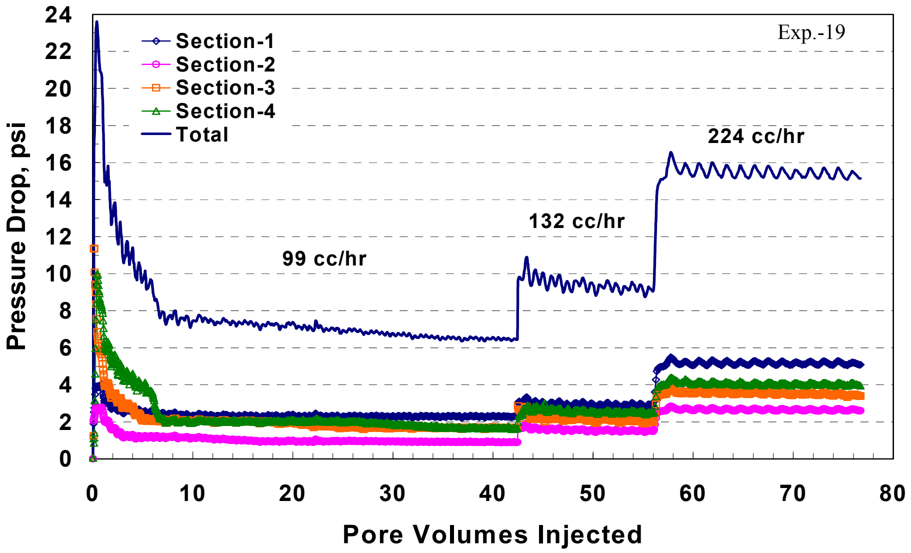

Figure 8.2: Pressure drop at different sections across the core during revaporization of condensate by methane at 1,200 psig.

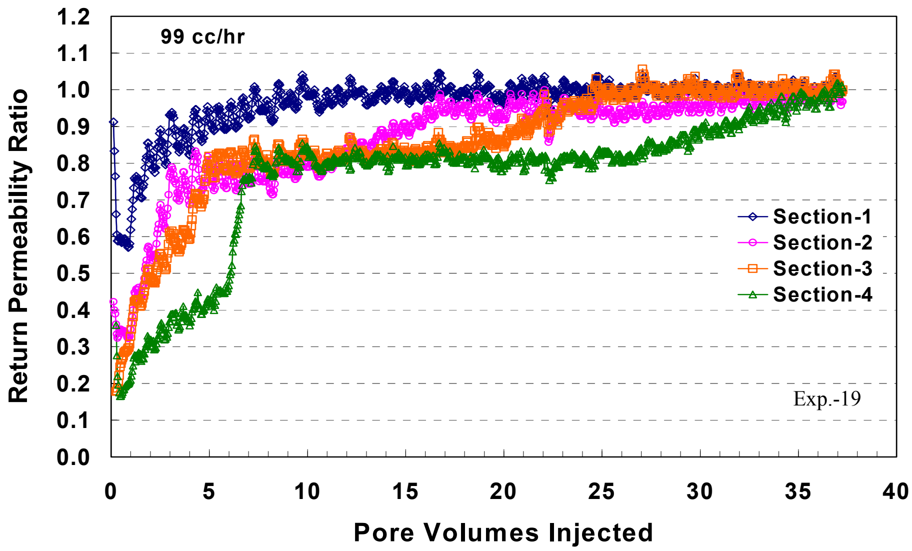

Figure 8.3: Return permeability ratio at different sections across the core during revaporization of condensate by methane at 1,200 psig.

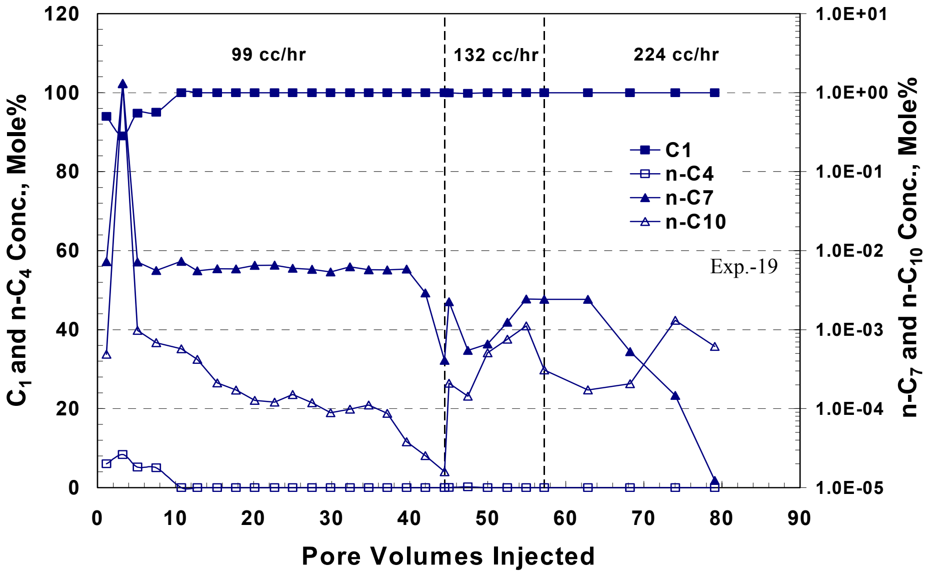

Figure 8.4: Composition of the core effluent during revaporization of condensate by methane at 1,200 psig and various flow rates.

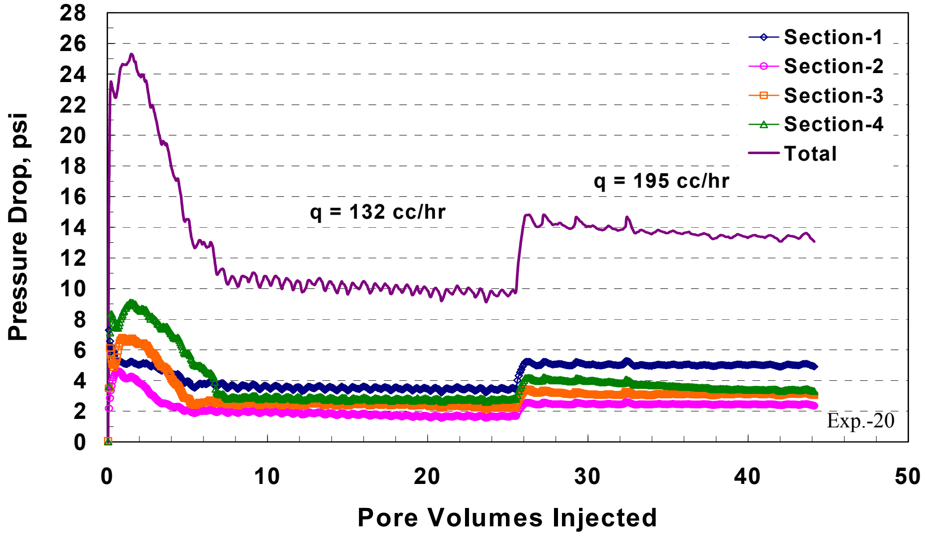

Figure 8.5: Pressure drop at different sections across the core during revaporization of condensate by methane at 1,200 psig.

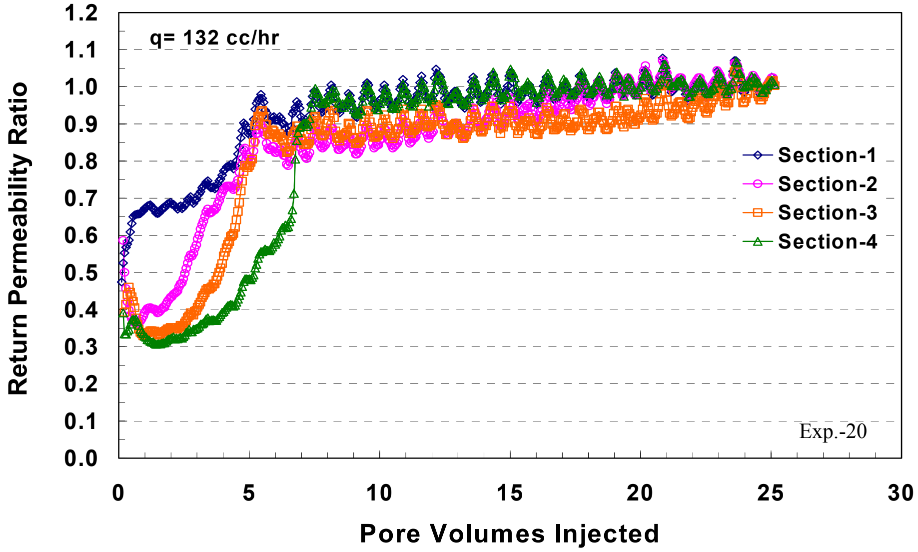

Figure 8.6: Return permeability ratio at different sections across the core during revaporization of condensate by methane at 1,200 psig.

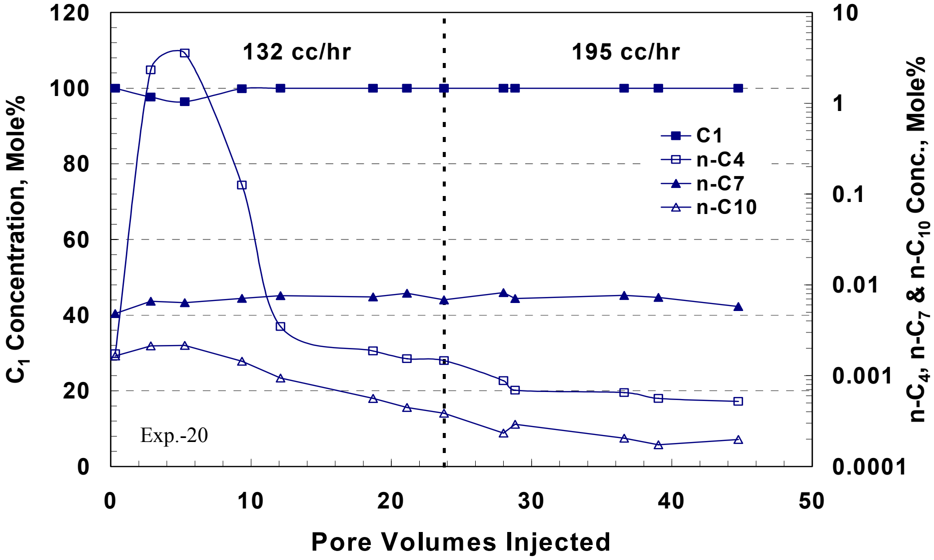

Figure 8.7: Composition of the core effluent during revaporization of condensate by methane at 1,200 psig.

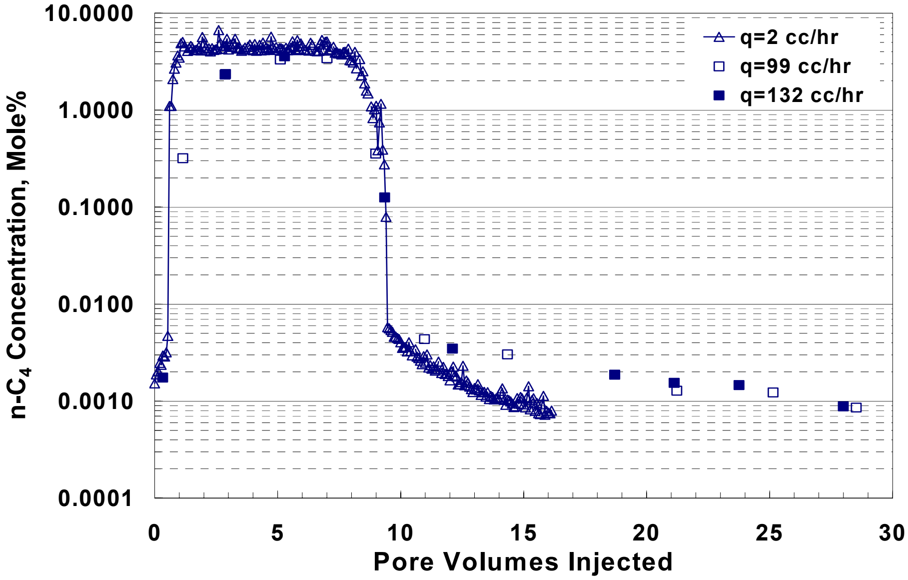

Figure 8.8: Concentration of n-butane in the core effluent during revaporization of condensate by methane at 1,200 psig and various flow rates.

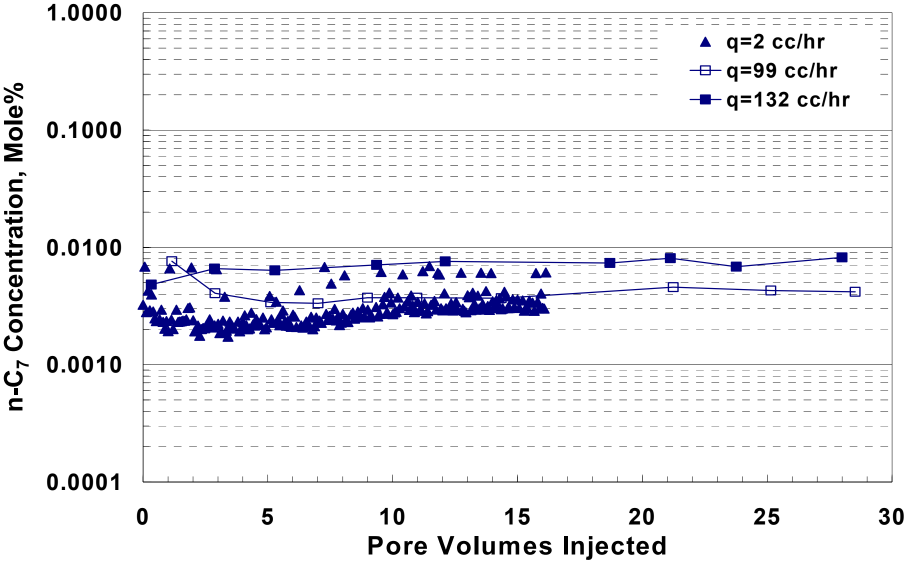

Figure 8.9: Concentration of n-heptane in the core effluent during revaporization of condensate by methane at 1,200 psig and various flow rates.

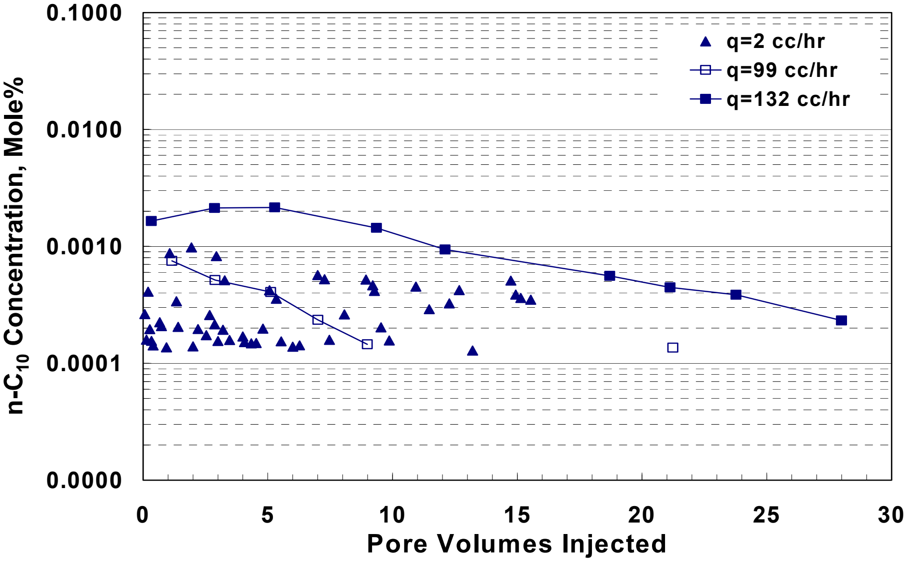

Figure 8.10: Concentration of n-decane in the core effluent during revaporization of condensate by methane at 1,200 psig and various flow rates.

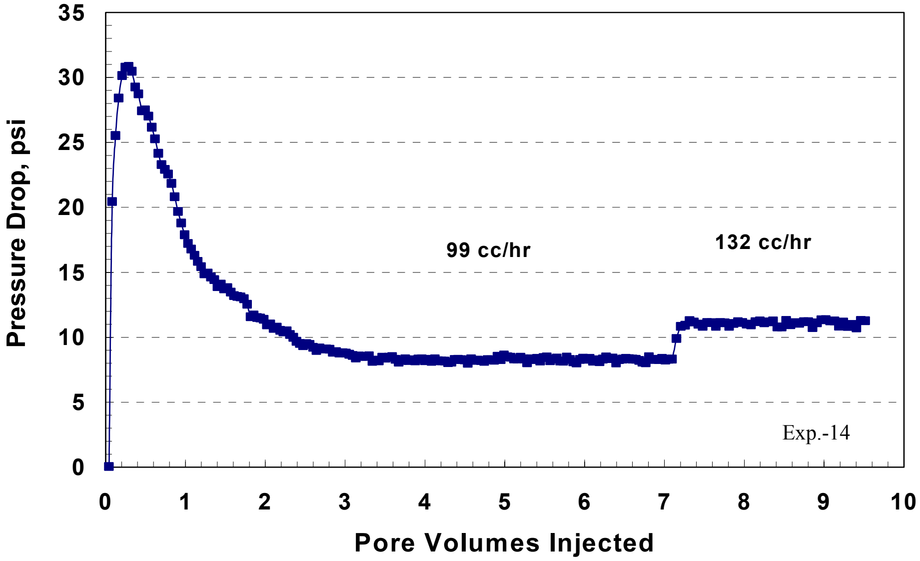

Figure 8.11: Pressure drop across the core during revaporization of condensate by methane at 3,000 psig.

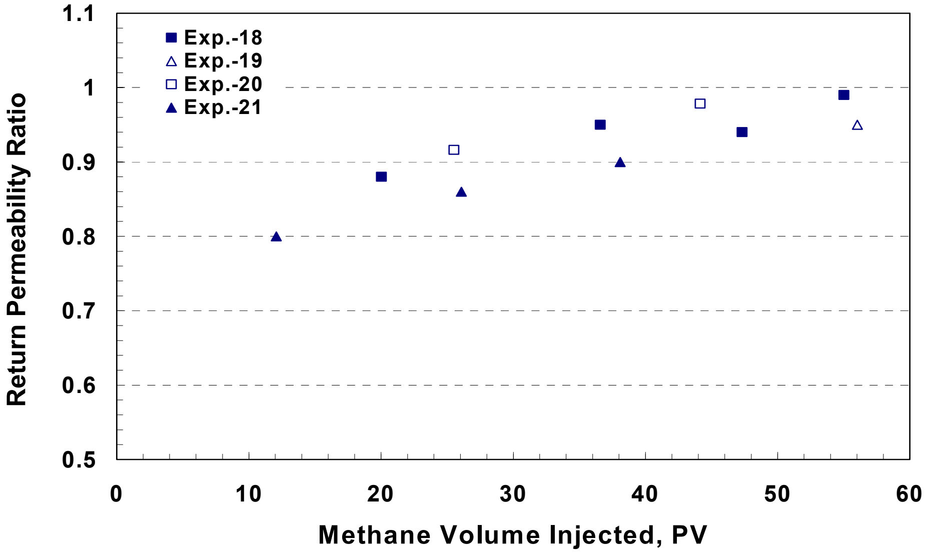

Figure 8.12: Return permeability ratio as a function of methane volume injected in Texas Cream limestone cores.

Chapter 9: Conclusions

The major conclusions of this experimental investigation of the behavior of gas condensate fluids are as follows:

- Gas relative permeability during two-phase steady-state flow of gas condensate mixtures decreased by 88 to 97% due to condensate and water blocking (see **Table 5.1**). Gas and condensate relative permeability values are almost equal at steady state flow of gas and condensate. Values as low as 0.04 were measured at the highest initial water saturation.

- Gas relative permeability decreased about the same percentage in high permeability cores (Berea) as in low permeability cores (Texas Cream limestone) at comparable trapping numbers.

- More severe reductions in gas relative permeability occurred during two-phase flow of gas and condensate at high initial water saturation than at low water saturation.

- Injection of methanol resulted in an enhanced flow period in both low and high permeability cores. The gas relative permeability increased by a factor of about 10. Subsequent, condensate accumulation is delayed for a certain time due to the presence of a methanol-rich liquid phase. During this time, the productivity index increased by more than an order of magnitude in both low and high permeability cores.

- The duration of the enhanced flow period is controlled by the volume of methanol injected and the mole fraction of methanol that partitions into the flowing gas phase after the treatment. Methanol treatments remove both water and condensate by a multi-contact miscible displacement if sufficient methanol is injected.
- Methanol treatments resulted in a significant but temporary enhancement in productivity for both low and high permeability cores. The removal of water blocks would be expected to have a long lasting impact on a well's PI. The condensate phase will reform and cause the PI to decrease again if the bottom hole pressure is the same following the treatment. However, in some cases the temporary removal of the condensate and/or water block may allow gas production at significantly lower pressure draw-down resulting in less condensate accumulation, perhaps even allowing the well to be produced at a bottom hole pressure above the dew point for a longer period of time than would otherwise be economic. In other cases due to operations such as lean gas injection in other wells some time in the past, the gas flowing to a given gas-condensate well may be less rich than what caused the original condensate block. Further investigation is needed to

evaluate the expected duration of the enhanced flow period under a variety of field conditions.

- The gas end-point relative permeability increased with flow rate, which is consistent with the general tendency for relative permeability to increase as the trapping number or capillary number increases.

- Methane was found to be effective at revaporizing residual condensate and restoring the initial core permeability. However, the revaporization process requires 10 to 100 pore volumes of methane to be effective.

- Dynamic condensate accumulation through the core was found to depend on the flow rate. As the flow rate increased, more pore volumes of two-phase flow are required to reach a steady state. When using the flashing method, a steady state was achieved at the expected pore volumes only at very low rates. All of these observations indicate that local equilibrium was not achieved at the high flow rates. At the highest flow rate, the residence time was only 9 minutes. This is evidently too little time for complete mass transfer to occur.

- Co-injection of equilibrium gas and condensate through the core resulted in a steady state being achieved at the expected number of pore volumes corresponding to the measured fractional flow.

- A methanol treatment applied to a gas condensate well in the Hatter's Pond field operated by Texaco was found to increase both gas and condensate production rates by a factor of 2 over the first four months and 50% thereafter. The increased rates were sustained over at least a ten-month period. Removal of water and condensate phases from the near wellbore region by the methanol resulted in a reduction in skin from 0.68 to –1.9.

The results presented in this dissertation can be used to help reservoir engineers evaluate and treat gas-condensate wells with reduced productivity. In light of this new data, the common perception that condensate blocking occurs only around low permeability wells should be re-examined. Reservoir engineers should be especially careful when evaluating the damage around well in high-permeability reservoirs if the well's pressure drawdown is high enough to result in wellbore pressures below the dewpoint over a long enough period of time to allow condensate accumulation near the well.

Appendix A

This appendix starts with a detailed example on calculations required for the gas mixture preparation. Then, the derivations of two-phase flow equations are discussed. In the final section, properties of methanol-water mixtures will be discussed.

A.1 GAS MIXTURE PREPARATION

This section demonstrates a numerical example on gas mixture preparation. Suppose we need to prepare a gas mixture consisting of the following components:

C_1 = 78.5 mole%

n-C_4 = 15.0 mole%

n-C_7 = 5.0 mole%

n-C_{10} = 1.5 mole%

The volume of the accumulator was measured with distilled water and found to be 1,431 mL. First of all, let us select a methane pressure of 1,600 psig. At 25°C and 1,600 psig, PREOS gives a molar volume of methane 182.22 mL/mole.

The number of moles of C_1 = 1,431/182.22 = 7.8531 moles.

Total number of moles = 7.8531/0.785 = 10.0040 moles

Therefore, the number of moles of the other components can be calculated as:

Moles of n-C_4 = 10.0040 * 0.150 = 1.5006 moles

Moles of n-C_7 = 10.0040 * 0.050 = 0.5002 moles

Moles of n-C_{10} = 10.0040 * 0.015= 0.1501 moles

Using the molecular weight given in g/mole, the amount of each n-C_7 and n-C_{10} in grams is:

Mass of n-C_7 = 0.5002 * 100.204 = 50.12 g

Mass of n-C_{10} = 0.1501 * 142.29 = 21.35 g

At 1,000 psig and 25°C, the PREOS gives a molar volume of n-C_4 equal to 94.13 mL/mole. Thus, the volume of n-C_4 that needs to be injected at 1,000 psig and 25°C using a RUSKA pump can be calculated as:

Volume of n-C_4 = 1.5006 * 94.13 = 141.25 mL

The volume of methane to be injected at the selected pressure (1,600 psig) is equal 1,431 mL. When these components are mixed together in this accumulator, the final pressure of the gas mixture is 1760 psig at room temperature.

A.2 FLOW RATES EQUATIONS

In coreflood experiments, two-phase flow was established by dropping the flowing pressure (1,200 psig) below the dewpoint while the upstream pressure (3,000 psig) was kept above the dewpoint pressure. This procedure allows dynamic condensate accumulation through the core. Therefore, it mimics formation of condensate bank in the near wellbore region in retrograde reservoirs. To achieve that the upstream back-pressure regulator pressure was kept at 3,000 psig and the pressure of the downstream back-pressure regulator that controlling the pressure in the core was gradually decreased to 1,200 psig. The injection pump rate is not the rate that is flowing through the core due to the difference in the flashing pressure before and after the upstream back-pressure regulator. In order to calculate the exact flow rates of both gas and oil (condensate) phases through the core, a mass balance needs to be performed across the upstream back-pressure regulator.

Figure A.1 shows a schematic diagram of the upstream back-pressure regulator during two-phase flow using a flashing method. A mass balance across the upstream back-pressure regulator can be represented as follows:

$$q\,\rho = q_g\,\rho_g + q_o\,\rho_o \qquad \text{(A.1)}$$

where

q = total flow rate of gas mixture at 3,000 psig

q_g = flow rate of gas-phase at 1,200 psig

q_o = flow rate of oil-phase at 1,200 psig

ρ = molar density of gas mixture at 3,000 psig

ρ_g = molar density of gas-phase at 1,200 psig

ρ_o = molar density of oil-phase at 1,200 psig

The molar densities of both gas and oil phases were obtained using a flash calculation for the gas mixture at 1,200 psig and 145°F. Since

$$q_{core} = \frac{q_g}{f_g} = \frac{q_o}{f_o} \tag{A.2}$$

then

$$q\,\rho = \frac{f_g}{f_o} q_o\,\rho_g + q_o\,\rho_o \tag{A.3}$$

multiplying Equation (A.3) by f_o and taking q_o as a common factor in the right-hand side results in

$$f_o q\,\rho = q_o\,(f_g\,\rho_g + f_o\,\rho_o) \tag{A.4}$$

solving Equation (A.4) for q_o gives the flow rate of oil phase:

$$q_o = \frac{f_o\,q\,\rho}{f_o\,\rho_o + f_g\,\rho_g} \tag{A.5}$$

doing the same procedure and solving for q_g drives the following equation for gas-phase flow rate:

$$q_g = \frac{f_g\, q\, \rho}{f_o\, \rho_o + f_g\, \rho_g} \tag{A.6}$$

A.3 PROPERTIES OF METHANOL-WATER MIXTURE

The viscosity of methanol in this dissertation was calculated based on an empirical correlation derived from measurements of viscosity reported on the literature (Mikhail and Kimel, 1961; Vargaftik, 1975). **Figure A.2** shows viscosity of methanol-water mixture at different temperatures (Mikhail and Kimel, 1961). As can be seen that the viscosity of methanol-water mixtures is not a linear function of concentration, but it has a maximum value at a methanol to water weight ratio of 2:5. Since pure methanol was injected through cores in coreflood experiments, its viscosity needs to be accurately predicted to calculate the actual core permeability to methanol. Therefore, measurements of methanol viscosity reported in the literature were correlated to predict the viscosity at the desired temperature (145°F). **Figure A.3** shows the viscosity of methanol as a function of temperature. The data indicates a polynomial correlation where the viscosity of methanol is decreased as the temperature increased. The correlation shows a very good prediction (R^2=0.9996) of methanol viscosity as a function of temperature. As a result, the viscosity of methanol (μ_{MeOH}) can be predicted at any temperature (T) using the following empirical correlation:

$$\mu_{MeOH} = 7.83296\times10^{-6}\,T^{2} - 4.66806\times10^{-3}\,T + 8.48775\times\text{-}01 \qquad \text{(A.7)}$$

Where viscosity of methanol (μ_{MeOH}) is in centipoises (cp) and the temperature in degree Fahrenheit (°F). This correlation gives a methanol viscosity of 0.3366 cp at 145°F. This value of viscosity has been used to calculate core permeability during methanol injection.

The viscosity of water has been calculated using the following empirical correlation (CRC, 53rd Edition):

$$\log_{10}\frac{\mu}{1.002} = \frac{1.3272\left(20-T\right)-0.001053\left(T-20\right)^{2}}{T+105} \qquad \text{(A.8)}$$

where μ in centipoises (cp) and T in degree Celsius (°C). This correlation is valid for temperatures range from 20 to 100°C. The calculated water viscosity at 145°F was found equal to 0.4477 cp.

Correlations developed by Lee et al. (1966) for calculating the viscosity of natural gases at elevated temperatures and pressures were used to estimate the viscosity of the gas single phase.

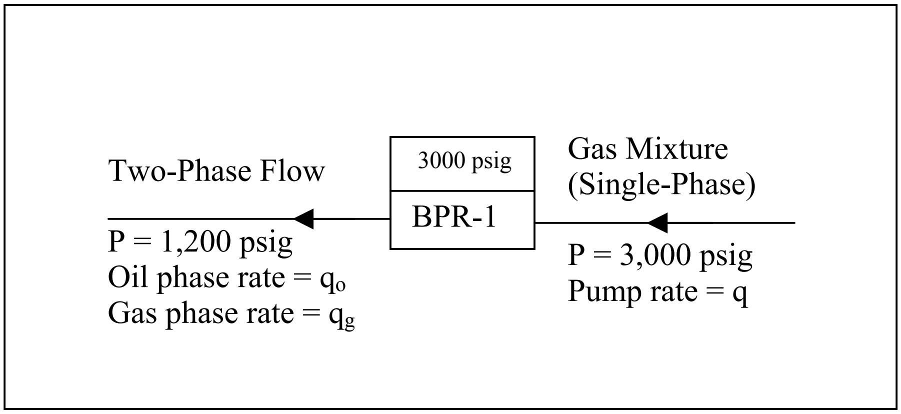

Figure A.1: A schematic diagram of upstream back-pressure regulator (BPR-1) during two-phase flow.

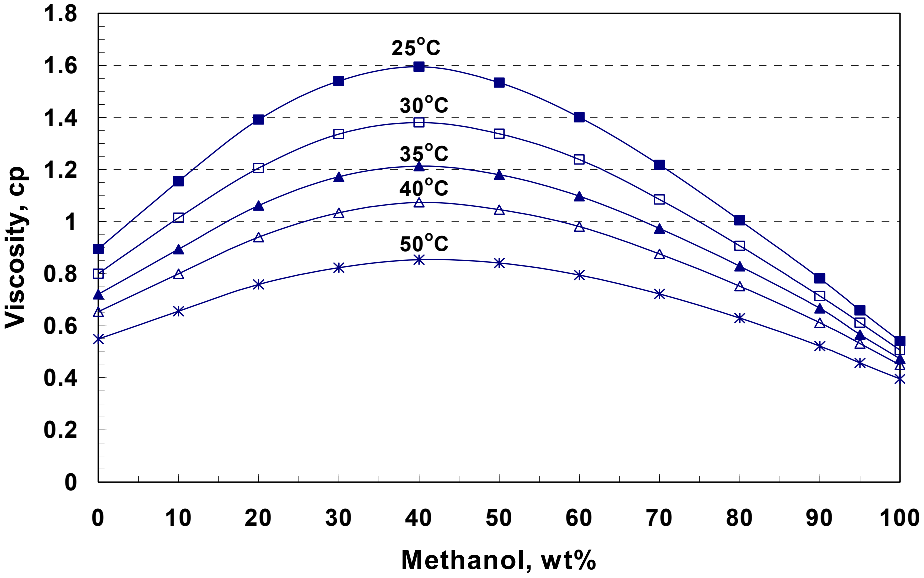

Figure A.2: Viscosity of methanol-water mixtures at different temperatures (Mikhail and Kimel, 1961).

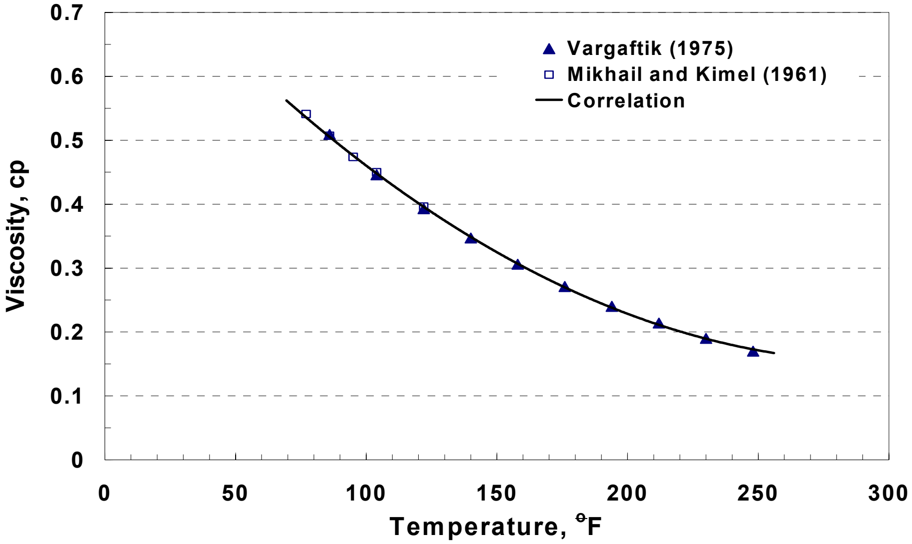

Figure A.3: Viscosity of methanol as a function of temperature.

Appendix B: Gas-Condensate Coreflood Experiments

This appendix summarizes all the coreflood experiments performed to study gas-condensate blocking and treatment in low and high permeabilities rocks.

B.1 Coreflood Experiment No. 4

B.1.1 Objective

The objective of this experiment is to investigate the effect of methanol treatment on the relative permeability of gas after a dynamic condensate accumulation. This experiment was performed on Texas Cream limestone core. There is no water present in the core (S_{wi}=0%).

B.1.2 Core Preparation

A core with a diameter of 0.972 inches and a length of 8.01 inches was cut from a Texas Cream limestone block. The core was dried in an oven at 95°C for more than 3 days. The core was wrapped with an aluminum foil and a heat-shrink Teflon. The wrapped core was placed into a Phoenix core-holder inside HTHP oven at 145°F. After 4 hours, an axial pressure was applied by screwing the end pieces of the core-holder. Then, an overburden pressure of 3,400 psig was applied using a hand pump.

B.1.3 Methane Flooding

The upstream and downstream back-pressure regulators were set to 3,000 psig. Methane gas was flowed at a flow rate of 44.8 cc/hr through the core until the pressure drop across the core stabilized. **Figure B.1** shows the pressure drop across the core during this stage. Two pressure transducers ($\Delta P_{total-1}$ and $\Delta P_{total-2}$) were used to measure the total pressure drop across the core. **Table B.1** gives the results of methane flooding. The average initial core permeability (at S_g=100%) was found equal to 2.75 md.

B.1.4 Gas Mixture (Single-Phase) Flow

The gas mixture (single-phase) was flowed through the core at 3,000 psig. The flow rate was 44.8 cc/hr. **Figure B.2** shows the pressure drop across the core during gas mixture flooding. The results are given in **Table B.2**.

B.1.5 Condensate Accumulation (Two-Phase)

Before the start of this stage, the inlet and outlet valves of the core were closed. Pressure of the downstream back-pressure regulator was decreased to 1,200 psig, while the pressure in the upstream back-pressure regulator was kept at 3,000 psig. Flow was started while the bypass was open until the pressure in the lines stabilized. Then, the bypass valve was closed and inlet and outlet valves

were open simultaneously. The flow rate was 44.8 cc/hr. This stage allowed the gas-condensate to dynamically accumulated through the core. The stage was stopped when the pressure drop across the core reached stable values. **Figure B.3** shows the pressure drop across the core during gas condensate accumulation. The results are given in **Table B.3**. Data needed to calculation relative permeability (μ_g=0.01396 cp, μ_o=0.23711 cp) for gas and oil phases were obtained using PREOS and UTCOMP.

B.1.6 Equilibrium Gas Flow

The pressure in the upstream back-pressure regulator was decreased to 1,200 psig. Gas-phase of the gas-mixture, which has a pressure of 1,200 psig (below dewpoint), was injected through the core at a flow rate of 44.8 cc/hr. The pressure drop across the core is shown in **Figure B.4**. This stage measures the gas end-point relative permeability (k^o_{rg}) before methanol as given in **Table B.4**.

B.1.7 Methanol Treatment

Pure methanol was injected through the core at an injection rate of 44.8 cc/hr and 1,200 psig. The volume of methanol injected was 20 PV. The pressure drop across the core stabilized at a value 84.54 psia as shown in **Figure B.5**.

B.1.8 Condensate Accumulation After Methanol

The pressure of the upstream back-pressure regulator was increased to 3,000 psig, while the pressure of the downstream back-pressure regulator was kept at 1,200 psig. The gas mixture was flashed through the core to bank condensate after the methanol treatment. **Figure B.6** depicts the pressure drop across the core during this stage. The measured gas and oil relative permeabilities are given in **Table B.5**. Data needed to calculate the relative permeabilities were also obtained from PREOS and UTCOMP.

B.1.9 Equilibrium Gas Flow After Methanol

The equilibrium gas was injected at a flow rate of 44.8 cc/hr. **Figure B.7** shows the pressure drop across the core during equilibrium gas flow at 1,200 psig. This stage gives the gas end-point relative permeability after the methanol treatment, and the measured values are given in **Table B.6**.

B.1.10 Summary of the Results of Experiment-4

Figure 8 compares the pressure drop during dynamic condensate accumulation through the core before and after an injection of 20 PV of methanol. Pressure drop across the core during injection of equilibrium gas before and after methanol injection is shown in **Figure B.9**. This figure indicates that the methanol treatment was effective to increase the gas end-point relative permeability by 51%. Summary of experimental results is given in **Table B.7**.

Table B.1: Initial core permeability measured with methane at 1,200 psig and a flow rate of 44.8 cc/hr.

	$\Delta P_{Total\text{-}1}$	$\Delta P_{Total\text{-}2}$
ΔP, psia	5.33	5.42
k, md	2.77	2.72

Table B.2: Core permeability measured during gas mixture (single-phase) flow at 1,200 psig and a flow rate of 44.8 cc/hr.

	$\Delta P_{Total\text{-}1}$	$\Delta P_{Total\text{-}2}$
ΔP, psia	7.45	7.42
k_g, md	3.83	3.85

Table B.3: Gas and oil relative permeabilities measured during dynamic condensate accumulation before methanol treatment at 1,200 psig and 44.8 cc/hr.

	$\Delta P_{Total\text{-}1}$	$\Delta P_{Total\text{-}2}$
ΔP, psia	39.84	38.70
k_{rg}	0.18	0.18
k_{ro}	0.23	0.24

Table B.4: Gas end-point relative permeability measured during equilibrium gas flow at 1,200 psig and 44.8 cc/hr.

	$\Delta P_{Total\text{-}1}$	$\Delta P_{Total\text{-}2}$
ΔP, psia	8.47	8.38
k_g, md	1.46	1.48
k^o_{rg}	0.382	0.384

Table B.5: Relative permeabilities measured during dynamic condensate accumulation after methanol treatment at 1,200 psig and 44.8 cc/hr.

	$\Delta P_{Total-1}$	$\Delta P_{Total-2}$
ΔP, psia	50.48	38.7
k_{rg}	0.14	0.18
k_{ro}	0.18	0.24

Table B.6: Gas end-point relative permeability measured during equilibrium gas flow after methanol treatment at 1,200 psig and 44.8 cc/hr.

	$\Delta P_{Total-1}$	$\Delta P_{Total-2}$
ΔP, psia	5.63	5.55
k_g, md	2.20	2.23
k^o_{rg}	0.574	0.580

Table B.7: Summary of experimental results for coreflood Experiment-4.

	Before Methanol	After Methanol
k_{rg}	0.18	0.14
k_{ro}	0.24	0.18
k^o_{rg}	0.384	0.580

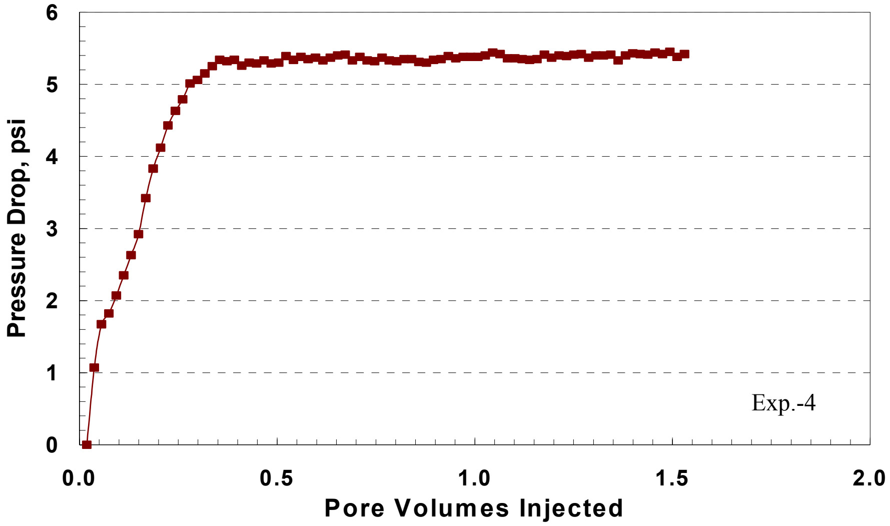

Figure B.1: Pressure drop across the core during methane flow at 3,000 psig and 44.8 cc/hr.

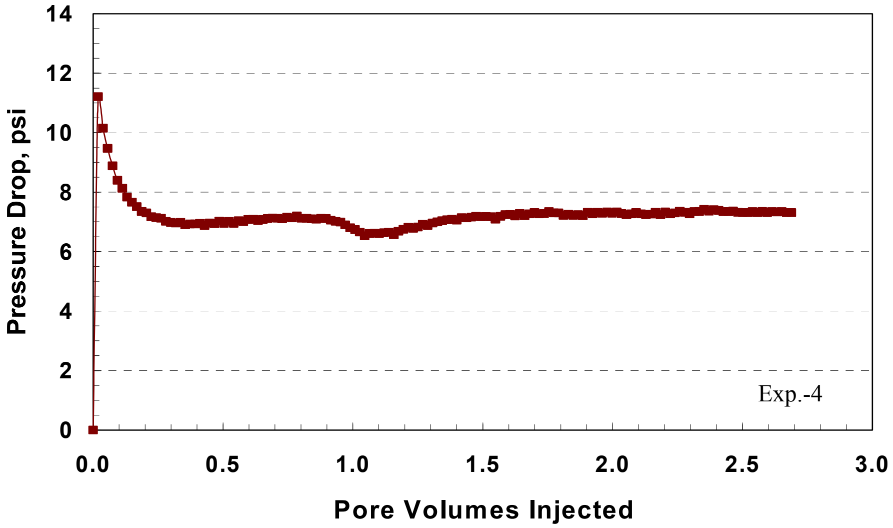

Figure B.2: Pressure drop across the core during gas mixture (single-phase) flow at 3,000 psig and 44.8 cc/hr.

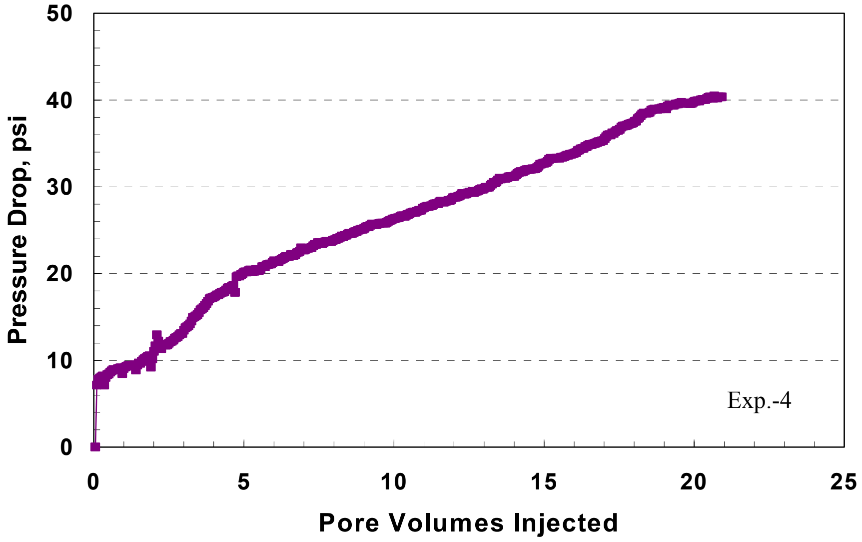

Figure B.3: Pressure drop across the core during dynamic condensate accumulation at 1,200 psig and 44.8 cc/hr.

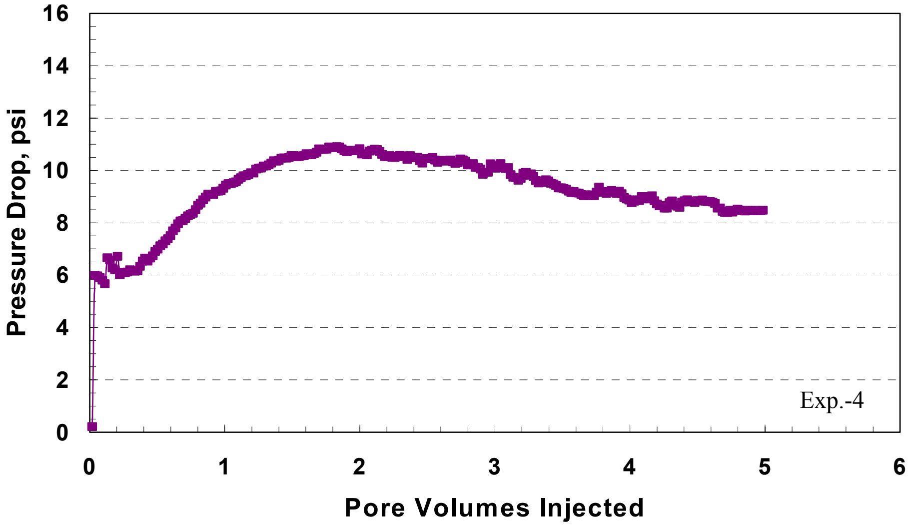

Figure B.4: Pressure drop across the core during equilibrium gas flow at 1,200 psig and 44.8 cc/hr.

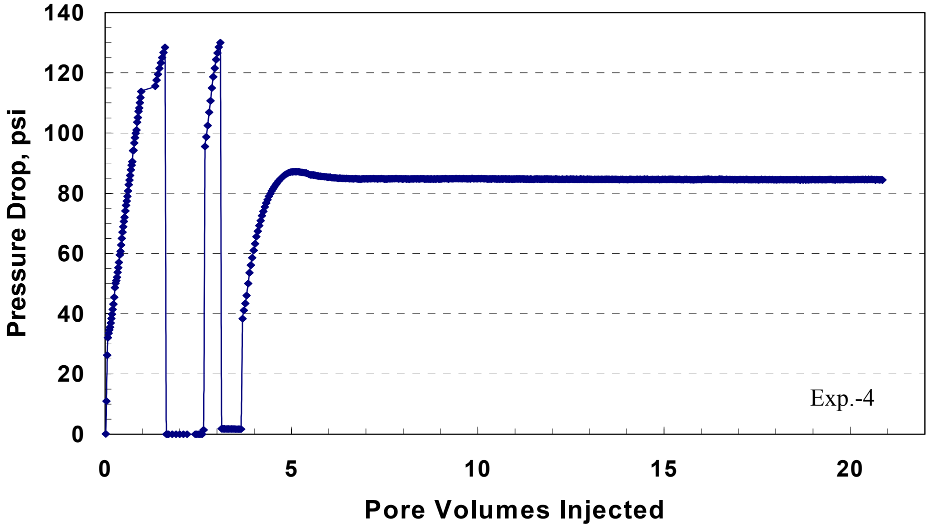

Figure B.5: Pressure drop across the core during methanol treatment at 1,200 psig.

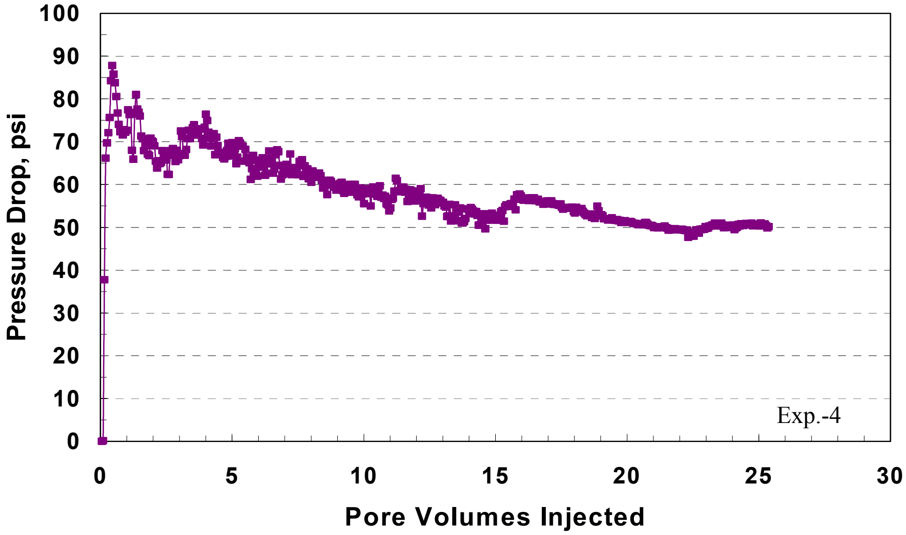

Figure B.6: Pressure drop across the core during condensate accumulation after the methanol treatment at 12,00 psig and 44.8 cc/hr.

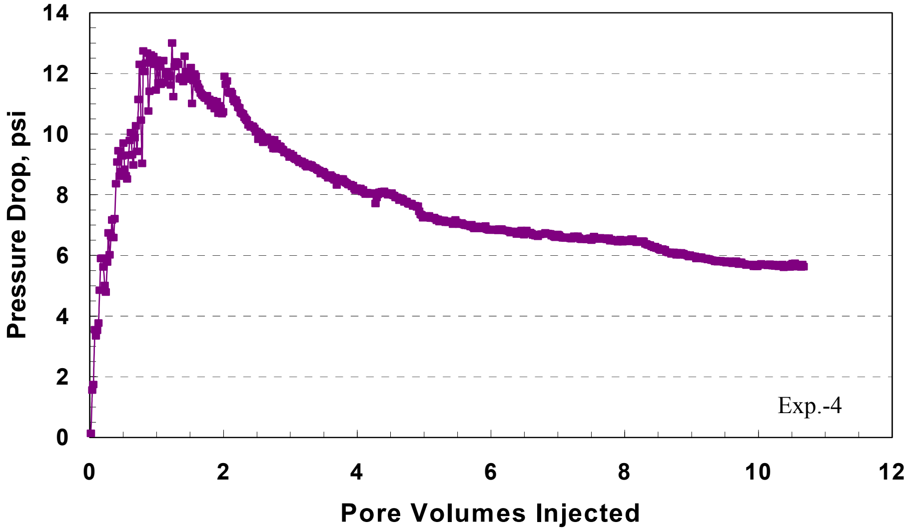

Figure B.7: Pressure drop across the core during equilibrium gas flow after the first methanol treatment at 1200 psig and 44.8 cc/hr.

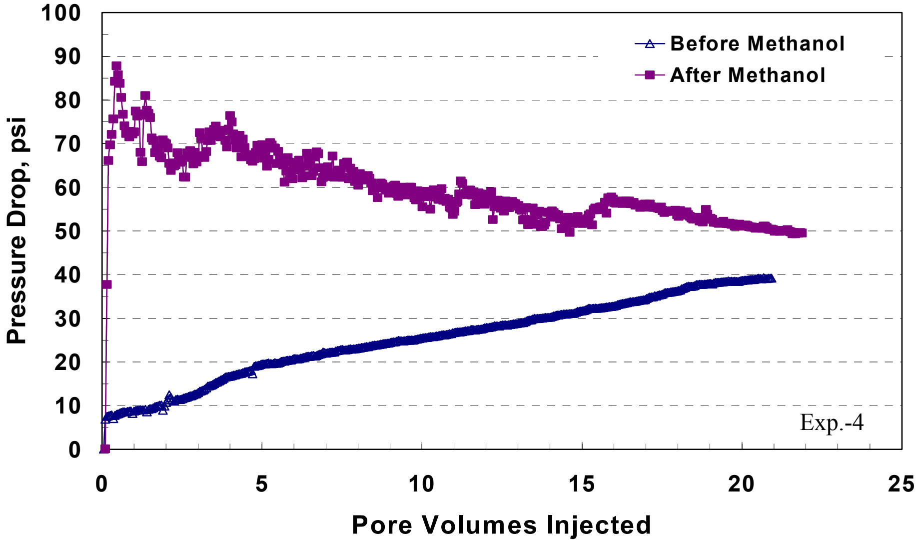

Figure B.8: Pressure drop across the core during dynamic condensate accumulation before and after methanol treatment at 1,200 psig and 44.8 cc/hr.

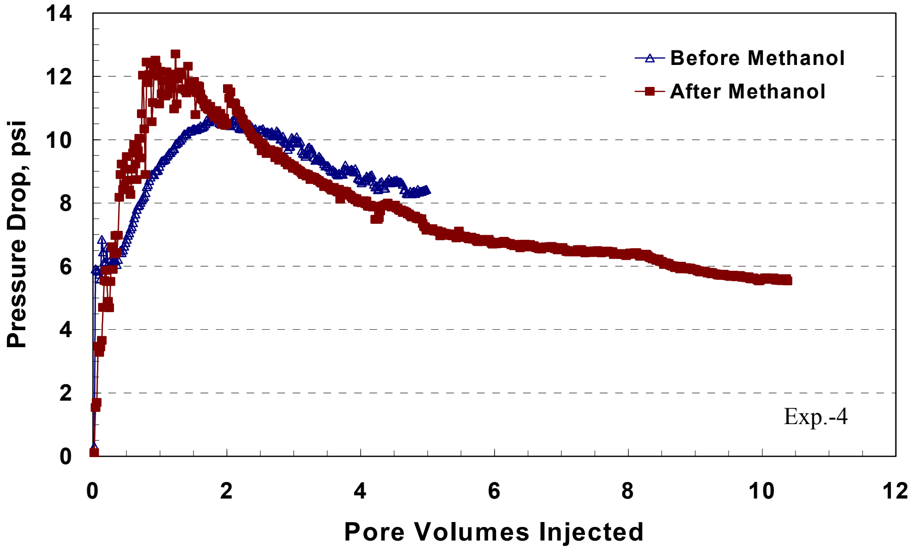

Figure B.9: Pressure drop across the core during equilibrium gas flow before and after methanol treatment at 1,200 psig and 44.8 cc/hr.

B.2 Coreflood Experiment No. 5

B.2.1 Objective

The objective of this experiment is to investigate the effect of methanol on the relative permeability of gas after gas-condensate accumulation in the presence of residual water saturation.

B.2.2 Core Preparation

A core with a diameter of 0.972 inches and a length of 8.00 inches was cut from Texas Cream Limestone block. The core was dried in an oven at 95°C for more than 3 days. The core was wrapped with an aluminum foil and a heat-shrink Teflon. The wrapped core was placed into a Phoenix core-holder inside HTHP oven at 145°F. After 4 hours, an axial pressure was applied by screwing the end pieces of the core-holder. Then, an overburden pressure of 3400 psig was applied.

B.2.3 Brine Permeability

In this stage the core was flooded with 0.5wt% $CaCl_2$ solution at atmospheric pressure and 145°F. An accumulator filled with 0.5wt% $CaCl_2$ solution was placed inside the oven. Initially, the core was vacuumed for more than 10 hours inside the oven. A burette filled with brine was connected to the inlet of the core. The brine was drawn from the burette by a vacuum pump. The pore volume of the core was found to be 20.20 mL. A RUSKA pump was used to displace the brine from the accumulator. The flow rate was 44.8 cc/hr. The brine flow was continued until the pressure drop across the core was stabilized. **Figure B.10** shows the pressure drop across the core during brine flooding. The viscosity of the brine was calculated at 145°F and found to be 0.4477 cp (CRC, 53rd Edition). **Table B.8** gives the initial core permeability measured with brine. The brine permeability was taken as the core effective permeability.

B.2.4 Methane Flooding at 2,000 psig

The upstream and downstream back-pressure regulator were set to 2,000 psig. Methane gas was flowed at a flow rate of 44.8 cc/hr through the core until the pressure drop across the core stabilized. Then, the flow rate was decreased to 19.2 cc/hr. After the pressure stabilized, the flow rate was increased back to 44.8 cc/hr. **Figure B.11** shows the pressure drop across the core during this stage. **Table B.9** gives the results of methane flooding. During this stage, effluents were collected using a fraction collector that was set to collect effluent each 1 minute. The cumulative water produced was 8.84 cm^3. This means that the residual water saturating (S_{wr}) at this stage reached 56.24%.

B.2.5 Methane Flooding at 3000 psig

The pressure of both the upstream and downstream back-pressure regulators was increased to 3,000 psig. Methane was flowed at a rate of 44.8 cc/hr. **Figure B.12** depicts the pressure drop across the core during methane flooding at 3,000 psig. During this stage, 2.30 mL of water were produced. By the end of this stage, the residual water saturation was decreased to 44.85%. **Table B.10** lists the relative permeability of the gas at residual water saturation.

B.2.6 Gas Mixture (Single-Phase) Flow

The gas mixture (single-phase) was flowed through the core at 3,000 psig. The flow rate was 44.8 cc/hr. **Figure B.13** shows the pressure drop across the core during gas mixture flooding. The results are given in **Table B.11**. In this stage, no water was collected in the effluent.

B.2.7 Condensate Accumulation (Two-Phase)

Before the start of this stage, the inlet and outlet valves of the core were closed. Pressure of the downstream back-pressure regulator was decreased to 1,200 psig, while the pressure in the upstream back-pressure regulator was kept at 3,000 psig. Flow was started while the bypass was open until the pressure in the lines stabilized. Then, the bypass valve was closed and inlet and outlet valves were open simultaneously. The flow rate was 44.8 cc/hr. This stage allowed the gas-condensate to dynamically accumulated through the core. The stage was stopped when the pressure drop across the core reached stable values. **Figure B.14** shows the pressure drop across the core during gas condensate accumulation. The quality of the data is not good due to leak occurred in one of the transducer after 50 PV. Therefore, an average value of pressure drop before the leak was used to calculate two phase relative permeabilities. Gas and oil relative permeabilities during condensate accumulation are given in **Table B.12**.

Data needed to calculation relative permeability for gas and oil phases (μ_g=0.01396 cp, μ_o=0.23711 cp) were obtained using PREOS and UTCOMP.

B.2.8 Equilibrium Gas Flow

The pressure in the upstream back-pressure regulator was decreased to 1,200 psig. The gas phase of the gas-mixture, which has a pressure of 1,200 psig (below dew point) was injected through the core at a flow rate of 44.8 cc/hr. The pressure drop across the core is shown in **Figure B.15**. This stage gives the gas end-point relative permeability (k^o_{rg}) before methanol and the measured values are given in **Table B.13**.

B.2.9 Methanol Treatment

Pure methanol was injected through the core at an injection rate of 44.8 cc/hr and 1,200 psig. The volume of methanol injected was 20 PV. The pressure drop across the core stabilized at a value 121.1 psia as shown in **Figure B.16**. The calculated permeability for methanol was 2.16 md.

B.2.10 Condensate Accumulation After Methanol

The pressure of the upstream back-pressure regulator was increased to 3,000 psig, while the pressure of the downstream back-pressure regulator was kept at 1,200 psig. The gas mixture was flashed through the core to bank condensate. **Figure B.17** depicts the pressure drop across the core during this stage. Gas and oil relative permeabilities are given in **Table B.14**.

B.2.11 Equilibrium Gas After Methanol

The equilibrium gas was injected at a flow rate of 44.8 cc/hr and a flowing pressure of 1,200 psig. **Figure B.18** shows the pressure drop across the core. This stage gives the gas end-point relative permeability after methanol injection, as given in **Table B.15**.

B.2.12 Summary of the Results of Experiment-5

Figure B.19 compares the pressure drop during condensate accumulation through the core before and after methanol (20 PV) treatment. As can be seen, methanol treatment was effective to delay the accumulation of condensate due to the presence of methanol-rich phase. An enhanced flow period with a minimum pressure drop prolongs for 16.9 PV before post-treatment accumulation. During the enhanced flow period, both gas and condensate relative permeabilities increased by order of magnitude: k_{rg}=0.36 and k_{ro}=0.47. Pressure drop across the core during injection of equilibrium gas before and after methanol injection is shown in **Figure B.20**. This figure indicates that the methanol treatment was effective to increase the gas relative permeability by 43%. **Figure B.21** shows the initial gas (methane) relative permeability at residual water saturation. Summary of experimental results is given in **Table B.16**.

Table B.8: Initial core permeability measured with 0.5 wt% $CaCl_2$ solution at atmospheric pressure and a flow rate of 44.8 cc/hr.

	ΔP_{Total}
ΔP, psia	178.93
k, md	1.94

Table B.9: Gas relative permeability measured during brine displacement with methane at 2,000 psig (S_{wr}=56.24%).

	q = 44.8 cc/hr		q = 19.2 cc/hr	
ΔP, psia	23.09	23.99	9.03	8.29
k_g, md	0.54	0.52	0.60	0.65
k_{rg}	0.28	0.27	0.31	0.33

Table B.10: Gas relative permeability measured during methane flow at 3,000 psig and 44.8 cc/hr (S_{wr}=44.85%).

	$\Delta P_{Total-1}$	$\Delta P_{Total-2}$
ΔP, psia	23.01	18.61
k_g, md	0.64	0.79
k_{rg}	0.33	0.41

Table B.11: Gas relative permeability measured during gas mixture (single-phase) flow at 3,000 psig and 44.8 cc/hr.

	$\Delta P_{Total-1}$	$\Delta P_{Total-2}$
ΔP, psia	43.12	31.49
k_g, md	0.66	0.91
k_{rg}	0.34	0.47

Table B.12: Gas and oil relative permeabilities measured during dynamic condensate accumulation at 1,200 psig and 44.8 cc/hr.

	$\Delta P_{Total-1}$
ΔP, psia	101.01
k_{rg}	0.14
k_{ro}	0.18

Table B.13: Gas end-point relative permeability measured during equilibrium gas flow before methanol treatment at 1,200 psig and 44.8 cc/hr.

	$\Delta P_{Total-1}$	$\Delta P_{Total-2}$
ΔP, psia	21.21	20.38
k_g, md	0.58	0.61
k^o_{rg}	0.300	0.313

Table B.14: Gas and oil relative permeabilities measured during condensate accumulation after methanol treatment at 1,200 psig and 44.8 cc/hr.

	$\Delta P_{\text{Total-1}}$
ΔP, psia	216.1
k_{rg}	0.06
k_{ro}	0.08

Table B.15: Gas end-point relative permeability measured during equilibrium gas flooding after methanol treatment at 1,200 psig and 44.8 cc/hr.

	$\Delta P_{\text{Total-1}}$	$\Delta P_{\text{Total-2}}$
ΔP, psia	14.32	14.25
k_g, md	0.86	0.87
k^o_{rg}	0.445	0.447

Table B.16: Summary of experimental results for coreflood Experiment-5.

	Before Methanol	After Methanol
k_{rg}	0.14	0.06
k_{ro}	0.18	0.08
k^o_{rg}	0.313	0.447

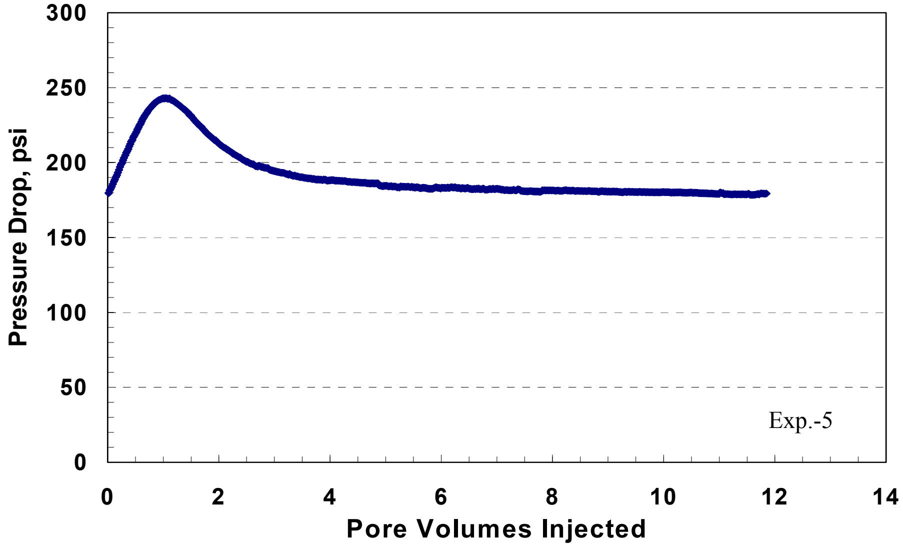

Figure B.10: Pressure drop across the core during brine (0.5 wt% $CaCl_2$) injection at atmospheric pressure and 44.8 cc/hr.

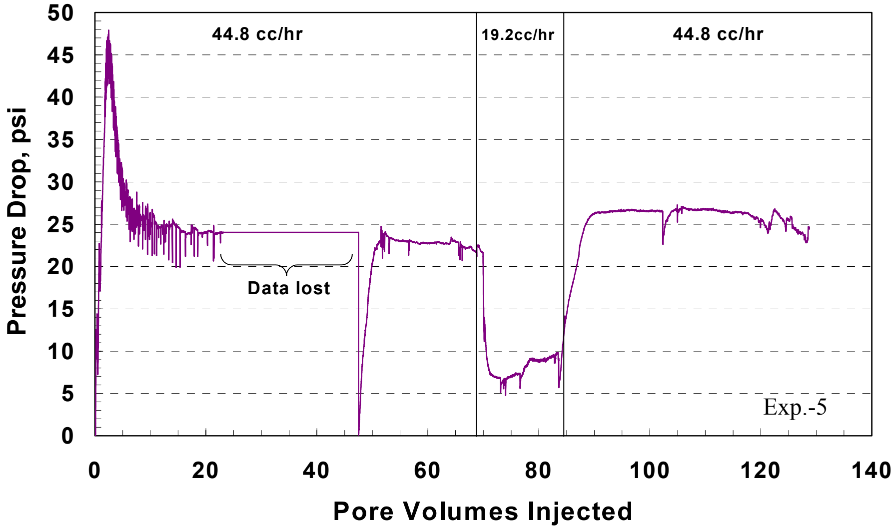

Figure B.11: Pressure drop across the core during methane flow to displace water from the core at 2,000 psig and various flow rates.

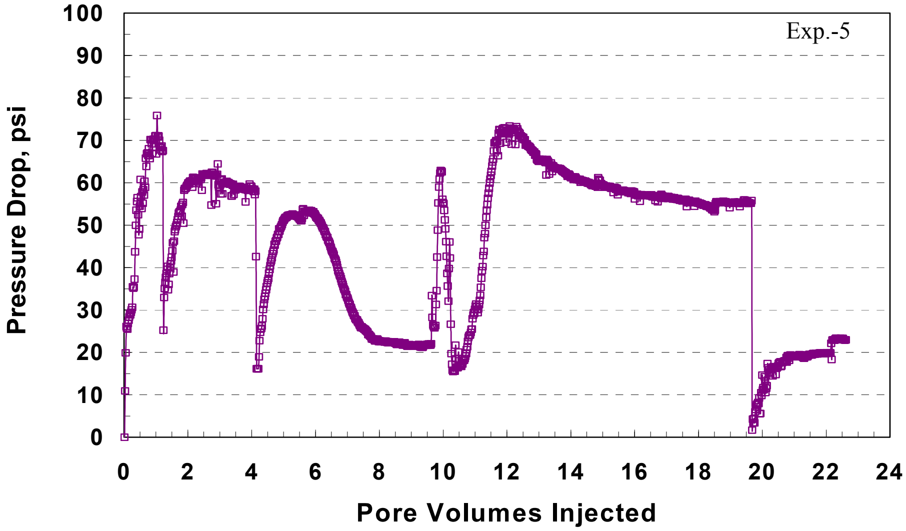

Figure B.12: Pressure drop across the core during methane flow at 3,000 psig and a flow rate of 44.8 cc/hr.

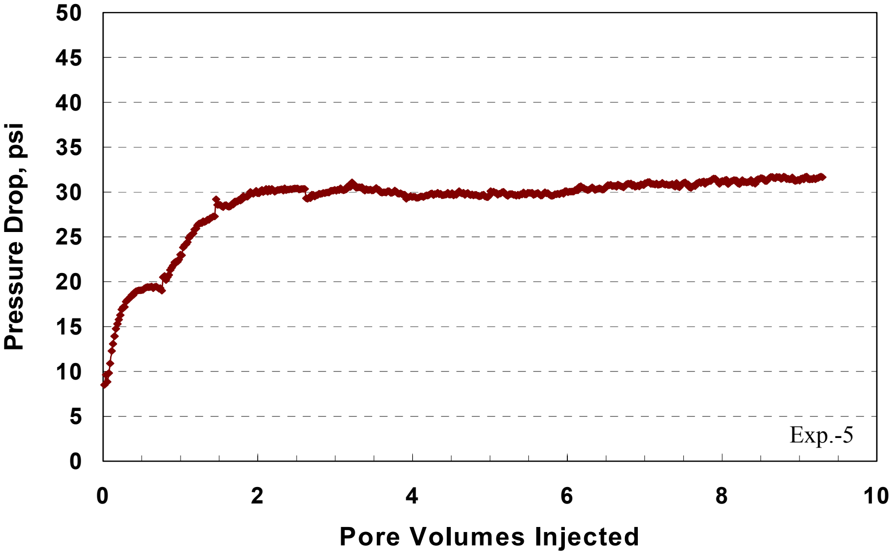

Figure B.13: Pressure drop across the core during gas mixture (single-phase) flow at 3,000 psig and 44.8 cc/hr.

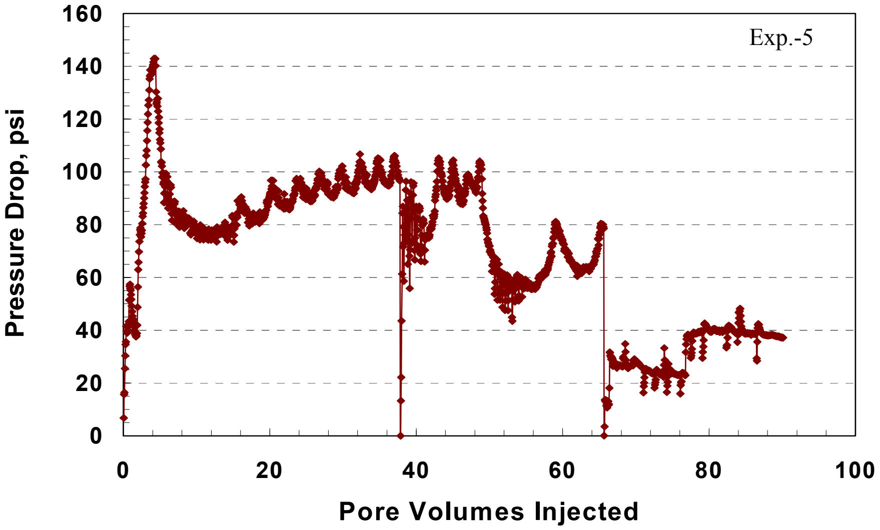

Figure B.14: Pressure drop across the core during dynamic condensate accumulation at 1,200 psig and 44.8 cc/hr.

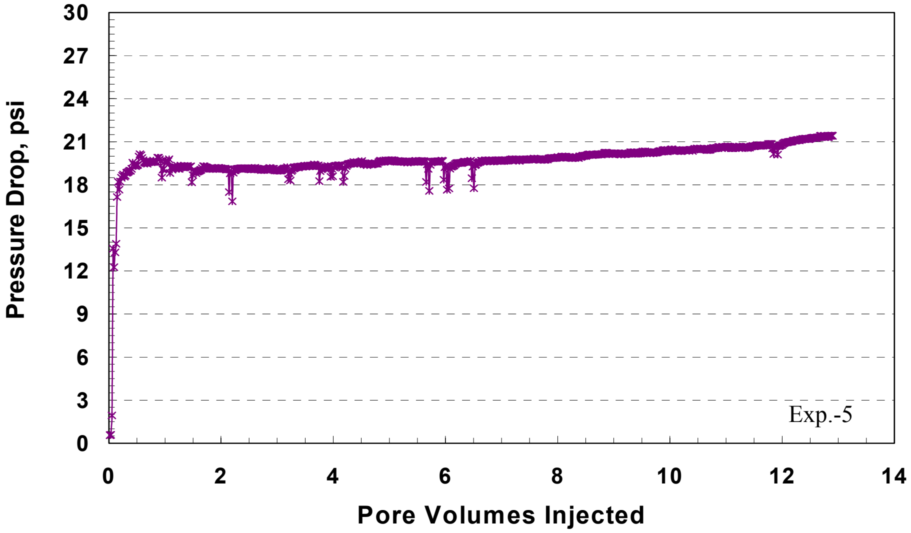

Figure B.15: Pressure drop across the core during equilibrium gas flow before methanol treatment at 1,200 psig and 44.8 cc/hr.

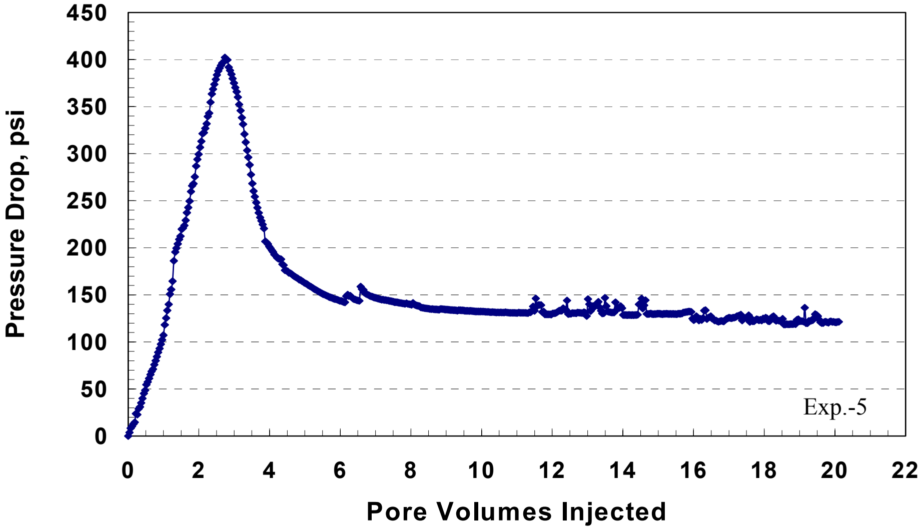

Figure B.16: Pressure drop across the core during methanol treatment at 1,200 psig and 44.8 cc/hr.

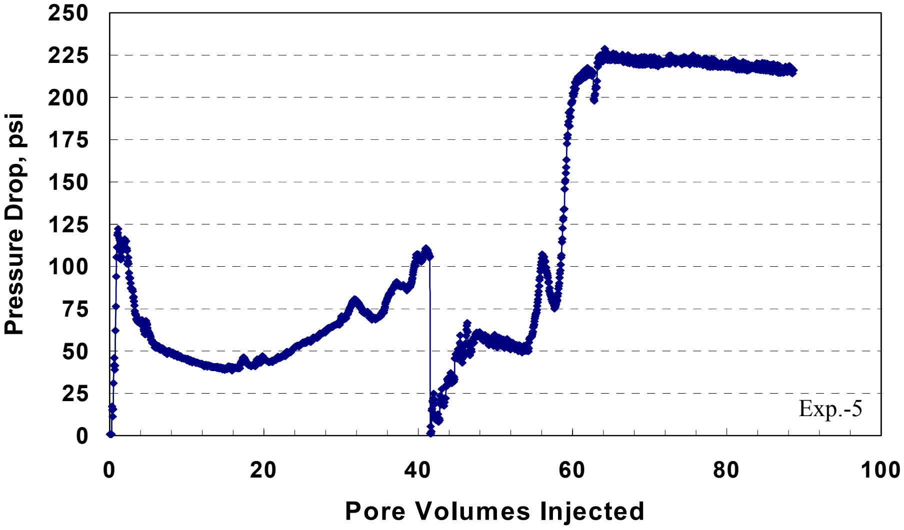

Figure B.17: Pressure drop across the core during condensate accumulation after methanol treatment at 1,200 psig and 44.8 cc/hr.

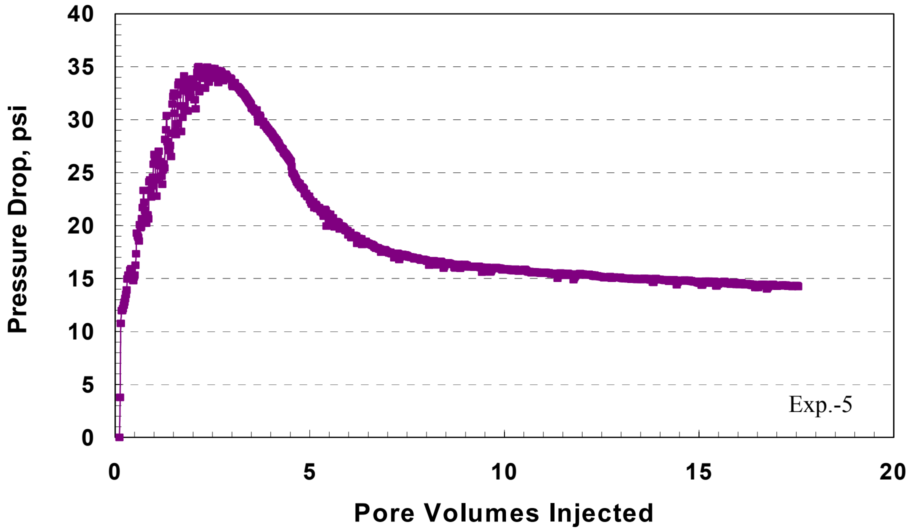

Figure B.18: Pressure drop across the core during equilibrium gas flow after methanol treatment at 1,200 psig and 44.8 cc/hr.

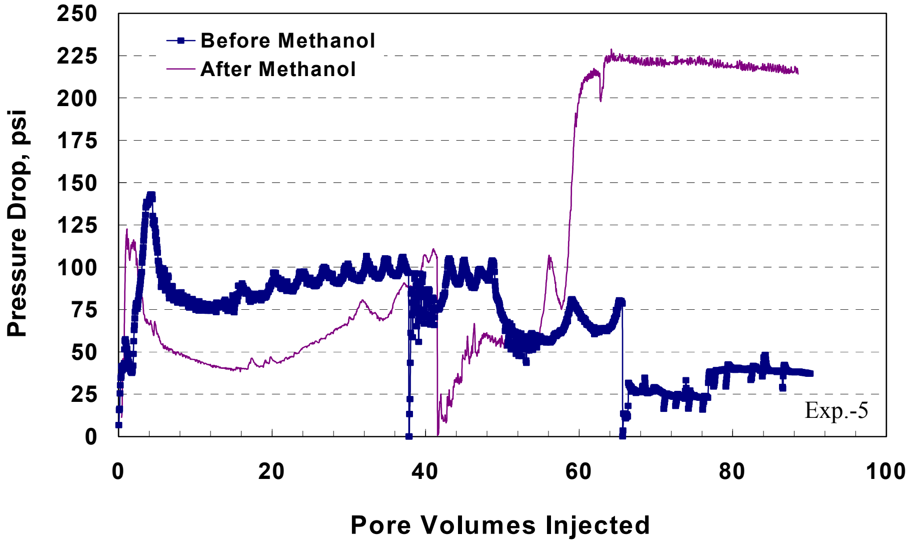

Figure B.19: Pressure drop across the core during condensate accumulation before and after methanol treatment at 1,200 psig and 44.8 cc/hr.

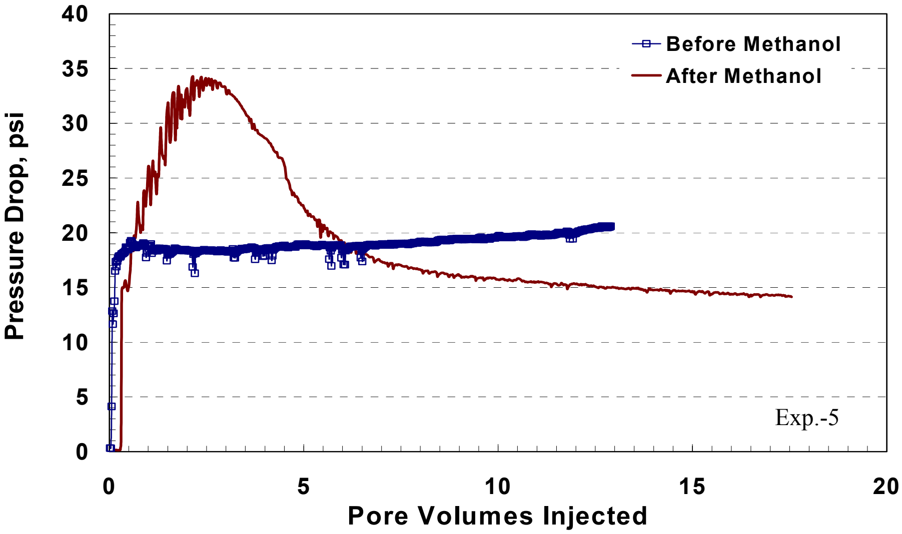

Figure B.20: Pressure drop across the core during equilibrium gas flow before and after methanol treatment at 1,200 psig and 44.8 cc/hr.

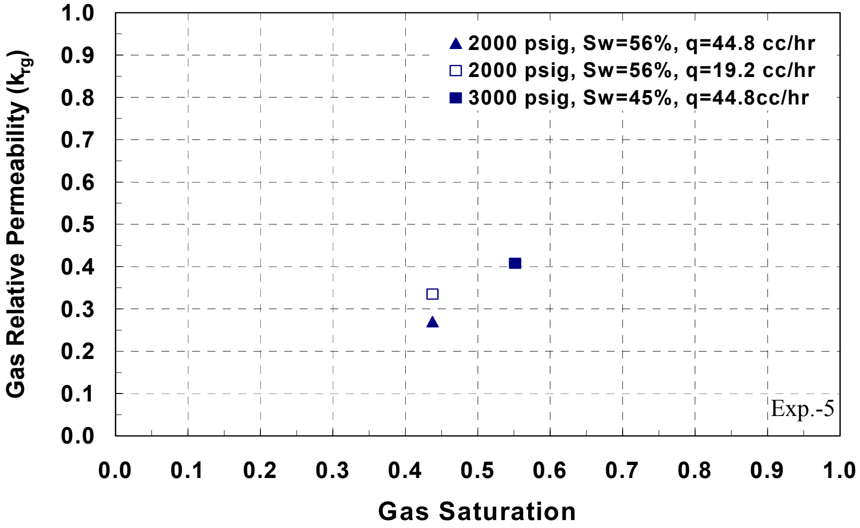

Figure B.21: Gas (methane) relative permeability data at different residual water saturations.

B.3 Coreflood Experiment No. 7

B.3.1 Objective

The objective of this experiment is to investigate the effect of multi-stage treatment of methanol on the relative permeability of gas after gas-condensate accumulation. This experiment was performed on Texas Cream Limestone. There was no water present in the core.

B.3.2 Core Preparation

A core with a diameter of 0.972 inches and a length of 8.01 inches was cut from Texas Cream limestone block. The core was dried in an oven at 95°C for more than 3 weeks. The core was wrapped with an aluminum foil and a heat-shrink Teflon. The wrapped core was placed into a Phoenix core-holder inside HTHP oven at 145°F. After 4 hours, an axial pressure was applied by screwing the end pieces of the core-holder. Then, an overburden pressure of 3,400 psig was applied.

B.3.3 Initial Core Permeability Measurements

The initial (absolute) core permeability was measured using varies single-phase gases. The pressure of both the upstream and downstream back-pressure regulators was set to 2,000 psig. Initially, nitrogen gas was flowed at a rate of 44.8 cc/hr. **Figure B.22** shows the pressure drop across the core during the flow of nitrogen at 2,000 psig. Then, methane was flowed through the core at the same flow rate. The pressure drop across the core during methane flooding is shown in **Figure B.23**. The pressure of both back-pressure regulators was increased to 3,000 psig. Methane was flowed through the core at 3,000 psig and a flow rate of 44.8 cc/hr. **Figure B.24** depicts the pressure drop across the core during methane flow at 3,000 psig. **Table B.17** gives the measured initial core permeability to nitrogen and methane at flowing pressure of 2,000 and 3,000 psig.

B.3.4 Gas Mixture (Single-Phase) Flow

The gas mixture (single-phase) was flowed through the core at 3,000 psig by setting the pressure of both back-pressure regulators to 3,000 psig. The flow rate was 44.8 cc/hr. **Figure B.25** shows the pressure drop across the core during gas mixture (single-phase) flooding. **Table B.18** gives the gas relative permeability to single-phase gas mixture at 3,000 psig. The measured values are close to those measured with nitrogen and methane. This confirms that the gas mixture is a single phase at 3,000 psig and flowing above its dewpoint pressure. Therefore, the preparation of this synthetic gas mixture was right.

B.3.5 Condensate Accumulation (Two-Phase)

Before the start of this stage, the inlet and outlet valves of the core were closed. Pressure of the downstream back-pressure regulator was decreased to 1,200 psig, while the pressure in the upstream back-pressure regulator was kept at 3,000 psig. Flow was started while the bypass was open until the pressure in the lines stabilized. Then, the bypass valve was closed and inlet and outlet valves

were open simultaneously. The flow rate was 44.8 cc/hr. This stage allowed the gas-condensate to dynamically accumulated through the core. The stage was stopped when the pressure drop across the core reached stable values. **Figure B.26** shows the pressure drop across the core during two-phase flow. Gas and oil relative permeabilities during two-phase flow are given in **Table B.19**. The gas relative permeability was reduced by 88% due to condensate blocking when the pressure was reduced below the dewpoint.

B.3.6 Equilibrium Gas Flow

The pressure in the upstream back-pressure regulator was decreased to 1,200 psig. The gas-phase of the gas mixture, which has a pressure of 1,200 psig (below dew point), was injected through the core at a flow rate of 44.8 cc/hr. The pressure drop across the core is shown in **Figure B.27**. This stage gave the gas end-point relative permeability (k^o_{rg}) before methanol treatment as listed in **Table B.20**.

B.3.7 The First Stage of Methanol Treatment

Pure methanol was injected through the core at an injection rate of 44.8 cc/hr and 1,200 psig. The volume of methanol injected was 20 PV. The pressure drop across the core stabilized at a value 138.62 psia as shown in **Figure B.28**. The calculated permeability for methanol was 1.89 md. This is the first stage of methanol treatment after condensate accumulation.

B.3.8 Two-Phase Flow After the First Stage of Methanol Treatment

The pressure of the upstream back-pressure regulator was increased to 3,000 psig, while the pressure of the downstream back-pressure regulator was kept at 1,200 psig. The gas mixture was flashed through the core to accumulate condensate. **Figure B.29** depicts the pressure drop across the core during this stage. This figure indicates that the pressure drop across the core started to increase after an injection of 31.3 PV of the two-phase. This means that the first methanol treatment was effective in delaying the condensate banking. After the evaporation of the methanol-rich phase from the core, condensate started to accumulate as implied by the increase in the pressure drop. **Table B.21** lists gas and oil relative permeabilities measured during condensate accumulation after the first treatment of methanol.

B.3.9 Equilibrium Gas After the First Methanol Treatment

The pressure of the upstream back-pressure regulator was decreased to 1,200 psig. The equilibrium gas was injected at a flow rate of 44.8 cc/hr**. Figure B.30** shows the pressure drop across the core. This stage gives the gas end-point relative permeability after methanol injection, as given in **Table B.22**.

B.3.10 The Second Stage of Methanol Treatment

The core was treated with the second stage of pure methanol. The flow rate of 44.8 cc/hr and the flowing pressure was 1,200 psig. The volume of methanol injected was 20 PV. The pressure drop across the core stabilized at a value 129.21 psia, which is close to the stabilized value of the first stage of methanol, as shown in **Figure B.31**. The calculated permeability for methanol was 2.02 md.

B.3.11 Two-Phase Flow After the Second Stage of Methanol Treatment

The pressure of the upstream back-pressure regulator was increased to 3,000 psig, while the pressure of the downstream back-pressure regulator was kept at 1,200 psig. The gas mixture was flashed through the core to bank condensate. **Figure B.32** shows the pressure drop across the core during two-phase flow after the second treatment of methanol. It can be seen that the pressure drop across the core started to increase after an injection of 66.2 PV of the two-phase. This indicates that the second treatment of methanol was so effective than the first one. However, the pressure drop continued to increase. The rate was dropped to 32 cc/hr when the pressure drop reached the maximum limit of the pressure transducer. Two-phase relative permeabilities are given in **Table B.23**.

B.3.12 Equilibrium Gas After the Second Methanol Treatment

The pressure of the upstream back-pressure regulator was decreased to 1,200 psig. The equilibrium gas was injected at a flow rate of 44.8 cc/hr. **Figure B.32** shows the pressure drop across the core. Pressure transducer # 6 had a leak through the bypass value. This transducer was closed, while pressure drop was measured using pressure transducer # 7. **Table B.24** gives the gas end-point relative permeability after methanol injection, as given in. The second treatment of methanol increased the gas relative permeability compared to the first treatment.

B.3.13 The Third Stage of Methanol Treatment

The core was treated with 20PV of methanol as the third stage. The flow rate of 44.8 cc/hr and the flowing pressure was 1,200 psig. The volume of methanol injected was 20 PV. The pressure drop across the core stabilized at a value 138.00 psia, which is close to the stabilized value of the first stage of methanol, as shown in **Figure B.34**. The calculated permeability for methanol was 1.90 md.

B.3.14 Two-Phase Flow After the Third Stage of Methanol Treatment

The pressure of the upstream back-pressure regulator was increased to 3,000 psig, while the pressure of the downstream back-pressure regulator was kept at 1,200 psig. The gas mixture was flashed through the core to bank condensate. **Figure B.35** shows the pressure drop across the core during two-phase flow after the third treatment of methanol. The pressure drop across the core showed the same trend as that observed after the second stage of methanol. However, the pressure drop started to increase after a flow of 78.8 PV of the two-phase. This result indicates that the third treatment of methanol delayed condensate accumulation for a longer period than that the previous two treatments. The flow rate was decreased to 11.2 cc/hr when the pressure drop across reached the limit of the pressure transducers. Gas and oil relative permeabilities during two-phase flow are given in **Table B.25**.

B.3.15 Equilibrium Gas After the Third Methanol Treatment

The equilibrium gas was injected at a flow rate of 44.8 cc/hr. **Figure B.36** shows the pressure drop across the core. The gas end-point relative permeability after methanol injection is given in **Table B.26**. The second treatment of methanol increased the gas relative permeability compared to the first treatment.

B.3.16 Summary of the Results of Experimen-7

Figure B.37 compares the pressure drop during two-phase flow through the core before and after methanol treatments. As can be seen, methanol treatment delays condensate accumulation and creates an enhanced flow period where the pressure drop reached a minimum value. **Table B.27** gives the measured gas and oil relative permeability values during the enhanced flow period.

Pressure drop across the core during equilibrium gas flow before and after methanol injection is shown in **Figure B.38**. This figure indicates that the methanol treatment was effective to increase the gas relative permeability. The first methanol treatment increased the gas relative permeability by 25%, while the second treatment increased it by 36%. The second treatment of methanol was so effective than the first one. The third treatment of methanol did not improve the gas relative permeability. **Table B.28** summarizes the experimental results of this coreflood experiment.

Table B.17: Initial core permeability measured using single-phase gases.

Gas	Pressure, psig	k, md
Nitrogen	2,000	2.97
Methane	2,000	2.49
Methane	3,000	2.32

Table B.18: Core permeability measured with gas mixture (single-phase) at 3,000 psig and 44.8 cc/hr.

	$\Delta P_{Total-1}$	$\Delta P_{Total-2}$
ΔP, psia	12.31	11.10
k_g, md	2.32	2.57

Table B.19: Oil and gas relative permeabilities measured during condensate accumulation stage before methanol at 1,200 psig and 44.8 cc/hr.

	$\Delta P_{Total-1}$
ΔP, psia	89.77
k_{rg}	0.12
k_{ro}	0.15

Table B.20: Gas end-point relative permeability measured during equilibrium gas flow before methanol treatment at 1,200 psig and 44.8 cc/hr.

	$\Delta P_{Total-1}$	$\Delta P_{Total-2}$
ΔP, psia	9.39	9.31
k_g, md	1.32	1.33
k^o_{rg}	0.569	0.517

Table B.21: Two-phase relative permeability measured during condensate accumulation after the first methanol treatment at 1200 psig.

	$\Delta P_{Total-1}$
ΔP, psia	121.61
k_{rg}	0.09
k_{ro}	0.11

Table B.22: Gas end-point relative permeability measured during equilibrium gas flow after the first methanol treatment at 1200 psig and 44.8 cc/hr.

	$\Delta P_{Total-1}$	$\Delta P_{Total-2}$
ΔP, psia	7.24	7.45
k_g, md	1.71	1.66
k^o_{rg}	0.737	0.647

Table B.23: Gas and oil relative permeabilities measured during condensate accumulation after the second methanol treatment at 1200 psig.

	$\Delta P_{Total-1}$
ΔP, psia	130.58
k_{rg}	0.06
k_{ro}	0.08

Table B.24: Gas end-point relative permeability measured during equilibrium gas flow after the second methanol treatment at 1,200 psig and 44.8 cc/hr.

	$\Delta P_{Total-1}$	$\Delta P_{Total-2}$
ΔP, psia	7.24	7.45
k_g, md	1.71	1.66
k^o_{rg}	0.737	0.647

Table B.25: Gas and oil relative permeabilities measured during condensate accumulation after the second methanol treatment at 1,200 psig

	$\Delta P_{Total-1}$
ΔP, psia	83.85
k_{rg}	0.03
k_{ro}	0.04

Table B.26: Gas end-point relative permeability measured during equilibrium gas flow after the third methanol treatment at 1,200 psig and 44.8 cc/hr.

	$\Delta P_{Total-1}$	$\Delta P_{Total-2}$
ΔP, psia	8.79	8.81
k_g, md	1.41	1.41
k^o_{rg}	0.608	0.547

Table B.27: Gas and oil relative permeability measured during the enhanced flow period of the two-phase flow at 1,200 psig.

	Before Methanol	After the first Methanol stage	After the second Methanol stage	After the third Methanol stage
k_{rg}	0.12	0.16	0.48	0.56
k_{ro}	0.15	0.20	0.63	0.73

Table B.28: Summary of the results for coreflood Experiment-7.

	Before Methanol	After the first Methanol stage	After the second Methanol stage	After the third Methanol stage
k_{rg}	0.12	0.09	0.06	0.03
k_{ro}	0.15	0.11	0.08	0.04
k^o_{rg}	0.517	0.647	0.704	0.547

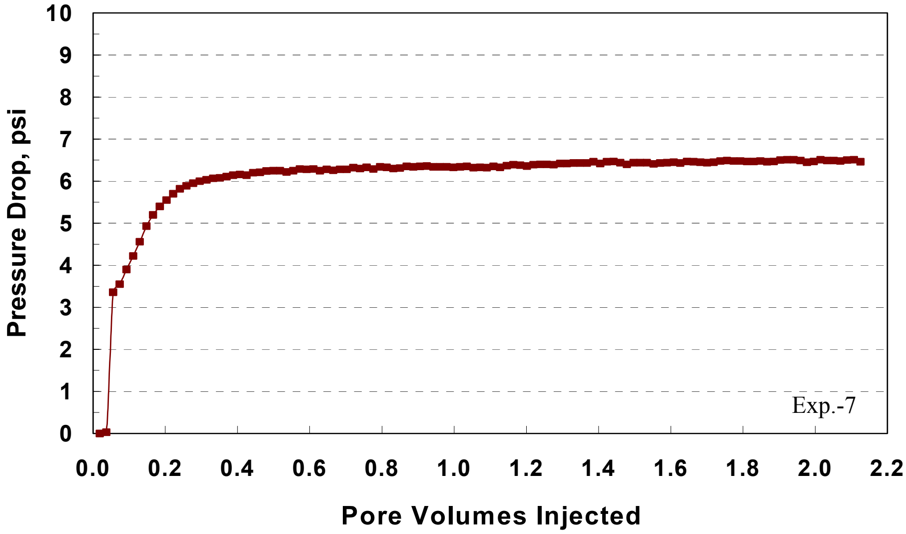

Figure B.22: Pressure drop across the core during nitrogen flow at 2,000 psig and 44.8 cc/hr.

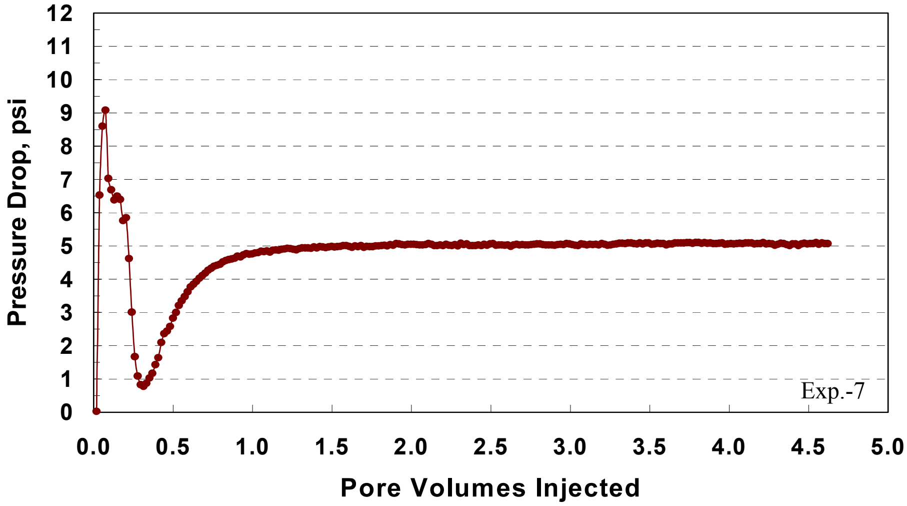

Figure B.23: Pressure drop across the core during methane flow at 2,000 psig and 44.8 cc/hr.

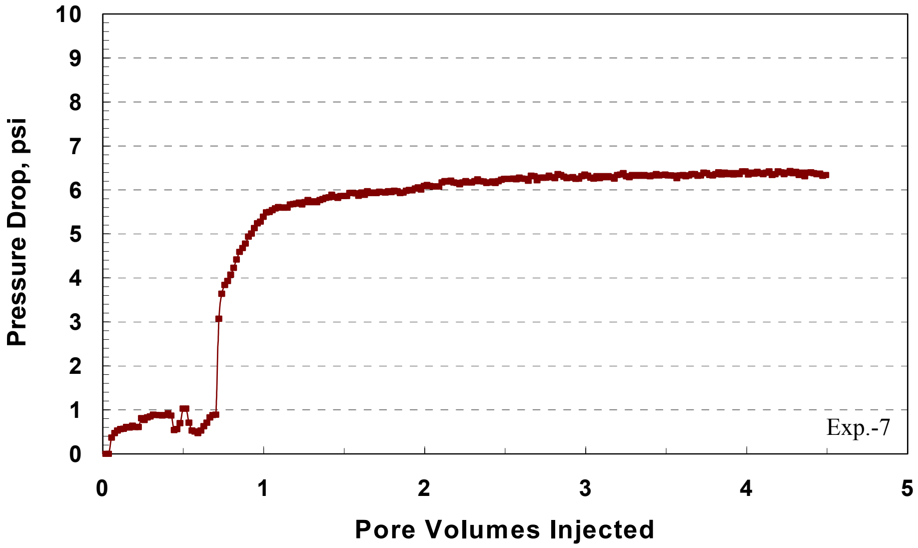

Figure B.24: Pressure drop across the core during methane flow at 3,000 psig and 44.8 cc/hr.

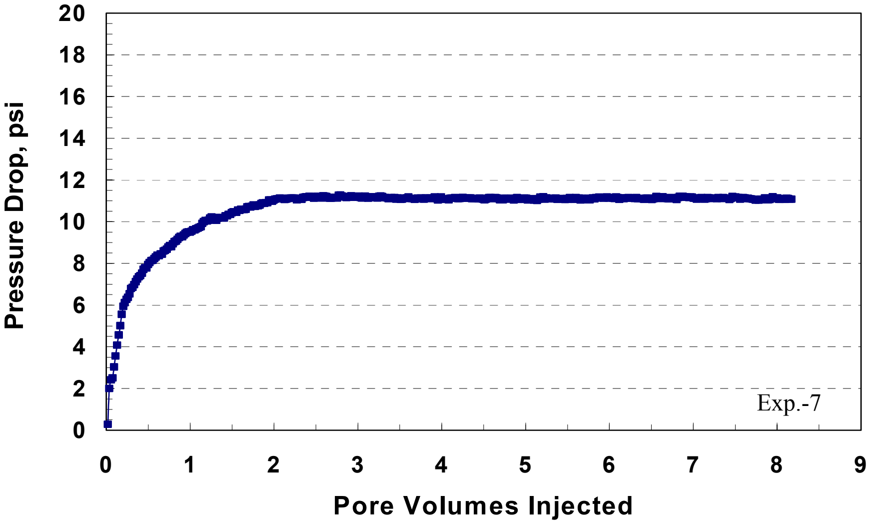

Figure B.25: Pressure drop across the core during gas mixture (single-phase) flow at 3,000 psig and 44.8 cc/hr.

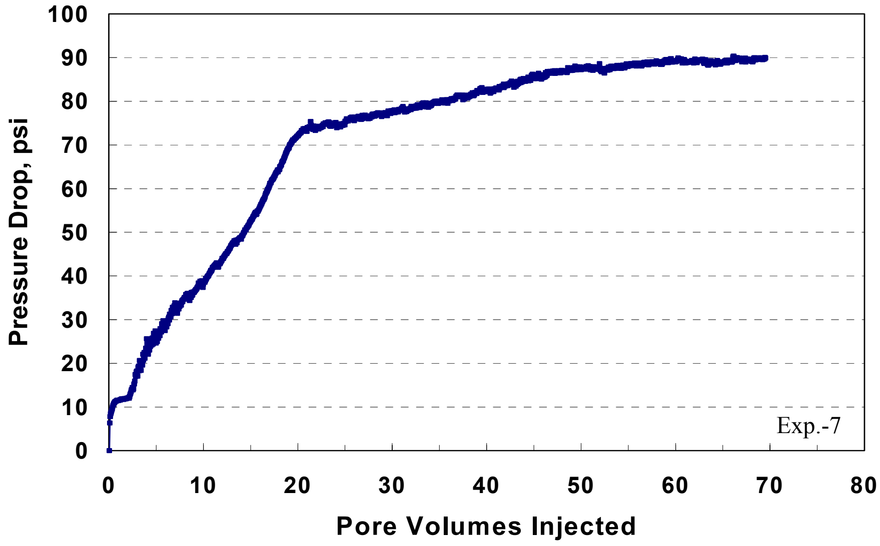

Figure B.26: Pressure drop across the core during condensate accumulation before methanol treatment at 1,200 psig and 44.8 cc/hr.

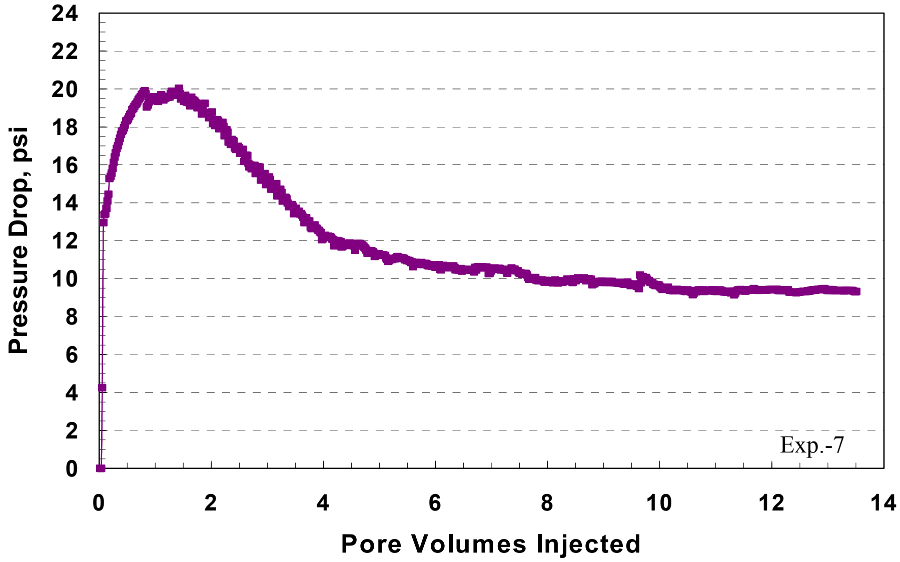

Figure B.27: Pressure drop across the core during equilibrium gas flow before methanol treatment at 1,200 psig and 44.8 cc/hr.

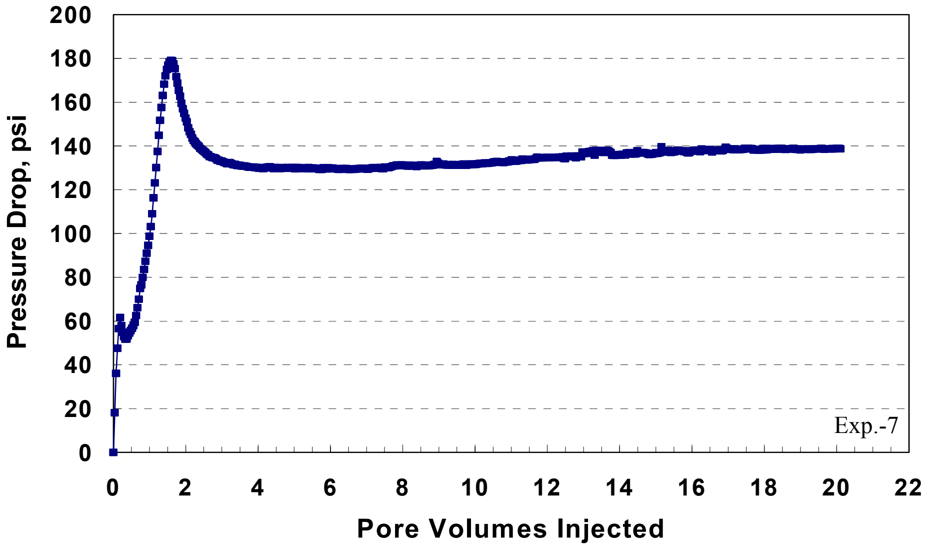

Figure B.28: Pressure drop across the core during the first stage of methanol treatment at 1,200 psig and 44.8 cc/hr.

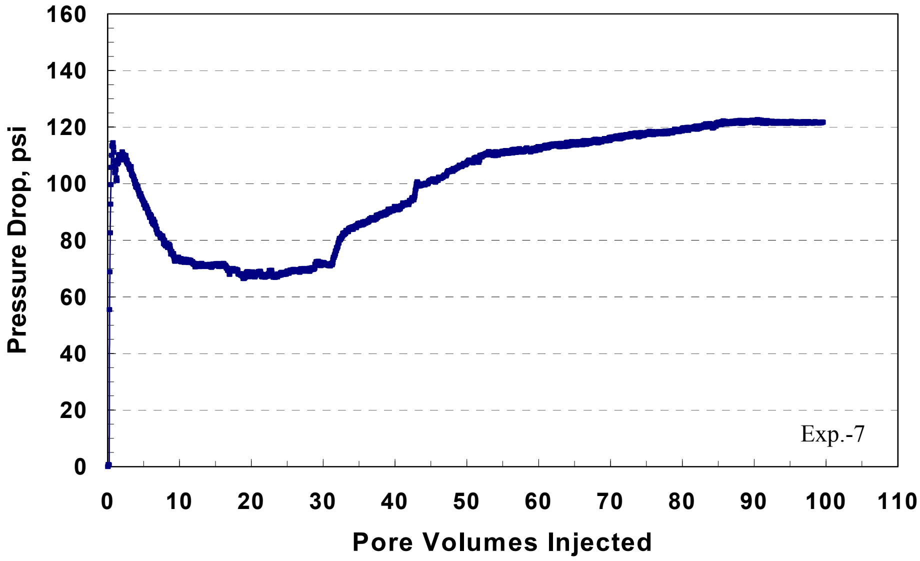

Figure B.29: Pressure drop across the core during condensate accumulation after the first methanol treatment at 1,200 psig and 44.8 cc/hr.

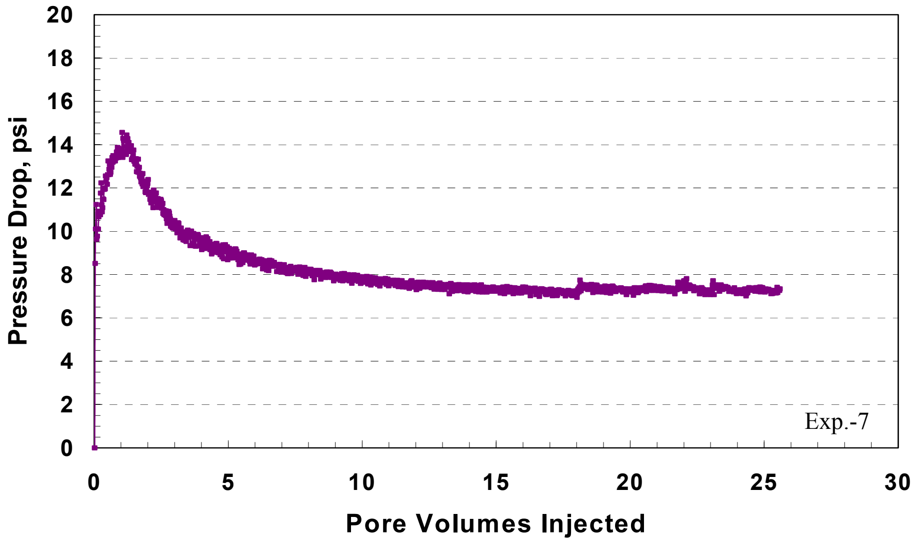

Figure B.30: Pressure drop across the core during equilibrium gas flow after the first methanol treatment at 1,200 psig and 44.8 cc/hr.

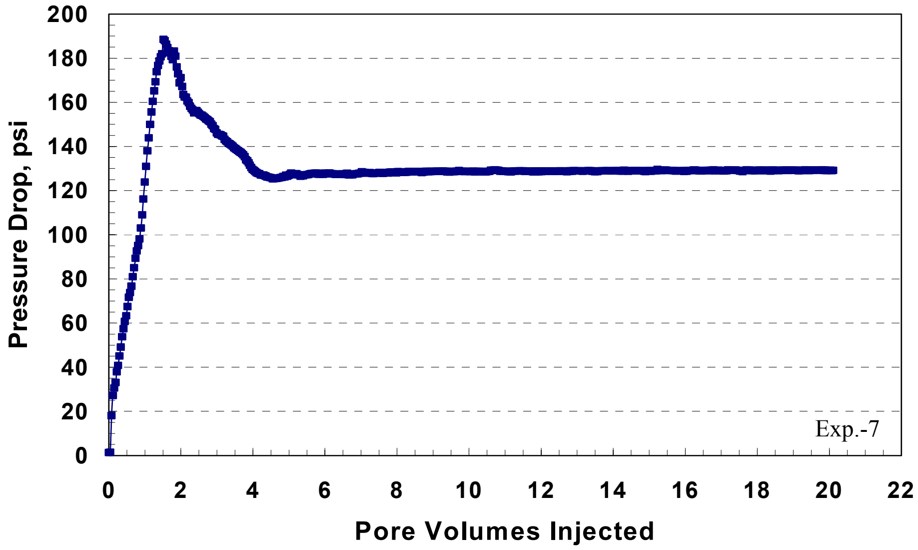

Figure B.31: Pressure drop across the core during the second methanol treatment at 1,200 psig and 44.8 cc/hr.

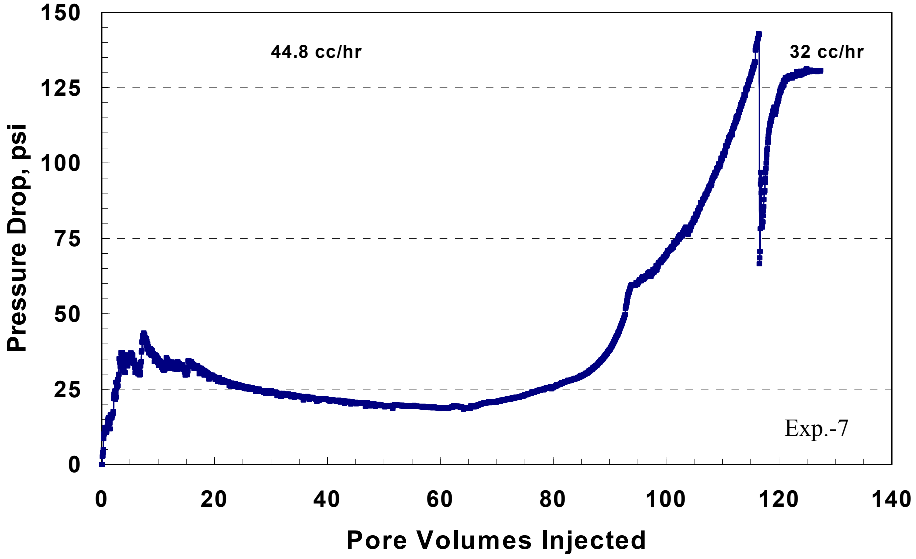

Figure B.32: Pressure drop across the core during condensate accumulation after the second methanol treatment at 1,200 psig.

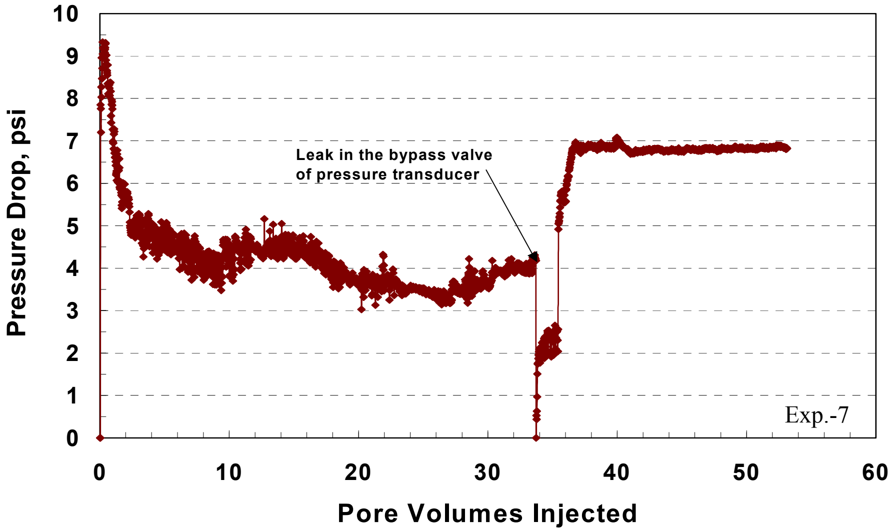

Figure B.33: Pressure drop across the core during equilibrium gas flow after the second methanol treatment at 1,200 psig and 44.8 cc/hr.

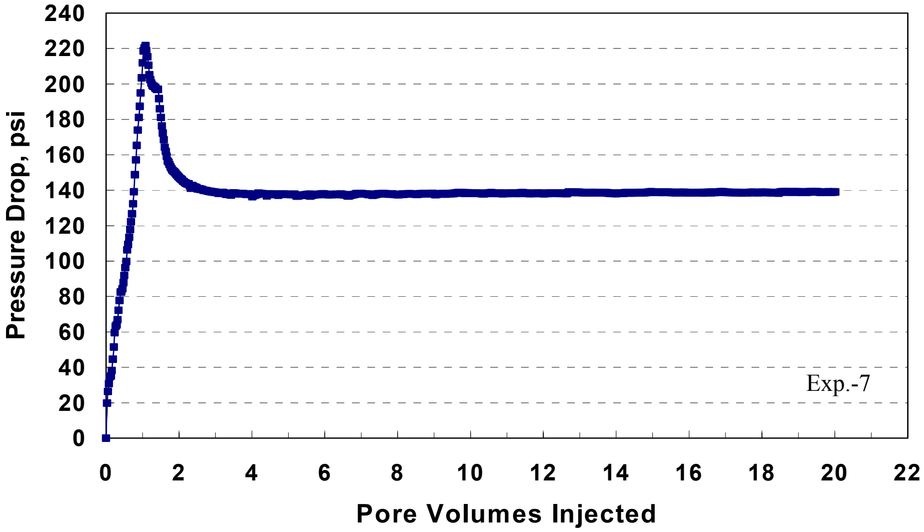

Figure B.34: Pressure drop across the core during the third methanol treatment at 1,200 psig and 44.8 cc/hr.

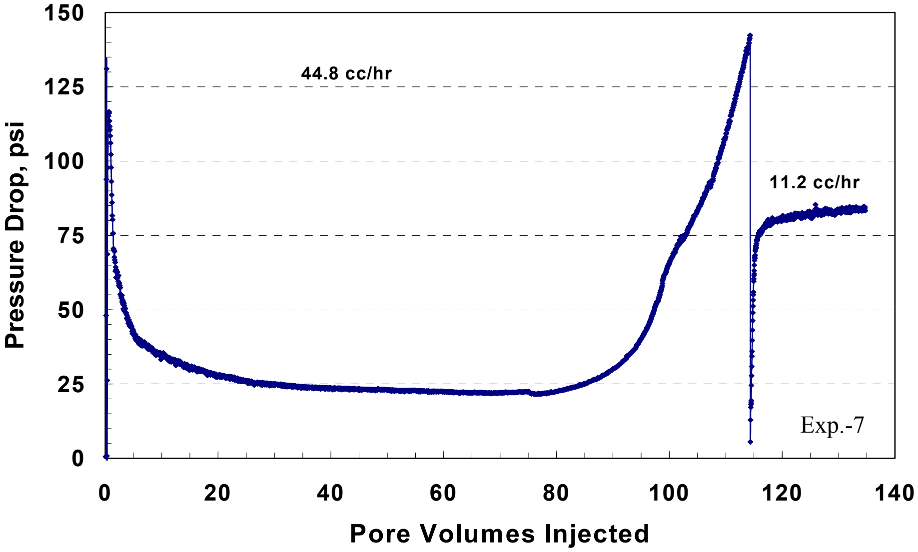

Figure B.35: Pressure drop across the core during condensate accumulation after the third methanol treatment at 1,200 psig.

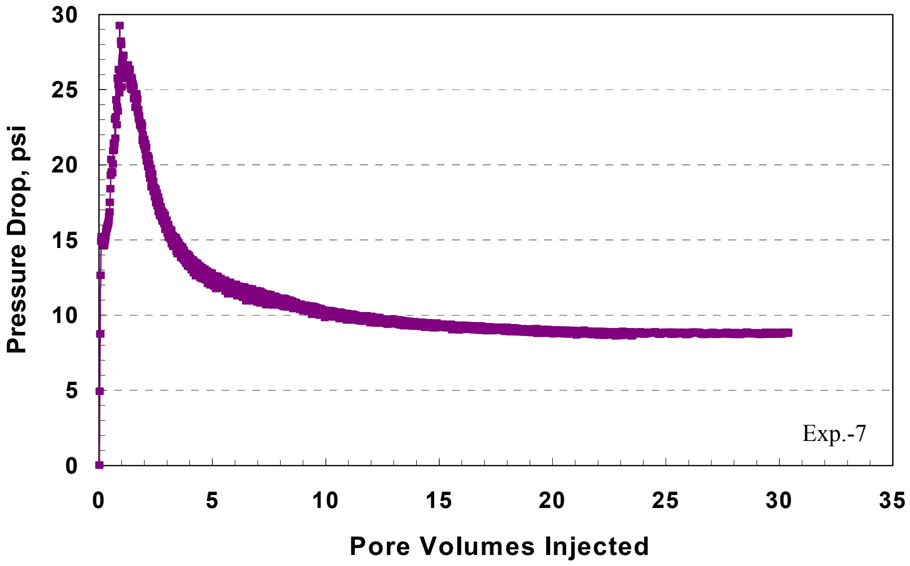

Figure B.36: Pressure drop across the core during equilibrium gas flow after the third methanol treatment at 1,200 psig and 44.8 cc/hr.

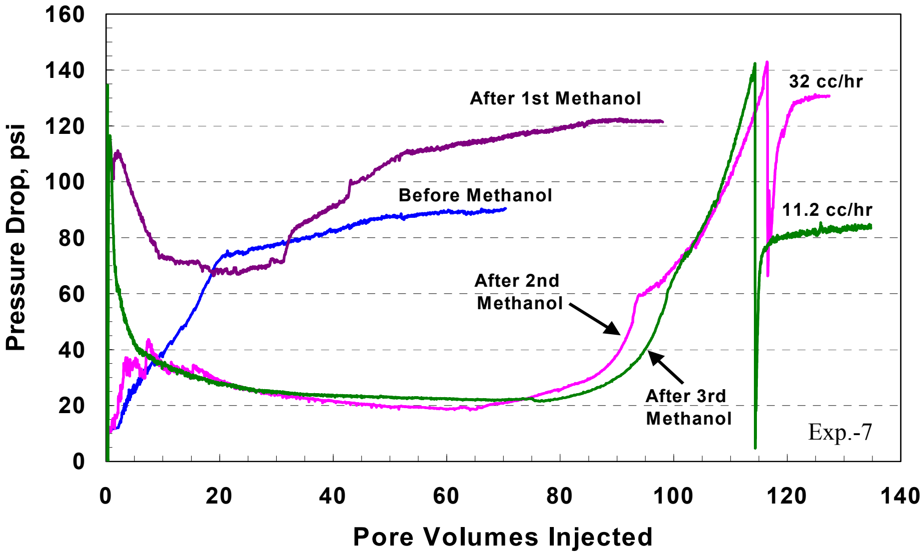

Figure B.37: Pressure drop across the core during dynamic condensate accumulation before and after methanol treatments at 1,200 psig and 44.8 cc/hr.

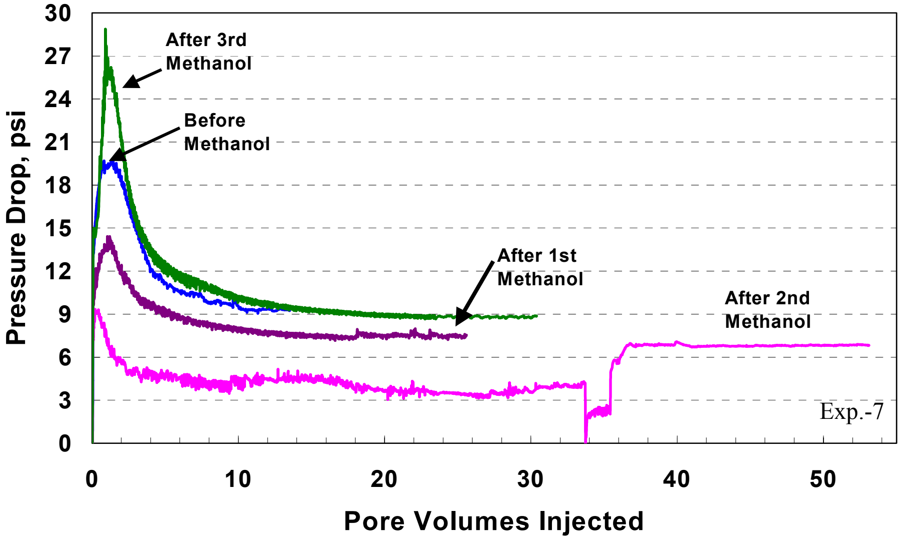

Figure B.38: Pressure drop across the core during equilibrium gas flow before and after methanol treatments at 1,200 psig and 44.8 cc/hr.

B.4 Coreflood Experiment No. 8

B.4.1 Objective

The objective of this experiment is to investigate the effect of multi-stage treatment of methanol on the relative permeability of gas after gas-condensate accumulation at an initial water saturation of 20%. This experiment was performed on a Texas Cream limestone core.

B.4.2 Core Preparation

A core with a diameter of 0.972 inches and a length of 8.01 inches was cut from Texas Cream limestone block. The core was dried in an oven at 95°C for more than 3 weeks. The core was wrapped with an aluminum foil and a heat-shrink Teflon. The wrapped core was placed into a Phoenix core-holder inside HTHP oven at 145°F. After 4 hours, an axial pressure was applied by screwing the end pieces of the core-holder. Then, an overburden pressure of 3,400 psig was applied.

B.4.3 Initial Core Permeability Measurement

The initial core permeability was measured using methane at a flowing pressure of 3,000 psig before introducing water saturation. The pressure of both the upstream and downstream back-pressure regulators was set to 3,000 psig. Methane gas was flowed at a rate of 44.8 cc/hr. **Figure B.39** shows the pressure drop across the core during the flow of methane at 3,000 psig. **Table B.29** gives the measured initial core permeability to methane at flowing pressure of 3,000 psig. The average initial core permeability is equal to 4.26 md.

B.4.4 Water Saturation Procedure

Water at a saturation of 20% was introduced into the core according to the following procedure:

1. The pressure of the core holder was depleted to an atmospheric pressure by disconnected the inlet and outlet lines from flow lines.
2. The outlet end of the core holder was connected to a vacuum pump. Then, the core was vacuumed for at 5 hours, while the inlet end was closed.
3. To get 20% water saturation, 4 ml of distilled water were injected from the inlet of the core holder using a burette, while a vacuum was pulled from the outlet end of the core holder.
4. The core holder was placed inside the oven (@ 145°F) and opened to atmospheric pressure. The core holder was set in the oven for 4 hours to reach an equilibrium temperature. Then, a series of push-pull cycles were applied using a RUSKA hand pump through the outlet of the core holder, while keeping the inlet of the core holder closed.
5. Between each push and pull cycle, a break of 15 minutes was taken to allow water vapor to distribute through the core.
6. The water saturation procedure was completed after 32 push-pull cycles.

B.4.5 Methane Flow at S_{wi} =20%

After the core was saturated with 20% of water, the permeability was measured using methane at a flowing pressure of 3,000 psig and a flow rate of 44.8 cc/hr. **Figure B.40** shows the pressure drop across the core during methane flow at a water saturation of 20%. The measured gas relative permeability at S_{wi} = 20% is given in **Table B.30**.

B.4.6 Gas Mixture (Single-Phase)

The gas mixture (single-phase) was flowed through the core at 3,000 psig. The flow rate was 44.8 cc/hr. **Figure B.41** shows the pressure drop across the core during gas mixture (single-phase) flooding. The single-phase gas relative permeability is given in **Table B.31**. In this stage, no water was collected in the effluent.

B.4.7 Condensate Accumulation (Two-Phase Flow)

Before the start of this stage, the inlet and outlet valves of the core were closed. Pressure of the downstream back-pressure regulator was decreased to 1,200 psig, while the pressure in the upstream back-pressure regulator was kept at 3,000 psig. Flow was started while the bypass was open until the pressure in the lines stabilized. Then, the bypass valve was closed and inlet and outlet valves were open simultaneously. The flow rate was 44.8 cc/hr. This stage allowed the gas-condensate to dynamically accumulated through the core. The stage was stopped when the pressure drop across the core reached stable values. **Figure B.42** shows the pressure drop across the core during the two-phase flow. The pressure drop across the core was gradually increased until it reached a plateau after 24 PV. Gas and oil relative permeabilities measured during condensate accumulation are given in **Table B.32**. Data needed to calculation relative permeability for gas and oil phases (μ_g=0.01396 cp, μ_o=0.23711 cp) were obtained using PREOS and UTCOMP.

B.4.8 Equilibrium Gas Flow

The pressure in the upstream back-pressure regulator was decreased to 1,200 psig. The gas-phase of the gas mixture, which has a pressure of 1,200 psig (below dewpoint), was injected through the core at a flow rate of 44.8 cc/hr. The pressure drop across the core is shown in **Figure B.43**. This stage gave the gas end-point relative permeability (k^o_{rg}) before methanol treatment, as listed in **Table B.32**.

B.4.9 The First Stage of Methanol Treatment

Pure methanol was injected through the core at an injection rate of 44.8 cc/hr and 1,200 psig. The volume of methanol injected was 20 PV. The pressure drop across the core stabilized at a value 55.39 psia as shown in **Figure B.44**. The calculated permeability for methanol was found to be 4.72 md.

B.4. 10 Two-Phase Flow After the First Stage of Methanol Treatment

The pressure of the upstream back-pressure regulator was increased to 3,000 psig, while the pressure of the downstream back-pressure regulator was kept at 1,200 psig. The gas mixture was flashed through the core to bank condensate. **Figure B.45** depicts the pressure drop across the core during this stage. This figure indicates that the pressure drop across the core started to increase after an injection of 36 PV of the two-phase. This means that the first methanol treatment was effective in delaying the condensate banking. The two-phase relative permeabilities are shown in **Table B.34**.

B.4.11 Equilibrium Gas After the First Methanol Treatment

The pressure of the upstream back-pressure regulator was decreased to 1,200 psig. The equilibrium gas was injected at a flow rate of 44.8 cc/hr. **Figure B.46** shows the pressure drop across the core. This stage gives the gas end-point relative permeability after methanol injection, as given in **Table B.35**. The first stage of methanol increased the gas relative permeability by 23%.

B.4.12 The Second Stage of Methanol Treatment

The core was treated with the second stage of pure methanol. The flow rate was 44.8 cc/hr and the flowing pressure was 1,200 psig. The volume of methanol injected was 20 PV. The pressure drop across the core stabilized at a value 62.63 psia, which is close to the stabilized value of the first stage of methanol, as shown in **Figure B.47**. The measured permeability for methanol was found equal to 4.18 md.

B.4.13 Two-Phase Flow After the Second Stage of Methanol Treatment

The pressure of the upstream back-pressure regulator was increased to 3,000 psig, while the pressure of the downstream back-pressure regulator was kept at 1,200 psig. The gas mixture was flashed through the core to bank condensate. **Figure B.48** shows the pressure drop across the core during two-phase flow after the second treatment of methanol. It can be seen that the pressure drop across the core started to increase after an injection of 70 PV of the two-phase. This indicates that the second treatment of methanol was so effective than the first one. Gas and oil relative permeabilities measured during this stage are given in **Table B.36**.

B.4.14 Equilibrium Gas After the Second Methanol Treatment

The pressure of the upstream back-pressure regulator was decreased to 1,200 psig. The equilibrium gas was injected at a flow rate of 44.8 cc/hr. **Figure B.49** shows the pressure drop across the core during equilibrium gas flow at 1,200 psig. This stage gives the gas end-point relative permeability after methanol injection, as given in **Table B.37**. The second treatment of methanol increased the gas relative permeability by 36% compared to the first treatment.

B.4.15 Two-Phase Flow (4th flow)

Since the second stage of methanol increased the relative permeability to a higher value of 0.92, it was proposed to investigate how methanol will prolong in preventing condensate banking. Two-phase gas mixture was flushed through the core as explained above. This stage is called as the forth flow of two-phase mixture. **Figure B.50** shows the pressure drop across the core during two-phase flow. The pressure drop across the core showed the same trend as that observed after the second stage of methanol. However, the pressure drop started to increase after a cumulative injection of 58.4 PV of the two-phase. This is really an interesting finding. This result indicates that there is some residual methanol in the core that delaying the accumulation of condensate. Gas and oil relative permeabilities are given in **Table B.38**.

B.4.16 Equilibrium Gas (4th stage)

The equilibrium gas was injected at a flow rate of 44.8 cc/hr and a pressure of 1,200 psig. **Figure B.51** shows the pressure drop across the core. This stage gives the gas end-point relative permeability after methanol injection, as given in **Table B.39**.

B.4.17 Two-Phase Flow (5th flow)

It was decided to flow the two-phase gas mixture to see if the residual methanol was removed by the previous stage of equilibrium gas. Two-phase gas mixture was flushed through the core as explained above. This stage is called as the fifth flow of two-phase mixture. **Figure B.52** shows the pressure drop across the core during two-phase flow. The pressure drop across the core showed the same trend as that for the forth stage of two-phase flow. The pressure drop started to increase after 62.4 PV of the two-phase. This result confirms that the residual methanol was not removed by the equilibrium gas and it may stay for a longer time. Two-phase relative permeability values are given in **Table B.40**.

B.4.18 Equilibrium Gas (5th stage)

The equilibrium gas was injected at a flow rate of 44.8 cc/hr and 1,200 psig. **Figure B.53** shows the pressure drop across the core. This stage gives the gas end-point relative permeability after methanol injection, as given in **Table B.41**.

B.4.19 Summary of the Results for Coreflood Experiment-8

Figure B.54 compares the pressure drop during two-phase flow through the core before and after methanol treatments. Pressure drop across the core during injection of equilibrium gas before and after methanol injection is shown in **Figure B.55**. This figure indicates that the methanol treatment was effective to increase the gas relative permeability. Summary of experimental results is given in **Table B.42**. The first methanol treatment increased the gas relative permeability by 23%, while the second treatment increased it by 36%. The second treatment of methanol was so effective than the first one. The removal of methanol by evaporation is very slow. Therefore, it stays for a longer time in the core. The residual methanol improves the productivity by postponing the accumulation of condensate. The treatment of methanol created an enhanced flow period where the pressure drop reached a minimum value. During this period, the productivity of the gas after the treatment is expected to maximize. Gas and oil relative permeabilities measured during the enhanced flow period are given in **Table B.43**. The first treatment of methanol increased both gas and oil (condensate) relative permeabilities during the enhanced flow period by a factor of 8 and 9, respectively. The enhancement of both relative permeabilities after the second treatment was higher (10-fold for k_{rg} and 11-fold for k_{ro}) than the first treatment.

Table B.29: Initial core permeability measured using methane at 3,000 psig and a flow rate of 44.8 cc/hr.

	$\Delta P_{Total-1}$	$\Delta P_{Total-2}$
ΔP, psia	3.61	3.33
k_g, md	4.09	4.43

Table B.30: Gas relative permeability measured during methane flow at S_{wi} =20%.

	$\Delta P_{Total-1}$	$\Delta P_{Total-2}$
ΔP, psia	3.78	3.47
k_g, md	3.90	4.26
k_{rg}	0.95	0.96

Table B.31: Gas relative permeability measured during gas mixture (single-phase) flow at 3,000 psig and 44.8 cc/hr.

	$\Delta P_{Total-1}$	$\Delta P_{Total-2}$
ΔP, psia	6.67	6.27
k_g, md	4.28	4.56
k_{rg}	~1.0	~1.0

Table B.32: Gas and oil relative permeabilities measured during condensate accumulation before methanol at 1200 psig and 44.8 cc/hr.

	$\Delta P_{Total-1}$
ΔP, psia	108.56
k_{rg}	0.06
k_{ro}	0.07

Table B.33: Gas end-point relative permeability measured during equilibrium gas flow before methanol at 1,200 psig and 44.8 cc/hr.

	$\Delta P_{Total-1}$	$\Delta P_{Total-2}$
ΔP, psia	3.97	4.03
k_g, md	3.12	3.08
$k°_{rg}$	0.729	0.675

Table B.34: Gas and oil relative permeability measured during two-phase flow after the first methanol treatment at 1,200 psig and 44.8 cc/hr.

	$\Delta P_{Total-1}$
ΔP, psia	98.10
k_{rg}	0.06
k_{ro}	0.08

Table B.35: Gas end-point relative permeability measured during equilibrium gas flow after the first methanol treatment at 1,200 psig and 44.8 cc/hr.

	$\Delta P_{Total-1}$	$\Delta P_{Total-2}$
ΔP, psia	3.35	3.28
k_g, md	3.70	3.78
$k°_{rg}$	0.865	0.829

Table B.36: Gas and oil relative permeabilities measured during condensate accumulation after the second methanol treatment at 1200 psig and 44.8 cc/hr.

	$\Delta P_{Total-1}$
ΔP, psia	111.93
k_{rg}	0.05
k_{ro}	0.07

Table B.37: Gas end-point relative permeability measured during equilibrium gas flow after the second methanol treatment at 1,200 psig and 44.8 cc/hr.

	$\Delta P_{Total-1}$	$\Delta P_{Total-2}$
ΔP, psia	2.91	2.97
k_g, md	4.26	4.17
k^o_{rg}	0.994	0.916

Table B.38: Gas and oil relative permeabilities measured during two-phase flow (4th flow stage) at 1,200 psig and 44.8 cc/hr.

	$\Delta P_{Total-1}$
ΔP, psia	119.90
k_{rg}	0.05
k_{ro}	0.06

Table B.39: Gas end-point relative permeability measured during equilibrium gas flow (4th stage) at 1,200 psig and 44.8 cc/hr.

	$\Delta P_{Total-1}$	$\Delta P_{Total-2}$
ΔP, psia	4.22	4.48
k_g, md	2.94	2.76
k^o_{rg}	0.686	0.606

Table B.40: Gas and oil relative permeabilities measured during two-phase flow (5th stage) at 1,200 psig and 44.8 cc/hr.

	$\Delta P_{Total-1}$
ΔP, psia	123.36
k_{rg}	0.05
k_{ro}	0.06

Table B.41: Gas end-point relative permeability measured during equilibrium gas flow (5th stage) at 1,200 psig and 44.8 cc/hr.

	$\Delta P_{Total-1}$	$\Delta P_{Total-2}$
ΔP, psia	2.86	2.79
k_g, md	4.34	4.44
k^o_{rg}	1.01	0.975

Table B.42: Summary of experimental results for coreflood Experiment-8.

	Before Methanol	After the first Methanol stage	After the second Methanol stage
k_{rg}	0.06	0.06	0.05
k_{ro}	0.07	0.08	0.07
k^o_{rg}	0.675	0.829	0.916

Table B.43: Gas and oil relative permeabilities measured during the enhanced flow period.

	Before Methanol	After the first Methanol stage	After the second Methanol stage
ΔP, psia	108.56	12.59	9.89
k_{rg}	0.06	0.48	0.62
k_{ro}	0.07	0.63	0.80

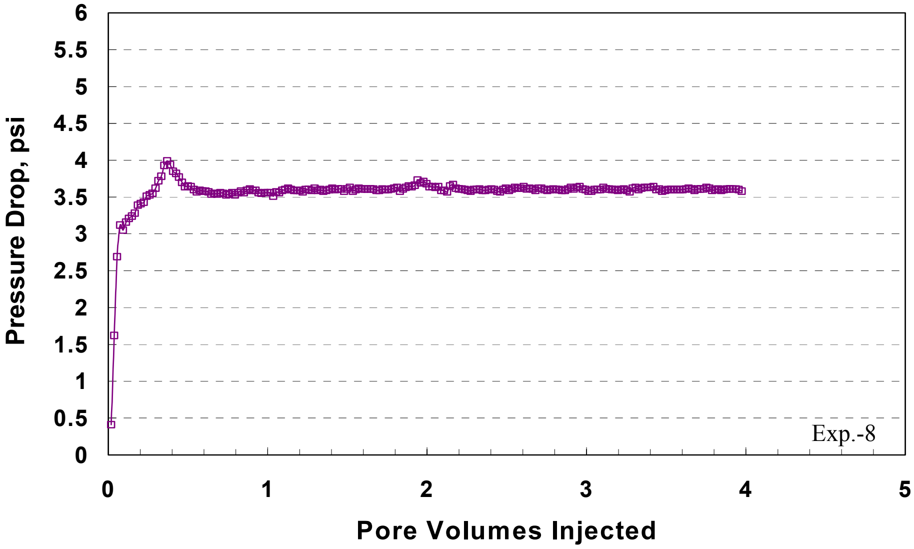

Figure B.39: Pressure drop across the core during methane flow before introducing water saturation at 3,000 psig and 44.8 cc/hr.

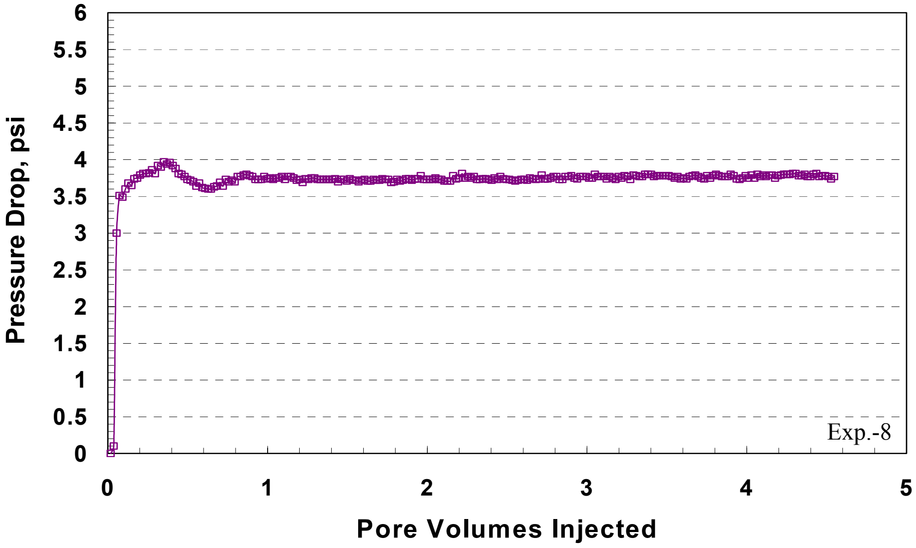

Figure B.40: Pressure drop across the core during methane flow at an initial water saturation of 20% at 3,000 psig and 44.8 cc/hr.

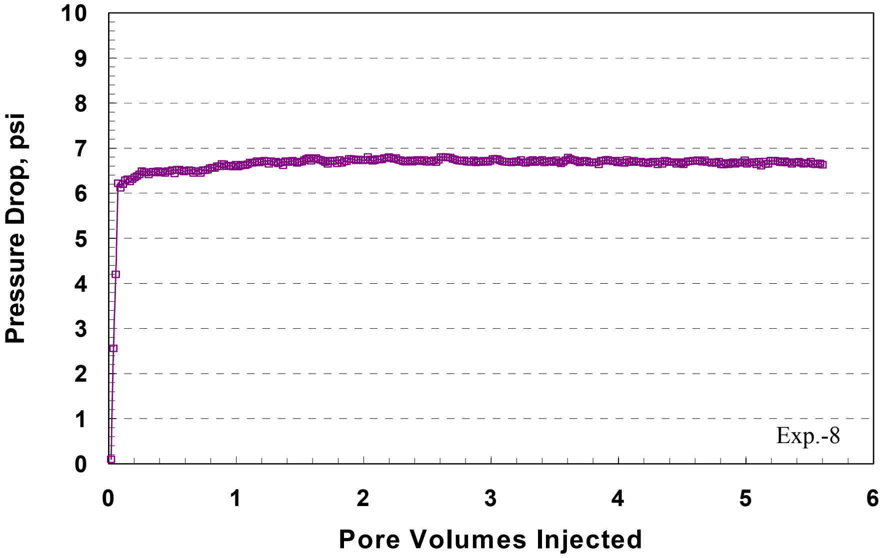

Figure B.41: Pressure drop across the core during gas mixture (single-phase) flow at 1,200 psig and 44.8 cc/hr.

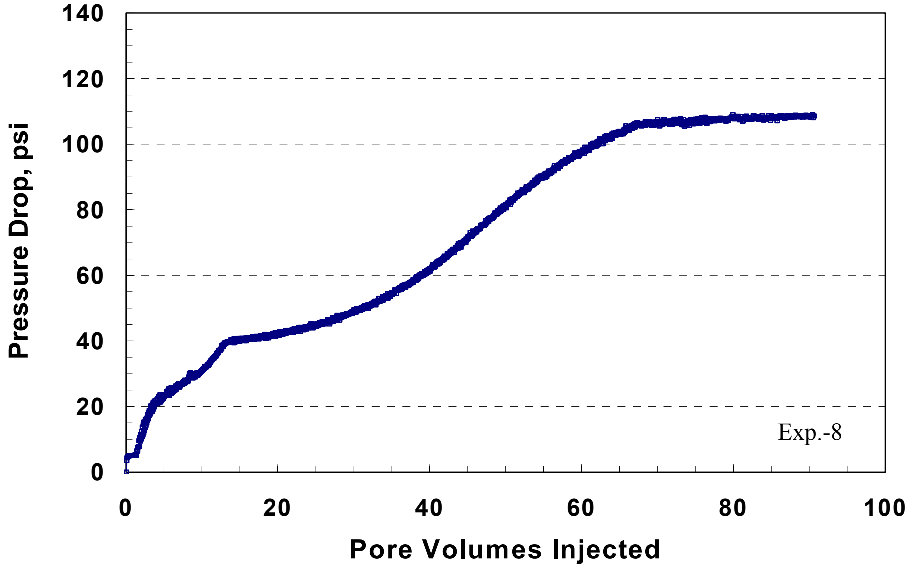

Figure B.42: Pressure drop across the core during condensate accumulation before methanol treatment at 1,200 psig and 44.8 cc/hr.

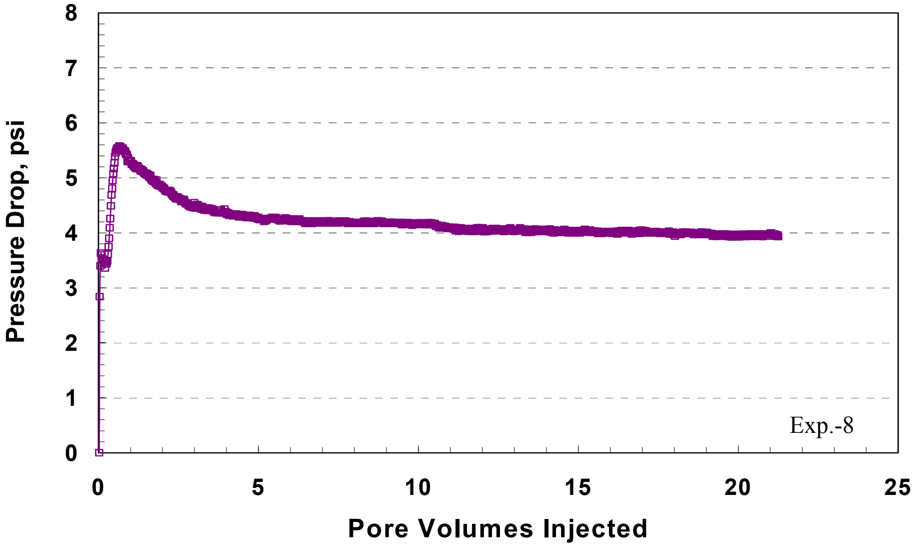

Figure B.43: Pressure drop across the core during equilibrium gas flow before methanol treatment at 1,200 psig and 44.8 cc/hr.

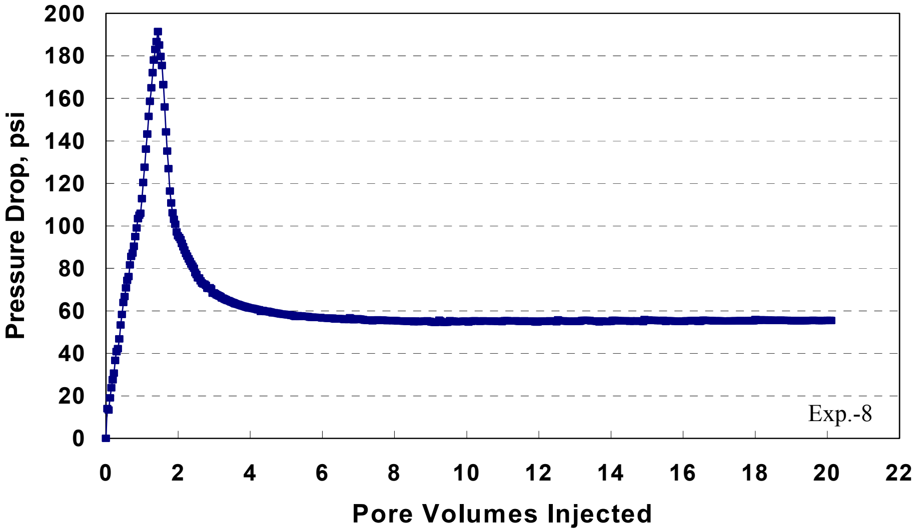

Figure B.44: Pressure drop across the core during the first methanol treatment at 1,200 psig and 44.8 cc/hr.

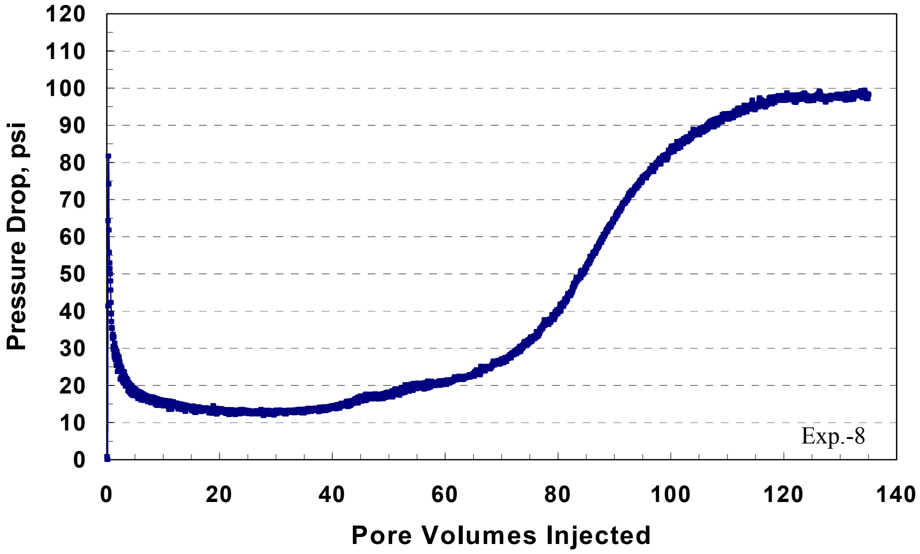

Figure B.45: Pressure drop across the core during condensate accumulation after the first methanol treatment at 1,200 psig and 44.8 cc/hr.

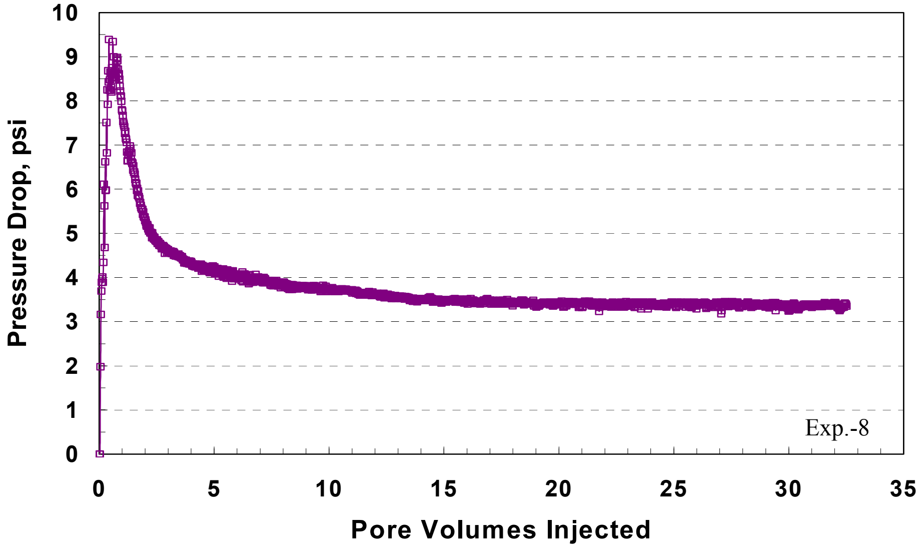

Figure B.46: Pressure drop across the core during equilibrium gas flow after the first methanol treatment at 1,200 psig and 44.8 cc/hr.

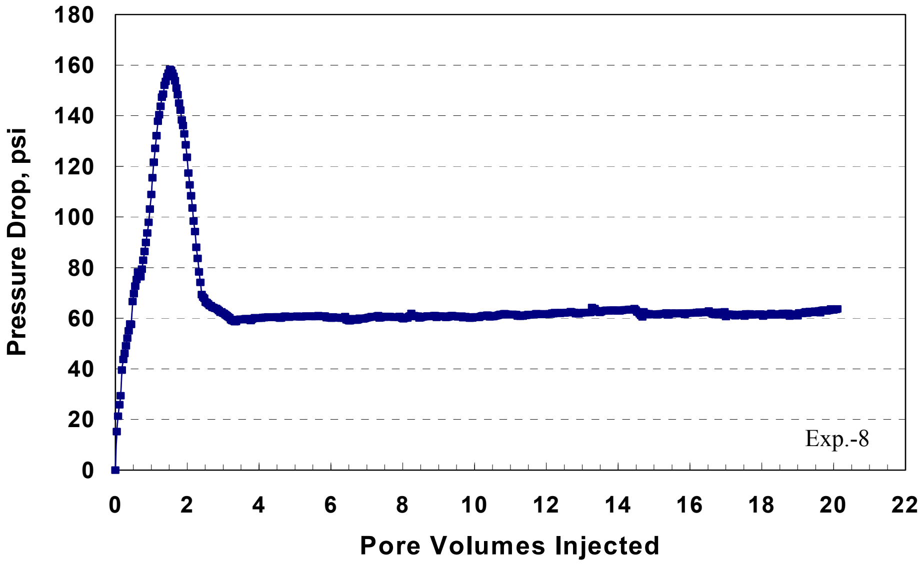

Figure B.47: Pressure drop across the core during the second methanol treatment at 1,200 psig and 44.8 cc/hr.

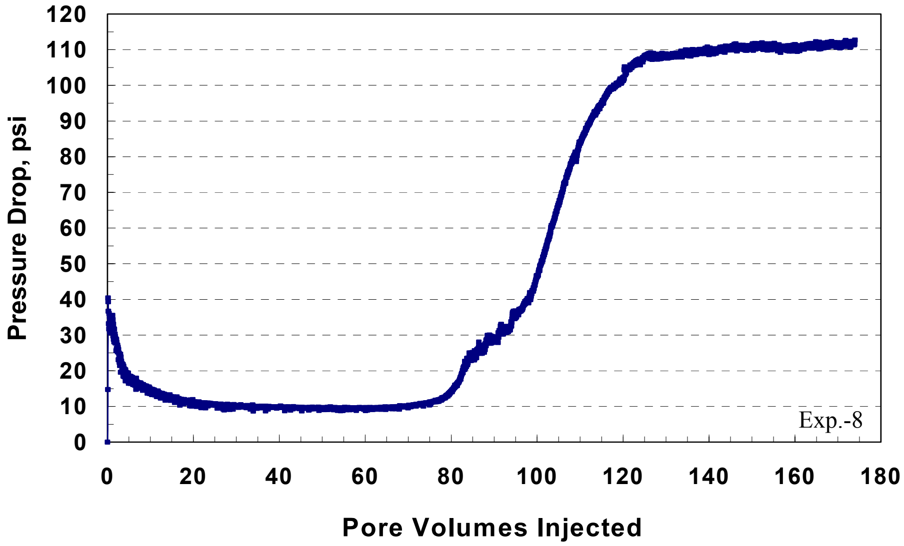

Figure B.48: Pressure drop across the core during condensate accumulation after the second methanol treatment at 1,200 psig and 44.8 cc/hr.

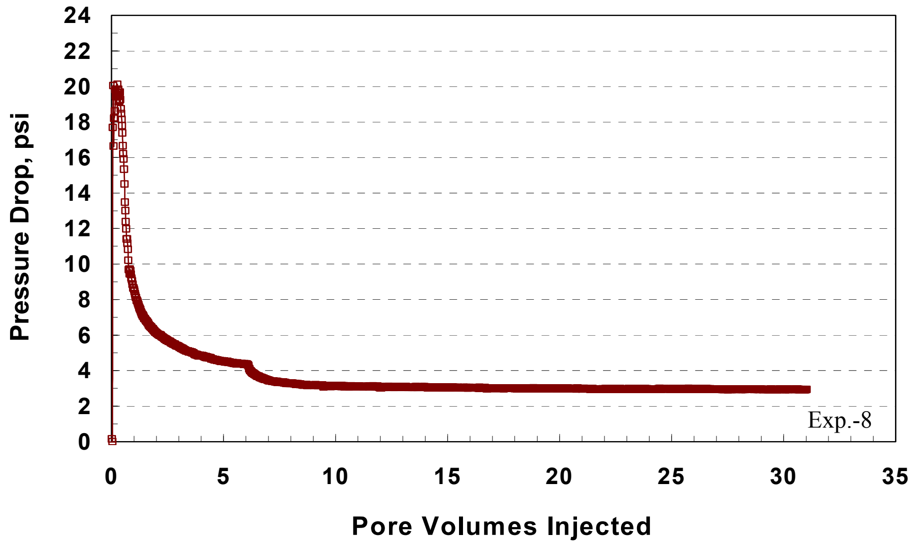

Figure B.49: Pressure drop across the core during equilibrium gas flow after the second methanol treatment at 1,200 psig and 44.8 cc/hr.

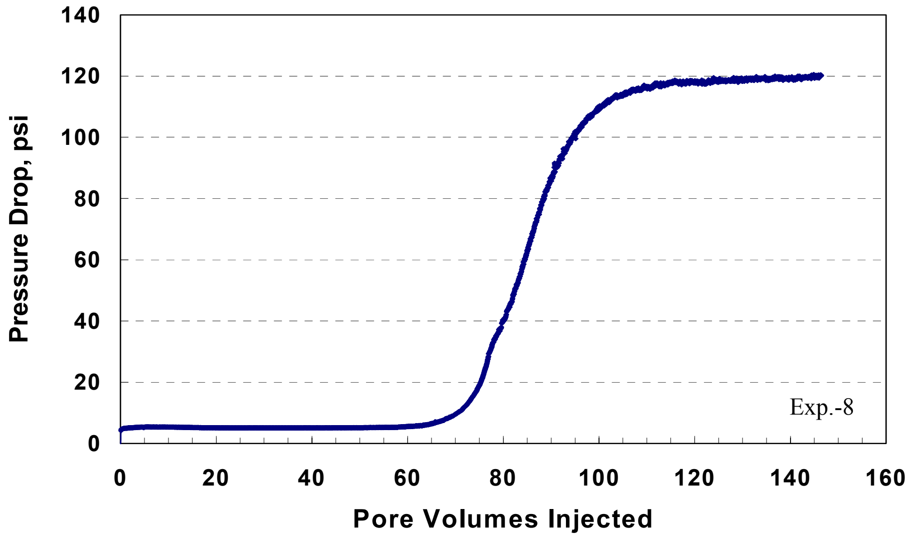

Figure B.50: Pressure drop across the core during condensate accumulation (4th flow) at 1,200 psig and 44.8 c/hr.

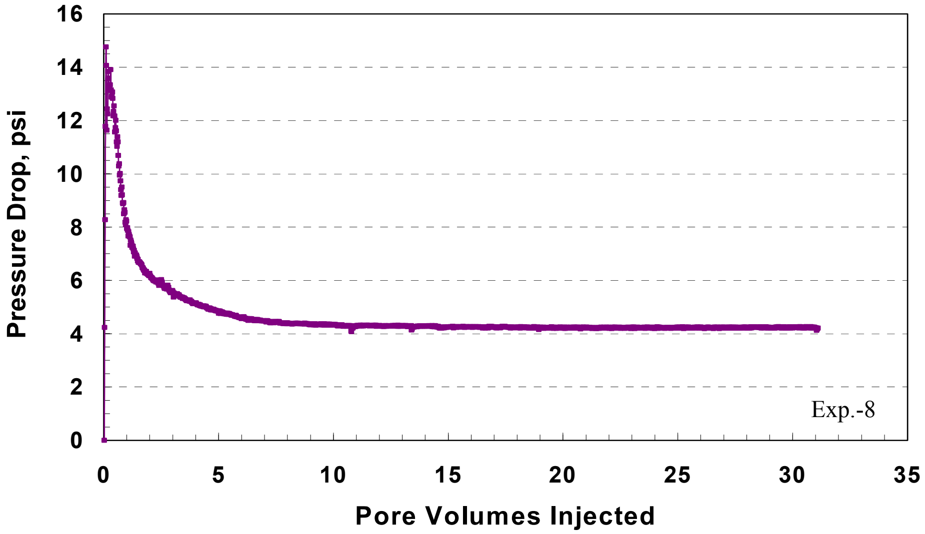

Figure B.51: Pressure drop across the core during equilibrium gas flow (4th flow) at 1,200 psig and 44.8 cc/hr.

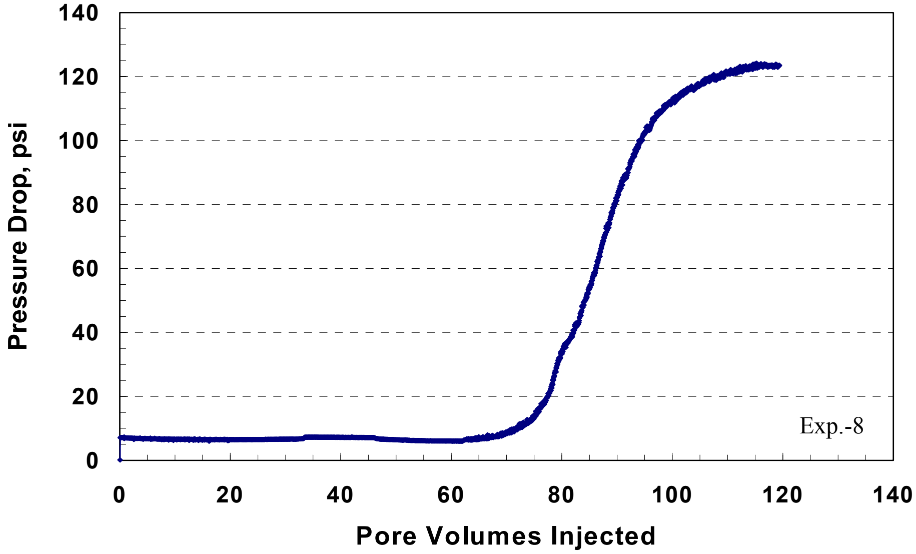

Figure B.52: Pressure drop across the core during condensate accumulation (5th flow) at 1,200 psig and 44.8 cc/hr.

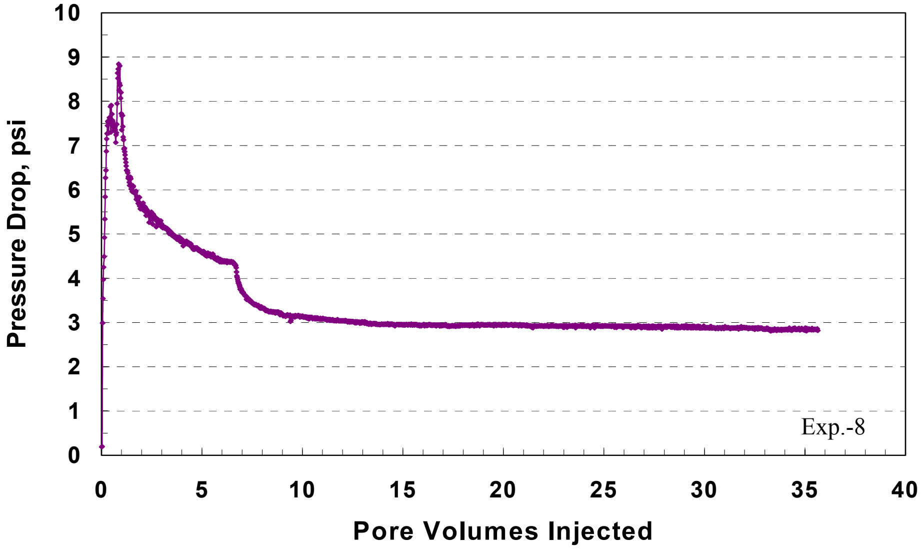

Figure B.53: Pressure drop across the core during equilibrium gas flow (5th flow) at 1,200 psig and 44.8 cc/hr.

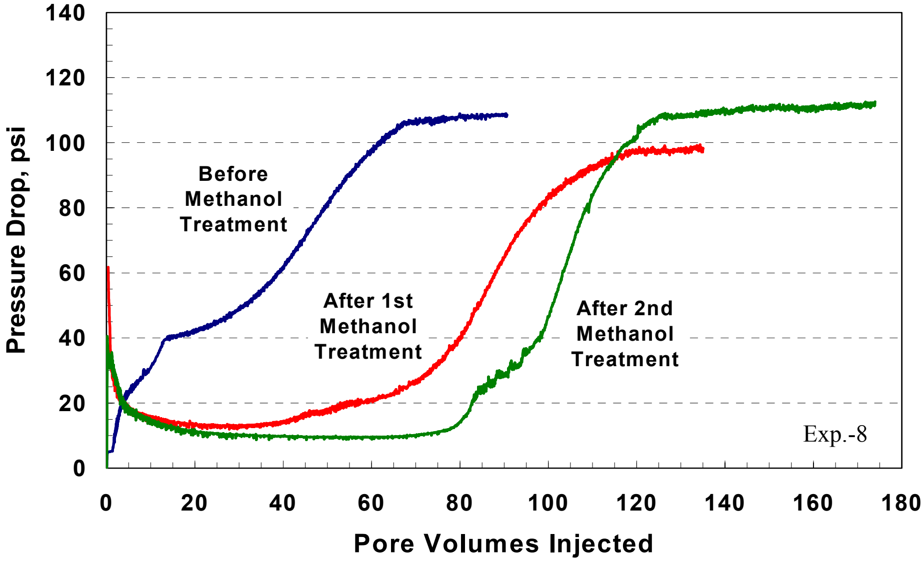

Figure B.54: Pressure drop across the core during condensate accumulation before and after methanol treatments at 1,200 psig and 44.8 cc/hr.

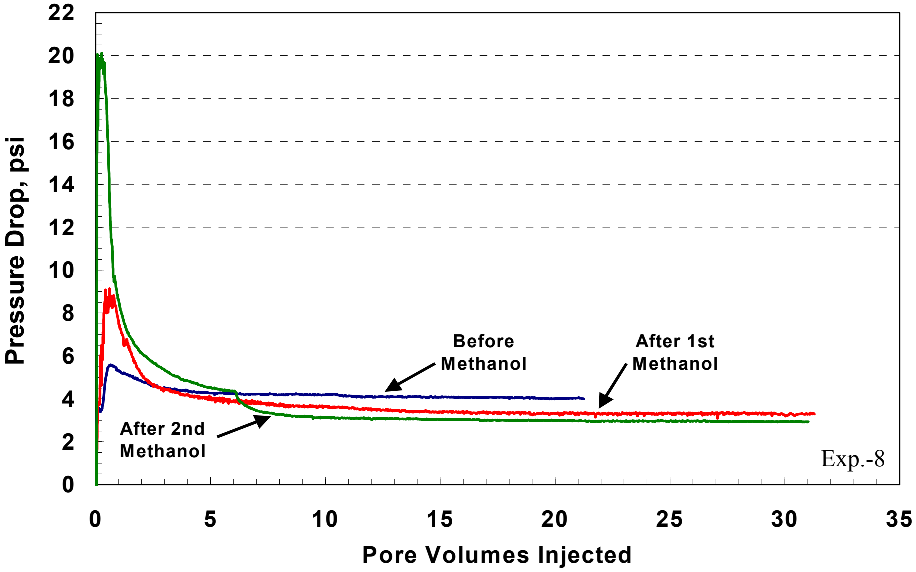

Figure B.55: Pressure drop across the core during equilibrium gas flow before and after methanol treatments at 1,200 psig and 44.8 cc/hr.

B.5 Coreflood Experiment No. 10

B.5.1 Objective

The objective of this experiment is to investigate the effect of multi-stage treatment of methanol on the relative permeability of gas after gas-condensate accumulation in at an initial water saturation of 20%. This experiment was performed on a Texas Cream limestone core. This is a repeat of Experiment-8 to confirm the obtained results

B.5.2 Core Preparation

A core with a diameter of 0.972 inches and a length of 8.01 inches was cut from Texas Cream limestone block. The core was dried in an oven at 95°C for more than 3 weeks. The core was wrapped with an aluminum foil and a heat-shrink Teflon. The wrapped core was placed into a Phoenix core-holder inside HTHP oven at 145°F. After 4 hours, an axial pressure was applied by screwing the end pieces of the core-holder. Then, an overburden pressure of 3,400 psig was applied.

B.5.3 Initial Core Permeability

The initial core permeability was measured using methane at a flowing pressure of 3,000 psig before introducing water saturation. The pressure of both the upstream and downstream back-pressure regulators was set to 3,000 psig. Methane gas was flowed at two flow rates: 60 and 120 cc/hr. **Figure B.56** shows the pressure drop across the core during the flow of methane at 3,000 psig. **Table B.44** gives the measured initial core permeability to methane at flowing pressure of 3,000 psig and various rates.

B.5.4 Water Saturation Procedure

Water at a saturation of 20% was introduced into the core according to the following procedure:

1. The pressure of the core holder was depleted to an atmospheric pressure by disconnected the inlet and outlet lines from flow lines.
2. The outlet end of the core holder was connected to a vacuum pump. Then, the core was vacuumed for at 5 hours, while the inlet end was closed.
3. To get 20% water saturation, 4 ml of distilled water were injected from the inlet of the core holder using a burette, while a vacuum was pulled from the outlet end of the core holder.
4. The core holder was placed inside the oven (@ 145°F) and opened to atmospheric pressure. The core holder was set for 4 hours to reach an equilibrium temperature. Then, a series of push-pull cycles were applied using the RUSKA hand pump through the outlet of the core holder.
5. Between each push and pull cycle, a break of 15 minutes was taken to allow water vapor to distribute through the core.

6. The water saturation procedure was completed after 32 push-pull cycles.

B.5.5 Methane Flow at S_{wi}=20%

After the core was saturated with 20% of water, the permeability was measured using methane at a flowing pressure of 3,000 psig and flow rates of 60 and 120 cc/hr. **Figure B.57** shows the pressure drop across the core during methane flow at a water saturation of 20%. The measured gas relative permeability is given in **Table B.45**.

B.5.6 Gas Mixture (Single-Phase) Flow

The gas mixture (single-phase) was flowed through the core at 3,000 psig. The flow rate was initially 60 cc/hr and then increased to 120 cc/hr. **Figure B.58** shows the pressure drop across the core during gas mixture (single-phase) flooding. The results are given in **Table B.46**. In this stage, no water was collected in the effluent.

B.5.7 Condensate Accumulation (Two-Phase Flow)

Before the start of this stage, the inlet and outlet valves of the core were closed. Pressure of the downstream back-pressure regulator was decreased to 1,200 psig, while the pressure in the upstream back-pressure regulator was kept at 3,000 psig. Flow was started while the bypass was open until the pressure in the lines stabilized. Then, the bypass valve was closed and inlet and outlet valves

were open simultaneously. The flow rate was 60 cc/hr. This stage allowed the gas-condensate to dynamically accumulated through the core. The stage was stopped when the pressure drop across the core reached stable values. **Figure B.59** shows the pressure drop across the core during two-phase flow. The pressure drop across the core was gradually increased until it reached a plateau after 134 PV. Gas and oil relative permeabilities measured during dynamic condensate accumulation are given in **Table B.47**. Data needed to calculation relative permeability for gas and oil phases (μ_g=0.01396 cp, μ_o=0.23711 cp) were obtained using PREOS and UTCOMP.

B.5.8 Equilibrium Gas Flow

The pressure in the upstream back-pressure regulator was decreased to 1,200 psig. Gas-mixture, which has a pressure of 1,200 psig (below dew point), was injected through the core at a flow rate of 60 cc/hr. The pressure drop across the core is shown in **Figure B.60**. This stage gave the gas end-point relative permeability (k^o_{rg}) before methanol treatment as given in **Table B.48**.

B.5.9 The First Stage of Methanol Treatment

Pure methanol was injected through the core at an injection rate of 60 cc/hr and 1,200 psig. The volume of methanol injected was 20 PV. The pressure drop across the core stabilized at a value 64.84 psia as shown in **Figure B.61**. The calculated permeability for methanol was found equal to 5.40 md.

B.5.10 Two-Phase Flow After the First Stage of Methanol Treatment

The pressure of the upstream back-pressure regulator was increased to 3,000 psig, while the pressure of the downstream back-pressure regulator was kept at 1,200 psig. The gas mixture was flashed through the core to bank condensate. **Figure B.62** depicts the pressure drop across the core during this stage. This figure indicates that the pressure drop across the core started to increase after an injection of 40.23 PV of the two-phase. This means that the first methanol treatment was effective in delaying the condensate banking. The measured two-phase relative permeability values are given in **Table B.49**.

B.5.11 Equilibrium Gas After the First Methanol Treatment

The pressure of the upstream back-pressure regulator was decreased to 1,200 psig. The equilibrium gas was injected at a flow rate of 60 cc/hr. **Figure B.63** shows the pressure drop across the core. This stage gives the gas end-point relative permeability after methanol injection, as given in **Table B.50**. The first stage of methanol increased the gas relative permeability by 35%.

B.5.12 Summary of the Results for coreflood Experiment-10

Figure B.64 compares the pressure drop during two-phase flow through the core before and after methanol treatments. Pressure drop across the core during injection of equilibrium gas before and after methanol injection is shown in **Figure B.65**. This figure indicates that the methanol treatment was effective to increase the gas relative permeability. The methanol treatment increased the gas relative permeability by 35%. The removal of methanol by evaporation is very slow. Therefore, it stays for a longer time in the core. The residual methanol improves the productivity by postponing the accumulation of condensate. Summary of experimental results is given in **Table B.51**. The results of this experiment are close to that obtained in Experiment-8. Even though the gas end-point relative permeability is high (~0.7) before methanol, treatment of methanol enhanced the gas productivity by a factor of 1.4. Methanol treatment resulted in an enhanced flow period where the pressure drop reached its minimum values. **Table B.52** gives the effect of methanol on gas and oil relative permeabilities during the enhanced flow period. During this enhanced period, condensate accumulation was delayed due to the presence of methanol-rich phase and gas productivity increased by a factor of 11.6.

Table B.44: Initial core permeability measured using methane at 3,000 psig.

	q = 60 cc/hr		q = 120 cc/hr	
	$\Delta P_{Total-1}$	$\Delta P_{Total-2}$	$\Delta P_{Total-1}$	$\Delta P_{Total-2}$
ΔP, psia	3.89	3.52	7.78	7.06
k, md	5.08	5.61	5.08	5.60

Table B.45: Core relative permeability to methane at an initial water saturation of 20% and 3,000 psig.

	q = 60 cc/hr		q = 120 cc/hr	
	$\Delta P_{Total-1}$	$\Delta P_{Total-2}$	$\Delta P_{Total-1}$	$\Delta P_{Total-2}$
ΔP, psia	4.63	4.20	9.22	8.33
k_g, md	4.27	4.71	4.29	4.75
k_{rg}	0.84	0.84	0.84	0.85

Table B.46: Gas relative permeability measured during gas mixture (single-phase) flow at 3,000 psig.

	q = 60 cc/hr		q = 120 cc/hr	
	$\Delta P_{Total-1}$	$\Delta P_{Total-2}$	$\Delta P_{Total-1}$	$\Delta P_{Total-2}$
ΔP, psia	8.21	7.45	17.57	15.52
k_g, md	4.66	5.13	4.35	4.93
k_{rg}	0.92	0.91	0.86	0.88

Table B.47: Gas and oil relative permeabilities measured during condensate accumulation before methanol treatment at 1,200 psig and 60 cc/hr.

	$\Delta P_{Total-1}$
ΔP, psia	118.90
k_{rg}	0.05
k_{ro}	0.07

Table B.48: Gas end-point relative permeability measured during equilibrium gas flow before methanol treatment at 1,200 psig and 60 cc/hr.

	$\Delta P_{Total-1}$	$\Delta P_{Total-2}$
ΔP, psia	4.23	4.28
k_g, md	3.97	3.87
k^o_{rg}	0.773	0.690

Table B.49: Gas and oil relative permeabilities measured during condensate accumulation after the first methanol treatment at 1,200 psig and 60 cc/hr.

	$\Delta P_{Total-1}$
ΔP, psia	103.53
k_{rg}	0.06
k_{ro}	0.08

Table B.50: Gas end-point relative permeability measured during equilibrium gas flow after the first methanol treatment at 1,200 psig and 60 cc/hr.

	$\Delta P_{Total-1}$	$\Delta P_{Total-2}$
ΔP, psia	3.15	3.17
k_g, md	5.27	5.24
k^o_{rg}	0.939	0.933

Table B.51: Summary of experimental results for coreflood Experiment-10.

	Before Methanol	After 20PV Methanol
k_{rg}	0.05	0.06
k_{ro}	0.07	0.08
k°_{rg}	0.69	0.933

Table B.52: Gas and oil relative permeabilities measured during the enhanced flow period.

	Before Methanol	After 20PV Methanol
k_{rg}	0.05	0.58
k_{ro}	0.07	0.75

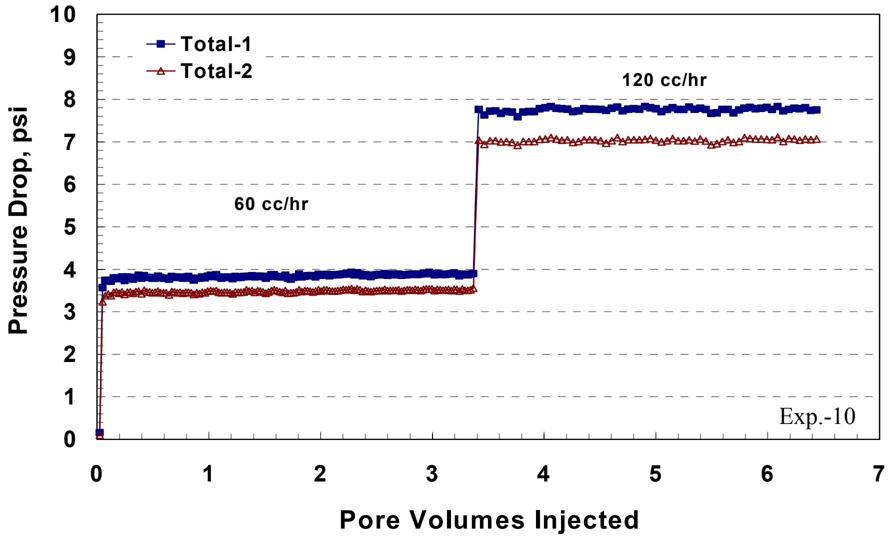

Figure B.56: Pressure drop across the core during methane flow before introducing water saturation at 3,000 psig.

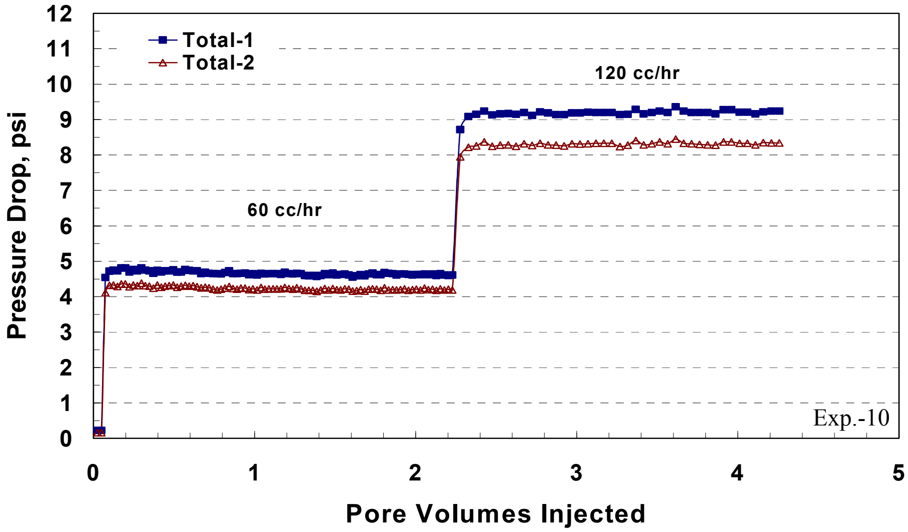

Figure B.57: Pressure drop across the core during methane flow at an initial water saturation of 20% and 3,000 psig.

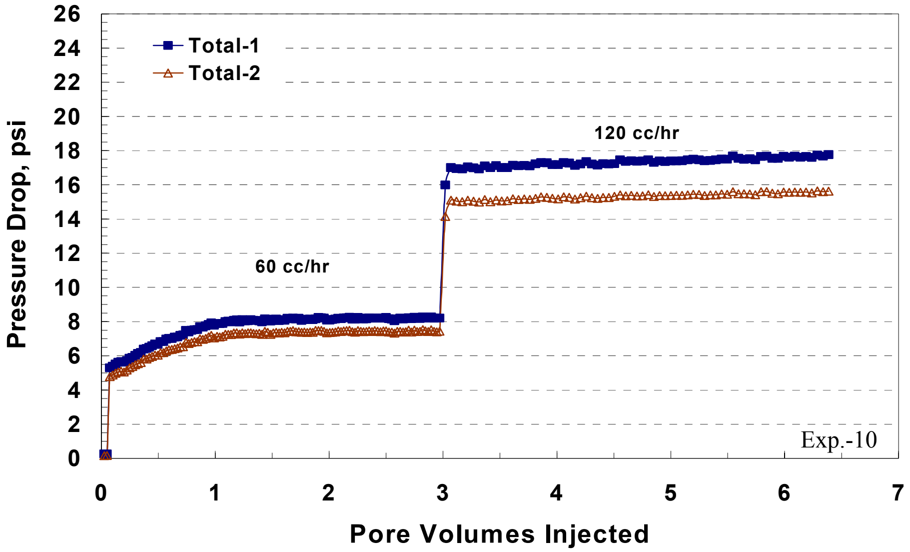

Figure B.58: Pressure drop across the core during gas mixture (single-phase) flow at 3,000 psig.

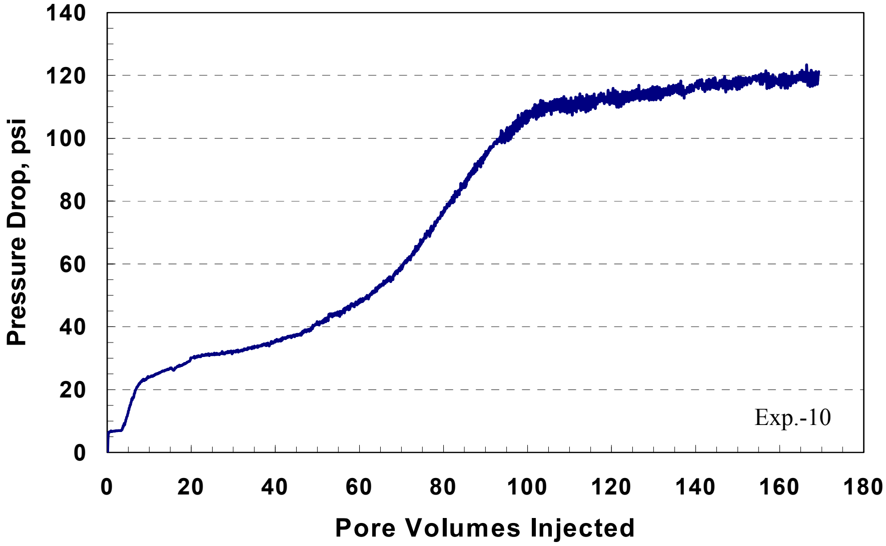

Figure B.59: Pressure drop across the core during dynamic condensate accumulation before methanol treatment at 1,200 psig and 60 cc/hr.

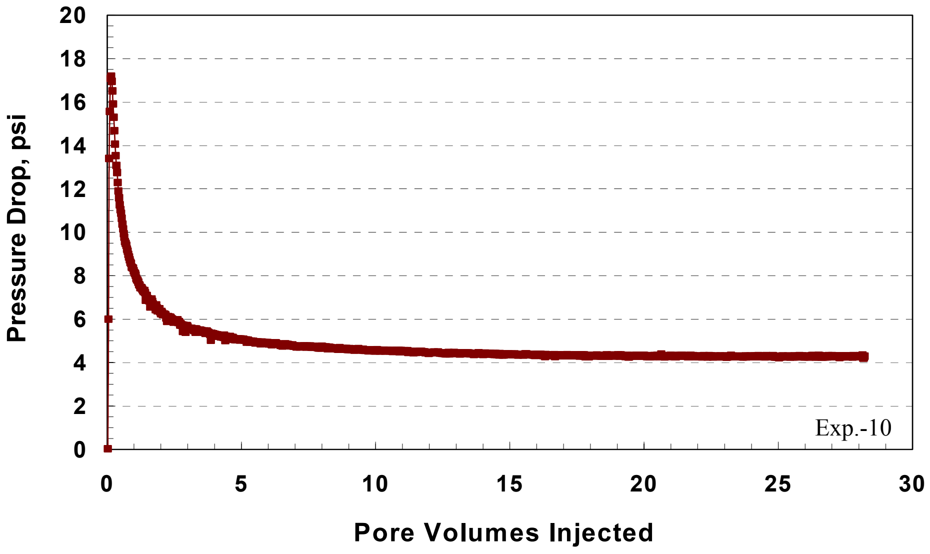

Figure B.60: Pressure drop across the core during equilibrium gas flow before methanol treatment at 1,200 psig and 60 cc/hr.

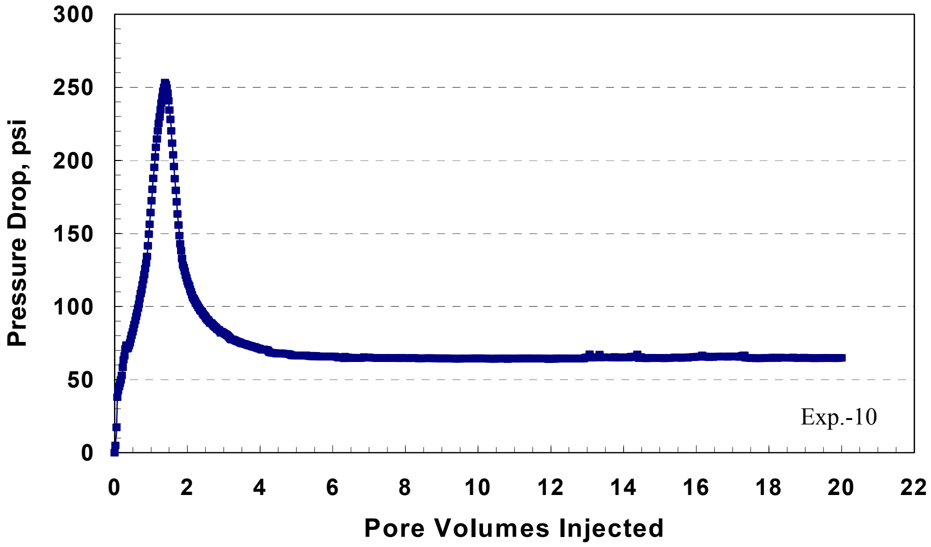

Figure B.61: Pressure drop across the core during the first methanol treatment at 1,200 psig and 60 cc/hr.

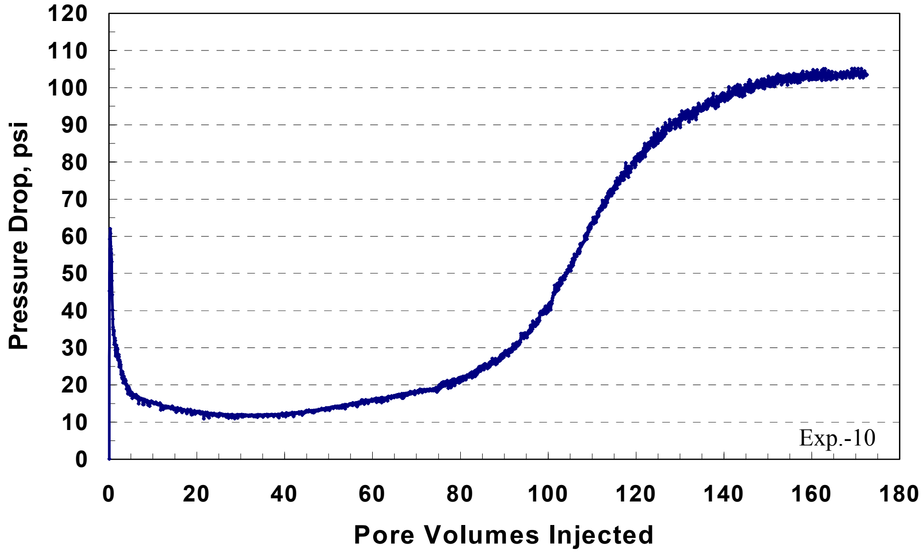

Figure B.62: Pressure drop across the core during condensate accumulation after the first methanol treatment at 1,200 psig and 60 cc/hr.

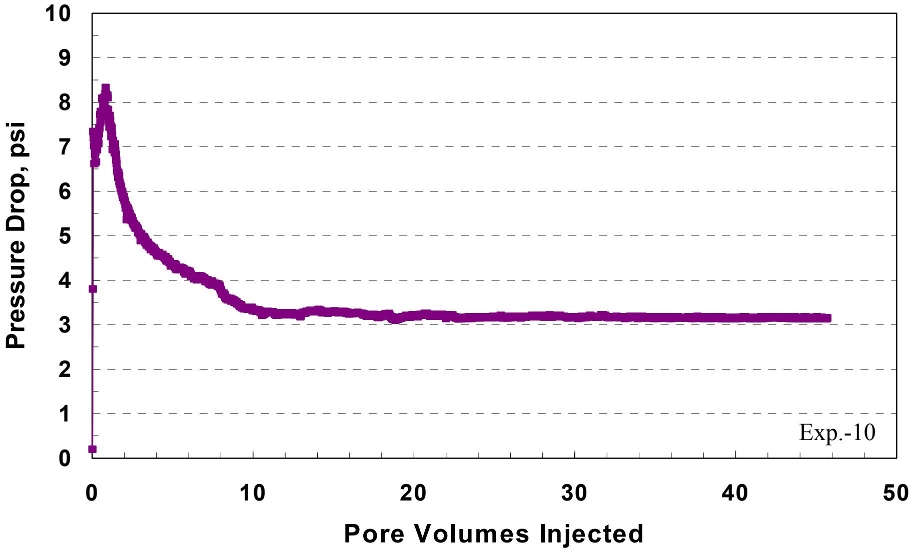

Figure B.63: Pressure drop across the core during equilibrium gas flow after the first methanol treatment at 1,200 psig and 60 cc/hr.

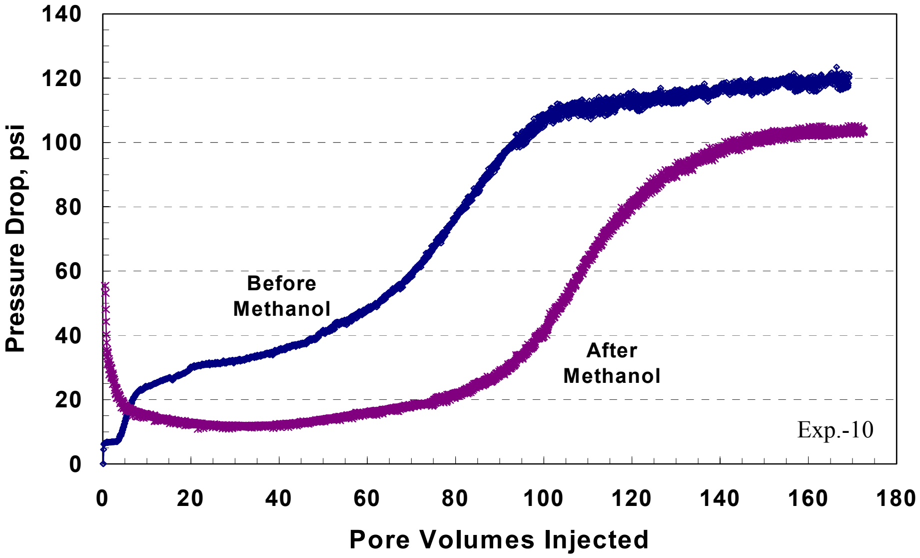

Figure B.64: Pressure drop across the core during condensate accumulation before and after methanol treatment at 1,200 psig and 60 cc/hr.

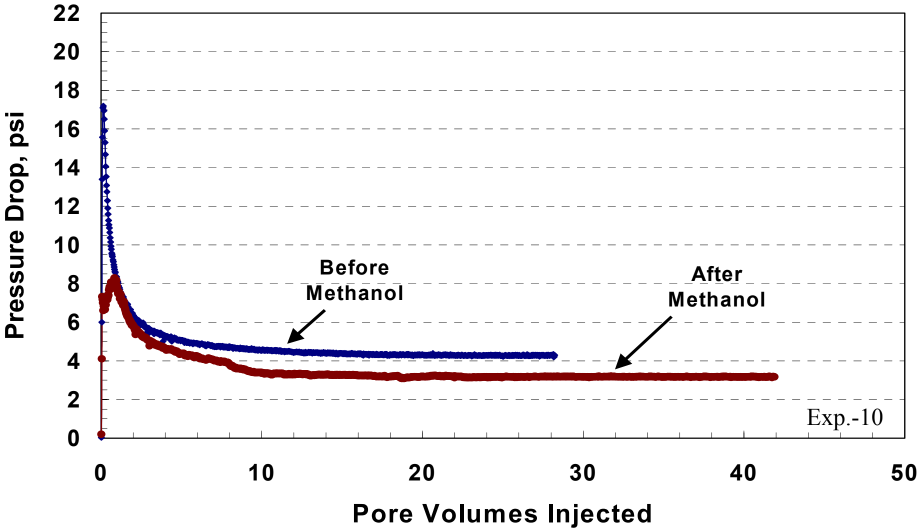

Figure B.65: Pressure drop across the core during equilibrium gas flow before and after methanol treatment at 1,200 psig and 60 cc/hr.

B.6 Coreflood Experiment No. 12

B.6.1 Objective

The objective of this experiment is to investigate the effect of multi-stage treatment of methanol on the relative permeability of gas after gas-condensate accumulation in highly permeable core. This experiment was performed on a Berea core (high permeability). There was no water present in the core (S_{wi}=0%).

B.6.2 Core Preparation

A plug sample 0.972 inches in a diameter and 8.01 inches long drilled from a Berea block parallel to the bedding planes. The core was dried in an oven at 95°C for more than 2 weeks. The core was wrapped with an aluminum foil and a heat-shrink Teflon to prevent diffusion of gases through the sleeve rubber. The wrapped core was placed into a Phoenix core-holder inside HTHP oven at 145°F. After 4 hours, an axial pressure was applied by screwing the end pieces of the core-holder. Then, an overburden pressure of 3,400 psig was applied.

B.6.3 Initial Core Permeability

The initial core permeability was measured using methane at a flowing pressure of 3,000 psig before introducing a single-phase gas mixture. The pressure of both the upstream and downstream back-pressure regulators was set to 3,000 psig. Methane gas was flowed at a high rate of 600 cc/hr. Two pressure transducers with a limit of 10 (Total-1) and 50 (Total-2) psia differential pressure were used. **Figure B.66** shows the pressure drop across the core during the flow of methane at 3,000 psig. **Table B.53** gives the measured initial core permeability to methane at a flowing pressure of 3,000 psig.

B.6.4 Gas Mixture (Single-Phase)

The gas mixture (single-phase) was flowed through the core at 3,000 psig. The flow rate was 600 cc/hr during this stage. **Figure B.67** shows the pressure drop across the core during gas mixture (single-phase) flooding. The measured initial core permeability during single-phase flow at 3,000 psig is given in **Table B.54**. The core permeability measured during this stage is close to the one measured initially with methane. The permeability (245.94 md) measured with the lowest-range pressure transducer was used as the absolute permeability (k at S_g = 100%) in the relative permeability calculations.

B.6.5 Condensate Accumulation (Two-Phase Flow)

Before the start of this stage, the inlet and outlet valves of the core were closed. Pressure of the downstream back-pressure regulator was decreased to 1,200 psig, while the pressure in the upstream back-pressure regulator was kept at 3,000 psig. Flow was started while the bypass was open until the pressure in the lines stabilized. Then, the bypass valve was closed and inlet and outlet valves were open simultaneously. The flow rate was 600 cc/hr. This stage allowed the gas-condensate to dynamically accumulated through the core. This simulates the condensate bank in the wellbore region. The stage was stopped when the pressure drop across the core reached stable values. **Figure B.68** shows the pressure drop across the core during two-phase flow. The pressure drop is sharply increased until it reached a value of 8.5 psia at 27.3 PV. Then, it is increased at a slower rate. This discontinuity would be due to capillary forces between flowing gas and condensate occupied the pores. The pressure drop across the core was gradually increased until it reached a plateau after 93.8 PV. The measured gas and oil relative permeabilities during condensate accumulation are given in **Table B.55**. Data needed to calculation relative permeability for gas and oil phases (μ_g=0.01396 cp, μ_o=0.23711 cp) were obtained using PREOS and UTCOMP. This result indicates that condensate bank would cause a severe reduction in gas productivity even in high permeability cores. This is considered as a new finding to the literature. In this experiment, the gas relative permeability reduced by 94% due to condensate accumulation.

B.6.6 Equilibrium Gas Flooding

The pressure in the upstream back-pressure regulator was decreased to 1,200 psig. An equilibrium gas, the gas phase of the gas mixture which has a pressure of 1,200 psig (below dewpoint), was injected through the core at a flow rate of 600 cc/hr. The pressure drop across the core is shown in **Figure B.69**. Gas end-point relative permeability measured during equilibrium gas flow is given in **Table B.56**. This stage gave the gas end-point relative permeability (k^o_{rg}) before methanol treatment. This stage results in a high gas end-point relative permeability (~0.90) since there was no water present in the core which have a high initial permeability.

B.6.7 The First Stage of Methanol Treatment

Pure methanol was injected through the core at an injection rate of 300 cc/hr and 1,200 psig. The volume of methanol injected was 20 PV. The pressure drop across the core stabilized at a value 5.23 psia as shown in **Figure B.70**. The calculated permeability for methanol was found equal to 334.90 md.

B.6.8 Two-Phase Flow After the First Stage of Methanol Treatment

The pressure of the upstream back-pressure regulator was increased to 3,000 psig, while the pressure of the downstream back-pressure regulator was kept at 1,200 psig. The flow rate of this stage was 600 cc/hr. The gas mixture was flashed through the core to bank condensate. **Figure B.71** depicts the pressure drop across the core during this stage. This figure indicates that the pressure drop across the core started to increase after an injection of 54.3 PV of the two-phase. The pressure drop profile shows the same trend as the two-phase flow before methanol. The first methanol treatment was effective in delaying the condensate banking for 54.3 PV due to the existence of an enhanced flow period that characterized with a minimum pressure drop. Gas and oil relative permeabilities are given in **Table B.57**.

B.6.9 Equilibrium Gas After the First Methanol Treatment

The pressure of the upstream back-pressure regulator was decreased to 1,200 psig. The equilibrium gas was injected at a flow rate of 600 cc/hr. **Figure B.72** shows the pressure drop across the core. This stage gives the gas end-point relative permeability after methanol injection, as given in **Table B.58**. The first stage of methanol increased the gas relative permeability by 6.5%. The most important is that the methanol delayed the condensate bank that expected to take place after the post-treatment production period.

B.6.10 The Second Stage of Methanol Treatment

Pure methanol was injected, as the second treatment, through the core at an injection rate of 300 cc/hr and 1,200 psig. The volume of methanol injected was 20 PV. The pressure drop across the core reached a value of 5.22 psia which is close to that for the first treatment. **Figure B.73** depicts the pressure drop across the core during the second treatment of methanol. The calculated permeability for this stage of methanol was found equal to 335.54 md.

B.6.11 Two-Phase Flow After the Second Stage of Methanol Treatment

The pressure of the upstream back-pressure regulator was increased to 3,000 psig, while the pressure of the downstream back-pressure regulator was kept at 1,200 psig. The flow rate was 600 cc/hr. **Figure B.74** depicts the pressure drop across the core during this stage. This figure shows the same behavior as the two-phase before methanol treatment, except it has shit to higher pore volumes.

This figure implies that the pressure drop across the core started to increase after an injection of 63.3 PV. This means that the second methanol treatment delayed the condensate more than the first one. The two-phase relative permeabilities are given in **Table B.59**. Therefore, more injection of methanol would stay for longer time during the post-treatment production period yielding high gas productivity.

B.6.12 Equilibrium Gas After the Second Methanol Treatment

The pressure of the upstream back-pressure regulator was decreased to 1,200 psig. The equilibrium gas was injected at a flow rate of 600 cc/hr. **Figure B.75** shows the pressure drop across the core. This stage gives the gas end-point relative permeability after methanol injection, as given in **Table B.60**. The second stage of methanol increased the gas relative permeability by 9.2%. The improvement obtained after the second treatment of methanol is higher than the first one. Multi-stage treatment of methanol will be more effective to enhance the productivity of gas wells, particularly when the bottom hole flowing pressure fell below the dewpoint pressure.

B.6.13 The Third Stage of Methanol Treatment

Methanol was injected, as the third treatment, through the core at an injection rate of 300 cc/hr and a flowing pressure of 1,200 psig. The volume of methanol injected was 20 PV. The pressure drop across the core reached a value of 5.13 psia. **Figure B.76** illustrates the pressure drop across the core during the third treatment of methanol. The calculated permeability for this stage of methanol was found to be 341.54 md.

B.6.14 Two-Phase Flow After the Third Stage of Methanol Treatment in the Reverse Direction Flow

The pressure of the upstream back-pressure regulator was increased to 3,000 psig, while the pressure of the downstream back-pressure regulator was kept at 1200 psig. In this stage, the flow rate was 600 cc/hr in the reverse direction (upward flow). This means that the two-phase enters the core from the bottom and exists from the top of the core. The flow direction was changed to investigate if the methanol reduces the interfacial tension of the condensate to very small values that enough to flow methanol-condensate mixture under the effect of gravity force. If this is true, the pressure drop will continue to buildup from the beginning of the flow without countering any delay.

Figure B.77 represents the pressure drop across the core during the two-phase flow in the upward direction. This result shows the same behavior of the two-phase after methanol treatments in the downward flow. This figure shows also that the pressure drop across the core started to increase after 60.3 PV. This delay in the condensate accumulation invalidates the proposed assumption. Possible explanation for this delay after the methanol treatment is that the residual methanol changed the phase-behavior of the gas mixture till it evaporates from the pores. Then, condensate started to build up and reduced the gas relative permeability. The evaporation process of methanol is a slow process since it is controlled by a mass transfer. The gas and oil relative permeability values are given in **Table B.61**. As can be seen the gas and oil relative permeability values decreased due to the flow against gravity forces.

B.6.15 Equilibrium Gas After the Third Methanol Treatment in the Reverse Direction

The pressure of the upstream back-pressure regulator was decreased to 1,200 psig. The equilibrium gas was injected in the upward direction at a flow rate of 600 cc/hr. **Figure B.78** shows the pressure drop across the core. The pressure drop reached a very small value (<0.4 psia) that yielded to a value of gas end-point relative permeability greater than one, as given in **Table B.62**. The gas created a channel through the core, while most of the liquid phase accumulated at the bottom of the core by the affect of gravity.

B.6.16 The Fourth Stage of Methanol Treatment in Horizontal Direction

Methanol was injected, as the fourth treatment, through the core in a horizontal direction at rate of 300 cc/hr and a flowing pressure of 1,200 psig. In this case, the core holder was put down horizontally on the floor of the oven without changing the flow lines. The volume of methanol injected was 20 PV. The pressure drop across the core reached a value of 5.21 psia. **Figure B.79** shows the pressure drop across the core during the fourth treatment of methanol in the horizontal direction. The measured core permeability to methanol was found to be 336.10 md which is close to that measured in the previous methanol treatments, regardless the flow direction.

B.6.17 Two-Phase Flow After the Fourth Stage of Methanol Treatment in the Horizontal Direction Flow

The pressure of the upstream back-pressure regulator was increased to 3,000 psig, while the pressure of the downstream back-pressure regulator was kept at 1,200 psig. In this stage, the flow rate was 600 cc/hr in the horizontal direction. **Figure B.80** represents the pressure drop across the core during the two-phase flow in the horizontal direction. This figure shows that the pressure drop across the core started to buildup after a production of 40.2 PV. This fast pressure buildup is due to the gravity segregation in the horizontal direction. The condensate accumulated in the lower part of the core while the gas flowed in the upper parts. This confirmed by the gradual increase in the pressure drop, where it took 75.0 PV for the pressure drop to reach a steady state following the enhanced flow period. The gas and oil relative permeability values are given in **Table B.63**. The gas relative permeability was decreased by 93%.

B.6.18 Equilibrium Gas After the Fourth Methanol Treatment in the Horizontal Direction

The pressure of the upstream back-pressure regulator was decreased to 1,200 psig. The equilibrium gas was flowed in the horizontal direction at a rate of 600 cc/hr. **Figure B.81** shows the pressure drop across the core during the flow of equilibrium gas in the horizontal direction. The pressure drop reached a maximum value of 7.4 psia and sharply decreased to reach a stable value of 0.74 psia. The initial high value of the pressure drop is due to the flow initiation of the liquid phase. The gas end-point relative permeability is given in **Table B.64**.

B.6.19 The Fifth Stage of Methanol Treatment in Downward Direction

The flow direction was changed into the downward direction. A pure methanol was injected, as the fifth treatment, through the core in downward direction at 300 cc/hr and 1,200 psig. The volume of methanol injected was 20 PV. The pressure drop across the core reached a value of 5.32 psia. **Figure B.82** shows the pressure drop across the core during the fifth treatment of methanol in the downward direction. The core permeability to methanol was 329.07 md.

B.6.20 Two-Phase Flow After the Fifth Methanol Treatment in the Downward Direction Flow at Lower Flow Rates

The pressure of the upstream back-pressure regulator was increased to 3,000 psig, while the pressure of the downstream back-pressure regulator was kept at 1,200 psig. In this stage, the flow rate was set initially to 120 cc/hr in the downward direction. **Figure B.83** shows the pressure drop across the core during the two-phase flow in the downward direction after the fifth methanol treatment at a lower rate. This result shows a delay of condensate banking by 70.3 PV at this lower rate. A new batch of the gas mixture was flowed because the first batch was not enough to reach a steady state. The pressure profile of the second batch is similar to that of the first one. The pressure drop reached a steady state value of 7.33 psia. When the flow rate was doubled (240 cc/hr), the pressure drop increased by 2-fold. The gas and oil relative permeability values are given in **Table B.65**. The results indicate that the condensate accumulation is not a rate dependent when it reached a steady-state. Flowing the two-phase flow at lower rate reduced the gas relative permeability compared to that flowed at higher rate.

B.6.21 Equilibrium Gas After the Fifth Methanol Treatment in the Downward Direction at Lower Flow Rates

The pressure of the upstream back-pressure regulator was decreased to 1,200 psig. The equilibrium gas was flowed in the downward direction at an initial flow rate of 600 cc/hr. The rate was reduced to 300 cc/hr after the pressure drop reached stabilized values. **Figure B.84** shows the pressure drop across the core during the flow of equilibrium gas in the downward direction after the fifth methanol treatment. The gas end-point relative permeability is given in **Table B.66**. The fifth methanol treatment increased the gas end-point relative permeability to a very high value of 0.95.

B.6.22 Summary of the Results of Coreflood Experiment-12

Gas relative permeability was decreased by more than 94% due to condensate accumulation in highly permeable cores. To our knowledge, the results obtained are new to the literature. Multi-stage of methanol treatment was effective to enhance the reduced gas relative permeability. The removal of residual methanol by evaporation is a very slow process. Therefore, it stays for a longer time in the core. The residual methanol improves the productivity by postponing the accumulation of condensate as shown in **Figure B.85**. Methanol stages helped to delay the condensate buildup following the treatment. **Figure B.86** shows the effect of methanol treatment volume on the post-treatment condensate accumulation delay. As can be seen, increasing the volume of methanol treatment yielded a more production time for gas after the treatment before countering the subsequent condensate bank.

Effect of methanol treatment on gas and oil relative permeabilities during condensate accumulation at steady state is given in **Table B.67**. As can be seen, the steady state two phase relative permeability values are all in the same range. Therefore, methanol is a temporary treatment to enhance gas productivity. On the other hand, gas productivity increased during the enhanced flow period where the condensate banking is postponed. **Table B.68** shows the effect of methanol treatment on gas and oil relative permeabilities during the enhanced flow period. After each methanol treatment, gas relative permeability increased by an order of magnitude relative to that before the treatment.

Table B.53: Initial core permeability measured using methane at a flow rate of 600 cc/hr and 3,000 psig.

	$\Delta P_{Total-1}$	$\Delta P_{Total-2}$
ΔP, psia	0.81	0.75
k_g, md	244.04	262.91

Table B.54: Core permeability measured during gas mixture (single-phase) flow at a flow rate of 600 cc/hr and 3,000 psig.

	$\Delta P_{Total-1}$	$\Delta P_{Total-2}$
ΔP, psia	1.56	1.42
k_g, md	245.94	268.85

Table B.55: Gas and oil relative permeabilities measured during condensate accumulation before methanol treatment at 600 cc/hr and 1,200 psig.

	$\Delta P_{Total-1}$
ΔP, psia	23.93
k_{rg}	0.06
k_{ro}	0.08

Table B.56: Gas end-point relative permeability measured during equilibrium gas flow before methanol treatment at 600 cc/hr and 1,200 psig.

	$\Delta P_{Total-1}$	$\Delta P_{Total-2}$
ΔP, psia	0.75	0.73
k_g, md	221.63	227.70
k^o_{rg}	0.901	0.926

Table B.57: Gas and oil relative permeabilities measured during condensate accumulation after the first methanol treatment at 600 cc/hr and 1,200 psig.

	$\Delta P_{Total-1}$
ΔP, psia	23.00
k_{rg}	0.06
k_{ro}	0.08

Table B.58: Gas end-point relative permeability measured during equilibrium gas flow after the first methanol treatment at 600 cc/hr and 1,200 psig.

	$\Delta P_{Total-1}$
ΔP, psia	0.70
k_g, md	236.02
k^o_{rg}	0.960

Table B.59: Gas and oil relative permeabilities measured during condensate accumulation after the second methanol treatment at 600 cc/hr and 1,200 psig.

	$\Delta P_{Total-1}$
ΔP, psia	21.00
k_{rg}	0.07
k_{ro}	0.09

Table B.60: Gas end-point relative permeability measured during equilibrium gas flow after the second methanol treatment at 600 cc/hr and 1,200 psig.

	$\Delta P_{Total-1}$
ΔP, psia	0.69
k_g, md	241.91
k^o_{rg}	0.984

Table B.61: Gas and oil relative permeabilities measured during condensate accumulation after the third methanol treatment in the reverse direction (upward flow) at 600 cc/hr and 1,200 psig.

	$\Delta P_{Total-1}$
ΔP, psia	24.87
k_{rg}	0.06
k_{ro}	0.08

Table B.62: Gas end-point relative permeability measured during equilibrium gas flow after the third methanol treatment in the reverse direction (upward flow) at 600 cc/hr and 1,200 psig.

	$\Delta P_{Total-1}$
ΔP, psia	0.29
k_g, md	567.96
k^o_{rg}	2.309

Table B.63: Gas and oil relative permeabilities measured during condensate accumulation after the fourth methanol treatment in the horizontal direction at 600 cc/hr and 1,200 psig.

	$\Delta P_{Total-1}$
ΔP, psia	22.49
k_{rg}	0.07
k_{ro}	0.09

Table B.64: Gas end-point relative permeability measured during equilibrium gas flow after the fourth methanol treatment in the horizontal direction at 600 cc/hr and 1,200 psig.

	$\Delta P_{Total-1}$
ΔP, psia	0.74
k_g, md	225.39
k^o_{rg}	0.916

Table B.65: Gas and oil relative permeabilities measured during condensate accumulation after the fifth methanol treatment in the downward direction at lower rates and 1,200 psig.

	q = 120 cc/hr	q = 240 cc/hr
ΔP, psia	7.33	14.47
k_{rg}	0.04	0.04
k_{ro}	0.05	0.05

Table B.66: Gas end-point relative permeability measured during equilibrium gas flow after the fifth methanol treatment in the downward direction at lower flow rates and 1,200 psig.

	q = 600 cc/hr	q = 300 cc/hr
ΔP, psia	0.71	0.42
k_g, md	232.71	199.57
k^o_{rg}	0.946	0.811

Table B.67: Summary of experimental results for coreflood Experiment-12.

	Before Methanol	After 1st Methanol	After 2nd Methanol	After 3rd Methanol	After 4th Methanol	After 5th Methanol
k_{rg}	0.06	0.06	0.07	0.06	0.07	0.04
k_{ro}	0.08	0.08	0.09	0.08	0.09	0.05
k^o_{rg}	0.901	0.960	0.984	>1	0.916	0.946

Table B.68: Gas and oil relative permeabilities measured during the enhanced flow period.

	Before Methanol	After 1st Methanol	After 2nd Methanol	After 3rd Methanol	After 4th Methanol	After 5th Methanol
ΔP, psia	23.93	2.47	2.26	4.26	2.76	0.41
k_{rg}	0.06	0.60	0.65	0.35	0.53	0.72
k_{ro}	0.08	0.78	0.85	0.45	0.70	0.94

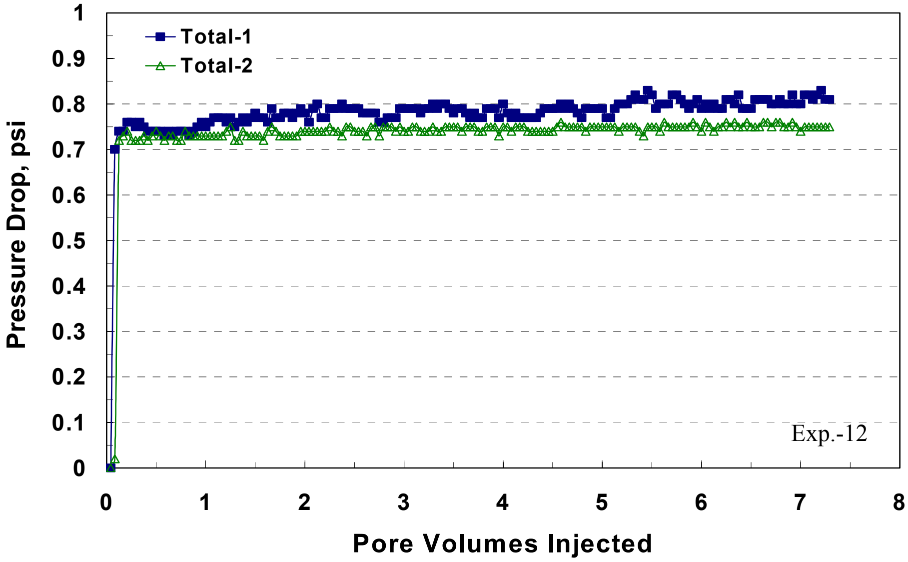

Figure B.66: Pressure drop across the core during methane flow at 600 cc/hr and 3,000 psig.

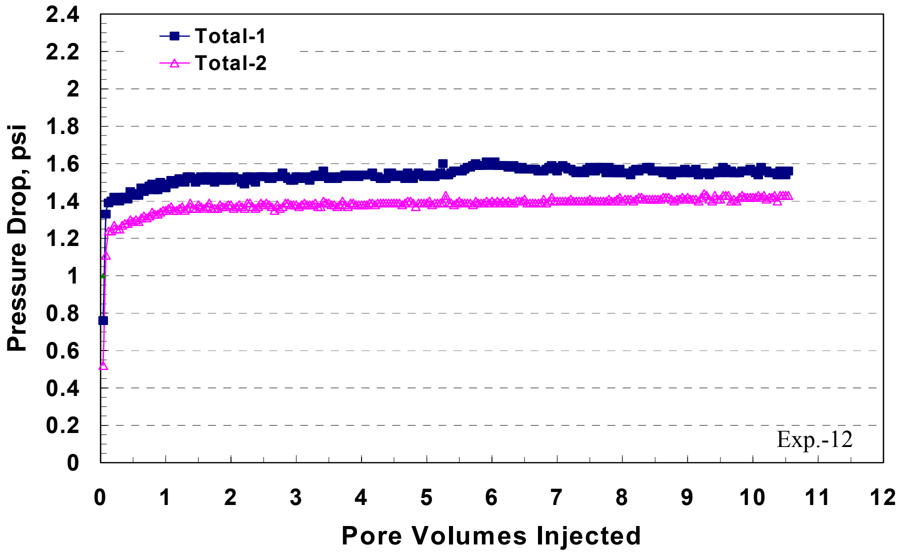

Figure B.67: Pressure drop across the core during gas mixture (single-phase) flow at 600 cc/hr and 3,000 psig.

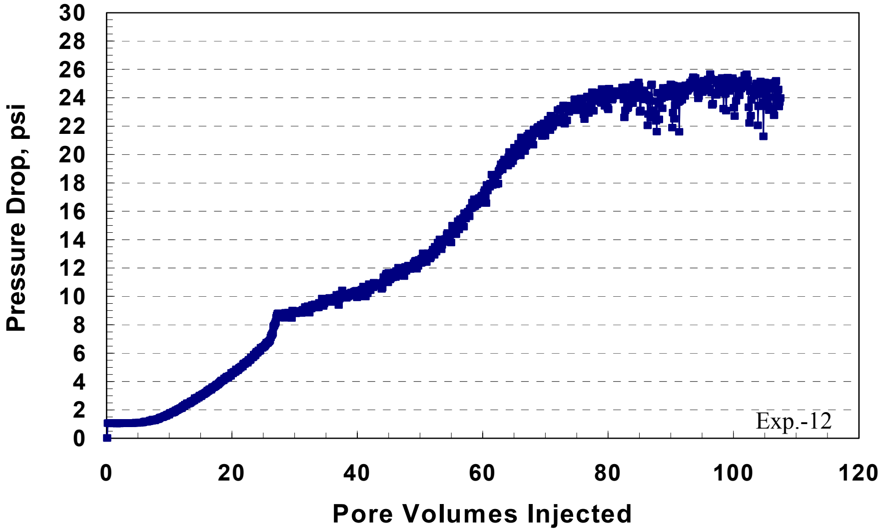

Figure B.68: Pressure drop across the core during condensate accumulation before methanol treatment in downward flow at 600 cc/hr and 1,200 psig.

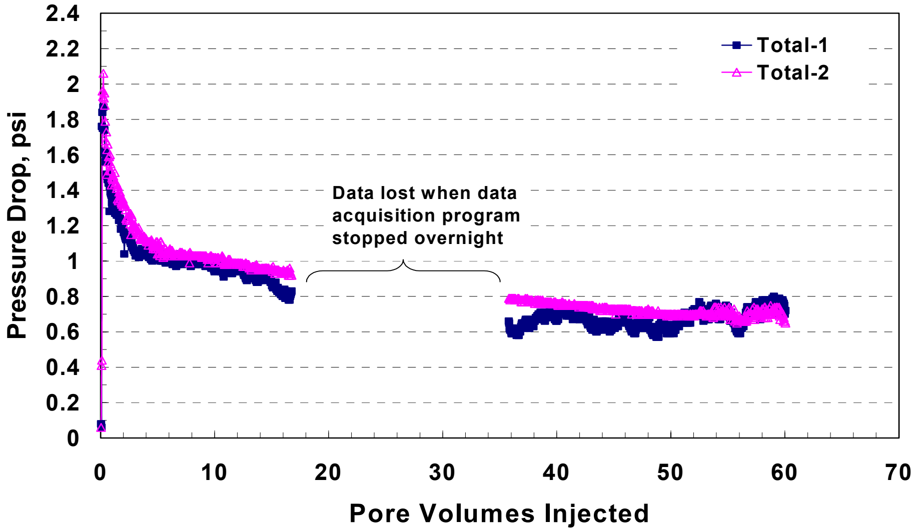

Figure B.69: Pressure drop across the core during equilibrium gas flow before methanol treatment at 600 cc/hr and 1,200 psig.

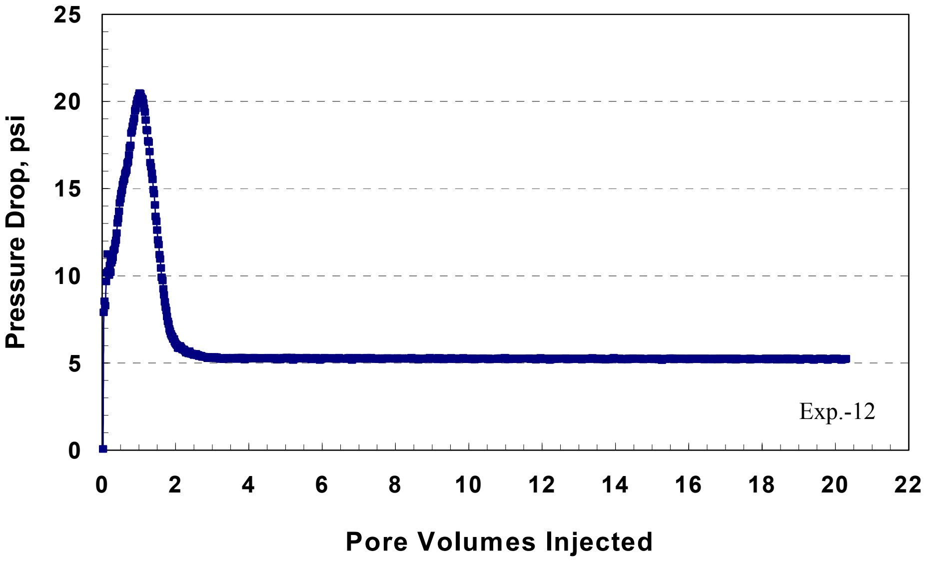

Figure B.70: Pressure drop across the core during the first methanol treatment at 300 cc/hr and 1,200 psig.

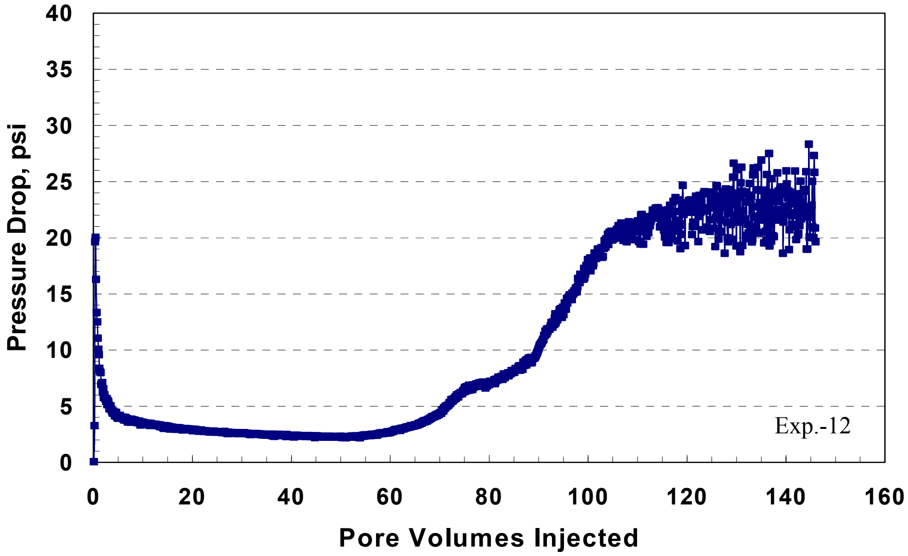

Figure B.71: Pressure drop across the core during condensate accumulation after the first methanol treatment at 600 cc/hr and 1,200 psig.

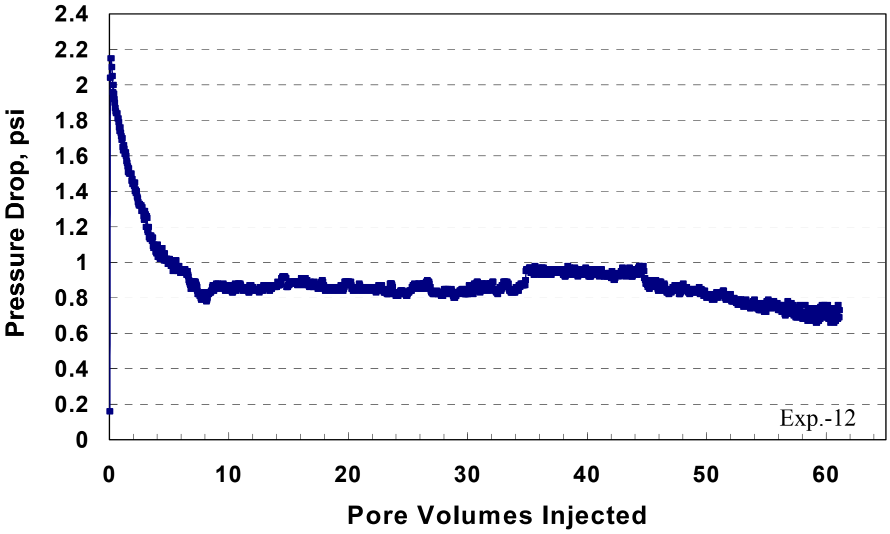

Figure B.72: Pressure drop across the core during equilibrium gas flow after the first methanol treatment at 600 cc/hr and 1,200 psig.

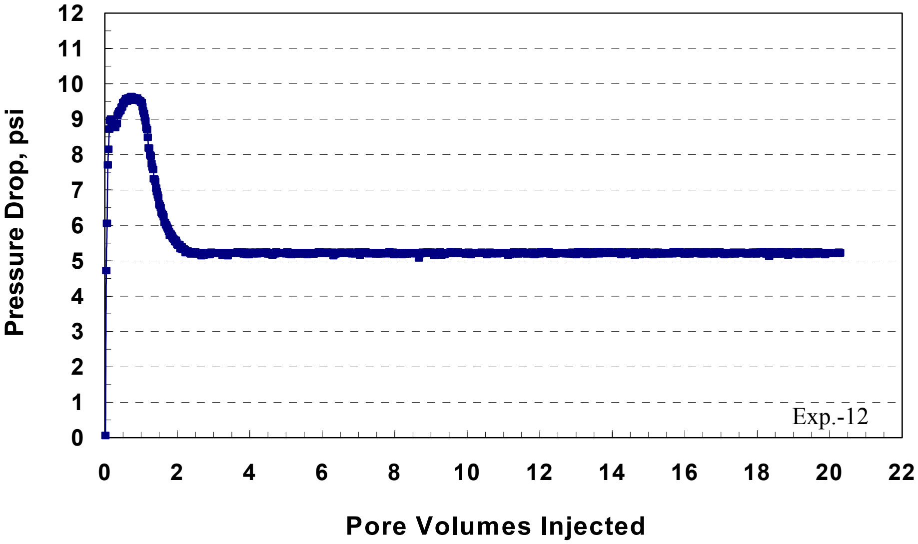

Figure B.73: Pressure drop across the core during the second methanol treatment at 300 cc/hr and 1,200 psig.

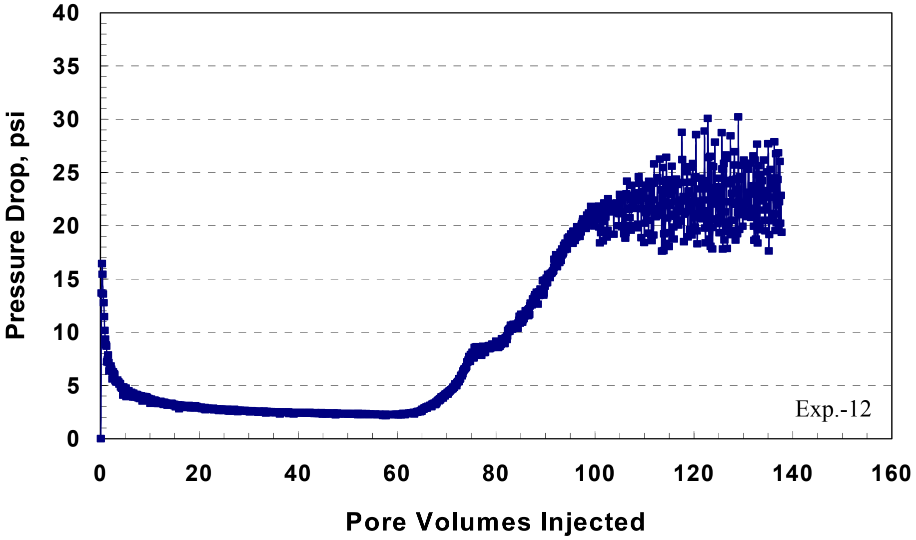

Figure B.74: Pressure drop across the core during condensate accumulation after the second methanol treatment at 600 cc/hr and 1,200 psig.

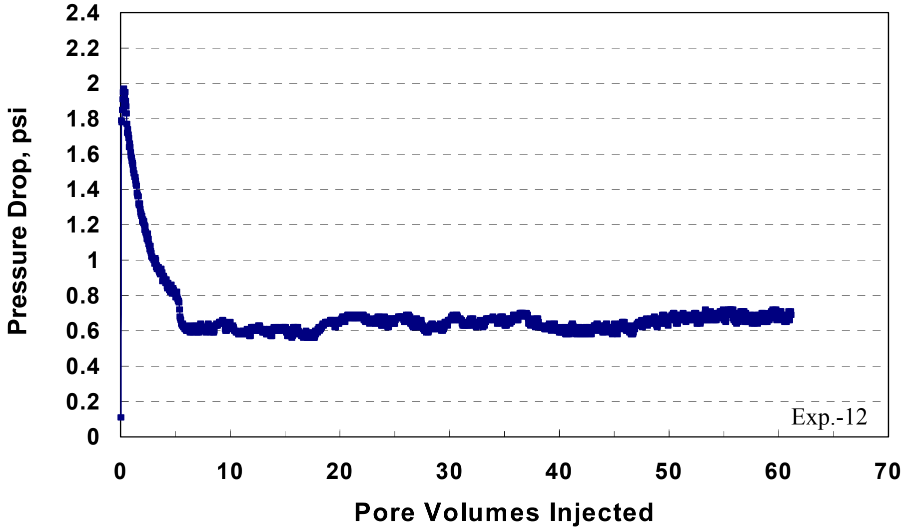

Figure B.75: Pressure drop across the core during equilibrium gas flow after the second methanol treatment at 600 cc/hr and 1,200 psig.

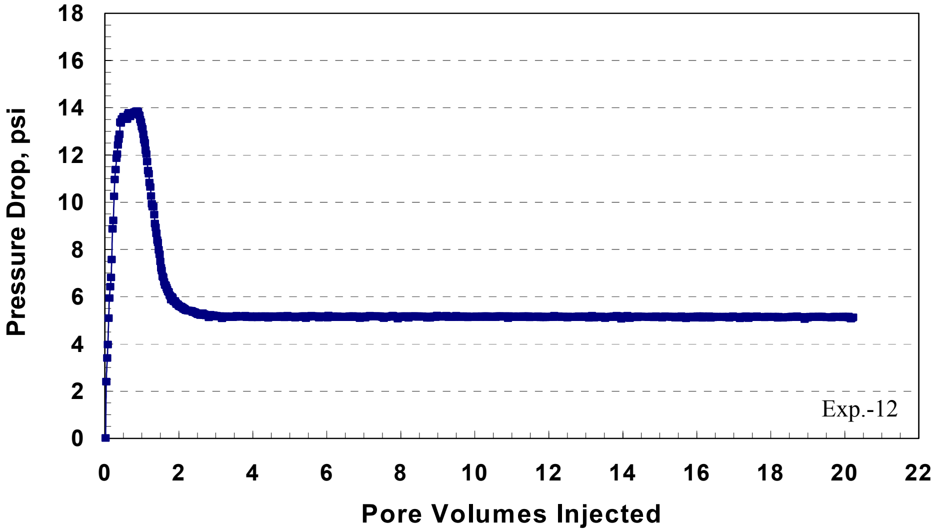

Figure B.76: Pressure drop across the core during the third methanol treatment at 300 cc/hr and 1,200 psig.

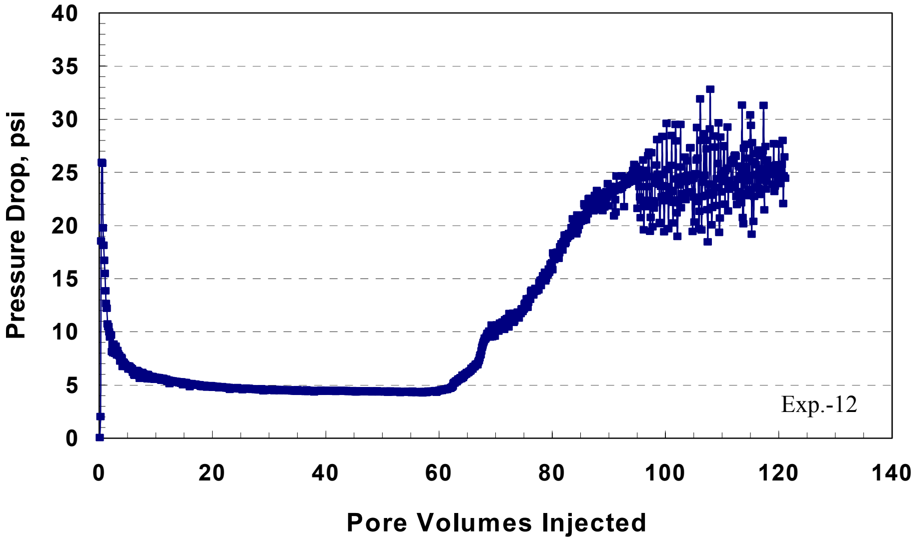

Figure B.77: Pressure drop across the core during condensate accumulation in the reverse direction (upward flow) after the third methanol treatment at 600 cc/hr and 1,200 psig.

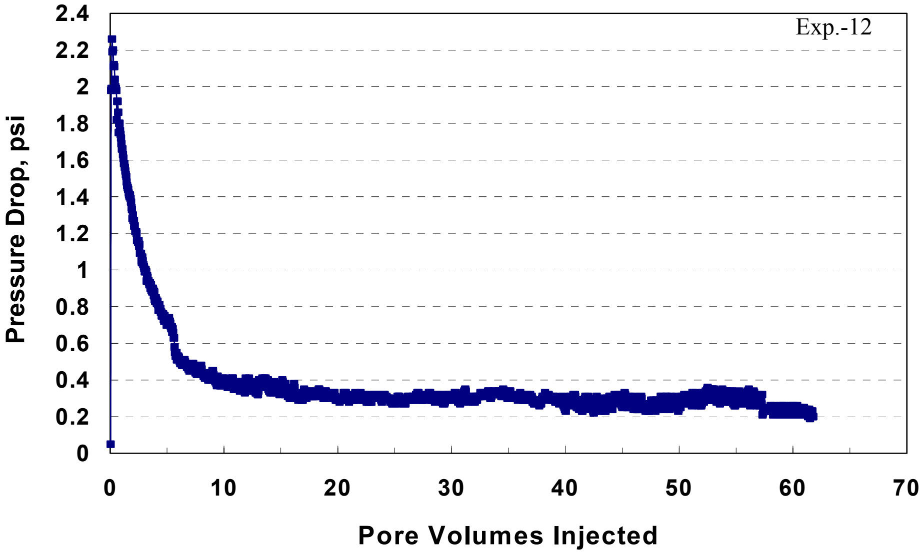

Figure B.78: Pressure drop across the core during equilibrium gas flow in the reverse direction (upward flow) after the third methanol treatment at 600 cc/hr and 1,200 psig.

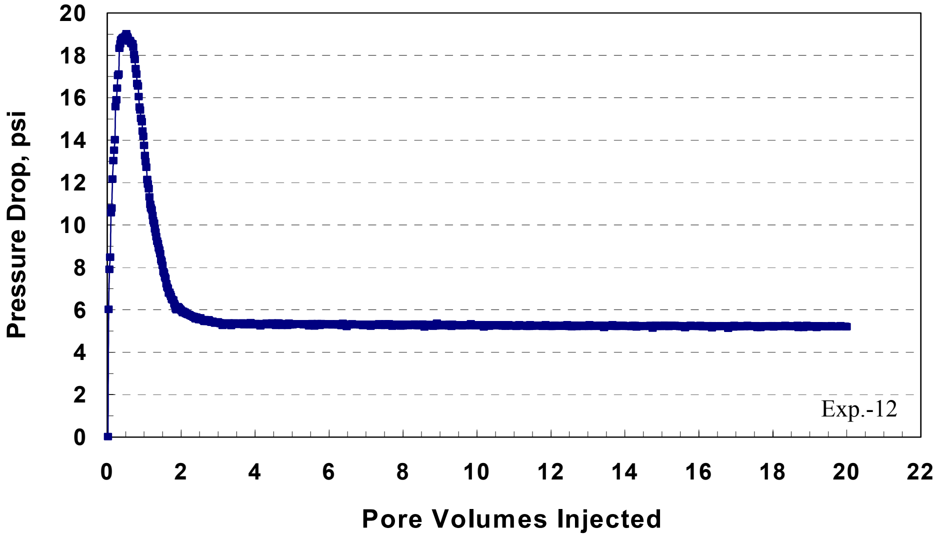

Figure B.79: Pressure drop across the core during the fourth methanol treatment in horizontal direction at 300 cc/hr and 1,200 psig.

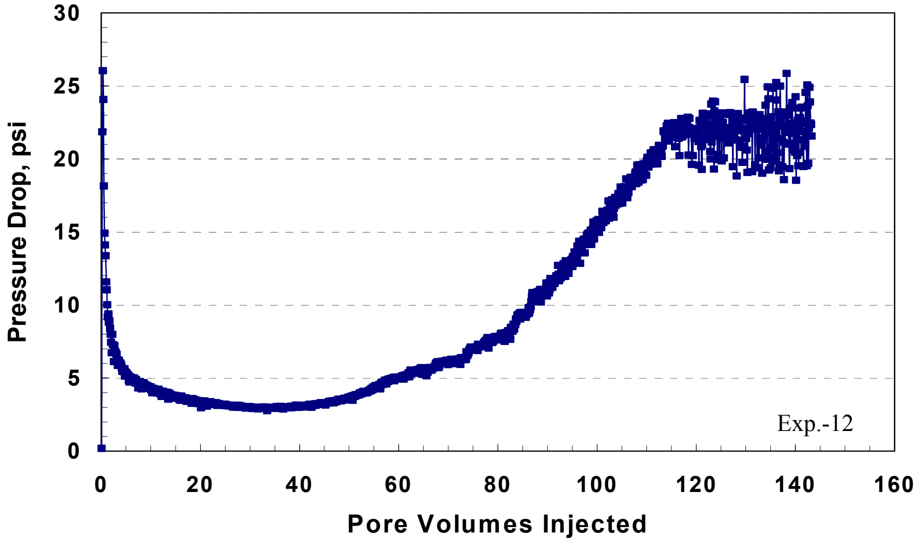

Figure B.80: Pressure drop across the core during condensate accumulation in the horizontal direction after the fourth methanol treatment at 600 cc/hr and 1,200 psig.

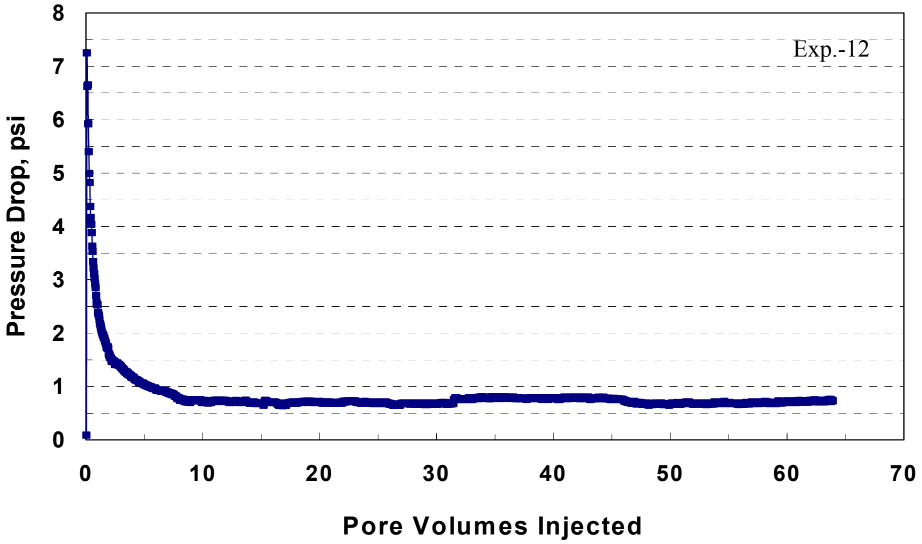

Figure B.81: Pressure drop across the core during equilibrium gas flow in the horizontal direction after the fourth methanol treatment at 600 cc/hr and 1,200 psig.

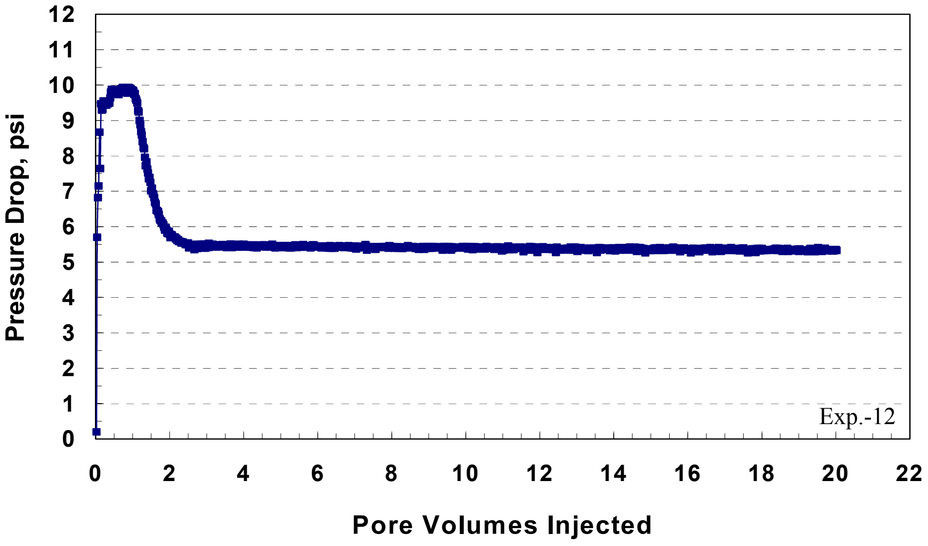

Figure B.82: Pressure drop across the core during the fifth methanol treatment in the downward direction at 300 cc/hr and 1,200 psig.

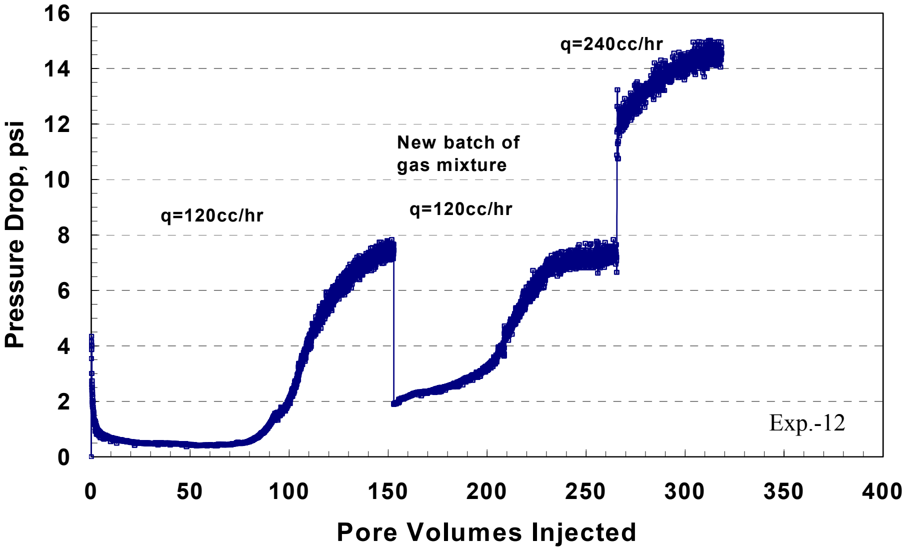

Figure B.83: Pressure drop across the core during condensate accumulation after the fifth methanol treatment at various rates and 1,200 psig.

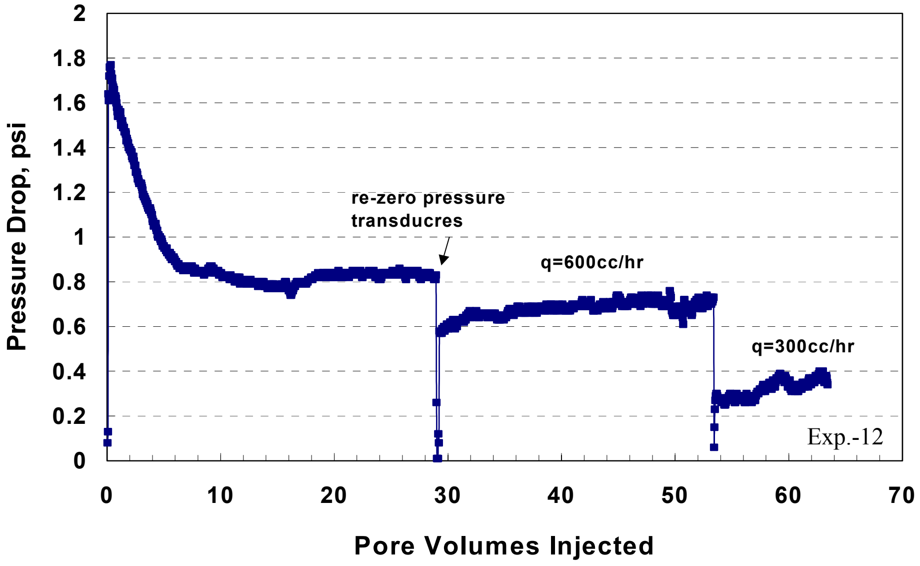

Figure B.84: Pressure drop across the core during equilibrium gas flow after the fifth methanol treatment at various rates and 1,200 psig.

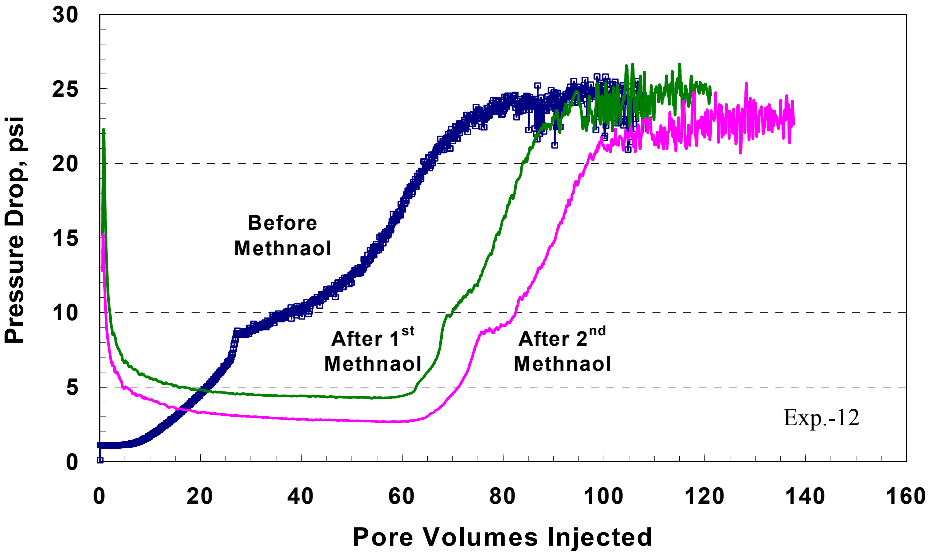

Figure B.85: Pressure drop across the core during condensate accumulation before and after methanol treatments at 600 cc/hr and 1,200 psig.

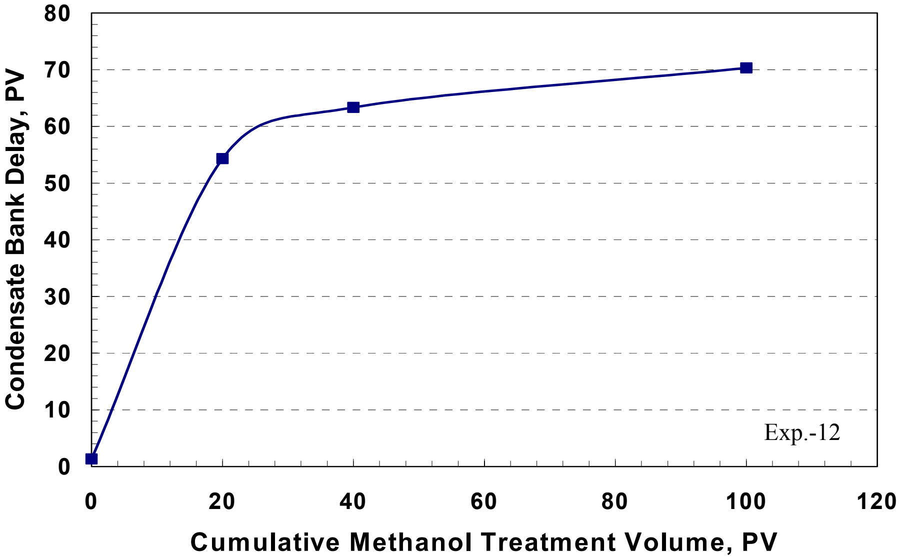

Figure B.86: Effect of methanol on post-treatment condensate accumulation delay followed the enhanced flow period in Berea core.

B.7 Coreflood Experiment No. 12a

B.7.1 Objective

The objective of this experiment is to investigate the effect of multi-stage treatment of methanol on the relative permeability of gas after gas-condensate accumulation in highly permeable core in the presence of residual water saturation. This experiment was performed on the Berea core that was used in Experiment-12.

B.7.2 Core Cleaning

Since this core was used in Experiment-12, methane was flowed through the core at different flow rates (600 and 800 cc/hr) at 1,200 psig to remove any movable hydrocarbons. The pressure drop across the core during the flow of methane is shown in **Figure B.87**. Two pressure transducers (Total-1 and Total-2) were used to measure the total pressure drop across the whole core. **Table B.69** gives the measured gas permeability at various flow rates at 1,200 psig. The initial core permeability at (S_g = 100%) was taken based on the average value of 378.27 md. Pure methanol was injected through the core at a flow rate of 300 cc/hr and 1,200 psig. The objective of this methanol stage is to remove any residual hydrocarbons from the core. **Figure B.88** depicts the pressure drop across the core during methanol flood. The pressure drop increased initially to a maximum value of 20 psia, then it sharply decreased to a reach a plateau value of 5.31 psia. The initial increase in pressure drop is due to the displacement of the gas from the core by the injected methanol. In other words, the pressure drop increased because the relative permeability of methanol is less than that of the methane. Once the methanol displaced methane from the core, it presents as a single phase where the pressure drop reached a stabilized value. The measured core permeability to methanol was 330.21 md. Since the measured permeability to methanol is the same as that measured in the pervious experiment during methanol treatments, this stage assure the core was completely cleaned from any residual hydrocarbons.

B.7.3 Water Saturation Stage

A brine consists of 3wt% NaCl and 0.5wt% $CaCl_2$ solution was injected through the core to displace the methanol. The brine was injected at two flow rates 300 and 150 cc/hr at a constant flowing pressure of 1,200 psig. **Figure B.89** shows the pressure drop profile during brine saturation stage. The pressure drop increased to a maximum value of 8.59 psia and then it decreased gradually to reach a stabilized value around 7.7 psia. Initially the brine displaced methanol from the core. Since both brine and methanol are liquid phases and have small difference in viscosities, their relative permeability values expected to be adjacent. **Table B.70** gives the measured permeability values using brine flow.

B.7.4 Methane Flood at Residual Water Saturation

Methane was flowed through the core at 1,200 psig to displace water until it reached residual water saturation. The residual water saturation was calculated by measuring the volume of water displaced in the effluent. **Figure B.90** shows the displacement of water by methane at 1,200 psig and different flow rates. **Table B.71** lists the measured residual water saturation with the corresponding value of gas relative permeability. It took many pore volumes (> 110 PV) of methane to displace the water to its residual saturation. This confirms that the evaporation of liquid by flowing gas is a very slow process. The measured residual water saturation was 38% and the gas relative permeability was 0.40.

B.7.5 Methane Flow at 3,000 psig

The core permeability was measured using methane at a flowing pressure of 3,000 psig before introducing a single-phase gas mixture. The pressure of both the upstream and downstream back-pressure regulators was increased to 3,000 psig. Methane gas was flowed at high rates of 800 and 600 cc/hr, respectively. **Figure B.91** shows the pressure drop across the core during the flow of methane at 3,000 psig. **Table B.72** gives the measured core permeability to methane at a flowing pressure of 3,000 psig. There was no water collected during this stage. Thus, the residual water saturation (38%) assumed not to be changed.

B.7.6 Gas Mixture (Single-Phase)

The gas mixture (single-phase) was flowed through the core at 3,000 psig. The flow rate was 600 cc/hr during this stage. **Figure B.92** shows the pressure drop across the core during gas mixture (single-phase) flooding. The results are given in **Table B.73**. The relative permeability measured during this stage is the same as the one measured with methane at 3,000 psig. This verifies that the gas mixture was flowed as a single phase above its dewpoint pressure.

B.7.7 Condensate Accumulation (Two-Phase Flow)

Before the start of this stage, the inlet and outlet valves of the core were closed. Pressure of the downstream back-pressure regulator was decreased to 1,200 psig, while the pressure in the upstream back-pressure regulator was kept at 3,000 psig. Flow was started while the bypass was open until the pressure in the lines stabilized. Then, the bypass valve was closed and inlet and outlet valves were open simultaneously. The flow rate was 600 cc/hr. This stage allowed the gas-condensate to dynamically accumulated through the core. This simulates the condensate bank in the wellbore region. The stage was stopped when the pressure drop across the core reached stable values. **Figure B.93** shows the pressure drop across the core during two-phase flow. The pressure drop is sharply increased until it reached a value of 23.50 psia at 12.10 PV. Then, it is increased at a slower rate. This discontinuity would be due to capillary forces between flowing gas phase and condensate accumulated in the core pores. The pressure drop across the core was gradually increased until it reached a plateau after 80.6 PV. This increase in pressure drop is higher than that of Experiment-12 that was conducted on the same core in the absence of water. This means that the presence of residual water would make the reduction in gas relative permeability due to condensate banking more badly. The measured gas and condensate relative permeabilities are given in **Table B.74**. Data needed to calculation relative permeability for gas and oil phases (μ_g=0.01396 cp, μ_o=0.23711 cp) were obtained using PREOS and UTCOMP. This result indicates that condensate bank would cause a severe reduction in gas productivity even in highly permeable cores. This is considered as a new finding to the literature. In this experiment, the gas relative permeability reduced by 97% due to condensate accumulation in the presence of residual water saturation.

B.7.8 Equilibrium Gas Flooding

The pressure in the upstream back-pressure regulator was decreased to 1,200 psig. The gas phase of the gas-mixture, which has a pressure of 1200 psig (below dewpoint), was injected through the core at a flow rate of 600 cc/hr. The pressure drop across the core is shown in **Figure B.94**. This stage gives the gas end-point relative permeability (k^o_{rg}) before methanol treatment as given in **Table B.75**. The gas end-point relative permeability (0.68) at S_{wr} of 38% is less than that (~0.90) at S_g = 100%.

B.7.9 The First Stage of Methanol Treatment

Pure methanol was injected through the core at an injection rate of 300 cc/hr and 1,200 psig. The volume of methanol injected was 20 PV. The pressure drop across the core stabilized at a value 6.82 psia as shown in **Figure B.95**. The measured permeability for methanol was found to be 256.95 md. Therefore, the methanol relative permeability was 0.68.

B.7.10 Two-Phase Flow After the First Stage of Methanol Treatment

The pressure of the upstream back-pressure regulator was increased to 3,000 psig, while the pressure of the downstream back-pressure regulator was kept at 1,200 psig. The rate of this stage was 600 cc/hr. The gas mixture was flashed through the core to bank condensate. **Figure B.96** depicts the pressure drop across the core during this stage. This figure indicates that the pressure drop across the core started to increase after an injection of 55.3 PV of the two-phase. Then, the pressure drop profile shows the same trend as that before methanol. The first methanol treatment was effective in delaying the condensate banking. The measured steady state gas and oil relative permeabilities are given in **Table B.76**.

B.7.11 Equilibrium Gas After the First Methanol Treatment

The pressure of the upstream back-pressure regulator was decreased to 1,200 psig. The equilibrium gas was injected at a flow rate of 600 cc/hr. **Figure B.97** shows the pressure drop across the core. This stage gives the gas end-point relative permeability after methanol injection, as given in **Table B.77**. The first stage of methanol increased the gas relative permeability by 42.2%. The methanol was effective to remove residual water saturation from the core as well as condensate. The most important is that the methanol delayed the condensate bank that expected to take place after the post-treatment production period.

B.7.12 The Second Stage of Methanol Treatment

Pure methanol was injected, as the second treatment, through the core at an injection rate of 300 cc/hr and 1,200 psig. The volume of methanol injected was 20 PV. The pressure drop across the core reached a value of 6.05 psia which is close to that for the first treatment. **Figure B.98** depicts the pressure drop across the core during the second treatment of methanol. The calculated permeability for this stage of methanol was 289.47 md, which corresponds to a relative permeability value of 0.77.

B.7.13 Two-Phase Flow After the Second Stage of Methanol Treatment

The pressure of the upstream back-pressure regulator was increased to 3,000 psig, while the pressure of the downstream back-pressure regulator was kept at 1,200 psig. The flow rate was 600 cc/hr. **Figure B.99** depicts the pressure drop across the core during this stage. This figure shows the same behavior as the two-phase before methanol treatment, except it has shit to higher pore volumes. This figure implies that the pressure drop across the core started to increase after an injection of 72.82 PV. This means that the second methanol treatment delayed the condensate more than the first one. The two-phase relative permeabilities are given in **Table B.78**. Therefore, more injection of methanol would stay for longer time during the post-treatment production period and yield high gas productivity.

B.7.14 Equilibrium Gas After the Second Methanol Treatment

The pressure of the upstream back-pressure regulator was decreased to 1,200 psig. The equilibrium gas was injected at a flow rate of 600 cc/hr. **Figure B.100** shows the pressure drop across the core. This stage gives the gas end-point relative permeability after methanol injection, as given in **Table B.79**. The second stage of methanol did not increase the gas relative permeability. The improvement obtained after the second treatment of methanol is lower than the first one. Multi-stage treatment of methanol will be more effectiveness to enhance the productivity of gas wells, particularly when the bottom hole flowing pressure fall below the dewpoint pressure.

B.7.15 The Third Stage of Methanol Treatment

Methanol was injected, as the third treatment, through the core at an injection rate of 300 cc/hr and a flowing pressure of 1,200 psig. The volume of methanol injected was 20 PV. **Figure B.101** illustrates the pressure drop across the core during the third treatment of methanol. The pressure drop across the core reached a value of 6.00 psia. The calculated permeability for this stage of methanol was equal to 292.08 md.

B.7.16 Two-Phase Flow After the Third Stage of Methanol Treatment at a Lower Rate

The pressure of the upstream back-pressure regulator was increased to 3,000 psig, while the pressure of the downstream back-pressure regulator was kept at 1200 psig. In this stage, the flow rate decreased to 138 cc/hr. **Figure**

B.102 represents the pressure drop across the core during the two-phase flow at this lower rate. This figure shows that the pressure drop across the core started to increase after 30.90 PV. The gas and oil relative permeability values are given in **Table B.80**. As can be seen, the gas and oil relative permeability values have higher values than that obtained at higher rates. This is due to the decrease in the capillary number that results to higher relative permeability.

B.7.17 Summary of the Results for Coreflood Experiment-12a

Figure B.103 shows the two-phase flow before and after methanol treatment. This result indicates that the gas relative permeability was decreased by more than 97% due to condensate accumulation even in highly permeable cores. To our knowledge, the results obtained are new to the literature. Methanol treatment was effective to enhance the reduced gas relative permeability, as given in **Table B.81**. Methanol treatment increased the gas end-point relative permeability by a factor of 1.5 as shown in **Figure B.104**. The removal of residual methanol by evaporation is a very slow process. Therefore, it stays for a longer time in the core. The residual methanol improves the productivity by postponing the accumulation of condensate. Methanol stages helped to delay the condensate buildup following the treatment.

Figure B.105 shows the effect of methanol treatment volume on the post-treatment condensate accumulation delay at different water saturations in Berea cores. As can be seen, increasing the volume of methanol treatment yielded a more production time for gas after the treatment before countering the subsequent condensate bank. **Figure B.106** depicts the effect of methanol treatment on the productivity index (PI) in Berea core. As can be seen, the productivity index increased by an order of magnitude during the enhanced flow period where the methanol postponed the accumulation of condensate. This is an interesting finding where the methanol treatment enhances the productivity directly after the treatment. **Table B.82** gives gas and oil relative permeabilities during the enhanced flow period during condensate accumulation. **Figure B.107** shows the gas relative permeability curve measured during this experiment. It is appears that the saturation window was very narrow for this core.

Table B.69: Initial core permeability measured using methane at 1,200 psig.

	q = 600 cc/hr		q = 800 cc/hr	
	$\Delta P_{Total-1}$	$\Delta P_{Total-2}$	$\Delta P_{Total-1}$	$\Delta P_{Total-2}$
ΔP, psia	0.40	0.44	0.52	0.58
k, md	374.73	343.40	381.82	344.71

Table B.70: Core permeability measured using brine at 1,200 psig.

	q = 300cc/hr		q = 150 cc/hr	
	$\Delta P_{Total-1}$	$\Delta P_{Total-2}$	$\Delta P_{Total-1}$	$\Delta P_{Total-2}$
ΔP, psia	7.71	7.80	3.85	3.75
k, md	302.08	298.90	302.62	310.68

Table B.71: Gas relative permeability measured during brine displacement with methane at 1,200 psig and various flow rates.

q, cc/hr	S_{wr}, %	ΔP, psia	k_g, md	k_{rg}
600	42.50	2.45	61.07	0.16
800	42.00	2.80	71.19	0.19
600	40.50	1.50	100.02	0.26
600	39.0	0.98	152.68	0.40
800	38.0	1.31	152.78	0.40

Table B.72: Core relative permeability at $S_{wr} = 38\%$ measured during methane flow at 3,000 psig.

	q=800cc/hr		q=600 cc/hr	
	$\Delta P_{Total-1}$	$\Delta P_{Total-2}$	$\Delta P_{Total-1}$	$\Delta P_{Total-2}$
ΔP, psia	2.18	2.19	1.56	1.53
k_g, md	121.03	120.22	126.50	120.22
k_{rg},	0.32	0.32	0.33	0.34

Table B.73: Gas relative permeability measured during gas mixture (single-phase) flow at 600 cc/hr and 3,000 psig.

	$\Delta P_{Total-1}$	$\Delta P_{Total-2}$
ΔP, psia	3.20	3.16
k_g, md	119.34	120.96
k_{rg},	0.32	0.32

Table B.74: Gas and oil relative permeabilities measured during condensate accumulation stage before methanol treatment at 600 cc/hr and 1200 psig.

	$\Delta P_{Total-1}$
ΔP, psia	30.85
k_{rg}	0.03
k_{ro}	0.04

Table B.75: Gas end-point relative permeability measured during equilibrium gas flow before methanol at 600 cc/hr and 1,200 psig.

	$\Delta P_{Total-1}$
ΔP, psia	1.14
k_g, md	145.83
k^o_{rg}	0.386

Table B.76: Gas and oil relative permeabilities measured during condensate accumulation after the first methanol treatment at 600 cc/hr and 1,200 psig.

	$\Delta P_{Total-1}$	$\Delta P_{Total-2}$
ΔP, psia	26.68	26.74
k_{rg}	0.04	0.04
k_{ro}	0.05	0.05

Table B.77: Gas end-point relative permeability measured during equilibrium gas flow after the first methanol treatment at 600 cc/hr and 1,200 psig.

	$\Delta P_{Total-1}$
ΔP, psia	0.45
k_g, md	365.77
k^o_{rg}	0.967

Table B.78: Gas and oil relative permeabilities measured during condensate accumulation after the second methanol treatment at 600 cc/hr and 1,200 psig.

	$\Delta P_{Total-1}$	$\Delta P_{Total-2}$
ΔP, psia	27.03	26.61
k_{rg}	0.04	0.04
k_{ro}	0.05	0.05

Table B.79: Gas end-point relative permeability measured during equilibrium gas flow after the second methanol treatment at 600 cc/hr and 1,200 psig.

	$\Delta P_{Total-1}$
ΔP, psia	0.54
k_g, md	305.38
k^o_{rg}	0.807

Table B.80: Gas and oil relative permeabilities measured during condensate accumulation after the third methanol treatment at 138 cc/hr and 1,200 psig.

	$\Delta P_{Total-1}$	$\Delta P_{Total-2}$
ΔP, psia	2.80	2.76
k_{rg}	0.08	0.08
k_{ro}	0.10	0.10

Table B.81: Effect of methanol treatment on two-phase relative permeabilities during condensate accumulation at 1,200 psig.

	Before Methanol	After 1st Methanol	After 2nd Methanol
k_{rg}	0.03	0.04	0.04
k_{ro}	0.04	0.05	0.05
k^o_{rg}	0.386	0.967	0.807

Table B.82: Gas and oil relative permeabilities measured during the enhanced flow period.

	Before Methanol	After 1st Methanol	After 2nd Methanol
k_{rg}	0.03	0.33	0.39
k_{ro}	0.04	0.43	0.51

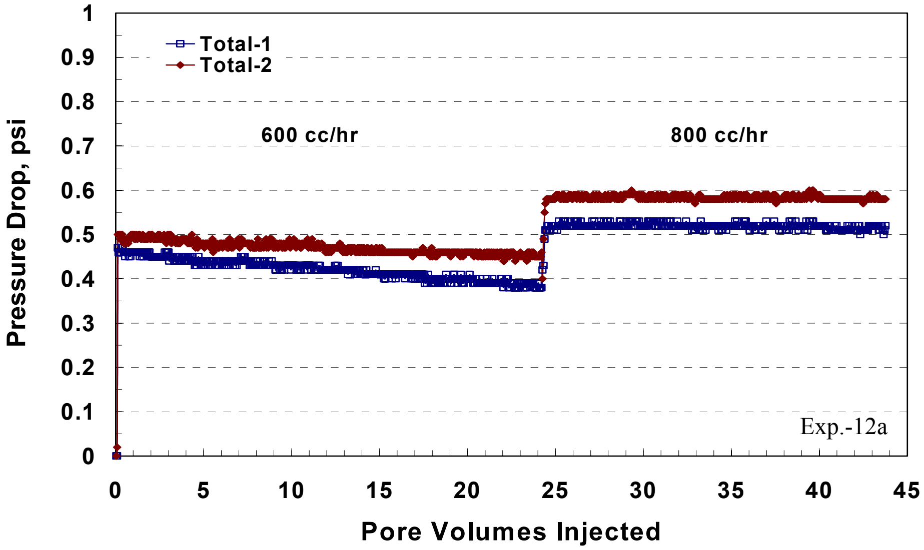

Figure B.87: Pressure drop across the core during methane flow before introducing water saturation at 1,200 psig.

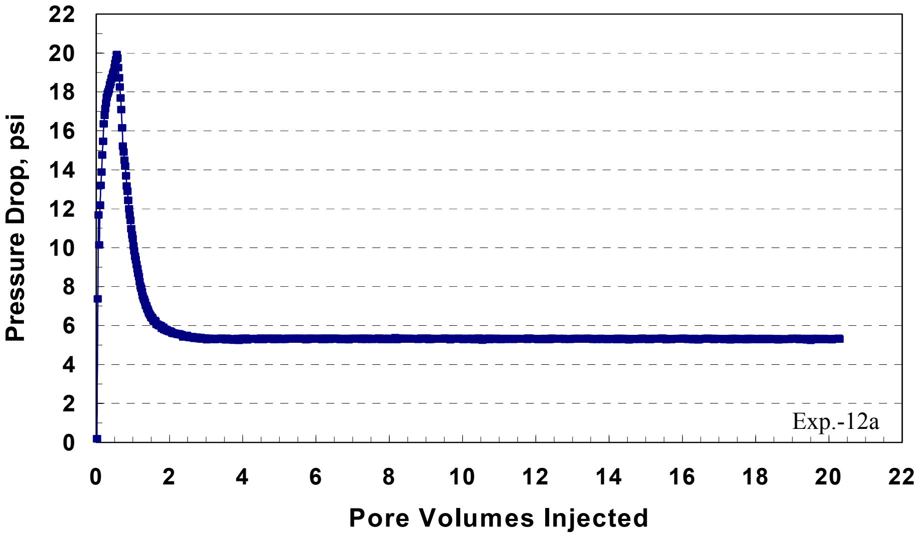

Figure B.88: Pressure drop across the core during methanol flow to clean the core at 300 cc/hr and 1,200 psig.

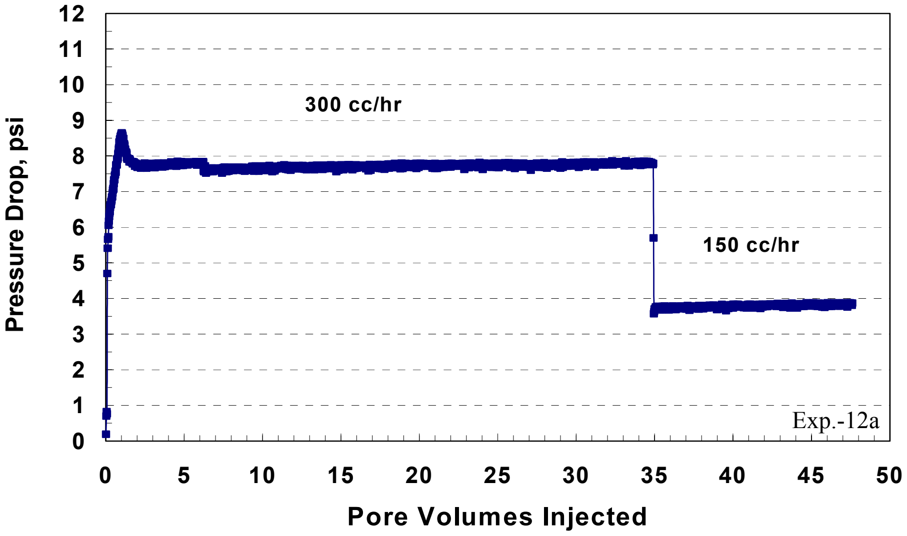

Figure B.89: Pressure drop across the core during brine (3wt% NaCl+0.5wt% $CaCl_2$) flooding at 1,200 psig.

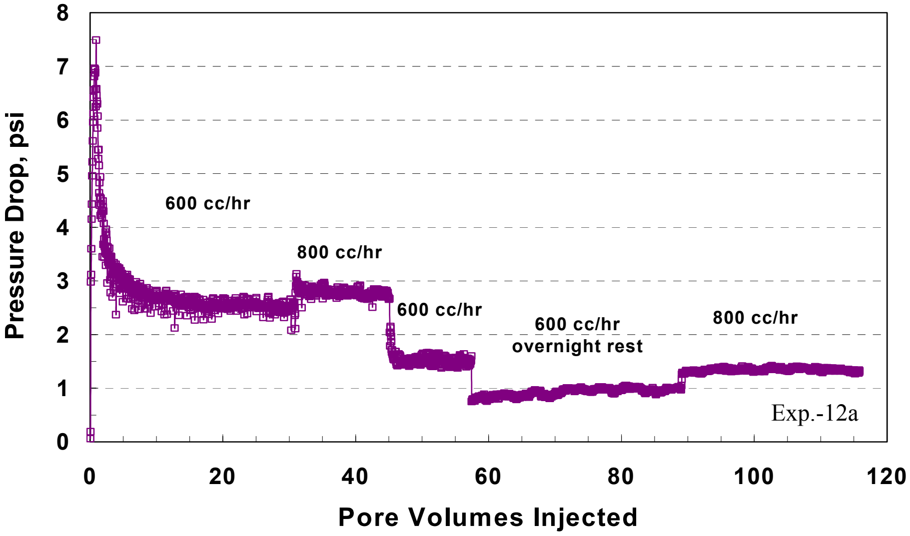

Figure B.90: Pressure drop across the core during brine displacement by methane at 1,200 psig and various flow rates.

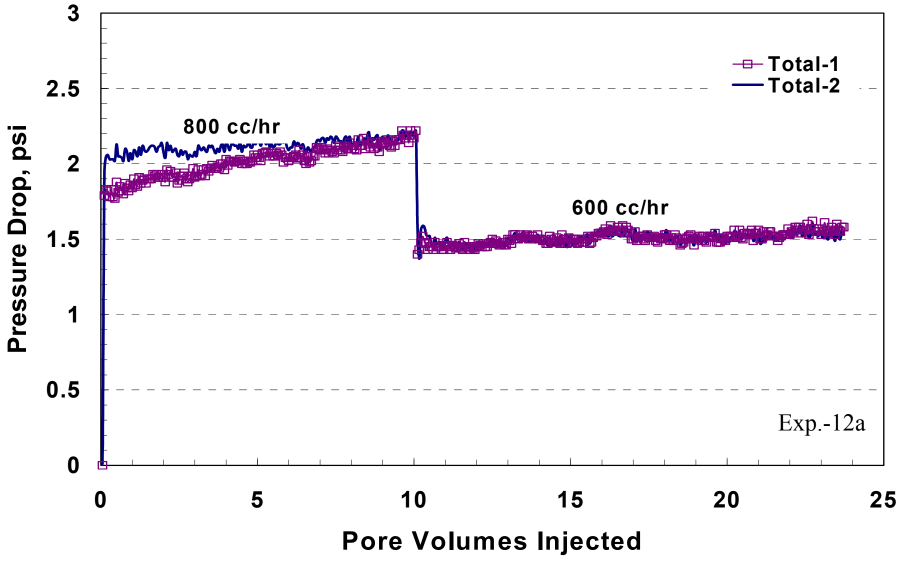

Figure B.91: Pressure drop across the core during methane flow at 3,000 psig.

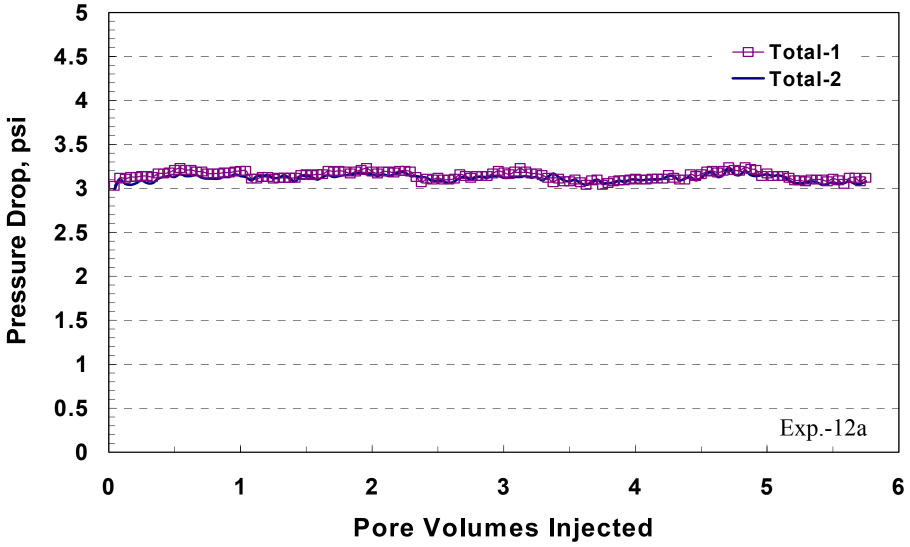

Figure B.92: Pressure drop across the core during gas mixture (single-phase) flow at 600 cc/hr and 3,000 psig.

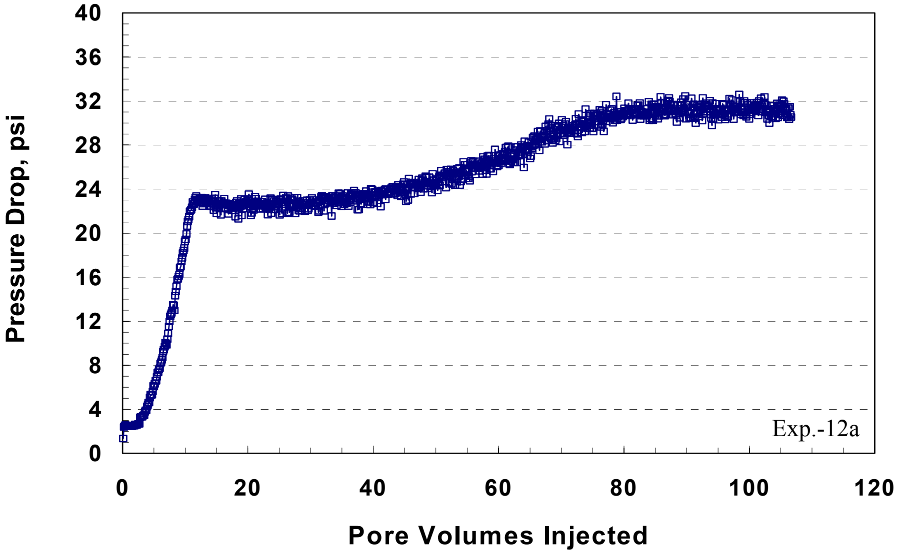

Figure B.93: Pressure drop across the core (Berea) during dynamic condensate accumulation before methanol treatment at 600 cc/hr and 1,200 psig.

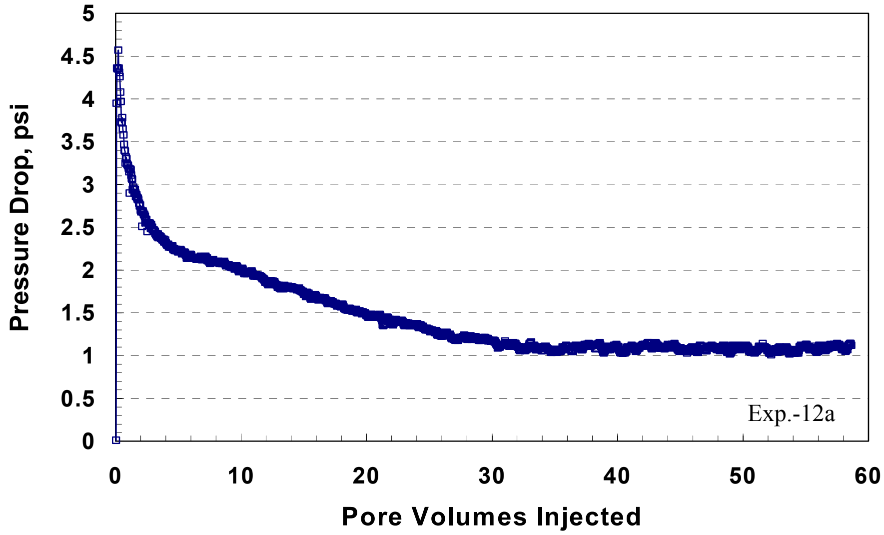

Figure B.94: Pressure drop across the core during equilibrium gas flow before methanol treatment at 600 cc/hr and 1,200 psig.

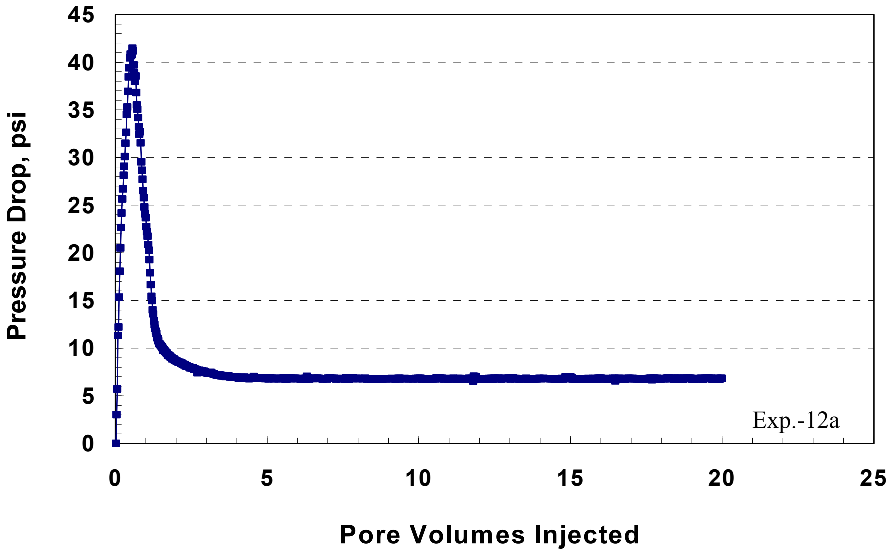

Figure B.95: Pressure drop across the core during the first methanol treatment at 300 cc/hr and 1,200 psig.

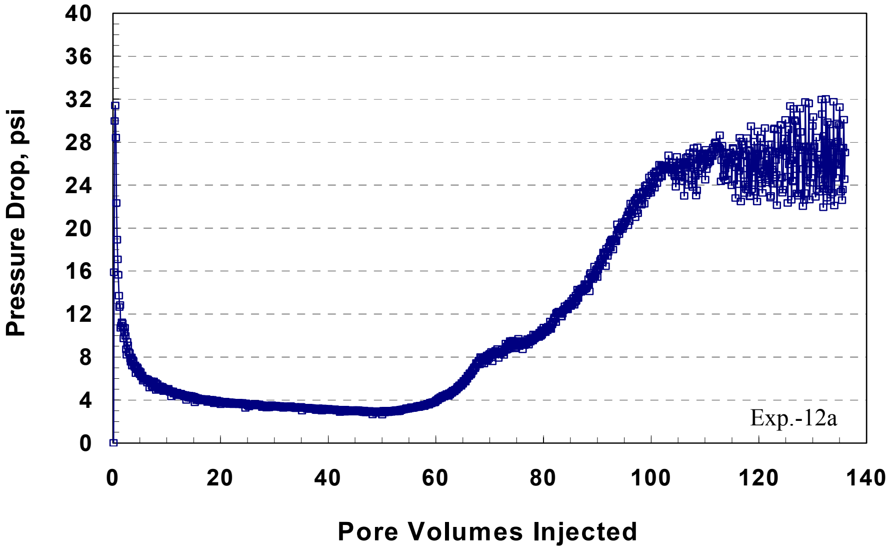

Figure B.96: Pressure drop across the core (Berea) during condensate accumulation after the first methanol treatment at 600 cc/hr and 1,200 psig.

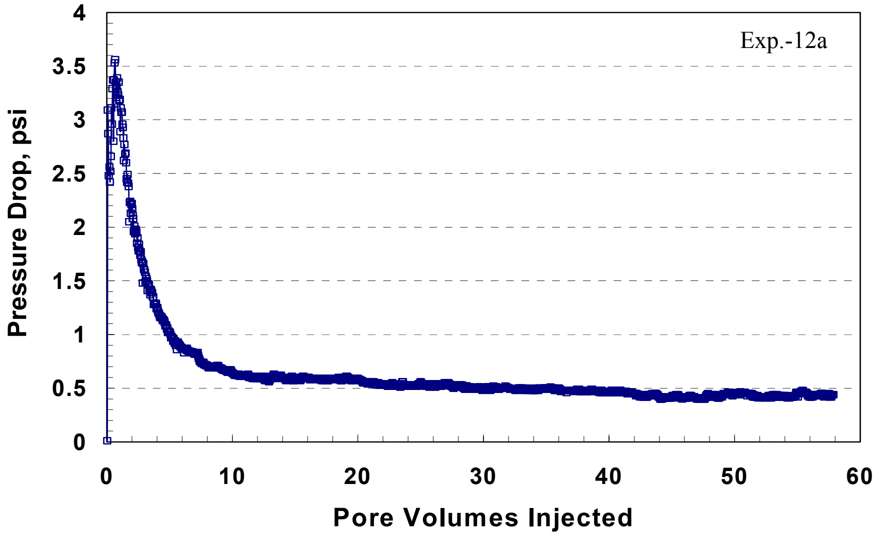

Figure B.97: Pressure drop across the core during equilibrium gas flow after the first methanol treatment at 600 cc/hr and 1,200 psig.

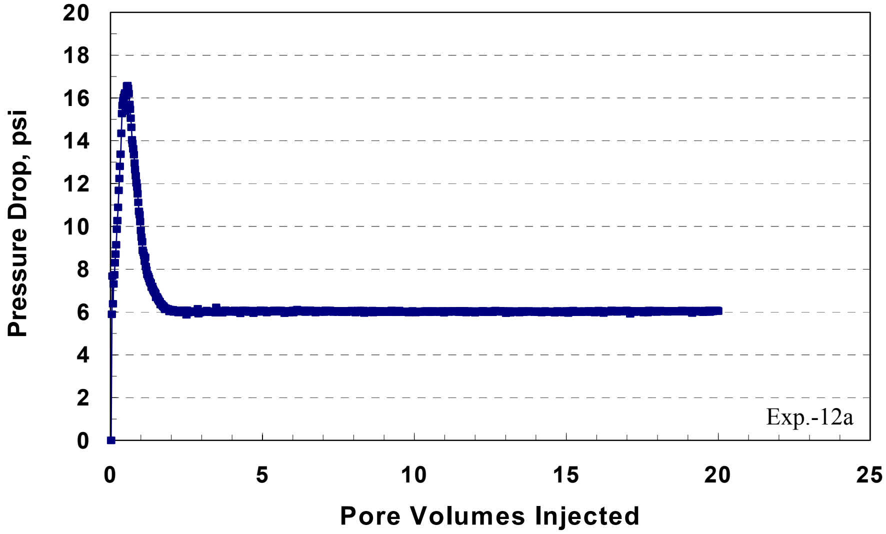

Figure B.98: Pressure drop across the core during the second methanol treatment at 300 cc/hr and 1,200 psig.

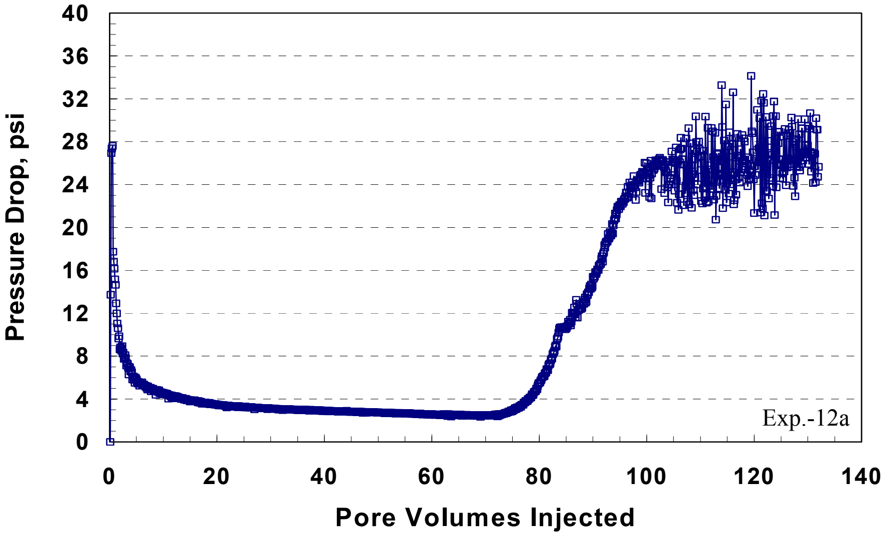

Figure B.99: Pressure drop across the core during condensate accumulation after the second methanol treatment at 600 cc/hr and 1,200 psig.

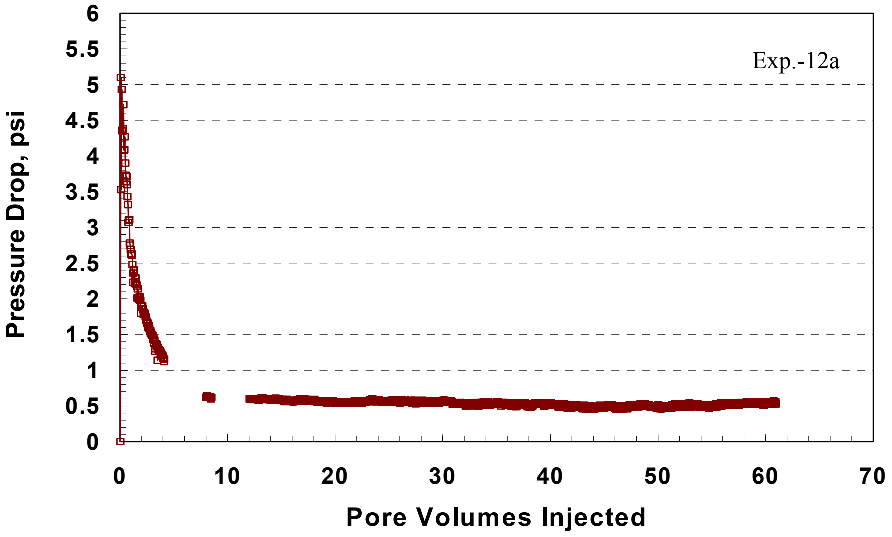

Figure B.100: Pressure drop across the core during equilibrium gas flow after the second methanol treatment at 600 cc/hr and 1,200 psig.

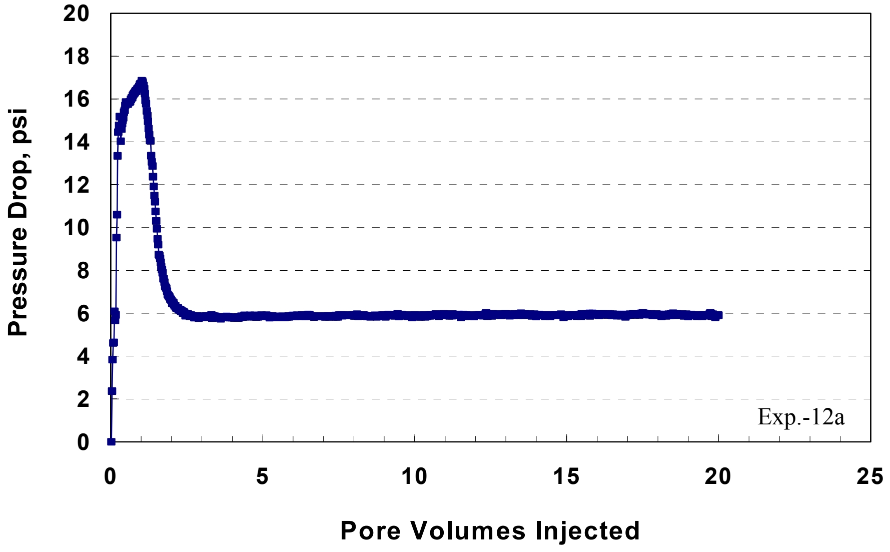

Figure B.101: Pressure drop across the core during the third methanol treatment at 300 cc/hr and 1,200 psig.

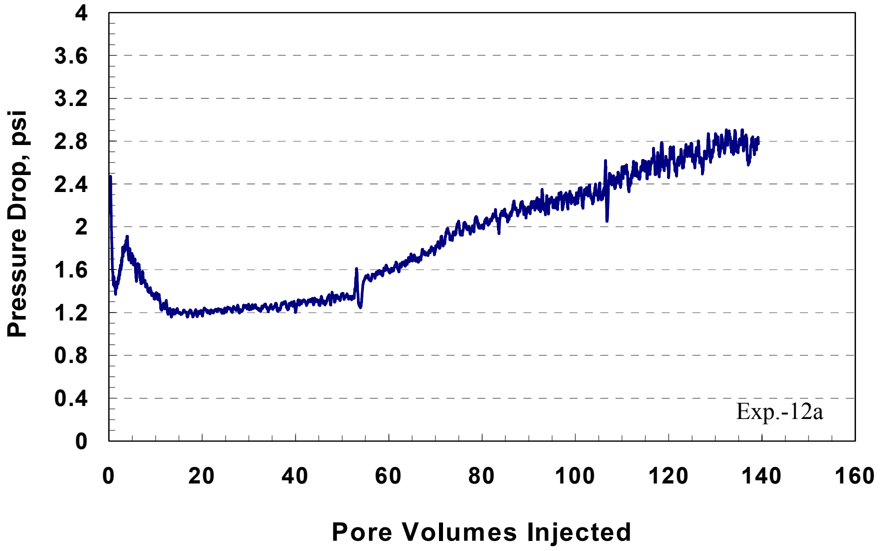

Figure B.102: Pressure drop across the core during condensate accumulation after the third methanol treatment at 138 cc/hr and 1,200 psig.

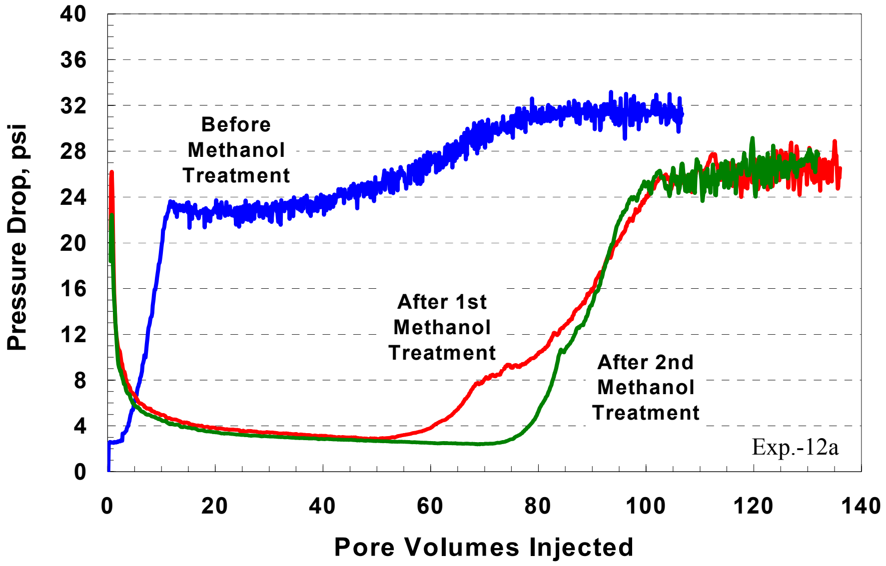

Figure B.103: Pressure drop across Berea core during condensate accumulation before and after methanol treatments at 600 cc/hr and 12,00 cc/hr.

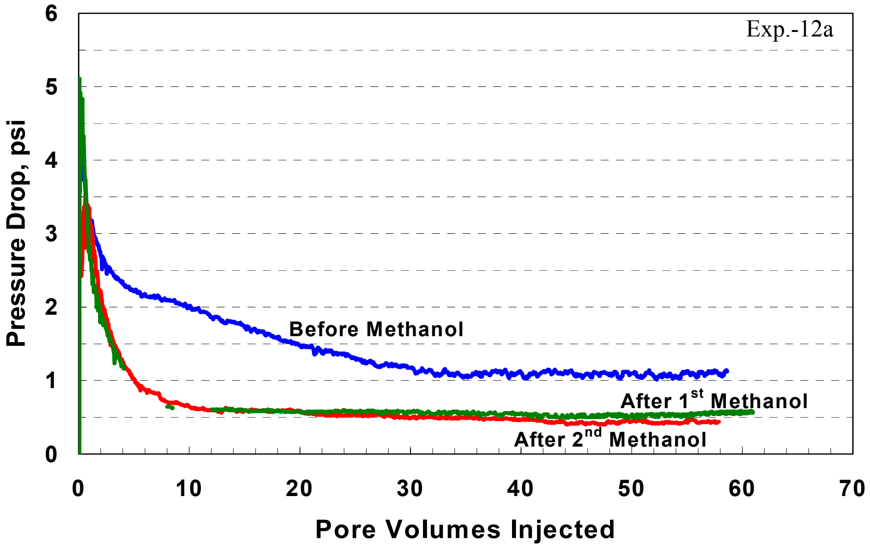

Figure B.104: Pressure drop across the core during equilibrium gas flow before and after methanol treatments at 600 cc/hr and 1,200 psig.

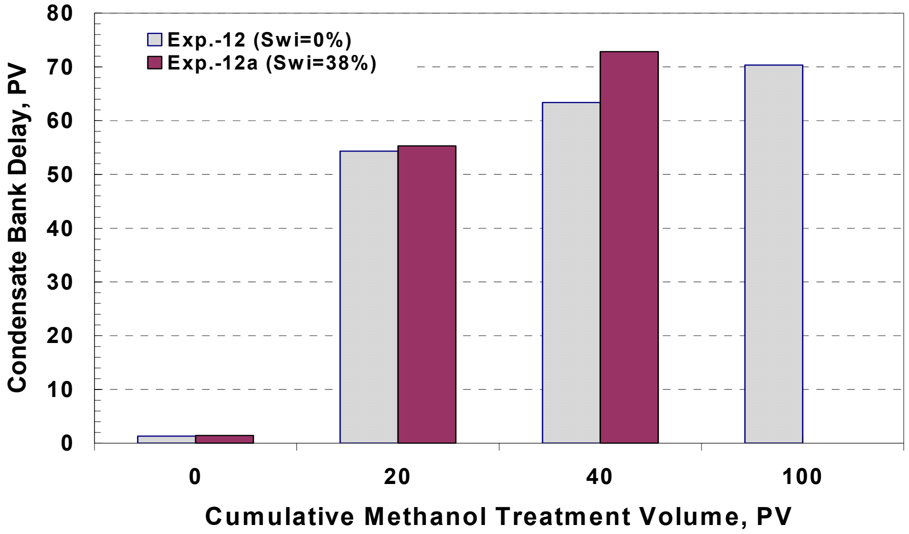

Figure B.105: Effect of methanol treatment volume on condensate bank delay in Berea cores.

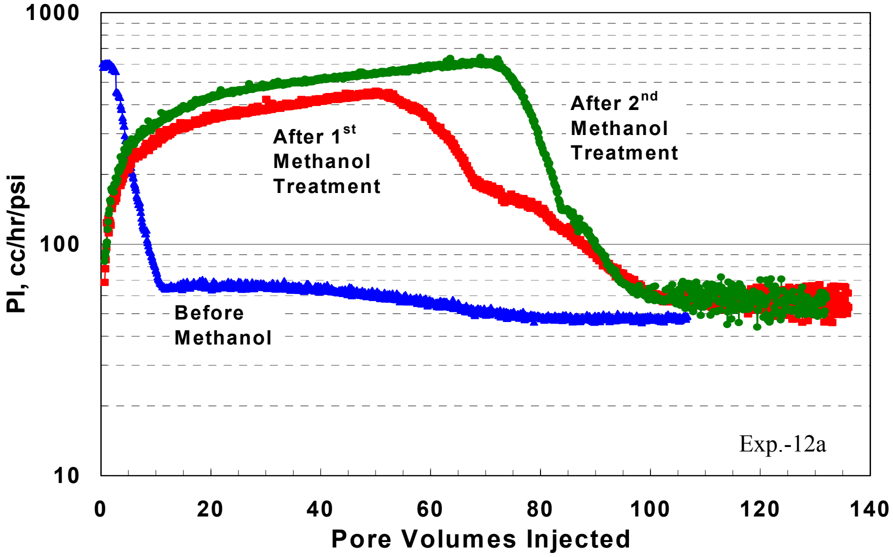

Figure B.106: Effect of methanol treatment on the productivity index (PI) profile in Berea cores.

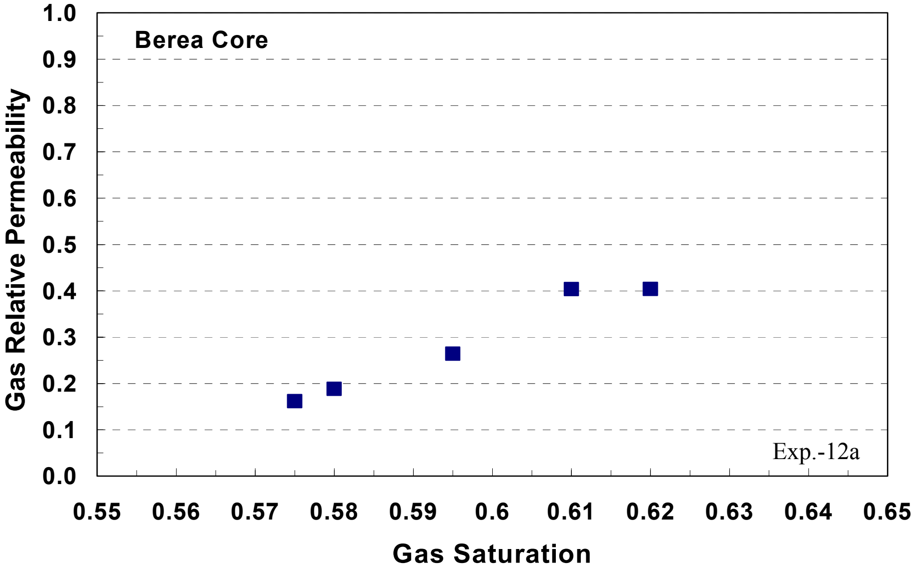

Figure B.107: Gas-water relative permeability data for Berea sandstone core.

B.8 Coreflood Experiment No. 13

B.8.1 Objective

The objective of this experiment is to investigate the effect of multi-stage treatment of methanol on the relative permeability of gas after gas-condensate accumulation in a low permeability core in the presence of high water saturation. This experiment was performed on a core from Texas Cream limestone. This experiment is a repeat for Experiment-5 to improve the quality of the obtained results.

B.8.2 Core Preparation

A core plug sample with a diameter of 0.972 inches and a length of 8.01 inches was drilled from a Texas Cream limestone block. The core was dried in an oven at 95°C for more than 2 weeks. The core was wrapped with an aluminum foil and a heat-shrink Teflon to prevent diffusion of gases through the sleeve rubber. The wrapped core was placed into a Phoenix core-holder inside HTHP oven at 145°F. After 4 hours, an axial pressure was applied by screwing the end pieces of the core-holder. Then, an overburden pressure of 3,400 psig was applied.

B.8.3 Initial Core Permeability Measurement

The initial core permeability was measured using methane at a flowing pressure of 1,200 psig before introducing the water saturation. The pressure of both the upstream and downstream back-pressure regulators was set to 1,200 psig. Methane gas was flowed at various rates. Two pressure transducers were used to measure the differential pressure across the core. **Figure B.108** shows the pressure drop across the core during the flow of methane at 1,200 psig. **Table B.83** gives the initial core permeability value to methane measured at a flowing pressure of 1,200 psig and various flow rates. The initial core permeability at S_g=100% was taken from an average value of 4.50 md.

B.8.4 Brine Flow at Atmospheric Pressure

A brine consists of 3wt% NaCl solution was flowed through the core at atmospheric pressure and 145°F. Initially, the core was vacuumed for 45 minutes. Then, brine was flowed through the core at two flow rates (132 and 69 cc/hr). The pressure drop profile is illustrated in **Figure B.109**. The measured brine permeability is very close to the initial value as given in **Table B.84**. This means that the brine saturated the core thoroughly since both single-phase permeability values are almost the same.

B.8.5 Methane Flow at 1200 psig

Methane gas was flowed at 1,200 psig through the core to displace water and reduced it to residual saturation. When the pressure drop across the core stabilized, flow rate was changed to a higher value and the corresponding saturation was measured. The flow rate was varied in the following sequence: 99, 132, 195, and 228 cc/hr. **Figure B.110** shows the pressure drop across the core during this stage. Effluents were collected using a fraction collector that was set to collect effluent each 1 minute during the flow of methane at 99 cc/hr. **Figure B.111** depicts the cumulative water volume produced during flow of methane at 99 cc/hr. The cumulative water produced increased with flow rate. **Table B.85** gives the gas relative permeabilities at different water saturations measured during water displacement by methane flooding. The residual water saturating (S_{wr}) at the end of this stage reached a value of 53.96%. From these data, a relative permeability curve for this core was generated as shown in **Figure B.112**.

B.8.6 Condensate Accumulation (Two-Phase Flow)

Before the start of this stage, the inlet and outlet valves of the core were closed. Pressure of the downstream back-pressure regulator was decreased to 1,200 psig, while the pressure in the upstream back-pressure regulator was kept at 3,000 psig. Flow was started while the bypass valve was open until the pressure in the lines stabilized. Then, the bypass valve was closed and inlet and outlet valves were open simultaneously. The flow rate was 60 cc/hr. This stage allowed the gas-condensate to dynamically accumulated through the core. This simulates the condensate bank in the wellbore region. The stage was stopped when the pressure drop across the core reached stable values. **Figure B.113** shows the pressure drop across the core during two-phase flow. The pressure drop was gradually increased until it reached a plateau value of 196 psia. This trend is similar to those observed in the previous experiments. The measured gas and oil relative permeabilities during condensate accumulation are given in **Table B.86**.

Data needed to calculation relative permeability for gas and oil phases (μ_g=0.01396 cp, μ_o=0.23711 cp) were obtained using PREOS and UTCOMP. In this experiment, the gas relative permeability reduced by 96% due to condensate accumulation in the presence of residual water saturation.

B.8.7 Equilibrium Gas Flooding

The pressure in the upstream back-pressure regulator was decreased to 1,200 psig. An Equilibrium gas, which is the gas-phase of the gas-mixture at a pressure of 1,200 psig (below dewpoint), was injected through the core at a flow rate of 99 cc/hr. The pressure drop across the core is shown in **Figure B.114**. This stage gives the gas end-point relative permeability (k^o_{rg}) before methanol treatment as given in **Table B.87**. This stage results in an increase in the gas end-point relative permeability due to displacement of condensate from the core.

B.8.8 The First Stage of Methanol Treatment

Pure methanol was injected through the core at an injection rate of 99 cc/hr and 1,200 psig. The volume of methanol injected was 20 PV. The pressure drop across the core stabilized at a value 131.6 psia as shown in **Figure B.115**. The measured permeability to methanol was found to be 4.39 md which is close to the initial core permeability. Thus, the methanol was effective to remove both residual water and condensate from the core.

B.8.9 Two-Phase Flow After the First Stage of Methanol Treatment

The pressure of the upstream back-pressure regulator was increased to 3,000 psig, while the pressure of the downstream back-pressure regulator was kept at 1,200 psig. The rate of this stage was 60 cc/hr. The gas mixture was flashed through the core to bank condensate. **Figure B.116** depicts the pressure drop across the core during this stage. This figure indicates that the pressure drop across the core started to increase after an injection of 52.96 PV of the two-phase. The pressure drop profile shows the same trend as the two-phase flow before methanol. The first methanol treatment was effective in delaying the condensate banking and gave an enhanced flow period of 52.96 PV where the pressure drop reached a minimum value. After that, the pressure drop started to increase due to the accumulation of condensate and the depletion of methanol-rich phase. The measured two-phase relative permeabilities are given in **Table B.88**.

B.8.10 Equilibrium Gas After the First Methanol Treatment

The pressure of the upstream back-pressure regulator was decreased to 1,200 psig. The equilibrium gas was injected at a flow rate of 99 cc/hr. **Figure B.117** shows the pressure drop across the core. This stage gives the gas end-point relative permeability after methanol injection, as given in **Table B.89**. The first stage of methanol increased the gas relative permeability by 54.8%. The most important finding is that the methanol delayed the condensate bank that expected to take place after the post-treatment production period.

B.8.11 The Second Stage of Methanol Treatment

Pure methanol was injected, as the second treatment, through the core at an injection rate of 99 cc/hr and 1,200 psig. The volume of methanol injected was 20 PV. The pressure drop across the core reached a value of 135.31 psia which is close to that for the first treatment. **Figure B.118** depicts the pressure drop across the core during the second treatment of methanol. The measured permeability for this stage of methanol was found equal to 4.27 md.

B.8.12 Two-Phase Flow After the Second Stage of Methanol Treatment

The pressure of the upstream back-pressure regulator was increased to 3,000 psig, while the pressure of the downstream back-pressure regulator was kept at 1,200 psig. The two-phase was flowed at two rates: 60 and 42 cc/hr, respectively. **Figure B.119** depicts the pressure drop across the core during this stage. This figure shows the same behavior as the two-phase before methanol treatment. This figure implies that the pressure drop across the core started to increase after an injection of 71.9 PV. This means that the second methanol treatment extended the enhanced flow period by a factor of 1.36 relative to the first treatment. The results are given in **Table B.90**. Therefore, more injection of methanol would stay for longer time during the post-treatment production period and result in high gas productivity.

B.8.13 Equilibrium Gas After the Second Methanol Treatment

The pressure of the upstream back-pressure regulator was decreased to 1,200 psig. The equilibrium gas was injected at a flow rate of 99 cc/hr. **Figure B.120** shows the pressure drop across the core. This stage gives the gas end point relative permeability after methanol injection, as given in **Table B.91**. The second stage of methanol increased the gas relative permeability by 37.7%. The improvement obtained after the second treatment of methanol is less than the first one. This is because the flow might not enough to restore the flow permeability. Multi-stage treatment of methanol will be more effective to enhance the productivity of gas wells, particularly when the bottom hole flowing pressure fell below the dewpoint pressure.

B.8.14 Summary of the Results for Coreflood Experiment-13

Gas relative permeability was decreased by more than 96% due to condensate accumulation. The reduction becomes severe in the presence of high water saturation. Multi-stage of methanol treatment was effective to enhance the reduced gas relative permeability. The removal of residual methanol by evaporation is a very slow process. Therefore, it stays for a longer time in the core. The residual methanol improves the productivity by postponing the accumulation of condensate. Methanol stages helped to delay the condensate buildup following the treatment as shown in **Figure B.121**. As can be seen, increasing the volume of methanol treatment yielded a more production time for gas after the treatment before countering the subsequent condensate banking. Gas and oil relative permeabilities during the enhanced flow period are given in **Table B.92**. The productivity of gas increased by an order of magnitude during the enhanced flow period. Methanol helped to remove condensate by a miscible displacement and did not cause damage to the core. **Table B.93** lists gas and oil relative permeabilities at steady state during condensate accumulation before and after methanol treatment. Methanol treatment also increased the gas end-point relative permeability as shown in **Figure B.122**.

Table B.83: Initial core permeability measured during methane flow at 1,200 psig and various flow rates.

q, cc/hr	ΔP, psia	k, md
195	10.84	4.49
44.8	2.60	4.29
69	3.64	4.75
132	7.31	4.51

Table B.84: Core permeability to brine (3wt% NaCl) at atmospheric pressure.

q, cc/hr	ΔP, psia	k_w, md
132	224.25	4.57
69	119.45	4.49

Table B.85: Gas relative permeability measured during brine displacement with methane at 1,200 psig.

q, cc/hr	ΔP, psia	k_g, md	k_{rg}	S_{wr}, %
99	21.87	1.13	0.25	55.45
132	27.24	1.21	0.27	54.95
195	36.46	1.33	0.30	54.46
228	40.25	1.41	0.31	53.96

Table B.86: Gas and oil relative permeabilities measured during condensate accumulation stage before methanol treatment at 60 cc/hr and 1200 psig.

	$\Delta P_{Total-1}$
ΔP, psia	196.45
k_{rg}	0.04
k_{ro}	0.05

Table B.87: Gas end-point relative permeability measured during equilibrium gas flow before methanol treatment at 99 cc/hr and 1,200 psig.

	$\Delta P_{Total-1}$	$\Delta P_{Total-2}$
ΔP, psia	11.27	11.49
k_g, md	2.43	2.38
k^o_{rg}	0.540	0.529

Table B.88: Gas and oil relative permeabilities measured during condensate accumulation after the first methanol treatment at 60 cc/hr and 1,200 psig.

	$\Delta P_{Total-1}$
ΔP, psia	132.44
k_{rg}	0.06
k_{ro}	0.08

Table B.89: Gas end-point relative permeability measured during equilibrium gas flow after the first methanol treatment at 99 cc/hr and 1,200 psig.

	$\Delta P_{Total-1}$	$\Delta P_{Total-2}$
ΔP, psia	7.21	7.42
k_g, md	3.80	3.69
k^o_{rg}	0.843	0.819

Table B.90: Gas and oil relative permeabilities measured during condensate accumulation after the second methanol treatment at 1,200 psig.

	q = 60 cc/hr	q = 42 cc/hr
ΔP, psia	121.41	90.47
k_{rg}	0.07	0.06
k_{ro}	0.09	0.08

Table B.91: Gas end-point relative permeability measured during equilibrium gas flow after the second methanol treatment at 99 cc/hr and 1,200 psig.

	$\Delta P_{Total-1}$	$\Delta P_{Total-2}$
ΔP, psia	8.52	8.34
k_g, md	3.21	3.28
k^o_{rg}	0.713	0.729

Table B.92: Gas and oil relative permeabilities measured during the enhanced flow period.

	Before Methanol	After 1st Methanol	After 2nd Methanol
k_{rg}	0.04	0.46	0.43
k_{ro}	0.05	0.61	0.56
k^{o}_{rg}	0.529	0.819	0.729

Table B.93: Gas and oil relative permeabilities measured at steady state during condensate accumulation at 60 cc/hr and 1,200 psig.

	Before Methanol	After 1st Methanol	After 2nd Methanol
k_{rg}	0.04	0.06	0.07
k_{ro}	0.05	0.08	0.09
k^{o}_{rg}	0.529	0.819	0.729

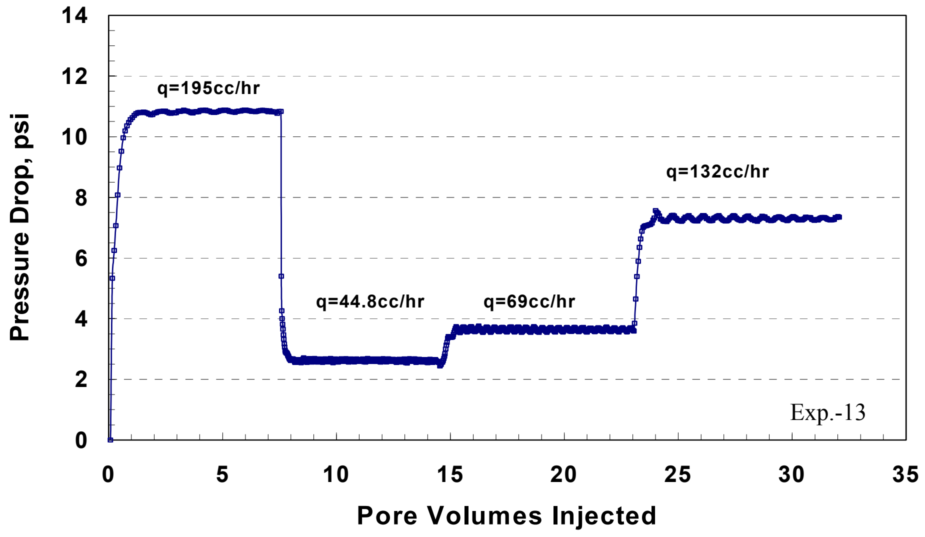

Figure B.108: Pressure drop across the core during methane flow at 1,200 psig.

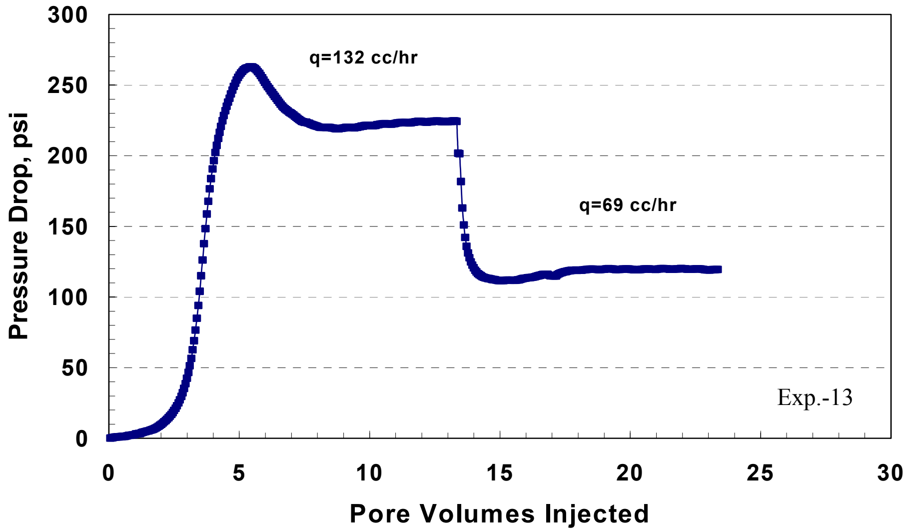

Figure B.109: Pressure drop across the core during flow of brine (3wt% NaCl) at atmospheric pressure and 145°F.

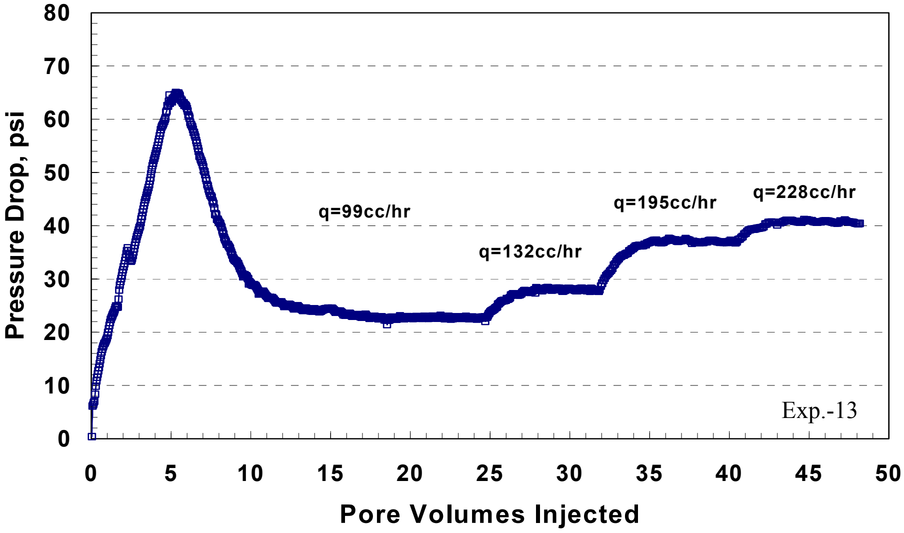

Figure B.110: Pressure drop across the core during displacement of brine by methane flow at 12,00 psig and various flow rates.

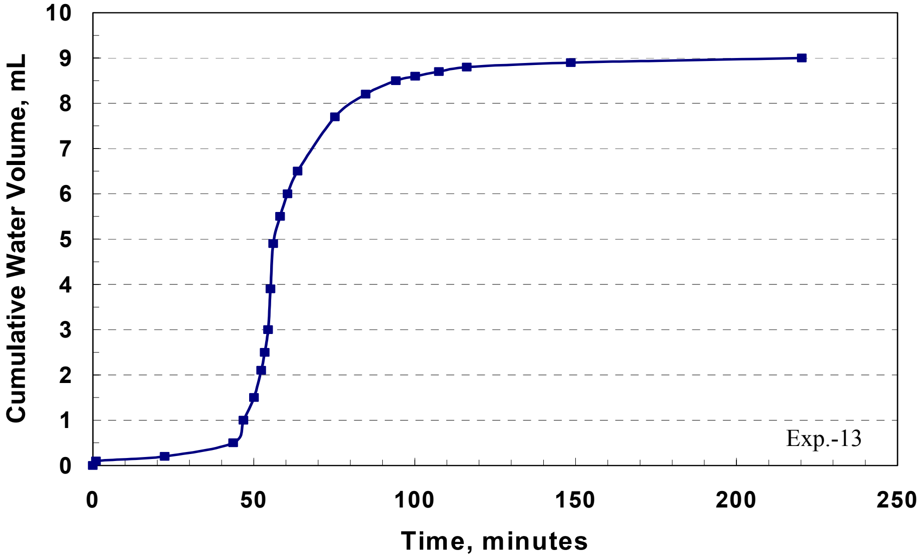

Figure B.111: Cumulative water volume collected in the core effluent during the displacement of brine by methane at 99 cc/hr and 1,200 psig.

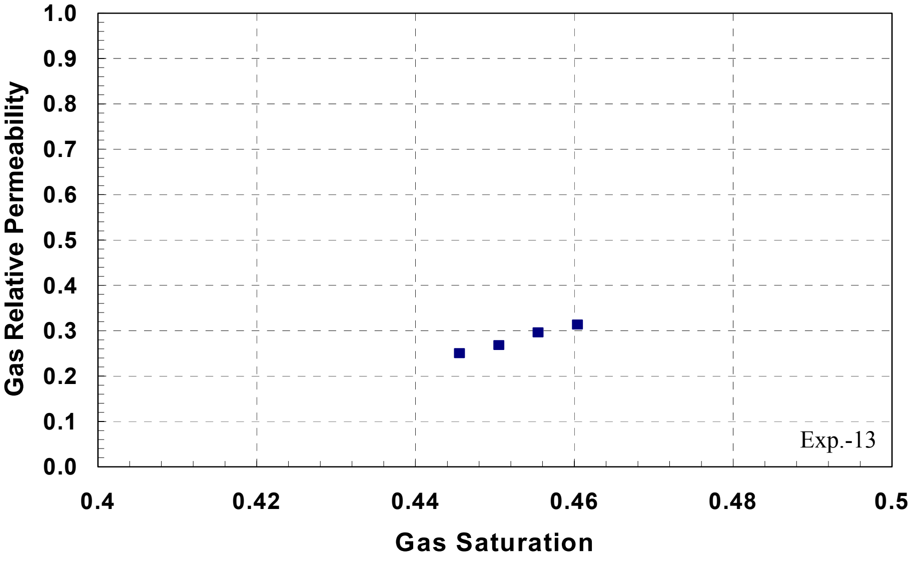

Figure B.112: Gas-water relative permeability data for Texas Cream limestone core.

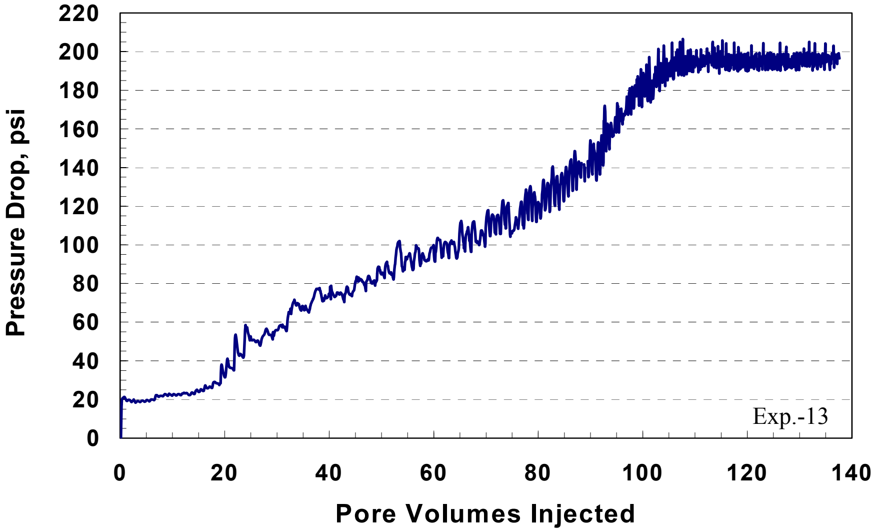

Figure B.113: Pressure drop across the core during condensate accumulation before methanol treatment at 60 cc/hr and 1,200 psig.

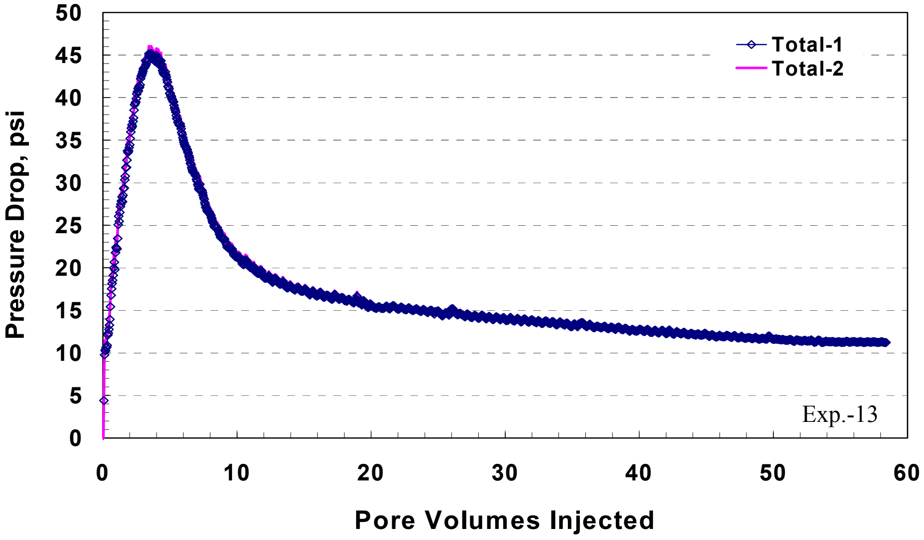

Figure B.114: Pressure drop across the core during equilibrium gas flow before methanol treatment at 99 cc/hr and 1,200 psig.

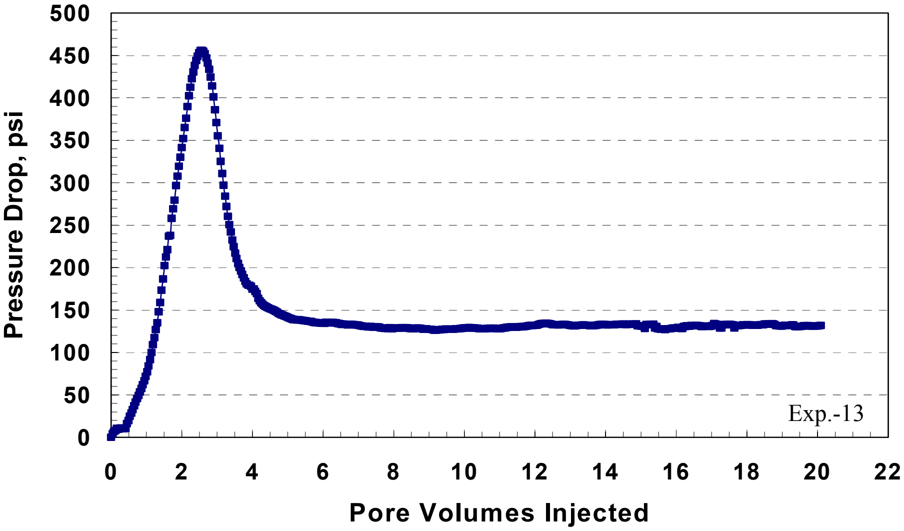

Figure B.115: Pressure drop across the core during the first methanol treatment at 99 cc/hr and 1,200 psig.

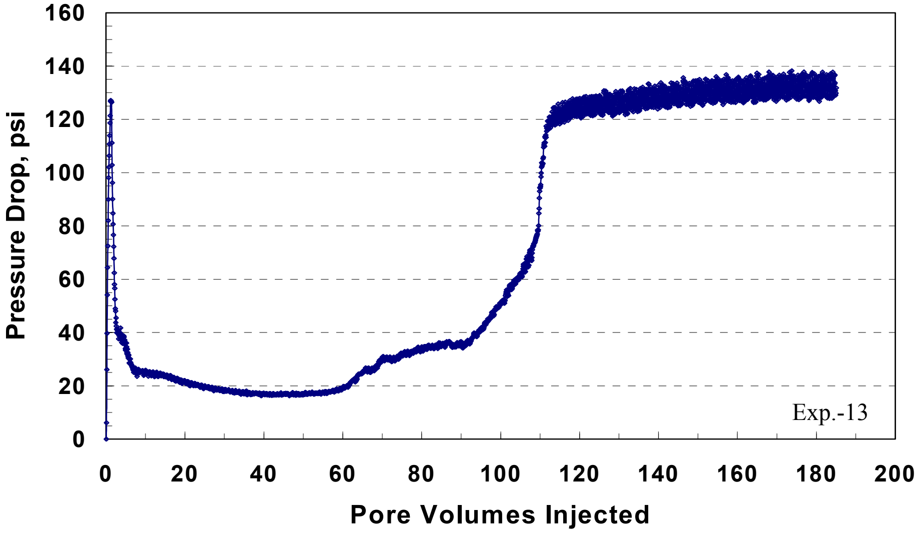

Figure B.116: Pressure drop across the core during condensate accumulation after the first methanol treatment at 60 cc/hr and 1,200 psig.

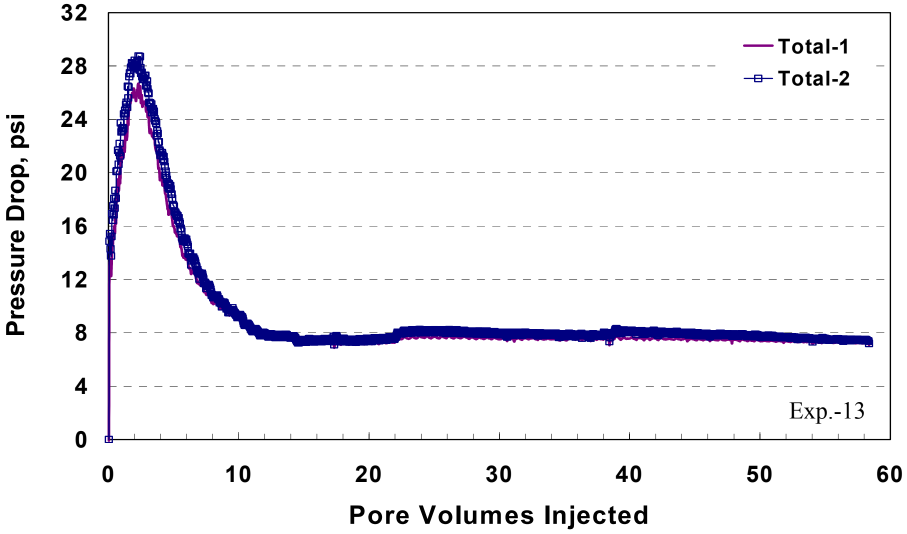

Figure B.117: Pressure drop across the core during equilibrium gas flow after the first methanol treatment at 99 cc/hr and 1,200 psig.

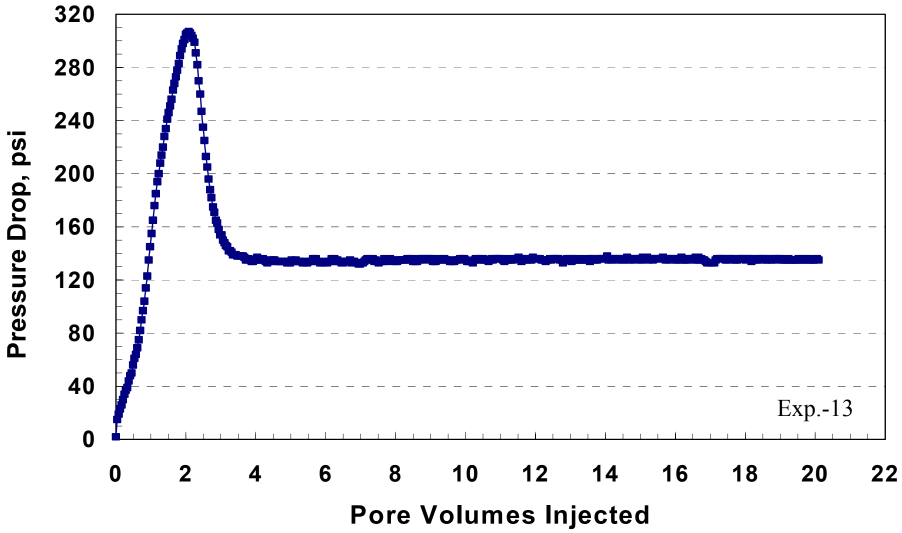

Figure B.118: Pressure drop across the core during the second methanol treatment at 99 cc/hr and 1,200 psig.

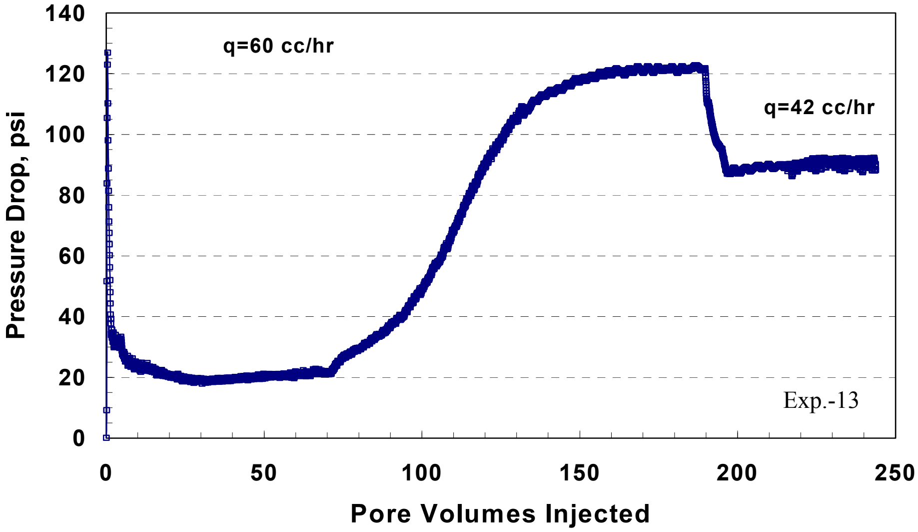

Figure B.119: Pressure drop across the core during condensate accumulation after the second methanol treatment at 1,200 psig.

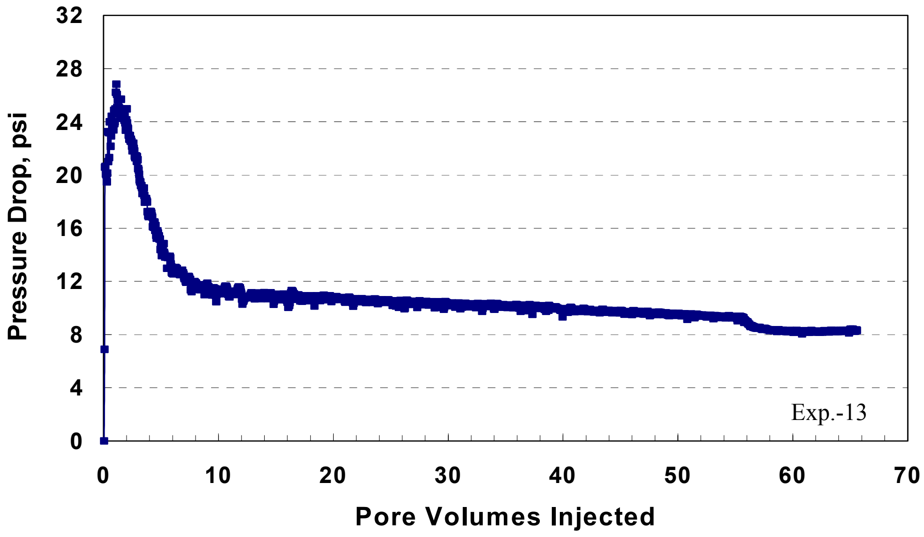

Figure B.120: Pressure drop across the core during equilibrium gas flow after the second methanol treatment at 99 cc/hr and 1,200 psig.

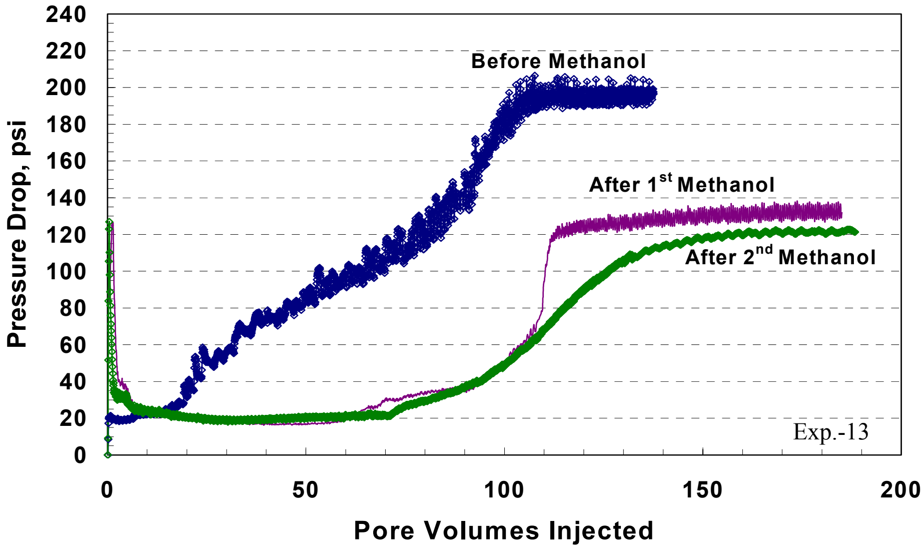

Figure B.121: Pressure drop across the core during condensate accumulation before and after methanol treatments at 60 cc/hr and 1,200 psig.

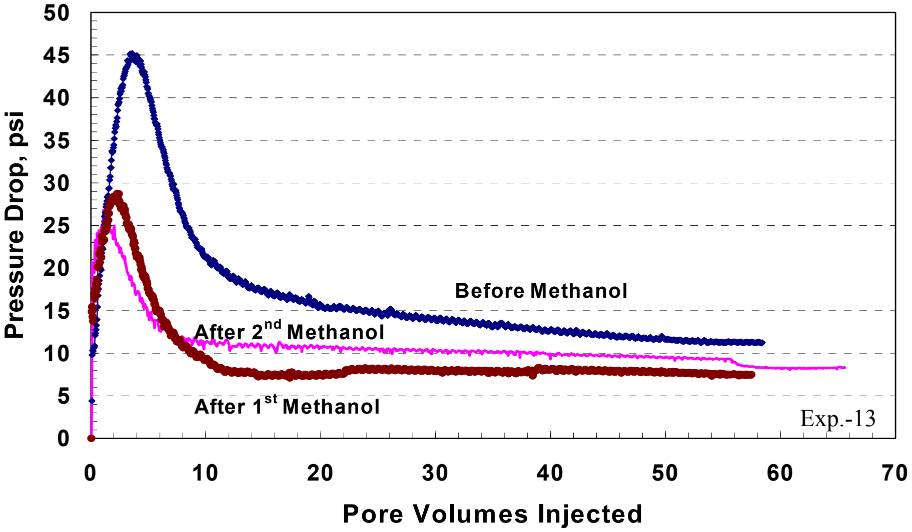

Figure B.122: Pressure drop across the core during equilibrium gas flow before and after methanol treatments at 99 cc/hr and 1,200 psig.

B.9 Coreflood Experiment No. 14

B.9.1 Objective

The objective of this experiment is to investigate the effect of flow rate on condensate accumulation. This experiment was performed on a core from Texas Cream limestone. There is no water present in the core.

B.9.2 Core Preparation

A core sample with a diameter of 0.972 inches and a length of 8.01 inches was drilled from Texas Cream limestone block. The core was dried in an oven at 95°C for more than 4 weeks. The core was wrapped with an aluminum foil and a heat-shrink Teflon to prevent diffusion of gases through the sleeve rubber. The wrapped core was placed into a Phoenix core-holder inside HTHP oven at 145°F. After 4 hours, an axial pressure was applied by screwing the end pieces of the core-holder. Then, an overburden pressure of 3,400 psig was applied.

B.9.3 Initial Core Permeability

The initial core permeability was measured using methane at a flowing pressure of 3,000 psig. The pressure of both the upstream and downstream back-pressure regulators was set to 3,000 psig. Methane gas was flowed at three different flow rates (90, 102, and 132 cc/hr). Two pressure transducers were used to measure the differential pressure across the core. **Figure B.123** shows the pressure drop across the core during the flow of methane at 3,000 psig. **Table**

B.94 gives the measured initial core permeability values to methane at a flowing pressure of 3,000 psig and different flow rates. The initial core permeability at S_g=100% was taken from an average value of 4.43 md.

B.9.4 Gas Mixture (Single-Phase) Flow

The gas mixture (single-phase) was flowed through the core at a pressure (e.g. 3,000 psig) above the dewpoint. Two flow rates: 99 and 132 cc/hr were used. **Figure B.124** shows the pressure drop across the core during gas mixture (single-phase) flooding. The core permeabilities measured during gas mixture flow are given in **Table B.95**. The obtained value of permeability is very close to the initial core permeability. This assures that the gas mixture flowed through the core as a single phase and was prepared correctly.

B.9.5 Condensate Accumulation (Two-Phase Flow)

Before the start of this stage, the inlet and outlet valves of the core were closed. Pressure of the downstream back-pressure regulator was decreased to 1,200 psig, while the pressure in the upstream back-pressure regulator was kept at 3,000 psig. Flow was started while the bypass valve was open until the pressure in the lines stabilized. Then, the bypass valve was closed and inlet and outlet valves were open simultaneously. This stage allowed the gas-condensate to dynamically accumulated through the core. This simulates the condensate bank in the wellbore region. The stage was stopped when the pressure drop across the core reached stable values. The initial flow rate was 6 cc/hr. Then, the flow rate was increased when the pressure drop reached a stabilized value. **Figure B.125** shows the pressure drop across the core during two-phase flow at 1,200 psig. The pressure drop was gradually increased until it reached a plateau value after 16.5 PV. This result confirms that condensate accumulation is a rate dependant. As the flow rate decreases, it reaches a steady state faster. Therefore, there is non-equilibrium effect that changes the phase behavior of the gas mixture.

Gas and oil relative permeabilities are given in **Table B.96**. As can be seen, the gas relative permeability reduced by 93% due to condensate accumulation. Even though condensate was accumulated at a lower rate (6 cc/hrs), it severely reduced gas productivity as those at higher flow rates.

B.9.6 Summary of the Results for Coreflood Experiment-15

Gas relative permeability was decreased by more than 93% due to condensate accumulation. The condensate accumulation shows a rate dependant. As the flow rate decreases, the condensate bank formed faster. In other words, it requires less pore volumes to reach a steady state than that accumulated at higher rates.

Table B.94: Initial core permeability measured during methane flow at 3,000 psig.

q, cc/hr	ΔP, psia	k, md
90	6.30	4.71
102	8.13	4.13
132	9.74	4.46

Table B.95: Core permeability measured during flow of gas mixture (single-phase) at 3,000 psig.

q, cc/hr	ΔP, psia	k_g, md
90	15.28	4.13
132	20.30	4.14

Table B.96: Gas and oil relative permeabilities measured during condensate accumulation stage at 1,200 psig and various flow rates.

q, cc/hr	ΔP, psia	k_{rg}	k_{ro}
6	10.50	0.078	0.101
12	22.26	0.073	0.096
20	38.00	0.072	0.093

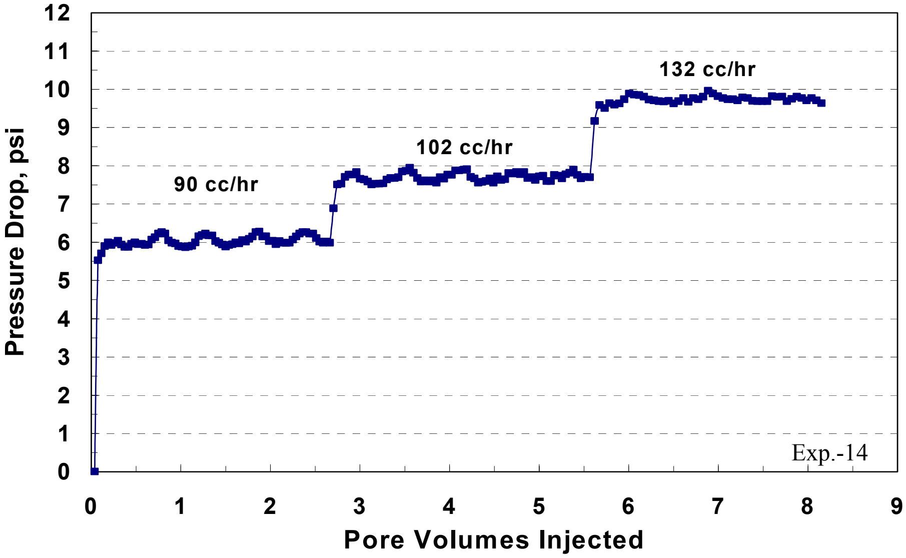

Figure B.123: Pressure drop across the core during methane flow at various flow rates and 3,000 psig.

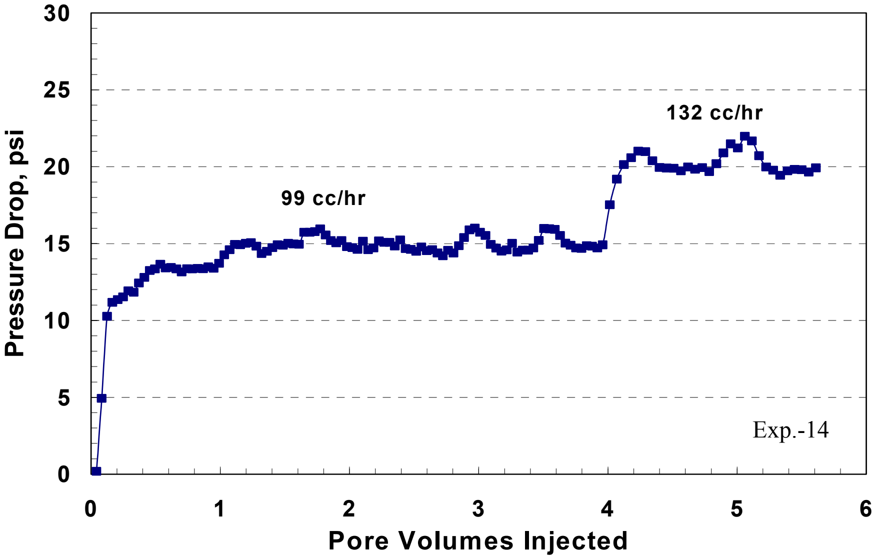

Figure B.124: Pressure drop across the core during gas mixture (single-phase) flow at 3,000 psig and different flow rates.

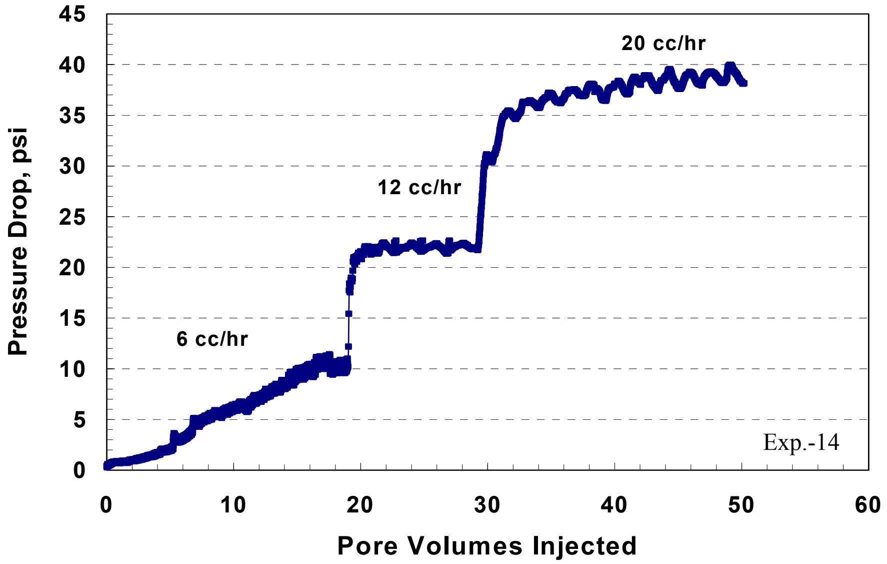

Figure B.125: Pressure drop across the core during dynamic condensate accumulation at 1,200 psig and different flow rates.

B.10 Coreflood Experiment No. 15

B.10.1 Objectives

The objectives of this experiment are: (1) to investigate the propagation of condensate bank through the core, (2) to study the effect of flow rate on condensate accumulation, and (3) to measure the dynamic fractional flow of both gas and oil phases at the steady state of two-phase flow. This experiment was performed on a core from Texas Cream limestone.

B.10.2 Core Preparation

A core plug sample with a diameter of 0.972 inches and a length of 8.01 inches was drilled from a Texas Cream limestone block. The core was dried in an oven at 95°C for more than 5 weeks. The core was wrapped with an aluminum foil and a heat-shrink Teflon to prevent diffusion of gases through the sleeve rubber. The wrapped core was placed inside a Phoenix core holder provided with multiple pressure ports that divide the core into four sections (2 inches in length each). An axial pressure was applied by screwing the end pieces of the core holder. Then, an overburden pressure of 3,400 psig was applied. Holes were drilled through the pressure tabs to open holes through the aluminum foil and the Teflon to allow gas flow from the core to the designated pressure tab. Four pressure transducers were connected to measure pressure drop across each section of the core, in addition to two pressure transducers to measure the total pressure drop across the whole core. The core holder was placed inside the oven at 145°F.

A windowed-PVT cell was installed in-line downstream of the core. The aim of installing the PVT cell is to measure the fractional flow of both gas and oil phases during two-phase flow through the experiment.

B.10.3 Initial Core Permeability

The initial core permeability was measured using methane at a flowing pressure of 3,000 psig. The pressure of both the upstream and downstream back-pressure regulators was set to 3,000 psig. Methane gas was flowed at two flow rates: 69 and 99 cc/hr. Four pressure transducers were used to measure the differential pressure across each section of the core. **Figure B.126** shows the pressure drop at different sections of the core during the flow of methane at 3,000 psig. **Table B.97** gives the measured initial core permeability values to methane at a flowing pressure of 3,000 psig. The variation of the measured permeability between the sections of the core indicates the heterogeneity of the core.

B.10.4 Gas Mixture (Single-Phase) Flow

The gas mixture (single-phase) was flowed through the core at a pressure (e.g. 3,000 psig) above the dewpoint. The single phase flowed through the core at a rate of 48 cc/hr. **Figure B.127** shows the pressure drop at different sections of the core during gas mixture (single-phase) flow at 3,000 psig. The measured core permeability values are given in **Table B.98**. The obtained values of permeability are very close to the initial core permeabilities measured with methane at 3,000 psig. This assures that the gas mixture flowed through the core as a single-phase and was prepared correctly.

B.10.5 Condensate Accumulation

Before the start of this stage, the inlet and outlet valves of the core were closed. Pressure of the downstream back-pressure regulator was decreased to 1,200 psig, while the pressure in the upstream back-pressure regulator was kept at 3,000 psig. Flow was started while the bypass valve was open until the pressure in the lines stabilized. Then, the bypass valve was closed and inlet and outlet valves were open simultaneously. This stage allowed the gas-condensate to dynamically accumulated through the core. This simulates the condensate bank in the wellbore region. The stage was stopped when the pressure drop across the core reached stable values. The flow rate was 18 cc/hr.

Figure B.128 shows the pressure at different sections across the core during condensate accumulation at 1,200 psig. The pressure drop in the first section was gradually increased until it reached a plateau value after 4.0 PV. Then, the pressure drop in section-2 started to increase. Therefore, the condensate bank propagates through each section until it reaches a steady state. The pressure drop in each section of the core took about 4.0 PV to reach a stabilized value. The condensate accumulation in the whole core reached a steady state after 16 PV. These results indicate that the condensate accumulation strongly depends on the flow rate. Therefore, non-equilibrium effect exists during the two-phase flow.

Gas and oil relative permeabilities measured during condensate accumulation are given in **Table B.99**. Condensate accumulation caused a severe damage to the core where the gas and oil relative permeabilities decreased to 0.165 and 0.215, respectively.

B.10.6 Dynamic Liquid Drop-out Measurements

Dynamic fractional flow of both gas and oil phases were measured using the windowed-PVT cell. When the pressure drop across the core during two-phase flow reached a steady state value, the core effluents were flowed through the PVT cell. The oil phase accumulates into the bottom of the cell, while the gas phase flow out from the top the cell. The volume of the accumulated oil was measured by recording the change in the height level as a function of time using a Cathetometer that has an accuracy of ±0.01 cm. The gas effluent from the PVT cell was connected to an accumulator that filled with water. The volume of displaced water is corresponding to the gas volume since the accumulator at 1,200 psig and 145°F. The displaced water was collected using a fractional collector.

Figure B.129 shows the cumulative hydrocarbon (HC) liquid volume collected during two-phase flow as a function of time at 1,200 psig and a pump rate of 18 cc/hr. This shows a linear relationship, where the flow rate is equal to the slop of the line. The measured flow rate of the gas phase was found to be 0.0378 mL/min. Cumulative volume of water displaced by gas during two-phase flow at steady state at 1,200 psig and 18 cc/hr is shown in **Figure B.130** as a function of time. This also shows a linear relationship between the cumulative volume of displaced water and time. Thus, the flow rate of the gas phase is equal to the slop of the line which was calculated as 0.6984 mL/min using a linear regression. The dynamic fractional flow factor of the oil phase was found equal to 5.13%. The measured dynamic liquid drop out is close to that measured from the CCE (static test) and calculated with EOS (7.14%). From **Figure B.128**, the fractional flow factor is around 6% since it took 16 PV of two-phase flow to reach a steady state. The small difference between the measured dynamic and static values is acceptable within the experimental errors.

B.10.7 Equilibrium Gas Flooding

The pressure in the upstream back-pressure regulator was decreased to 1,200 psig. An equilibrium gas, which is the gas phase of the gas-mixture at a pressure of 1,200 psig (below dewpoint), was injected through the core at a flow rate of 99 cc/hr. The pressure drop across the core during equilibrium gas flow is shown in **Figure B.131**. This stage gives the gas end-point relative permeability (k^o_{rg}) before methanol treatment, as given in **Table B.100**. This stage results in an increase in the end-point gas relative permeability due to displacement of condensate from the core. However, the residual condensate reduced the gas end-point relative permeability to 0.577.

B.10.8 The First Stage of Methanol Treatment

Pure methanol was injected through the core at an injection rate of 99 cc/hr and 1,200 psig. The volume of methanol injected was 20 PV. The pressure drop across the core stabilized at a value 164.1 psia as shown in **Figure B.132**. The calculated permeability for methanol was found equal to 3.52 md, which is close to the initial core permeability. Thus, the methanol was effective to remove condensate from the core.

B.10.9 Condensate Accumulation after the First Methanol Treatment

The pressure of the upstream back-pressure regulator was increased to 3,000 psig, while the pressure of the downstream back-pressure regulator was kept at 1,200 psig. The pump rate of this stage was 18 cc/hr. The gas mixture was flashed through the core to bank condensate. **Figure B.133** depicts the pressure drop at different sections across the core during this stage. However, some of the data was lost when the data acquisition program stopped while the flow continued overnight. Therefore, we cannot say if there is an enhanced flow period even though the pressure drop increased after the lost data period. Gas and oil relative permeabilities during this stage are given in **Table B.101**. The methanol treatment was effective to increase the gas and oil relative permeabilities by 13%. The pump rate (@ 3000 psig) was increased to 27 cc/hr when the steady state was reached. The rate of both oil and gas phases were measured at two different pump rates as shown in **Figures B.134** and **B.135**. The measured gas and oil flow rate during two-phase flow at 1,200 psig are given in

Table B.102. The fractional flow of gas phase was found to be 6.44 and 6.61% measured at a pump rate of 18 and 27 cc/hr, respectively. These values are in consistent with expected ones obtained from the CCE and EOS calculations.

B.10.10 Equilibrium Gas After the First Methanol Treatment

The pressure of the upstream back-pressure regulator was decreased to 1,200 psig. The equilibrium gas was injected at a flow rate of 99 cc/hr. **Figure B.136** shows the pressure drop across the core. This stage gives the gas end-point relative permeability after methanol injection, as given in **Table B.103**. The first stage of methanol increased the gas relative permeability a 17.5%.

B.10.11 The Second Stage of Methanol Treatment

Pure methanol was injected, as the second treatment, through the core at an injection rate of 20 cc/hr and 1,200 psig. This stage of methanol was flowed at a lower rate to increase the contact time between the injected methanol and the residual condensate. The volume of methanol injected was 20 PV. **Figure B.137** depicts the pressure drop across the core during the second treatment of methanol. The pressure drop across the core reached a value of 31.15 psia. The calculated permeability for this stage of methanol was found equal to 3.75 md.

B.10.12 Two-Phase Flow After the Second Stage of Methanol Treatment

The pressure of the upstream back-pressure regulator was increased to 3,000 psig, while the pressure of the downstream back-pressure regulator was kept at 12,00 psig. The two-phase was injected at a flow rate of 18 cc/hr. **Figure B.138** depicts the pressure drop across the core during this stage. This figure shows an enhanced flow period of 60 PV where the pressure drop reached a minimum value. Therefore, the second methanol treatment was effective compared to the first one. It seems that injecting methanol at lower rate may increase the methanol saturation in the core and miscibility of condensate. Gas and oil relative permeabilities during the enhanced flow period of two-phase flow are listed in **Table B.104**. The gas and oil relative permeabilities increased by a factor of 3.8 during the enhanced flow period. After the enhanced flow period had vanished, the pressure drop increased in each sections of the core due to the propagation of condensate bank. The delay in the post-treatment accumulation was because of the presence of a methanol-rich phase that inhibits condensate banking. Once the condensate accumulate after the evaporation of methanol-rich phase, the oil and gas relative permeabilities were reduced to those before the treatment, as given in **Table B.105**.

B.10.13 Equilibrium Gas After the Second Methanol Treatment

The pressure of the upstream back-pressure regulator was decreased to 1200 psig. The equilibrium gas was injected at a flow rate of 99 cc/hr. **Figure B.139** shows the pressure drop across the core. This stage gives the gas end-point relative permeability after methanol injection, as given in **Table B.106**. The second stage of methanol increased the gas end-point relative permeability by 60%. The improvement obtained after the second treatment of methanol is more than the first one. This means that the first methanol treatment was not sufficient to displace the condensate bank. Another possibility is that the injection rate of the first methanol was to high to clean the whole core from condensate. Multi-stage treatment of methanol will be more effectiveness to enhance the productivity of gas wells, particularly when the bottom hole flowing pressure fell below the dewpoint pressure.

B.10.14 Summary of the Results for Coreflood Experiment-15

Gas relative permeability was decreased by more than 84% due to condensate accumulation when the flowing pressure falls below the dewpoint. Multi-stage of methanol treatment was effective to enhance the reduced gas relative permeability. The removal of residual methanol by evaporation is a very slow process. Therefore, it stays for a longer time in the core and form an enhanced flow period where the gas productivity increased. The residual methanol improves the productivity by postponing the accumulation of condensate. Methanol stages helped to delay the condensate buildup following the treatment. The productivity of gas increased by an order of magnitude during the enhanced flow period. Methanol helped to remove condensate by a miscible displacement and did not cause damage to the core. **Table B.107** lists gas and oil relative permeabilities during condensate accumulation at steady state before and after methanol treatment. Methanol treatment increased the gas end-point relative permeability.

Table B.97: Initial core permeability measured using methane at 3,000 psig.

	Gas Permeability, md	
	q = 69 cc/hr	q = 99 cc/hr
Section-1	2.57	2.41
Section-2	4.49	4.50
Section-3	3.22	2.95
Section-4	4.01	3.83
Whole Core	3.14	2.94

Table B.98: Core permeability measured with gas mixture (single-phase) at a flow rate of 48 cc/hr and 3,000 psig.

	k_g, md
Section-1	2.40
Section-2	4.09
Section-3	2.79
Section-4	3.67
Whole Core	2.79

Table B.99: Gas and oil relative permeabilities measured during condensate accumulation stage at 1,200 psig and 18 cc/hr.

	ΔP, psia	k_{rg}	k_{ro}
Section-1	5.65	0.118	0.154
Section-2	3.25	0.204	0.266
Section-3	3.35	0.198	0.259
Section-4	3.93	0.169	0.221
Whole Core	16.13	0.165	0.215

Table B.100: Gas end-point relative permeability measured during equilibrium gas flow before methanol at 1,200 psig and 99cc/hr.

	ΔP, psia	k^o_{rg}
Section-1	2.91	0.479
Section-2	1.66	0.842
Section-3	2.11	0.659
Section-4	3.53	0.395
Whole Core	9.65	0.577

Table B.101: Gas and oil relative permeabilities measured during condensate accumulation after the first methanol treatment at 1,200 psig and 18 cc/hr.

	ΔP, psia	k_{rg}	k_{ro}
Section-1	5.93	0.112	0.146
Section-2	2.89	0.229	0.299
Section-3	3.14	0.212	0.276
Section-4	3.66	0.181	0.237
Whole Core	14.25	0.186	0.243

Table B.102: Measured gas and oil rates during two-phase flow at steady state at 1,200 psig and different pump rates.

Pump Rate, mL/hr	18	27
Gas Rate, mL/min	0.6431	0.9799
Oil Rate, mL/min	0.0443	0.0694
f_o, vol.%	6.44	6.61
f_g, vol.%	93.56	93.39

Table B.103: Gas end-point relative permeability measured during equilibrium gas flow after the first methanol treatment at 1,200 psig and 99 cc/hr.

	ΔP, psia	k^o_{rg}
Section-1	2.60	0.628
Section-2	1.77	0.925
Section-3	2.08	0.785
Section-4	3.62	0.452
Whole Core	9.57	0.684

Table B.104: Gas and oil relative permeabilities measured during the enhanced flow period of the two-phase after the second methanol treatment at 1,200 psig and 18 cc/hr.

	ΔP, psia	k_{rg}	k_{ro}
Section-1	1.39	0.478	0.624
Section-2	0.48	>1.0	>1.0
Section-3	0.89	0.746	0.974
Section-4	2.18	0.305	0.398
Whole Core	4.21	0.631	0.824

Table B.105: Gas and oil relative permeabilities measured during condensate accumulation at steady state after the second methanol treatment at 1,200 psig and 18 cc/hr.

	ΔP, psia	k_{rg}	k_{ro}
Section-1	11.22	0.059	0.077
Section-2	5.75	0.115	0.151
Section-3	5.96	0.111	0.145
Section-4	5.92	0.112	0.147
Whole Core	27.07	0.098	0.128

Table B.106: Gas end-point relative permeability measured during equilibrium gas flow after the second methanol treatment at 1,200 psig and 99 cc/hr.

	ΔP, psia	k^o_{rg}
Section-1	2.14	0.763
Section-2	1.30	1.258
Section-3	1.79	0.914
Section-4	2.45	0.668
Whole Core	7.12	0.918

Table B.107: Gas and oil relative permeabilities measured during condensate accumulation at steady state at 1,200 psig.

	Before Methanol	After 1st Methanol	After 2nd Methanol
k_{rg}	0.165	0.186	0.098
k_{ro}	0.215	0.243	0.128
k^{o}_{rg}	0.577	0.684	0.918

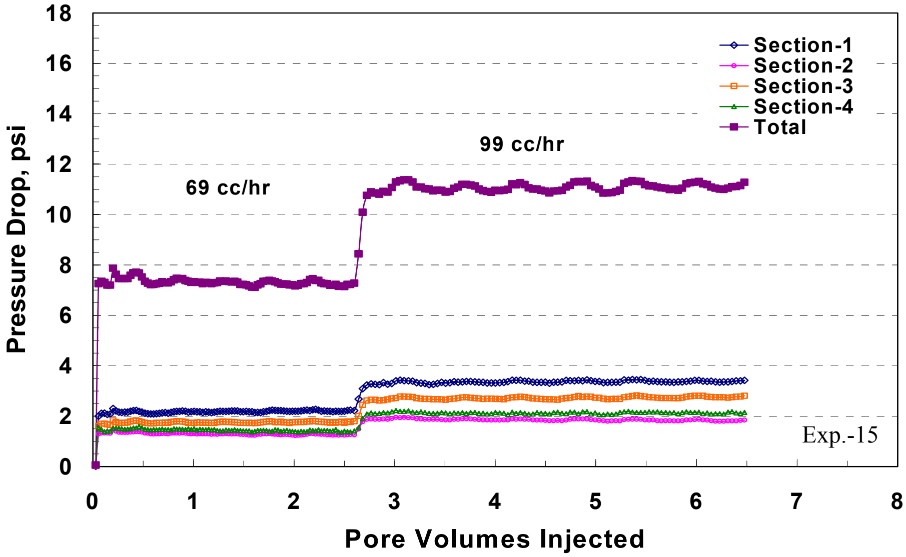

Figure B.126: Pressure drop at different sections across the core during methane flow at 3,000 psig and various rates.

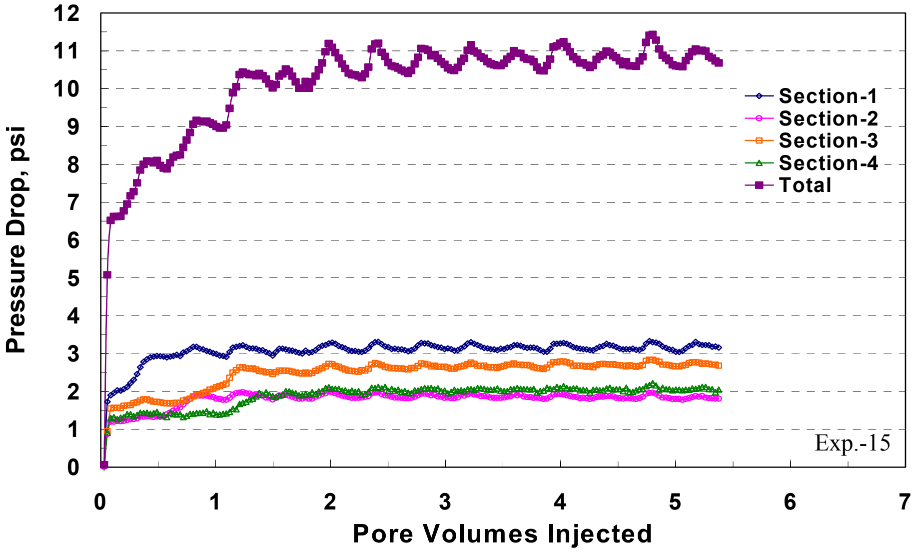

Figure B.127: Pressure drop at different sections across the core during gas mixture (single-phase) flow at 48 cc/hr and 3,000 psig.

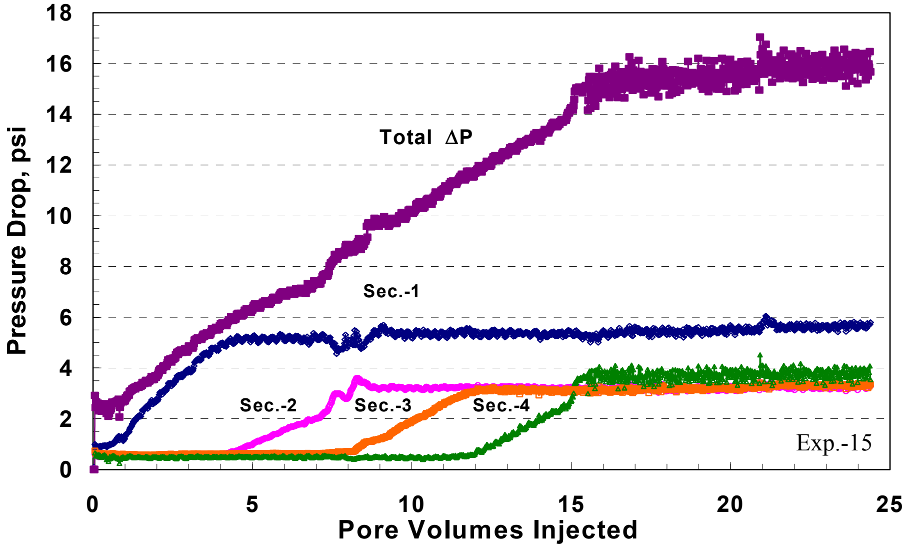

Figure B.128: Pressure drop at different sections across the core during condensate accumulation at 18 cc/hr and 1,200 psig.

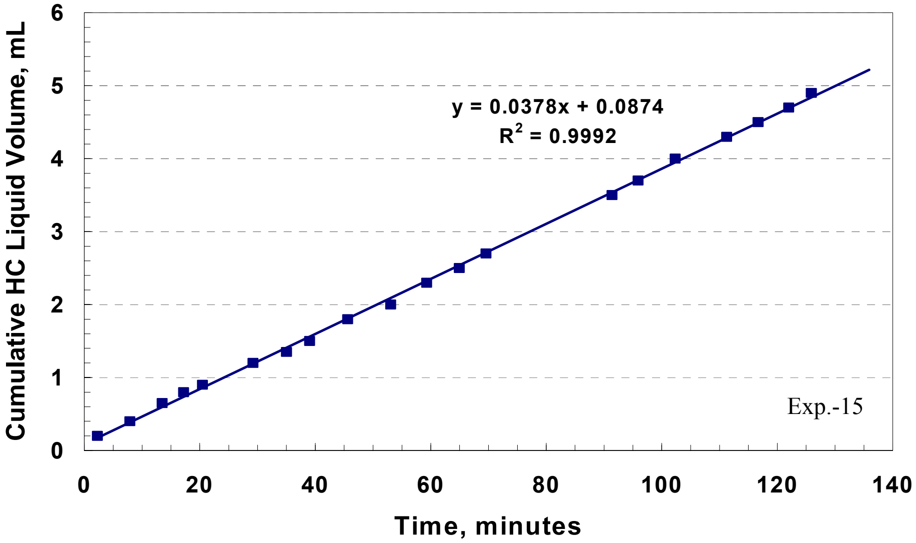

Figure B.129: Cumulative hydrocarbon liquid volume during two-phase flow at steady state at 18 cc/hr and 1,200 psig.

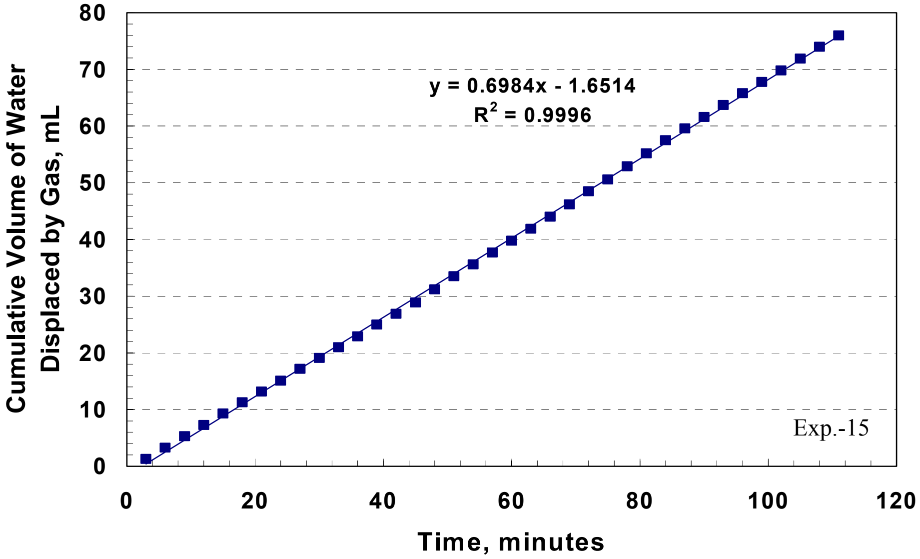

Figure B.130: Cumulative volume of water displaced by gas-phase during two-phase flow at steady state at 18 cc/hr and 1,200 psig.

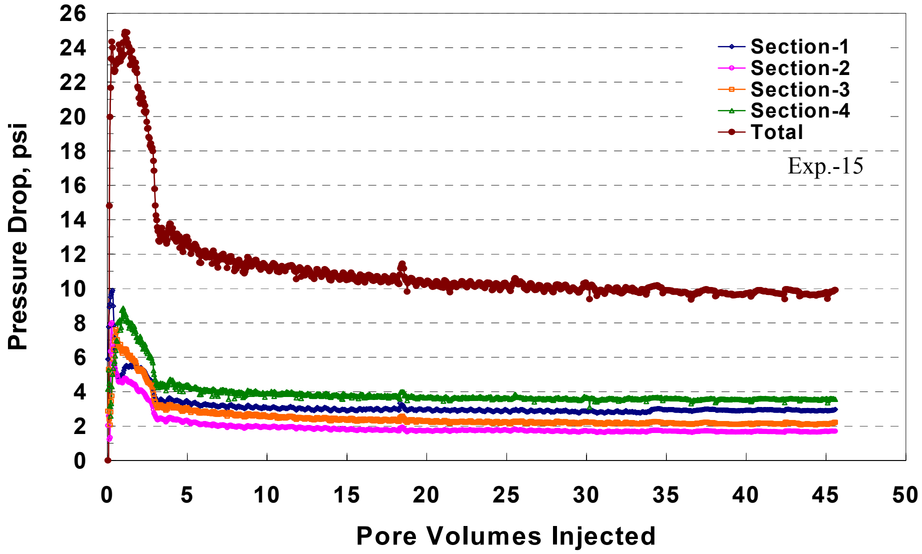

Figure B.131: Pressure drop at different sections across the core during equilibrium gas flow at 99 cc/hr and 1,200 psig.

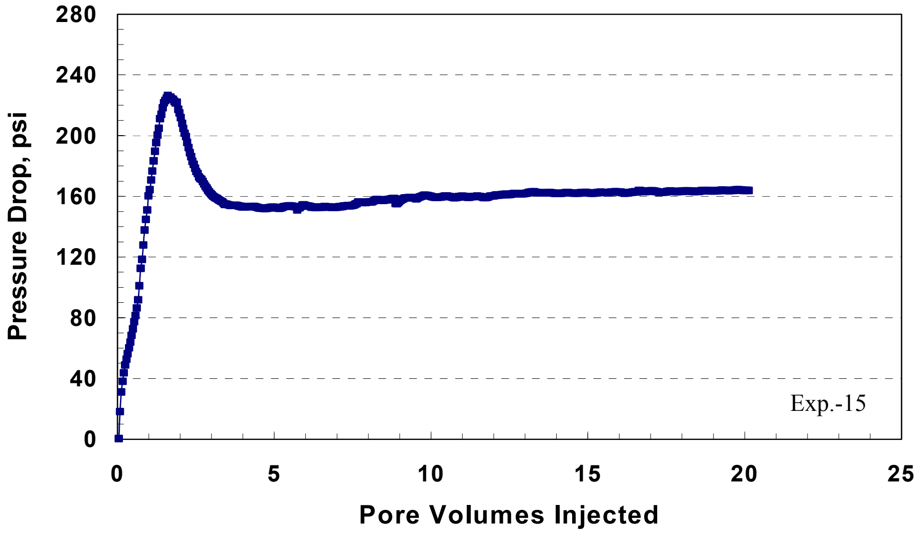

Figure B.132: Pressure drop across the core during the first methanol treatment at 99 cc/hr and 1,200 psig.

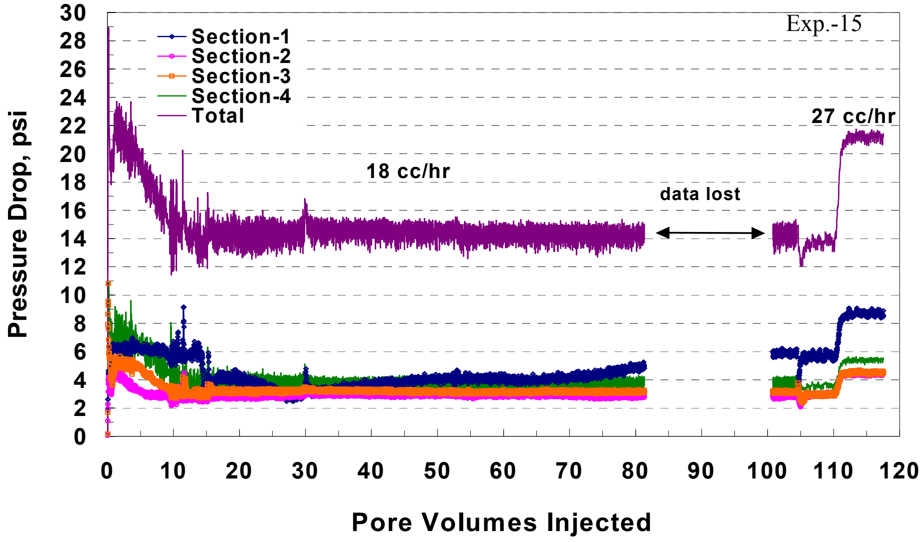

Figure B.133: Pressure at different sections across the core during condensate accumulation after the first methanol treatment at 1,200 psig.

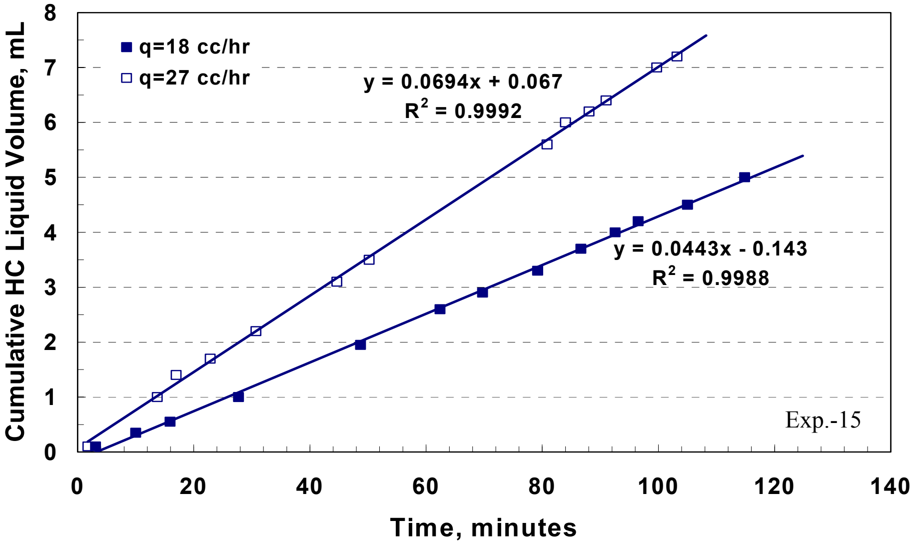

Figure B.134: Cumulative hydrocarbon liquid volume during two-phase flow at steady state at 1,200 psig and various pump rates.

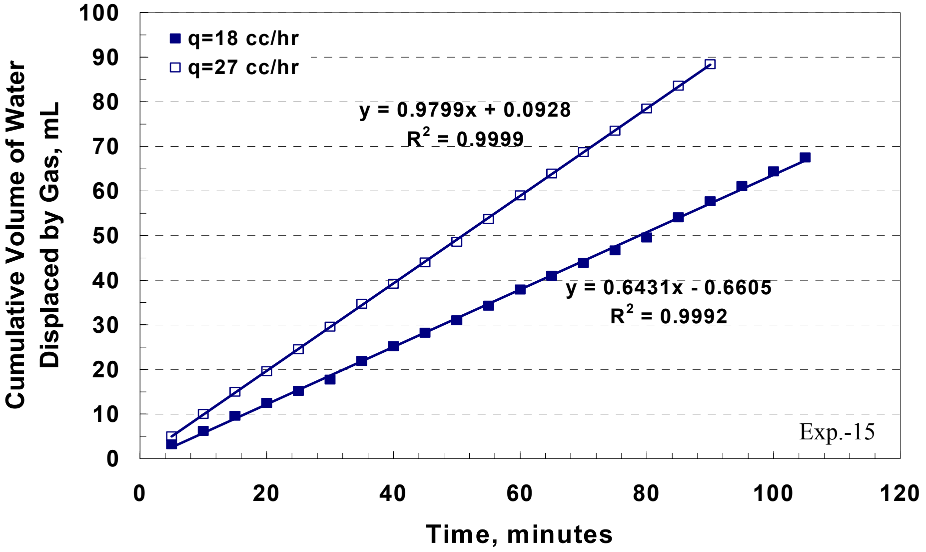

Figure B.135: Cumulative volume of water displaced by gas-phase during two-phase flow at steady state at 1,200 psig and various pump rates.

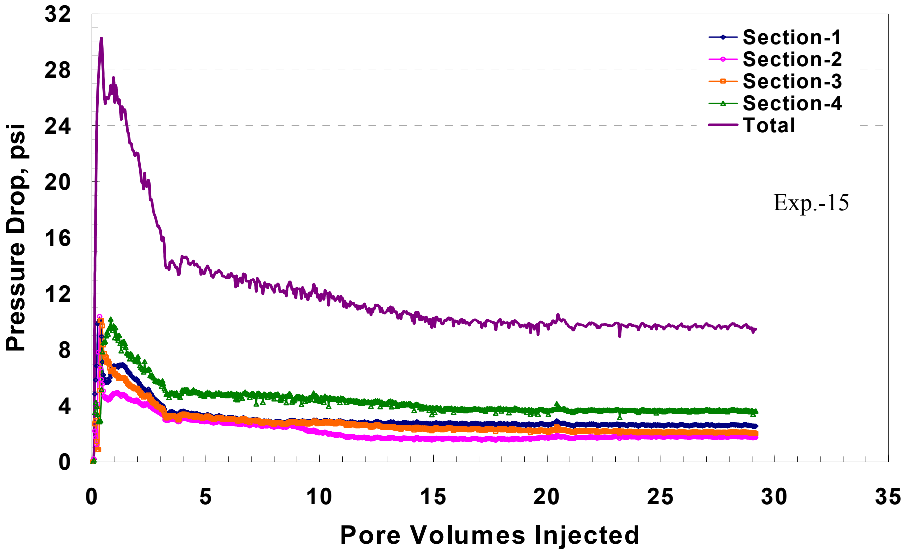

Figure B.136: Pressure drop at different sections across the core during equilibrium gas flow after the first methanol treatment at 99 cc/hr and 1,200 psig.

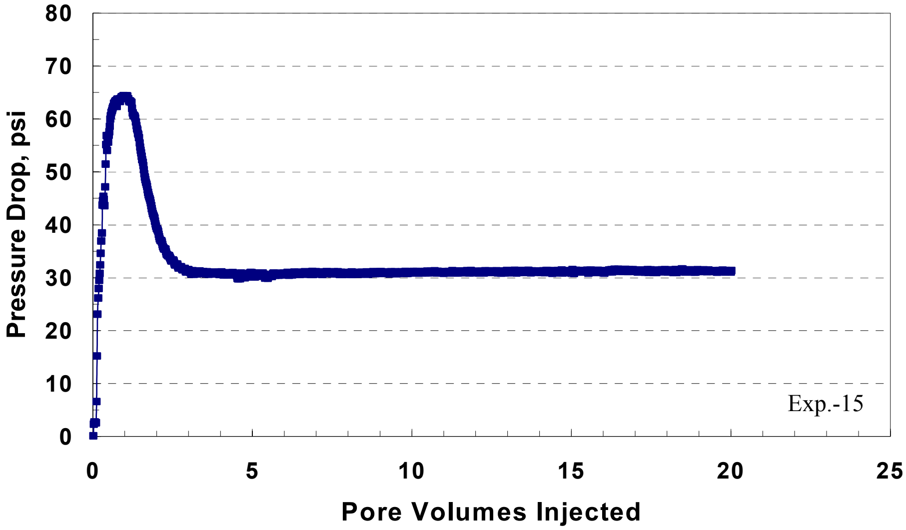

Figure B.137: Pressure drop across the core during the second methanol treatment at 20 cc/hr and 1,200 psig.

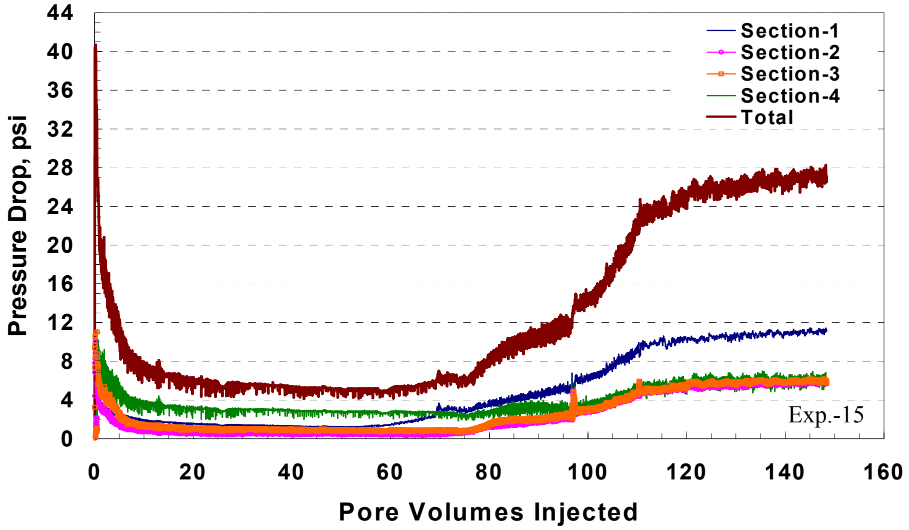

Figure B.138: Pressure drop at different sections across the core during condensate accumulation after the second methanol treatment at 18 cc/hr and 1,200 psig.

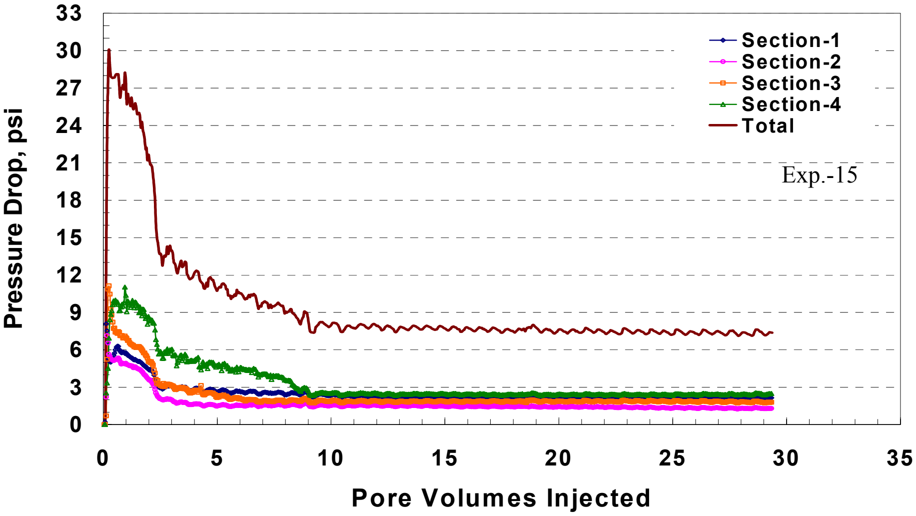

Figure B.139: Pressure drop at different sections across the core during equilibrium gas flow after the 2nd methanol treatment at 99 cc/hr and 1,200 psig.

B.11 Coreflood Experiment No. 16

B.11.1 Objectives

The objectives of this experiment are: (1) to investigate the propagation of condensate bank through the core, (2) to study the effect of flow rate on condensate accumulation, and (3) to measure the dynamic fractional flow of both gas and oil phases at the steady state of two-phase flow. This experiment was performed on a core from Texas Cream limestone. There was no water present in the core.

B.11.2 Core Preparation

The core used in this experiment is the same one used in Experiment-15. The core was cleaned with methanol to remove the residual condensate. Methane gas was flowed through the core at 1,200 psig to restore its initial gas permeability. **Figure B.140** shows pressure drop at different sections across the core during methane flow at 1,200 psig and various rates. Once the pressure stabilized during this stage, flowing pressure was increased to a value above the dewpoint to assure that no condensate present in the core.

B.11.3 Methane Flow

The initial core permeability was measured using methane at a flowing pressure of 3,000 psig. The pressure of both the upstream and downstream back-pressure regulators was set to 3,000 psig. Methane gas was flowed at two flow rates: 99 and 132 cc/hr. Four pressure transducers were used to measure the differential pressure across each section of the core. **Figure B.141** shows the pressure drop at different sections of the core during the flow of methane at 3,000 psig. **Table B.108** gives the measured initial core permeability values to methane at a flowing pressure of 3,000 psig. The measured permeability values are close to those obtained in Experiment-15. Therefore, the core was cleaned and its initial permeability was restored.

B.11.4 Gas Mixture (Single-Phase) Flow

The gas mixture (single-phase) was flowed through the core at a pressure (e.g. 3,000 psig) above the dewpoint. The single phase flowed through the core at two rates: 99 and 132 cc/hr. **Figure B.142** shows the pressure drop at different sections of the core during gas mixture (single-phase) flow at 3,000 psig. The measured core permeability values are given in **Table B.109**. The obtained values of permeability are very close to the initial core permeabilities measured with methane at 3,000 psig. This assures that the gas mixture flowed through the core as a single phase and was prepared correctly.

B.11.5 Condensate Accumulation

Before the start of this stage, the inlet and outlet valves of the core were closed. Pressure of the downstream back-pressure regulator was decreased to 1,200 psig, while the pressure in the upstream back-pressure regulator was kept at 3,000 psig. Flow was started while the bypass valve was open until the pressure in the lines stabilized. Then, the bypass valve was closed and inlet and outlet valves were open simultaneously. This stage allowed the gas-condensate to dynamically accumulated through the core. This simulates the condensate bank in the wellbore region. The stage was stopped when the pressure drop across the core reached stable values. The two-phase was flowed at a pump rate of 6 cc/hr.

Figure B.143 shows the pressure at different sections across the core during condensate accumulation at a pump rate of 6 cc/hr and 1,200 psig. The pressure drop in the first section was gradually increased until it reached a plateau value after 3.8 PV. Then, the pressure drop in section-2 started to increase. Therefore, the condensate bank propagates through each section until it reaches a steady state. The pressure drop in the other sections of the core took about 3.0 PV to reach a stabilized value. The condensate accumulation in the whole core reached a steady state after and a cumulative injection of 9.6 PV of two-phase flow. These results indicate that the condensate accumulation strongly depends on the flow rate. Therefore, non-equilibrium effect exists during the two-phase flow. Gas and oil relative permeabilities during condensate accumulation are given in **Table B.110**. Condensate accumulation caused a severe damage to the core where the gas and oil relative permeabilities decreased to 0.182 and 0.237, respectively. These results are close to those obtained in the previous experiment since the same core was used in both experiments.

B.11.6 Dynamic Liquid Drop-out Measurements

Dynamic fractional flow of both gas and oil phases were measured using the windowed-PVT cell. When the pressure drop across the core during two-phase flow reached a steady state value, the core effluents were flowed through the PVT cell. The oil phase accumulates into the bottom of the cell, while the gas phase flow out from the top the cell. The volume of the accumulated oil was measured by recording the change in the height level as a function of time using a Cathetometer that has an accuracy of ±0.01 cm. The gas effluent from the PVT cell was connected to an accumulator that filled with water. The volume of displaced water is corresponding to the gas volume since the accumulator at 1,200 psig and 145°F. The displaced water was collected using a fractional collector.

Figure B.144 shows the cumulative hydrocarbon liquid volume collected during two-phase flow as a function of time at 1,200 psig and various pump rates. This shows a linear relationship, where the flow rate is equal to the slop of the line. Cumulative volume of water displaced by gas during the two-phase flow at steady state at 1200 psig and different rates is shown in **Figure B.145** as a function of time. This also shows a linear relationship between the cumulative volume of displaced water and time. Thus, the flow rate of the gas phase is equal to the slop of the. **Table B.111** lists the measured gas and oil rates during two-phase flow at steady state and 1,200 psig. The measured dynamic fractional flow factor of oil phase (f_o) is close to that measured from the CCE (static test) and the calculated with PREOS (7.14%). The small difference between the measured dynamic and static values is acceptable within the experimental errors.

Figure B.146 shows the pressure drop across the core during two-phase flow at steady state at 1,200 psig and various rates. The measured gas and oil relative permeabilities at each rate are given in **Table B.112**. As can be seen that as the flow rate increased, the relative permeability of both oil and gas phase decreased due to increase in condensate saturation. These results are in agreement with those obtained by Chen et al. (1999) and Mott et al. (2000).

B.11.7 Equilibrium Gas Flooding

The pressure in the upstream back-pressure regulator was decreased to 1,200 psig. An equilibrium gas, which is the gas-phase of the gas-mixture at a pressure of 1200 psig (below dewpoint), was injected through the core at a flow rate of 99 cc/hr. The pressure drop across the core is shown in **Figure B.147**. This stage gives the gas end-point relative permeability (k^o_{rg}) before methanol treatment, as given in **Table B.113**. This stage results in an increase of in the end-point gas relative permeability due to displacement of condensate from the core. However, the residual condensate reduced the gas end-point relative permeability to 0.510.

B.11.8 Summary of the Results of Coreflood Experiment-16

Based on the obtained results, condensate banking is strongly dependant on the flow rate. As the flow rate decreased, condensate accumulates faster and reduces the gas relative permeability. **Figure B.148** shows the pore volumes injected of two-phase flow to reach steady state as a function of pump rate (@ 3,000 psig). This figure indicates a clear evidence of non-equilibrium effects during condensate accumulation. At higher flow rates, the two-phase flow needs longer time to reach steady state due to the stripping of condensate by flowing gas phase. This result is in agreement with field observations where wells flowing at higher rates without countering any severe reduction in gas productivity even though the bottom hole flowing pressure is below the dewpoint. Therefore, problems of condensate banking are unpredictable due to the non-equilibrium effects.

Figure B.149 shows gas and oil relative permeabilities as a function of capillary number. As the flow rate was increased, relative permeability of both gas and oil phases decreased due to the increase in condensate saturation since the flow rate was increased at each steady state period. The interfacial tension increased as the condensate saturation was increased.

Table B.108: Initial core permeability measured using methane at 3,000 psig.

	Initial Core Permeability, md	
	q = 99 cc/hr	q = 132 cc/hr
Section-1	2.49	2.47
Section-2	3.97	3.99
Section-3	2.95	3.05
Section-4	3.16	3.48
Whole Core	2.45	2.58

Table B.109: Core permeability measured with gas mixture (single-phase) at 3,000 psig.

	Core Permeability, md	
	q = 99 cc/hr	q = 132 cc/hr
Section-1	2.73	2.71
Section-2	4.56	4.51
Section-3	3.23	3.12
Section-4	4.13	4.06
Whole Core	2.93	2.92

Table B.110: Gas and oil relative permeabilities measured during condensate accumulation stage at 6 cc/hr and 1,200 psig.

	ΔP, psia	k_{rg}	k_{ro}
Section-1	1.96	0.115	0.151
Section-2	0.92	0.217	0.322
Section-3	1.07	0.212	0.276
Section-4	1.24	0.183	0.238
Whole Core	4.98	0.182	0.237

Table B.111: Measured gas and oil rates during two-phase flow at steady state at 1,200 psig and different pump rates (@ 3,000 psig).

Pump Rate, cc/hr	q_g, mL/min	q_o, mL/min	f_o, %
6	0.2273	0.0129	5.37
18	0.6570	0.0468	6.65
36	1.3473	0.1004	6.94
60	2.3573	0.1738	6.87
99	4.1276	0.3028	6.83

Table B.112: Gas and oil relative permeabilities measured during condensate accumulation at 1,200 psig and various pump rates.

Pump Rate, cc/hr	N_c	k_{rg}	k_{ro}
6	2.96×10^{-8}	0.182	0.237
18	8.87×10^{-8}	0.161	0.211
36	1.77×10^{-7}	0.162	0.212
60	2.96×10^{-7}	0.155	0.202
99	4.88×10^{-7}	0.145	0.189

Table B.113: Gas end-point relative permeability measured during equilibrium gas flow at 1,200 psig and 99 cc/hr.

	ΔP, psia	k^{o}_{rg}
Section-1	3.19	0.665
Section-2	1.94	0.651
Section-3	2.71	0.563
Section-4	4.11	0.410
Whole Core	11.76	0.510

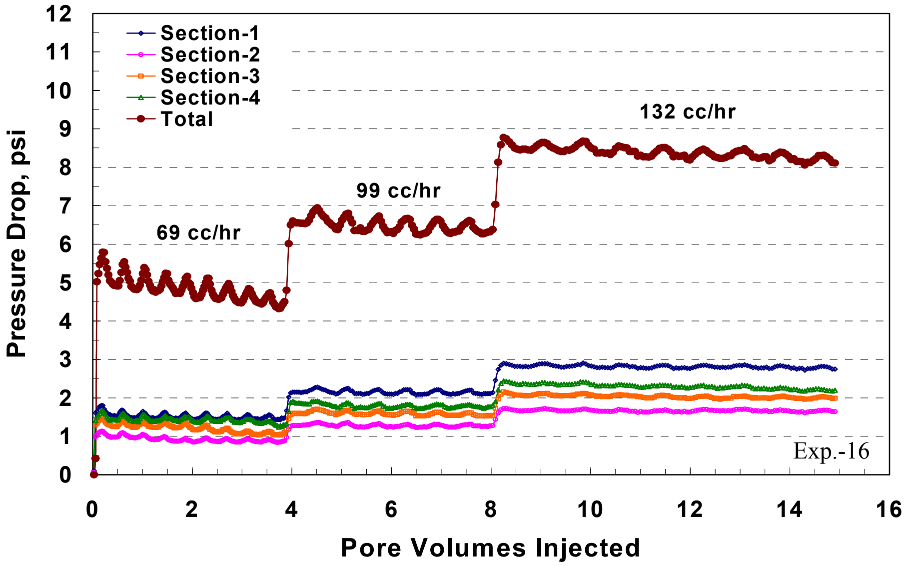

Figure B.140: Pressure drop at different sections across the core during methane flow at 1,200 psig and various flow rates.

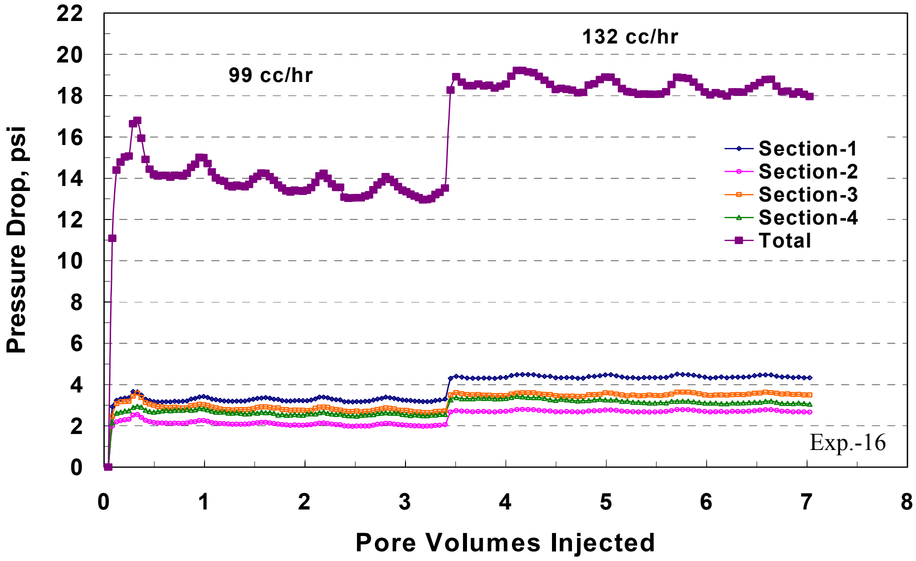

Figure B.141: Pressure drop at different sections across the core during methane flow at 3,000 psig and various flow rates.

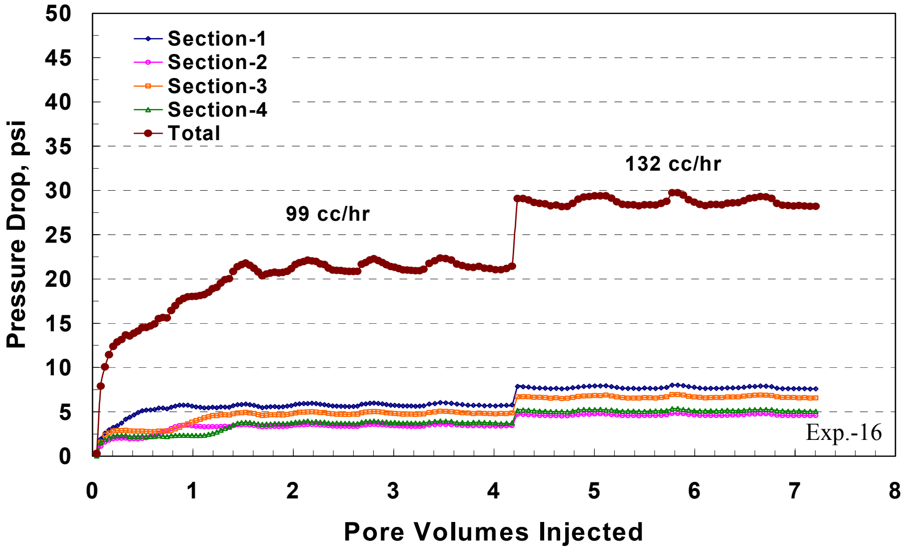

Figure B.142: Pressure drop at different sections across the core during gas mixture (single-phase) flow at 3,000 psig.

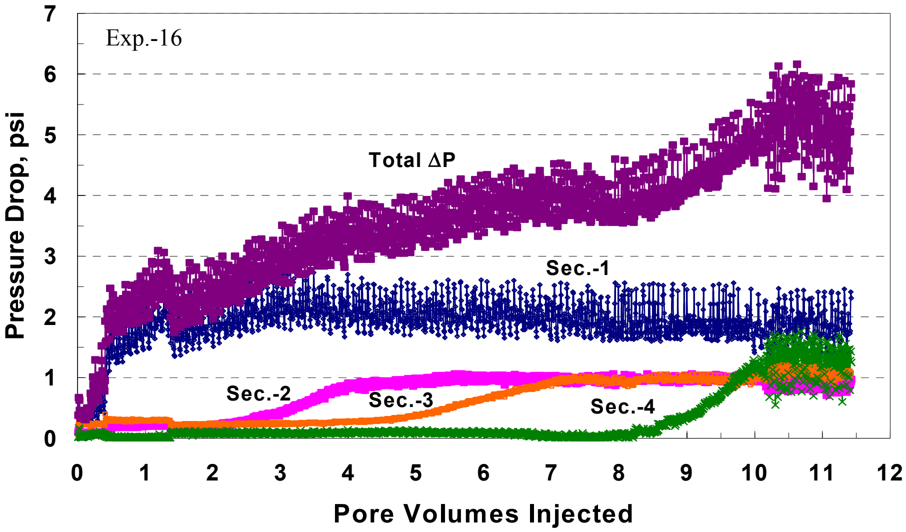

Figure B.143: Pressure drop at different sections across the core during condensate accumulation at 1,200 psig and a pump rate of 6 cc/hr.

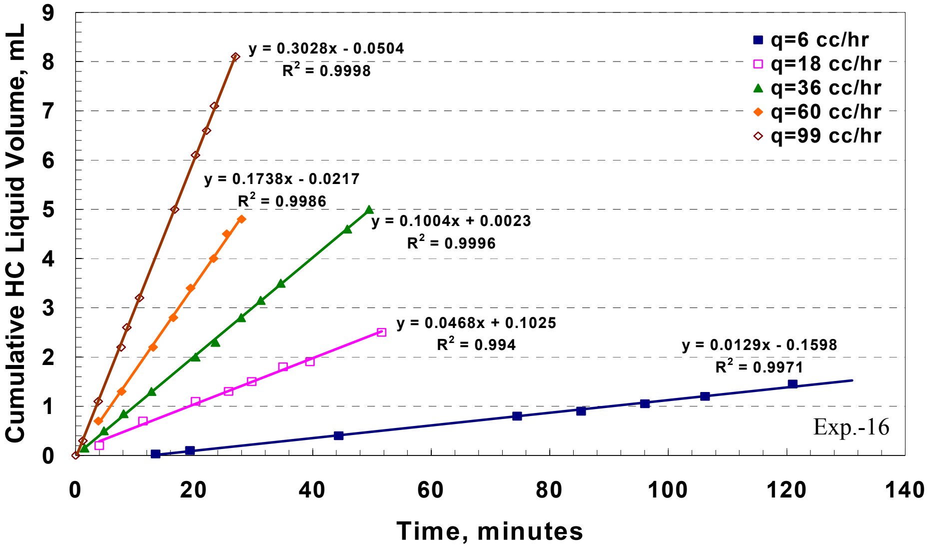

Figure B.144: Cumulative hydrocarbon (HC) liquid volume collected during two-phase flow at steady state at 1,200 psig and various pump rates.

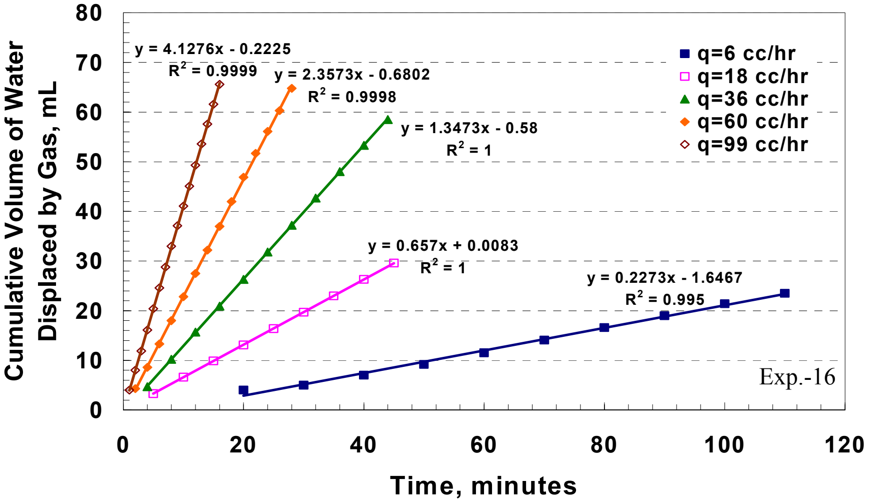

Figure B.145: Cumulative volume of water displaced by gas during two-phase flow at steady state at 1,200 psig and various pump rates.

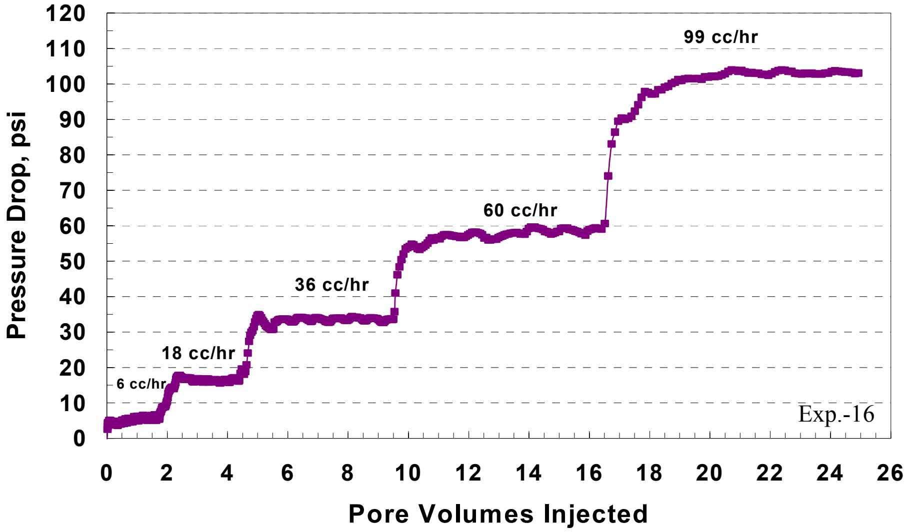

Figure B.146: Pressure drop across the core during two-phase flow at steady state at 1,200 psig and different pump rates.

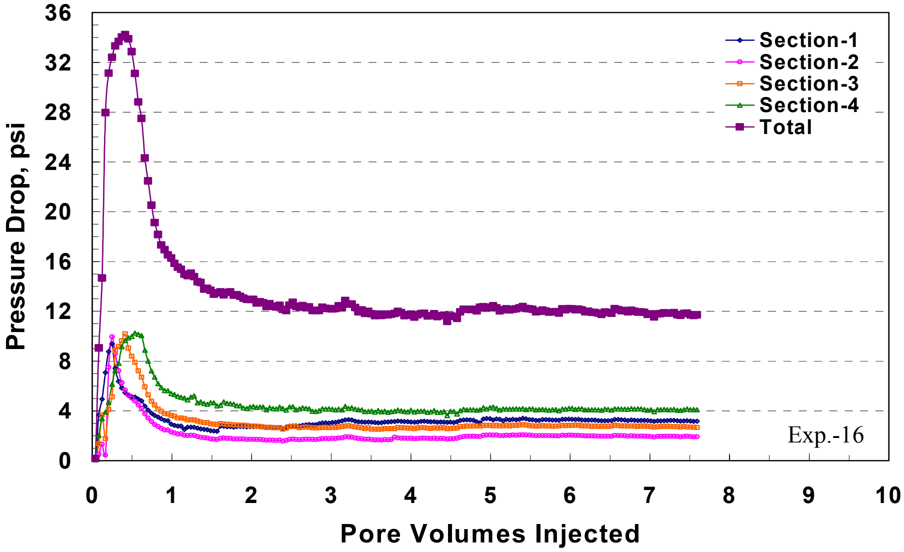

Figure B.147: Pressure drop at different sections across the core during equilibrium gas flow at 1,200 psig and 99 cc/hr.

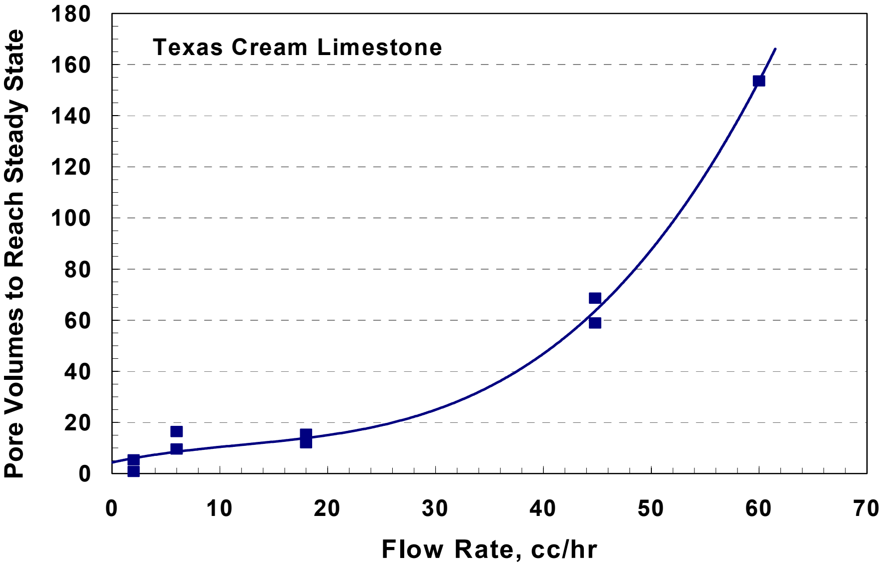

Figure B.148: Effect of flow rate (@3,000 psig) on condensate accumulation.

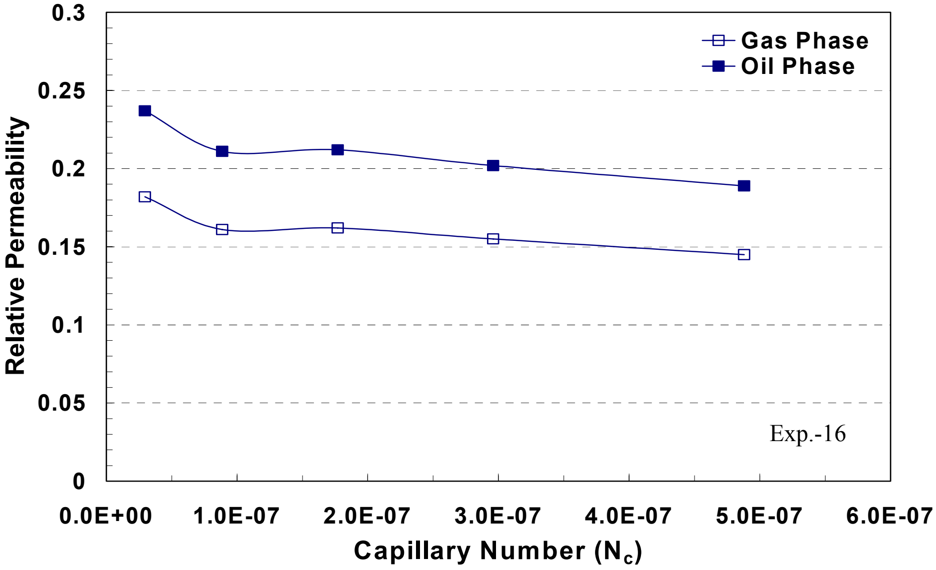

Figure B.149: Gas and oil relative permeabilities as a function of capillary number.

B.12 Coreflood Experiment No. 17

B.12.1 Objectives

The objectives of this experiment are: (1) to investigate the propagation of condensate bank through the core at low flow rate of 2 cc/hr, and (2) to study the revaporization of condensate by methane flooding. This experiment was performed on a core from Texas Cream limestone.

B.12.2 Core Preparation

The core used in this experiment is the same one used in Experiments 15 and 16. Methane gas was flowed through the core at 1,200 psig to restore its initial gas permeability. **Figure B.150** shows pressure drop at different sections across the core during methane flow at 1,200 psig and various flow rates. This figure indicates that the removal of condensate by methane flooding is a very slow process since convective mass transfer from the condensate film into the flowing gas phase controls it. Once the pressure stabilized during this stage, flowing pressure was increased to a value above the dewpoint to assure that no condensate present in the core.

B.12.3 Methane Flow

The initial core permeability was measured using methane at a flowing pressure of 3,000 psig. The pressure of both the upstream and downstream back-pressure regulators was set to 3,000 psig. Methane gas was flowed at two rates: 99, 132 and 162 cc/hr, in sequence. Four pressure transducers were used to measure the differential pressure across each section of the core. **Figure B.151** shows the pressure drop at different sections of the core during the flow of methane at 3,000 psig. **Table B.114** gives the measured initial core permeability values to methane at a flowing pressure of 3,000 psig. The measured permeability values are close to those obtained in the pervious experiments (15 and 16) since the same core was used. Therefore, the core was cleaned and restored its initial permeability.

B.12.4 Gas Mixture (Single-Phase) Flow

The gas mixture (single-phase) was flowed through the core at a pressure (e.g. 3,000 psig) above the dewpoint. The single phase flowed through the core at two rates: 99 and 132 cc/hr. **Figure B.152** shows the pressure drop at different sections of the core during gas mixture (single-phase) flow at 3,000 psig. The pressure drop increased because the viscosity of the gas mixture is larger than that of the displaced fluid (methane). As can be seen, the gas mixture propagated through each section of the core till it breakthrough where the pressure drop stabilized at each section of the core. The measured core permeability values are given in **Table B.115**. The obtained values of permeability are very close to the initial core permeabilities (for each section) measured with methane at 3,000 psig. This assures that the gas mixture flowed through the core as a single phase and was prepared correctly.

B.12.5 Condensate Accumulation

Before the start of this stage, the inlet and outlet valves of the core were closed. Pressure of the downstream back-pressure regulator was decreased to 1,200 psig, while the pressure in the upstream back-pressure regulator was kept at 3,000 psig. Flow was started while the bypass valve was open until the pressure in the lines stabilized. Then, the bypass valve was closed and inlet and outlet valves were open simultaneously. This stage allowed the gas-condensate to dynamically accumulated through the core. This simulates the condensate bank in the wellbore region. The stage was stopped when the pressure drop across the core reached stable values. The two-phase was flowed at a pump rate of 2 cc/hr.

Figure B.153 shows the pressure at different sections across the core during condensate accumulation at 1,200 psig at a pump rate of 2 cc/hr. The pressure drop in the first section was gradually increased until it reached a plateau value after 2.5 PV. Then, the pressure drop in section-2 started to increase. Therefore, the condensate bank propagates through each section until it reaches a steady state. The condensate accumulation in the whole core reached a steady state after 5.5 PV. Since this stage was conducted at a lower flow rate, condensate accumulation reached a steady state faster compared to that flowed at higher flow rates. Therefore, local equilibrium between gas and condensate phases was achieved at lower flow rates. These results indicate that the condensate accumulation strongly depends on the flow rate. Gas and oil relative permeabilities during condensate accumulation are given in **Table B.116**. Condensate accumulation caused a severe damage to the core where the gas and oil relative permeabilities decreased to 0.127 and 0.166, respectively. These results are close to those obtained in the previous experiments since the same core was used in both experiments.

B.12.6 Revaporization of Condensate by Methane Flooding

Methane was flowed through the core directly after condensate accumulation stage. The flowing pressure of methane was 1,200 psig at various flow rates. The aim of this stage is to investigate the revaporization of condensate by methane flooding. The effluent of the core were analyzed with the GC through this stage. **Figure B.154** shows the pressure drop at different sections across the core during revaporization of condensate by methane flow at 1,200 psig. Initially, the pressure drop across the core sharply increased to 31 psi to displace the high condensate saturation from the core. Then, the pressure drop started to decrease gradually till it reached a steady state value after an injection of 15 PV. **Table B.117** lists the measured core permeability during revaporization of condensate by methane flow at different flow rates. The measured permeability values indicate methane was effective to restore the initial core permeability by revaporization of condensate from the pores, even though it required more pore volumes.

Figure B.155 shows the components concentration of the core effluent during this stage. Initially, methane displaced the heavy components from the core as shown in the peak of their concentrations with the corresponding increase in the pressure drop (**Figure B.154**). Methane displaced all of n-butane from the core in the first 10 PV of the flood. However, concentrations of both n-heptane and n-decane gradually decreased until they were completely removed from the core after 56 PV of methane flood. These results indicate that revaporization of condensate by methane is a very slow process since it is controlled by a mass transfer.

Table B.114: Initial core permeability measured using methane at 3,000 psig.

	Gas Permeability, md		
	q = 99 cc/hr	q = 132 cc/hr	q = 162 cc/hr
Section-1	2.66	2.37	3.37
Section-2	3.99	3.86	3.82
Section-3	3.38	3.06	2.94
Section-4	3.20	3.22	3.25
Whole Core	3.45	2.70	2.69

Table B.115: Core permeability measured during gas mixture (single-phase) flow at 3,000 psig.

	Permeability, md	
	q = 69 cc/hr	q = 42 cc/hr
Section-1	2.71	2.80
Section-2	4.50	4.29
Section-3	3.16	2.88
Section-4	4.12	3.90
Whole Core	3.48	3.06

Table B.116: Gas and oil relative permeabilities measured during condensate accumulation stage at 1,200 psig and 2 cc/hr.

	ΔP, psia	k_{rg}	k_{ro}
Section-1	1.52	0.066	0.086
Section-2	0.45	0.219	0.287
Section-3	0.40	0.247	0.323
Section-4	1.02	0.097	0.127
Whole Core	3.14	0.127	0.166

Table B.117: Gas permeability measured during revaporization of condensate by methane flow at 1,200 psig and different flow rates.

	Gas Permeability, md			
	q = 99 cc/hr	q = 132 cc/hr	q = 224 cc/hr	q = 132 cc/hr
Section-1	3.05	3.00	2.91	3.16
Section-2	4.98	4.82	4.78	5.05
Section-3	3.40	3.95	3.82	3.96
Section-4	2.94	3.53	3.65	3.62
Whole Core	3.59	3.90	3.83	3.96

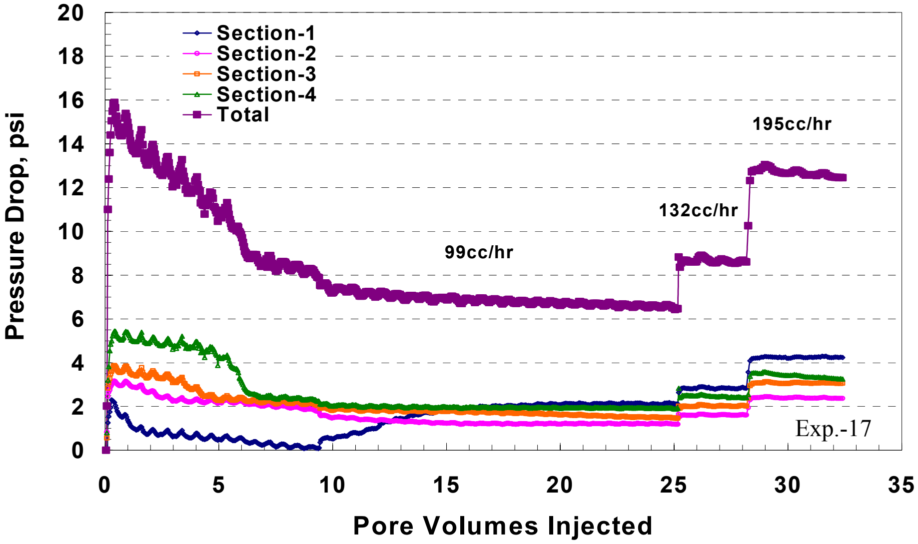

Figure B.150: Pressure drop at different sections across the core during methane flow at 1,200 psig and various flow rates.

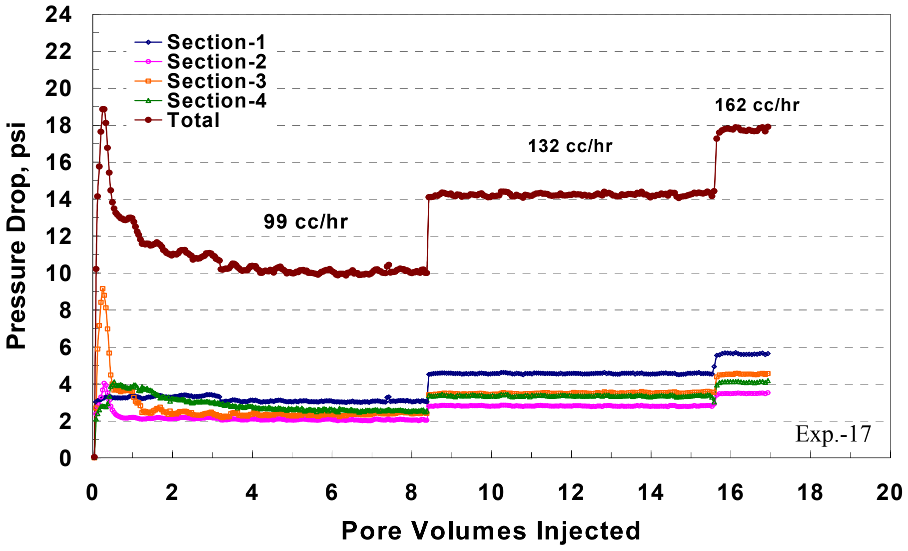

Figure B.151: Pressure drop at different sections across the core during methane flow at 3,000 psig and various flow rates.

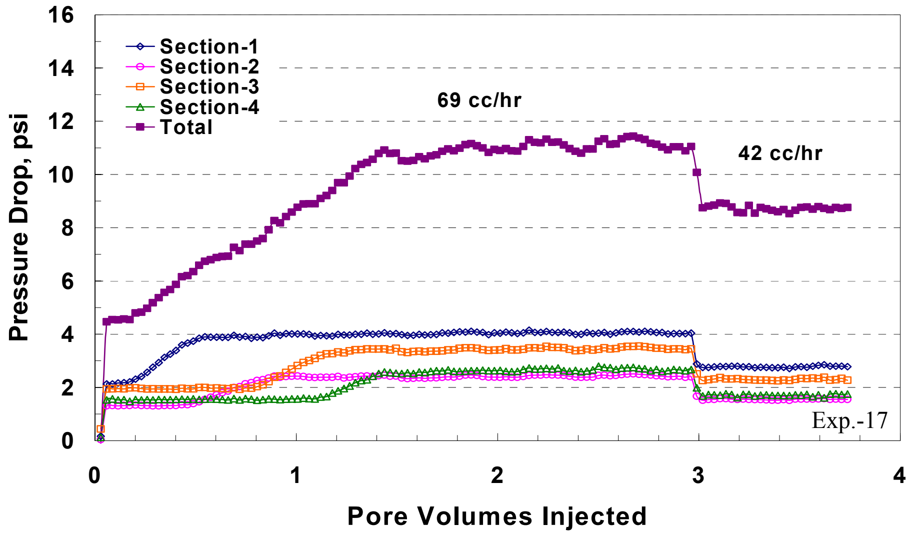

Figure B.152: Pressure drop at different sections across the core during gas mixture (single-phase) flow at 3,000 psig.

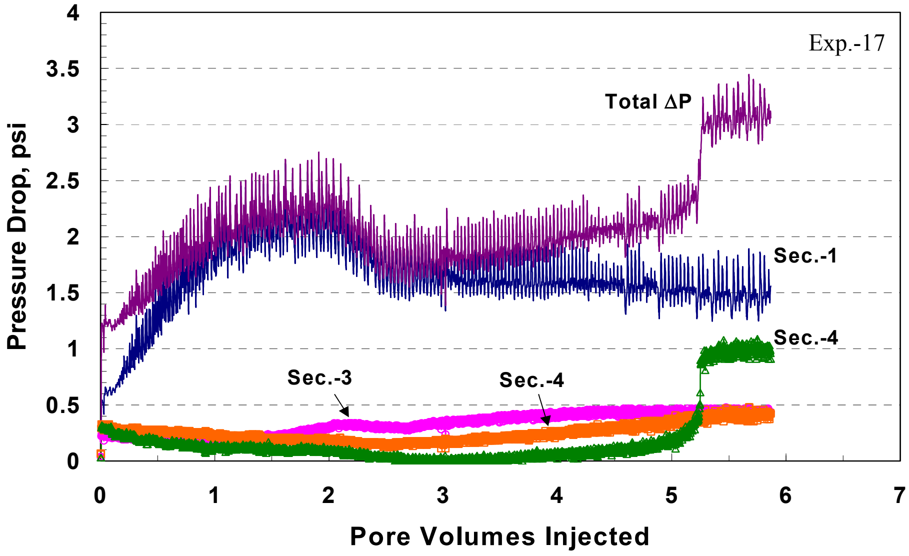

Figure B.153: Pressure drop at different sections across the core during dynamic condensate accumulation at 1,200 psig and 2 cc/hr.

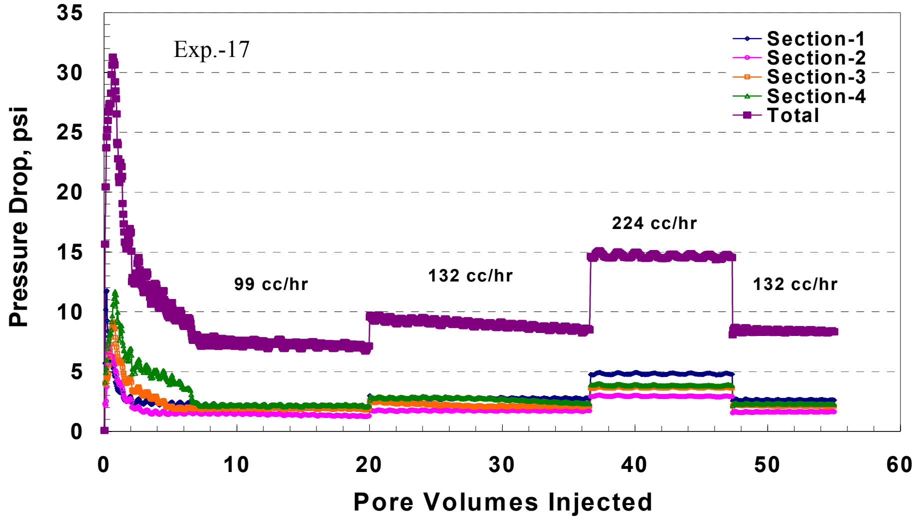

Figure B.154: Pressure drop at different sections across the core during revaporization of condensate by methane flow at 1,200 psig.

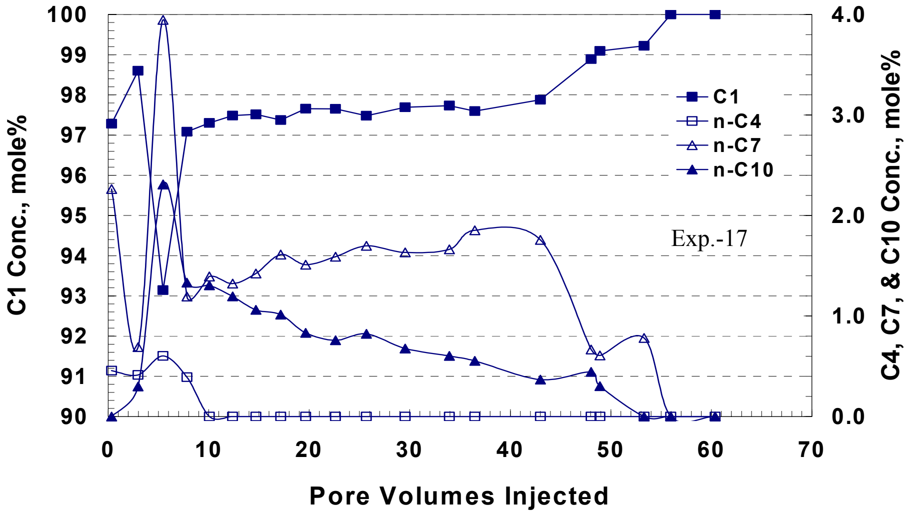

Figure B.155: Components concentrations in the effluent of the core during revaporization of condensate by methane flooding at 1,200 psig.

B.13 Coreflood Experiment No. 18

B.13.1 Objectives

The objectives of this experiment are: (1) to investigate the propagation of condensate bank through the core using co-injection of both gas and condensate phases simultaneously at a higher flow rate, (2) to study the non-equilibrium behavior during two-phase flow, and (3) to analyze the effluent of the core by the gas chromatograph. This experiment was performed on a core from Texas Cream limestone.

B.13.2 Core Preparation

The core used in this experiment is the same one used in Experiments 15, 16 and 17. Methane gas was flowed through the core at 1,200 psig to restore its initial gas permeability. **Figure B.156** shows pressure drop at different sections across the core during methane flow at 1,200 psig and various flow rates. This figure indicates that the removal of condensate by methane flooding is a very slow process since convective mass transfer from the condensate film into the flowing gas phase controls it. **Table B.118** gives the measured restored core permeability at various flow rates. The restored core permeability (k = 3.82 md) is very close to the initial one measured (k = 3.87 md) in Experiment-17, since the same core was used in both experiments. Therefore, methane evaporated all the residual condensate from the core.

B.13.3 Two-Phase Flow

The equilibrium gas and condensate phases were stored each in a separate rodded-piston accumulator. Each accumulator was set vertical inside the oven and connected a RUSKA pump. The equilibrium gas phase accumulator connected to the pump from the bottom, so the gas flow will be from the top-end of the accumulator. On the other hand, the condensate accumulator connected to the pump from the top-end where the condensate will flow from the bottom end. The flow rate of each pump was selected in order to get a constant fractional flow around 7%. The injected phases were mixed together before they enter the upstream back-pressure regulator. Before the start of this stage, the inlet and outlet valves of the core were closed. Pressure in the upstream and downstream back-pressure regulators was set to 1,200 psig. Flow was started while the bypass valve was open until the pressure in the lines stabilized. Then, the bypass valve was closed and inlet and outlet valves were open simultaneously. This stage allowed flow of equilibrium gas and condensate phases simultaneously through the core. The stage was stopped when the pressure drop across the core reached stable values.

The flow rate of gas phase was 132 cc/hr and the condensate phase was flowed at a rate of 10 cc/hr. These flow rates give a liquid fractional flow factor of 7.0% that is very close to that one calculated using dynamic accumulation. These flow rates are equivalent to a single-phase flow rate of 52.9 cc/hr at 3,000 psig and flashing into two-phase at 1,200 psig. **Figure B.157** shows the pressure at different sections across the core during two-phase flow at 1,200 psig. The pressure drop in the first section was gradually increased until it reached a plateau value after 2.7 PV. Then, the pressure drop in section-2 started to increase. Therefore, the condensate bank propagates through each section until it reaches a steady state. The condensate accumulation in the whole core reached a steady state after 11.5 PV. Since this stage was conducted using a co-injection of condensate and gas phases, condensate accumulation reached a steady state faster compared to that performed using dynamic flashing method at the same flow rate and fractional flow. For instance, two-phase flow using flashing method reached a steady state after 60 and 152 PV at a flow rate of 44.8 and 60 cc/hr, respectively. Therefore, local equilibrium between gas and condensate phases was not achieved during dynamic flashing, except at very low flow rates. These results indicate that the condensate accumulation strongly depends on the flow rate.

Gas and oil relative permeabilities during co-injection of two phases are given in **Table B.119**. Condensate accumulation caused a severe damage to the core where the gas and oil relative permeabilities decreased to 0.161 and 0.207, respectively. These results are close to those obtained in the previous experiments since the same core was used in both experiments, even though the condensate accumulation methods were different. After that, the co-injection of two phases was resumed at lower flow rate. The flow rates of gas and condensate phases were set to 32 and 2.5 cc/hr, respectively. **Figure B.158** shows the pressure drop at different sections across the core during co-injection to two phases at 1,200 psig at steady state. The measured gas and oil relative permeabilities are given in **Table B.120**. The relative permeabilities decreased as the flow rate was decreased due to the capillary effects.

B.13.4 Equilibrium Gas Flow

The pressure in the upstream back-pressure regulator was checked and set to 1,200 psig. Gas-mixture, which has a pressure of 1,200 psig (below the dewpoint), was injected through the core at a flow rate of 99 cc/hr. The pressure drop at different sections across the core during equilibrium gas flow is shown in **Figure B.159**. This stage gives the gas end-point relative permeability (k^o_{rg}) before methanol treatment, as given in **Table B.121**. The obtained gas end-point relative permeability is 0.60. This value is similar to those obtained in the previous experiments in the absence of initial water saturation.

B.13.5 The First Stage of Methanol Treatment

Pure methanol was injected through the core at an injection rate of 20 cc/hr and 1,200 psig. The volume of methanol injected was 20 PV. The pressure drop across the core stabilized at a value 31.66 psia as shown in **Figure B.160**. The calculated permeability for methanol was found equal to 3.69 md. The effluent of the core were switched to a fraction flow collector that was set to collect effluent in graduated-glass tubes each 15 minutes. The volume of the collected liquid was measured for each phase. **Figure B.161** shows methanol-rich phase as a function of cumulative pore volumes injected during methanol treatment. At the start of methanol injection, gas phase was produced from the core for 0.5 PV. Then, two phases consisted of methanol and hydrocarbons were observed in the collected effluent. This means that the methanol treatment was effective to displace residual condensate from the core. The presence of two phases because hydrocarbons have a very little solubility in methanol as previously discussed in the phase behavior studies chapter. After an injection of 1.75 PV of methanol, only methanol-rich phase was collected in the effluent. Analyses of gas chromatograph showed these samples contained a mixture of methanol, n-heptane, and n-decane. The hydrocarbons represent a trace amount during the methanol treatment.

B.13.6 Two-Phase Flow After the First Stage of Methanol Treatment

The equilibrium gas and condensate phases were injected simultaneously through the core after the first methanol treatment at 1,200 psig. The used flow rate was 64 and 5 cc/hr for the gas and condensate phases, correspondingly. This stage allowed the condensate to accumulate through the core to assess the effectiveness of methanol treatment. **Figure B.162** depicts the pressure drop at different sections across the core during co-injection of gas and condensate phases at 1,200 psig. Initially, the pressure drop across the core increased to 40 psia to displace methanol from the core. The measured volume of liquid displaced by two-phase was found equal to 17 mL (0.85 PV). This liquid consisted of methanol and hydrocarbons mixture. Then, the pressure drop decreased gradually as the accessible methanol produced. This figure did not show any sign of an enhanced flow period that was observed during dynamic condensate accumulation (flashing method). The existence of the enhanced flow period in the previous experiments was mainly due to the non-equilibrium behavior of two-phase flow. Gas and oil relative permeabilities measured during this stage are listed in **Table B.122**.

B.13.7 Equilibrium Gas After the First Methanol Treatment

The pressure of the upstream back-pressure regulator was set to 1,200 psig. The equilibrium gas was injected at a flow rate of 99 cc/hr. **Figure B.163** shows the pressure drop across the core. This stage gives the gas end-point relative permeability after methanol injection, as given in **Table B.123**. The methanol treatment neither increased the gas end-point nor damages the core. However, the treatment was temporary effective to remove condensate blocking from the core.

B.13.8 The Second Stage of Methanol Treatment

Pure methanol was injected through the core at an injection rate of 20 cc/hr and 1,200 psig. The volume of methanol injected was 20 PV. The pressure drop across the core stabilized at a value 32.0 psia as shown in **Figure B.164**. The calculated permeability for methanol was found equal to 3.65 md that is similar to the one obtained during the first treatment. **Figure B.165** shows methanol-rich phase as a function of cumulative pore volumes injected during methanol treatment. This figure shows the same trend observed during the first methanol treatment. This means that the methanol treatment was effective to displace residual condensate from the core. In addition, the gas chromatograph analyses showed these samples contained a mixture of methanol, n-heptane, and n-decane. The hydrocarbons represent a trace amount during the methanol treatment.

B.13.9 Two-Phase Flow After the Second Stage of Methanol Treatment

The equilibrium gas and condensate phases were injected simultaneously through the core after the first methanol treatment at 1,200 psig. The used flow rate was 64 and 5 cc/hr for the gas and condensate phases, respectively. This stage allowed the condensate to accumulate through the core to assess the effectiveness of the second methanol treatment. **Figure B.166** depicts the pressure drop at different sections across the core during co-injection of gas and condensate phases at 1,200 psig. Initially, the pressure drop across the core increased to 38 psia to displace methanol from the core. The measured volume of liquid displaced by two-phase was found equal to 17.5 mL (0.88 PV). This liquid consisted of methanol and hydrocarbons mixture. These results as the same those obtained after the first methanol treatment. Then, the pressure drop decreased gradually as the methanol produced. This figure also did not show any sign of an enhanced flow period that was observed during dynamic condensate accumulation (flashing method). This stage confirms that the existence of the enhanced flow period in the previous experiments was mainly due to the non-equilibrium behavior of two-phase flow. Gas and oil relative permeabilities measured during this stage are listed in **Table B.124**.

B.13.10 Equilibrium Gas After the Second Methanol Treatment

The pressure of the upstream back-pressure regulator was set to 1,200 psig. The equilibrium gas was injected at a flow rate of 99 cc/hr. **Figure B.167** shows the pressure drop across the core. This stage gives the gas end-point relative permeability after methanol injection, as given in **Table B.125**. The methanol treatment did not increase the gas end-point nor damage the core. However, the treatment was temporary effective to remove condensate blocking from the core. **Figure B.168** illustrates components concentrations during equilibrium gas flow. The concentration of heavy components (n-C_7 and n-C_{10}) initially increased to reach maximum values at 1.52 and 0.85 mole%. This increase is due to the displacement of condensate from the pores. Then, the concentration of n-C_7 and n-C_{10} decreased and reached the same amount in the equilibrium gas. The obtained results showed that the residual condensate did not change the composition of the flowing gas as long as they are in equilibrium. However, the composition would expect to vary if a non-equilibrium fluid is flowing (e.g. C_1 or N_2).

B.13.11 The Third Stage of Methanol Treatment

Pure methanol was injected through the core at an injection rate of 20 cc/hr and 1,200 psig. The volume of methanol injected was 20 PV. The pressure drop across the core stabilized at a value 31.83 psia, as shown in **Figure B.169**. The calculated permeability for methanol was found equal to 3.67 md that is similar to the values obtained during the first and second treatment.

B.13.12 Dynamic Condensate Accumulation (Two-Phase Flow)

Since the previous methanol treatments did not give an enhanced flow period during two-phase flow using the co-injection method, we decided to perform dynamic condensate accumulation using the flashing method. Before the start of this stage, the inlet and outlet valves of the core were closed. Pressure of the upstream back-pressure regulator was increased to 3,000 psig, while the pressure in the downstream back-pressure regulator was kept at 1,200 psig. Single-phase flow (gas mixture above the dewpoint) was started while the bypass valve was open until the pressure in the lines stabilized. Then, the bypass valve was closed and inlet and outlet valves were open simultaneously. The gas mixture flow rate was set to 20 cc/hr (@ 3,000 psig). This flow rate gives a gas phase flowing at a rate of 49.81 cc/hr and a condensate phase flowing at 3.83 cc/hr at 1,200 psig. This stage allowed the gas-condensate to dynamically accumulated through the core. This mimics what happen in the wellbore region in retrograde reservoirs. The stage was stopped when the pressure drop across the core reached stable values.

Figure B.170 shows the pressure drop at different sections across the core during dynamic condensate accumulation after the third methanol treatment at

1,200 psig. The pressure drop was sharply increased to reach a maximum value of 84 psi to displace methanol from the core. The total volume of methanol collected in the effluent was 10.5 mL (0.53 PV), which is less than that collected during the co-injection. Therefore, the residual methanol saturation would be expected higher in this stage. Then, it gradually reduced to reach a minimum value 8.12 psia. Therefore, flashing the gas mixture gives an enhanced flow period that prolongs for more than 30 PV. As been stated before, the volume of methanol treatment controls the duration of the enhanced flow period. After the evaporation of residual methanol from the core, the pressure drop started to build-up due to the accumulation of condensate and reached a plateau value of 52.2 psia. This result confirms that non-equilibrium behavior is dominant during dynamic condensate accumulation than that during co-injection. Since the dynamic condensate accumulation (flashing method) is more representative to retrograde reservoirs than co-injection method, non-equilibrium behavior needs to be considered in gas reservoir studies. Gas and oil relative permeabilities measured during dynamic condensate accumulation are given in **Table B.126**. In this experiment, the gas relative permeability reduced by 94%.

B.13.13 Equilibrium Gas Flooding

The pressure in the upstream back-pressure regulator was decreased to 1,200 psig. An equilibrium gas, which is the gas-phase of the gas-mixture at a pressure of 1,200 psig (below dewpoint), was injected through the core at a flow rate of 99 cc/hr. The pressure drop across the core is shown in **Figure B.171**.

Table B.127 lists the gas end-point relative permeability (k^{o}_{rg}) after the third methanol treatment. This stage results in an increase in the gas end-point relative permeability due to displacement of condensate from the core**.** **Figure B.172** depicts components concentrations during equilibrium gas flow after the third methanol treatment. The heavy components were displaced during the first 10 PV and reach their concentration in the equilibrium gas.

B.13.14 The Fourth Stage of Methanol Treatment

Pure methanol was injected through the core at an injection rate of 20 cc/hr and 1200 psig. The volume of methanol injected was 20 PV. The pressure drop across the core stabilized at a value 32.75 psi, as shown in **Figure B.173**. The measured permeability for methanol was found equal to 3.57 md, which is close to the initial core permeability.

B.13.15 Two-Phase Flow After the Fourth Stage of Methanol Treatment

The pressure of the upstream back-pressure regulator was increased to 3,000 psig, while the pressure of the downstream back-pressure regulator was kept at 1,200 psig. The flow rate of the single-phase at 3,000 psig was 2 cc/hr. This low rate was selected to see if the enhanced flow period is either controlled by the two-phase flow method (flashing or co-injection) or non-equilibrium behavior. Dynamic condensate accumulation was found to achieve equilibrium at this low flow rate. The gas mixture was flashed through the core to dynamically accumulate condensate. **Figure B.174** depicts the pressure drop across the core during this stage. This figure indicates that there is no enhanced flow period. Therefore, the enhanced flow period is mainly controlled by the non-equilibrium behavior of the two-phase flow. Gas and oil relative permeabilities measured during dynamic condensate accumulation after the fourth methanol treatment are given in **Table B.128**. These values are very close to those obtained during co-injection of two phases. Accordingly, this low flow rate (2 cc/hr) provides equilibrium status for the two-phase flow.

B.13.16 Summary of the Experimental Results

Flowing the equilibrium gas and condensate phases simultaneously through the core at a fixed fractional flow factor formed a condensate bank that reduced the permeability by more than 85%. The two-phase flow reached a steady state faster during the co-injection of equilibrium phases than that in dynamic flashing method. Methanol treatment was effective to displace condensate blocking from the core, but it did not provide an enhanced flow period during the co-injection method. The enhanced flow period was committed to be a function of non-equilibrium behavior of two-phase flow. Condensate accumulation is strongly dependent on the flow rate. Equilibrium was achieved at low flow rates.

Table B.118: Initial core permeability measured using methane at 1,200 psig.

	q = 99 cc/hr	q = 132 cc/hr	q = 224 cc/hr	q = 132 cc/hr
Section-1	3.05	3.00	2.91	3.16
Section-2	4.98	4.82	4.78	5.05
Section-3	3.40	3.95	3.82	3.96
Section-4	2.94	3.53	3.65	3.62
Whole Core	3.59	3.90	3.83	3.96

Table B.119: Gas and oil relative permeabilities measured during co-injection of equilibrium gas (q=132 cc/hr) and condensate (q=10 cc/hr) phases at 1,200 psig.

	ΔP, psia	k_{rg}	k_{ro}
Section-1	23.41	0.089	0.115
Section-2	8.70	0.241	0.310
Section-3	9.35	0.224	0.288
Section-4	10.61	0.197	0.254
Whole Core	52.07	0.161	0.207

Table B.120: Gas and oil relative permeabilities measured during co-injection of equilibrium gas (q=32 cc/hr) and condensate (q=2.5 cc/hr) phases at 1,200 psig and steady state.

	ΔP, psia	k_{rg}	k_{ro}
Section-1	6.52	0.078	0.103
Section-2	2.88	0.176	0.234
Section-3	2.67	0.190	0.252
Section-4	3.75	0.135	0.180
Whole Core	18.07	0.112	0.149

Table B.121: Gas end-point relative permeability measured during equilibrium gas flow at 99 cc/hr and 1,200 psig.

	ΔP, psia	k_g	k°_{rg}
Section-1	3.07	2.04	0.647
Section-2	1.74	3.60	0.713
Section-3	2.42	2.59	0.655
Section-4	3.59	1.75	0.482
Whole Core	10.59	2.37	0.598

Table B.122: Gas and oil relative permeabilities measured during co-injection of equilibrium gas (q=64 cc/hr) and condensate (q=5 cc/hr) phases after the first methanol treatment at 1,200 psig.

	ΔP, psia	k_{rg}	k_{ro}
Section-1	7.24	0.140	0.186
Section-2	7.05	0.144	0.191
Section-3	6.60	0.154	0.204
Section-4	7.33	0.138	0.184
Whole Core	29.92	0.136	0.180

Table B.123: Gas end-point relative permeability measured during equilibrium gas flow after the first methanol treatment at 99 cc/hr and 1,200 psig.

	ΔP, psia	k_g	k°_{rg}
Section-1	3.17	1.97	0.626
Section-2	1.75	3.58	0.709
Section-3	2.17	2.89	0.730
Section-4	3.89	1.61	0.444
Whole Core	10.58	2.37	0.599

Table B.124: Gas and oil relative permeabilities measured during co-injection of equilibrium gas (q=64 cc/hr) and condensate (q=5 cc/hr) phases after the second methanol treatment at 1,200 psig.

	ΔP, psia	k_{rg}	k_{ro}
Section-1	9.13	0.111	0.147
Section-2	4.15	0.245	0.325
Section-3	4.41	0.230	0.305
Section-4	5.49	0.185	0.245
Whole Core	22.29	0.182	0.242

Table B.125: Gas end-point relative permeability measured during equilibrium gas flow after the second methanol treatment at 99 cc/hr and 1,200 psig.

	ΔP, psia	k_g	k°_{rg}
Section-1	3.66	1.71	0.543
Section-2	1.73	3.63	0.719
Section-3	2.07	3.02	0.764
Section-4	3.46	1.81	0.501
Whole Core	10.43	2.40	0.607

Table B.126: Gas and oil relative permeabilities measured during dynamic condensate accumulation (flashing method) after the third methanol treatment at 1,200 psig and a pump rate of 20 cc/hr (@3,000 psig).

	ΔP, psia	k_{rg}	k_{ro}
Section-1	19.67	0.040	0.052
Section-2	10.78	0.073	0.096
Section-3	11.37	0.069	0.091
Section-4	10.95	0.072	0.094
Whole Core	52.65	0.060	0.078

Table B.127: Gas end-point relative permeability measured during equilibrium gas flow after the third methanol treatment at 99 cc/hr and 1,200 psig.

	ΔP, psia	k_g	k°_{rg}
Section-1	2.28	2.75	0.870
Section-2	1.30	4.81	0.953
Section-3	1.85	3.40	0.857
Section-4	3.57	1.76	0.485
Whole Core	9.11	2.75	0.696

Table B.128: Gas and oil relative permeabilities measured during dynamic condensate accumulation (flashing method) after the fourth methanol treatment at 1,200 psig and a pump rate of 2 cc/hr (@3,000 psig).

	ΔP, psia	k_{rg}	k_{ro}
Section-1	0.74	0.107	0.140
Section-2	0.37	0.215	0.281
Section-3	0.33	0.239	0.312
Section-4	1.10	0.072	0.094
Whole Core	2.41	0.131	0.171

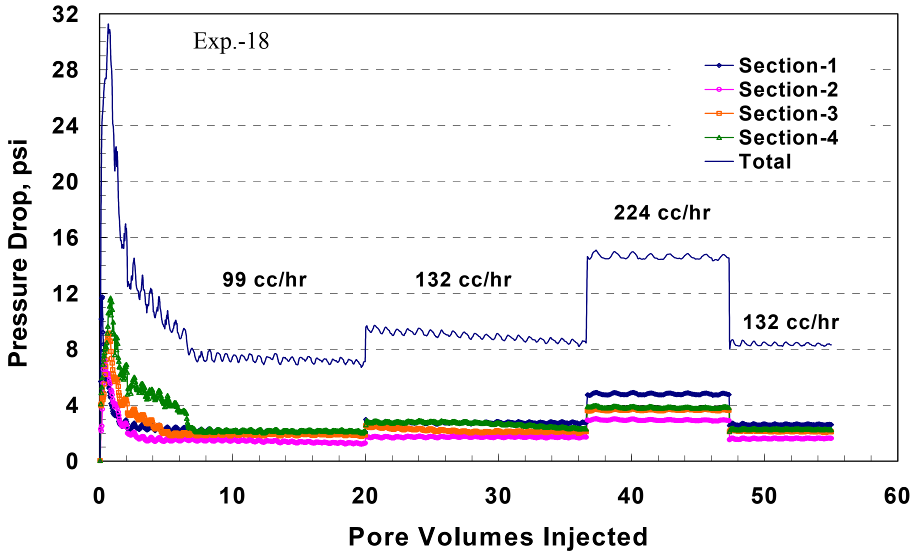

Figure B.156: Pressure drop at different sections across the core during methane flow at 1,200 psig and various rates.

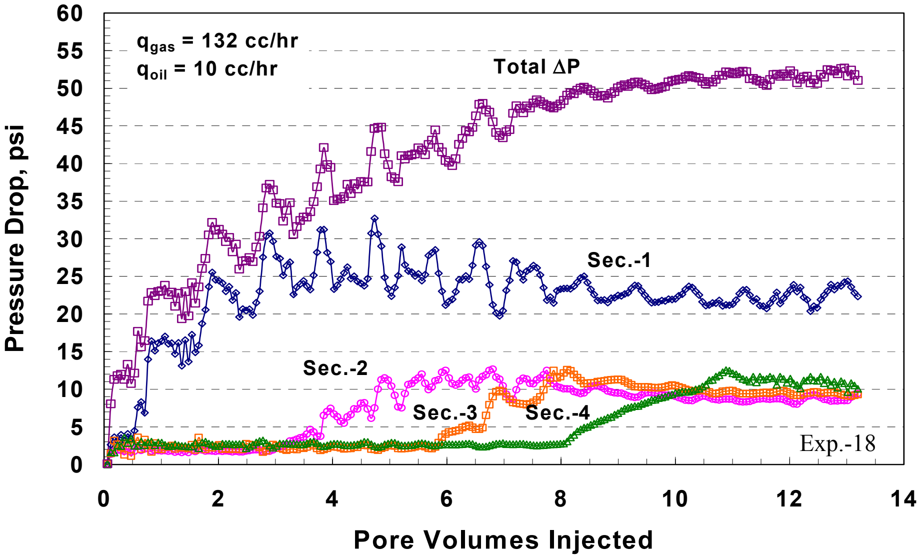

Figure B.157: Pressure drop at different sections across the core during co-injection of equilibrium gas and condensate phases at 1,200 psig.

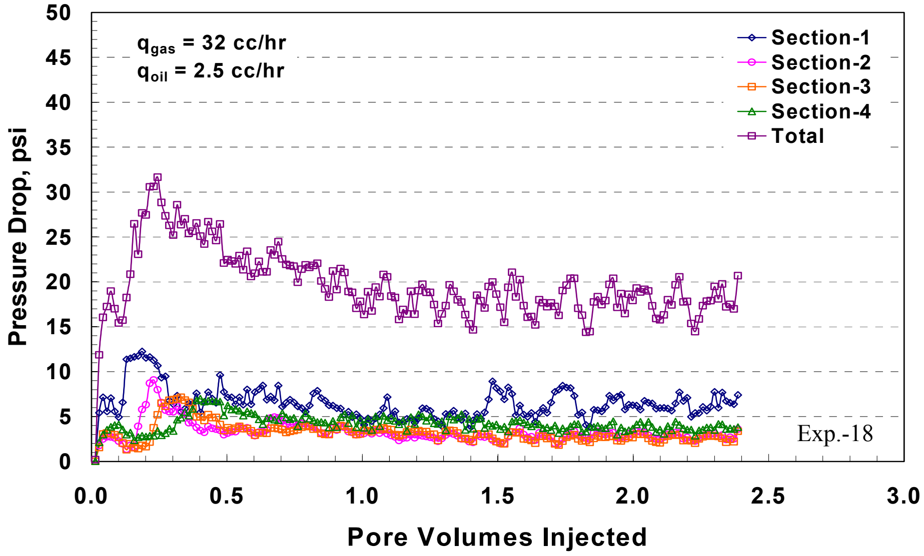

Figure B.158: Pressure drop at different sections across the core during co-injection of equilibrium gas and condensate phases at 1,200 psig at steady state.

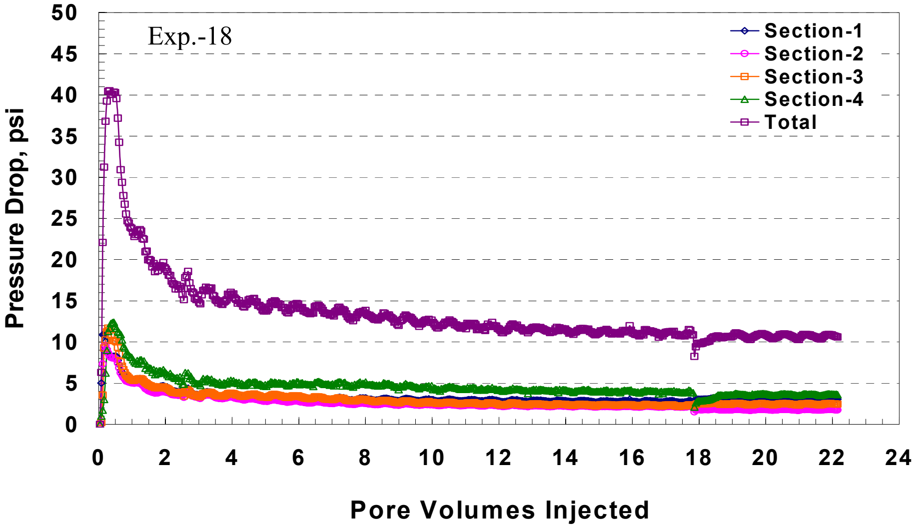

Figure B.159: Pressure drop at different sections across the core during equilibrium gas flow at 99 cc/hr and 1,200 psig.

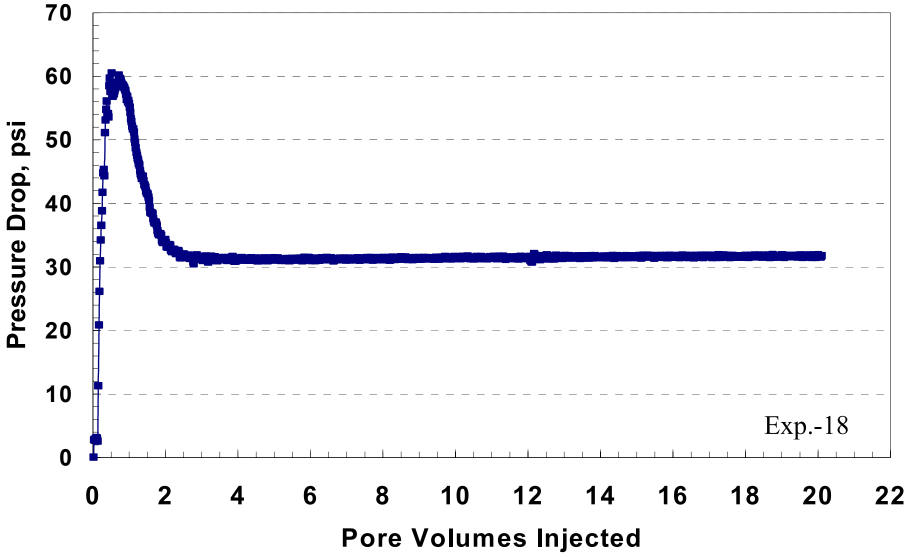

Figure B.160: Pressure drop across the core during the first methanol treatment at a flow rate of 20 cc/hr and 1,200 psig.

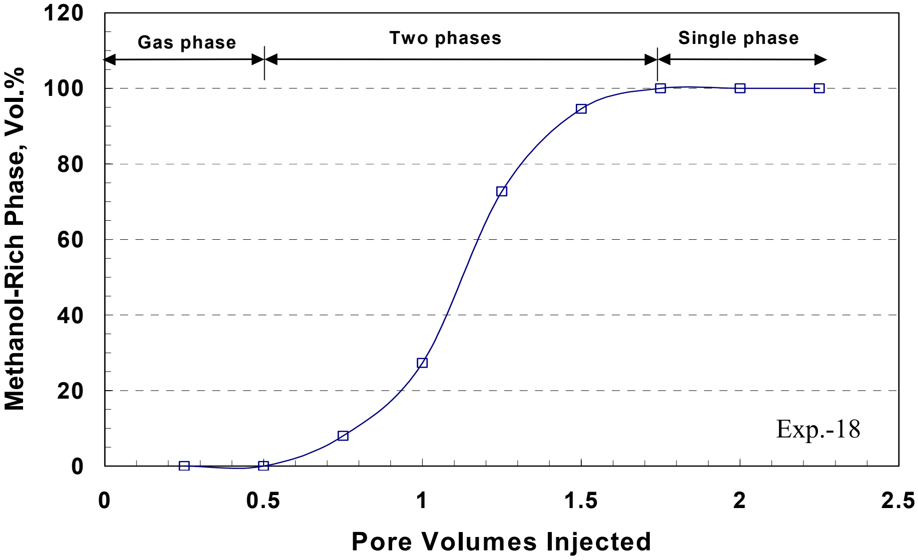

Figure B.161: Methanol-rich phase measured during the first methanol treatment.

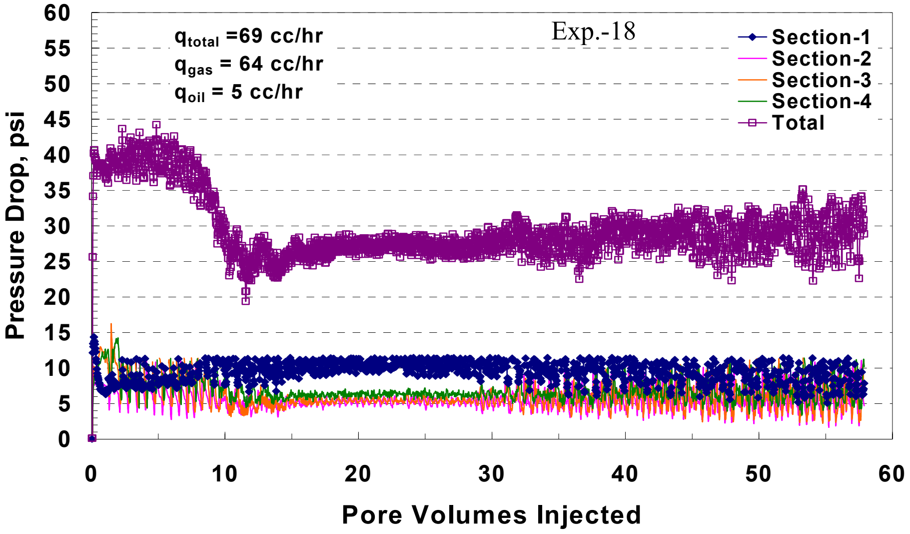

Figure B.162: Pressure drop at different sections across the core during co-injection of equilibrium gas and condensate phases after the first methanol treatment at 1,200 psig.

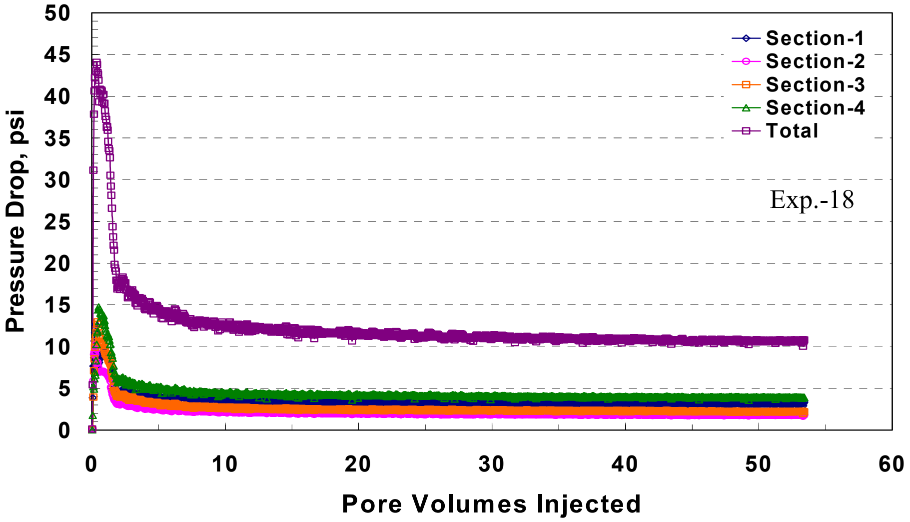

Figure B.163: Pressure drop at different sections across the core during equilibrium gas flow after the first methanol treatment at 99 cc/hr.

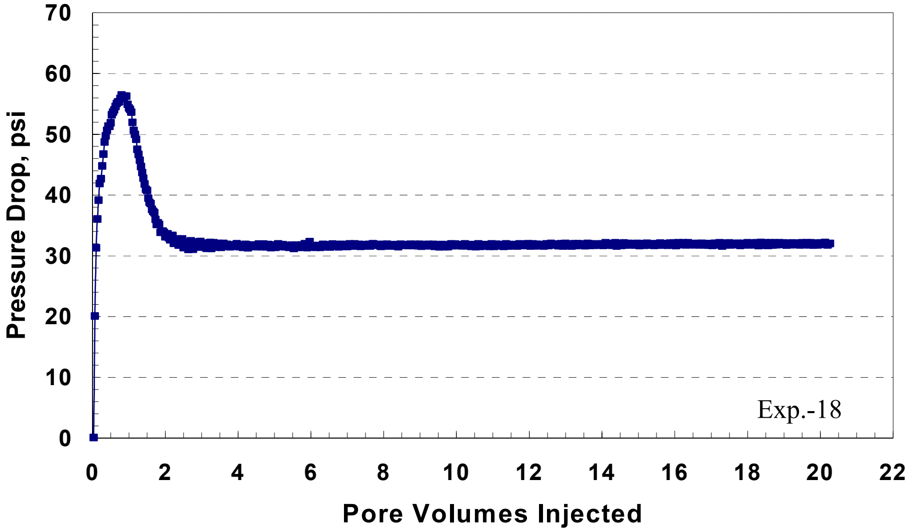

Figure B.164: Pressure drop across the core during the second methanol treatment at a flow rate of 20 cc/hr and 1,200 psig.

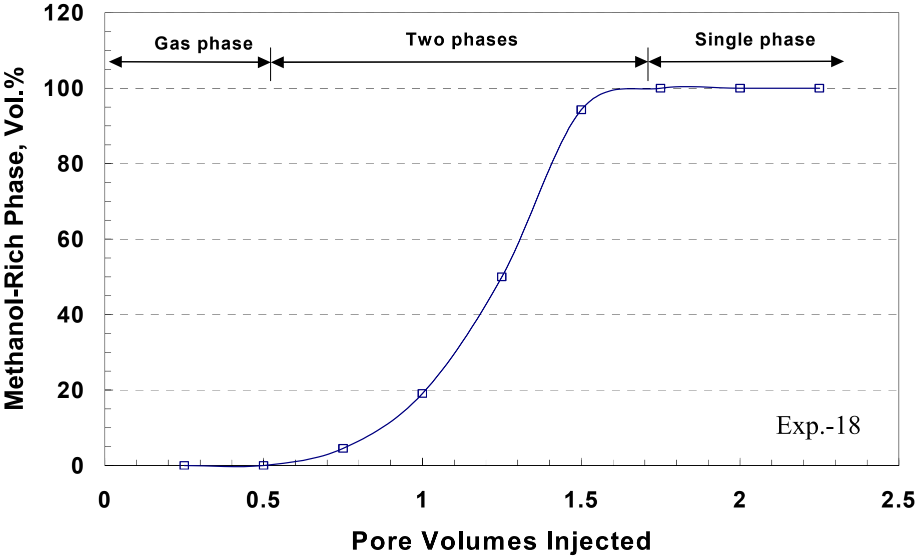

Figure B.165: Methanol-rich phase measured during the second methanol treatment.

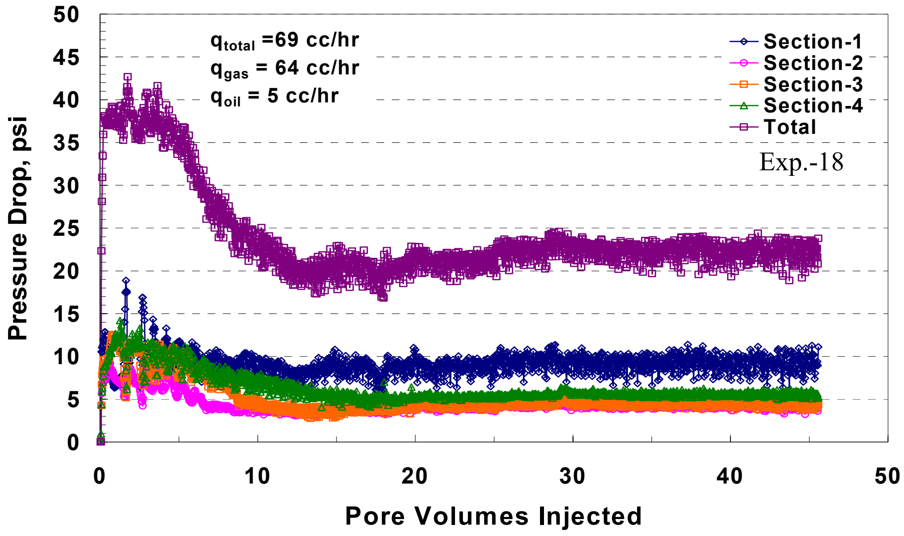

Figure B.166: Pressure drop at different sections across the core during co-injection of equilibrium gas and condensate phases after the second methanol treatment at 1,200 psig.

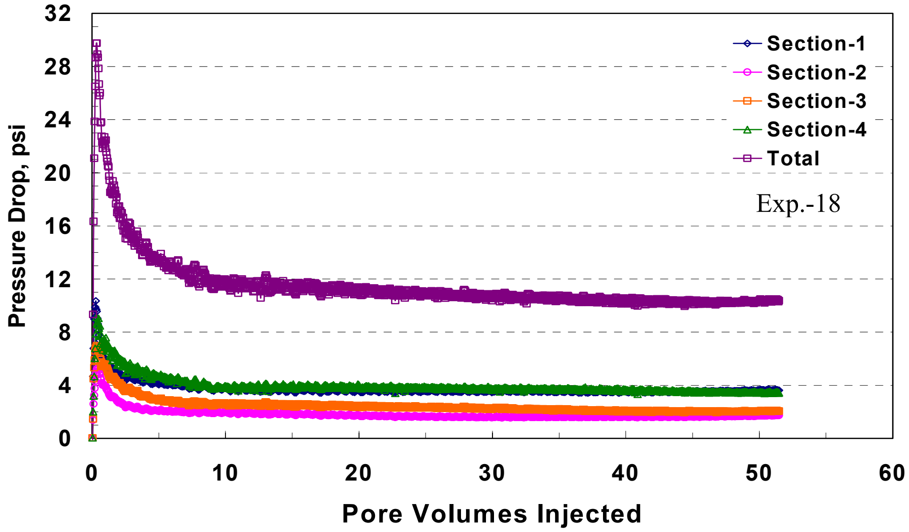

Figure B.167: Pressure drop at different sections across the core during equilibrium gas flow after the first methanol treatment at 99 cc/hr.

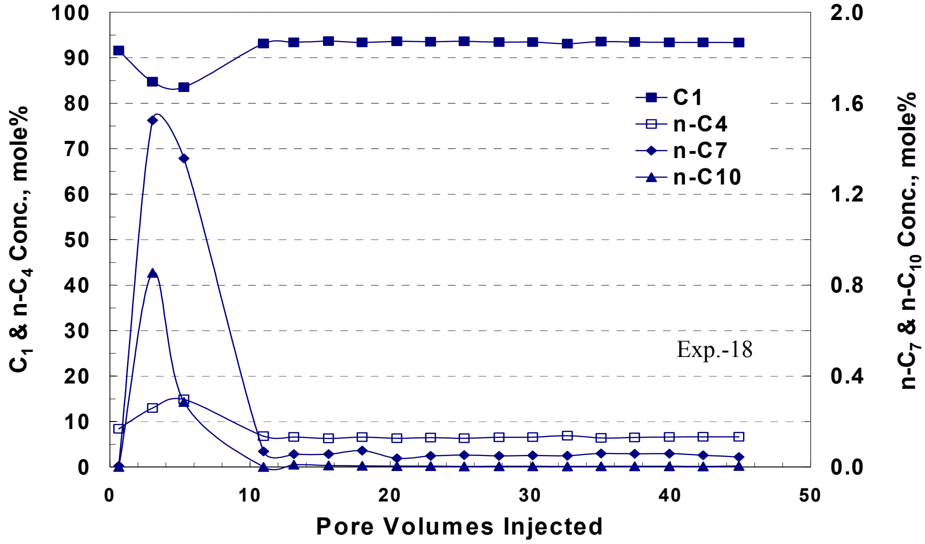

Figure B.168: Components concentrations during equilibrium gas flow after the second methanol treatment.

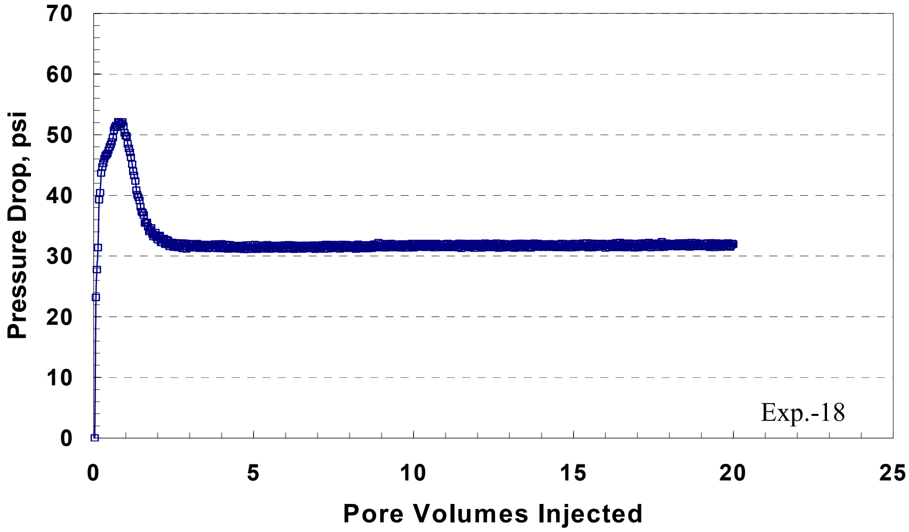

Figure B.169: Pressure drop across the core during the third methanol treatment at a flow rate of 20 cc/hr and 1,200 psig.

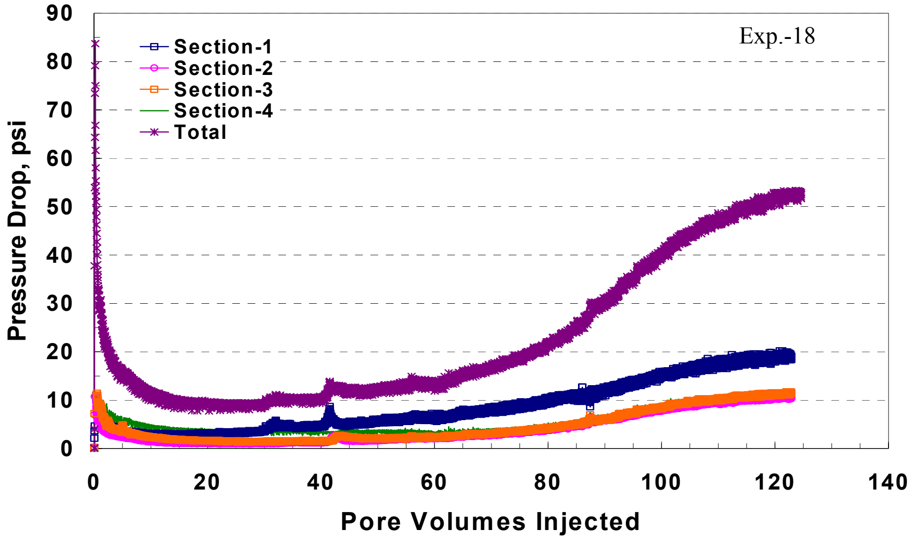

Figure B.170: Pressure drop at different sections across the core during dynamic condensate accumulation after the third methanol treatment at a pump rate of 20 cc/hr and 1,200 psig.

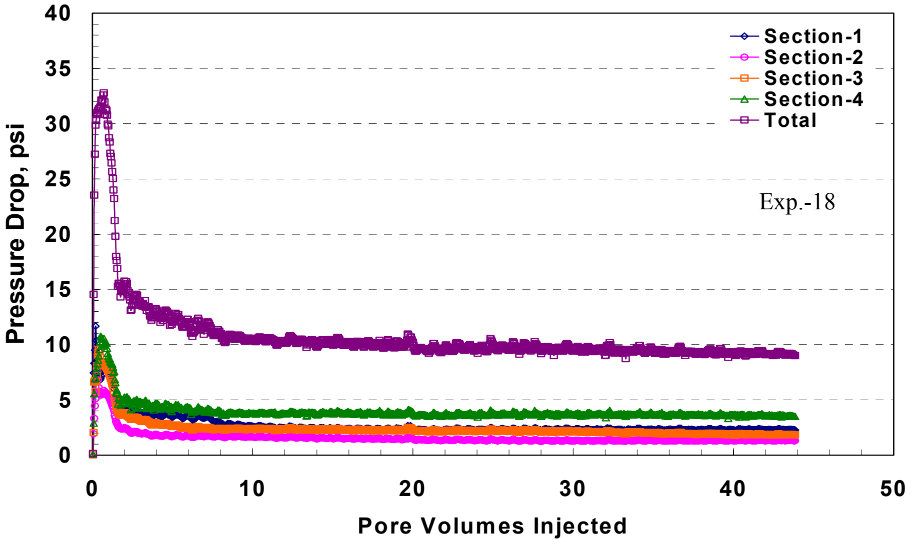

Figure B.171: Pressure drop at different sections across the core during equilibrium gas flow after the third methanol treatment at 99 cc/hr and 1,200 psig.

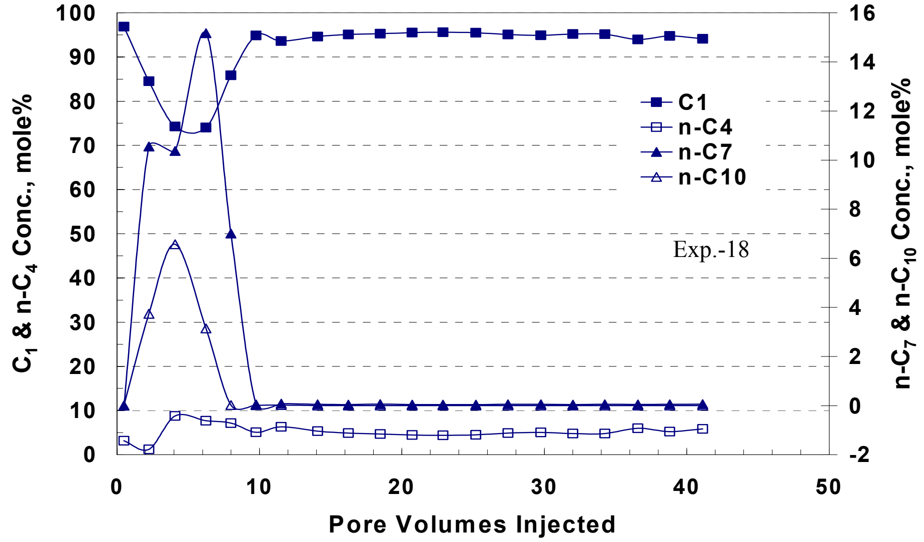

Figure B.172: Components concentrations during equilibrium gas flow after the third methanol treatment.

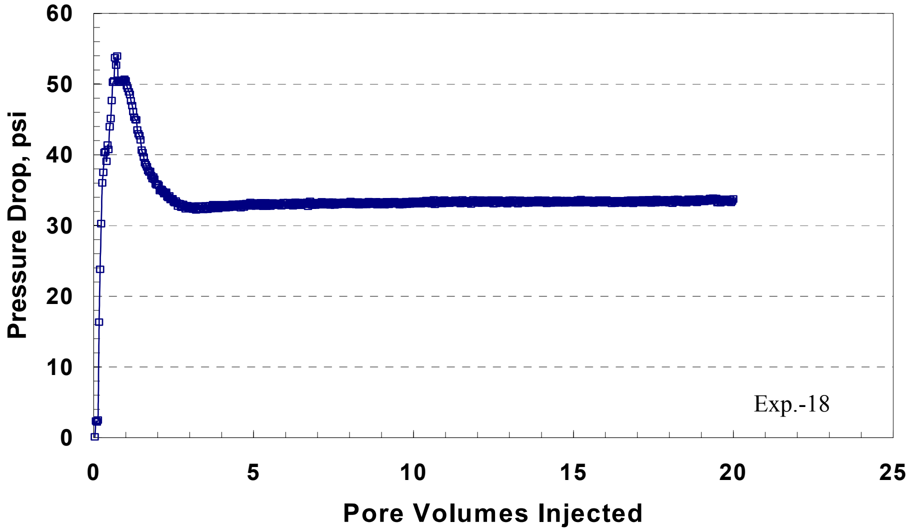

Figure B.173: Pressure drop across the core during the fourth methanol treatment at a flow rate of 20 cc/hr and 1,200 psig.

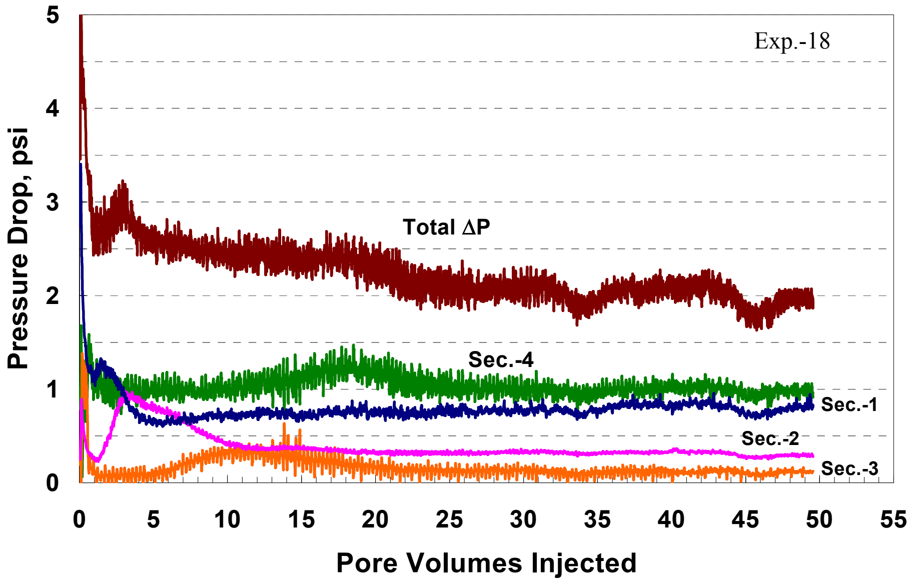

Figure B.174: Pressure drop at different sections across the core during dynamic condensate accumulation after the fourth methanol treatment at a flow rate of 2 cc/hr and 1,200 psig.

B.14 Summary of Experiment No. 19

B.14.1 Objectives

The objectives of this experiment are: (1) to determine the evaporation rate of residual condensate by methane flow, (2) to analyze the composition of the core effluent during two-phase flow at higher rate using dynamic flashing, (3) to determine the evaporation rate of methanol by methane flow, and (4) to study the effect of flowing pressure on condensate accumulation. This experiment was performed on a Texas Cream limestone core.

B.14.2 Revaporization of Condensate with Methane

The core used in this experiment is the same one used in Experiments 15, 16, 17 and 18. The core has been saturated with condensate during Experiment-18. Methane gas was flowed through the core at 1,200 psig and various flow rates to revaporize the condensate and see if it restores the initial core permeability. **Figure B.175** shows pressure drop at different sections across the core during methane flow at 1,200 psig and various flow rates. At the flow rate of 99 cc/hr, the pressure drop across the core gradually decreased until it reached a stabilized value after 40 PV. This result indicates that the removal of condensate by methane flooding is a very slow process since convective mass transfer from the condensate film into the flowing gas phase controls it. **Table B.129** gives the measured restored core permeability at various flow rates. The average restored permeability (k = 3.70 md) is very close to the initial one measured (k = 3.82 md) in Experiment-18, since the same core was used in both experiments. Therefore, methane revaporized all the residual condensate from the core.

Figure B.176 shows the composition of the core effluent during revaporization of condensate with methane flow at 1,200 psig. Once methane was flowed through the core, it displaced the residual condensate and creating flowing channels. The concentrations of n-C_4, n-C_7, and n-C_{10} components increased to a maximum value of 8.36, 1.30, and 1.31 mole%, in sequence, after an injection of 3.2 PV of methane. The increases in these concentrations associated with the increase in the pressure drop (**Figure B.175**). This means that methane faced a resistance from the residual condensate to be displaced. The flow initiation pressure drop, calculated from the difference between the maximum pressure drop and the stabilized value, required to displace the condensate was found equal to 17 psia. Then, components concentrations gradually decreased in the effluent. Methane removed all the n-C_4 from the core after 10 PV were injected. However, the revaporization of n-C_7, and n-C_{10} is a very slow process since they are presented in a liquid form and may adsorb on the core pores. Once the flow rate was increased to 132 cc/hr, the concentrations of n-C_7, and n-C_{10} increased again in the effluent. This is because methane flowed through more pores that may not accessible at the lower rates. Although the core permeability was restored after 70 PV of methane flood, trace amount of n-C_{10} was detected in the effluent. Accordingly, revaporization of condensate with methane flood is very slow process and may not reliable to be used in immature fields.

B.14.3 Methane Flow at 3,000 psig

The pressure in both the upstream and downstream back-pressure regulators was set to 3,000 psig. Methane was flowed through the core at a flowing pressure of 3,000 psig that is above the dewpoint of the used gas mixture. **Figure B.177** shows the pressure drop at different sections across the core during methane flow at 3,000 psig and various flow rates. The pressure drop at each section reached a plateau value after and injection of 2 PV. The measured core permeability at each flow rate is given in **Table B.130**. The measured core permeability is consistence at each flow rate. However, the measured core permeability ($k = 2.74$ md) to methane at 3,000 psig is less than the initial permeability ($k = 3.70$ md). Trace amounts (<0.0004 mole%) of n-C_7 and n-C_{10} were detected by the GC in the effluent. Thus, the core is still having some of the condensate and this stage of methane was not able to displace it. This is probably due to the high pressure that traps the condensate.

B.14.4 Gas Mixture (Single-Phase)

Gas mixture was flowed through the core as a single-phase at 3,000 psig and two flow rates: 99 and 132 cc/hr. The pressure drop at different sections across the core during single-phase flow is illustrated in **Figure B.178**. The pressure drop increased initially to displace methane that has lower viscosity, from the core. Once the methane was completely displaced, the pressure drop stabilized at each section of the core. **Table B.131** lists the measured core permeability during single-phase flow at 3,000 psig. The obtained values of permeability are very close to those measured with the previous methane flood. Therefore, the gas mixture was flooded through the core as a single-phase since the flowing pressure is above the dewpoint.

B.14.5 Dynamic Condensate Accumulation

Before the start of this stage, the inlet and outlet valves of the core were closed. Pressure of the upstream back-pressure regulator was kept at 3,000 psig, while the pressure in the downstream back-pressure regulator was gradually decreased to 1,200 psig. During the gradual decrease of the pressure, the PVT cell that connected to the end of the coreholder was monitored. At the start, the PVT cell's window looks clear since the gas mixture presents as a single-phase. A Fog (black color) was formed inside the PVT cell when the pressure reached a value of 2,778 psig. Then, the window looked clear and droplets of liquid were formed at a pressure of 2,743 psig. This pressure is close to the measured dewpoint pressure (2,792 psig) of the gas mixture. Once the pressure of the downstream reached to 1,200 psig, single-phase flow (gas mixture above the dewpoint) was injected at 3,000 psig through the upstream back-pressure regulator and flashed into gas and condensate phases at the inlet of the core that was kept at 1,200 psig, while the bypass valve was open until the pressure in the lines stabilized. Then, the bypass valve was closed and inlet and outlet valves were open simultaneously. The gas mixture flow rate was set to 42 cc/hr (@ 3,000 psig). This flow rate gives a gas phase flowing at a rate of 104.59 cc/hr and a condensate phase flowing at 8.04 cc/hr at 1,200 psig. This stage allowed the gas-condensate to dynamically accumulated through the core. This mimics what happen in the wellbore region in retrograde reservoirs. The stage was stopped when the pressure drop across the core reached stable values.

Figure B.179 shows the pressure drop at different sections across the core during dynamic condensate accumulation at 1,200 psig. This figure shows how the condensate back propagates through the core. The pressure drop across Section-1 reached a plateau value after 5.7 PV. Then, the pressure drop across Section-2 started to increase at the arrival of condensate bank and so on. The condensate bank took around 5.7 PV in each section of the core. The two-phase flow reached a steady state in the core after an injection of 22.6 PV. Since this volume is larger than that expected at a fractional flow of 7.14%, non-equilibrium behavior extended it since the flow rate was high. **Table B.132** gives gas and oil relative permeabilities measured during dynamic condensate accumulation at 1,200 psig and 42 cc/hr. The measured values are the same as those determined in the pervious experiments since the same core was used in all of them.

Composition concentrations of the effluent during are illustrated in **Figure B.180**. The concentration of each component was almost constant during the condensate accumulation stage. To better understand the compositional analysis, the concentration of each component was normalized to its concentration in the equilibrium gas as shown in **Figure B.181**. This figure indicates that the amount of each component detected during the two-phase flow is less than that in the equilibrium gas. Therefore, non-equilibrium dominates since the flow was high and local equilibrium between flowing gas and condensate phases was not accomplished.

The condensate and gas volume ratio in the PVT cell was adjusted to be 7% by drawing some of the condensate out of the cell and balanced the pressure with the gas phase at 1,200 psig. Then, the cell was isolated from the flow lines and shut-in for 2 days. Then, the gas phase was charged into GC for compositional analysis without any further pumping. Composition concentrations were normalized to the values in the equilibrium gas as shown in **Figure B.182**. The composition of the gas phase are close to those in the equilibrium gas since it was left in contact with condensate phase inside the PVT cell for 2 days. This finding confirms that local equilibrium during two-phase is sensitive to flow rate. The concentration of n-C_{10} components is larger than that in the equilibrium gas due to the instability of the GC measurements to its very small amount.

B.14.6 Methanol Treatment

Pure methanol was injected through the core at an injection rate of 36 cc/hr and 1,200 psig. The volume of methanol injected was 20 PV. The pressure drop across the core during methanol injection is shown in **Figure B.183**. The pressure drop across the core increased to a maximum value of 282 psia since it has a larger viscosity than the two-phase present in the core. Then, it gradually decreased to reach a constant value of 58.96 psig. The measured permeability to methanol was found equal to 3.57 md. The measured permeability to methanol is the same as that restored by methane flow after revaporization of condensate. This value confirms that residual condensate was existed during the methane and gas mixture flows at 3,000 psig. So, methanol treatment is proven to be an effective way to get rid of residual condensate and restore the initial permeability.

B.14.7 Revaporization of Methanol with Methane Flow

The purpose of this stage is to determine the evaporation rate of methanol from the core to assess the persistence of methanol treatment. Methane was flowed directly after the methanol treatment at 1,200 psig and various flow rates. **Figure B.184** depicts the pressure drop at different sections across the core during revaporization of methanol by methane flood. The pressure drop was sharply increased to reach a maximum value of 57.7 psia to displace methanol from the core. The total volume of methanol collected in the effluent was 11.1 mL (0.55 PV), which is close to that collected in the previous experiment. The amount of liquid methanol collected is corresponding to a residual methanol saturation of 44.5%. This saturation is quite high unless the methanol was displaced as a vapor too. **Table B.133** lists the measured gas permeability to methane after the revaporization of methanol at 1,200 psig and different flow rates. The obtained permeability values are less than the initial core permeability. Although large volumes of methane (76 PV) were injected, the methanol was not completely evaporated from the core. The volume of methane stage was insufficient to clean up the core and restore its initial permeability. Accordingly, methanol injection is a long-lasting treatment, but it is a temporary solution to remove condensate blocking as found in the previous experiments.

B.14.8 Methane Flow at 2,500 psig

The pressure of the upstream and downstream back-pressure regulators was increased to 2,500 psig. Methane was injected through the core at two flow rates: 132 and 195 cc/hr, in sequence. **Figure B.185** shows the pressure drop across the core during methane flow at 2,500 psig. The pressure drop increased to 48.7 psia and gradually decreased to reach a plateau value of 22 psia at 132 cc/hr. The measured core permeability to methane at 2,500 psig is given in **Table B.134**.

B.14.9 Dynamic Condensate Accumulation at 2,500 psig

The aim of this stage is to investigate the effect of flowing pressure on condensate accumulation. The pressure of the upstream back-pressure regulator was increased to 3,000 psig, while the downstream back-pressure regulator was kept at a pressure of 2,500 psig. The single-phase mixture was injected at a flow rate of 42 cc/hr at 3,000 psig and flashed at the inlet of the core into gas and condensate phases. Flash calculation using the PREOS at 145°F and 2,500 psig performed on the gas mixture resulted in a liquid dropout (LDO) of 18.18%, as given in **Table B.135**. The calculated flow rates for the gas and condensate phases at 2,500 psig are 41.74 and 9.27 cc/hr, respectively.

Figure B.186 shows the pressure at different sections across the core during dynamic condensate accumulation at 2,500 psig. The pressure drop in all sections of the core increased at the same time, expect in Section-2. This is because Section-2 has the highest permeability (**Table B.129**) where small changes in the pressure drop could not be measured. After that, the pressure drop across the core gradually decreased until it leveled-down. It seems that the condensate phase started to mobilize with the gas phase since it is flowing at a high fractional flow (18.18%). Once the condensate fills most of the accessible pores, it starts to move with the gas phase in the effluent. So, a drainage process took place after the fill-up of pores. As can be seen from **Figure B.186**, steady state was reached after a cumulative injection of 5.5 PV of two-phase flow. Fewer pore volumes were required to reach steady state at 2,500 psig compared to 1,200 psig (~22 PV) since the liquid dropout is higher at 2,500 psig.

The dynamic fractional flow of condensate was measured by recording the volume of hydrocarbon inside the PVT cell as a function of time. **Figure B.187** shows the cumulative hydrocarbon volume collected during dynamic condensate accumulation through the core at 2,500 psig and 42 cc/hr. The first curve was measured during condensate accumulation period at which the pressure drop was increasing, while the second curve was at a steady state when the pressure drop stabilized. During condensate accumulation, the measured fractional flow of condensate was found equal to 27.32% which is higher than the calculated one. This high value indicates that condensate was moving from the beginning of the flow and a drainage process took place resulted in a high volume of a movable condensate bank. At steady state, the condensate phase was moving with the gas phase at a fractional flow of 17.07%, which is very close to the calculated value.

Gas and oil relative permeabilities measured during dynamic condensate accumulation through the core at 42 cc/hr and 2,500 psig are given in **Table B.136**. Condensate accumulation caused a severe damage to the core where the gas and oil relative permeabilities decreased to 0.125 and 0.090, respectively. These results are less than those obtained at 1,200 psig. The gas relative permeability decreased more at high pressure, but still below the dewpoint, because the associated liquid dropout is high too.

The GC analyzed the effluent gas phase during dynamic condensate accumulation through the core at 2,500 psig. The concentration of each component determined by the GC was normalized to its concentration in the equilibrium gas phase (**Table B.135**). **Figure B.188** shows the normalized concentrations of the gas-phase composition during dynamic condensate accumulation through the core at 42 cc/hr and 2,500 psig. During condensate accumulation, the effluent gas phase has very small amounts of n-C_4, n-C_7, and n-C_{10} than those in the equilibrium gas at the same pressure (2,500 psig). Most of the heavy components were dropped out in the PVT cell resulted to a very high measured liquid dropout (27.32%). Therefore, the compositional analysis supports the high value of the measured liquid dropout and the existence of a drainage process during condensate accumulation period. At steady state period, compositional analysis also indicates the flowing gas phase is very close to the equilibrium gas. The non-equilibrium behavior at this high pressure (2,500 psig) has less effect than that at 1,200 psig, especially at steady state.

B.14.10 Summary of the Results for Coreflood Experiment-19

Condensate can be revaporized by methane flood, but it requires large volumes of methane to be injected. The revaporization of residual condensate by methane is very slow process since it is controlled by mass transfer and may not be practical in the field. Non-equilibrium behavior influenced on the condensate accumulation and extended the period to reach steady state. Compositional analyses showed that the gas mixture has different composition concentrations when it is flowing at higher rates compared to the equilibrium gas phase. Dynamic condensate accumulation at 2,500 psig resulted in a severe reduction in core permeability. The dynamic fractional flow measured during two-phase flow at 2,500 psig agreed with the calculated value. Fewer pore volumes of two-phase flow were required to reach steady state at 2,500 psig compared to 1,200 psig (~22 PV) since the liquid dropout is higher at 2,500 psig. The non-equilibrium behavior at high pressure (2,500 psig) has less effect on condensate accumulation than that at 1,200 psig, especially at steady state.

Table B.129: Initial core permeability measured during revaporization of condensate with methane flow at 1,200 psig.

	q = 99 cc/hr	q = 132 cc/hr	q = 224 cc/hr
Section-1	2.69	2.90	2.72
Section-2	6.83	5.53	5.31
Section-3	3.67	4.14	4.05
Section-4	3.74	3.33	3.47
Whole Core	3.83	3.63	3.63

Table B.130: Core permeability measured during methane flow at 3,000 psig.

	q = 99 cc/hr	q = 132 cc/hr	q = 228 cc/hr
Section-1	2.36	2.35	2.32
Section-2	3.76	3.79	3.75
Section-3	2.26	2.27	2.15
Section-4	3.11	3.24	3.26
Whole Core	2.76	2.79	2.72

Table B.131: Core permeability measured during gas mixture (single-phase) flow at 3,000 psig.

	q = 99 cc/hr	q = 132 cc/hr
Section-1	2.66	2.59
Section-2	4.59	4.48
Section-3	2.69	2.58
Section-4	4.06	3.98
Whole Core	2.12	2.17

Table B.132: Gas and oil relative permeabilities measured during dynamic condensate accumulation at 42 cc/hr and 1,200 psig.

	ΔP, psia	k_{rg}	k_{ro}
Section-1	16.28	0.141	0.184
Section-2	8.65	0.124	0.162
Section-3	9.34	0.171	0.224
Section-4	10.10	0.178	0.233
Whole Core	44.30	0.155	0.202

Table B.133: Core permeability measured during revaporization of methanol by methane flood at 1,200 psig.

	q = 132 cc/hr	q = 195 cc/hr	q = 228 cc/hr
Section-1	2.20	2.44	2.58
Section-2	3.89	3.82	4.39
Section-3	2.42	2.55	2.68
Section-4	1.39	1.51	1.57
Whole Core	2.24	2.37	2.52

Table B.134: Core permeability measured during methane flow at 2,500 psig.

	q = 132 cc/hr	q = 195 cc/hr
Section-1	2.37	2.46
Section-2	2.16	2.67
Section-3	1.43	1.56
Section-4	1.23	1.38
Whole Core	1.84	1.98

Table B.135: Flash calculation using the PREOS at 145°F.

	Concentration, mole%		
Component	Single-Phase at 3,000 psig	Gas-Phase at 2,500 psig	Liquid-Phase at 2,500 psig
C_1	78.50	85.727	60.368
n-C_4	15.00	11.509	23.759
n-C_7	5.00	2.361	11.620
n-C_{10}	1.50	0.403	4.252
Density, lbmole/ft^3	0.6719	0.52976	0.65884
Viscosity, cp	0.0388	0.0235	0.0762
LDO, vol.%	100	81.82	18.18

Table B.136: Gas and oil relative permeabilities measured during dynamic condensate accumulation through the core at 42 cc/hr and 2,500 psig.

	ΔP, psia	k_{rg}	k_{ro}
Section-1	8.84	0.174	0.125
Section-2	5.88	0.123	0.089
Section-3	8.57	0.125	0.090
Section-4	6.45	0.188	0.135
Whole Core	36.89	0.125	0.090

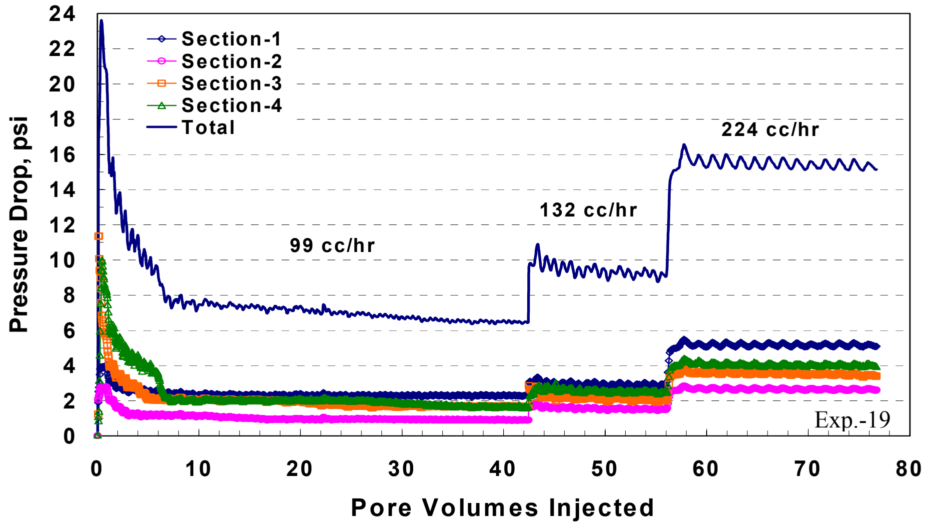

Figure B.175: Pressure drop at different sections across the core during revaporization of condensate with methane at 1,200 psig.

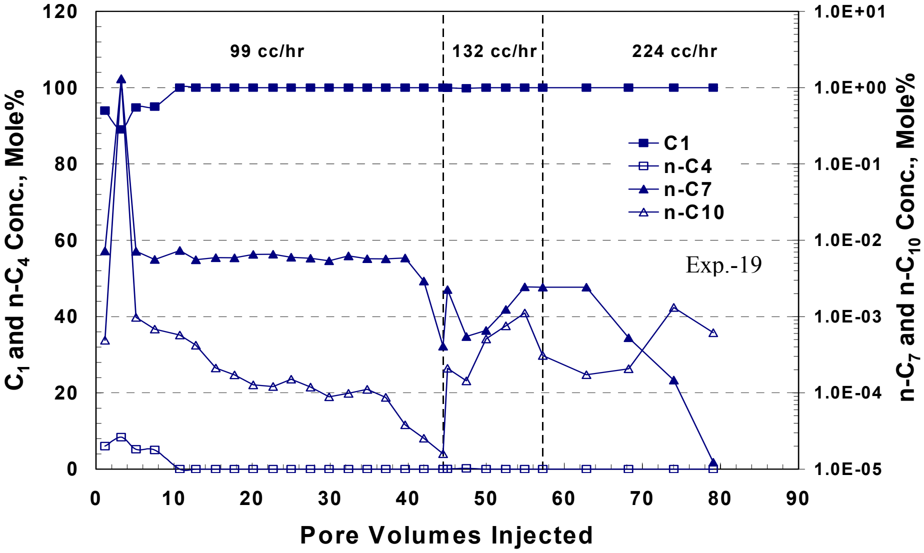

Figure B.176: Composition of the core effluent during revaporization of condensate with methane at 1,200 psig.

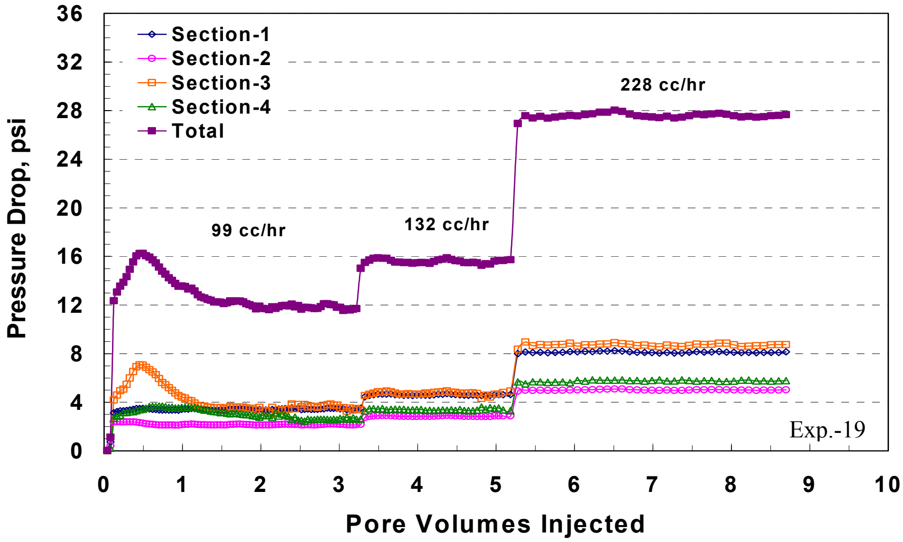

Figure B.177: Pressure drop at different sections across the core during methane flow at 3,000 psig and various flow rates.

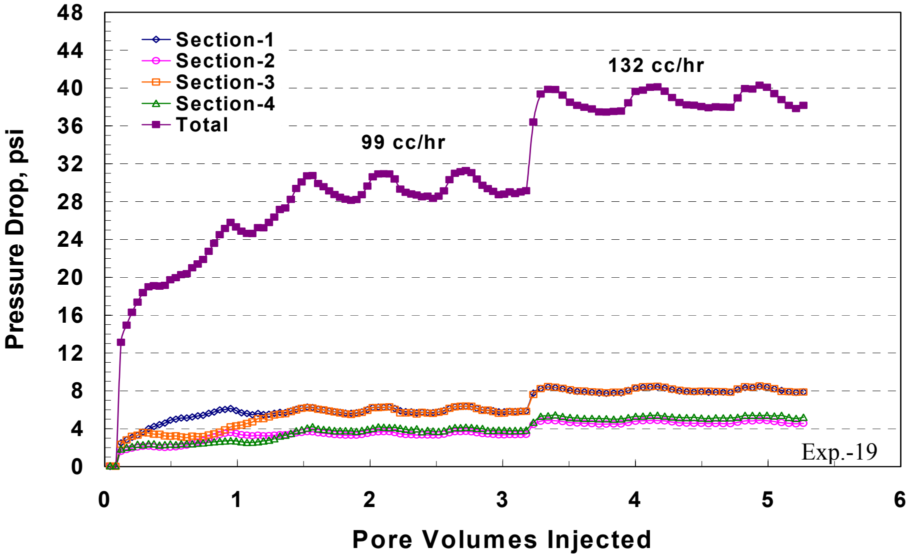

Figure B.178: Pressure drop at different sections across the core during gas mixture (single-phase) flow at 3,000 psig.

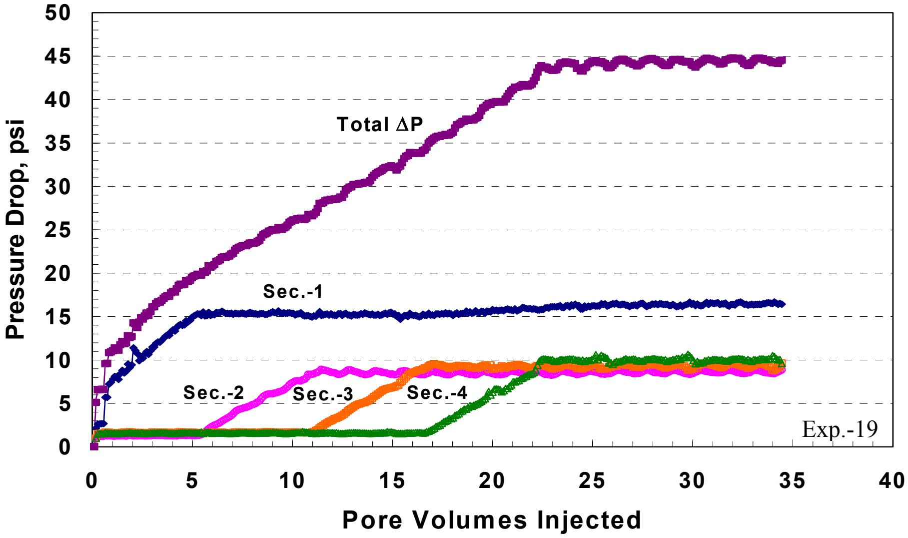

Figure B.179: Pressure drop at different sections across the core during dynamic condensate accumulation at 42 cc/hr and 1,200 psig.

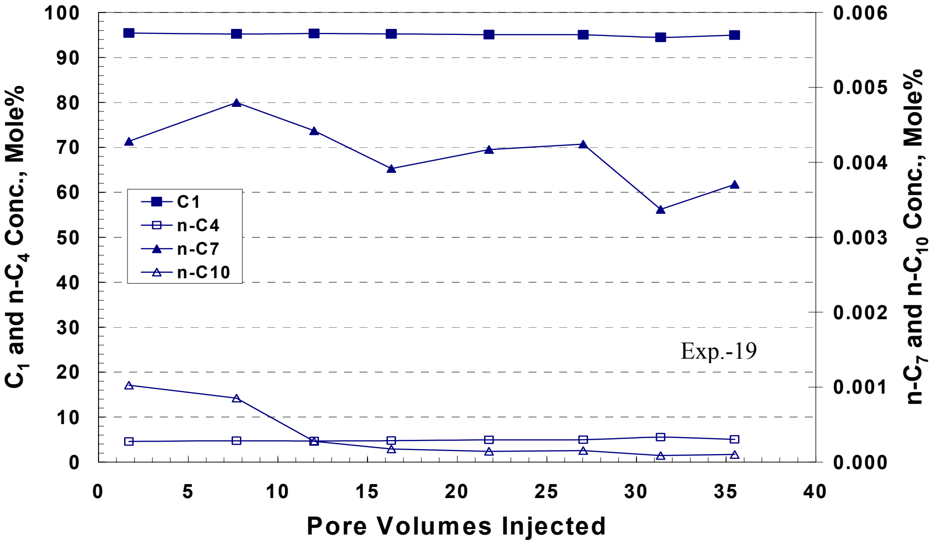

Figure B.180: Composition of the core effluent during dynamic condensate accumulation at 1,200 psig and 42 cc/hr.

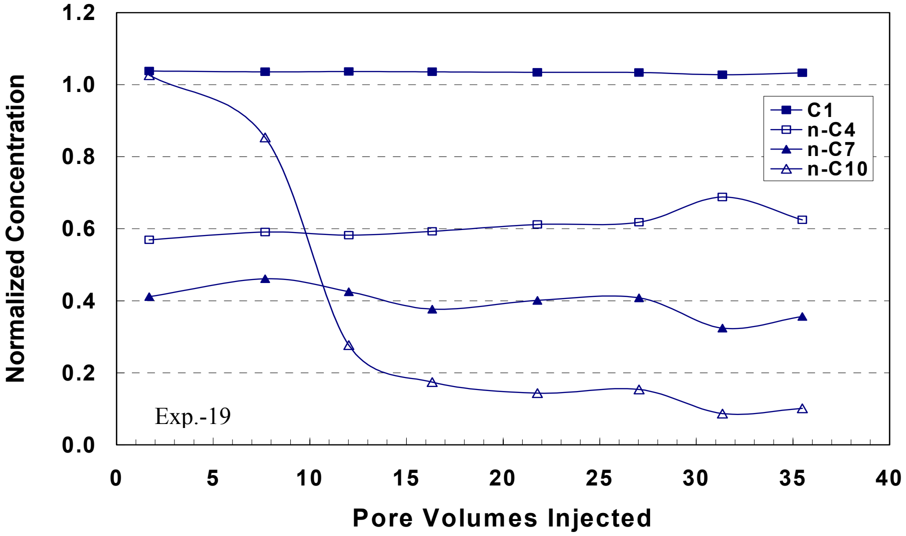

Figure B.181: Normalized concentration of the core effluent during dynamic condensate accumulation at 1,200 psig and 42 cc/hr.

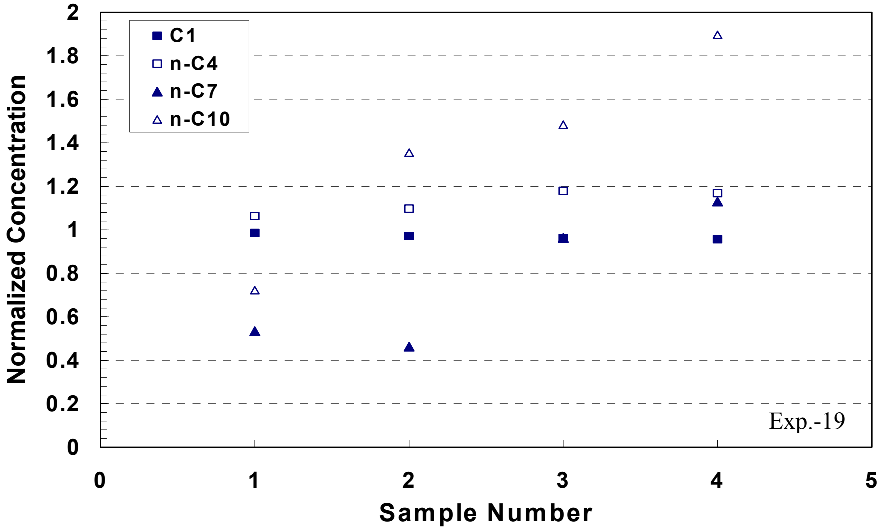

Figure B.182: Normalized concentrations of the gas phase that was in equilibrium with condensate phase inside the PVT cell at 1,200 psig.

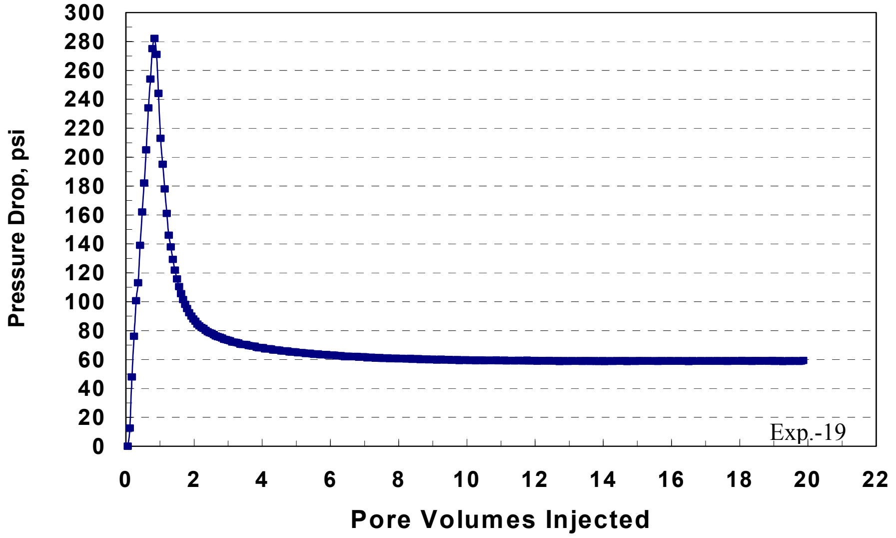

Figure B.183: Pressure drop across the core during methanol flow at 1,200 psig and 36 cc/hr.

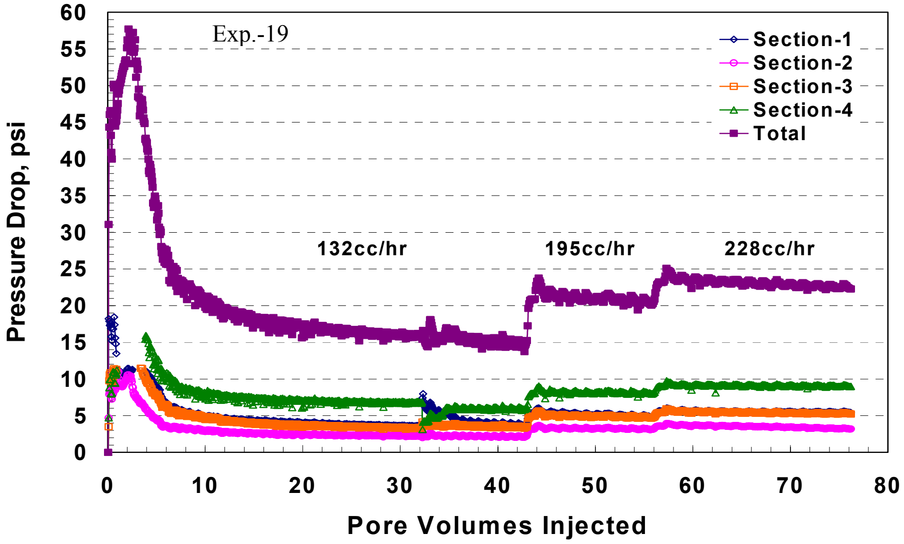

Figure B.184: Pressure drop at different sections across the core during revaporization of methanol with methane at 1,200 psig.

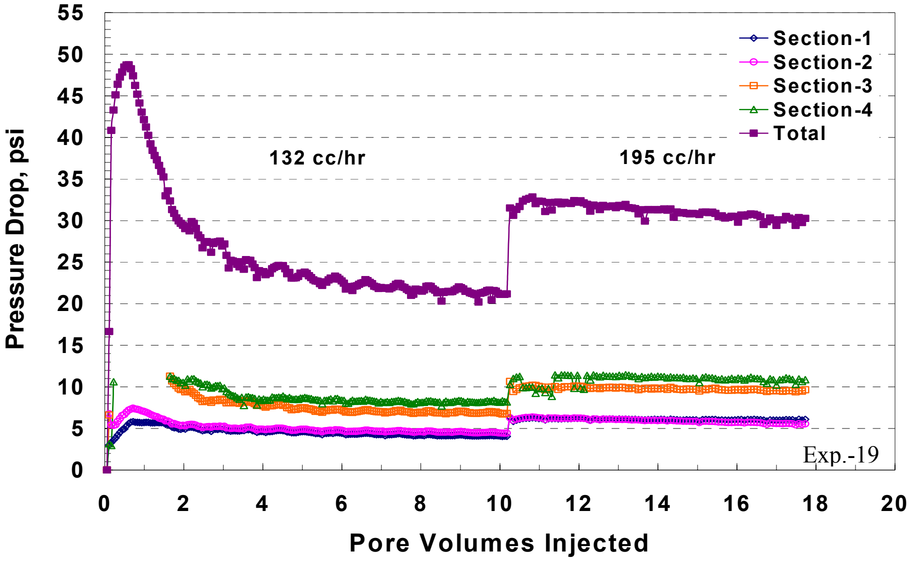

Figure B.185: Pressure drop at different sections across the core during methane flow at 2,500 psig.

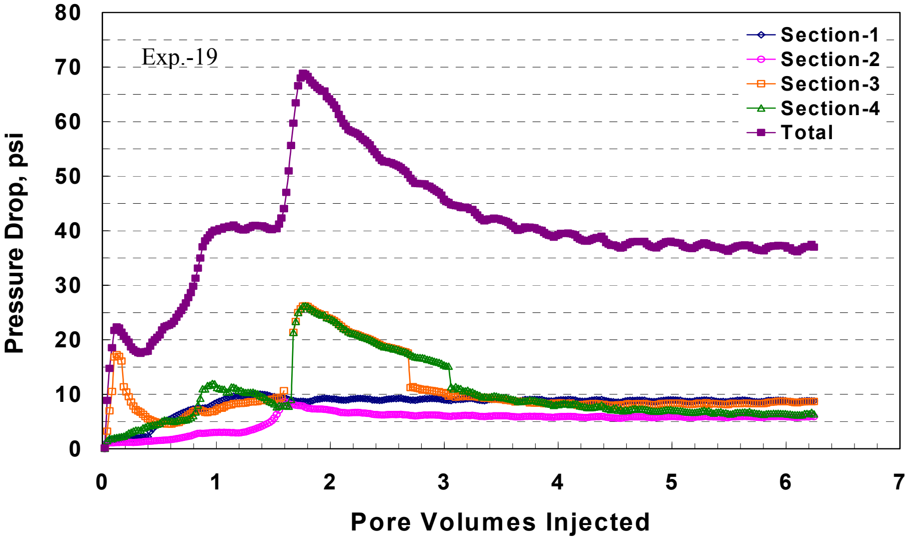

Figure B.186: Pressure drop at different sections across the core during dynamic condensate accumulation at 42 cc/hr and 2,500 psig.

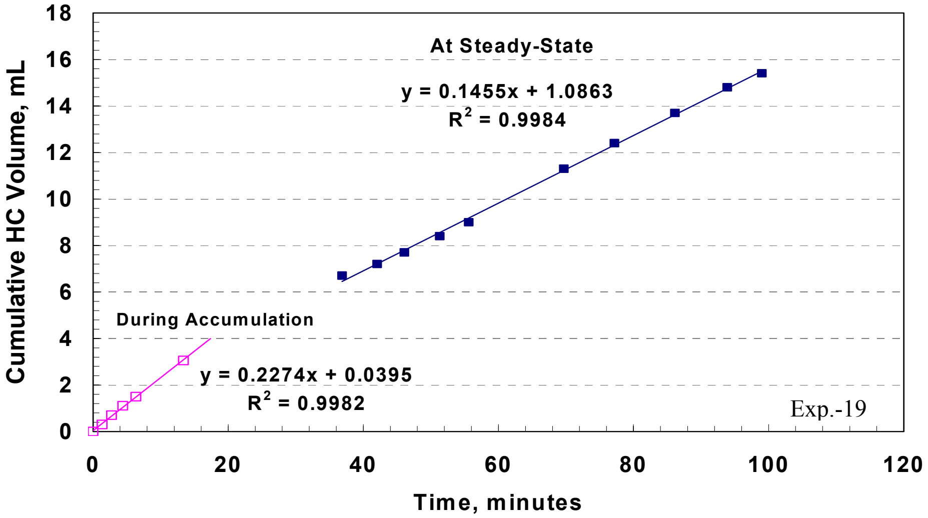

Figure B.187: Cumulative hydrocarbon liquid volume collected during two-phase flow through the core at 2,500 and 42 cc/hr.

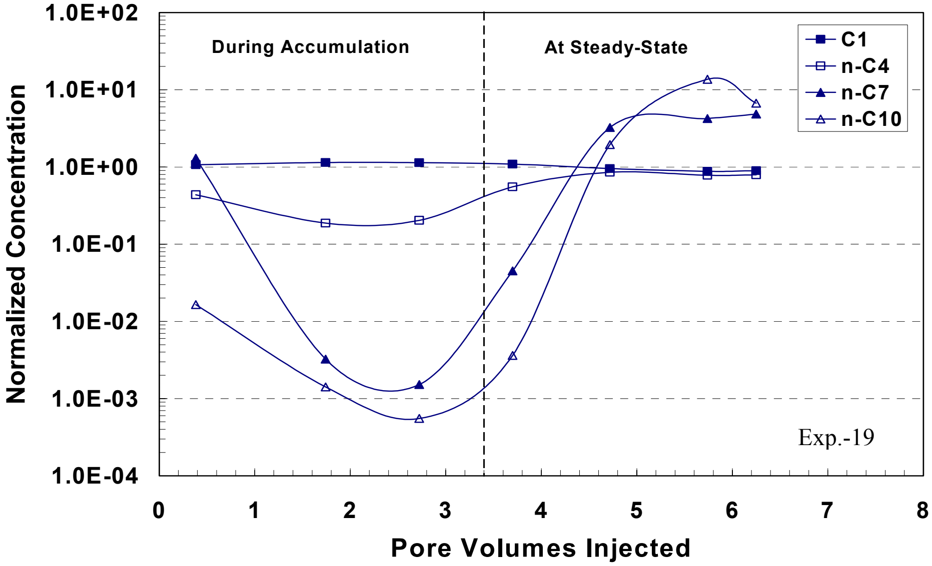

Figure B.188: Normalized concentrations of the gas phase composition during dynamic condensate accumulation through the core at 42 cc/hr and 2,500 psig.

Appendix C: Characterizing Flow Properties of Cores

This appendix describes the study of flow properties and heterogeneity of cores. This study was performed on Texas Cream limestone and Antolini sandstone cores. Tracer tests were performed to measure petrophysical properties including: porosity, permeability, dispersion coefficient, and dispersivity. The appendix starts with an introduction that gives a background and equations needed to calculate the petrophysical properties. The second section explains the apparatus used in tracer tests. Then, experimental results will be discussed for each core.

C.1 Introduction

Hydrodynamic dispersion is a mass transport mechanism in which a miscible fluid displaces another fluid in a porous medium. The displaced fluid tends to mix with the displacing fluid. This results in a development of a mixing or transition zone at the front in which the concentration of the injected fluid decreases. Experiments showed that the mixing zone grows with time or with the distance traveled (Coats and Smith, 1964; Bear, 1972; Brigham, 1974; Baker, 1977; Peters et al., 1996). Dispersion coefficient is usually determined by measuring the concentration of a tracer in the effluent and calculating the longitudinal dispersion coefficient from the breakthrough curve using the convection-dispersion equation:

$$\frac{\partial C}{\partial t}+\frac{u}{\phi R_f}\frac{\partial C}{\partial x}-\frac{D_L}{R_f}\frac{\partial^2 C}{\partial x^2}=0 \qquad \text{(C.1)}$$

where

C = Tracer concentration

u = fluid flux, q/A

D_L = longitudinal dispersion coefficient

ϕ = average porosity of the porous medium

R_f = a retardation factor (≥1) that accounts for adsorption of the tracer by the porous medium

The analytical solution of this equation depends on the set of initial and boundary conditions that describe the tracer experiments. Generally, all solutions give alike results when the porous medium is long compared with the length of the mixed zone (Brigham, 1974). An approximate solution, in a dimensionless form, for the case of no adsorption (R_f = 1) and a displacement of two miscible fluids having equal densities and viscosities is (Peters et al., 1996):

$$C_D(x_D, t_D) = \frac{1}{2}\left[\operatorname{erfc}\left(\sqrt{N_{Pe}}\left[\frac{x_D - t_D}{2\sqrt{t_D}}\right]\right)\right] \tag{C.2}$$

where erfc is the complementary error function. The dimensionless variables are defined as follows:

$$C_D = \frac{C(x, t) - C_i}{C_j - C_i} \tag{C.3}$$

$$x_D = \frac{x}{L} \tag{C.4}$$

$$t_D = \frac{q\,t}{A\phi L} \tag{C.5}$$

$$N_{Pe} = \frac{q\,L}{A\phi D_L} \tag{C.6}$$

where,

C_i = initial tracer concentration

C_j = injected tracer concentration

L = length of the porous medium

q = volumetric injection rate

A = cross-sectional area of the porous medium

t = injection time

ϕ = average porosity of the porous medium

N_{pe} = Peclet number

The Peclet number is defined as the ratio of the convection to dispersion transport mechanisms. The mixing zone length is defined as the distance between two symmetric concentrations points, such as C_D=0.1 and C_D=0.9. The growth of the mixing zone length is given by (Lake, 1989; Peters et al., 1996):

$$\Delta x_D = 3.625\sqrt{\frac{t_D}{N_{Pe}}} \tag{C.7}$$

or in a dimensional form by:

$$\Delta x = 3.625\sqrt{D_L t} \tag{C.8}$$

The longitudinal dispersion coefficient can be determined by plotting C_D versus t_D for the breakthrough curve as follows:

$$D_L = \frac{qL}{A\phi}\left(\frac{J_{0.9} - J_{0.1}}{3.625}\right)^2 \tag{C.9}$$

where

$$J_{0.9} = \frac{1 - t_D}{\sqrt{t_D}} \text{ for } C_D = 0.9$$

$$J_{0.1} = \frac{1 - t_D}{\sqrt{t_D}} \text{ for } C_D = 0.1$$

Perkins and Johnston (1963) developed a correlation between longitudinal dispersion coefficient and Peclet number. They found that at a Peclet number less than 0.02, the diffusion and dispersion coefficients are equal in the porous medium. Both molecular diffusion and mechanical dispersion contribute to the dispersion coefficient. The molecular diffusion is resulting from variations in tracer concentration within the liquid phase. At values of Peclet number are greater than 6, the dispersion coefficient is dominated by mechanical dispersion and the effect of molecular diffusion can be neglected. Under the conditions of most reservoir rocks, the value of the Peclet number is greater than 6 (Bear, 1972). The longitudinal dispersion coefficient can be calculated as:

$$D_L = \frac{\alpha_L q}{A\phi} \tag{C.10}$$

where α_L is the longitudinal dispersivity of the porous medium. The longitudinal dispersivity is a primary petrophysical property of the porous medium.

This chapter deals with the study of heterogeneity of two types of cores using tracer tests. The longitudinal dispersion coefficient and dispersivity were calculated using the above equations.

C.2 Apparatus

UV Spectrophotometer Model 559 was used to measure the concentration of a tracer in the solution. Tungsten-bromide and deuterium lamps were used as light sources. The detector is a side-window photo-multiplier that having a wavelength range up to 900 nm. The UV Spectrophotometer has a wavelength accuracy of ±0.5 nm and a wavelength repeatability of ±0.1 nm. The working wavelength range is from 190 to 900 nm. The Spectrophotometer is connected to a flowchart recorder that provides pulses on a chart paper. This apparatus is running in a fully automated manner. This instrument is capable to measure Absorbance, Transmittance, Concentration, Single beam, and derivative. In this study, we used it to measure the Absorbance, which then converted to a concentration using a calibration curve.

C.3 Tracer Calibration Curve

The UV Spectrophotometer was calibrated using Potassium Iodide (KI) solution. A granular form of KI was purchased from EM Science Inc. with an assay > 99%. Standard solutions of predetermined concentrations (0-35 ppm) of KI were prepared in deionized water. The lower and upper wavelength limits used in this calibration were 190 and 275 nm, respectively. The UV Absorbance readings were normalized to the base line. **Table C.1** gives the UV Absorbance (%) for each standard solution. **Figure C.1** depicts the calibration curve for determining the concentration of KI from the UV Absorbance. This figure shows a linear relationship between the concentration and the UV Absorbance reading. The data of calibration curve was correlated using a linear regression. Therefore, the concentration of KI in the solution can be determined using the following linear relationship:

$$\text{KI Concentration (ppm)} = 0.3596 * \text{UV Absorbance (\%)} - 0.6526 \qquad \text{(C.11)}$$

C.4 Experimental Procedure

Core flow experiments were conducted using a Phoenix coreholder. Cores used have a diameter of 1 inch and a length of 6 inches. The core holder has two pressure tabs that measure pressure drop at different sections of the core. Pressure drop across the core was measured using Validyne pressure transducers. Pressure readings were transmitted from the pressure transducers to a Tracor Westronics DDR10 digital recorder during coreflood experiments. These experiments were conducted on two types of cores: Texas Cream limestone and Antolini cores. Texas Cream limestone cores were brought from Georgetown, Texas, while Antolini cores were obtained from Ashfork quarry in Flagstaff, Arizona.

Cores were cut from a cubic block that brought from the rock source. They were dried in an oven at 90°C for more than two days. Weight of a dry core was recorded. Then, the core was immersed in a 3wt% NaCl brine inside a vacuum desiccator. Vacuum was applied from the top of the desiccator for 24 hours to ensure full saturation. The saturated core was weighed and placed inside the core holder. An overburden pressure of 1,000 psig was applied using mineral oil with an Enerpac hand pump. The brine of 3wt% NaCl was injected at a constant rate using a Beckman reciprocating pump (Model 100A). Then, a slug of predetermined concentration of KI solution was injected and displaced with the brine through the core. Effluent samples were collected using an ISCO fraction flow collector during the coreflood experiments. The collected effluent samples were analyzed to determine KI concentration using the UV Spectrophotometer. Brine was displaced with n-decane until the core reached its residual water saturation. This is the first drainage process. Then, brine injection was resumed to displace n-decane to its residual oil saturation. This is the first forced imbibition process. The second drainage process was conducted by displacing the brine with n-decane.

C.5 Results and Discussion

C.5.1 Texas Cream Limestone Core

The porosity of Texas Cream core was measured with a fluid displacement with a wetting fluid, e.g. 3wt% NaCl brine, and found to be 17%. The pore volume of the core was 13.13 cm^3. The initial core permeability was 4.31 md. A slug (16.2 cm^3) of KI solution was injected and displaced with the brine. The injected tracer concentration (C_j) has a UV Absorbance of 87.5% that corresponds to a concentration of 30.81 ppm. The concentration of the tracer in the effluent was normalized as given in Equation (C.3). **Figure C.2** shows the normalized tracer concentration as a function of cumulative pore effluent. After an injection of 1 pore volume, the tracer slug started to be detected in the core effluent. The concentration of the tracer in the effluent reached a value close to the injected concentration (C_D=1.0) after a displacement of 2.31 pore volumes. Therefore, the amount of tracer that breakthroughs (1.31 PV) is almost the same amount injected (1.23 PV) within experimental errors. The tracer profile shows also a tail after the breakthrough due to adsorption. **Figure C.3** shows the breakthrough curve in the Texas Cream limestone core. The breakthrough curve takes the form of the S-shaped curve due to hydrodynamic dispersion (Bear, 1972). The longitudinal dispersion coefficient was calculating by using Equation (C.9) and found equal to 1.599×10^{-2} cm^2/s.

Figure C.4 depicts the growth of the mixing zone length with time for a tracer test in Texas Cream limestone core. It can be seen that the growth of mixing zone grows linearly with the square root of time as given in Equation (C.8). The analytical solution presented in Equation (C.2) was computed for the breakthrough curve of the tracer test in Texas Cream limestone core. **Figure C.5** compares the experimental and analytical concentration profiles for the tracer test. This figure indicates a good agreement between the experimental data and the analytical solution. The value of the Peclet number for this core was found to be 36.87. This means that the dispersion coefficient is dominated by mechanical dispersion. The average longitudinal dispersivity of the Texas Cream limestone core was calculated to be 0.4133 cm using Equation (C.10).

During the displacement of brine by n-decane, the residual water saturation (S_{wr}) reached a value of 14.87%. **Figure C.6** shows fractional flow curves for this process. The oil end-point relative permeability (k_{ro}) reached a value of 0.92 at this residual water saturation. Then, the core was shut-in for 18 hours to allow the oil to redistribute through the core. The fractional flow curves for both water and oil are given in **Figure C.7**. The forced imbibition process resulted in a residual oil saturation (S_{or}) of 41.33% and a water end-point relative permeability (k_{rw}) of 0.68. This reduction in water relative permeability is due to introducing of the oil. The experiment was shut-in for 15 hours. **Figure C.8** shows fractional flow curves for the second drainage process. The oil end-point relative permeability reached a value of 0.48 at the end of the second drainage process. At this stage, the residual water saturation increased by 8.4%. The reduction in oil relative permeability indicates that this porous medium is apparently a water-wet. **Figure C.9** illustrates the end-point relative permeability curves for the Texas Cream limestone core.

C.5.2 Antolini Core

The Antolini core has a sandstone mineralogy. The initial permeability to brine was found to be 68.42 md. However, this core is more permeable than the

Texas Cream limestone, it has a lower average porosity of 12.95%. The slug volume of the injected tracer was 16.6 cm^3. The injected tracer had a concentration of 31.17 ppm of KI. **Figure C.10** shows the normalized tracer concentration as a function of cumulative pore effluent. The tracer appeared in the effluent after an injection of 0.88 PV. The tracer concentration reached a value close to the injected one at 1.87 PV of cumulative pore effluent. After breakthrough, the tracer profile gradually decreased and showed a tailing trend. The breakthrough curve follows the S-shape form curve, as illustrated in **Figure C.11**. Therefore, hydrodynamic dispersion dominates in this type of porous medium. The longitudinal dispersion coefficient was computed from the breakthrough curve using Equation (C.9) and found equal to 0.03275 cm^2/s.

The growth of the mixing zone length is linearly related to the square root of time as shown in **Figure C.12**. The tracer test in Antolini core satisfies the relationship between the mixing zone length and time according to Equation (C.8). **Figure C.13** depicts experimental and analytical concentration profiles for the tracer test in Antolini core. This result indicates a good agreement between the experimental data and the analytical solution. The Peclet number and the longitudinal dispersivity for Antolini were found 47.28 and 0.3223 cm, respectively. Coreflood experiments were not conducted on this core.

C.6 Summary of Results

This chapter showed experimental results of tracer testes conducted on Texas Cream limestone and Antolini sandstone cores. Petrophysical properties measured included: porosity, permeability, dispersion coefficient, and dispersivity are given in **Table C.2**. Tracer testes indicated that hydrodynamic dispersion is dominated in both porous media. Experimental data showed an agreement with the analytical solution. The development of the mixing zone grows linearly with the square root of time.

Table C.1: UV readings for standard solutions of KI used for calibration.

Concentration, ppm	UV Absorbance, %
0	0
5	16.5
10	29.5
20	60.5
30	86.5
35	96.0

Table C.2: Summary of the results for tracer tests.

	Texas Cream Core	Antolini Core
Diameter, in.	1.0	1.0
Length, in.	6.0	6.0
Total Porosity, %	17.01	12.95
Absolute Permeability, md	4.31	68.42
Peclet Number	36.87	47.28
D_L, cm^2/s	0.01599	0.03275
α_L, cm	0.41333	0.32233

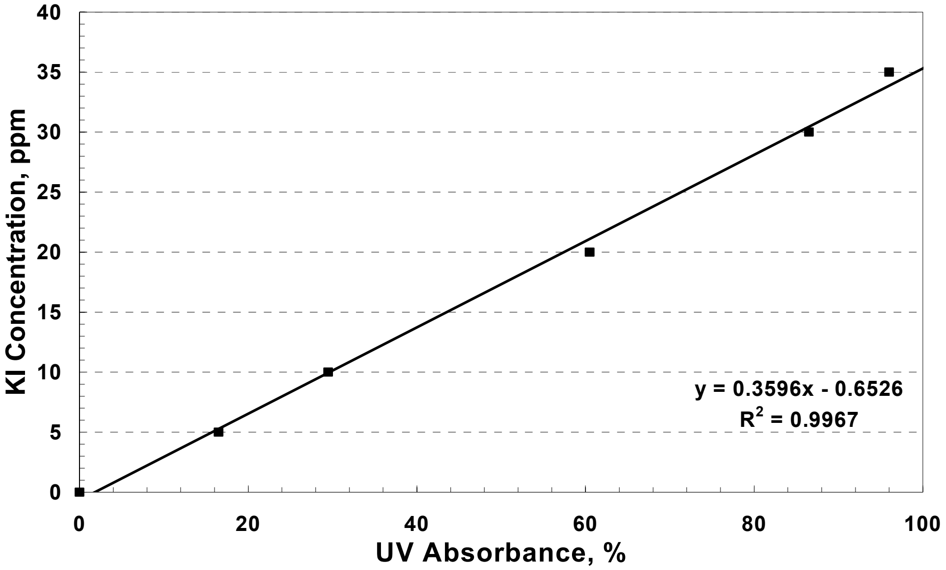

Figure C.1: Calibration curve for measuring concentration of KI in solutions.

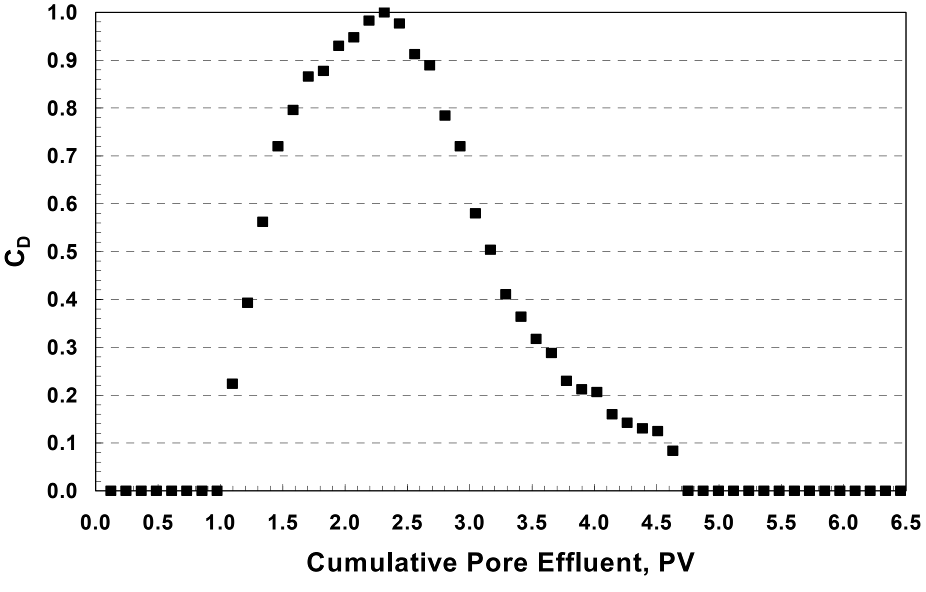

Figure C.2: Normalized tracer concentration profile for Texas Cream limestone core.

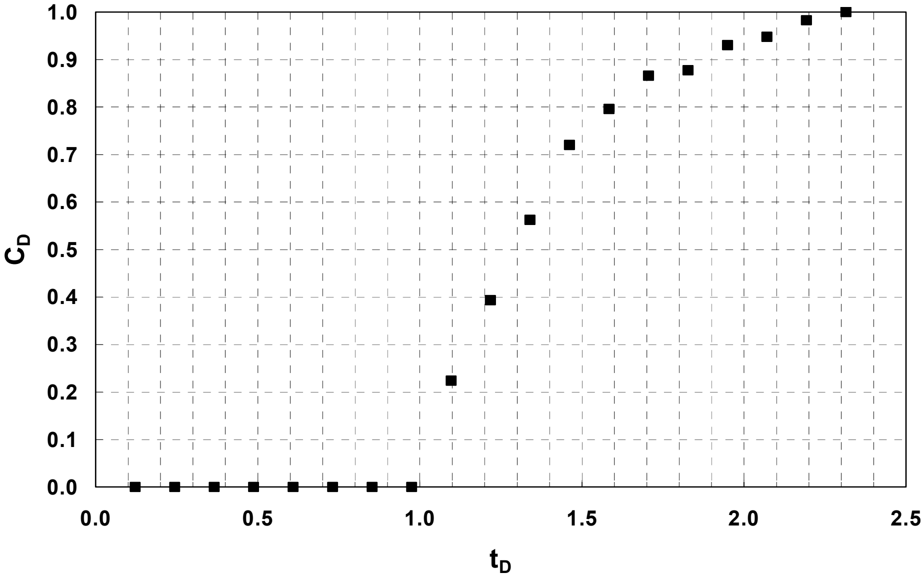

Figure C.3: Breakthrough curve for tracer test in Texas Cream limestone core.

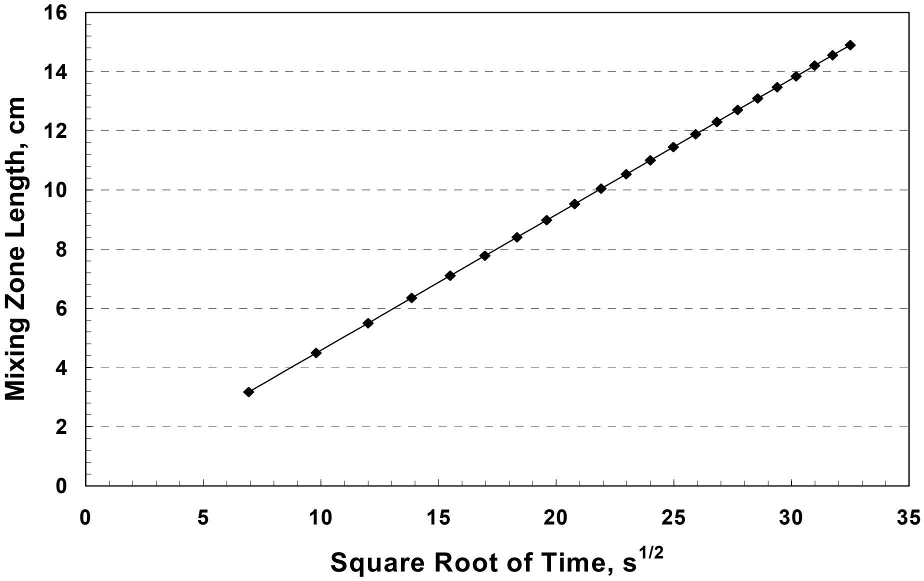

Figure C.4: Growth of mixing zone length with time in Texas Cream limestone core.

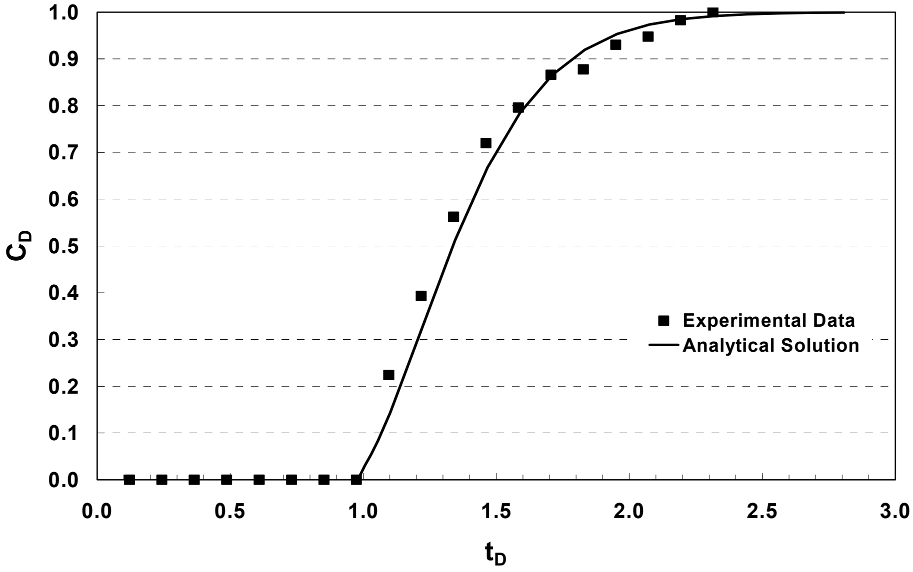

Figure C.5: Experimental and analytical concentration profiles for the tracer test in Texas Cream limestone core.

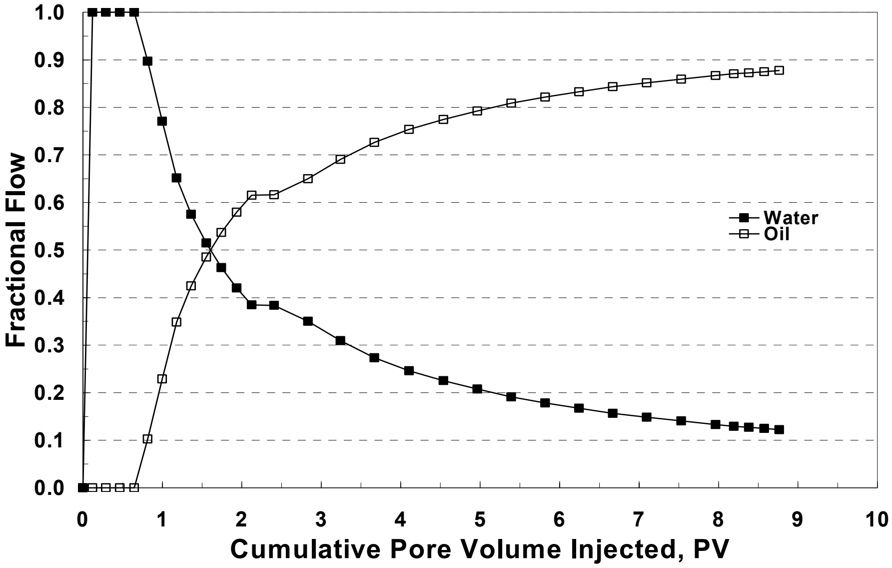

Figure C.6: Fractional flow curves for the first drainage process for Texas Cream limestone core.

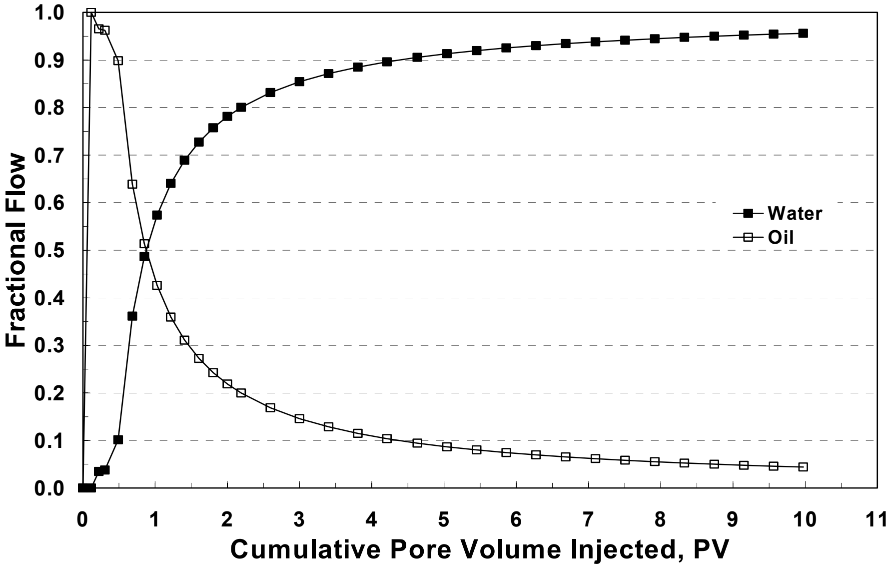

Figure C.7: Fractional flow curves for the forced imbibition process for Texas Cream limestone core.

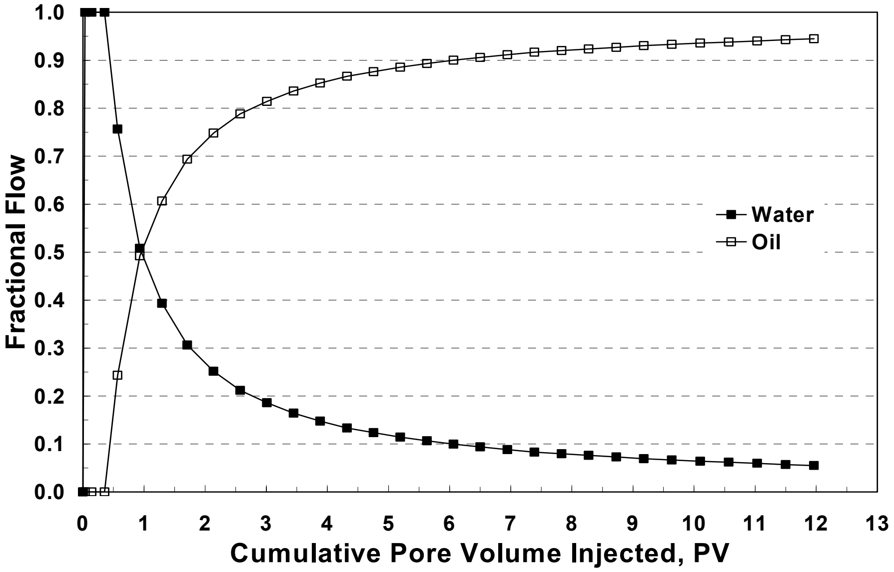

Figure C.8: Fractional flow curves for the second drainage process for Texas Cream limestone core.

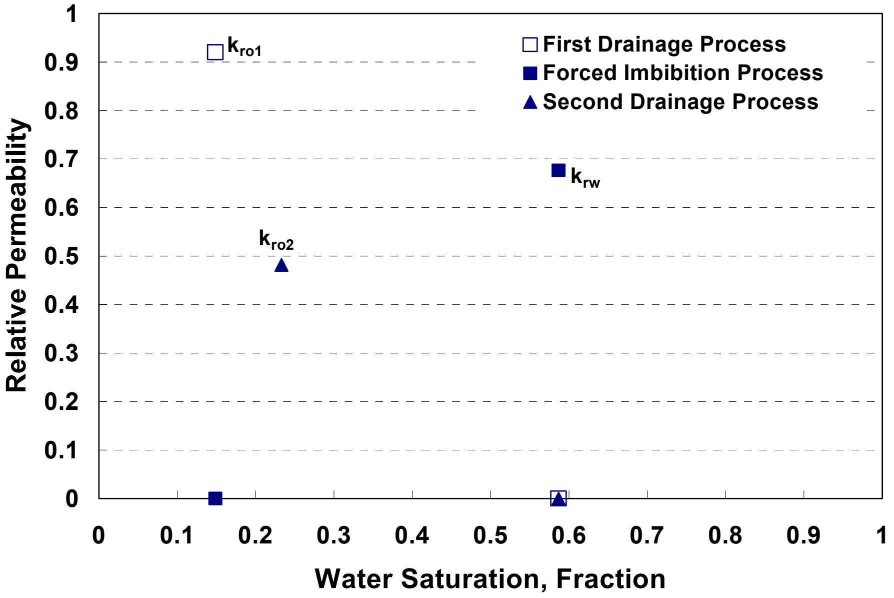

Figure C.9: Water and oil end-point relative permeability data for Texas Cream limestone core.

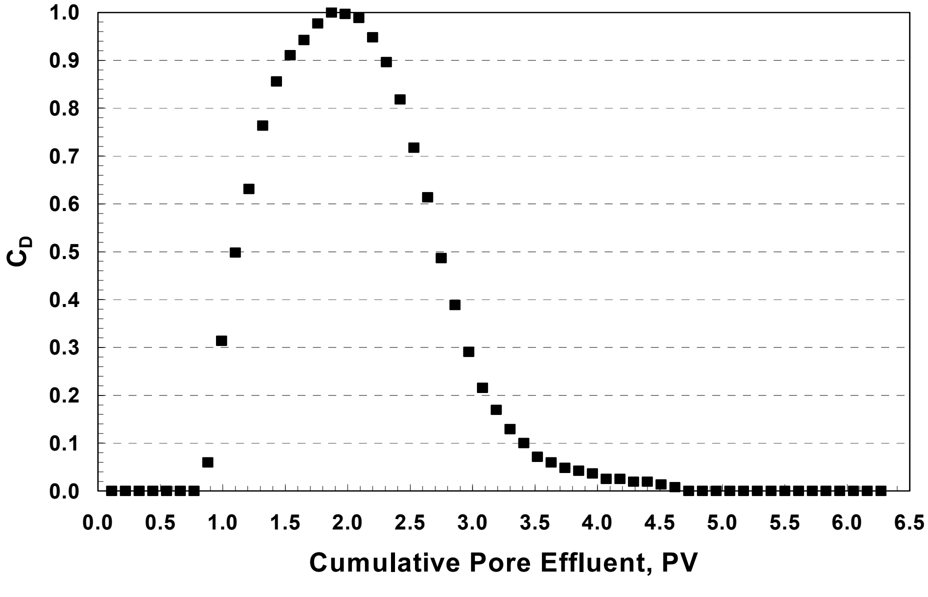

Figure C.10: Normalized tracer concentration profile for Antolini core.

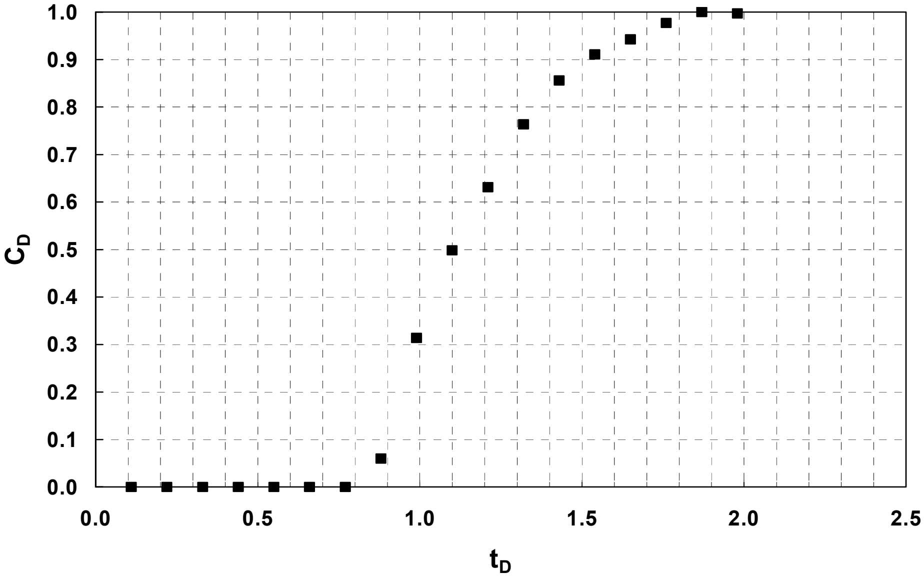

Figure C.11: Breakthrough curve for tracer test in Antolini core.

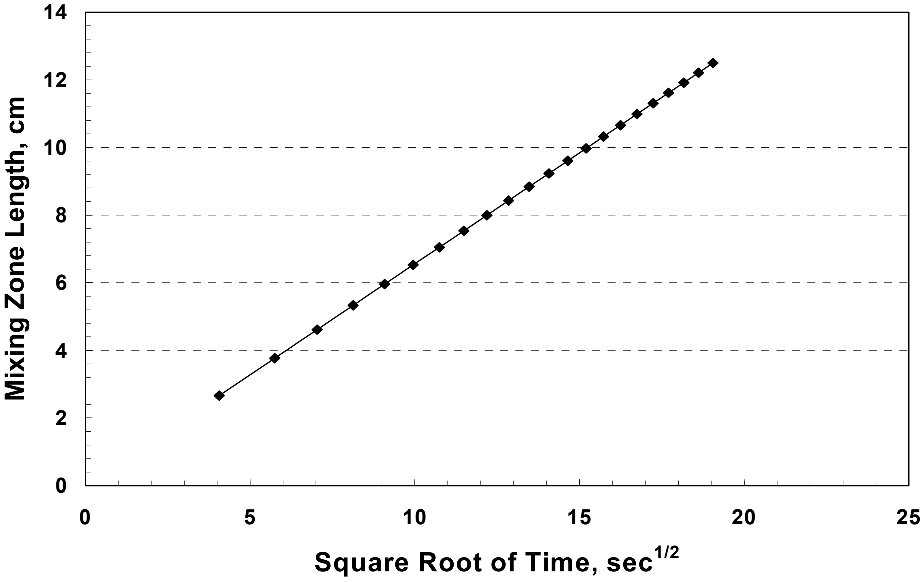

Figure C.12: Growth of mixing zone length with time Antolini core.

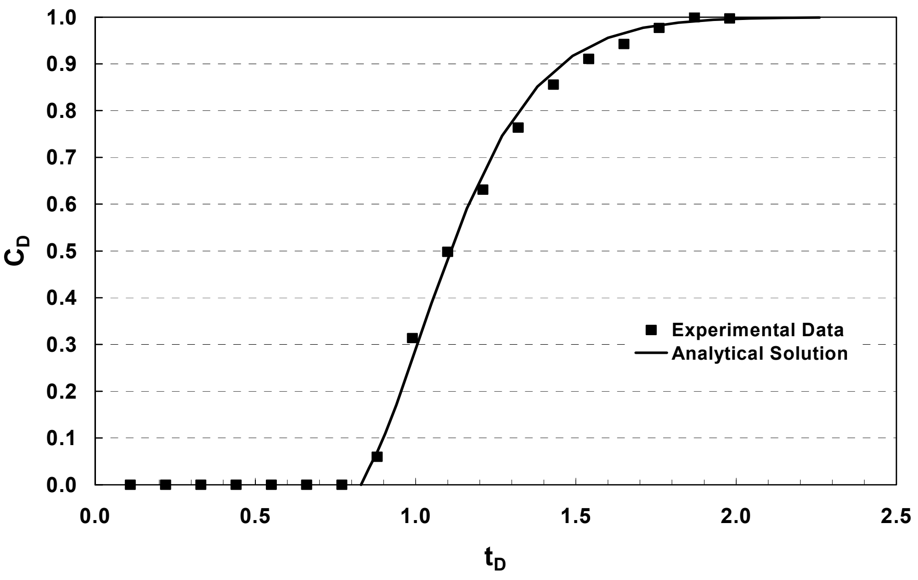

Figure C.13: Experimental and analytical concentration profiles for the tracer test in Antolini core.

References

Abel, W., Jackson, R.F., and Wattenbarger, R.A.: "Simulation of a Partial Pressure Maintenance Gas Cycling Project with a Compositional Model, Carson Creek Field, Alberta," *JPT* (January 1970), 38-46.

Afidick, D., Kaczorowski, N.J., and Bette, S.: "Production Performance of Retrograde Gas Reservoir: A Case Study of the Arun Field," paper SPE 28749 presented at the 1994 SPE Asia Pacific Oil and Gas Conference, Melbourne, Australia, Nov. 7-10.

Ahmed, M., Al-Qahtani, M. Y., and Zillur, R.: "Quantifying Production Impairment Due To Near-Wellbore Condensate Dropout and Non-Darcy Flow Effects in Carbonate and Sandstone Reservoirs With and Without Hydraulic Fractures in the Ghawar Field, Saudi Arabia," paper SPE 77552 presented at the 2002 SPE Annual Technical Conference and Exhibition, San Antonio, TX, September 29-October 2.

Ahmed, T., Evans, J., Kwan, R., and Vivian, T.: "Wellbore Liquid Blockage in Gas-Condensate Reservoirs," paper SPE 51050 presented at the 1998 SPE Eastern Regional Meeting, Pittsburgh, PA, November 9-11.

Al-Anazi, H.A., Pope, G.A., Sharma, M.M., and Metcalfe, R.S.: "Laboratory Measurements of Condensate Blocking and Treatment for Both Low and High Permeability Rocks," paper SPE 77546 presented at the SPE Annual Technical Conference and Exhibition, San Antonio, TX, 29 September-2 October, 2002.

Al-Anazi, H.A., Walker, J.G., Pope, G.A., Sharma, M.M., and Hackney, D.F.: "A Successful Methanol Treatment in a Gas-Condensate Reservoir: Field Application," paper SPE 80901 presented at the 2003 SPE Production & Operations Symposium, Oklahoma City, Oklahoma, March 22-23.

Ali, J.K., McGauley, P.J., and Wilson, C.J.: "Experimental Studies and Modeling of Gas Condensate Flow Near the Wellbore," paper SPE 39053 presented at the fifth Latin American and Caribbean Petroleum Engineering Conference and Exhibition, Rio de Janeiro, Brazil, 30 August-3 September 1997.

Amaefule, J.O. and Handy, L.L.: "The Effect of Interfacial Tensions on Relative Oil/Water Permeabilities of Consolidated Porous Media," *SPEJ* (June 1982), 371-381.

Antoci, J.C., Briggiler, N.J., and Chadwich, J.A.: "Crosslinked Methanol: Analysis of a Successful Experience in Fracturing Gas Wells," paper SPE 69585 presented at the 2001 SPE Latin American and Caribbean Petroleum Engineering Conference, Buenos Aires, Argentina, March 25-28.

Asar, H. and Handy, L.L.: "Influence of Interfacial Tension on Gas/Oil Relative Permeability in a Gas-Condensate System," *SPERE* (February 1988), 257-264.

Ayyalasomayajula, P., Sharma, R., Walker, J.G., Sharma, M.M., and Pope, G.A.: "Phase Behavior Modeling of Hydrocarbon-Methanol-Water Mixtures by Peng-Robinson and SAFT Equations of State," paper SPE 77575 presented at the 2002 SPE Annual Technical Conference and Exhibition, San Antonio, TX, September 29 - October 2.

Ayyalasomayajula, S.P.: "Prediction of Bulk and Interfacial Thermodynamic Properties of Polar Mixtures by Statistical Associating Fluid Theory," Ph.D. dissertation, The University of Texas at Austin, 2003.

Baker, L.E.: "Effects of Dispersion and Dead-End Pore Volume in Miscible Flooding," *SPEJ* (June 1977), 219-227.

Bardon, C. and Longeron, D.G.: "Influence of Very Low Interfacial Tension on Relative Permeability," *SPEJ* (October 1980), 391-401.

Barnum, R.S., Brinkman, F.P., Richardson, T.W., and Spillette, A.G.: "Gas Condensate Reservoir Behavior: Productivity and Recovery Reduction Due to Condensation," paper SPE 30767 presented at the 1995 SPE Annual Conference and Exhibition, Dallas, TX, October 22-25.

Bear, J.: *Dynamics of Fluids in Porous Media*, Elsevier, New York, 1972.

Bird, R.B., Stewart, W.S., and Lightfood, E.N.: *Transport Phenomena*, John Wiley & Sons Inc., New York, 1960.

Blom, A.M.P., Hagoort, J., and Soetekouw, D.P.N.: "Relative Permeability at Near-Critical Conditions," paper SPE 38935 presented at the 1997 SPE Annual Technical Conference and Exhibition, San Antonio, Texas, October 5-8.

Blom, S.M.P. and Hagoort, J.: "The Combined Effect of Near-Critical Relative Permeability and Non-Darcy Flow on Well Impairment by Condensate Drop-Out," paper SPE 39976 presented at the 1998 SPE Gas Technology Symposium held in Calgary, Alberta, Canada, March 15-18.

Boersma, D.M. and Hagoort, J.: "Displacement Characteristics of Nitrogen vs. Methane Flooding in Volatile-Oil Reservoirs," *SPERE* (November 1994) 261-265.

Boom, W., Wit, K., Zeelenberg, J.P.W., Weeda, H.C., and Maas, J.G.: "On the Use of Model Experiments for Assessing Improved Gas-Condensate Mobility Under Near-Wellbore Flow Conditions," paper SPE 36714 presented at the 1996 SPE Annual Technical Conference and Exhibition, Denver, Colorado, October 6-9.

Bourbiaux, B.J. and Limborg, S.G.: "An Integrated Experimental Methodology for a Better Prediction of Gas-Condensate Flow Behavior," paper SPE 28931 presented at the SPE 69th Annual Technical Conference and Exhibition, New Orleans, LA, September 25-28, 1994.

Brigham, W.E.: "Mixing Equations in Short Laboratory Cores," *SPEJ* (February 1974), 91-99.

Briones, M., Zamvrano, J.A., and Zerpa, C.: "Study of Gas-Condensate Well Productivity in Santa Barbara Field, Venezuela, by Well Test Analysis," paper SPE 77538 presented at the 2002 SPE Annual Technical Conference and Exhibition, San Antonio, TX, September 29 - October 2.

Brownell, L.E. and Katz, D.L.: "Flow of Fluids Through Porous Media-Part II," *Chem. Eng. Prog.* 43, No. 11, 601, 1947.

Chaback, J.J. and Williams, M.L.: "*p-x* Behavior of a Rich-Gas Condensate in Admixture with CO_2 and (N_2 + CO_2)," SPERE (February 1994) 44-50.

Chen, H.L., Wilson, S.D., and Monger-McClure, T.G.: "Determination of Relative Permeability and Recovery for North Sea Gas-Condensate Reservoirs," *SPERE* (August 1999), 393-402.

Coats, K.H. and Smith, B.D.: "Dean-End Pore Volume and Dispersion in Porous Media," *SPEJ* (March 1964), 73-84.

Danesh, A., Henderson, G.D., and Peden, J.M.: "Experimental Investigation of Critical Condensate Saturation and Its Dependence on Interstitial Water Saturation in Water-Wet Rocks," *SPERE* (August 1991), 336-342.

Danesh, A., Henderson, G.D., Krinis, D., and Peden, J.M.: "Experimental Investigation of Retrograde Condensation in Porous Media at Reservoir Conditions," paper SPE 18316 presented at the 63rd Annual Technical Conference and Exhibition, Houston, TX, October 2-5, 1988.

Du, L., Walker, J.G., Pope, G.A., Sharma, M.M., and Wang, P.: "Use of Solvents to Improve the Productivity of Gas Condensate Wells," paper SPE 62935 presented at the 2000 SPE Annual Technical Conference and Exhibition held in Dallas, TX, October 1-4.

Eckles, W.W. Jr., Prihoda, C., and Holden, W.W.: "Unique Enhanced Oil and Gas Recovery for Very High-Pressure Wilcox Sands Uses Cryogenic Nitrogen and Methane Mixture," *JPT* (June 1981), 971.

Engineer, R.: "Cal Canal Field, California: Case History of a Tight and Abnormally Pressured Gas Condensate Reservoir," paper SPE 13650 presented at the 1985 SPE California Regional Meeting, Bakersfield, CA, March 27-29.

Fevang, Ø. and Whitson, C.H.: "Modeling Gas Condensate Well Deliverability," *SPERE* (November 1996) 221-230.

Gatlin, C.: "The Miscible Displacement of Oil and Water From Porous Media by Various Alcohols," Ph.D. Dissertation, The Pennsylvania State University, August 1959.

Givens, J.W.: "A Method of Predicting Revaporization of Retrograde Condensate by Dry-Gas Injection," *SPEJ* (March 1969) 21-27.

Gondouin, M., Iffly, R., and Husson, J.: "An Attempt to Predict the Time Dependence of Well Deliverability in Gas Condensate Fields," *SPEJ* (June 1967), 113-124.

Gravier, J., Lemouzy, P., Barroux, C., and Abed, A.F.: "Determination of Gas-Condensate Relative Permeability on Whole Cores Under Reservoir Conditions," *SPEFE* (February 1986), 9-15.

Henderson, G.D., Danesh, A., Tehrani, D.H., and Peden, J.M.: "An Investigation Into the Processes Governing Flow and Recovery in Different Flow Regimes in Gas Condensate Reservoirs," paper SPE 26661 presented at the 68th Annual Technical Conference and Exhibition of the SPE, Houston, Texas, 3-6 October 1993.

Henderson, G.D., Danesh, A.S., and Peden, J.M.: "Waterflooding of Gas-Condensate Fluids in Cores Above and Below the Dewpoint," paper SPE 22636 presented at the 66th Annual Technical Conference and Exhibition, Dallas, TX, October 6-9, 1991.

Hernández, J.M., Fernández, C.T., and Scianca, N.M.: "Methanol as Fracture Fluid in Gas Wells," paper SPE 27007 presented at the III Latin American/Caribbean Petroleum Engineering Conference, Buenos Aires, Argentina, April 27-29,1994.

Huang, W.W., Bellamy, R.B., and Ohnimus, S.W.: "A Study of Nitrogen Injection for Increased Recovery From a Rich Retrograde Gas/Volatile Oil Reservoir," paper SPE 14059 presented at the 1986 SPE International Meeting on Petroleum Engineering, Beijing, March 17-20.

Jamaluddin, A.K.M., Thomas, S.Y.J., D'Cruz, D., and Nighswander, J.: "Experimental and Theoretical Assessment of Using Propane to Remediate Liquid Buildup on Condensate Reservoirs," paper SPE 71526 presented at the 2001 SPE Annual Technical Conference and Exhibition, New Orleans, LO, September 30-October 3.

Jianfen, D., Shilun, L., and Lei S.: "Effect of Porous Medium Adsorption on Percolation Law of Condensate-Gas Mixture," paper SPE 50926 presented at the 1998 SPE International Conference and Exhibition, Beijing, China, 2-6 November 1998.

Kamath, J. and Laroche, C.: "Laboratory Based Evaluation of Gas Well Deliverability Loss Due to Waterblocking," paper SPE 63161 presented at the 2000 SPE Annual Technical Conference and Exhibition, Dallas, TX, October 1-4.

Kumar, R.: "Productivity Improvement of Gas-Condensate Wells by Fracturing," MS Thesis, The University of Texas at Austin, August 2000.

Lake, L.W.: *Enhanced Oil Recovery*, Englewood Cliffs, N.J. Prentice Hall, 1989.

Lee, A.L., Gonzalez, M.H., and Eakin, B.E.: "The Viscosity of Natural Gases," *JPT* (August 1966), 997-1000.

Lee, S. and Chaverra, M.: "Modeling and Interpretation of Condensate Banking for the Near Critical Cupiagua Field," paper SPE 49265 presented at the 1998 SPE Annual Technical Conference and Exhibition, New Orleans, LA, September 27-30.

Leemput, L.E.C., Bertram, D.A., Bentley, M.R., and Gelling, R.: "Full Field Reservoir Modeling of Central Oman Gas/Condensate Fields," paper SPE 30757 presented at the 1995 SPE Annual Technical Conference and Exhibition, Dallas, TX, October 22-25.

Lefebvre du Prey, E.J.: "Factors Affecting Liquid-Liquid Relative Permeabilities of a Consolidate Porous Medium," *SPEJ* (February 1973), 39-47.

Li, S., Zheng, X., Dai, Z., Luo, K., Chen, G., and Liu, N.: "Investigation of Revaporization of Retrograde Condensate," paper SPE 68170 presented at the 2001 SPE Middle East Show, Manama, Bahrain, March 17-20.

Lombard, J.M., Longeron, D.G., and Kalaydjian, F.J.M.: "Influence of Connate Water and Condensate Saturation on Inertial Effects in Gas/Condensate Reservoirs," SPEJ (September 2000) 5 (3), 301-308.

Luo, K., Li, S., Zheng, X., Chen, G., Dai, Z., and Liu, N.: "Experimental Investigation into Revaporization of Retrograde Condensate by Lean Gas Injection," paper SPE 68683 presented at the 2001 SPE Asia Pacific Oil and Conference and Exhibition, Jakarta, Indonesia, April 17-19.

Malone, M.R.: "Fracturing with Crosslinked Methanol in Water-Sensitive Formations," paper SPE 70009 presented at the 2001 SPE Permian Basin Oil and Gas Recovery Conference, Midland, TX, May 15-16.

Marker, M.F.: "Simulation of the Use of Solvents in Gas-Condensate Reservoirs," MS Thesis, Technical University of Denmark, Fall 2000.

McLeod, H.O. and Coulter, A.W.: "The Use of Alcohol in Gas Well Stimulation," paper SPE 1663 presented at the SPE Eastern Regional Meeting, Columbus, Ohio, November 10-11, 1966.

McLeod, H.O., McGinty, J.E., and Smith, G.F.: "Deep Well Stimulation With Alcoholic Acid," paper SPE 1558 presented at the 41st Annual Fall Meeting of the Society of Petroleum Engineers of AIME, Dallas, TX, October 2-5, 1966.

Mikhail, S.Z. and Kimel, W.R.: "Densities and Viscosities of Methanol-Water Mixtures," *Journal of Chemical and Engineering Data*, Vol. 6, No. 4, October 1961, 533-537.

Morel, D.C., Lomer, J.F., Morineau, Y.M., and Putz, A.C.: "Mobility of Hydrocarbon Liquids in Gas Condensate Reservoirs: Interpretation of Depletion Laboratory Experiments," paper SPE 24939 presented at the 67th Annual Conference and Exhibition of the SPE, Washington, DC, October 4-7, 1992.

Morel, D.C., Nectoux, A., and Danquigny, J.: "Experimental Determination of The Mobility of Hydrocarbon Liquids during Gas Condensate Reservoir Depletion: Three Actual Cases," paper SPE 38922 presented at the SPE Annual Technical Conference and Exhibition, San Antonio, TX, 5-8 October 1997.

Moses, P.L. and Wilson, K.: "Phase Equilibrium Considerations in Using Nitrogen for Improved Recovery from Retrograde Condensate Reservoirs," *JPT* (February 1981), 256.

Mott, R., Cable, A., and Spearing, M.: "Measurements and Simulation of Inertial and High Capillary Number Flow Phenomena in Gas-Condensate Relative Permeability," paper SPE 62932 presented at the 2000 SPE Annual Technical Conference and Exhibition, Dallas, TX, October 1-4.

Mott, R.: "Engineering Calculations of Gas Condensate Well Productivity," paper SPE 77551 presented at the 2002 SPE Annual Technical Conference and Exhibition, San Antonio, TX, 29 September-2 October.

Mott, R.E., Cable, A.S., and Spearing, M.C.: "Measurements of Relative Permeabilities for Calculating Gas-Condensate Well Deliverability," *SPE Res. Eval. & Eng.* (December 2000), 3 (6), 473-479.

Narayanaswamy, G.: "Well Productivity of Gas Condensate Reservoirs," MS Thesis, The University of Texas at Austin, August 1998.

Narayanaswamy, G., Pope, G.A., and Sharma, M.M.: "Predicting Gas Condensate Well Productivity Using Capillary Number and Non-Darcy Effects," paper SPE 51910 presented at the 1999 SPE Reservoir Simulation Symposium, Houston, TX, February 14-17.

Odeh, A.S.: "Effect of Viscosity Ratio on Relative Permeability," *Trans.*, AIME (1959) 216, 346-352.

Ortiz, J. and McLane, J.E.: "Low-pH Methanol: An Alternative for Stimulation in Water-Sensitive, Tight, Dirty Sandstones," *SPEPE* (May 1986), 195-202.

Perkins, T.K. and Johnston, D.C.: "A Review of Diffusion and Dispersion in Porous Media, " *SPEJ* (March 1963), 70-84.

Perry, R.H.: *Perry's Chemical Engineerings' Handbook*, 6th Ed., McGraw-Hill Book Inc., New York, 1984, Chap. 3, pp. 97-100.

Peters, E.J., Gharbi, R., and Afzal, N.: "A Look at Dispersion in Porous Media Through Computed Tomography Imaging," *J. Pet. Sci. Eng.*, 15 (1996), 23-31.

Piers, A.P., Correa, A.C.F., Mohamed, R.S., and Sousa Jr., R.: "Optimization of Lean Gas Injection in Gas-Condensate Reservoirs," paper SPE 31004 presented at the 1995 Eastern Regional Meeting, Morgantown, West Virginia, September 19-21.

Pope, G.A., Wu, W., Narayanaswamy, G., Delshad, M., Sharma, M.M., and Wang, P.: "Modeling Relative Permeability Effects in Gas-Condensate Reservoirs with a New Trapping Model," *SPE Res. Eval. & Eng.* (April 2000) 3 (2), 171.

Raimondi, P. and Torcaso, M.A.: "Mass Transfer Between Phases in a Porous Medium: A Study of Equilibrium," *SPEJ* (March 1965) 51-59.

Rai, R.R.: "Gas Condensates Relative Permeability Parametric Study and Core Flood Simulation" Thesis, The University of Texas at Austin, December 2003.

Rajeev, K.: "Productivity Improvement of Gas-Condensate Wells by Fracturing," Thesis, The University of Texas at Austin, August 2000.

Roy, R.S. and Sharma, M.M.: "The Relative Importance of Solids and Filtrate Invasion on the Flow Initiation Pressure," paper SPE 68949 presented at the 2001 SPE European Formation Damage Conference, The Hague, The Netherlands, May 21-22.

Saeidi, A. and Handy, L.L.: "Flow and Phase Behavior of Gas Condensate and Volatile Oils in Porous Media," paper SPE 4891 presented at the 44th Annual California Regional Meeting of the SPE of AIME, San Francisco, California, April 4-5, 1974.

Sänger, P. and Hagoort, J.: "Recovery of Gas Condensate by Nitrogen Injection Compared with Methane Injection," *SPEJ* (March 1998), 26-33.

Shapiro, A.A., Potsch, K., Kristensen, J.G., and Stenby, E.H.: "Effect of Low Permeable Porous Media on Behavior of Gas Condensates," paper SPE 65182 presented at the SPE European Petroleum Conference, Paris, France, 24-25 October 2000.

Sharma, R.: "Modeling Gas Condensate Reservoir and Development of a New Hybrid Well Model," MS Thesis, The University of Texas at Austin, May 2003.

Siregar, S., Hagoort, J., and Ronde, H.: "Nitrogen Injection vs. Gas Cycling in Rich Retrograde Condensate-Gas Reservoirs," paper SPE 22360 presented at the 1992 SPE International Meeting on Petroleum Engineering, Beijing, China, March 24-27.

Smith, L.R. and Yarborough, L.: "Equilibrium Revaporization of Retrograde Condensate By Dry Gas Injection," *SPEJ* (March 1968) 87-94.

Stoudt, E.L., Thomas, A.R., Ginger, E.P., and Vinopal, R.J.: "Geological Reservoir Characterization for Engineering Simulation, Hatter's Pond Field, Mobile County, Alabama," paper SPE 24713 presented at the 1992 SPE Annual Conference and Exhibition, Washington, DC, October 1-4.

Thomas, R.D. and Ward, D.C.: "Effect of Overburden Pressure and Water Saturation on Gas Permeability of Tight Sandstone Cores," *JPT* (February 1972), 120-124.

Vargaftik, N.B.: *Tables on the Thermophysical Properties of Liquids and Gases in Normal and Dissociated States*, 2nd Edition, John Wiley & Sons, Inc., 1975, 405.

Walker, J.G.: "Laboratory Evaluation of Alcohols and Surfactants to Increase Production from Gas-Condensate Reservoirs," Thesis, The University of Texas at Austin, December 2000.

Walls, J.D., Nur, A.M., and Bourbie, T.: "Effects of Pressure and Partial Water Saturation on Gas Permeability in Tight Sands: Experimental Results," *JPT* (April 1982), 930-36.

Weast, R.C. (ed.): *Handbook of Chemistry and Physics*, CRC Press Inc., 63rd Edition., 1982-1983.

Wheaton, R.J. and Zhang H.R.: "Condensate Banking Dynamics in Gas Condensate Fields: Compositional Changes and Condensate Accumulation Around Production Wells," paper SPE 62930 presented at the 2000 SPE Annual Technical Conference and Exhibition, Dallas, TX, October 1-4.

Whitson, C.H., Fevang, Ø., and Saevareid, A.: "Gas Condensate Relative Permeability for Well Calculations," paper SPE 56476 presented at the 1999 SPE Annual Technical Conference and Exhibition, Houston, TX, October 3-6.

Wilson, J.W.: "Determination of Relative Permeability Under Simulated Reservoir Conditions," *AIChE Jour.* (1956) 2, 94.

Wu, W., Wang, P., Delshad, M., Wang, C., Pope, G.A., and Sharma, M.M.: "Modeling Non-Equilibrium Mass-Transfer Effects for A Gas Condensate Field," *In Situ* (2000) 24(2&3), 139-162.

Yu, X., Lei, S., Liangtian, S., and Shilun, L.: "A New Method for Predicting the Law of Unsteady Flow Through Porous Medium on Gas Condensate Well," paper SPE 35649 presented at the SPE Program Conference held in Calgary, Alberta, Canada, 28 April-1 May, 1996.

Vita

Hamoud Ali Al-Anazi was born in Hail, Saudi Arabia, on August 23, 1971, the son of Ali Faleh Al-Anazi and Nada Al-Anazi. He holds a Bachelors Degree of Science in Chemical Engineering from King Fahd University of Petroleum and Minerals (KFUPM), Dhahran, Saudi Arabia. In October 1994, he was hired as a Lab Scientist in the Research and Development Center of Saudi Aramco. His research interests were wells stimulation, formation damage, and conformance control. He is a member in the Society of Petroleum Engineers (SPE). He published several papers in SPE and ACS conferences and SPE journals. He was awarded a sponsorship from Saudi Aramco to pursue advanced degrees in Petroleum Engineering. In January 1998, he entered the Graduate School at the University of Texas at Austin. He was awarded a Master Degree in Petroleum Engineering on December 1999. Then, he was admitted in the PhD program in Petroleum Engineering at the University of Texas at Austin. Hamoud won 2nd place in MS division in 2002 and 3rd place in PhD division in 2003 of the SPE Contest Paper held in the University of Texas at Austin.

Permanent address: P.O. Box 1235
Dhahran, 31311
Saudi Arabia

This dissertation was typed by the author.